PROCEEDINGS

of the

ZEL'DOVICH MEMORIAL

International Conference on Combustion

Moscow, 12-17 September 1994

COMBUSTION,

DETONATION,

SHOCK WAVES

COMBUSTION,
DETONATION,
SHOCK WAVES

Edited by

S. M. Frolov
Semenov Institute of Chemical Physics, Moscow, Russia

PROCEEDINGS
of the
ZEL'DOVICH MEMORIAL

International Conference on Combustion
Moscow, 12–17 September 1994

Volume 2

Russian Section of the Combustion Institute

Acknowledgments

The Organising Committee

Preface

Professor Yakov Borisovich Zel'dovich was one of the most eminent scientists of the 20th century. He made outstanding contributions to the development of the modern theory of combustion and detonation, physics of explosion and shock waves, nuclear physics and physics of elementary particles, theory of gravitation and cosmology, astrophysics and X-ray astronomy.

In 1994 he would turn 80. The idea of organizing the International Conference on Combustion dedicated to the 80th birthday anniversary of Prof. Yakov Zel'dovich (Zel'dovich Memorial) evoked a warm response among scientists all over the world. The Conference is a tribute of respect to this person, and contributes to further development of science and strengthening the international combustion community.

The Technical Program of the Zel'dovich Memorial contained 48 invited plenary lectures and more than 200 poster presentations at 8 Sessions:

1. Kinetics;

2. Ignition and Steady-State Flame Propagation;

3. Diffusion and Heterogeneous Combustion;

4. Turbulent Combustion;

5. Unsteady Combustion;

6. Detonation;

7. Combustion and Detonation Analogies;

8. Intensive Shock Waves and Extreme States of the Matter.

Round Table Discussions on the particular topics of current interest in the combustion science were organized to stimulate informal exchange of ideas.

The Proceedings of the Conference entitled **Combustion, Detonation, Shock Waves** are published in two volumes. Volume 1 includes complete manuscripts of invited plenary lectures. Volume 2 includes extended abstracts of poster presentations.

In this volume, **Combustion, Detonation, Shock Waves, Volume 2**, the papers selected for poster presentation have been arranged according to the corresponding Sessions.

Contributions to **Session 1, Kinetics,** deal mainly with environmental aspects of combustion processes. The well-known Zel'dovich mechanism of NO_x formation has been used in relevant studies by *Gostintsev and Gamera, Heitland et al., Kondrikov, Pesce-Rodrigues and Fifer, Sobolev and Karasev.* Peculiarities of soot and particulate formation phenomenon are reported by *Calcote and Gill, Krestinin, Mansurov, Roth and von Gersum, Tesner and Shurupov.* The problems of pollutant reduction in various industrial applications are studied by *Barrakat et al., Chae et al., Sternberg et al.*

The nonthermal mechanism of flame propagation, first predicted by Zel'dovich, is studied by *Nagorny et al.* for the silane mixtures. The effect of translational nonequilibrium on the gas-phase reactions behind a shock wave propagating in a multi-component mixture is reported by *Kulikov* as the development of Zel'dovich ideas. *Skrebkov* presents an approach for studying chemical kinetics – vibrational energy transfer interactions in nozzle flows.

A new semi-empirical mechanism of *iso*-octane and *n*-heptane preflame oxidation under conditions relevant to spark ignition engines is suggested by *Basevich et al.* A detailed kinetic mechanism of auto-ignition and combustion of simple sulphur-containing gas-phase molecular systems H–S–O and C–S–O is developed by *Basevich et al, Bruno et al.* study the effect of hydrogen peroxide on the ignition delay time of $CH_4/O_2/Ar$ mixtures. *Tsyganov et al.* report the new detailed scheme of carborane oxidation in water vapor. Also presented are the results of investigations of condensed-phase kinetics in energetic materials (*Kriger et al., Manelis et al., Sinditskii et al.*), and of the effect of extraneous factors on flame propagation (*Gromovenko and Begishev, Karpov et al., Popov et al., Yagodnikov and Voronetskii*).

Contributions to **Session 2, Ignition and Steady-State Flame Propagation,** are basically in line with the Zel'dovich–Frank-Kamenetskii theory developed in late 30s *Assovskii* offers the review of current studies of ignition and extinction of gasifiable rocket propellants. The structure of combustion waves is studied theoretically by *Bykov et al., Chan et al., Chernysh et al., Drozdov et al., Khusid and Rabinovich, Stepanov. Sepiyarskii* reports the wave theory of ignition taking into account the transition from heating by an external source to that by a chemical reaction. Experimental studies of gas-phase flame characteristics (*D'yukov et al., Fialkov et al., Shebeko et al.*) and solid propellant ignition and combustion (*Bakhman and Lobanov, Dudyrev et al., Fernandez-Pello, Fogelzang et al., Trofimov et al., Zenin and Finjakov*) are also presented. The comparative study of various metallized fuel-rich propellants for future air-breathing rocket ramjets and current solid propulsion systems is suggested by *Athawale et al.*

A great variety of contributions is made at **Session 3, Diffusion and Heterogeneous Combustion.** Two review papers by *Goltsiker et al.* and *Shevchuk and Florko* present some historical information on the development of this field of science and highlight the existence of various mechanisms of ignition and flame propagation in heterogeneous systems. The papers by *Chuchalin* and *Wang et al.* deal with modeling

of gas-phase diffusion flames. Researchers from the Institute of Chemical Kinetics and Catalysis, Novosibirsk (*Kakutkina et al., Korzhavin et al., Pron et al., Zamashchikov et al.*) report the new theoretical and experimental results on filtrational and fluidizing combustion, as well as combustion of foamy structures.

Ignition and combustion regimes of a hydrocarbon droplet (film) are studied by *Bloshenko, Chiu and Hwang*, and *Jarosinski et al.* A number of papers (*Babuk et al., Ermakov et al., Meinkohn, Shafirovich and Goldshleger, Valov et al.*) deal with theoretical and experimental investigations of ignition and combustion of metal particles (aluminum, magnesium, etc.).

Istratov et al. report the results of observations of powder combustion in a test engine under conditions close to its stable operation. *Strunin et al.* study the properties of ammonium nitrate, an oxidizer in explosives and solid rocket propellants. Specific features of SHS waves are investigated by *Aldushin et al., Khusid et al., Pivkina and Frolov.*

Coal combustion is the topic of papers by *Biede, Elperin and Krasovitov, Golovina et al., Gremyachkin and Buyanov, Sørensen et al.* Particular attention is paid to heterogeneous reactions in coal-particle interior. Korean researchers, *Jurng et al.*, present the results of investigations of waste car tire utilization by means of burning tire chips in a specially designed burner.

Session 4, Turbulent Combustion, has a number of noteworthy contributions. Papers by *Beretta et al.* and *Frost et al.* deal with the pdf approach in modeling turbulent combustion. In the former paper, the effect of temperature fluctuations on NO emission in turbulent nonpremixed gas flames is studied numerically. In the latter paper, the authors analyze the pdf transport equation for a simple-geometry diffusion flame. *Lipatnikov* studies theoretically the correlation between the turbulence and preflame auto-ignition in spark ignition engines. *Karpov et al.* study an apparent paradox arising under premixed turbulent combustion of specially composed mixtures.

The problem of large-area fires is studied by *Gostintsev et al., Kuhl et al.* present the results of direct numerical simulation of 3D turbulent flow fields in explosions.

Borissov et al. present a new model describing the velocity field and flame shape for the helical propagation of a flame front. A comparative study of turbulence models applied to confined swirling flows is made by *Trinh*. Pulsed Jet Combustion is studied theoretically by *Deshovskii et al.* (zero-dimensional thermochemical model) and *Frolov et al.* (3D computer simulation).

In **Session 5, Unsteady Combustion,** *Arkhipov* presents a review of studies on active control of burning solid propellant charges. *Alexandrov et al., Filimonov and Kidin, Garbei et al.*, and *Lissotchkin* contribute to different aspects of the theory of unsteady propellant combustion. Mathematical models of particular transient phenomena are suggested by *Bykov and Pushkaryeva* (continuous stirred-tank reactor), *Kaptsov and Bykov* (reaction–diffusion problem), *Cowperthwaite* (Lagrange's problem

with finite rate of chemical energy release).

A few papers deal with different mechanisms of flame instability. *Gostintsev* and *Istratov* examine fractal flow patterns arising due to boyancy-driven upward motion of the flame ball. When studying the hydrodynamic instability of premixed flames, *Minaev* concludes that nonlinear stabilization of the instability can be expected to occur under certain conditions. *Cambray et al.* study flame wrinkling in a weakly turbulent gas, *Popov* applies a zero-range potential method to study stability of plane flame front, *Segal* studies the effect on flame stability of a viscosity change during chemical transformation. *Rumanov* derives the conditions for the onset of flame self-oscillations. When analyzing thermal instability of flame front, *Strunin et al.* observe transitions from one-head spin regime to chaotic regime of instability.

Fire-storm originating during large-area fires is numerically realized by *Gostintsev* and *Ryzhov*.

A new method of abnormal combustion diagnostics in internal combustion engines is suggested by *Chae et al.* A spark plug is used as an ionization probe which allows, together with pressure measurements, to identify oscillatory combustion phenomena. *Afanas'iev et al.* report experimental results on the excitation conditions for a kinetic singing flame. *Stolin and Stelmakh* analize thermal instability for the system consisting of the rod heater surrounded by a ceramic layer. They predict critical phenomena caused by nonmonotonic dependence of ceramic thermal conductivity on temperature.

Section 6, Detonation, appeared to be the most representative by the number of contributions. Zel'dovich fundamental ideas serve as a basis for continued research in this field of combustion science. In general, all the contributions can be subdivided according to the following topics: *Detonation Initiation, Propagation, Structure, Properties of Detonation Products, Applications.*

The papers on *Detonation Initiation* include both theoretical and experimental contributions. Shock initiation of condensed high explosives (HE) is studied by *Chernyshev et al., Gatilov et al., Morozov et al., Plaksin et al.; Wang Zhiping and Wei Yuzhang; Ryabykh et al.*, use fast electrons for initiation, *Dubovik* applies initiation by impact, *Fang Qing et al.* study detonation excitation by a high-velocity projectile. Mechanisms of detonation initiation in gases are studied in a number of papers. *Levin et al.* present a numerical simulation of direct initiation of plane and cylindrical detonation waves. *Vasiljev*, using a high-velocity blunt body for initiating detonation in oxyacetylene mixture, arrives at the new mechanism of ballistic wave transformation to detonation. A few papers deal with the experimental verification of the Zel'dovich mechanism of spontaneous detonation onset. *Chan et al.* report the results of detonation initiation by focusing a sufficiently weak shock wave in a oxyhydrogen mixture. For creating ignition delay gradients in a combustible mixture *Medvedev et al.* use an explosion venting technique, while *Sochet et al.* dilute the mixture nonuniformly with air. An alternative treatment of the spontaneous detonation onset is suggested by *Subbotin*, based on experimental observations in an explosion chamber with a periphery crevice.

viii

Contributions on various aspects of Detonation to Deflagration Transition (DDT) problem are also presented. *Ermolaev et al.* suggest a new experimental approach for studying DDT in HE and substantiate it theoretically. *Noskov et al.* study the effect of τ on isentropic processes in a shock-compressed gas (resulting in static temperature maximum in a supersonic boundary layer) on the location of 'explosion in explosion'. *Smirnov et al.* report the results of numerical simulation and experimental observations of DDT phenomena in gases.

Specific features of Detonation Propagation in various media are studied by *Bondarenko and Vedin, Sun Chengwei and Gao Wen* (condensed HE); *Lee et al.* (nitromethane in porous medium), *Aslanov* (spray detonation); *Khasainov and Veyssiere* (hybrid two-phase mixtures); *Goldshtein et al.* (gas mixtures in porous media); *Presles et al.* (pure gaseous nitromethane–oxygen mixture); *Gao Wen et al.* and *Zhao Tonghu et al.* study the problem of detonation diffraction.

Detonation Structure is the topic of papers by *Fokeev et al.* (detonation cell calculations); *He and Lee* (substantiation for the necessity of transverse waves in detonation structure), and *Vidal et al.* (2D computer simulation). *Ershow* studies theoretically the structure of gaseous detonation under conditions of very high frictional losses (*e.g.*, in porous medium). *Pinaev* reports unique experimental results on 'vacuum' detonation, a new phenomenon which widens our knowledge on explosion modes.

Studies of detonation products properties, such as electric strength and conductivity (*Chernyshev and Ivanov*), and composition (*Volk*) are aimed at solution of applied problems. *Bityurin et al.* and *Zhdan et al.* present experimental findings oriented at detonation applications. *Novikov* reviews the studies on Rarefaction Shock Waves (RSW), first predicted by Zel'dovich, and emphasizes the practical significance of RSW collision technique.

Section 7, Combustion and Detonation Analogies, presents contributions in which the methods of the combustion theory are applied to other phenomena. Various aspects of radiation heat transfer are studied by *Andersen* and *Shon*. *Borissov et al.* use the Zel'dovich approach, developed for studying thermodiffusional flame instability, for modeling detonation structure. Self-organization phenomena are the topics of the paper by *Danilenko and Vladimirov*. *Hari et al.* apply the ideas developed in the combustion theory to the problem of convectional dissipation structures in a horizontal layer of fluid heated from below. Processes in reactors are studied by *Pushkin and Rubanov* and by *Ryabinin*. *Fletcher* presents the review of theoretical and experimental studies of melt/water explosions. Physical ideas in this field of science are based on the theory of detonation. In line with this topic is the paper by *Gostintsev and Sukhanov*. *Grigorjev et al.* present the study of chemical condensation phenomena based on Frenkel–Zel'dovich theory. *Varlamov* reviews the mechanisms of condensed phase structure formation during heterogeneous solidification. Thermal bistability of an electric circuit consisting of two resistors is studied by *Rumanov* as an analogy of surface reaction behavior studied by Zel'dovich and Frank-Kamenetskii. *Khudyaev*

contributes to the Kolmogorov–Petrovskii–Piskunov problem by extending the class of relevant boundary conditions.

Koslov and *Kuznetsov* report about the new physical phenomenon, termed optical deflagration, which is the result of interaction between powerful laser beams with water. *Shlensky and Vainshtein* present the measured thermolysis data of highly energetic materials.

Session 8, Intensive Shock Waves and Extreme States of the Matter, contains 5 papers. *Balagansky and Gryaznov* study experimentally the phenomenon of desensitization of multiply shocked HE. *Dolgoborodov* discusses the new design of the Fast Shock Tube aimed to achieve high dynamic pressures and to study hypervelocity penetration. *Gorel'skii and Zelepugin* have developed a mathematical model for compaction processes and initiation of exothermic combustion reactions in SHS systems. *Kulikov* studies translational and chemical nonequilibrium behind a shock wave. *Losev et al.* present the detailed mechanism of chemical reactions in high-temperature air behind a strong shock wave.

S. M. Frolov
Editor

SESSION 1. Kinetics

EXTINCTION PROPERTIES OF SMOKE FROM BURNING HEATING OIL

M. Barrakat*, J. M. Souil*, C. Breillat*, J. P. Vantelon*,
V. G. Knorre†

*Laboratoire de Chimie Physique de la Combustion, University of Poitiers , Ecole Nationale Supérieure de Mécanique et d'Aérotechnique, Site du Futuroscope — BP 109, Chasseneuil du Poitou — 86960 Futuroscope Cedex, France
†Moscow State Technical University MADI, Leningradski Prospekt 64, Moscow, 125829 Russia

The production of smoke by fires presents a major risk. In addition to toxic potential, it may obscure visibility, often impeding action or escape. Moreover, its constituents can represent a radiating medium affecting strongly the heat flux distribution in the surroundings. The former aspect is rather specific and is dealt with appropriate procedures based on chemical and biological testing. The two latter aspects lead generally to quantify smoke particulates absorption and scattering properties through the measurement of light extinction coefficients. Nevertheless, the extinction coefficient is an extensive property of the considered medium and characterizing is not sufficient. Thus, it can be rather expressed as the product of the extinction coefficient per unit mass concentration (termed specific extinction area) and the mass concentration of smoke particle: $k_e = \sigma C$ [1]. This quantity σ can be expressed on soot-mass basis σ_s or, since in many practical application the mass of soot is not obtained, on fuel-loss-mass basis σ_f. Then, in open systems, σ_f may be obtained from measurements of extinction coefficient k_e, smoke volume flow V, and mass loss rate of fuel m_f, i.e. $\sigma_f = k_e V / m_f$.

Experiments were performed at a laboratory scale, in an original flow-through system, well suited for the measurements of interest (k_e, V and m_f), and ensuring reliability, repeatability and possibility to conduct tests of longer duration (Fig. 1). Ventilation being one of the most important parameters controlling smoke behavior and properties, a confined system with monitored air supply was used, combustion being always fuel-controlled. These experiments, with limited and variable ventilation conditions, permitted to change the smoke dilution, i.e. the particle concentration. Another variable parameter was the wavelength of the (visible range) laser source used for extinction measurements.

Heating oil was chosen as the fuel to be used in the present experiments. It gives off substantial amounts of smoke and exhibits a fairly constant burning behavior. Moreover, it is a fuel commonly used and often involved in accidental fires.

It was possible to determine, at each wavelength, a specific extinction area σ_f. This quantity appeared to be independent of the ventilation conditions (Fig. 2), and its

1
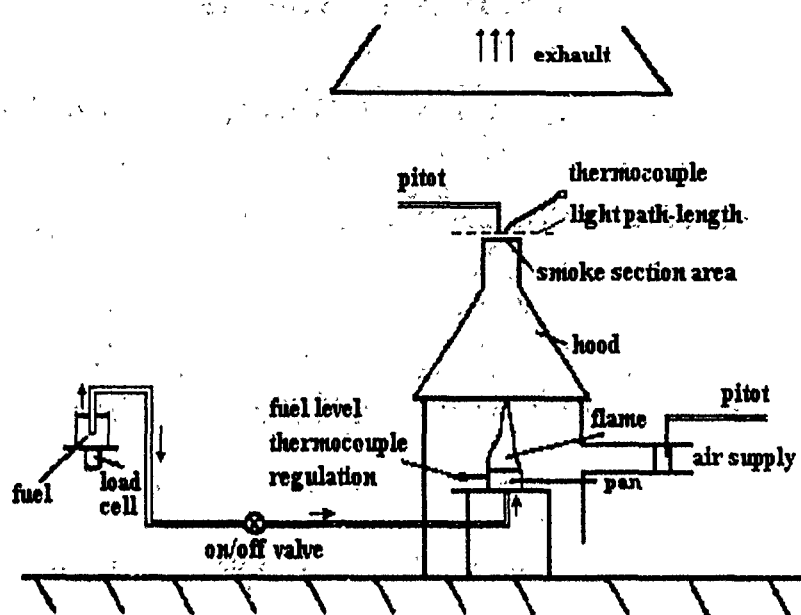
Figure 1: Experimental setup.
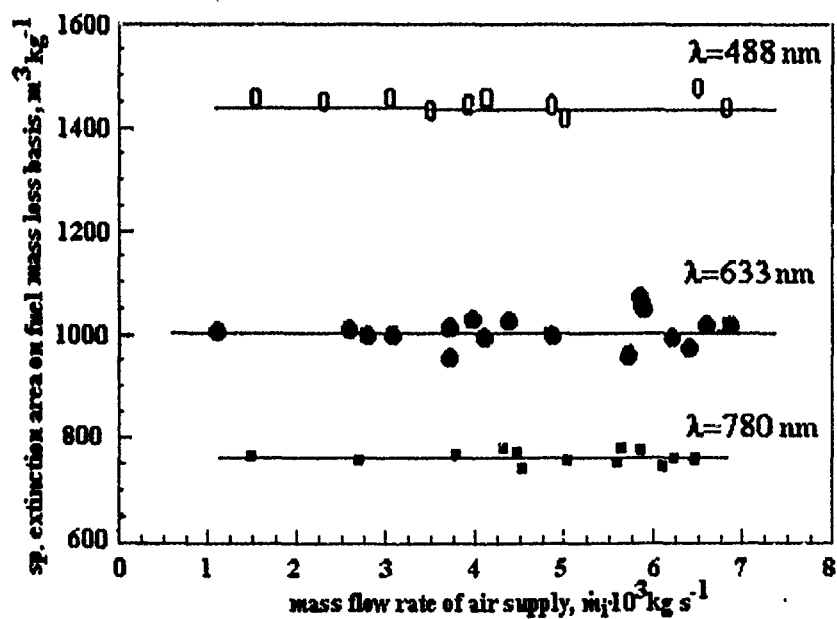
Figure 2: Dependence of the specific extinction areas on fuel mass loss basis on mass flow rate of air supply.

values indicated a high smoke potential of the heating oil (for instance about 1000 m^2kg^{-1} at 633 nm). This is consistent with fuel chemical nature (large proportion of unsaturated and aromatic compounds).

Concerning the wavelength effect, the small-particle limit of Mie theory can be applied to soot, and the results showed an approximate relationship of the form $\sigma_f = 4.45 \cdot 10^6/\lambda^{1.3}$ with λ expressed in nanometers. The value 1.3 of the dispersion coefficient, in the visible range of the spectrum, is consistent with the hydrogen content in soot (high H/C ratio).

The multi-wavelength transmission data also made it possible to determine the soot particle size [2] and therefore the yield of smoke (the fraction of mass loss of fuel converted to soot), number density of soot particles and soot particles volume fraction. For the small-particle limit of Mie theory, the Rayleigh approximation can be applied:

$$Q_e = Q_a = 24\alpha \frac{nk}{(n^2 - k^2 + 2)^2 + 4n^2k^2)} = 24\alpha F_a(\lambda),$$

where $\alpha = 2\pi r/\lambda$, and n and k are, respectively, the real part and the imaginary part of the complex refractive index m.

The ratio of the two extinction coefficients for two different wavelengths is independent of the particle size distribution, so that

$$\left[\frac{k_{e\lambda_i}}{k_{e\lambda_j}}\right]_{Rayleigh} = \frac{\lambda_j}{\lambda_i}\frac{F_a(\lambda_i)}{F_a(\lambda_j)}.$$

In the large particle limit, $Q_e \rightarrow 2$ and $k_{e\lambda_i}/k_{e\lambda_j} \rightarrow 1$; then, to obtain information on the particle size, a normalized extinction coefficient is introduced:

$$X_{ij} = \frac{k_{e\lambda_i}/k_{e\lambda_j} - 1}{\left[k_{e\lambda_i}/k_{e\lambda_j} - 1\right]_{Rayleigh}}.$$

Figure 3 shows the evolution of this ratio as a function of the mean radius of particles. Referring the values obtained for σ_f to these theoretical curves determines the mean radius for the particles of interest. Due to the nonlinear nature of the normalized extinction evolution with radius, it is better to use the three experimental ratios even though only two of them are independent.

The mean particle radius r_m deduced is approximately 0.035 μm and agrees with electron microscopy measurements.

The specific extinction area σ_f can be further expressed as

$$\sigma_f = \frac{3\varepsilon Q_e}{4\rho_s r_m},$$

where ρ_s is the soot particle density and ε the yield of smoke (fraction of the mass loss of fuel converted to soot).
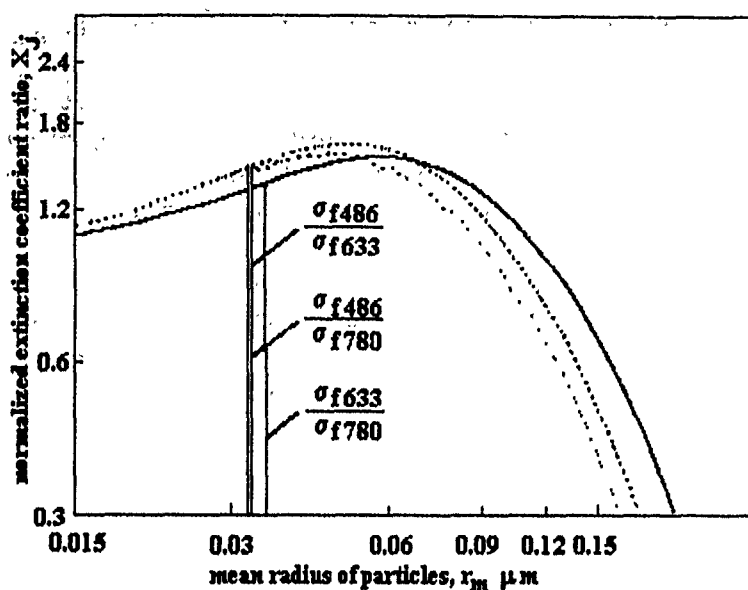
Figure 3: Normalized extinction coefficient ratio as a function of the mean radius of particles.

Substituting the values of Q_e/r_m calculated as above, we deduced the mean value of 0.13 for ε. The number density of soot particles and the soot volume fraction were then calculated, showing a direct proportionality with the mass flow rate of air supply.

At last, the specific extinction area deduced from the soot mass ($\sigma_s = \sigma_f/\varepsilon = 7700$ m^2kg^{-1}), which is a basic concept in smoke extinction properties normalization, appears to be in fairly good agreement with the roughly constant values generally reported for all fuels burning in the flame mode.

References

[1] Babrauskas, V., *J. Fire and Flammability*, 1981, **12**, 51–64.

[2] Bard, S., Pagni, P. J., *J. Heat Transfer*, 1981, **103**, 357–362.

REACTION MECHANISMS OF *iso*-OCTANE AND *n*-HEPTANE AUTOIGNITION UNDER CONDITIONS RELEVANT TO SPARK-IGNITION ENGINES

V. Ya. Basevich*, A. A. Belyaev*, W. Brandstätter†, S. M. Frolov*, M. G. Neigauz*, R. Tatschl†

*Semenov Institute of Chemical Physics, Kosygin Str., 4, Moscow, 117977 Russia
†AVL LIST GmbH, Kleiststrasse 48, A-8020 Graz, Austria

Introduction

The kinetic schemes employed in studying combustion processes in SI engines must take into account the phenomenological features typical for hydrocarbon fuel oxidation at high pressures and moderate temperatures. This implies that both low- and high-temperature oxidation mechanisms should be incorporated into a kinetic scheme [1]. Combination of the two subschemes can provide a model of two-stage auto-ignition. Hydrocarbons exhibiting two-stage auto-ignition are known to be characterized by substantial widening of self-ignition limits. According to the qualitative analysis [1] and quantitative estimations [2], abnormal combustion in SI engines ('knock') can be caused by two-stage autoignition of unburnt mixture pockets.

This paper deals with a new detailed reaction mechanism developed for studying autoignition of *iso*-octane, *n*-heptane and their mixtures under conditions similar to those in the end gas of SI engines. To implement the mechanism in multidimensional fluid dynamic codes, its systematic reduction has been performed.

Reaction Mechanism

Modeling of two-stage autoignition of hydrocarbon fuels is based on the well-known principle discussed elsewhere [1, 3]. At low temperatures, chain branching is assumed to proceed via alkil peroxide decomposition, whereas at larger temperatures decomposition of hydrogen peroxide and reactions involving formaldehyde are dominant. With a further temperature increase, the branching tends to proceed mainly through the reaction of H atom with oxygen. The transition between the branching mechanisms is a result of the temperature increase in the course of decomposition of the alkil peroxide radical RO_2.

The kinetic mechanism of *iso*-octane and *n*-heptane oxidation includes two groups of reactions.

The first one is the autoignition group including 29 reactions involving 13 reactants. The autoignition group includes reactions describing cool flames and two-stage autoignition at certain critical values of Arrhenius parameters. It includes competing reactions (specific for *iso*-octane and *n*-heptane) which ensure the transition between low- to high-temperature oxidation mechanisms. In addition, a few empirical reactions

5

are included to reduce C_7 and C_8 to C_1 and C_2 hydrocarbons. The autoignition sub-scheme under consideration differs from the existing reaction mechanisms, although the basic steps involved are represented by well-known processes.

The second group of reactions is the detailed mechanism of oxidation of C_1 and C_2 hydrocarbons containing 255 reactions involving 30 reactants [4]. In the present paper, it is modified for the use at high initial pressures.

Validation of the reaction mechanism was performed by comparing the predicted autoignition delay times to the available measurement data. The ignition delay times are calculated for constant-volume conditions.
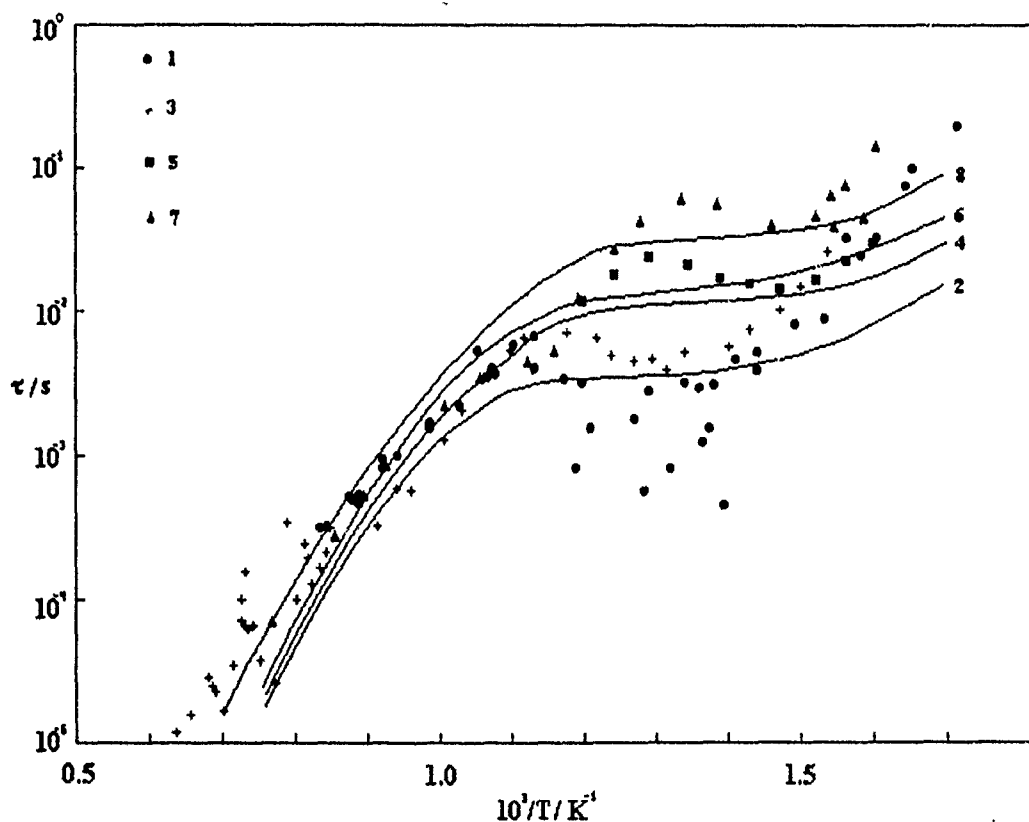

Figure 1: Comparison of predicted (curves) and measured (points) ignition delays for stoichiometric n-heptane–iso-octane–air mixtures at initial pressure 15 bar. 1, 2 — n-heptane–air; 3, 4 — 40% n-heptane + 60% iso-octane–air; 5, 6 — 10% n-heptane + 90% iso-octane–air; 7, 8 — iso-octane–air.

Validation

To compare the predicted results to the measured data, experimental studies using rapid-compression and shock-tube techniques were considered. Of interest are the experimental conditions close to those in the end gas in SI engines, namely, the temperatures $600 \text{ K} < T < 1200 \text{ K}$, the pressures 15 bar $< p <$ 100 bar, and the equivalence ratios $0.5 < \phi < 2.0$.

An example of the comparison of the predicted and measured results is shown in Fig. 1. The predicted curves are compared to the available experimental data for the ignition delays of stoichiometric mixtures of n-heptane (1, 2), 40% n-heptane + 60% iso-octane (3, 4), 10% n-heptane + 90% iso-octane (5, 6) and iso-octane (7, 8) with air at the initial pressure $p = 15$ bar over a wide range of initial temperatures.

Figure 1 exhibits a significant scatter of the measured results for iso-octane (3 groups of points: Halstead et al, Teichmann, and Fieweger et al) and for n-heptane (5 groups: Ciezki et al, Teichmann, Taylor et al, Scheuermeyer et al, and Roegener). For similar initial conditions, the ignition delay times differ by a factor of 2 to 7. Moreover, different authors observed qualitatively different dependencies of $\lg\tau$ vs. $1/T$ for iso-octane. The discrepancies observed are most likely due to the difference in experimental and measuring techniques and the definitions of ignition delay employed in the respective studies.

It is evident that the iso-octane–air mixture exhibits longer ignition delays than the n-heptane–air and blended fuel–air mixtures. The difference is more pronounced at low temperatures. At high temperatures, the ignition delays for different fuel–air mixtures become close. Clearly, all the predicted curves are S-shaped. This is an evidence of two oxidation mechanisms involved, namely, low-temperature ($T < 700$ K) and high-temperature ($T > 900$ K). Between these temperature ranges, there is a transition region where the process of autoignition is two-staged.

Mechanism Reduction

Implementation of a reaction mechanism in a multidimensional fluid dynamic code requires reducing it to the shortest possible scheme. The reduction procedure employed has been reported in [5].

The use of the procedure resulted in developing a reduced reaction mechanism including 21 reactions involving 13 reactants. This mechanism shows a good agreement with experimental data and with the results obtained using the complete reaction mechanism.

Conclusion

A detailed reaction mechanism has been developed and validated with the view of studing autoignition of iso-octane, n-heptane and their mixtures in air in a wide range of initial conditions in terms of temperature (600–1200 K), pressure (15–100

7

bar), and equivalence ratio (0.5–2.0). The mechanism includes 284 reactions involving 43 reactants. A reduced reaction mechanism including 21 reactions among 13 reactants has also been developed. It approximates, with a good accuracy, the results of detailed calculations, based on the complete reaction mechanism, within the ignition delay time.

References

[1] Sokolik A. S. *Self-ignition, Flame and Detonation in Gases*, Israel Program for Scientific Translation, Jerusalem, 1963.

[2] Frolov S. M., Gelfand B. E., Tsyganov S. A. In: *Progr. Astron. Aeron. Dynamics of Detonations and Explosions — Detonations*, AIAA Inc., New York, 1990, **133**, 133.

[3] Lewis G., von Elbe G., *Combustion, Flames and Explosions of Gases*, Academic Press, New York, 1961.

[4] Basevich V. Ya. In: *Handbook of Heat and Mass Transfer* (N. P. Cheremisinoff, Ed.), Gulf Publ.Co., Houston, 1990, 769.

[5] Karasevich Yu. K., Neigauz M. G. In: *Direct and Inverse Problems in Chemical Kinetics* (V. I. Bykov, Ed.), Nauka, Novosibirsk, 1993, 248 (in Russian).

THE KINETIC MODELING OF LAMINAR FLAMES OF H_2S AND CS_2

V. Ya. Basevich, V. I. Vedeneev, V. S. Arutyunov

Semenov Institute of Chemical Physics, Kosygin str. 4, Moscow, 117977 Russia

This work completes the first stage of the development of the detailed kinetic mechanisms of self-ignition and combustion of relatively simple sulphur-containing gas-phase molecular systems: H–S–O and C–S–O. Experimental studies of gas-phase hydrogen sulfide oxidation (H–S–O) and carbon disulfide oxidation (C–S–O) were conducted in a number of works. Some of these works were reviewed in [1, 2], where detailed kinetic mechanisms of these processes were also suggested and kinetic simulation of self-ignition

Table 1: Flame propagation velocities u_n for hydrogen sulfide/oxygen mixtures at $P = 1$ atm.

Mixture (%)				u_n (cm/s)				
H$_2$S	O$_2$	Ar	N$_2$	Exp.	Calc.			
				293 K	293 K	485 K	630 K	715 K
5.1	13.9	81.0	—	9.1	4.3	5.9	11.3	13.5
6.1	20.4	—	73.5	8.0	1.8	2.5	5.0	

in these systems was carried out. In this work we compare the results of computations of laminar flames in hydrogen sulfide and carbon disulfide with experimental data.

One-dimensional steady (propagation of laminar flame was described by the standard set of equations [3] with boundary conditions similar to those in [4]. The kinetic mechanisms for both H–S–O and C–S–O systems were supplemented with the missing backward reactions. The Arrhenius parameters of backward reactions were calculated using the respective equilibrium constants. Apart from that, some rate constants were updated by [5].

Hydrogen Sulfide Oxidation (H–S–O system)

In this case, the primary kinetic mechanism [1], after introducing additional backward reactions, was reduced to 146 reactions (104 forward and 42 backward reactions) and 22 particles. It was done as proposed in [6] without significant loss of accuracy. This set of differential equations was solved using the standard program [7]. The accuracy of the reaction rates of the majority of elementary reactions in this mechanism being within the factor 2–5, the same accuracy may be expected for these calculations.

The predictions were compared with the experimental results of [8]. Table 1 shows that the laminar flame velocities calculated at the initial temperature $T_0 = 293$ K are substantially lower than the experimental values. It is well known that a metal grid used to stabilize a flat flame affects its parameters. The most important factor is the heat transfer from the heated grid to the fresh gas mixture, which changes the initial gas temperature. The computations were made for various values of T_0 down to the minimum temperature measured in [8] by a thermocouple in the vicinity of metal grid. The final temperature was kept constant by adjusting the value of specific heat used in computations. It is evident that experimental values are within the predicted region for Ar-diluted mixtures and close to the calculated values for N$_2$-diluted mixtures.

Carbon Disulfide Oxidation (C–S–O system)

In this case, the mechanism was simpler [2], so there was no need to reduce it.
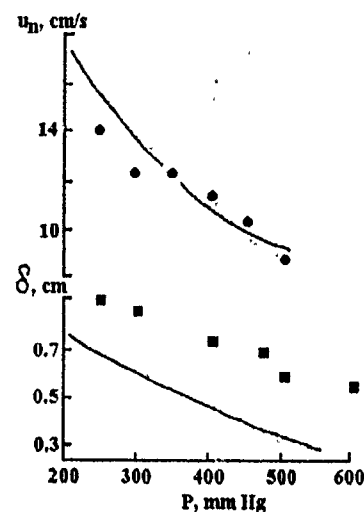
Figure 1: The pressure dependence of flame velocity and reaction zone width in carbon disulfide flame ($T_0 = 293$ K, $[CS_2]_0 = 2.2\%$, $[O_2]_0 = 20.5\%$, $[N_2] = 77.3\%$).

The numerical results of calculations were also compared with flat flame experiments [9]. To obtain satisfactory agreement it was necessary to change only the rate constant of termination reaction $SO + O_2 + M = SO_3 + M$, which had to be equal or lower than $k_0 = 5 \cdot 10^7 \ l^2/mole^2 s$ at zero activation energy. Figure 1 shows the pressure dependencies of calculated and experimental normal flame velocities and the reaction zone widths. The correspondence is satisfactory for both curves.

References

[1] Chernyshova A. V., Basevich V. Ya., Vedeneev V. I., Arutyunov V. S., *Izvestiya Akad. Nauk SSSR, Ser. Khim.*, 1990, 1956 (in Russian).

[2] Chernyshova A. V., Basevich V. Ya., Vedeneev V. I., Arutyunov V. S., *Izvestiya Akad. Nauk SSSR, Ser. Khim.*, 1992, 812 (in Russian).

[3] Kondratyev V. N., Nikitin E. E., *Kinetics and Mechanism of Gasphase Reactions*, Nauka, Moscow, 1974 (in Russian).

[4] Bischoff K. B., *J. Chem. Eng. Soc.*, 1961, **16**, 131.

[5] Westley F., Herron J. T., Cvetanovic J. J., *US Dep. Commer. Nat. Bur. Stand., Nat. Stand. Ref. Data Ser.*, 1987.

[6] Karasevich Yu. K., Neigauz M. G. In: *Direct and Inverse Problems in Chemical Kinetics*, (V. I. Bykov Ed.), Nauka, Novosibirsk, 1993, 248 (in Russian).

[7] Belyaev A. A., Posvyanski V. S., *Inform. Bull. of USSR Algoritm and Programm Foundation*, 1985, 3, 35 (in Russian).

[8] Levy A., Merryman E. L., *Comb. Flame*, 1965, **9**, 229.

[9] Egerton A., Sen D., *Proc. 4th Symp. (Int.) on Comb.*, Williams & Wilkins, 1953, 321.

AUTOIGNITION OF CH4/O2/AR MIXTURES: THE EFFECT OF HYDROGEN PEROXIDE

C. Bruno*, V. I. Golovitchev[†], M. L. Pilia[†]

Dip. Meccanica e Aeronautica, Università di Roma I, Roma, Italy
[†] *CRS4 Research Center, Cagliari, Italy*

Control of ignition processes by addition of promoters to the combustible mixtures is an increasingly interesting method for improving the performance of practical combustion systems [1]. Compounds used as the promoters (additives reducing ignition delay time) include free radicals, nitrogen oxides, peroxides, etc. The purpose of this study is to investigate the effects of hydrogen peroxide, H_2O_2, on the ignition delay times for $CH_4/O_2/Ar$ mixtures. This a mixture was chosen because reliable experimental data on ignition delay times for promoter-free mixtures are available from [2]. In this paper, other additives, such as H_2 and C_3H_8, were also investigated. Strictly speaking, they can be considered as easily ignitable fuels rather than promoters. Their influence can be explained on a thermal basis, while H_2O_2 primarily acts as a gaseous catalyst.

The ignition delay time is related to the "latent period" of a premixed combustion process, when temperature remains nearly constant. The mixture components, however, may undergo substantial charges. In this study, a computer model [3] was used to predict the mixture parameters as functions of time, and the ignition delay time was defined as the time at which the rate of temperature rise sharply increases (the point of inflection).

Table 1: The reaction mechanism of $CH_4/O_2/Ar$ mixtures

Reaction		a_f^r	ζ_f^r	E_{af}^r	M_i
$CH_3 + H + M$	$\rightleftharpoons$ $CH_4 + M$	$8.00 \cdot 10^{26}$	-3.00	0.	all components
$CH_4 + O_2$	$\rightleftharpoons$ $CH_4 + HO_2$	$7.90 \cdot 10^{13}$	0.00	56000.	—
$CH_4 + H$	$\rightleftharpoons$ $CH_3 + H_2$	$2.20 \cdot 10^{04}$	3.00	8750.	—
$CH_3 + OH$	$\rightleftharpoons$ $CH_3 + H_2O$	$1.60 \cdot 10^{06}$	2.10	2460.	—
$CH_4 + O$	$\rightleftharpoons$ $CH_3 + OH$	$1.02 \cdot 10^{09}$	1.50	8604.	—
$CH_4 + H_2O$	$\rightleftharpoons$ $CH_3 + H_2O_2$	$1.80 \cdot 10^{11}$	0.00	18700.	- -
$CH_3 + O$	$\rightleftharpoons$ $CH_2O + H$	$8.00 \cdot 10^{13}$	0.0	0.	—
$CH_3 + OH$	$\rightleftharpoons$ $CH_2 + H_2O$	$7.50 \cdot 10^{06}$	2.0	5000.	—
$CH_3 + H$	$\rightleftharpoons$ $CH_2 + H_2$	$9.00 \cdot 10^{13}$	0.0	15100.	—
$CH_2 + H$	$\rightleftharpoons$ $CH + H_2$	$1.00 \cdot 10^{18}$	-1.56	0.	—
$CH_2 + OH$	$\rightleftharpoons$ $CH + H_2O$	$1.13 \cdot 10^{07}$	2.0	3000.	—
$CH_2 + OH$	$\rightleftharpoons$ $CH_2O + H$	$2.50 \cdot 10^{13}$	0.0	0.	—
$CH + O_2$	$\rightleftharpoons$ $HCO + O$	$3.30 \cdot 10^{13}$	0.0	0.	—
$CH + O$	$\rightleftharpoons$ $CO + H$	$5.70 \cdot 10^{13}$	0.0	0.	—
$CH + OH$	$\rightleftharpoons$ $HCO + H$	$3.00 \cdot 10^{13}$	0.0	0.	—
$CH + CO_2$	$\rightleftharpoons$ $HCO + CO$	$3.40 \cdot 10^{12}$	0.0	690.	—
$CH + H_2O$	$\rightleftharpoons$ $CH_2O + H$	$1.17 \cdot 10^{15}$	-0.75	0.	—
$CH_2 + CO_2$	$\rightleftharpoons$ $CH_2O + CO$	$1.10 \cdot 10^{11}$	0.0	1000.	—
$CH_2 + O$	$\rightleftharpoons$ $CO + H + H$	$5.00 \cdot 10^{13}$	0.0	0.	—
$CH_2 + O$	$\rightleftharpoons$ $CO + H_2$	$3.00 \cdot 10^{13}$	0.0	0.	—
$CH_3 + O_2$	$\rightleftharpoons$ $CO_2 + H + H$	$1.60 \cdot 10^{12}$	0.0	1000.	—
$CH_2 + O_2$	$\rightleftharpoons$ $CH_2O + O$	$5.00 \cdot 10^{13}$	0.0	9000.	—
$CH_2 + O_2$	$\rightleftharpoons$ $CO_2 + H_2$	$6.90 \cdot 10^{11}$	0.0	500.	—
$CH_2 + O_2$	$\rightleftharpoons$ $CO + H_2O$	$1.90 \cdot 10^{10}$	0.0	$-1000.$	—
$CH_2 + O_2$	$\rightleftharpoons$ $CO + OH + H$	$8.60 \cdot 10^{10}$	0.0	$-500.$	—
$CH_2 + O_2$	$\rightleftharpoons$ $HCO + OH$	$4.30 \cdot 10^{10}$	0.0	$-500.$	—
$CH_2 + OH$	$\rightleftharpoons$ $HCO + H_2O$	$3.43 \cdot 10^{09}$	1.18	$-447.$	—
$CH_2O + H$	$\rightleftharpoons$ $HCO + H_2$	$2.19 \cdot 10^{08}$	1.77	3000.	—
$CH_2O + M$	$\rightleftharpoons$ $HCO + H + M$	$3.31 \cdot 10^{16}$	0.0	81000.	all components
$CH_2O + O$	$\rightleftharpoons$ $HCO + OH$	$1.80 \cdot 10^{13}$	0.0	3630.	—
$HCO + OH$	$\rightleftharpoons$ $H_2O + CO$	$1.00 \cdot 10^{14}$	0.0	0.	—
$HCO + M$	$\rightleftharpoons$ $H + CO + M$	$2.50 \cdot 10^{14}$	0.0	16802.	all components
$HCO + H$	$\rightleftharpoons$ $CO + H_2$	$1.19 \cdot 10^{13}$	0.25	0.	—

Each of N_r elementary chemical reactions involving N_s species are represented in the general form

$$\sum_{s=1}^{N_s} \nu_{sr}' X_s \underset{k_b^r}{\overset{k_f^r}{\rightleftharpoons}} \sum_{s=1}^{N_s} \nu_{sr}'' X_s, \qquad r = 1, N_r$$

where X_s represents one mole of s-species, ν_{sr}' and ν_{sr}'' are the stoichiometric coefficients, k_f^r and k_b^r are the rate coefficients for forward and backward stages of the r-th reaction and are used in the generalized Arrhenius form

$$k_f^r = a_f^r T^{\zeta_f^r} \exp(-Ta_f^r/T),$$

Table 1 (continued)

Reaction		a_f^r	ζ_f^r	E_{af}^r	M_i
HCO + O	$\rightleftharpoons$ CO + OH	$3.00 \cdot 10^{13}$	0.00	0.	—
HCO + O	$\rightleftharpoons$ CO$_2$+ H	$3.00 \cdot 10^{13}$	0.00	0.	—
HCO + O$_2$	$\rightleftharpoons$ HO$_2$+ CO	$3.30 \cdot 10^{22}$	-0.40	0.	—
CO + O +M	$\rightleftharpoons$ CO$_2$ + M	$6.17 \cdot 10^{14}$	0.0	3000.	all components
CO + OH	$\rightleftharpoons$ CO$_2$+ H	$1.51 \cdot 10^{07}$	1.30	$-758.$	—
CO + O$_2$	$\rightleftharpoons$ CO$_2$+ O	$1.60 \cdot 10^{13}$	0.00	41000.	—
HO$_2$+ CO	$\rightleftharpoons$ CO$_2$ + OH	$5.80 \cdot 10^{13}$	0.0	22934.	—
CH$_2$+ CH$_4$	$\rightleftharpoons$ CH$_3$+ CH$_3$	$4.00 \cdot 10^{13}$	0.0	0.	—
CH$_2$+ O$_2$	$\rightleftharpoons$ CO + OH + H	$3.00 \cdot 10^{13}$	0.0	0.	—
CH$_2$+ H$_2$	$\rightleftharpoons$ CH$_3$+ H	$7.00 \cdot 10^{13}$	0.0	0.	—
CH$_2$+ H	$\rightleftharpoons$ CH$_2$+ H	$2.00 \cdot 10^{14}$	0.0	0.	—
H$_2$ + O$_2$	$\rightleftharpoons$ OH + OH	$1.70 \cdot 10^{13}$	0.0	47780.	—
H$_2$ + OH	$\rightleftharpoons$ H$_2$O + H	$1.17 \cdot 10^{09}$	1.30	3626.	—
O + OH	$\rightleftharpoons$ O$_2$+ H	$4.00 \cdot 10^{14}$	-0.5	0.	—
O + H$_2$	$\rightleftharpoons$ OH + H	$5.06 \cdot 10^{04}$	2.67	6290.	—
H + O$_2$ + M_4	$\rightleftharpoons$ HO$_2$ + M_4	$3.61 \cdot 10^{17}$	-0.72	3590.	all components
OH + H$_2$O	$\rightleftharpoons$ H$_2$O + O$_2$	$7.50 \cdot 10^{12}$	0.0	0.	—
H + HO$_2$	$\rightleftharpoons$ OH + OH	$1.40 \cdot 10^{14}$	0.0	1073.	—
O + HO$_2$	$\rightleftharpoons$ O$_2$ + OH	$1.40 \cdot 10^{13}$	0.0	1073.	—
OH + OH	$\rightleftharpoons$ O + H$_2$O	$6.00 \cdot 10^{08}$	1.3	0.	—
H + H +M	$\rightleftharpoons$ H$_2$ +M	$1.00 \cdot 10^{18}$	-1.00	0.	all components
H + OH +M	$\rightleftharpoons$ H$_2$O +M	$1.60 \cdot 10^{22}$	-2.00	0.	all components
H + O +M	$\rightleftharpoons$ OH +M	$6.20 \cdot 10^{16}$	-0.60	0.	all components
O + O +M	$\rightleftharpoons$ O$_2$ + M	$1.89 \cdot 10^{13}$	0.0	$-1788.$	all components
H + HO$_2$	$\rightleftharpoons$ H$_2$ + O$_2$	$1.25 \cdot 10^{13}$	0.0	0.	—
HO$_2$+ HO$_2$	$\rightleftharpoons$ H$_2$O$_2$+ O$_2$	$2.00 \cdot 10^{12}$	0.0	0.	—
HO$_2$ + M	$\rightleftharpoons$ OH + OH +M	$1.30 \cdot 10^{17}$	0.0	45500.	all components
H$_2$O$_2$+ H	$\rightleftharpoons$ HO$_2$+ H$_2$	$1.60 \cdot 10^{12}$	0.0	3800.	—
H$_2$O$_2$+ OH	$\rightleftharpoons$ H$_2$O + HO$_2$	$1.0 \cdot 10^{13}$	0.0	1800.	—
H + HO$_2$	$\rightleftharpoons$ O + H$_2$0	$3.10 \cdot 10^{10}$	0.0	3590.	—
H + OH +M	$\rightleftharpoons$ HO$_2$ + M	$1.0 \cdot 10^{16}$	0.0	0.	all components
H$_2$O$_2$+ H	$\rightleftharpoons$ H$_2$0 + OH	$1.0 \cdot 10^{13}$	0.0	3590.	—

Reaction rates coefficients are given in $[\text{cm}^3\text{mol}^{-1}\text{s}^{-1}]$, M_i is the third body.

$$k_b^r = a_b^r T^{\zeta_b^r} \exp(-T a_b^r / T).$$

The reaction rate parameters a_r, ζ^r, and Ta^r, listed in Table 1, are taken mainly from [4]. The mechanism was "tuned" to high temperature conditions and the pressure-dependent nature of the "fall-off" reactions [1] was neglected.

The mathematical model designed to describe the time evolution of reacting mixtures parameters, in an adiabatic, constant-pressure environment, is formulated as an

13

initial-value problem for the set of ordinary differential equations (ODEs)

$$\frac{dy_i}{dt} = f_i(\bar{y}) = M w_i \sum_{r=1}^{N_r} (\nu_{ir}'' - \nu_{ir}') \dot{\omega}_r,$$

$$(y_i)_{t=0} = y_i^o, \qquad i = 1, N_s,$$

$$H(t) = \sum_{i=1}^{N_s} y_i h_i(T) = const.$$

Here H, $h_i(T)$ are the total enthalpy and enthalpies of i-species, respectively. $M w_i$ is the i-th molecular mass, T is the temperature, and the variable $\dot{\omega}_r$ is the rate of the r-th reaction defined in terms of the mass action Arrhenius kinetics. The steady-state point in the calculations corresponds to the equilibrium state. Since the time required to reach an equilibrium generally exceeds by several orders of magnitude the characteristic times associated with the fastest reactions, the initial value problem must be solved by methods suitable for so-called "stiff" ODEs.

To integrate numerically the set of "stiff" ODEs, a linear, multi-step method developed by Gear was used. The ignition delays were first compared with the experimental data for additive-free $CH_4/O_2/Ar$ mixtures [2]. This comparison was performed to assess the accuracy of the kinetic mechanism in the absence of additives. A satisfactory agreement with the experimental data for the selected series 1B, 1C, 2B, 4A is clearly demonstrated in Figs. 1–4. The results for $CH_4/O_2/Ar$ mixtures in the presence of hydrogen peroxide (in molar percentage) shows a substantial monotonic reduction of ignition delay times, which is a new finding. Hydrogen peroxide has proved to be more efficient than, for example, H_2, as can be seen in Fig. 4. Hydrogen peroxide, like most of the promoters, decomposes quickly via

$$H_2O_2 + M \rightleftharpoons OH + OH + M,$$
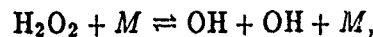
thereby introducing free radicals OH into the mixture and accelerating the chain reactions as a gas-phase catalyst. In this case, the H and OH distributions exhibit two peaks: the first one is related to H_2O_2 decomposition, and the second one to the combustion of the main fuel.

This is why the definition of ignition delay time by H and OH peaks is not adequate. These results indicate that moderate H_2O_2 addition reduces delay times by about one order of magnitude in the temperature (1525–2025 K) and the pressure (2.55–13.01 atm) ranges of the experiments in [2]. These effects can be used to shorten methane/air flames.

References

[1] Zamansky, V. M., Borisov, A. A. *Prog. Energy Comb. Sci.*, 1992, **18**, 297, 2.

Ignition delays for $CH_4/O_2/Ar$ mixtures
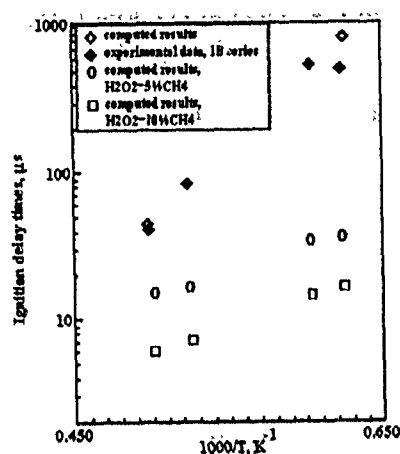
Figure 1: Effect of H_2O_2 on $CH_4/O_2/Ar$ mixtures ignition delay times and comparison with experimental (additive-free) data (Lifshitz, A., et al., Comb. and Flame. 16, 311, 1971).

◊ computed results

◆ experimental data, 1B series

○ computed results, $H_2O_2 = 5\%$ CH_4

□ computed results, $R_2O_2 = 10\%$ CH_4
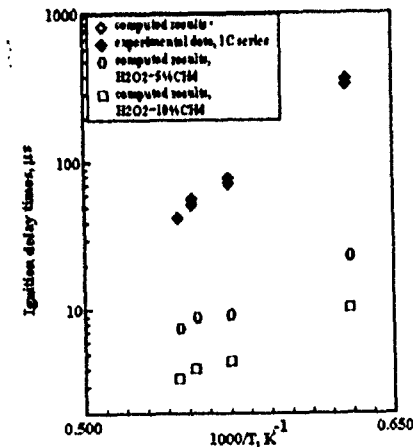
Figure 2: Effect of H_2O_2 on $CH_4/O_2/Ar$ mixtures ignition delay times and comparison with experimental (additive-free) data.

◊ computed results

◆ experimental data, 1C series

○ computed results, $H_2O_2 = 5\%$ CH_4

□ computed results, $H_2O_2 = 10\%$ CH_4
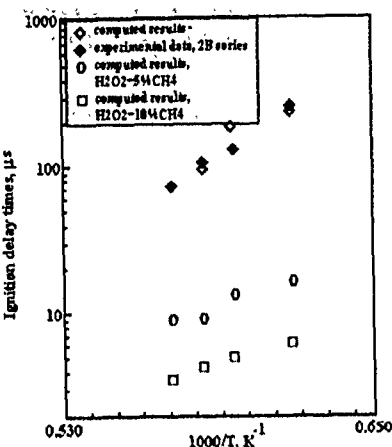
Figure 3: Effect of H_2O_2 on $CH_4/O_2/Ar$ mixtures ignition delay times and comparison with experimental (additive-free) data.

◊ computed results

◆ experimental data, 2B series

○ computed results, $H_2O_2 = 5\%$ CH_4

□ computed results, $H_2O_2 = 10\%$ CH_4
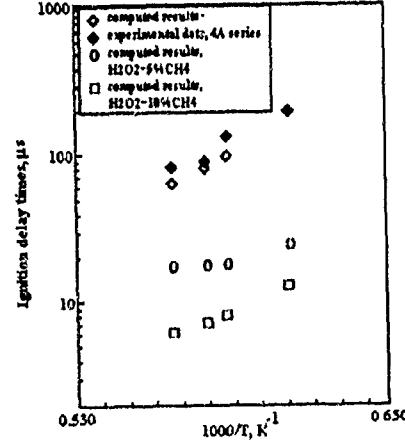

Figure 4. Effect of H_2O_2 on $CH_4/O_2/Ar$ mixtures ignition delay times and comparison with experimental data (additive: H_2).

◊ computed results

◆ experimental data, 4A series

○ computed results, $H_2O_2 = 5\%$ CH_4

□ computed results, $H_2O_2 = 10\%$ CH_4

[2] Lifshitz, A. *et al. Comb. and Flame,* 1971, **16**, 311.

[3] Golovitchev, V. I., Brenner, G. *DLR Institute of Theoretical Fluid Mechanics Internal Publication* IB 221–93 A 18, 1993.

[4] Miller, J. A., Bowman, C. T. *Prog. Energy Comb. Sci.,* 1989, **15**, 287.

DEVELOPMENT OF THE CHEMICAL KINETICS FOR AN IONIC MECHANISM OF SOOT FORMATION IN FLAMES

H. F. Calcote, R. J. Gill

AeroChem Research Laboratories, Inc.
P.O. Box 12, Princeton, NJ 08542 USA

At soot threshold the only property of the flame that changes is the character of the flame ions. Small ions increase to large ions. The basic premise of the ionic mechanism of soot formation is that the chemiion HCO^+ grows to a very large size to become an incipient soot particle of about 500 to 1,000 Å. To model the ionic mechanism it is necessary to develop a kinetic scheme involving chemiionization (source of original ions), ion-molecule reactions (ion growth mechanism), ion-electron recombination (removal of ions), and ion diffusion. For a refined mechanism, ion oxidation, electron attachment, and cation-anion recombination should be included. Modeling this process is complicated by the lack of thermodynamic and kinetic data on ionic reactions at flame temperatures and for large ions. We have therefore set out to determine the required data. In this presentation we discuss the development of the chemical kinetic data base: the thermodynamic development and application to a specific flame are presented elsewhere. The philosophy has been to obtain reasonable values and make reasonable assumptions to compare with experimental data. If reasonable agreement is obtained, the estimates and assumptions will be refined.

Electronically excited CH^* reacts with an oxygen atom to produce the chemiion HCO^+, which, through a series of ion-molecule reactions, produces $C_3H_3^+$, an ion which is observed in large concentrations in fuel rich and sooting flames. This ion then reacts with several small neutral species, e.g. C_2H_2, C_4H_2, C_3H_3 and allene, to produce larger ions which continue to grow through a series of ion-molecule reactions producing larger and larger ions. Simultaneously, as the ions grow they are neutralized by reacting with

electrons or anions, producing neutral by-product polycyclic aromatic hydrocarbons, that can continue to grow to soot through the "free radical mechanism". These neutral reactions probably play only a minor role.

In developing this mechanism only ionic species which have been observed in flames have been included and all observed ions have been accounted for. This is a more stringent constraint than has been applied to the free radical mechanism. Selected reaction rate coefficients are presented in Table 1.

Ion–Molecule Reactions: When available, experimental rate coefficients were used, but these are available only for small ions. In general, experimental rates are very close to the rate calculated by the average dipole orientation, ADO, theory:

$$k = \frac{2\pi e}{\mu^{1/2}}\left[\alpha^{1/2} + C\mu_D\left(\frac{2}{\pi k T}\right)^{1/2}\right] \tag{1}$$

where, μ is the reduced mass, α is the polarizability of the neutral reactant, C is a locking constant and μ_D is the dipole moment of the neutral reactant. For nonpolar species such as C_2H_2, C_4H_2 and allene, the major neutral growth species in the ionic model, Eq.(1) reduces to the Langevin equation which does not have a temperature coefficient. For polar species such as C_3H_3, propargyl radical; the increased rate due to the dipole is small at flame temperatures (about 25%) so the dipole term in Eq.(1) is neglected.

In the Langevin theory, the ion is treated as a point charge. This is not realistic for large ions. We have thus extended the Langevin theory to consider the finite dimensions of the ion. The ion is considered as a conducting sphere of finite radius, for which, in free space, the charge is uniformly distributed over the surface. When a polarizable neutral molecule approaches an ion, under the influence of the ion electric field, it becomes a dipole. This acts to redistribute the surface charge on the ion and increases the electric field strength between the neutral and the ion. To apply the extended Langevin theory to our set of reactions, we fit the results of a detailed calculation to estimate the A and n terms in the classical Arrhenius equation.

The size of the ions was deduced from experimental ion mobility, κ, data and Langevin's ion mobility equation:

$$\kappa = \frac{A}{\sqrt{\rho(\varepsilon_r - 1)}}\left(1 + \frac{M}{m}\right)^{1/2} \tag{2}$$

where M is the MW of the neutral and m is the MW of the ion, ε_r is the relative permittivity of the neutral and ρ is the gas density and A is a complicated function of pressure. The ion diameters, d (in Å), are related to ion mass by the empirical equation:

$$\ln(d) = -1.375 + 2.154\ln(\ln(m)) \tag{3}$$

The correlation coefficient for this equation was 0.999.

Table 1: Selected reaction rate coefficients.
$k = AT^n e^{-E/RT}$ (K, kJ, moles, cm^3, s)
$C_3H_3^+$ linear; $H_3C_3^+$ cyclic; C_3H_4 = allene; $H_yC_x^+$, $C_xH_{(y-n)}H_n^+$, etc.
represent isomers of the same ion.

Chemiionization Reactions

							A	n	E
C_2	+	OH	$\rightarrow$	CH^*	+	CO	3.4E+12	0	0
C_2H	+	O_2	$\rightarrow$	CH^*	+	CO_2	4.5E+15	0	105
CH^*			$\rightarrow$	CH			1.7E+06	0	0
CH^*	+	O	$\rightarrow$	HCO^+	+	e	4.8E+14	0	0

Ion–Molecule Reactions

								A	n	E
HCO^+	+	H_2O	$=$	H_3O^+	+	CO		1.9E+15	0	0
HCO^+	+	C_2H_2	$=$	C_2H_3	+	CO		8.1E+13	0.31	0
HCO^+	+	C_3H_4	$=$	$H_3C_3^+$	+	H_2	+ CO	8.1E+13	0.31	0
$C_3H_3^+$	+	M	$=$	$H_3C_3^+$	+	M		8.6E+13	0.31	0
$C_3H_3^+$	+	C_2H_2	$=$	$C_5H_2H^+$	+	H_2		8.6E+13	0.31	0
$C_3H_3^+$	+	C_4H_2	$=$	$C_5H_2H^+$	+	C_2H_2		7.3E+13	0.31	0
$C_5H_2H^+$	+	C_3H_4	$=$	$H_5C_6^+$	+	C_2H_2		9.5E+13	0.31	0
$C_{19}H_{11}^+$	+	C_2H_2	$=$	$C_{21}H_{11}^+$	+	H_2		1.3E+14	0.32	0
$C_{20}H_{11}^+$	+	C_2H_2	$=$	$C_{22}H_{13}^+$				1.3E+14	0.32	0
$C_{21}H_{11}^+$	+	C_2H_2	$=$	$C_{23}H_{13}H^+$				1.3E+14	0.32	0
$C_{22}H_{13}$	+	C_2H_2	$=$	$C_{24}H_{13}^+$	+	H_2		1.3E+14	0.33	0

Ion–Electron Recombination Reactions

							A	n	E
H_3O^+	+	e	$\rightarrow$	H_2O	+	H	1.3E+19	-0.5	0
HCO^+	+	e	$\rightarrow$	CO	+	H	7.4E+18	-0.68	0
$C_3H_3^+$	+	e	$\rightarrow$	C_2H_2	+	CH	1.1E+19	-0.5	0
$C_5H_2H^+$	+	e	$\rightarrow$	C_2H	+	C_3H_2	1.3E+19	-0.5	0
$C_{14}H_8H_3^+$	+	e	$\rightarrow$	$C_{14}H_{10}$	+	H	2.1E+19	-0.5	0
$C_{23}H_{13}^+$	+	e	$\rightarrow$	$C_{22}H_{12}$	+	CH	2.5E+19	-0.5	0

The Langevin equation accounts only for the number of collisions, it does not include collision efficiency. There is considerable evidence that the rate of ion–molecule reactions is directly proportional to the exothermicity of the reaction, $-\Delta H_r$, this is used in weighting the paths in a multi-path reaction.

One of the major problems in working with large ions is their identification; mass spectrometry gives mass only and the number of carbon and hydrogen atoms has been determined by the use of isotopes. Thus for a given molecular formula there can be several isomeric structures. We thus include isomers in the reaction scheme when their free energies of formation are close. Reactions are always written toward increasing molecular size; thus the free energy of reaction becomes more positive as the temperature is increased. The forward reaction rate coefficient is limited so that the reverse reaction never exceeds the Extended Langevin rate.

Ion–Electron Recombination: The ions disappear by either cation–electron or cation–anion dissociative recombination. Cation recombination rate coefficients with anions are about two orders of magnitude lower than with electrons. Further, anion concentrations which have been measured are about two orders of magnitude smaller than electron concentrations but there are no good measurements of electron or anion concentrations in sooting flames. There is, however, evidence for the presence of large anions in sooting flames. Anions are neglected for the present.

In choosing product channels for the large cation–electron dissociative recombination reactions, only molecules observed in sooting flames have been considered as products. Reaction rate coefficients for cation–electron reactions are not strongly temperature dependent, but do increase with the size of the ion.

The rate of ion recombination, α, is estimated by the equation for the rate of collision of electrons with particles:

$$\alpha = \frac{\pi d^2}{4} \left(\frac{8kT}{\pi m_e}\right)^{1/2} \left(1 + \frac{e^2}{(2\pi \varepsilon_0 d)kT}\right) \tag{4}$$

in which d = the ion diameter, m_e = the electron mass, and ε_0 = permittivity of free space. The ion diameters were calculated as described above. Equation (4) gives a $T^{-1/2}$ temperature dependence which compares favorably with experiments for H_3O^+. The values calculated by Eq. (4) were about twice the measured values, so the calculated values were divided by 2. If there is an error in our recombination rates it is probably on the high side.

EFFECTS OF NO_x REMOVAL WITH PULSE STREAMER. CORONA DISCHARGE

J. O. Chae*, G. Vasiliev[†], D. S. Han[‡], S. C. Chung[‡], Y. S. Jeong[‡]

*Dept. of Mech. Eng., Inha Univ., Inchon, Korea
[†]Inst., Heat and Mass Transfer, Minsk, Byelourussia
[‡]Dept. of Mech. Eng., Graduate school, Inha Univ., Inchon, Korea

It is very important to investigate the removal of the emission of air pollutants caused by the recent increase in energy demand, especially NO_x, which results from the combustion of fossil fuels and gives rise to the photochemical smog and acid rains destroying the ecosystem. Therefore, the advanced technologies of NO_x removal must be urgently developed. The advanced technology of Pulsed Streamer Corona (refer to as PSC) discharge removes air pollutants by a high voltage pulse and a corona discharge which forms a current channel of brushlike structure in the reactor.

In this study, this advanced technology was investigated as concerns the effects of NO_x removal and parametric screening studies. The PSC discharge used for aftertreatment is a possible candidate as an advanced technology for NO_x removal.

The results of this study are as follows:

1. The NO contained in streamer gases is converted to NO_2 by oxidation and is to be decomposed mainly to nitrogen and oxygen for NO_x removal.

2. The NO_x concentration is maintained at a lower value through higher input power, although it is drastically decreased with earlier power input, and there is an optimum point in terms of input power or residence time for NO_x removals depending on the NO concentration in mixture.

3. It is very efficient to increase the input frequency for NO_x removal, since NO concentration is decreased continuously with no change in NO_2 concentration in the streamer gas.

4. An addition of ammonia to the streamer gas enhances the rates of NO_x removal markedly.
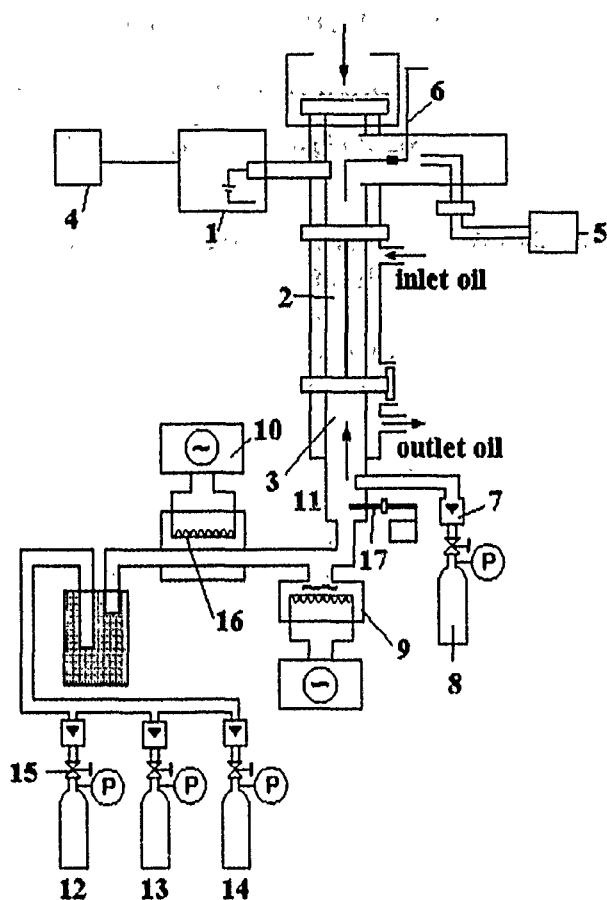
Figure 1: Schematic of experimental apparatus.

1.	PSC generator	7.	Flow meter	13.	O_2 gas bomb
2.	Reactor	8.	NH_3 gas bomb	14.	N_2 gas bomb
3.	Streamer gas	9.	Evaporator	15.	Regulator
4.	Oscilloscope	10.	Thermo-regulator	16.	Heating element
5.	NO_x analyzer	11.	Mixer	17.	Inlet temperature
6.	Outlet temperature	12.	NO gas bomb		

THE FORMATION OF NITROGEN OXIDES IN ATMOSPHERIC ELECTRIC DISCHARGES

Yu. A. Gostintsev, Yu. V, Gamera

Semenov Institute of Chemical Physics, Kosigin Str. 4, Moscow, 117977 Russia

The oxide and dioxide of nitrogen (generally known as the nitrogen oxides NO_x) are of vital importance in the chemistry of the atmosphere. They are among the troposphere components initiating photochemical smog formation. NO_x, along with the combinations of chlorides and hydrogen in the stratosphere, control the content of O_3 in the ozone layer of Earth. This necessitates a comprehensive study of the sources of NO_x.

The pattern of NO_x formation in a natural atmospheric lightning shown below is based on the kinetic scheme proposed by Ya. B. Zel'dovich for the shock wave caused by a linear spark discharge, modeled by the laws of instantaneous cylindrical explosion.

The principles of thermal nitrogen oxide formation in air are formulated in [1], the chain character of the process was established and, in the approximation of quasistationary concentrations of oxygen and nitrogen atoms, the kinetic equation of the process was obtained. For cooled or heated air, the equation is

$$\frac{d\xi}{d\varphi} = \frac{\tau_g}{\tau_c} \left\langle 1 - \left(\frac{\xi}{\varphi}\right)^2 \right\rangle. \tag{1}$$

Here, $\xi = \varphi C/(C)$, $(C) = K_1 \langle C_1 C_2 \rangle^{0.5} \varphi$, $\varphi = \exp(-\theta/T)$, $\tau_g = \langle d\ln\varphi/dt \rangle^{-1}$, and $\tau_c = \langle K_2 \varphi^n (C_1 \rho/\mu)^{0.5} \rangle^{-1}$; ρ, T, and μ are, respectively, the density, temperature and molecular mass of air; t is time; C, C_1, and C_2 are the molar fractions of NO, N_2, O_2; (C) is the equilibrium value of C; τ_g and τ_c are the characteristic times of temperature variation and chemical reaction (the sign of τ_g defines the direction of temperature variation $\tau_g > 0$ for heating, $\tau_g < 0$ for cooling); K_1, K_2, θ, and n are the Arrhenius parameters.

If the air density and temperature vary in accordance with the equation

$$\frac{d\ln|\rho^{0.5}\tau_g|}{d\ln\varphi} = \frac{1}{\alpha} - n = const,$$

then Eq. (1) is integrable in terms of modified cylindrical functions. For cooling, $\lim_{t\to\infty} \varphi \to 0$, and one can find the frozen concentration of oxide as $C_f = \lim_{\varphi\to 0} C$.

Analysis shows that, in the case of $\alpha^{-1} \leq 1$, $C_f = 0$ is possible. The physical implication of this result is that, under the conditions of the time of chemical transformation being much shorter than the characteristic time of the variation of gasdynamic parameters, the concentration of NO_x during the entire process remains close to equilibrium

and the freezing does not occur. If $\alpha^{-1} > 1$, then

$$\tilde{C}_f = (C_0)(0.5Z_0)^{-\alpha} \frac{\Gamma(1-\alpha')}{\Gamma(\alpha')} \frac{I_{-\alpha'}(Z_0)C_0 + I_{1-\alpha'}(Z_0)(C_1}{I_{\alpha'}(Z_0)C_0 + I_{\alpha'-1}(Z_0)(C_0)} \tag{2}$$
$$\alpha' = 0.5(1-\alpha); \qquad Z = \left| \frac{\alpha\tau_g}{\tau_c} \right|.$$

Here, $I_m(x)$ is the modified Bessel function, $\Gamma(x)$ is the gamma function.

In Eq. (2) and henceforth, suffix "0" refers to the initial values of the variables.

In the particular case of $\alpha = n^{-1} = 0.2$, the solution to Eq. (2) coincides with that obtained in [1, 2].

According to the views presented in [3, 4] and in line with the law of energy similarity of the shock wave of linear spark discharge to that of an instant cylindrical explosion [5], the cooling of a Lagrangian particle following the discharge in air is governed by the equations

$$\frac{T}{T_0} = 1 + \omega_1 \ln\left(\frac{t}{t_0}\right), \quad \frac{\rho}{\rho_0} = \left(\frac{t_0}{t}\right)^{2\omega}; \quad \omega_1 = 2\omega(\gamma - 1).$$

Here, $\rho_0 = \frac{\gamma+1}{\gamma-1}\rho_a$ and $T_0 = \frac{\mu(\gamma-1)}{2R(\gamma+1)^2 t_0}\left\langle\frac{\beta\varepsilon}{\rho_a}\right\rangle^{0.5} = \frac{\mu\beta E}{2R(\gamma+1)\rho_0 r^2}$ are the density and temperature at the shock wave front at the moment of time t_0 at the distance r from the symmetry axis, r is the Lagrangian coordinate, ρ_a is the density of undisturbed air, R is the universal gas constant, γ is the exponent of the Poisson adiabat; E is the energy density per unit length of the discharge, $\omega = \frac{\gamma+2}{(\gamma+1)^2}$, and β is a coefficient depending only on γ.

In this case,

$$Z_0 = \frac{K_2 \alpha \varphi_0^{\frac{1}{\alpha}}}{2R\theta\omega_1(\gamma+1)} \exp\left(\frac{\omega-1}{\omega_1}\right)\left\langle\frac{\beta E\mu(\gamma-1)C_1}{\omega_1(\gamma+1)}\right\rangle^{0.5}, \quad \alpha = \left\langle n - \frac{(1-\omega)}{\omega_1 \ln\varphi_0}\right\rangle^{-1}. \tag{3}$$

The accumulation of NO in lightnings is completely described by (2) and (3) at definite values of E, γ. As we can see from the above formulas, at $\omega < 1$ $(\gamma > 1)$, a critical radius exists, determined by the condition $\alpha = 1$. Within the volume $r \leq r_{cr}$, $C_f = 0$. Also, $C_f \to 0$ as $r \to \infty$.

Therefore, the characteristic distribution of $C_f(r)$ has a maximum C_f^* at any value of E.

We can take $E_s = 0.5$ MG/m to be the typical value of E for the pressure in the discharge 200 atm and the diameter of the channel 20 cm. If $E = E_s$ and γ is equal to 1.4, the total output of nitrogen oxides M_s, obtained by integrating $C_f(r)$ over the Lagrangian coordinate, is $M_s = 0.1$ mol/m, and the maximum NO_x concentration $C_{f_s}^* = 6.86 \cdot 10^{-2}$ is observed at the distance of 0.12 m from the symmetry axis. The average volume fraction in the discharge channel is equal to $5 \cdot 10^{-2}$, which is very close

23

to the experimentally detected amount of $4 \cdot 10^{-2}$, obtained using an electric-arc heater [6].

For γ reduced to 1.2 the maximum meaning of $C_{f_s}^*$ is lower only by 6.4%. Thus, the possible "dustiness" of the air, while reducing the value of γ [4], does not affect $C_{f_s}^*$ very much. We can observe a different picture in the dependence of the total output M_s on γ. With decreasing γ, the value of M_s falls sharply. For examples for $\gamma = 1.2$ $M_s = 0.027$ mol/m.

The quantities C_f and M are modelled by scaling with the energy E per unit length, different from E_s:

$$C_f^* = C_{f_s}^* \left\langle \frac{E_s}{E} \right\rangle^{0.1}, \qquad M = M_s \left\langle \frac{E}{E_s} \right\rangle^{0.9} \left[1 + 0.03 \ln \left(\frac{E}{E_s} \right) \right].$$

For the average lightning length about 5 km, the output of nitrogen oxides is 0.5 kmol/lightning ($\gamma = 1.4$, $E = E_s$).

Approximately 100 lightnings occur on Earth every second [7], which results in global production rate of nitrogen oxides 50 MT NO per year. Comparing this with the results of research of NO_x formation in powerful air explosions [8], we can conclude that every hour thunderstorms add to the troposphere approximately the same amount of NO_x as a megatonne nuclear explosion.

References

[1] Zel'dovich Ya. B., Sadovnikov P. Ya. Frank-Kamenetskii D. A. *The Nitrogen Oxidation in Burning*. Moscow, Publishing House of Academy of Sciences of USSR, 1947 (in Russian).

[2] Klyachko B. S. *Dokl. Akad. Nauk USSR*, 1987, **236**, 3, 661 (in Russian).

[3] Raizer Yu. P. *Zhurnal Fizicheskoi Khimii*, 1959, **33**, 3, 700 (in Russian).

[4] Sedov L. I. *The Methods of Similarity and Dimensionality in Mechanics*. Moscow, Nauka Publ., 1981 (in Russian).

[5] Askaryan G. A., Rabinovich M. C., Savchenko M. M., Stepanov V. K. *Pis'ma Zh. Exp. Tekhn. Fiz.*, 1967, **5**, 5, 150 (in Russian).

[6] Orth R. C., Billig F. S., Grenlevsky P. *Progress in Aeron. and Astron.*, 1972, 34.

[7] Brimblcumb P. *The Structure and Chemistry of the Atmosphere*. Moscow, Mir, 1988 (in Russian).

[8] Gostintsev Yu. A., Gamera Yu. V. *Khimicheskaya Fizika*, 1994, **13**, 2, 114 (in Russian).

THE EFFECT OF LIGHT ON THE VELOCITY OF FLAME PROPAGATION IN SYSTEMS CONTAINING CHLORINE

O. L. Gromovenko, I. R. Begishev

Higher Technical School of Firefighting Engineering, Moscow, Russia

Combustible gas mixtures containing chlorine can ignite under exposure to light. The influence of light intensity on the concentration range of photothermal ignition of 1,1-difluoroethane–chlorine and dichloromethane–chlorine mixtures was studied in [1, 2].

The dependence of flame propagation velocities in Cl_2–H_2 and ClF–Cl_2–H_2 mixtures at low pressures on the degree of preliminary chlorine photodissociation under the action of short UV pulses was determined in [3].

In chlorine-containing combustible systems at atmospheric pressure, the rate of formation of the initial centers of reaction (chlorine atoms) decreases sharply along the direction of the light beam, due to light absorption. The ignition occurs in the vicinity of the light source, and then a flame spreads over the whole mixture. The transparency of the reacting medium increases as chlorine burns out. This leads to the growth of photoinitiation rate ahead of the zone of chemical reactions. Under the continuous action of the light flux, its influence on combustion characteristics can be detected at a considerable distance from the light source. In this work, we examine the process of flame propagation in chlorine–difluoromethane and chlorine–hydrogen under the continuous action of light.

Experimental Procedure

The studies of ignition and flame propagation were conducted in steel reaction vessels 0.051 m in diameter with lengths ranging from 0.55 to 1.0 m, positioned horizontally. The initial mixtures in the vessel had the atmospheric pressure and room temperature. The light from a DRT–1000 mercury lamp was let into the vessel through a quartz window at one of its ends. The maximum intensity of the light flux was $2 \cdot 10^{21}$ quantum $m^{-2}s^{-1}$. At the same vessel end, ignition was performed by a red-hot Ni–Cr wire. The temperature regime of the process was monitored using eight tungsten–rhenium thermocouples 20 mm in diameter. The thermocouples were positioned along the cylinder axis at various distances from the quartz window. The thermocouple output signals were fed into a PEVM EC–1840 computer, where they were processed to obtain the dependence $T = f(t)$. The times at which flame reached the thermocouples were determined by the sharp increase in the temperature.
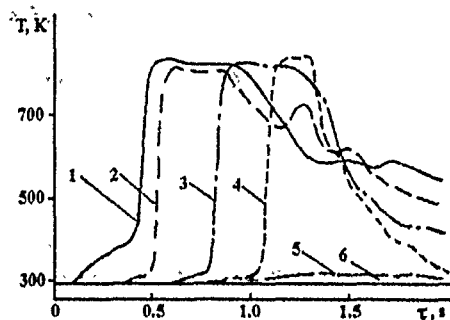
Figure 1: Variation in temperature of CF_2H_2–Cl_2 mixture (67%:33%) at the points with the following coordinates: (1) 0.027 m; (2) 0.1 m; (3) 0.23 m; (4) 0.3 m; (5) 0.38 m; (6) 0.454 m.

Results

The experiments with difluoromethane were carried out in a tube 1 m long at concentrations ranging from 13.5 to 66% vol. The apparent velocity of flame propagation changed along the length of the reaction vessel. The maximum values were observed at 0.1–0.3 m from the reactor end. As combustion spread over the bulk of the mixture, its rate decreased, and the apparent velocity reached a constant value at the distance of 0.8–0.85 m. The flame speed and its temperature depended on the mixture composition. The maximum values were recorded for the stoichiometric mixture (33.3%), $V \sim 10$ m/s and $T = 1300$ K, the minimum values corresponding to the limiting mixtures were 0.25 m/s and 900 K, respectively.

A substantial influence of light on the flame velocity was found for mixtures close to the rich flammability limit. When the mixture of 66% CF_2H_2 and 34% Cl_2 was ignited by light, the flame velocity was maximum near the ignition end of the reactor and equal to 1.12 m/s. When the mixture was ignited by the red-hot metal wire the maximum flame velocity was also observed in this part of the reactor, but its numerical value differed by more than two times and was 0.53 m/s. In determining the rich flammability limit, we found that, under exposure to light, in the mixtures beyond this limit (66–67%), the ignitiondriven wave propagated over a certain distance from the ignition end of the reactor. The temperature profiles for such a mixture at various locations along the reactor axis are given in Fig. 1. We can see that the flame propagation is detected sequentially by four thermocouples, the last of which is positioned at the distance of 0.3 m, and the next thermocouple indicates only a 15 K increase in temperature.

The influence of light on the velocity of flame propagation in chlorine–hydrogen mixtures is most pronounced in the vicinity of the rich flammability limit. The experi-
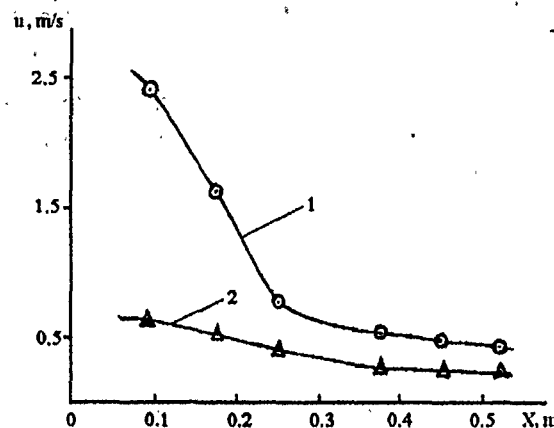
Figure 2: Variation in apparent flame velocity in H_2–Cl_2 mixture (87% : 13%) versus the length of the reactor at the ignition: (1) by light; (2) by red-hot wire.

ments were conducted in a reaction vessel 0.55 m long. The rich limit was found to be 87.5% vol. As is seen in Fig. 2, the flame velocity at all measurement locations is higher under the exposure to light. In this case, the flame velocity at 0.1 m from the ignition end of the reactor is almost four times higher than that in the experiments with ignition by the red-hot wire. At hydrogen concentrations ranging from 87.5 to 89%, flame propagation over 0.3–0.38 m was observed only under the action of continuous light flux.

Discussion and Conclusions

Thus, in chlorine-containing systems the light affects the flame propagation velocity near the rich flammability limit. This can be attributed to the following. First, the decrease in the rate of photoinitiation with the length of the reaction vessel occurs more smoothly in mixtures with lower chlorine content. Secondly, in such systems, as a rule, complete combustion of chlorine takes place, and, therefore, the reacted mixture becomes more transparent at the wave bands of light absorption by chlorine. Thirdly, it is very important that, under the conditions of the experiments, the calculated rates of chlorine atom formation due to thermal and photochemical dissociation are of the same order at temperatures 800–900 K. These are precisely the temperatures typical for premixed flame close to the flammability limit.

References

[1] Begishev I. R., Poluektov V. A. Belikov A. K., *et al.* In: *Kinetics of Chemical Reactions, Proc. 9th All-Union Symp. on Combustion and Explosion*, Chernogolovka, 1989, 12–15 (in Russian).

[2] Begishev I. R., Belikov A. K., Nechitailo V. G., *Fizika Goreniya Vzriva*, 1991, **27**, 2, 21–25 (in Russian).

[3] Suetinov A. P., Moskvin Yu. L. In: *Combustion of Heterogeneous and Gaseous Systems, Proc. 8th All-Union Symp. on Combustion and Explosion*, Chernogolovka, 1986, 3–5 (in Russian).

NEW ECOLOGY ENGINES: A RESULT OF THE ZEL'DOVICH MECHANISM

H. Heitland*, G. Rinne[†], K. Wislocki[†]

Heitech-Engenieurbüro, Wolfsburg, Germany
[†]*Poznan Politechnical Institute, Poland*

State of the Art and Further Development

In today's urban traffic, passenger cars are driven mostly at part load. Even the best engines, such as diesel engines, are characterized at part loads by specific fuel consumption at least twice as high as the minimum at its best point. Only for this reason, hybrid-drive systems combining at least two different principles have a chance. For example, the Electro–Diesel–Hybrid runs at part load with the electric engine at a much better efficiency than the diesel engine, which takes over at higher loads. The development of engines with hybrid combustion systems, such as stratified charge engines, was given up too early when the cars were equipped with 3-way catalysts on Otto engines or supercharged Diesel engines. With new combustion systems, a better consumption and cleaner exhaust gas can be jbtained, as compared with combustion in modern engines. Spontaneous combustion should take place in the bulk of the residual hot exhaust gases, which can be implemented best in two-stroke engines. Only that portion of the burnt gas should be removed out of the cylinder which is equivalent to the newly burnt charge. It seems to be possible to avoid any kind of afterburners in order to save costs.

Prescription of the Mixture Exhaust Stratified Charge (MESC) Ecology Engine (Fig. 1)

In order to avoid the aforementioned disadvantages of the known engines, we have developed a new working procedure for a two-stroke engine, applied for German and US patents, and started our research.

The working cycle includes the following steps:
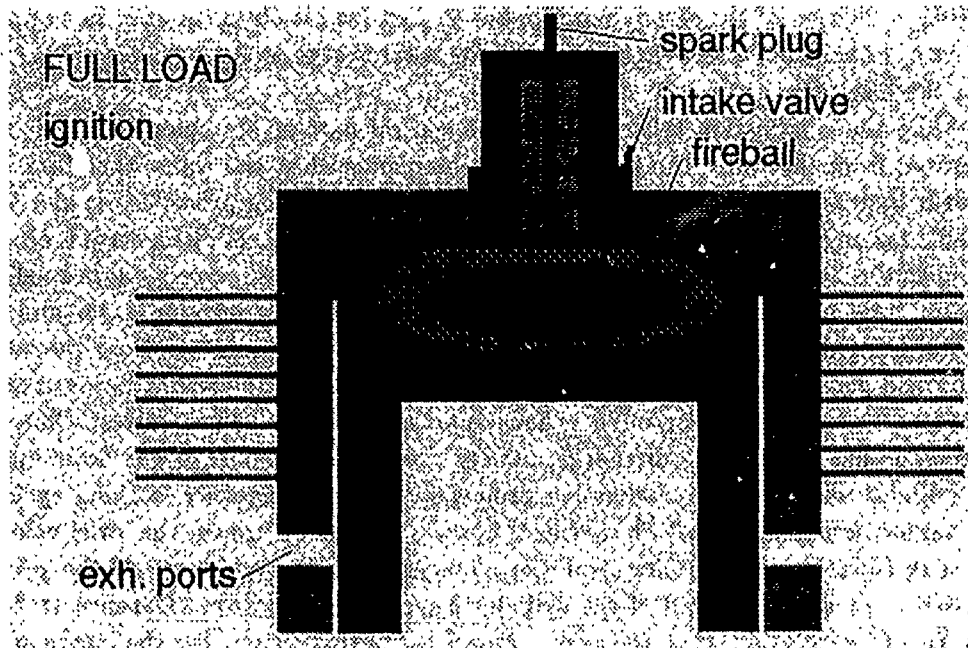
Figure 1: Principle of the MESC–engine.

(1) compression of the burned gases remaining in the cylinder,

(2) intake of a combustible air-fuel mixture into a limited zone of the combustion chamber, where the mixing of the air-fuel mixture and the burned gas will be minimized,

(3) ignition of the combustible air-fuel mixture in the limited zone of the combustion chamber,

(4) controlled rapid combustion in a fireball,

(5) expansion of the in-cylinder charge, and

(6) controlled discharge of a given burned gas quantity which equals the burned gas quantity produced by the combustion of the air-fuel mixture introduced into the cylinder in the next cycle.

After the discharge, the residual burned gases remain in the cylinder and will be compressed. A very lean combustible fuel–air mixture will be brought into these residuals, where only after combustion the mixing process should take place, in order to obtain a very low emission of nitrogen oxides. After the expansion of the in-cylinder charge only the amount of burned gas to be discharged is equal to that formed in the following cycle by the combustion of the air-fuel mixture brought into the cylinder, and

a strong reduction of the aerodynamic losses at part load is obtained even in comparison with unthrottled diesel engines, where the total charge in the cylinder always has to be discharged.

While the combustion takes place in the central part of the cylinder and is well separated from the walls, the flame cannot be quenched at the walls; therefore, less unburnt hydrocarbons remain in the burned gas. The working procedure is also very suitable for engine operation with self-ignition and for the use of alternative fuels. To minimize the mixing process between the air-fuel mixture and the residual burned gas layer, as well as the undesirable mixing process between the burning gases and the residual burned gas during the expansion, separation of the mixture from the residual burned gases is achieved by aerodynamic means, such as the swirl motion created by means of tangentially oriented exhaust ports or shrouded inlet valves. Thus, it is secured that, during the discharge, mainly the previously burned gas flows out of the cylinder and the new combustion products remain for another working cycle in the combustion chamber. With a central bowl in the piston crown, the swirl velocity increases (due to a squish effect) at the moment when the periphery of the piston, together with the inner wall of the cylinder head, forms a narrow clearance at TDC (Top Dead Center) and when the gas is pressed out of this region. For the intake of the air-fuel mixture, many different procedures exist. The favoured working procedure is the use of air-blast nozzles as a source of pulsed jet combustion (as proposed by A. K. Oppenheim), which has already been successfully tested in a combustion bomb.

Computer Model of the NO Production Using the Zel'dovich Mechanism (Figs. 1–4)

For the MESC engine (Fig. 1) having the effective compression ratio of 10 and a tisplacement volume of 1 liter, a computer model was developed. In the model, the engine process was simulated with a very lean methane/air mixture blown into the cylinder late in the compression stroke, ignited by the spark plug at a crank angle of 30 °C before TDC and burned completely in a centrally located fireball at 25 °C after TDC, and subsequent mixing. Assuming a linear burning rate and neglecting the heat released in combustion of the dissociated products O, N and the NO formed in the burned gas, the temperature–time (Fig. 2) and the pressure–volume (Fig. 3) diagrams were calculated for three different loads and air/fuel equivalence ratios. Fig. 2 shows that with the air/fuel equivalence ratio of 2.1, the temperatures in the fireball always remain below 2500 °C and in the rest of the burned gas below 700 °C. The integration of the pressure curves of Fig. 3, combined with the data of the ideal process, where combustion takes place instantaneously at TDC, yields the internal efficiencies and the mean effective pressure. The internal efficiency is highest at part load and drops to the normal values characteristic of common spark-ignition engines at full load, which clearly shows the part-load advantage of the MESC engines as compared with the modern engines. The load is controlled by the amount of the fuel/air mixture fed into

air-fuel ratio 2.1
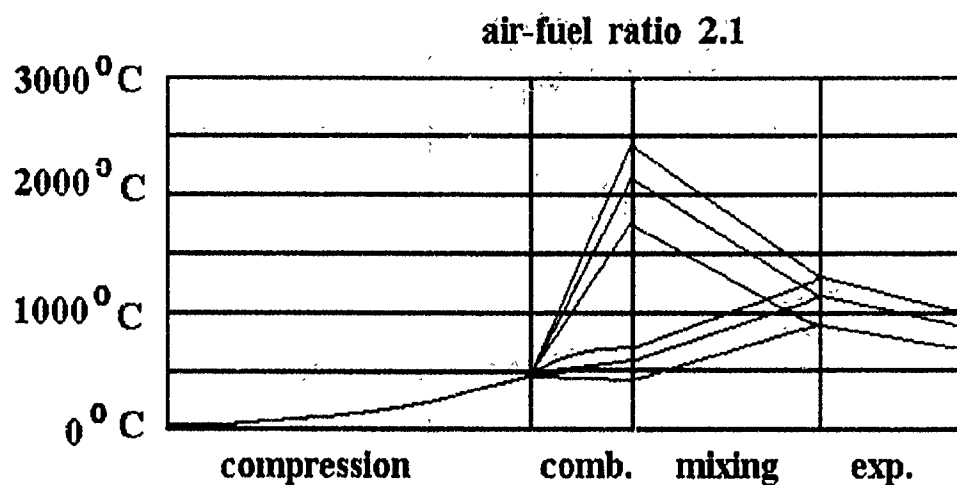
Figure 2: Temperature–time diagram.
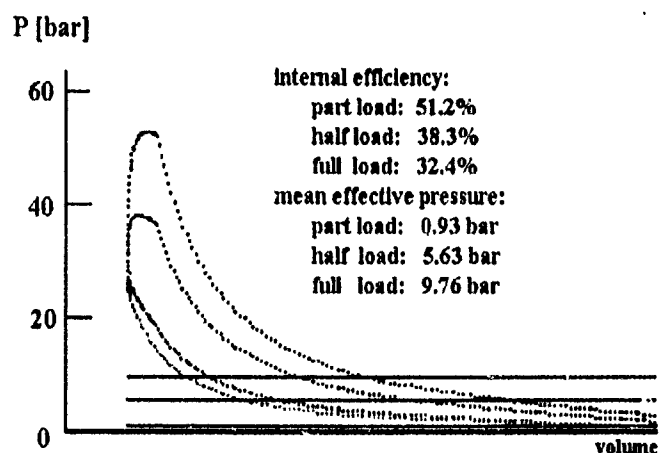
Figure 3: Pressure–volume diagram.

| Internal efficiency:		Mean effective pressure:	
part load:	51.2%	part load:	0.93 bar
half load:	38.3%	half load:	5.63 bar
full load:	32.4%	full load:	9.76 bar
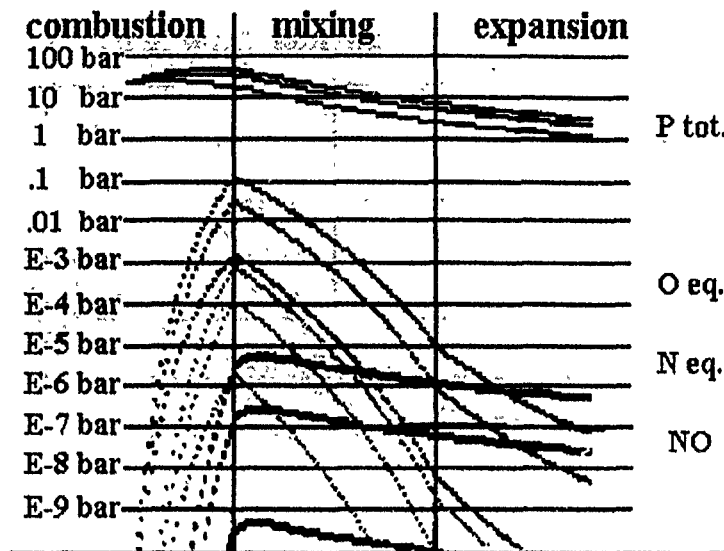
Figure 4: Partial pressure–time diagram.

the combustion chamber. The model is based on the Zel'dovich mechanism for the formation of nitrogen monoxide in the exhaust gas

$$N_2 + O \rightarrow NO + N \quad \text{and} \quad O_2 + N \rightarrow NO + O$$
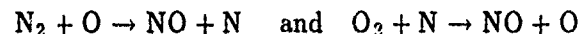
starting with the reactions for dissociation of $O_2 \rightarrow 2O$ and $N_2 \rightarrow 2N$ at chemical equilibrium and using the formula $k_f = A T^n \exp\left(-E/R_m T\right)$ for the reaction rates with the units kcal, m, s and K. It has been shown that only in the fireball the temperature was sufficiently high to result in any appreciable concentration of nitrogen monoxide. Calculations for leaner mixtures (of air/fuel relative ratios greater than 2), where the maximum cycle temperatures were below 2500 °C, also gave no indication of the formation of any substantial amount of NO. But the richer mixture of relative air/fuel ratio of 1.6 increased the NO concentration by the factor of 100. As the curves in Fig. 4 indicate, the formation of NO is very sensitive not only to temperature but also to pressure. Therefore, at full load the partial pressure increased by the factor of 10, as compared with half load, and the factor of 1000, as compared with idling. In order to verify these results, more detailed information was obtained from a computer simulation program for combustion in a bomb. With these encouraging theoretical results **the future ecology engines should**

- **be built as cheap two-stroke stratified charge engines without catalytic converters,**

- start with the engine design for part-load behavior and not for full load,

- work always with a very lean air/fuel mixture with its relative ratio around 2,

- employ pulsed air-blast systems for fireball combustion in the midst of the cylinder, and

- discharge only the amount of burned gas formed during single combustion cycle.

A STUDY OF SPATIAL DEVELOPMENT OF CHAIN BRANCHING PROCESS BY MEANS OF HIGH-SPEED SCHLIEREN CINEMATOGRAPHY

V. P. Karpov, N. M. Rubtsov, O. T. Ryzhkov, S. M. Temchin,
V. I. Chernysh, V. V. Azatyan

Semenov Institute of Chemical Physics, Moscow, Russia
Institute of Structural Macrokinetics, Chernogolovka, Russia

The wide application of SiO_2 thin films deposited by LPCVD method [1] in integrated circuits (IC) processing evokes an increasing interest to silane oxidation processes. It is important, in particular, to develop methods of SiO_2 aerosol detection, because the presence of its particles reduces the output of ICs in technological processes. In this connection, the information on spatial development of relevant chain branching reactions is quite necessary. It is well known that the self-ignition of silane–oxygen mixtures originates on the reactor surface. This phenomenon is due to the fact that heterogeneous chain branching plays an important role in the oxidation mechanism [2]. Furthermore, the ignition originating on the reactor walls can spread into the volume even under the conditions of dominant role played by heterogeneous chain termination. In addition, there has been no information on direct cinematography of chain self-ignition. This work elucidates some of the questions mentioned.

In the present work, both forced and spontaneous ignition of dichlorosilane (DCS) – oxygen mixtures were studied by high-speed schlieren cinematography over the temperature range of 298–373 K. Heated steel or quartz reactors of cylindrical shape with
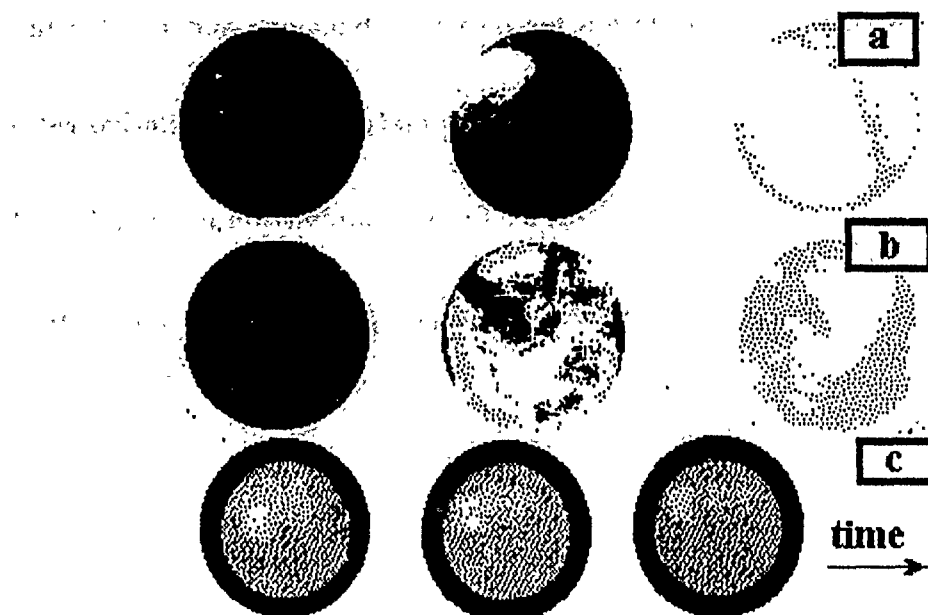
Figure 1: Cinematography of self-ignition in dichlorosilane–oxygen mixtures ($P = 7$ Torr (a), 8 Torr (b)); the behavior of prism images with self-ignition (c), $P = 7$ Torr. $T = 373$ K, $(SiH_2Cl_2) = 25\%$, $P_I = 5.5$ Torr, 1000 frames/s.

the diameters of 10 and 4 cm, respectively, had inlets for electrical power supply and gas evacuation, as well as optical windows. In a number of experiments the instrumental cell consisting of two copper plates was inside the 10-cm reactor. Constant electrical field of intensity up to 200 V/cm was applied between the plates (without glow discharge).

The results of two tuns of filming of self-ignition by schlieren cinematography are shown in Fig. 1(a–b). The induction periods are 1 s (a) and 1.2 s (b). One can see that, according to the equation $\tau = x^2/2D$, a 2 cm thick mixture layer is heated up to the surface temperature in 0.1 s (τ is the characteristic heating time, x is the characteristic dimension, and D is the mass diffusivity which is close to the thermal diffusivity). Nevertheless, the self-ignition originates on the reactor surface either locally (a) or uniformly over the surface, including the reactor butt-ends (b). The different regimes of chain ignition development appear to depend on the state of the surface before ignition. The dependence of the induction periods on the evacuation depth also indicates the increase in the surface influence with the evacuation depth, leading to an induction period of 4 s. The above-mentioned phenomena would not occur in the case of ignition by a heated surface. Thus, the active role of surface in self-ignition is due to the reactions of adsorbed atoms and radicals participating in chain propagation.

The direct cinematography of self-ignition development was carried out using streak photography in the 4-cm reactor. For $P = 6$ Torr, [DCS] = 20% the induction period

was 3.5 s at 373 K. Based on the above equation for τ, the heating time of the reactor volume is estimated at 0.25 s, i.e., during the induction period the heating of mixtures is completed. It has been shown that in this case self-ignition also originates on the reactor surface. Then the ignition spreads across the volume and turns to oscillations. One can also see, based on the estimated value of $\tau = x^2/2D$, that the heat released would not be dissipated on the reactor surface during the self-ignition. On the other hand, the aerosol formation can cause a decrease in the value x. Thus, the oscillations observed must be isothermic.

It has been revealed that, at the final stage of ignition in either regime, images of the rectangular window of the camera prism are recorded in the schlieren frames of the reactor. These images vary in location and brightness during about 1 s and then disappear (Fig. 1c). It has been shown that the images of SiO_2 aerosol clouds emerging just after ignition give rise to this phenomenon. Thus, the schlieren technique is highly suitable for studying heterophase chain processes.

In the following experiments the instrumental cell with 200 V/cm applied was located in the reactor. It has been shown that if the field was applied before self-ignition, then the prism images would completely disappear. This implies that the field applied has an influence on the formation of the new phase. This phenomenon also indicates charged particles formation in DCS oxidation and, therefore, corresponds to the changes in conductivity observed in this process [3]. Thus, it has been shown that the application of a constant electrical field (without glow discharge) eliminates undesired SiO_2 aerosol from the reactor volume during self-ignition of silane–oxygen mixtures.

It has been shown that 30% SF_6 added to the initial DCS (5% in oxygen) also reduces the amount of SiO_2 aerosol formed. Furthermore, the SF_6 addition results in substantial decrease in both flame propagation velocity and the lower limit of self-ignition. (The value of this limit is 1.5 times higher than without SF_6 in 5% DCS in oxygen). It is generally known that SF_6 molecules slowly react with atoms and radicals under the conditions studied here. The first vibrational level of SF_6 is too low to be of importance in V–V energy exchange processes. Thus, the SF_6 molecules interact rapidly with the charged particles (e.g. free electrons) formed in DCS oxidation. Hence, the charged particles do play an important role in the ignition of silanes.

This work has been supported by the Russian Foundation for Fundamental Research.

References

[1] Chapple-Sokol J. D., Gordon R. G. *Thin Sol. Films.* 1989, **171**, 291.

[2] Azatyan V. V., Aivazyan R. G. *Kinetika Kataliz*, 1986, **27**, 5, 1086 (in Russian).

[3] Azatyan V. V., Lukashov A. S., Nagorny S. S., Rubtsov N. M. *et al. Kinetika Kataliz*, 1993, **34**, 3, 404 (in Russian).

THE KINETICS OF CHEMICAL REACTIONS IN PHYSICO-CHEMICAL WAVES

B. N. Kondrikov

Mendeleev University of Chemical Technology
Miusskaya Sq. 9, Moscow, A-190 Russia

The main result of this work is the evaluation of the general dependences associated with the influence of high temperatures, ultra-high pressures, high reactant concentrations, and rapid variations in these parameters on the kinetics and mechanisms of chemical reactions in physico-chemical waves, mainly in deflagration and detonation waves. The hypothesis that was examined and supported is as follows: irrespective of any specific features of the physico-chemical waves considered, there are regions of conditions in the waves, where the rates and mechanisms of chemical reactions depend primarily on the values of thermodynamic parameters and concentrations but do not depend on their gradients and time derivatives, and thus the reaction rate is a special kind of a function of state.

The data published in the literature are rather contradictory. On the one hand, we have the evidence that the hypothesis formulated above is valid in a certain (though, sometimes rather broad) region of the conditions in deflagration and detonation waves. Sometimes, simple extrapolation of regular kinetic data to the (P, V, T) conditions in the reaction zone of the wave provides a very good correlation between the extrapolated and experimental reaction rates. On the other hand, in many works quantum mechanical and Monte-Carlo computations have been used to show that the actual state of the reactants in the wave is substantially more complicated than it is usually assumed, and that the reactions in the wave are characterized by more complicated specific mechanisms and kinetic functions than we commonly believe they are. The last point is corroborated by numerous examples of strong distinction between the reaction rates and mechanisms in the waves and under the conditions commonly encountered in measurements.

At the end of the 70s, we discovered the existence of a strong catalytic effect of very low content (up to 0.02%) of additives on the decomposition of nitromethane in a detonation wave by measuring the limiting diameter of the high-velocity detonation (HVD) [1]. A further progress in the investigations led us to the conclusion that many decomposition reactions of nitrocompounds in HVD waves can be strongly accelerated by additives of both basic and acidic nature. The chain-reaction mechanism explaining these facts was proposed by Ya. B. Zel'dovich. It has also been shown that nonsaturated organic compounds can play the role of catalysts promoting the oxidation and decomposition reactions in HVD waves [2]. All the data obtained could be quantitatively explained by conventional chemical kinetic relationships.

At the end of the 80s, we recalculated the kinetic constants of HVD decomposition and oxidation reactions of nitromethane, ethylene glycol dinitrate, nitroglycerin and trinitrotoluene using the precise dependences of the HVD limiting diameter on the initial temperature. The kinetic constants for the first three compounds have been shown to reasonably agree with the data obtained at low and moderate pressures. The rate of trinitrotoluene decomposition reaction under HVD conditions turned out to be 300 times higher than the reaction rate at ~ 1 atm [3].

Quite recently, we conducted a comparative study of reactions in the mixtures of polynitrocompounds with sulphuric and nitric acids under the conditions of conventional kinetic measurements and HVD waves. The mechanisms of the reactions have been found to be somewhat different, but a strong correlation between them has been shown to exist [3].

A little earlier, reactions of water solutions of organic salts of perchloric acid were investigated in this laboratory in low- and high-velocity detonation (LVD and HVD) waves, as well as in a strong electric discharge. The solutions have been shown to react very rapidly at the relatively low pressure of LVD. The reaction rate and its kinetic constants were estimated [4]. The reaction rates in LVD waves and in the electric discharges are abnormally high (the activation energy, 58 kJ/mole, is the lowest of all the explosives studied). The reaction rate at the HVD pressure, in contrast to the data just mentioned, is unusually small, so that without certain catalytic additives the HVD does not propagate. It is interesting to note that the solutions of perchloric acid salts under LVD conditions also retain the capability of being catalyzed by small additives of metal ions. It is a relatively rare example of LVD catalytic reactions.

A new method of measurement of the kinetic parameters of chemical conversion in detonation was developed recently in our works [5]. Detonation of nearly homogeneous charges of solid and liquid substances near the failure diameter is accompanied by spin waves propagating along helical paths on the cylinder surface. The spin pitch depends on the detonation velocity of the charge and the activation energy of chemical reaction. The results obtained for trinitrotoluene containing 15% RDX show that the activation energy derived from the experimental data by this method coincides with the value computed from the failure diameter versus initial temperature dependence mentioned above.

Some of the results obtained have not been given any conclusive explanation to the present time.

It is well known that many organic substances in the solid crystalline state decompose by a factor of a few tens slower than in the liquid or gas phase. The state of solids, liquids and gases in strong shock or detonation waves is usually considered to be that of molecular crystal, where the molecules occupy the sites and interact with each other as if they are the centres of a tightly packed crystalline lattice. However, all detonating explosives behave kinetically as if they consist of liquid rather than solid reactants.

The influence of static pressure on the decomposition rates of certain nitrocompounds was investigated. Some of them, such as nitroparaffines with α-hydrogen atom,

exhibited strong dependences of the rates on pressure presumably due to the aci-ion formation. However, nitromethane, which is the main representative of these compounds, does not seem to comply with the conclusion. In fact, the kinetic constants of the substance do not exhibit any pressure effect under detonation conditions. At the same time, the decomposition of trinitrotoluene (see above) is strongly accelerated when the substance is compressed in a detonation wave for diameters near the failure conditions.

A phenomenon of special interest is the formation of diamonds in the reaction zones of detonation waves. Some investigators attribute it to the stepwise variation in the slope of $D(\rho_0)$ curves for carbon-rich substances. Our data do not agree with this suggestion.

References

[1] Kondrikov B. N. *et al. Dokl. Akad. Nauk SSSR*, 1977, **233**, 3, 402 (in Russian).

[2] Kondrikov B. N. In: *Progress in Astronautics and Aeronautics*, 1983, **87**, 426.

[3] Gamezo V. N. *PhD (CS) Thesis*, MUCHT, 1993 (in Russian).

[4] Kondrikov B. N.*et al. Fizika Goreniya Vzriva*, 1988, **24**, 3, 75 (in Russian).

[5] Kozak G. D., Kondrikov B. N., Oblomsky V. B. *ibid*, 1989, **25**, 4, 459; 1992, **28**, 2, 195 (in Russian).

KINETICS AND MECHANISM OF SOOT FORMATION FROM METHANE

A. V. Krestinin

Institute of Chemical Physics in Chernogolovka, Chernogolovka, Russia

Introduction

Two main hypothetical mechanisms of the soot particle nucleation are discussed in the current literature. The first one [1] is based on the assumption concerning the

formation of soot particles by chemical coagulation of sufficiently large molecules of polyaromatic hydrocarbons. This hypothesis requires no knowledge about the soot nucleus. The other one assumes that a soot nucleus is first formed and it grows to become a soot particle [2]. An idea was also forward that the decisive contribution to the formation of a soot nucleus is due to the reactions of higher polyenes formed in abundance in the soot formation zone [3].

The hypothesis about the formation of soot nuclei from higher polyenes was taken as a basis for the numerical model developed earlier [4], which made it possible to calculate the kinetics of pyrolysis and to obtain the key kinetic characteristics of soot formation from acetylene, including the induction period τ, the final number density of soot particles N_{total}, the rate of heterogeneous surface growth and the rate of nucleation J. These numerical results adequately reproduce the experimental data [5, 6]. The present paper reports the numerical results obtained within the framework of this model for pyrolysis and soot formation from methane.

Description of the Model

Gas-phase reactions of the model include the scheme of methane thermal decomposition [7] and the formation of polyenes [8]. The main path of this process can be represented by the following scheme:

$$CH_4 \xrightarrow{-H} CH_3 + CH_3 \longrightarrow C_2H_5 \xrightarrow{-H} C_2H_4 + H \xrightarrow{-H_?} C_2H_3 \xrightarrow{-H}$$

$$C_2H_2 + C_2H \xrightarrow{-H} C_4H_2 + C_2H \longrightarrow \ldots C_{2n}H_2 + C_2H \xrightarrow{-H} C_{2n+2}H_2 \ldots \qquad n = 3, 4, \ldots$$
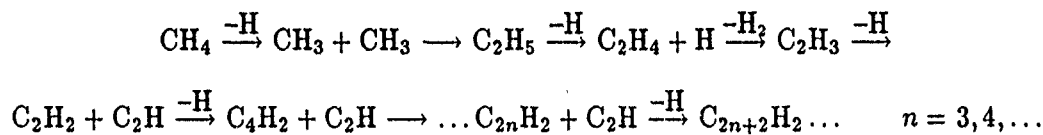
It is supposed that all gaseous components take part in the surface growth of soot particles and that the rate constant of the heterogeneous reactions do not depend on the particle size. The formation of a soot nucleus (Z) is simulated by the reactions which involve higher polyenes:

$$C_{14}H_2 + C_{2n}H_2 \longrightarrow Z, \qquad n = 5\text{-}7.$$
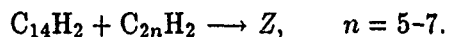
The description assumed implies [5] that

(a) sufficiently large polyyne molecules react easily with each other, which results in formation of a soot nucleus,

(b) this process is irreversible, and

(c) the polyenes provide a decisive contribution to the surface growth of the particles themselves during massive nuclei formation.

The set of equations of the model includes conservation equations for all chemical components of the gas and soot particles, as well as an equation for the mean diameter
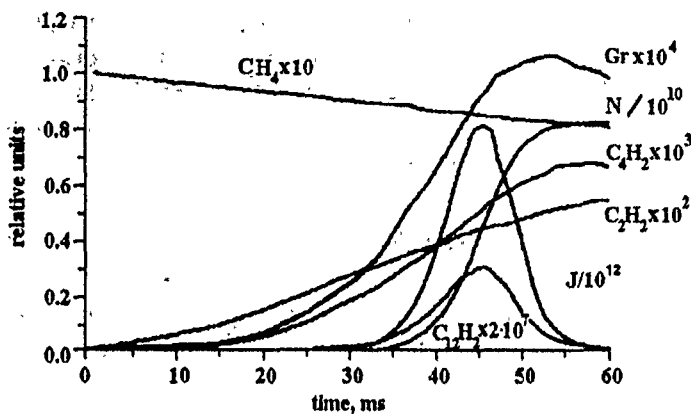
Figure 1: Thermal decay of methane. Calculation for the mixture 10% CH_4 in He, 10^5 Pa, 1573 K. Concentration of species in mole fractions, $[M] = 7.65 \cdot 10^{-6}$ mol/cm^3. Concentration of soot particles N in cm^{-3}, rate of nucleation J in cm^{-3}s^{-1}, Gr is the growth rate in g·cm^{-2}s^{-1}.

of particles:

$$\frac{d[X_i]}{dt} = \text{contribution of homogeneous reactions} + \text{contribution of heterogeneous reactions}$$

$$\frac{dN}{dt} = J, \qquad \langle d \rangle = N^{-1} \int\limits_0^t J(s)ds \left[\int\limits_s^t w(u)du + d_0 \right],$$

where $[X_i]$ denotes the concentration of the gaseous component X_i, mole/cm^3; J is the rate of nucleation, mole/cm^3/s; d_0 is the soot nucleus diameter, cm; $w(t)$ is the growth rate of an individual particle, cm/s.

Coagulation of soot particles is not taken into account in this numerical implementation of the model. Evaluation of the numerical results showed [5] that the error in the calculation of the soot surface area due to neglecting coagulation does not exceed 20–30% at temperatures below 1800–2000 K.

Numerical Results

Figure 1 shows the structure of the soot formation process during methane pyrolysis. The key features of the process are the following:

(1) formation of new soot nuclei occurs in an explosive manner at the end of the induction period during which acetylene and higher polyenes are accumulating; concentrations of polyenes reach at this time their maxima and then decrease;

(2) during the nucleation and immediately after it, the rapid surface growth of soot particles continues, mainly due to the contribution of heterogeneous destruction of polyenes.

Computations yield the following expressions for the basic kinetic parameters of the pyrolysis (10^5 Pa, 20% CH_4/He):

		Calculation:	Experiment [9]:
N_{total}	(cm^{-3})	: $1.5 \cdot 10^{22} \exp\left(-\frac{44500}{T}\right)$	$4.0 \cdot 10^{20} \exp\left(-\frac{40500}{T}\right)$
J	$(cm^{-3}s^{-1})$	: $1.1 \cdot 10^{32} \exp\left(-\frac{73000}{T}\right)$	—
τ	(s)	: $3.9 \cdot 10^{-9} \exp\left(\frac{32500}{T}\right)$	—

Conclusions

The quantitative non-empirical model, based on the idea of soot particles nucleation from polyenes and tested earlier by simulation of soot formation process from acetylene, is generally confirmed by results of simulation of thermal methane decomposition.

References

[1] Frenklach M., Clary D. W., Gardiner W. C. Jr., Stein S. E. *Proc. 20th Symp. (Int.) on Comb.*, The Combustion Institute, 1984, 887.

[2] Tesner, P. A. *Formation of Carbon from Hydrocarbons in Gas Phase.* Moscow, Khimiya, 1972 (in Russian).

[3] Bonne U., Homann K. H., Wagner H. Gg. *Proc. 10th Symp. (Int.) on Comb.*, The Combustion Institute, 1965, 503–512.

[4] Krestinin, A. V. *Khimicheskaya Fizika*, 1987, **6**, 342 (in Russian).

[5] Krestinin, A. V. *Khimicheskaya Fizika*, 1994, **13**, 121 (in Russian).

[6] Krestinin, A. V., Tesner, P. A., Shurupov, S. V. *Proc. 2nd Conf. (Int.) on Carbon Black.* Mulhouse, 1993, 39.

[7] Hidaka Y., Nakamura T., Tanaka H., Ihami K., Kawano H. *Int. J. Chem. Kinet.*, 1990, *22*, 701.

[8] Kiefer, J. H., von Drasek, W. A. *Int. J. Chem. Kinet.*, 1990, **22**, 747.

[9] Tesner P. A., Shurupov S. V. *Submitted to Zel'dovich Memorial.*

THE KINETIC MODEL OF PULSE INITIATION OF HEAVY METAL AZIDES

V. G. Kriger, A. V. Kalensky, L. G. Buluscheva, V. V. Murakhtanov

Kemerovo State University, Kemerovo, Russia

Initiation of Heavy Metal Azides (HMA) by laser and electron pulses have the following common aspects [1-4]:

1. The criterion for initiation depends on the pulse duration t. At $t < 30$ ns, the critical role is played by the energy flux density of the pulse ($H \simeq 4$ mJ/cm^2 and $H \simeq 130$ mJ/cm^2, respectively, for laser and electron pulses). At $t > 300$ ns, the criterion for initiation is based on the power density of a pulse [1-3].

2. There is an evidence that an induction period τ is rather long, $\tau \gg t$ and decreases with increasing energy flux density of the pulse [1, 3, 4].

3. In the 77–425 K range, H and τ weakly depend on the temperature of the sample [2, 4].

Of all the models considered elsewhere, only the model of sample initiation due to accumulation of energy at hot spots enables us to evaluate H, which leads to results close to those obtained experimentally. However, the model fails to account for the change of critical parameters of initiation for short and long pulses, induction period versus energy density, H versus the sample size, etc.

Also, qualitative common peculiarities of the initiation by laser and electron pulses, insufficient T-dependence of the processes, the induction period exceeding the pulse duration — all these indicate that HMA initiation results from the processes inside the crystal under irradiation, which allows us to put forward a hypothesis of HMA initiation due to the branching chain reactions.

One of the possible model reactions is considered in the present paper.

1. The generation of electron–hole (eh) pairs by pulsed radiation is described as

$$O \xrightarrow{\ G\ } e + p, \qquad G = \frac{H\alpha}{tE}, \tag{1}$$

where $E = 10$ eV is the energy of eh pair generation, $\alpha = 50$ cm^{-1} is the absorption factor, H is the energy density of the initiating pulse.

2. The reaction of the chain termination is the recombination of electrons and holes on the local centres in the bulk and on the surface. The recombination rate of the carriers is

$$V_{rp} = k_r p, \tag{2}$$

where $k_r \simeq 10^6$–10^7 s^{-1}, and $t = 1/k_r \sim 10^{-6}$–10^{-7} s is the recombination time of eh pairs for wide forbidden zone semiconductors.

3. The interaction of free holes (N_3^0 radicals) to form an intermediate complex followed by its decomposition into N_2 with the energy consumed by the generation of carriers is the chain development stage

$$2p \xrightarrow{k_2} A \xrightarrow{k_1} 3N_0 + K(n+p) + 2p + 2F + Q. \tag{3}$$
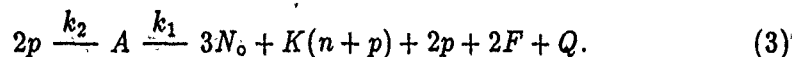
The reaction (3) was computed using the MNOO method. The thermal effect of the reaction was determined, $Q = 12.69$ eV. The width x and the height h of the activated barrier of the decomposition of the complex were found out ($x = 0.15$ Å, $h = 0.31$ eV). The rate constant of the reaction was evaluated by assuming the tunnel mechanism of the reaction.

Two holes are required to create an A complex, while the structure of the HMA energetic zone provides for the generation of three holes ($K = 1$) due to the reaction energy. Thus, the branching chain reaction in HMA is described by the equations

$$\begin{aligned}
\frac{dp}{dt} &= G - 2k_2 p^2 - k_r p + 3k_1 A, \\
\frac{dA}{dt} &= k_2 p^2 - k_1 A.
\end{aligned} \tag{4}$$

The analysis of the kinetics of the process during the stages of the generation of eh pairs, the induction period, the extinction of the reaction dependiny on the energy density of an initiating pulse was carried out. Presented below are the critical concentration of holes by the end of the pulse (p_k^o) and the induction period (p_k^u):

$$\begin{aligned}
p_k^o &= \frac{k_r}{k_2} + \frac{2k_r^2}{k_2 k_1}, \\
p_k^u &= \frac{k_r}{k_2}.
\end{aligned} \tag{5}$$

By solving Eq. (4) for a short-duration pulse one obtains the equation for the critical density of energy,

$$H_k = \frac{E\left(\dfrac{2k_r^2}{k_1 k_2} + \dfrac{k_r}{k_2}\right)}{\alpha}. \tag{6}$$

At larger t, the critical parameter is the power density of a pulse:

$$M_k = \frac{E k_r^2}{4 k_2 \alpha}. \tag{7}$$

43

At smaller t, we obtain the approximate dependence of the critical energy density on the pulse duration,

$$H_k(\tau) = \frac{\tau k_r E \left(\frac{2k_r^2}{k_1 k_2} + \frac{k_r}{k_2} \right)}{(1 - \exp(-k_r \tau)) \alpha}. \tag{8}$$

When the parameters of the system are $k_1 = 7 \cdot 10^6$ s^{-1}, $k_2 = 8.2 \cdot 10^{-12}$ cm^{3}s^{-1}, $k_r = 9 \cdot 10^6$ s^{-1}, the theoretical dependence $H_k(t)$ fits the experimental dependence best of all (the rms deviation $\beta = 3.8\%$ is substantially larger than the accuracy of the experiment).

According to the model, the induction period depends on the relative energy density of the pulse ($X = H/H_k$) and is constant for different types of initiation:

$$\tau(X) = -\frac{1}{k_r B} \log \left(\frac{(10(B - A)X + B + A)X(2X + 1)}{(2X^2 + 4X + B^2)(X - 1)} \right), \tag{9}$$

with $A = \frac{3}{2} \frac{k_1}{k_r} + 1$, $B = \sqrt{A^2 + \frac{12k_1 X}{k_r}}$.

Also, when the parameters of the system are $k_1 = 3.3 \cdot 10^6$ s^{-1}, $k_r = 2.8 \cdot 10^6$ s^{-1}, the theoretical dependence $\tau(x)$ fits the experimental data best under exposure to both laser and electron irradiation. The result points to a single mechanism of the reaction resulting in the HMA explosion under different types of initiation.

The critical energy density does depend the concentration of recombination centres. If we assume the recombination centres concentration distribution in simultaneously synthesized crystals to correspond to Gauss distribution:

$$W(N) = \sqrt{\frac{\phi}{2\pi}} \exp \left(-\frac{\phi}{2} (\overline{N} - N)^2 \right), \tag{10}$$

one can obtain the dependence of HMA initiation probability on the pulse energy density close to experimental when $\overline{N} = (4 \pm 0.4) \cdot 10^{13}$ cm^{-3}, ($\phi = 5.5 \cdot 10^{-26}$ cm^6).

The degrees of a sample decomposition in subcritical regimes were calculated. The radiation chemical yield of N_2 has been shown to depend on the ratio $H/H_k < 1$, and when $H \simeq 0.5 H_k$ it is ≤ 0.3 molecules/100eV, which is in a good agreement with the experiment.

Conclusion

The model for chain initiation of HMA complemented by the diffusion and recombination of carriers on the surface enables us to describe qualitatively and quantitatively almost all the effects observed in experimental initiation of HMA.

References

[1] Dolganov V. S. *Khimiya Vysokikh Energii*, 1993, **27**, 1, 55–58 (in Russian).

[2] Aleksandrov E.I. *Fizika Goreniya Vzriva*, 1984, **20**, 6, 104–108 (in Russian).

[3] Hagan J.T., Chaudhri M.M. *J. Materials Science*, 1981, **16**, 2457–2466.

[4] Aleksandrov E.I., Voznyuk A.G. *Fizika Goreniya Vzriva*, 1978, **14**, 4, 86–91 (in Russian).

THE POSSIBILITY OF A CONSIDERABLE INCREASE IN THE RATES OF GAS REACTIONS IN THE FRONT OF A SHOCK WAVE

S. V. Kulikov

Institute of Chemical Physics in Chernogolovka, Chernogolovka, 142432 Russia

Studies of translational nonequilibrium in the front of a shock wave spreading in a three-component gas are important for the understanding of the peculiarities of the threshold physicochemical processes initiated by the shock wave [1]. Such studies were performed using Monte Carlo methods with constant weighting factors [2, 3]. Molecules were assumed to be hard spheres. The results obtained for a mixture of components 1, 2 and 3 with the molecular mass ratio $m_1 : m_2 : m_3 := 1 : 20 : 80$ and the number density ratio $n_1 : n_2 : n_3 = 100 : 1 : 1$ are shown in Figs. 1 and 2. In this case, the ratio of the elastic cross-sections of molecules is $\sigma_1 : \sigma_2 : \sigma_3 = 1 : 2 : 2$ and the Mach number of the wave $M = 4$.

Figure 1 shows the profiles of relative velocities $u_{0i} = (u_i - u_a)/(u_b - u_a)$ (solid curves 1, 2 and 3) and relative temperatures $T_{0i} = (T_i - T_b)/(T_a - T_b)$ (solid curves 4, 5 and 6) of components 1, 2 and 3, respectively, $(i = 1, 2, 3)$. Here, subscripts a and b refer to the variables ahead of and behind the shock wave, respectively. The distance x is measured in the units of the mean free path of molecules in the flow ahead of the wave, λ. Similar calculations were carried out in [4] using Navier–Stokes-level equations, and the results, shown by the broken curves in Figure 1, are close to those given above.
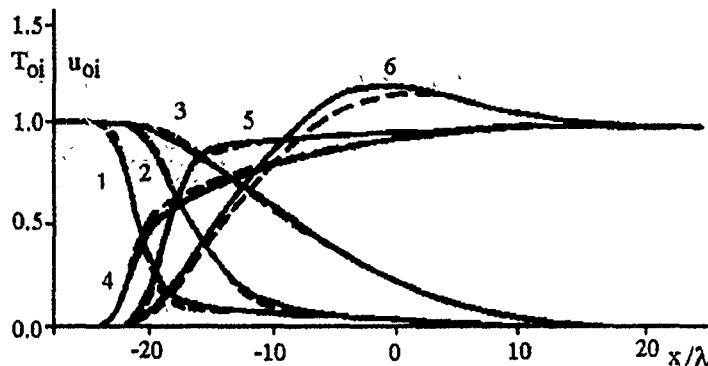
Figure 1: Profiles of relative velocities and temperatures of components for the mixture with number density ratio 100:1:1.
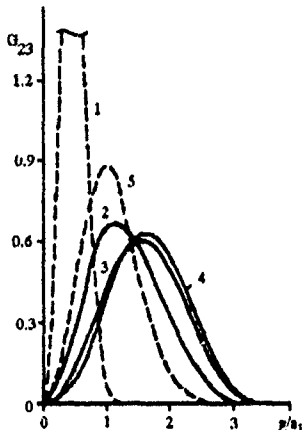

Figure 2: Distribution functions G_{23} in the wave front for the mixture with number density ratio 100:1:1.

Figure 2 shows the distribution functions G_{23} of the relative velocities g normalized with respect to the velocity of sound a_1 in the gas mixture ahead of the wave for the pairs of molecules of components 2 and 3. Curves 1 and 5 are the equilibrium distributions ahead of and behind the wave. Curves 2, 3 and 4 show the distributions in the front at distances $x = -16$, -14 and -10, respectively. One can see that, at $g > 1.5$, the distributions 2, 3 and 4 substantially exceed the equilibrium distribution 5. These superequilibria are about 15 at $g = 2.4$ and about 50000 at $g = 4.57$ for curve 4.

This effect appears at the leading edge of the wave, persists over a distance about 30 and reaches a maximum at $x = -10$, where the difference between the velocities of components 2 and 3 also reaches a maximum. In this case, the number of collisions of molecular pairs moving at high relative velocities in the front are substantially greater than under the equilibrium conditions behind the wave. This must appreciably affect the threshold physicochemical processes initiated by the shock wave in reactive mixtures of similar type. This influence must persist despite the narrowness of the zone of superequilibrium, due to the high degree of the superequilibrium. The effect can be conspicuous behind the wave in the avalanche-type chain processes, when even a
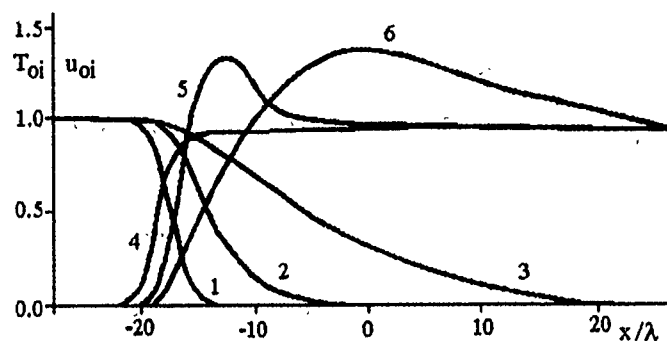
Figure 3: Profiles of relative velocities and temperatures of components for the mixture with number density ratio 1000:1:1.

relatively small extent of physical and chemical transformations in the nonequilibrium zone may have a significant influence on the entire flow.


Figure 4: Distribution functions G_{23} in the wave front for the mixture with number density ratio 1000:1:1.

The distributions of relative velocities for pairs of molecules of species 1 and 3, 2 and 2, 3 and 3 in the front also exceed their equilibrium values behind the wave. However, these superequilibria are not so overwhelming.

A somewhat greater effect was computed for a similar case with different number density ratio: $n_1 : n_2 : n_3 = 1000 : 1 : 1$. Figures 3 and 4 show u_{0i}, T_{0i}, and G_{23}. The notation is the same as in Figs. 1 and 2. These superequilibria are about 1000 at $g = 2.4$ and about 10000000 at $g = 3.9$ for curve 4.

The results obtained for $M = 5$ and mixture with $m_1 : m_2 : m_3 = 1 : 5 : 10$ and $\sigma_1 = \sigma_2 = \sigma_3$ show the absence of a significant effect of the superequilibrium over a wide range of number density ratios.

The computations have confirmed the conjecture of [1] concerning the potentially strong role played by translational nonequilibrium in the multi-component gas in the front of a shock wave threshold physicochemical processes.

References

[1] Zel'dovich Ya. B., Genich A. P., Manelis G. B., *Dokl. Akad. Nauk SSSR*, 1979, **248**, 2, 349–351 (in Russian).

[2] Genich A. P., Kulikov S. V., Manelis G. B., Chereshnev S. L. *Sov. Tech. Rev. B. Therm. Phys.*, 1992, **4**, 1, 1.

[3] Genich A. P., Kulikov S. V., Manelis G. B., Chereshnev S. L. *Proc. 17th Symp. (Int.) on RGD*, 1991, 175.

[4] Ruyev G. A., Fomin V. M., Shavaliev M. Sh. *Proc. 17th Symp. (Int.) on RGD*, 1991, 183.

AUTOWAVE REGIMES OF CHEMICAL REACTIONS IN A CONDENSED PHASE

G. B. Manelis, L. P. Smirnov, V. A. Strunin

Institute of the Chemical Physics in Chernogolovka, Chernogolovka, 142432 Russia

Introduction

The propagation of a chemical transformation in the form of traveling waves due to the strongly nonlinear dependence of the reaction rate on temperature (thermal mechanism) and conversion depth (diffusion mechanism) is a well-known phenomenon.

The basic specific feature of reactions in a condensed phase is the effect of mechanical stresses on reaction kinetics. The spatial inhomogeneity of mechanical stress and the feedback effect of the chemical transformation on the structure of the material and the stress distribution makes possible the autolocalization of reactions and the occurrence of chemical processes in the autowave regime (deformation mechanism).

The Diffusion Mechanism

It has been shown that certain autowave processes can involve a relatively wide reaction zone associated with the diffusion of the product, created in the initial substance, into the new phase [1–3]. An example of reversible first-order reaction was considered

48

in [1]. Its examination shows that the reaction takes place in a more or less narrow zone close to the phase boundary. The overall process can develop irreversibly until its completion due to the fact that the product emerges in the form of a separate phase. A substantial increase in the pre-exponential factor of the observed kinetic relationships and higher values of the activation energy of the bulk reaction occur in the moving zone, as compared with the topochemical reaction on the phase boundary.

The Thermal Mechanism. Many chemical reactions in a condensed phase have relatively low values of activation energy and/or thermal effect as compared with typical combustion reactions. Computer modelling of nonsteady regimes of these processes was carried out in [4-5]. The existence of the autowave regimes of weakly exothermic reactions in condensed phase was experimentally revealed in [6-7]. It was shown for the first time that the peak temperature can exceed the adiabatic value.

The Deformation Mechanism

The effect of mechanical stresses on the elementary act of chemical transformation and the kinetics of solid-state reactions have been considered in [8-9]. A major part of these works dealt with mechanical breakdown (fracture). In the case of simple irreversible reaction, the initial damage develops at an almost constant rate followed by explosive growth of the number of bond ruptures. In the case of reversible reaction, critical phenomena are possible. The actual form of the critical condition is readily found by the Semenov method. The different effects of the stresses at the individual stages of a complex chemical process may lead to the appearance of qualitatively different kinetic regimes of reaction progress depending on the applied load.

Autolocalization is a specific feature of the breakdown reaction. It has been shown [10] that the accumulation of bond ruptures in a structurally homogeneous material results in formation of a crack. In a structurally inhomogeneous material, cracks and their nuclei exist from the very beginning. The growth of a crack is an example of chemical reaction proceeding by an autowave mechanism. The reaction is localized in a small spatial region at the tip of the crack where the stresses are concentrated. Rupture of the bonds in this region leads to the overstressing of the intact bonds including those which are located further down the path of the crack, and the process is reproduced. The rapid growth of the reaction rate suggests invoking methods developed in combustion theory in modeling the crack growth. A detailed treatment of the kinetics of crack growth has been presented in [11-12].

In the case of crack growth driven by an autowave chemical process, the advance of the breakdown zone is due to the work done by extraneous forces. However, autowave processes can also be supported by an exothermic reaction accelerated by mechanical stresses, when the energy released is partially consumed to create spatially inhomogeneous stresses in the sample. An autowave mechanochemical process, in which the stresses are reproduced due to the difference between the densities of reactants and products, was discovered for the first time during a study of the thermal decomposition

of ammonium perchlorate [13]. Stresses and deformations in the neighbourhood of the growing reaction-centre cause dislocations to move along the slip planes. As a consequence of the interaction of these crystal defects with one another, this motion leads to the multiplication of the dislocations and thereby to an increase in the reaction rate and the entrainment of the new spatial regions, reached by the dislocations, in the reaction zone. Modelling of this process has shown that the propagation velocity of the steady reaction front is determined, to a considerable extent, by the parameters responsible for the rate of multiplication of the dislocations whereas the true rate constant only slightly affects the front velocity.

The existence of linear and planar defects in materials with irregular structure was postulated in [14–15]. It has been discovered [16] that the propagation of the reaction wave in glassy systems can be initiated by pulsed mechanical action of different kinds. In the phenomenological model constructed in [17], the propagation of the reaction front is governed by equations similar in form to the equations of flame propagation, the difference being that the heat release rate depends on the temperature gradient. The model proposed in [17] predicted the existence of two propagation regimes of a reaction wave which was subsequently confirmed experimentally. An alternative model of this phenomenon was recently presented in [18].

References

[1] Manelis G. B., Strunin V. A. *Dokl. Akad. Nauk SSSR*, 1969, **187**, 362 (in Russian).

[2] Strunin V. A., Manelis G. B. *Zhurnal Fizicheskoi Khimii*, 1972, **46**, 8, 1991 (in Russian).

[3] Manelis G.B. *et al. Dokl. Akad. Nauk SSSR*, 1981, **259**, 5, 1135 (in Russian).

[4] Merzhanov A. G. *et al. Dokl. Akad. Nauk SSSR*, 1968, **180**, 639 (in Russian).

[5] Manelis G. B., Smirnov L. P. *Fizika Goreniya Vzriva*, 1976, **3**, 354 (in Russian).

[6] Manelis G. B., Smirnov L. P. *et al. Report of the Branch of the Institute of Chemical Physics*, Chernogolovka, 1962 (in Russian).

[7] Manelis G. B., Smirnov L. P. *Fizika Goreniya Vzriva*, 1976, **5**, 665 (in Russian).

[8] Deyun E. V. *et al. Uspekhi Khimii*, 1980, **49**, 8, 1574 (in Russian).

[9] Popov A., Rapoport N., Zaikov G. *Oxidation of Stressed Polymers*. New York, Gordon & Breach, 1991.

[10] Manelis G. B. *et al. Khimicheskaya Fizika*, 1984, **3**, 1, 79 (in Russian).

[11] Barenblatt G. I. *et al. Izvestiya Akad. Nauk SSSR, Ser. Mekhanika Tverdogo Tela*, 1966, **6**, 107; 1967, **2**, 148 (in Russian).

[12] Manelis G. B., Polianchik E. V., Smirnov L. P. In: *Kinetics and Mechanism of Chemical Solid-state Reactions.* Minsk, 1975, 31 (in Russian).

[13] Raevskii A. V., Manelis G. B. *Dokl. Akad. Nauk SSSR,* 1963, **160**, 1136 (in Russian).

[14] Somigliana C. *R. C. Accad. Lincei,* 1914, **23**, 463.

[15] Oleinik E. F. *et al. Vysokomolek. Soedin.,* 1993, **35**, 11, 1819 (in Russian).

[16] Barelko V. V. *et al. Uspekhi Khimii,* 1990, **59**, 3, 353 (in Russian).

[17] Barelko V. V. *et al. Khimicheskaya Fizika,* 1983, **2**, 980 (in Russian).

[18] Knyazeva A. G. *Fizika Goreniya Vzriva,* 1994, **1**, 44 (in Russian).

LOW-TEMPERATURE SOOT FORMATION

Z. A. Mansurov

Al-Faraby Kazakh State National University, Al-Faraby St. 71, Almaty, 480121 Kazakhstan

Introduction

Despite the vast number of works concerning the processes of soot formation [1, 2], currently there is no established understanding of the problems of soot particle nucleation and growth in hydrocarbon combustion. Studies of soot and polycyclic aromatic hydrocarbons (PAHs) in flames are of interest from the environmental perspective as carcinogenic substances and a source of new carbon-based materials.

We have studied soot and PAH formation in methane and propane flames in twin heated reactor sections [3, 4], independently varying the temperatures of the first (T_1) and second (T_2) sections, flow velocity and mixture composition. Physical and chemical properties of the soot obtained have been studied, and a number of PAHs has been identified. The effects of the electric fields applied to the zone of soot formation have been studied.

Experimental and Discussion

Soot formation in low-temperature methane and propane combustion was studied in the heated twin reactors [3, 4]. The experiments with methane–oxygen mixtures were performed at the atmospheric pressure, varying the temperature of the first section (T_1)

from 673 K to 873 K, the temperature of the second section (T_2) from 873 K to 1223 K, the residence time from 1.7 s to 10.2 s, the ratio of components being $CH_4:O_2 = 1.63 : 1.90$ and $2.1:1$. In comparison with propane–oxygen flames, the regime of soot formation in methane–oxygen flames is usually observed at lower reactor temperatures ($T_1 = 423$ K, $T_2 = 773$–973 K), $t = 2$ s and the ratio of components $C_3H_8:O_2 = 1.53 : 1$. Flame temperature was measured by a chromel-alumel thermocouple ($d = 50$ μm) in a thin quartz coating preventing radical recombination and heating.

Temperature profiles in propane–oxygen flames were measured along the axis of the second reactor section at $T_1 = 423$ K and $T_2 = 773$ K, 873 K and 973 K. A limiting maximum temperature of the flame was determined, which is independent of the temperature of the second reactor section. However, the change in T_2 appears to be significant and probably gives some evidence of the limiting stage in the combustion regime with soot formation. One can speculate that the soot formation field under consideration is the field of reaction rate with a negative temperature exponent, since an increase in the initial T_2 does not lead to a corresponding increase in the combustion rate.

Sampling of gaseous products and soot along the reactor axis was performed by means of a quartz probe with inner diameter 70 μm. Low-temperature IR spectroscopy with cooling by liquid nitrogen was used to analyze the products of propane–oxygen flames. The analysis of IR spectra of the samples have shown that even ahead of the luminescence zone small quantities of propylene, water, formaldehyde, acetylene and carbon monoxide can be found against the background of main propane combustion products. An increase in CO_2 and C_6H_6 concentrations has been observed at the inner boundary of the luminous zone. In the afterburn zone we found small amounts of CO_2, C_2H_2, benzene, the concentration of which was increasing, and soot particles with PAHs adsorbed on their surface.

Soot samples, further extracted in benzene for PAHs isolation, were picked out in propane flames with $C_3H_8:O_2 = 0.81 : 1$. Their content was found to increase from 8.0% in the preflame zone to 23.8% in the afterburn zone.

The extracts analysis by UV fluorescence spectroscopy made it possible to identify the following PAHs: pyrene, fluoranthene, anthantrene, 1,12-benzperene, coronene. The results of probing show that the reactions of hydrocarbon formation up to benzene proceed homogeneously in the gas phase. In samples taken from gas phase benzene concentration continuously increases, as well as that of the PAHs adsorbed on soot surface. In the adsorbed benzene, C–H bonds weaken, which can significantly decrease the value of the energy barrier of addition and condensation reactions. Thus, in analyzing the mechanism of soot formation it is necessary to take into account a possibility of PAH formation on the soot surface, which in this case plays the role of the third particle.

We also used the same burner as in the previous experiments to study the electric field effects on the n=methane soot formation process at low temperatures. The electrodes were introduced along the axis of the second reactor section at its opposite

ends.

A series of experiments on the electric field effects on the size of the formed soot particles was conducted. In particular, we have obtained the dependence of soot particle diameter on the potential applied. As the potential was increased to 1 kV, the soot particle diameter decreased, and a further increase in the potential had a weaker effect on the diameter. This is consistent with the data of F. J. Weinberg [5]. The experiments included reversing the polarities of the electrodes. The decrease in soot particle diameter was less pronounced in the case of the opposite directions of the electric field and the gas flow.

According to the X-ray phase photography analysis, the soot obtained was a mixture of three phases with the diffractional content at $Q = 3.7$ (phase 1), $Q = 9.44–10$ (phase 2), $Q = 12.0–12.7$ (phase 3), which contents are as follows: phase 1 varied from 12% to 14%, phase 2 from 27% to 31%, and phase 3 from 57% to 60%. According to the group chromatographic analysis of the data, the extracts contained up to 70% of polyaromatic hydrocarbons, 17% of resins, 10–11% of asphaltene, 1–2% of paraffin and naphthenic hydrocarbons.

In the benzene extracts of the soot obtained, pyrene, fluorentene, coronene, anthantrene, 1–2 benzperylene were identified by IR and UV spectroscopy. In the fluorescence spectra of *iso*-octane extracts, there are intense bands with peaks at 429 nm, 456 nm, and 487 nm. The quantum output of the observed fluorescence is not less than 0.3, which provides some evidence of the polyaromatic hydrocarbon formation with great quantum outputs of fluorescence in the blue area of the spectrum.

We have proposed a reaction scheme based on the molecular-chain carbene mechanism for the polyaromatic compounds and soot, which allowed us to explain the formation of the identified substances.

Thus, based on the literature and experimental data, the following reaction scheme of PAH and soot formation in low-temperature hydrocarbon combustion is possible: the diffusion of H atoms from the combustion zone to the preflame zone; formation of ions, radicals, ethane and ethylene, buildup radicals and ions, the formation of C_2H_2, C_3H_6, C_6H_{12}, C_6H_6, CH_2O from olefins; PAH formation and coagulation with participation of ions in soot formation.

References

[1] Haynes B. S., Wagner H. Gr. *Prog. Energy Comb. Sci.*, 1981, **7**, 229.

[2] Longwell J. P. In: *Proc. 19-th Symp. (Int.) on Combust.* The Combustion Institute, 1982, 1339.

[3] Gukasyan Z. A., Mantashyan A. A. *et al. Fizika Goreniya Vzriva*, 1976, **12**, 789 (in Russian).

[4] Mansurov Z. A., Tuleutaev B. K. *et al. Neftekhimiya*, 1989, **29**, 2, 188 (in Russian).

[5] Mayo P. J., Weinberg F. J. *Proc. Roy. Soc.*, 1970, **319**, 351.

[6] Mansurov Z. A., Pesierev V. I. *et al. Archivum Combustionis*, 1990, **10**, 1–4, 209.

FLAME PROPAGATION IN DICHLOROSILANE–OXYGEN MIXTURES AND SiO₂ THIN FILM DEPOSITION

S. S. Nagorny, N. M. Rubtsov, S. M. Temchin, V. V. Azatyan

Institute of Structural Macrokinetics, Chernogolovka, Russia

One phenomenon of great interest and importance, predicted by Ya. B. Zel'dovich, is the mode of flame propagation caused neither by preheating, nor by heat transfer [1]. This phenomenon is due to nonlinear chain branching reactions. However, until recently the factors responsible for the nonthermal flame propagation have not been taken into account in a number of cases. It should be noted that the large concentrations of free atoms and radicals in chain flames and the high rate constants of chain interaction reactions indicate the important role of the branching reactions even under distinctly adiabatic conditions. After the theoretical prediction [1], the nonthermal flame propagation was observed in a number of combustion processes. However, the elementary acts of nonlinear branching were identified only in two reactions [2, 3]. This purely chain phenomenon is important for both theoretical description of chain processes and applications involving low-temperature thin film deposition. In this work, the reactions of mono- and dichlorosilane (MCS, DCS) oxidation were examined from these perspectives.

The flame propagation was studied in a heated quartz tube $\leq$ cm in diameter and 100 cm long and a heated cylindrical steel reactor 10 cm in diameter with optical windows for schlieren cinematography. The latter was equipped with a calibrated pressure transducer. The quartz reactor was equipped with photomultipliers positioned lengthwise at regular intervals. Ignition was provided by a spark source or a rapidly heated nichrome wire coil.

The quartz cooled reactor for SiO₂ deposition had a removable cover and inlets for electrical power supply and gas evacuation. The heater with silicon substrate was installed at the lower end inside the reactor. The deposition was performed in single runs of the initiated flame, the pressure being close to the lower flammability limit.

It has been shown, using both methods mentioned above, that the flame propagates along the tube at a constant speed, and both lower (P_I) and upper (P_{II}) flammability limits have been observed (Fig. 1). It has also been shown that for $P \leq 1.7P_I$ the
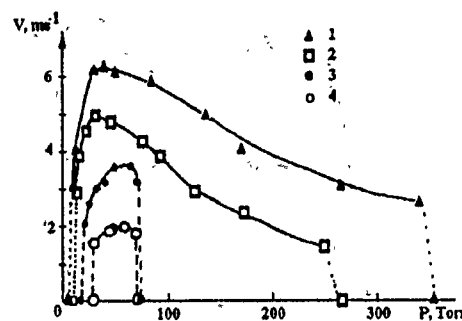
Figure 1: The flame propagation speed versus pressure in DSC-oxygen mixtures. $T = 373$ K; 1 — 2.9% DCS + 48.5% O_2 + 48.5% N_3; 2 — 2.9% DCS + 97.1% O_2; 3 — 2.5% MCS + 97.5% O_2 (503 K); 4 — 2% DCS + 98% O_2.

preheating by ΔT is not sufficient for shifting the gas mixture composition to the self-ignition domain, and the flame propagation is nonthermal. Under these conditions the characteristic time of heat release is much greater than the time of flame propagation over the distance equal to the reactor radius (5 cm). As has been shown for DCS oxidation in [4], the role of nonlinear chain branching in the reactions studied is quite significant. The dependence of flame propagation speed on the choice of inert gas (Ar, N_2) is also shown in Fig. 1. It has been shown that the highest flame propagation speeds are reached in DCS-Ar-O_2 mixtures, followed by N_2 and pure O_2. The nature of diluent affects P_{II} only, which means that the effects of these gases differ in terms of their efficiency as the third body in termolecular chain termination reactions. The most efficient third body is O_2 for both MCS and DCS oxidation, as shown in our recent work [5].

The nonthermal flame propagation phenomena were used for SiO_2 thin film deposition. The film thickness after 50 flame runs amounted to 0.2 μm, and SiO_2 was deposited uniformly over substrate surface. The Auger spectra for this film are shown in Fig. 2. The Auger spectrum for the initial film prior to ion etching contains Si peaks (63 and 78 eV) due to Si-O-Si bonds and O, C, and Cl peaks (Fig. 2a). The latter two peaks disappear after ion etching, i.e., they are caused by surface contamination (Fig. 2b). The absence of chlorine atoms indicates that they do take part mainly in the gas-phase elementary oxidation reactions resulting in HCl formation. The peak-to-peak Si/O ratio in the Auger spectrum corresponds to the stoichiometric SiO_2. It has been shown that the ion etching rate for the film obtained is only 3.5 times higher than that for the thermal SiO_2 film, i.e., the films obtained in present work are comparable to those obtained by Si surface oxidation.

55
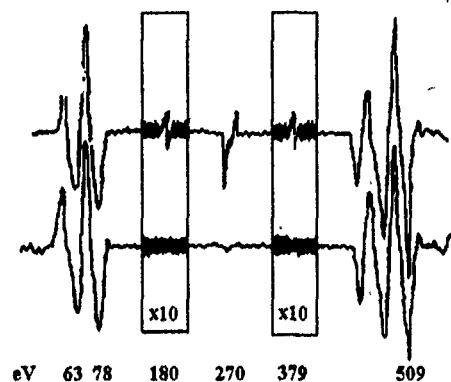
Figure 2: Auger spectra of 0.14 μm thick SiO_2 film: (a) prior to Ar^+ etching; (b) after 5 min Ar^+ etching.

The uniformity and homogeneity of the film on the silicon substrate surface were examined in a special study. The Auger spectra of three different portions of the film surface, located at the vertices of a triangle with 2-cm sides, were recorded after 5-min ion etching. It has been shown that the Auger spectra obtained for these portions are identical, whereas no overetching down to silicon substrate has been observed. Thus, thin SiO_2 films obtained in the present work are uniform and chemically homogeneous. The proposed deposition in single flame runs is important for the synthesis of very thin dielectric layers in integrated circuits based on Josephson transitions.

This work has been supported by the Russian Foundation for Fundamental Research.

References

[1] Zel'dovich, Ya. B., Frank-Kamenetskii, D. A. *Dokl. Akad. Nauk SSSR*, 1938, **19**, 693 (in Russian).

[2] Voronkov, V. G., Semenov N. N. *Zhurnal Fizicheskoi Khimii*, 1939, **13**, 1695 (in Russian).

[3] Azatyan, V. V. *et al. Izvestiya Akad. Nauk SSSR*, 1976, 7, 1459 (in Russian).

[4] Vartanyan, A. A. *PhD (CS) Thesis*, 1991. Chernogolovka, 185 (in Russian).

[5] Rubtsov, N. M., Temchin, S. M., *Khimicheskaya Fizika*. 1992, **11**, 1, 125 (in Russian).

CLEAN BURNING SOLID PROPELLANTS

Rose Pesce-Rodriguez, Robert A Fifer

US Army Research Laboratory, AMSRL–WT–PC, Aberdeen Proving Ground, MD 21005-5066, USA

Incomplete combustion of solid gun propellants is a common occurrence during the firing of both experimental and fielded gun systems. The products of this phenomenon include toxic gases such as CO, NO, and HCN, as well as reactive solid residues. The residues remaining in the breech after the firing may lead to "cook-off"-related accidents, and to the generation of additional toxic gas products and smoke. The objective of this investigation is to develop clean-burning solid propellants that will:

- have reduced levels of toxic/carcinogenic combustion products such as NO and HCN;

- burn quickly/efficiently without the need for lead-based burn-rate catalysts;

- undergo more complete combustion and reduce the amount of unburned residue in gun breeches.

"DENOX" agents have been shown to be effective in eliminating NO_x (primarily nitric oxide, NO) production in internal combustion engines and other devices. In these applications, the DENOX agents are NH_x- (e.g., NH_2- or NH_3-) containing species that serve as reducing agents by reacting with any NO present to reduce it to N_2. In nitrate ester- or nitramine-based solid gun and rocket propellants, NO is produced from the $-NO_2$ groups in the energetic oxidizer (e.g., RDX), polymer (e.g., nitrocellulose NC), or plasticizer (e.g., nitroglycerine NG). Potentially, NH_x-based reducing agents could be incorporated into solid propellants to reduce the NO to N_2 at or near the burning propellant surface; the increased near-surface energy release should also lead to more complete combustion (i.e. more "final" products and less solid residue) and reduced generation of other toxic/carcinogenic products. Preliminary results indicate that levels of NO, as well as of HCN can be reduced when, for example, ammonium carbonate is used as a propellant additive in LOVA formulations. Results for this and other experimental formulations will be presented and discussed.

FLAMMABILITY OF HYDROGEN–OXYGEN–STEAM MIXTURES AT ELEVATED PRESSURES AND TEMPERATURES

O. E. Popov, A. Yu. Kusharin, G. L. Agafonov

Semenov Institute of Chemical Physics, Moscow, Russia

Experimental investigations of flammability limits in hydrogen–oxygen mixtures diluted by steam were carried out at initial pressures up to 2 MPa and initial temperatures up to 500 K. The effects of pressure, temperature, and mixture composition on the concentration limits were determined. It has been shown that the absorption of thermal radiation by steam affects the flammability limits and extends the range of flammability with increasing initial pressure. The lean flammability limit is mainly controlled by hydrogen diffusion and the initial pressure does not affect this limit.

Introduction

The problem of flammability limits and near-limit phenomena has been studied experimentally and theoretically over years. The Zel'dovich theory [1] is a significant contribution to the understanding of the problem, which makes it possible to predict the limits in the narrow tubes. Application to the safety of nuclear power plants requires the knowledge of flammability of hydrogen–oxygen–steam mixtures at elevated pressures and temperatures. It is known that, in a light-water reactor, a large amount of hydrogen may be produced by radiolysis and metal–water reactions as a consequence of a severe accident. This paper extends the previous work of the present authors on hydrogen–oxygen–steam mixtures [2] to the domain of non-stoichiometric compositions.

The aim of the present work is to investigate combustion of such mixtures with a high content of steam in the near-limit region at elevated pressures and explain certain trends in flammability. To this end, we used both experimental and computational approaches.

Experimental

Two heated chambers (16 and 5 l in volume) were employed in the experiments. The first chamber was a vertical cylindrical vessel 0.5 m long with ignition at the bottom. The second chamber was a spherical vessel with central ignition. Both of these vessels were kept at a fixed temperature. The temperature difference between the upper and lower ends of the vessels did not exceed 1–2 K. Pressure and temperature were recorded by transducers and thermocouples. The maximum mass percentage of hydrogen at a given percentage of steam in a hydrogen–oxygen–steam mixture, for which ignition by a sufficiently powerful source (about 1–2 J) did not cause a noticeable increase in pressure, was used as the definition of the limit.
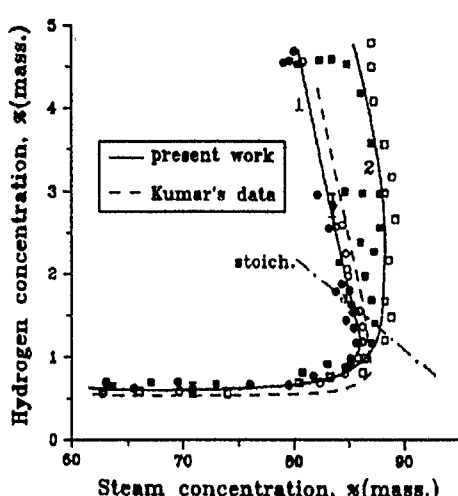
Figure 1: Flammability limits in H_2–O_2–H_2O mixtures. (1) $T_0 = 373$ K, $P_0 = 0.13$–0.17 MPa; (2) $T_0 = 473$ K, $P_0 = 1.85$–2.5 MPa.
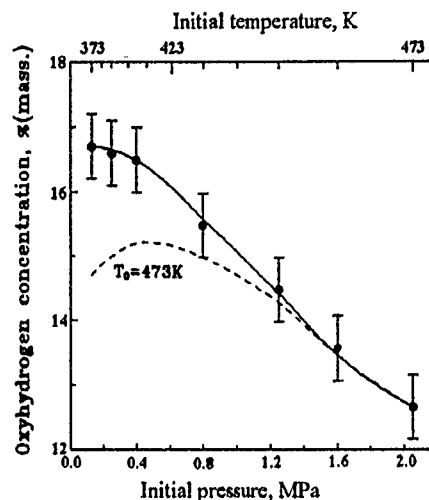
Figure 2: Limiting mass concentration of stoichiometric oxyhydrogen in H_2–O_2–H_2O mixtures as a function of initial pressure.

Computational Procedure

A theoretical model for one-dimensional spherical laminar flames involving detailed kinetics and thermal radiation has been developed. One of the purposes of this model was to compute the burning velocity for near-limit mixtures. The model allowed us to compare temperature and concentration profiles at different pressures. In addition, the model provided the transport coefficients of reactants and radiation characteristics of flames.

Results and Discussion

The flammability limits for hydrogen–oxygen–steam mixtures over the range of equivalence ratios 0.12–2.5 are shown in Fig. 1 at 373 K and 473 K. The curves with circles and squares correspond to 0.1 MPa and 1.6 MPa of steam pressure, respectively. The stoichiometric hydrogen–oxygen (oxyhydrogen) composition is shown by the dash-dot line. These results, obtained in a spherical chamber at near-atmospheric pressure, correlate reasonably with the experimental data measured by Kumar in the standard tube [3]. According to Fig. 1, the increase in temperature to 473 K and in pressure to 2–2.2 MPa affects the flammability limits and extends the flammability range. This effect manifests itself in the near-stoichiometric and rich mixtures with a large content of steam.

Figure 2 illustrates the effect of the reduction of limiting concentration with increasing initial pressure for stoichiometric oxyhydrogen premixed with steam. The

limit curve at a fixed temperature has a maximum at 0.4–0.6 MPa. An analysis of experimental and computational results has shown that thermal radiation from the flames and absorption of radiation by the steam affect the burning velocity of near-limit mixtures. This additional factor is of primary importance for the flammability limits in hydrogen–oxygen–steam mixtures at elevated pressures. The lean flammability limit is mainly governed by the diffusion of hydrogen, and the initial pressure does not affect this limit.

References

[1] Zel'dovich, Ya. B. *Theory of Combustion and Detonation of Gases*, Moscow, Gostekhteorizdat, 1944 (in Russian).

[2] Kogarko, S. M., Lyamin, A. G., Popov, O. E., Kusharin, A. Yu., Dubrovin, A. V. *IAEA–TC–427.6*, Vienna, 1984.

[3] Kumar, R. K. *J. Fire Sci.*, 1985, **3**, 3, 245–262.

HIGH-TEMPERATURE KINETICS IN AEROSOLS CONTAINING CARBONACEOUS PARTICLES

Paul Roth, Sabine von Gersum

Institut für Verbrennung und Gasdynamik, Universität Duisburg, Lotharstrasse 1, 47048 Duisburg, Germany

Introduction

Carbon is the most peculiar element in nature. The capability of carbon atoms to combine with each other by single as well as by double and triple bonds results in formation of carbon chains and various ring structures. The immense number of organic carbon compounds comprises the main energy source on earth. During combustion, soot particles originate from regions of low oxygen content. One possible mechanism to reduce the amount of soot produced in a combustion chamber is the soot particle oxidation in hot post-flame gases. Successful oxidation requires a detailed knowledge of the efficiency of potential oxidizers and the kinetics of oxidation under various reaction
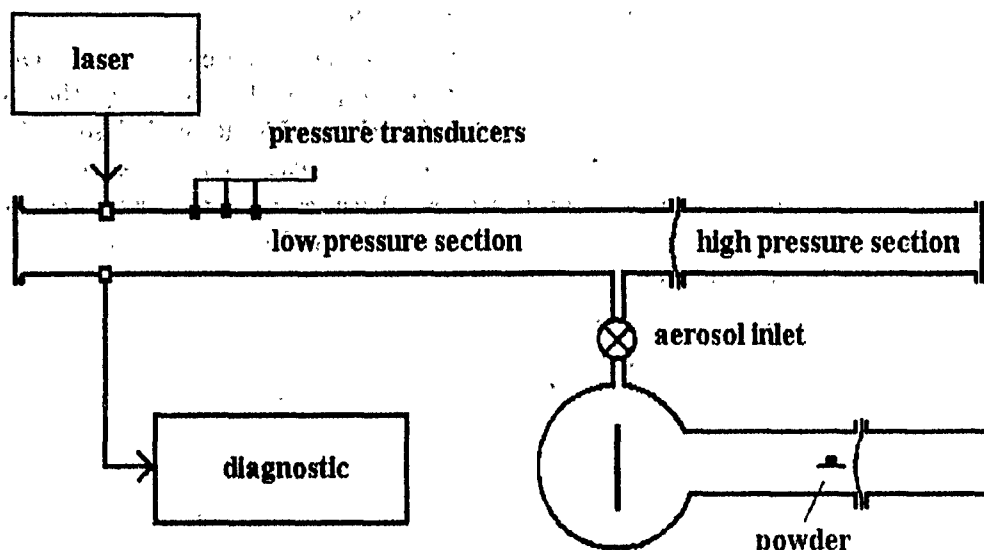
Figure 1: Experimental setup.

conditions. In the first part of this paper, a method for the investigation of soot particle oxidation under well-known reaction conditions is presented.

Apart from the two well-known carbon modifications, diamond and graphite, a third stable form was discovered by Kroto *et al.* [1]. They found a molecule consisting of 60 carbon atoms, which was exceptionally stable. They proposed a soccer-ball-shaped structure where the carbon atoms are at the edges of 12 pentagons and 20 hexagons. The second part of this paper describes experiments on the thermal decomposition and oxidation of fullerene C_{60} at temperatures $T > 1900$.

Experimental

The experimental setup employed in the studies of soot particle and fullerene kinetics is schematically shown in Fig. 1. It consists of:

- an aerosol generator, which is basically a small shock tube, by means of which the powder deposited on the flat plate was dispersed by an expansion wave;

- the main shock tube, by which the aerosol was heated up to the reaction temperatures;

- a particle and an Infrared-Diode–Laser diagnostic unit monitoring the progress in the reaction kinetics of the carbonaceous materials;

- an intensified CCD camera used to measure the spectral emission during pyrolysis and oxidation of fullerene C_{60}.

61

The post-shock temperatures and pressures were evaluated from shock velocity measurement data using one-dimensional conservation equations.

In the experiments on both the soot and the fullerene oxidation, CO and CO_2 are expected to be the reaction products. The optical setup used for measuring these gas-phase concentrations consisted of a narrow-bandwidth tunable IR–diode laser, a 0.5-m monochromator and an infrared detector. The laser was pulsed at a frequency about 25 kHz and could be tuned to single absorption lines. Measurements of CO were performed using the 0–1 P8 absorption line at $\nu = 2111.54$ cm^{-1} and CO_2 was measured using the $00^\circ 0$–$00^\circ 1$ R 28 transition ($\nu = 2369.09$ cm^{-1}).

In the soot oxidation experiments, the particle properties were characterized on the basis of laser light extinction measurements at three different wavelengths. For this purpose, an Ar + laser (488 nm), a He–Ne laser (633 nm), and a diode laser (780 nm) were employed. The optical dispersion quotient method, as described by Brandt *et al.* [2], was used to determine the mean particle size and the particle number density.

During the fullerene C_{60} pyrolysis, the time-dependent emission was monitored by an intensified CCD camera (Fa. LA Vision, Germany) allowing a time shift of the optical information. For this purpose, only a few lines at the top of the CCD sensor chip were illuminated for a certain time interval. The stored spectral information was stepwise transferred, line by line, to the dark zone of the CCD chip, which served as a memory. In this manner, the spectral as well as the temporal behaviour of the emitted light could be recorded. The spectral changes of the quantum efficiency of the intensifier were taken into account. From the time-dependent intensity profiles at characteristic wavelengths, the disappearance of C_{60} or the formation of decomposition products could be inferred.

Soot Particle Oxidation

The oxidation of soot particles by O_2, NO and O was studied in different series of experiments. The post-shock temperature ranged from 1500 K to 3500 K at pressures of about $p = 1$ bar. The soot particles were dispersed in the inert gas (argon) containing different gaseous compounds. The oxidizing species, O_2 or NO, could be added directly to the initial aerosol and heated up to reaction temperature by the shock wave, together with other aerosol constituents. In the case of the radical species O, the gas-phase precursor N_2O was added to the initial aerosol. N_2O is known to decompose very rapidly at temperatures $T > 1600$ K to form O atoms and other species via a kinetically well controlled process.

The experiments on soot/O_2/Ar aerosols were performed at temperatures 1500 K $< T < 3450$ K, at which O_2 is thermally stable. The only detectable reaction product was CO. Very small amounts of CO_2 were sometimes measurable at the end of the disposable measurement time. The soot oxidation rate is therefore represented by the initial slope of the CO concentration profiles at early reaction times. Assuming the
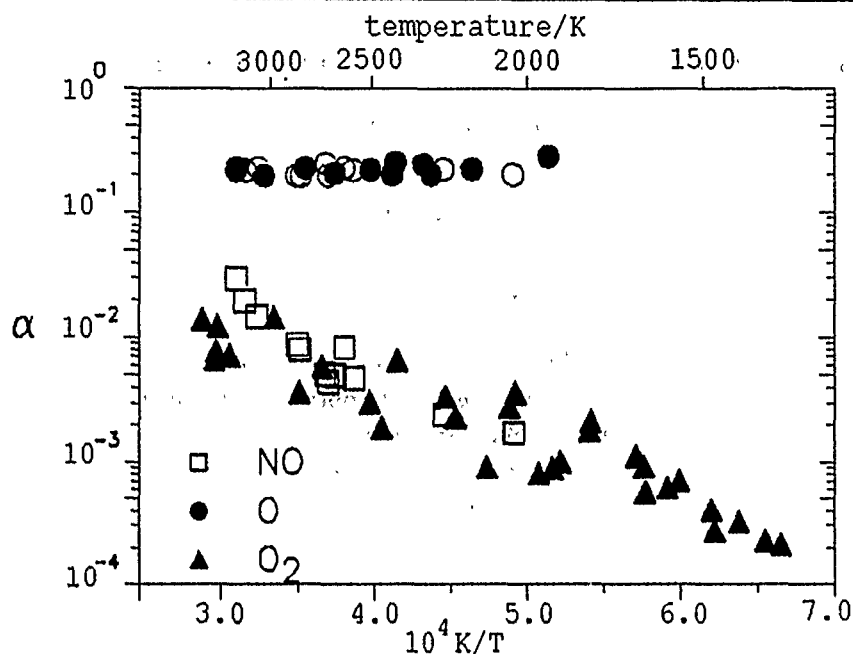
Figure 2: Reaction probabilities for soot particle oxidation by O_2, NO and O.

global heterogeneous reaction

$$C_S + \frac{1}{2}O_2 \rightarrow CO,$$
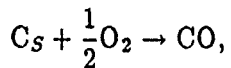
the measured CO formation rates can be transformed into reaction probabilities by

$$\alpha_{O_2} = \frac{d[CO]/dt}{2a_p Z_{O_2}}$$

The number of oxygen collisions per unit time and unit area Z_{O_2} can be determined from the Hertz–Knudsen equation. The reacting particle surface ap per unit volume of the suspension was determined from extinction measurements. The reaction probabilities α_{O_2} for soot particle oxidation by O_2 are shown as closed triangles in the Arrhenius representation of Fig. 2. The reaction probabilities depend on the partial pressure of oxygen and decrease with temperature. Their values are in a good agreement with the results on soot and graphite oxidation by molecular oxygen reported in the literature [3–5].

The oxidation of soot particles dispersed in NO/Ar mixtures containing 8 – 24% NO was studied in the temperature range of 2033 K $\leq T \leq$ 3500 K. Although NO is known to be relatively stable, it decomposes under the given reaction conditions, forming other potentially soot-oxidizing species. A computer simulation of the NO decomposition, based on a mechanism including 11 gas-phase reactions, showed that O_2 and O had to be taken into consideration in interpreting the measured CO concentration profiles.

63

Also, the following three global heterogeneous reactions were introduced:

$$C_S + O \rightarrow CO \qquad\qquad (H1)$$

$$C_S + \frac{1}{2}O_2 \rightarrow CO \qquad\qquad (H2)$$

$$C_S + NO \rightarrow CO + \frac{1}{2}N_2 \qquad\qquad (H3)$$

The reaction probabilities could be determined by fitting the calculated CO concentration profiles to the measured ones. The results obtained are shown in Fig. 2. The reaction probability α_{NO} exhibits Arrhenius behaviour and can be well represented by $\alpha_{NO} = 1.82 \exp(-1500\ K/T)$. Its values agree well with results obtained by Rosner et al. [6], Bradley et al. [1], and, recently, by Cadman et al.

The soot oxidation by O atoms was studied in N_2O/Ar mixtures containing dispersed particles. At temperatures between 1940 K and 3200 K, N_2O decomposes relatively fast. Computer simulations of the gas-phase kinetics showed that, along with N_2 and O, considerable amounts of NO and O_2 were also produced. As in the case of the soot/NO/Ar reactive system, all measured CO concentration profiles were fitted to the computed ones using the same reaction mechanism as described before. The individual reaction probabilities for the soot particle oxidation by O atoms are summarized as closed circles in Fig. 2. As in the previous case, the scattering of the data is relatively low and the mean value $\alpha_O = 0.23$ is temperature independent.

Thermal Decomposition and Oxidation of Fullerene C_{60}

To investigate the thermal and chemical stability of C_{60} at temperatures above 1900 K, again, the shock wave technique was applied. In each experiment, 100 mg of C_{60} powder containing 1% of C_{70} (Fa. Hoechst, Germany) was filled into the aerosol generator. It was dispersed by an expansion wave resulting in an aerosol containing C_{60} particles of initial size about 300 nm. The C_{60} aerosol was filled into the shock tube and heated up to reaction temperatures by a shock wave. It can be assumed that several subsequent processes occur in the shock-heated C_{60}/Ar aerosol. Because of the relatively high vapour pressure of C_{60}, the solid agglomerated carbonaceous particles start to evaporate behind the shock wave with the typical evaporation time of 40 μs. This behaviour is different from that of the soot which survives in the particulate form even at temperatures as high as 3500 K. Depending on the temperature, the C_{60} vapour starts to decompose or react with the decomposition products, as can be observed by the spectral emission behaviour.

In the first series of experiments, the emission characteristics of high-temperature fullerene C_{60} vapour were studied in the temperature range 1900 K $\leq T \leq$ 3340 K by means of the CCD camera in the spectral range 280 nm $\leq \lambda \leq$ 560 nm. The emission at $\lambda = 490$ nm was typical for C_{60}, and the emission band at $\lambda = 518$ nm was identified to result from C_2. From the temporal behaviour of E_{490} and E_{518} emissions normalized

64
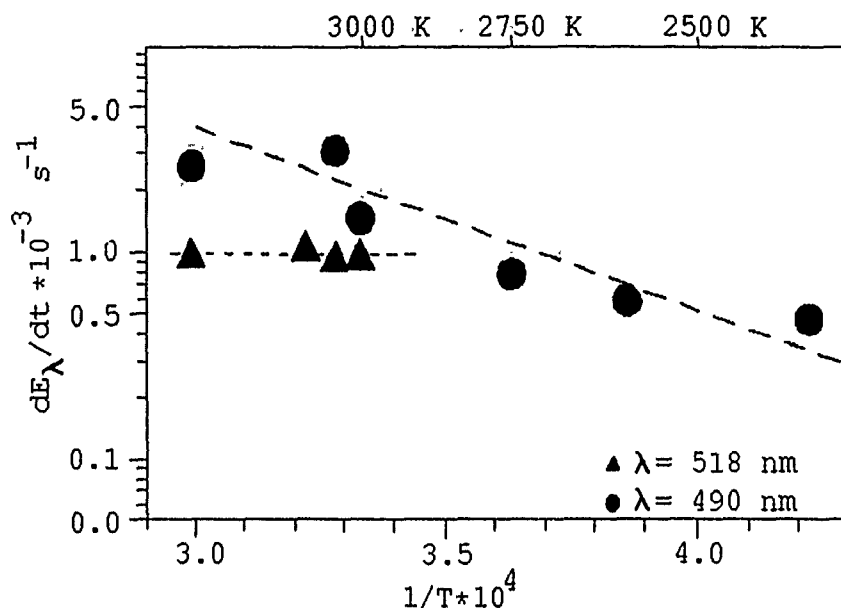
Figure 3: Disappearance rate of emission at $\lambda = 490$ nm and $\lambda = 518$ nm during C_{60} pyrolysis.

by the respective maximum values, the disappearance rates were determined, as shown in the Arrhenius diagram of Fig. 3. The measured dE_{518}/dt are nearly independent of temperature, whereas the values of dE_{480}/dt show the apparent activation energy of 199 kJ/mol, which is about four times of 4 lower than the activation energy determined by Sandler et al. [7] for the reaction $C_{60} \rightarrow C_{58} + C_2$. This indicates that the secondary reaction of C_{60} and C_2 must be considered under our reaction conditions, insofar as the measured emissions are representative for the species concentration at all. To get some information about the chemical stability of fullerene with respect to oxidation, some experiments on C_{60} dispersed in O_2/Ar mixtures were performed. Their results will be presented in the full paper.

Acknowledgement

References

[1] Kroto, H. W., Heath J. R., O'Brien S. C., Curl R. F., Smalley R. E. Nature, 1985, **318**, 162.

[2] Brandt, O., Roth P. Comb. Flame, 1989, **77**, 69.

[3] Rosner, D. E., Allendorf H. D. *AIAA Journal*, 1965, **3**, 1522.

[4] Park, C., Appleton J. P. *Comb. Flame*, 1973, **20**, 369.

[5] Bradley, D., Dixon-Lewis G., El-Din Habik S., Mushi E. M. J. *Proc. 20th Symp. (Int.) on Combustion*, The Combustion Institute, Pittsburgh, 1985, 931.

[6] Rosner, D. E., Allendorf H. D. *AIAA Journal*, 1968, **6**, 650.

[7] Sandler, P., Lifshitz C., Klots C. E. *Chemical Physics Letter*, 1992, **200**, 5, 445.

THE CATALYTIC BEHAVIOR OF CHEMICALLY BONDED METALS IN THE COMBUSTION OF ENERGETIC MATERIALS CONTAINING VARIOUS OXIDIZERS

V. P. Sinditskii, A. E. Fogelzang, T. Ya. Dutova, V. Y. Egorshev

Department of Chemical Engineering, Mendeleev University of Chemical Technology, Miusskaya Sq. 9, Moscow, 125820 Russia

Most of the combustion catalysis studies have been focused on double-base and composite propellants, i.e. on the systems in which nitrogen and chlorine oxides act as oxidizers. The results of these studies have demonstrated that the metals efficiently catalyzing certain systems, are usually not catalysts for others. The purpose of the present work is to elucidate how the catalytic activity of a metal depends on the nature of the oxidizer.

In order to avoid the difficulties of interpretation related to the uniformity of catalyst distribution and the effects of particle size, complex compounds (CCs) of the $[ML_n]X_2$ type were used as the objects of the investigation. These compounds may be considered as model compositions with metal ion, fuel ligand and oxidizer anion mixed on the molecular level. The salts of the corresponding acids with a ligand, L·HX, may be well taken for comparison as noncatalyzed systems. Ethylenediamine, $H_2NCH_2CH_2NH_2$, (En) is an excellent candidate for the fuel ligand, because it can form complex compounds with a variety of metals, as well as relatively stable salts with strongly oxidizing acids (HNO_2, HNO_3, $HClO_3$, $HClO_4$, $HBrO_3$, HIO_3, HIO_4). Transition metals, Ni(II) and Cu(II), which are known to readily participate in redox reactions, and also Zn and Cd, which are generally in the bivalent state, were taken to be the central ions in the CCs.

The burning rate of the CCs and salts of En was determined in a constant-pressure bomb by the method described in [1, 2].

The simplest way of analyzing the catalytic activity of a metal ion in combustion is to compare the trends observed in combustion of various CCs with En salts of the same anions. Despite some uncertainty related to the difference between the energy properties of CCs and En·2HX within the scope of this approach, the data obtained for all oxidizers can be used to put the metals in the order of decreasing catalytic activity: Cu > Ni > Cd ≫ Zn.

Previous studies of combustion of the ammonium salts of various inorganic acids–oxidizers have shown that the burning rate increases with the standard potential E_0 of oxidizer [3, 4]. The authors have explained this trend by assuming that the redox reactions in the flame are rate-controlling. A comparison of the mass burning rates of the salts, U_m, obtained in the present work, with the standard potentials of acid-oxidizers leads to similar conclusions.

The kinetics of many reactions including electron transfer (ET) as the rate-controlling stage is known to be described by the Marcus theory [5, 6], which predicts the existence of a correlation between the rate constant (k) and the driving force of reaction $(E_0^{ox} - E_0^{red})$:

$$k = \exp\left(-\frac{\Delta G^*}{RT}\right),$$

$$\Delta G^* = \frac{\lambda}{4}\left(1 + \frac{\Delta G^{0'}}{\lambda}\right) + Z_1 Z_2 \frac{e^2 f}{\varepsilon r_{12}},$$

$$\Delta G^{0'} = \Delta G^0 + (Z_1 - Z_2 - 1)\frac{ef}{\varepsilon r_{12}},$$

$$\Delta G^0 \ (\text{kcal/mol}) = -23.06(E_0^{ox} - E_0^{red}),$$

where ΔG^* is the standard activation energy of ET, r_{12} is the collision distance, e is the electron charge, λ is the reorganization energy consisting of the reorganization energies of the reactant molecules and the medium, f is the factor reflecting the effect of ionic strength, $\Delta G^{0'}$ is the corrected standard free energy of ET; ΔG^0 is the standard free energy of ET, E_0^{ox} and E_0^{red} are the standard potentials of electron donor oxidation and acceptor reduction.

Since, according to Ya. B. Zel'dovich [7], the burning rate depends on the rate of the leading reaction its value may be used for the analysis in terms of free energy change by Marcus theory.

The En·2HX combustion data represented by $\ln U_m$ versus the corresponding values of $G^{0'}$ are well described by a straight line (Fig. 1), which, in our opinion, suggests that electron transfer is the rate-controlling stage in the combustion process.

The known oxidation mechanism of coordination compounds of transition metals involves initial conversion of M(II) to M(III) with subsequent electron abstraction from the ligand [8]. As indicated in [9], coordination usually results in that a M^{3+}/M^{2+} redox
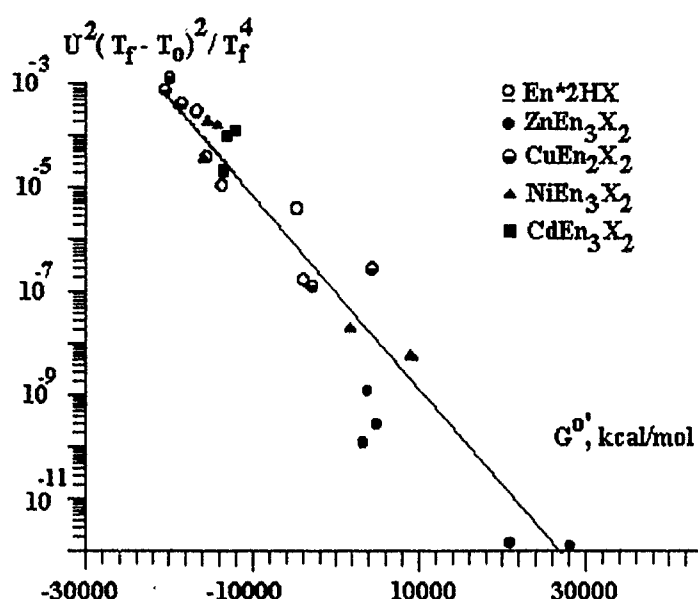
Figure 1: Dependence of the mass burning rate of complex compounds and En·2HX on corrected standard free energies of electron transfer. Solid line is drown through En·2HX points.

pair is available at lower potentials, and therefore, coordination can offer the possibility to oxidize Cd(II) to form the uncommon Cd(III). In the case of complexes of Zn, the redox potential of Zn^{3+}/Zn^{2+} (≈ 4 V) is too high for similar conversion to occur and, thus, it is the ligand that has to be oxidized. The detailed information about the En complexes is limited, and we are forced to rely on an estimation following [10]. The combustion data on the CCs as a function of $G^{0'}$ show a general trend similar to that characteristic of En salts (Fig. 1). Therefore, we can speculate that the redox reactions are rate-controlling in CCs combustion, and the role of metal as the catalyst amounts to facilitating ET from ligand to oxidizer. Thus, in the system with a given oxidizer, the metal ion would exhibit catalytic activity in combustion only when it is capable of changing its oxidation state and when the oxidizer can facilitate this transition.

References

[1] Fogelzang A. E., Egorshev V. Yu., Sinditskii V. P. et al. Dokl. Akad. Nauk SSSR, 1985, 282, 1449 (in Russian).

[2] Fogelzang A. E., Egorshev V. Yu., Sinditskii V. P., Dutov M. D. *Comb. Flame*, 1991, **87**, 123.

[3] Fogelzang A. E., Adzhemian B. Ja., Svetlov B. C. *Dokl. Akad. Nauk SSSR*, 1971, **199**, 6, 1296 (in Russian).

[4] Fogelzang A. E., Adzhemian B. Ja., Svetlov B. C. *Proc. 3rd All-Union Symp. on Comb. and Explosion*, Moscow, Nauka, 1971, 63 (in Russian).

[5] Eberson L. *Electron Transfer Reactions in Organic Chemistry*. Berlin, Springer–Verlag, 1987.

[6] Marcus R. A. *J. Chem. Phys.*, 1967, **26**, 867.

[7] Zel'dovich Ya. B. *Zhurnal Eksperimentalnoi Teoreticheskoi Fiziki*, 1942, **12**, 498 (in Russian).

[8] Barefield E. K., Mocelle M. T. *J. Amer. Chem. Soc.*, 1975, **97**, 4238.

[9] Yatsimirskii K. B. *Teoreticheskaya Eksperimentalnaya Khimiya*, 1986, **3**, 280 (in Russian).

[10] Yakoi H., Addison A. *Inorg. Chem.*, 1971, **16**, 1341.

DIFFERENT MEANS OF DESCRIPTION OF THE CHEMICAL AND VIBRATIONAL KINETICS IN A COMPLEX GAS MIXTURE

O. V. Skrebkov

Institute of Chemical Physics in Chernogolovka, Chernogolovka, Russia

There is a broad class of problems requiring joint consideration of chemical reaction kinetics and vibrational energy transfer processes in the dynamics of reactive gaseous systems. This class of problems includes dynamics of explosions, combustion, flows around bodies, and nozzle flows, as well as multicomponent flows involving complex interaction between kinetics and gasdynamics, with the time scale of the gas flow being of the same order as the vibrational relaxation time. It is natural that simplified

kinetic schemes are necessarily employed in the numerical studies of such systems. The extent of simplification is determined by the particular gasdynamic conditions and the purpose of the computation. The use of the macroscopic kinetics [1–4] in the form of equations for mean vibrational energies and concentrations is one of the approaches that drastically reduce the number of kinetic equations, as compared to the detailed microscopic description in the form of population balance equations. However, simplified models are questionable with regard to their validity and accuracy. The answer to this question can be given by detailed solution of elementary kinetic problems on the micr ...copic level, i.e., by studying the simplest systems (in terms of composition and gasdynamics).

The results of solution of the isothermal problem of vibrational relaxation in a binary mixture of diatomic molecules treated as anharmonic oscillators with substantially different fundamental vibrational frequencies (the mixtures are $CO + O_2$, HCL $+ H_2$, $CO + HF$) for various concentrations and initial conditions, formulated within the framework of microscopic description, are presented in this paper. A quantitative comparison of micro- and macroscopic descriptions of the vibrational kinetics has been performed for these systems. The initial conditions used in the computations are characteristic of nozzle flows and combustion processes. For microscopic description of kinetics, we used the population balance equations (see, for example, [5]) incorporating all possible processes of the type

$$\{f; s\} \overset{P_{ij}^{(q)}}{\rightleftarrows} \{f - l_{ig}; s + l_{jq}\}, \tag{1}$$

occurring in molecular collisions of the anharmonic oscillators. Here, $P_{ij}^{(q)} = P\left\{ \begin{array}{cc} f, & f - l_{ig} \\ s, & s + l_{jq} \end{array} \right\}$ is the rate constant of the q-th process in which l_{iq} quanta of the i-th molecule in the vibrational state f are exchanged for l_{iq} quanta of the j-th molecule in the vibrational state s. The quantity $S_i = \sum_f f x_{if}$ (mean vibrational quantum stored in the i-th mixture component) is used for comparison; x_{if} is the relative population at the vibrational level f. Under the harmonicity assumption for molecular vibrations, we have equations for the mean energies $E_i = S_i^{harm}$ (see, for example, [1]). On the whole, the agreement between the results for S_i and E_i can be estimated only as qualitative. The agreement can be improved and brought to an approximate quantitative level for individual stages or the entire process by introducing into the equations for E_i constant anharmonicity-correcting (in time-average terms) multipliers for the rate constants. However, the validity of this parametric method of correction for anharmonicity within the framework of macroscopic description is limited to the cases of either the simplest compositions (for example, a small admixture in the Boltzmann thermostat) or systems with relatively low vibrational excitation $(S_i(0) < 1.0)$.

The knowledge of vibrational level populations of individual mixture components and their variation in chemical and vibrational interactions is of primary importance

for solving a number of problems (e.g., those arising in modeling upper atmosphere processes, working fluid flows in chemical lasers [6], laser emission [7], and combustion or detonation wave structure). However, a consistent microscopic formulation of multicomponent vibrational kinetics equations and solving them simultaneously with gasdynamics equations would be impractical because of the absence of detailed knowledge of elementary kinetics.

A formulation in which one group of components and vibrational states is treated microscopically and the other macroscopically significantly reduces the number of vibrational states and associated elementary processes taken into account, as compared to the consistently microscopic approach. An example of such a combined formulation of the kinetic equations is given in this paper. Here, the subsystem considered microscopically is a mixture of diatomic molecules treated as anharmonic oscillators chemically and vibrationally interacting with one another and with the remaining generally polyatomic components comprising the macroscopic subsystem. In addition to the elementary processes (1) within the microscopic subsystem and the macroscopic subsystem [2], the collisions of molecules of components treated microscopically with the molecules of macroscopic components must be taken into account. These include:

(a) microscopic reactions of the form

$$\sum_i \nu_{ir} Y_i(f) + \sum_{j \neq i} \nu_{ir} Y_j \overset{k_r(f)}{\underset{k_r'(f)}{\rightleftharpoons}} \sum_i \nu_{ir}' Y_i(f) + \sum_{j \neq i} \nu_{ir}' Y_j, \tag{2}$$
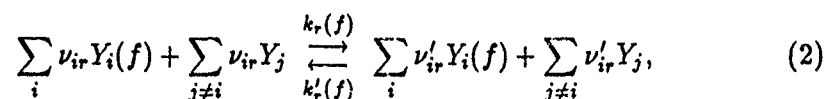
where $Y_i(f)$ is the i-th chemical component in the vibrational state f, and $k_r(f)$, $k_r'(f)$ are the rate constants of the r-th forward and backward microscopic chemical reactions; one of the stoichiometric coefficients ν_{ir} or ν_{ir}' of the i-th component is assumed to be zero;

(b) detailed vibrational relaxation of the molecules treated microscopically and modeled by anharmonic oscillators during their collisions with the molecules treated macroscopically and modeled by harmonic oscillators

$$\{f; v_m v_n\} \overset{P_{ij}^{(q)}}{\rightleftharpoons} \{f - l_{iq}; v_m - l_{mq}, v_n + l_{nq}\}. \tag{3}$$
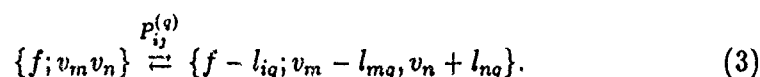
In the q-th process, a change in the quantum number f of the anharmonic oscillator of the i-th species by $\pm l_{iq}$ is accompanied by a change in the quantum numbers v_m and v_n of the m-th and n-th harmonic oscillators of the species j by $\pm l_{mq}$ and $\pm l_{nq}$, respectively. Within the framework of the harmonic oscillator model for the m-th and n-th modes, a process of type (3) is characterized by the probability $P_{ij}^{(q)}(f) = P \left\{ \begin{array}{cc} f, & f - l_{nq} \\ l_{mq}, & 0 \\ 0, & l_{mq} \end{array} \right\}.$

For given translational gas temperature and pressure (or density), the mixture state is determined by the component concentrations n_i per unit mass of mixture, mean energies E_k of the modes treated macroscopically, and the relative populations of the microscopic vibrational levels x_{if}.

The kinetic equations combining micro- and macroscopic descriptions in a reacting complex gas mixture are derived from the complete population balance equations by appropriate summation over the vibrational states of harmonic oscillators, v_m and v_n. As a consequence, additional terms appear on the right-hand sides of equations for E_i, n_i, and x_{vi}. These terms correspond to the processes of types (2) and (3) and correctly describe the chemical and vibrational behavior of both microscopic and macroscopic components considered.

The formulation of this kinetic problem is closed by the analytical expression for the rate constant of process (3), which is obtained by solving the corresponding dynamic problem.

References

[1] Biryukov A. S., Gordiets B. F. *Zhurnal Prikladnoi Mekhaniki Tekhicheskoi Fiziki*, 1972, **6**, 29 (in Russian).

[2] Vasil'ev V. M., Kulikov S. V., Skrebkov O. V. *ibid*, 1977, **4**, 13 (in Russian).

[3] Kulikov S. V., Skrebkov O. V., Vasil'ev V. M. *Khimicheskaya Fizika*, 1983, **2**, 8, 1038 (in Russian).

[4] Kulikov S. V., Skrebkov O. V. *Sov. J. Chem. Phys.*, 1990, **7**, 2, 384.

[5] Nikitin E. E., Osipov A. I. *Vibrational Relaxation in Gases*. Moscow, VINITI Publ., 1977 (in Russian).

[6] Bashkin A. S., Igoshin V. I. Oraevskiy A. N., Shcheglov V. A. *Chemical Lasers*, Moscow, Nauka, 1982 (in Russian).

[7] *Nonequilibrium Vibrational Kinetics*. (Capitelli M. Ed.) Berlin–Heidelberg–New-York–Tokyo, Springer–Verlag, 1986.

PECULIARITIES OF NITRIC OXIDES LIBERATION DURING TWO-STAGE BURNING

L. M. Sobolev, V. A. Karasev

Institute for Agriculture, Kostroma, Russia

Two-stage stratified burning reduces the requirements for octane number of petrol, improves fuel economy [1] and sharply decreases the amount of pollutants, especially nitric oxides NO_x in the exhaust gases. The design of double-bowl-in-head combustion chamber with four valves (Fig. 1) provides the conditions for two-stage stratified charge combustion and also makes it possible to study NO_x formation in the separate bowls 5 and 6 of the combustion chamber, sampling exhaust gases at point 7, and the total amount of NO_x at point 8.
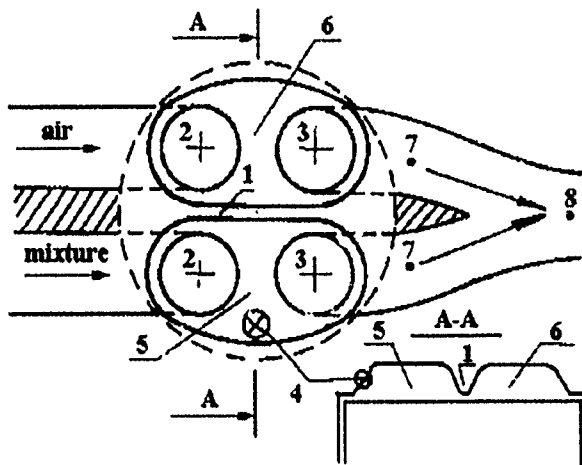
Figure 1: The diagram of stratified charge formation and two-stage combustion. 1 — dividing bulge; 2, 3 — intake and exhaust valves; 4 — spark plug; 5, 6 — the space with spark plug and the space without a spark plug; 7, 8 — exhaust gas sampling points.

The compositions of stratified charge in the separate volumes of the combustion chamber influence greatly the NO_x formation in the engine (Fig. 2). In the conventional open combustion chamber, the maximum amount of NO_x corresponds to the mixture with the relative air/fuel ratio $\alpha \approx 1.1$. According to the thermal theory of NO_x formation developed by Ya. B. Zel'dovich, the temperature of the working fluid is close to maximum, and there is enough free oxygen under these conditions. During the two-stage combustion the maximum amount of NO_x is formed when the lean mixture with $\alpha_0 \approx 1.4$ is used, but different amounts of NO_x are formed in the separate spaces of
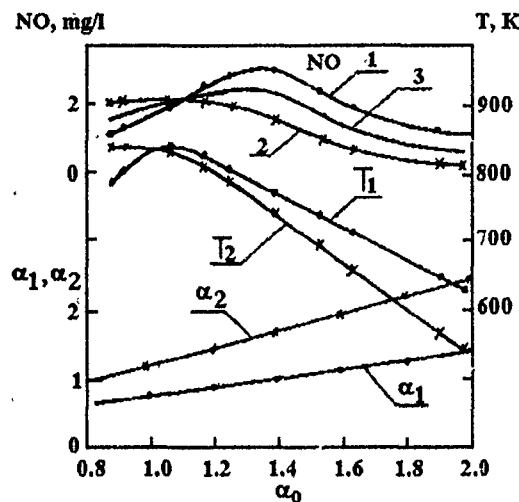
Figure 2: The effect of fuel mixture composition on NO_x formation at compression ratio $\varepsilon = 8.2$: *1* — in the first space; *2* — in the second space; *3* — total amount of NO_x.

the combustion chamber. Under these conditions, the fuel mixture with $\alpha_1 = 1.0$–1.1 is burned in the space with a spark plug, which creates favourable conditions for NO_x formation. At the same time the leaner fuel mixture $\alpha_2 \approx 1.5$–1.6 with a larger amount of free oxygen is burned in the space without a spark plug, but the flame temperature is low, which results in the amount of NO_x in the second space two times lower than in the first one.

During combustion of the rich mixture of common strength $\alpha_0 \approx 0.9$, one can observe a converse pattern of NO_x emission from two-space combustion chamber. In the first space, the fuel mixture is enriched up to $\alpha_1 \approx 0.6$, which sharply decreases the temperature of the charge behind the flame front and reduces the amount of NO_x, under the condition of the deficit of free oxygen, by three times. In the space without the spark plug the fuel mixture composition is close to stoichiometric, so that NO_x formation is maximum from this space.

Increasing compression ratio up to $\varepsilon = 11.7$ maintains the mechanism of nitric oxides formation at charge stratification (Fig. 3a), but the total amount of NO_x is nearly two times more than during two-stage stratified charge combustion in the engine with $\varepsilon = 8.2$. The sharp increase in NO_x emission from an engine with high compression ratio is due to the increasing flame temperature and the concentration of reactants in the unit mass of the working fluid.

If fuel mixtures of the same composition are burned in the two-space combustion chamber (Fig. 3b), the character of NO_x formation changes completely. In two-stage burning of the uniform fuel mixture, maximum NO_x formation corresponds to $\alpha_0 \approx 1.1$, as in one-space combustion chamber. Nonstratified rich fuel mixture combustion
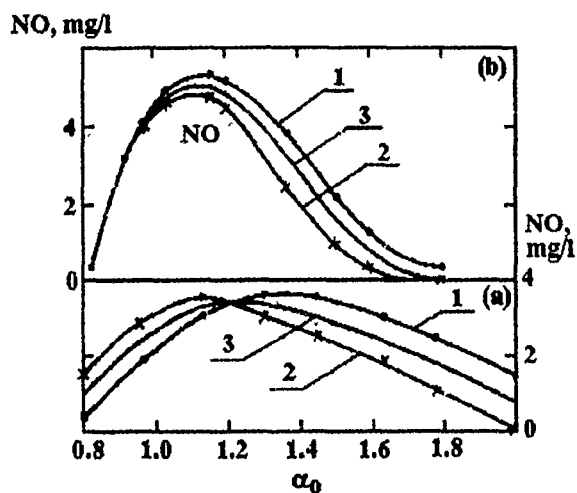
Figure 3: The effect of fuel mixture composition on NO_x formation at compression ratio $\varepsilon = 11.7$: a — stratified fuel mixture; b — nonstratified fuel mixture; 1, 2, 3 — the same as in Fig. 2.

results in equal NO_x emission from both of the spaces. Two-stage combustion of lean nonstratified fuel mixtures takes place under equal thermal conditions of the working fluid at equal concentration of free oxygen in both spaces, some decrease of the amount of NO_x in the second space is due to the reduction of combustion duration in this space and, as a result, to a decrease in the time of contact of chemically inert nitrogen with free oxygen.

References

[1] Sobolev L. M. *Chemical Physics of Combustion and Explosion Processes*, Chernogolovka, 1989, 48–50 (in Russian).

[2] Zel'dovich Ya. B., Sadovnikov P. Ya., Frank-Kamenetskii D. A. *Nitrogen oxidation in combustion. USSR Acad. Sci. Publ.*, 1947 (in Russian).

PROCESS ENGINEERING CONCERNING REDUCED-POLLUTANT THERMAL DISPOSAL OF HIGH-MOLECULAR ORGANIC RESIDUES FROM THE CRUDE OIL INDUSTRY

J. Sternberg, E. h. R. Jeschar, R. Scholz

Institut für Energieverfahrenstechnik, TU Clausthal, Germany

Currently, the investigations concerning the reduced-pollutant thermal disposal of high-molecular organic residual containing solids from the crude oil and lignite industry of the former East German Republic are being carried out in a combustion chamber. These inves   ons are conducted within the scope of a joint research project by the Institute   ᵡnergy Processing Technology and Chemical Engineering of the TU Bergakademie Freiberg and the Institute for Energy Processing Technology of the TU Clausthal. The research project is sponsored by the Deutsche Forschungsgemeinschaft (DFG). The residues from the high-conversion soaker cracking process (HSC residue) as well as tar–oil–solid mixtures (TOS residue) remaining after the pressurized degasification of lignite briquettes are used. Earlier investigations were carried out with a variety of residues such as visbreaker residual oil and petrol cokes [1].

The possibility of thermal disposing in a burning chamber firing process is initially determined by the physical properties of the type of fuel used. The choice of a suitable process procedure is furthermore dependent on the goal or objective aimed at and the amount of pollutants. The types of pollutants to be influenced through primary measures are, on the one hand, pollutants such as carbon monoxide (CO), hydrocarbons (C_xH_y), and soot, as well as other similar compounds, and, on the other hand, nitrogen oxides (NO_x). The main nitrogen oxide formation mechanisms are the thermal NO formation, the prompt NO formation and the fuel NO formation. The knowledge about the formation mechanism of the thermal NO is fully understood and recorded. However, in the case of the fuel and the prompt NO formation the knowledge and the understanding of the processes is far less complete. This is due to the reactions which occur at the flame front which are far more complex. In the case of the technical firings the so far frequently disregarded prompt NO formation cannot nowadays be ignored anymore since the permissible concentration of the pollutants is very low. Hence, the prompt NO formation has to be taken into account when optimizing a system. The combustion technical measures as shown in Fig. 1 for the reduction of the emission of pollutants can at times compete against one another; for example, the generation of fuel-rich reaction conditions reduces the nitrous oxide formation but promotes the formation of soot. The most recent developments have shown very clearly that, especially with respect to the emission of nitrogen oxides, considerable reduction potential
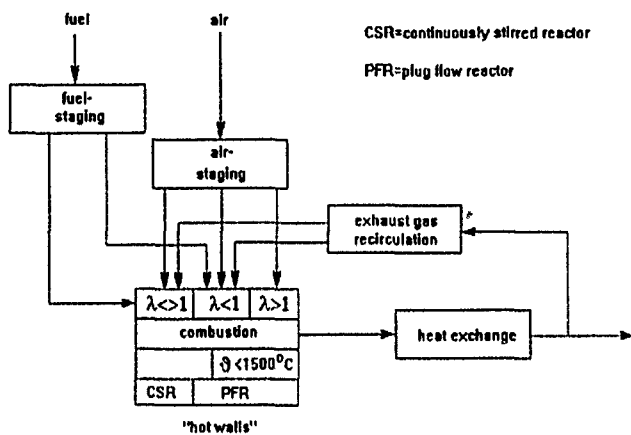
Figure 1: Aspects to process procedure conceptions of combustion. CSR = continuously stirred reactor; PFR = plug flow reactor.

through consistent application of primary measures exists, which has until now been fully exploited [2].

The optimization of the controlled combustion process (staging) with an existing reduction potential with respect to the pollutants mentioned above is represented by examples from the research conducted on the combustion of visbreaker and HSC residual oil and petrolcokes.

The difference in the liquid fuels mainly lies in the viscosity, as shown in Fig. 2. The viscosity of visbreaker residual oil is nearly the same as that of crude oil.

First investigations with conventional atomization systems have not led to satisfying results (Fig. 3) with respect to the atomization behavior, the achieved degree of burnout, and the nitrogen oxide emission in the case of the HSC residual oil combustion. This can be attributed to the quality of atomization achieved. To improve the atomization, the concept, as proposed by [4] of a prefilming nozzle was developed further and for the first time employed in a combustion system. The working principle is represented in Fig. 4. The nozzle system consists of three concentric lances. The fuel is centrally fed through the transport lance. The swirling primary air creates a fuel film on the inner side of the prefilming lance due to occurring thrust tensions. This film is then blown off by the atomization air resulting from the appearing forces. The experimental results of a second series of combustion of HSC residual oil using the prefilming nozzle are also shown in Fig. 3. In comparison to the first series of experiments, employing the prefilming nozzle resulted in a problem-free operation. The nitrogen oxide emission in the second experimental series was, at least, equivalent to that obtained with the visbreaker residual oil sometimes even better burnout characteristics.

Combustion of petrol cokes using the disposal of solid residuals as an example has been reported in [1].
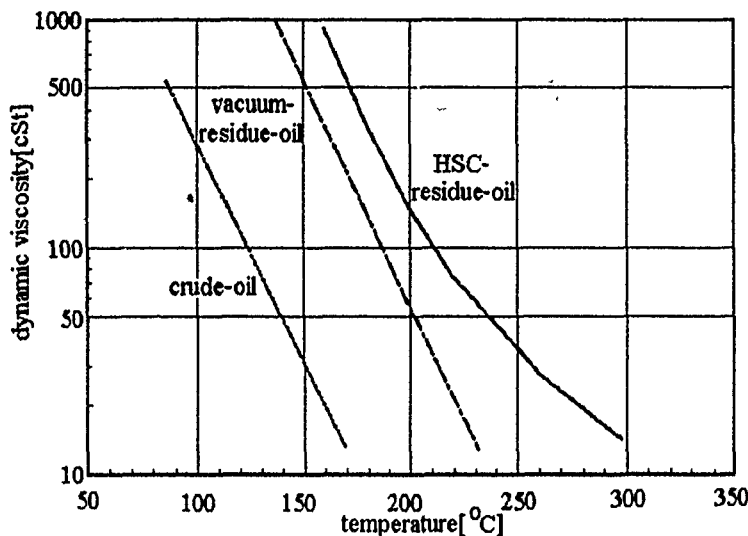
Figure 2: Temperature dependence of the dynamic viscosity of crude oil, vacuum oil, and HSC residual oils.
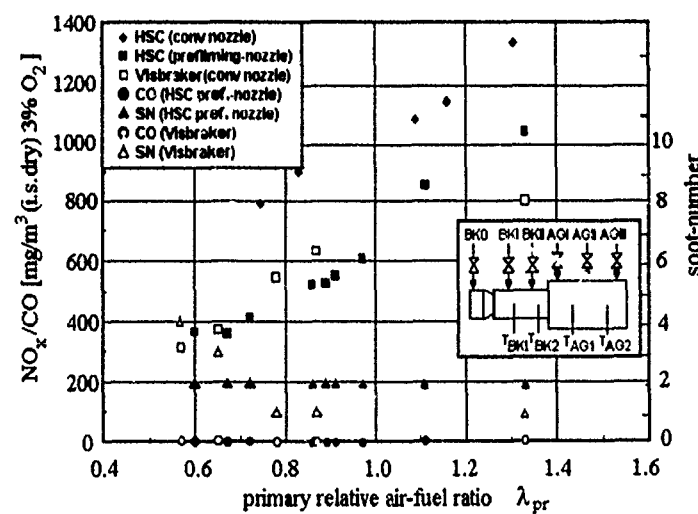
Figure 3: Comparison of the experimental results for the two-stage combustion of HSC and visbreaker residual oil.
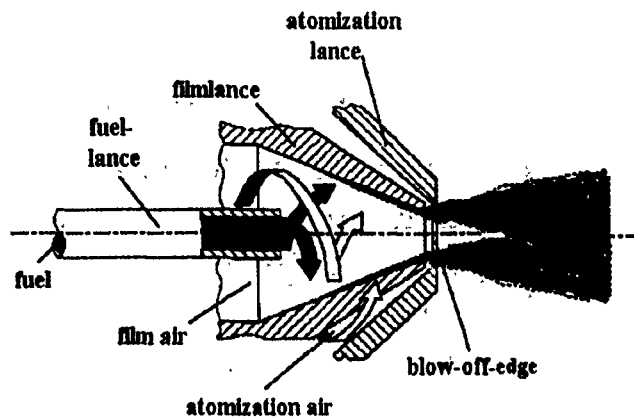
Figure 4: Working principle of the 'prefilming' nozzle.

References

[1] Jeschar, R., Scholz, R., Krone, T., Schopf, N., Kloppner, G., Malek, C., Sternberg, J. *DFG–Report (SFB 134/C4)*, 1992.

[2] Scholz, R., Jeschar, R., Beckmann, M., Sternberg, J. *Proc. PTS–WAF–Seminar*, 1992.

[3] Scholz, R., Sternberg, J. *Proc.: Energie und Umwelt'94*, Freiberg/Sachsen 23.3.–25.3.94.

[4] Glaser, H. W. *VDI–Fortschrittsberichte*, **7**: Stromungstechnik, 166, VDI Verlag Dusseldorf, 1989.

KINETICS OF SOOT FORMATION IN PYROLYSIS OF HYDROCARBONS AND THEIR MIXTURES

P. A. Tesner, S. V. Shurupov

All-Russian Institute of Natural Gas, VNIIGAZ, p/o Razvilka, Moscow Region, 142717 Russia

Despite the vast amount of data available in literature [1–4], soot formation in hydrocarbon pyrolysis has not been sufficiently investigated.

A technique for studying soot formation in hydrocarbon pyrolysis under isothermal conditions has been developed in VNIIGAZ [5].

Table 1.

Hydrocarbon	Particle number density (N/cm^{-3})
methane	$9.4 \cdot 10^{20}[\mathrm{CH_4}]\exp\left(-\frac{39400}{T}\right)$
acetylene	$3.0 \cdot 10^{22}[\mathrm{C_2H_2}]\exp\left(-\frac{41000}{T}\right)$
benzene	$2.7 \cdot 10^{21}[\mathrm{C_6H_6}]\exp\left(-\frac{35300}{T}\right)$
toluene	$2.3 \cdot 10^{21}[\mathrm{C_7H_8}]\exp\left(-\frac{35300}{T}\right)$
xylene	$1.7 \cdot 10^{21}[\mathrm{C_8H_{10}}]\exp\left(-\frac{35300}{T}\right)$

	Induction periods (τ_{ind}/s)
methane	$1.0 \cdot 10^{-9}[\mathrm{CH_4}]^{-0.9}\exp\left(\frac{21600}{T}\right)$
acetylene	$3.8 \cdot 10^{-9}[\mathrm{C_2H_2}]^{-0.9}\exp\left(\frac{19000}{T}\right)$
benzene	$6.2 \cdot 10^{-12}[\mathrm{C_6H_6}]^{-0.8}\exp\left(\frac{26700}{T}\right)$

	Rate of soot particles inception ($V/(\mathrm{cm}^{-3}{\cdot}\mathrm{s}^{-1})$)
methane	$7.2 \cdot 10^{29}[\mathrm{CH_4}]^{1.9}\exp\left(-\frac{61000}{T}\right)$
acetylene	$6.1 \cdot 10^{30}[\mathrm{C_2H_2}]^{1.9}\exp\left(-\frac{60000}{T}\right)$
benzene	$3.3 \cdot 10^{32}[\mathrm{C_6H_6}]^{1.8}\exp\left(-\frac{62000}{T}\right)$

$[\mathrm{CH_4}]$, $[\mathrm{C_2H_2}]$, and $[\mathrm{C_6H_6}]$ are the mole fractions.

Very simple patterns were observed using this technique. The soot particle number density for all hydrocarbons under study has been demonstrated to depend linearly upon hydrocarbon concentration. The activation energies of soot aerosol formation, as well as the expressions for soot particle number density for methane, acetylene, benzene,
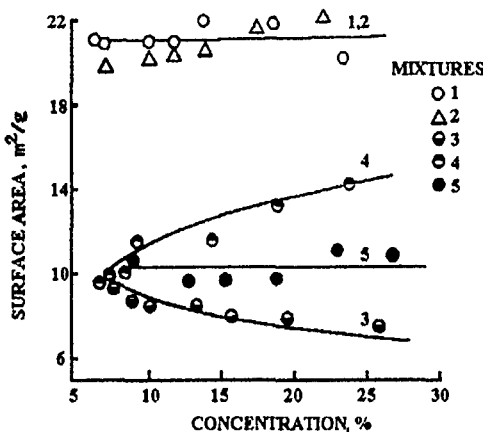
Figure 1: Surface area of soot vs composition of the mixture. Mixtures: 1 — acetylene-helium; 2 — benzene-helium; 3-5 — acetylene-benzene-helium; 3 — acetylene concentration is constant: 7.5%; 4 — benzene concentration is constant: 8.0%; 5 — acetylene and benzene concentrations are equal. X axis (Mixtures 3-4): the concentration of the hydrocarbon added; (Mixture 5) the concentration of each hydrocarbon.

toluene and xylene, were obtained (Table 1). The induction periods were measured to calculate the rate of soot particles formation.

The equations obtained enable us to make a quantitative comparison between hydrocarbons as regards their soot formation affinity under pyrolysis. At 1700 K, the relative affinities to soot formation in pyrolysis (the ratio of N_1/N_2 per one carbon atom, as well as the ratio of soot particles numbers in 1 g of soot equalled A_1^3/A_2^3, where A is the surface area, m^2/g) of acetylene benzene, toluene, xylene and methane amount to 6:6:5:3.3:1, respectively.

Employing the isothermic technique in the study of soot formation from hydrocarbon mixtures has resulted in observation of a new phenomenon, namely inhibition of soot particle formation [5]. First, for acetylene-benzene mixture, it has been shown that soot particles are formed from acetylene only, the soot formation from benzene being completely inhibited. Benzene is consumed by soot particle growth only. That is why a soot dispersion is lower for acetylene-benzene mixture than for individual hydrocarbons (Figs. 1-3).

A similar effect has been observed in the following mixtures: methane-benzene, benzene-xylene, benzene-naphthalene and benzene-anthracene. It has been demonstrated that, in the pyrolysis of methane-benzene mixtures, the soot particle were formed from benzene or acetylene, while methane was consumed by soot particle growth. In the pyrolysis of benzene-xylene mixture, the soot particle are formed from xylene, benzene being consumed only by particle growth. In the pyrolysis of benzene-naphthalene and benzene-anthracene mixtures, the soot particles are formed
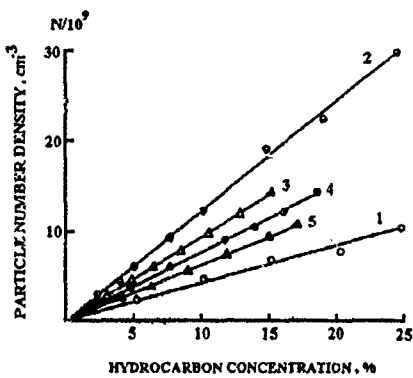
Figure 2: Particle number density vs. hydrocarbon concentration in helium. *1* — methane, *2* — acetylene, *3* — benzene, *4* — toluene, *5* — xylene; Temperature: *1, 2* — 1300 °C, *3, 4, 5* — 1200 °C.
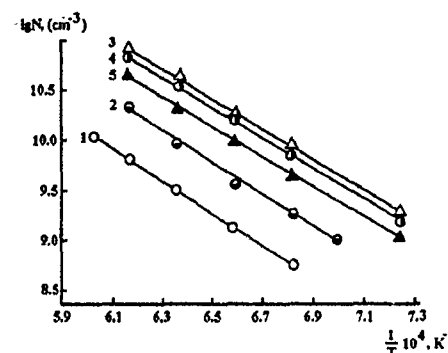
Figure 3: Particle number density vs reciprocal temperature. *1* — methane, *2* — acetylene, *3* — benzene, *4* — toluene, *5* — xylene.

from naphthalene or anthracene, benzene being consumed by particle growth only.

An explanation of the effect of inhibition can be given in terms of the difference in induction periods of soot particle formation. The soot particles are formed from the hydrocarbon with the shorter induction period. The hydrocarbon with the longer induction period is only consumed by particle growth as the soot nuclei are destroyed on the surface of the particles formed. Obviously, the inhibition observed is a common pattern of soot formation in the pyrolysis of hydrocarbons mixtures.

References

[1] Tesner P. A. *Formation of Solid Carbon from Hydrocarbons in Gas Phase.* Moscow, Khimiya, 1972 (in Russian).

[2] Lahaye J., Prado G. In: *Chemistry and Physics of Carbon.* (Walker P. L., Thrower P. A. Eds.) New York, Marcel Dekker, 1978, 14, 167.

[3] Haynes B. S., Wagner H. Gg. *Prog. Energy Comb. Sci.*, 1981, **7**, 229.

[4] Prado G., Lahaye J. In: *Particulate Carbon.* (Siegla D. C., Smith W. G. Eds.), New York, Plenum Press, 1981, 143.

[5] Tesner P. A., Shurupov S. V. *Comb. Sci. Techn.*, 1993, **92**, 61.

MECHANISMS OF CARBORANE 1,6–$C_2B_4H_6$
HIGH-TEMPERATURE OXIDATION IN WATER VAPOR

S. A. Tsyganov, V. G. Slutsky, E. S. Severin, E. V. Bespalov

Semenov Institute of Chemical Physics, Kosygin str. 4, Moscow, 117977 Russia

Abstract

The reactivity of carborane 1,6–$C_2B_4H_6$ in water vapor at 930–1750 K and 0.02–3.0 MPa is experimentally investigated, and a detailed oxidation scheme is proposed.

Introduction

High-temperature oxidation kinetics for compounds consisting of C, H, and N atoms has been described in a vast number of publications, among which the works by Zel'dovich [1] play an important role. The results of these works serve as a basis for the studies of the poorly investigated oxidation kinetics for compounds containing B, H, and C atoms. Carboranes ($C_2B_nH_{n+2}$, $3 \leq n \leq 10$) belong to this class of compounds. Carboranes are organoboron compounds with boron and carbon atoms forming cage structures. Under normal conditions, they are stable, non-toxic, and have high energetic characteristics due to the considerable boron content.

Experimental

Gaseous carborane–4 (1,6–$C_2B_4H_6$, Fig. 1) appears to be a convenient object for investigations. Experiments on self-ignition of the 0.038 $C_2B_4H_6$ + 0.462 H_2O + 0.5 Ar gaseous mixture at $930K \leq T \leq 1750$ K and $P(\pm 10\%) = 0.02$ MPa, 0.9 MPa, 1.7 MPa, and 3.0 MPa were carried out in a preheated (403 ± 3 K) rapid compression machine and behind reflected shock waves in a preheated (403 ± 3 K) shock tube [2].

Results and Discussion

The results are shown in Fig. 1. For comparison, the ignition delay τ is also shown in Fig. 1 versus temperature for the stoichiometric propane/air mixture at $P = 0.9$ MPa.

It follows from Fig. 1 that carborane–4 is a highly reactive compound: at $P = 0.9$ MPa and $T > 1200$ K its reactivity in water vapor exceeds that of propane in air by a factor of 3 to 7. Furthermore, the ignition delay for carborane/water vapor mixture decreases with the increasing pressure at $T > 1200$ K, but is pressure independent at $T < 1000$ K.
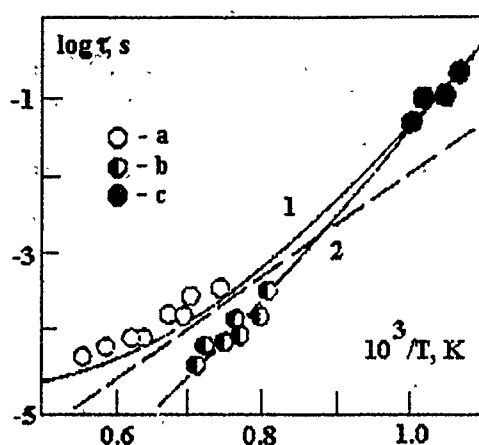
Figure 1: Ignition delays for 0.038 $C_2B_4H_6$ + 0.462 H_2O + 0.5 Ar mixture. Experimental results: (a), (b), and (c) correspond to P = 0.02 MPa, 0.9 MPa, and 0.9 MPa $\leq P \leq$ 3.0 MPa, respectively. Predicted results: lines 1 and 2 are the predictions for P = 0.02 MPa and P = 0.9 MPa obtained using the scheme of Table 1. Broken line corresponds to self-ignition of stoichiometric propane/air mixture at P = 0.9 MPa [6].

Table 1: Kinetic scheme of carborane 1,6–$C_2B_4H_6$ oxidation in water vapor (kcal/mol, cm^3/(mol·s)).

	Reaction			$\log_{10} A$	E	$-\Delta H_{298}$
1	$C_2B_4H_6$	$\longrightarrow$	BH_2–$C_2B_3H_4$	12.5	59.0	−28.1
2	BH_2–$C_2B_3H_4$	$\longrightarrow$	$C_2B_4H_6$	9.6	30.0	28.1
3	BH_2–$C_2B_3H_4$	$\longrightarrow$	H_2 3 + H_2	11.3	3.3	33.4
4	3 + H_2O	$\longrightarrow$	4 + H_2	11.3	3.3	27.1
5	4 + H_2O	$\longrightarrow$	$B(OH)_3$ + $C_2B_3H_5$	11.3	3.3	16.6
6	$C_2B_3H_5$ + H_2O	$\longrightarrow$	6 + H_2	13.0	20.0	33.4
7	6 + H_2O	$\longrightarrow$	7 + H_2	13.0	20.0	33.4
8	7 + H_2O	$\longrightarrow$	8 + H_2	13.0	20.0	33.4
9	8 + H_2O	$\longrightarrow$	9	13.0	20.0	13.4
10	9 + H_2O	$\longrightarrow$	10 + $B(OH)_3$	11.3	3.3	30.4
11	10 + H_2O	$\longrightarrow$	11	11.3	3.3	30.4
12	11 + H_2O	$\longrightarrow$	12 + $B(OH)_3$	11.3	3.3	30.4
13	12 + H_2O	$\longrightarrow$	13 + CH_4	11.3	3.3	30.4
14	13 + H_2O	$\longrightarrow$	$B(OH)_3$ + CH_4	11.3	3.3	30.4
15	H_3BO_3	$\longrightarrow$	HBO_2 + H_2O	14.1	54.5	−48.0
16	HBO_2 + H_2O	$\longrightarrow$	H_3BO_3	11.8	11.9	48.0
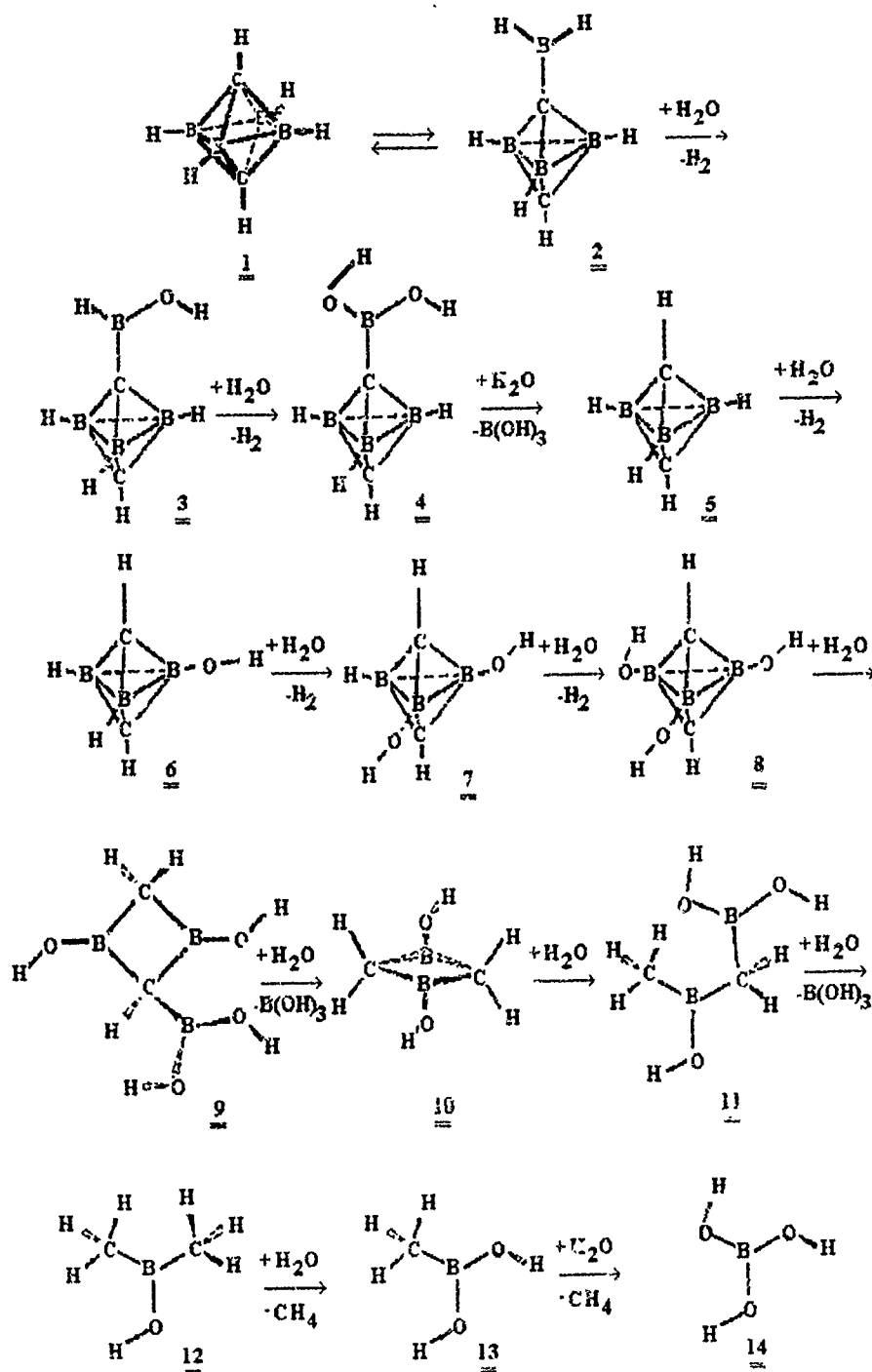
Figure 2: Sequence of carborane 1.6–$C_2B_4H_6$ oxidation in water vapor.

The computed [3] equilibrium constant

$$K_p = 10^{2.95} \exp\left(-\frac{29 \text{ kcal}}{RT}\right) \tag{1}$$

between carborane–4 and its active C–BH_2 isomer (Fig. 2), which contains a trivalent B atom in an exo–BH_2 group, points to the high concentration of these isomers at elevated temperatures (for example, at $T = 1500$ K the equilibrium concentration of C–BH_2 isomer is 6.7%). Like the BH_3 molecule, the C–BH_2 isomer actively reacts with water vapor, which explains the high reactivity of carborane–4 in water vapor.

Orthoboric acid, hydrogen, and the lower carborane–3, $C_2B_3H_5$, are the products of C–BH_2 isomer/water vapor interaction (Fig. 2). The constants for reactions of C–BH_2 isomer and its derivatives with water vapor are equal to the reaction rate constant of $BH_3 + H_2O$

$$k_{BH_3+H_2O} = 10^{11.3} \exp\left(-\frac{3.3 \text{ kcal}}{RT}\right) \text{ cm}^3\text{mol}^{-1}\text{s}^{-1} \tag{2}$$

The estimation of the carborane–3 −− water vapor reaction rate constant yields

$$k_{C_2B_3H_4+H_2O} = 10^{13} \exp\left(-\frac{20 \text{ kcal}}{RT}\right) \text{ cm}^3\text{mol}^{-1}\text{s}^{-1} \tag{3}$$

The full oxidation scheme for carborane–4/water vapor system is given in Fig. 2 and Table 1. A comparison of the experimental results on self-ignition at $P = 0.9$ MPa and $T < 1000$ K with computations made it possible to determine the rate constant of direct carborane–4 isomerization

$$k_1 = 10^{12.5} \exp\left(-\frac{59 \text{ kcal}}{RT}\right) \text{ s}^{-1}, \tag{4}$$

and to obtain from Eq. (1) the constant of the reverse isomerization

$$k_{-1} = 10^{9.6} \exp\left(-\frac{30 \text{ kcal}}{RT}\right) \text{ s}^{-1} \tag{5}$$

The ignition delays computed by the full scheme satisfactorily describe the experimental data in the entire range of the investigated temperatures and pressures (Fig. 1).

References

[1] Zel'dovich Ya. B., Barenblatt G. I., Librovich V. B., Makhviladze G. M. *Mathematic Theory of Combustion and Explosion.* Moscow, Nauka, 1980 (in Russian).

[2] Tsyganov S. A., Slutsky V. G., Severin E. S., *et al. Dokl. Akad. Nauk SSSR*, 1991, **317**, 269 (in Russian).

[3] Slutsky V. G., Hofman M., Schleyer P. v. R. *Mendeleev Comm.*, 1994, **2**, 12

THE EFFECT OF ELECTRIC FIELD ON IGNITION AND COMBUSTION PROCESSES OF COMBUSTIBLE GASES, DUST AND LIQUIDS

D. A. Yagodnikov, A. V. Voronetskii

Moscow

Gaseous fuels

The blow-off characteristics of the propane–air premixed flame at the atmospheric pressure in a bunsen burner with electric field (EF) applied were investigated. In preliminary experiments, constant potential 0.9 kV was created between the burner nozzle (negative electrode) 10 mm in diameter and coaxial metal ring electrode 75 mm in diameter. In this case, longitudional EF was realized. Figure 1 shows that the blow-off velocity V increases at different propane flow rates G and reaches a peak at the distance $x = 40$–60 mm between the nozzle exit and the ring electrode. It is known that the effect of EF on ignition and combustion processes is realized by means of ionic wind [1] (coinciding in direction with positive ions movement) or, otherwise because of intensification of chemical reactions [2] (in the presence of nitrogen). Therefore, with negative voltage applied to the nozzle, the ionic wind directed toward the burner nozzle moves the hot gases, which explains the increase in the blow-off velocity.

Also, flame structure was studied by recording ionization current i at various positions of the ring electrode and various equivalence ratios ϕ. The measurements have shown that a maximum i is reached at some distance from the nozzle. Its position moved from the nozzle with increasing propane flow rate (decreasing ϕ), and the value of i increase with fuel-rich premixed flame height in the range of 90–140 mm. At the highest peak of i (at $\phi = 0.37$) fine soot particles form in combustion products, which increases electrical conductivity of the flame [1]. The extrema of $i(x)$ are attributable to the existence of flame regions where positive ions, electrons and soot particles concentrations are the highest.

It has been found that at EF voltage 0.9 kV and ionization current maximum 0.002 mA, emitted Joule heat power is above 1.8 mW and cannot intensify ignition and combustion processes.

In the second series of experiments, cylindrical grid electrodes at the height 200 mm were used to create a transverse EF. The grids were made of stainless steel 0.5-mm diameter wire with mesh size 1 to 1 mm. The experimental results are presented in Fig. 3 at the negative potential 0.9 kV at the burner nozzle. It has been established that blow-off velocity grows as the cylindrical electrode diameter D decreases at various values of G. These points to an additional EF tension. The enhancement can be explained by the effect of ionic wind directed to the burner nozzle. In conclusion, it

87
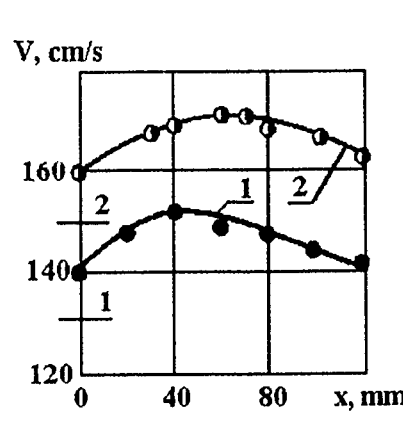
Figure 1: Flame blow-off characteristics at $G = 8$ (*1*) and 12 (*2*) mg/s. Dashed lines — values V by zero-field.
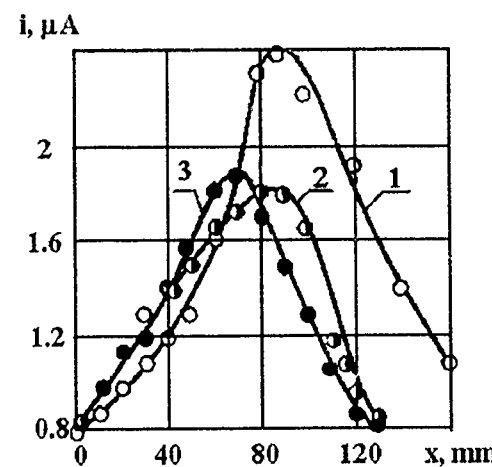
Figure 2: Dependence of i on x at $f = 0.37$ (*1*), 0.46 (*2*) and 0.53 (*3*).
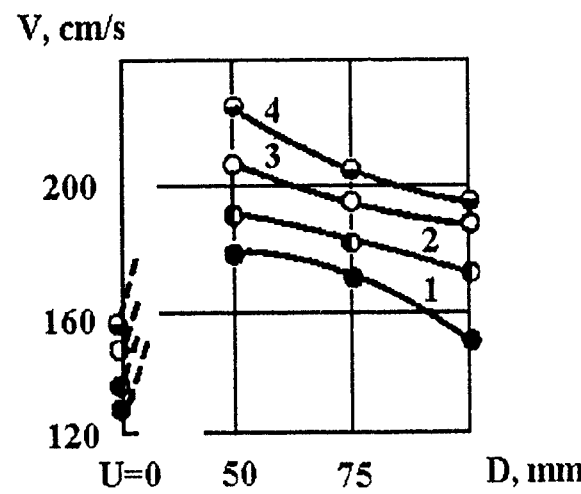
Figure 3: Flame blow-off characteristics at $G = 8$ (*1*), 10 (*2*), 11 (*3*), 12 mg/s (*4*).

can be mentioned that the blow-off velocity in the second series was by 18–20% higher for identical conditions.

Combustible Dust

In the present work, we proposed to use a diffusion bunsen-type dust flame to study the EF effect on metal fuel combustion. An aluminum polydisperse powder is used with mass-average particle diameter about 25 μm. The dust flame was stabilized on a 15-mm diameter burner nozzle. The pilot flame of temperature 2000 K sufficed to ignite aluminum particles. Electric field was created between the nozzle and a 75-mm diameter cylindrical grid electrode.

In the test with negative voltage 0.9 kV applied to the nozzle, flame fluctuations and periodical variations of flame surface were observed: the conical shape evolves to the shape of umbrella. This is due to the motion of aluminum oxide particles towards the cylindrical electrode, which results in an increase in the ionization current from 0.001 mA (without aluminum particles combustion) to 0.1 mA. Thus, dust flame electrical conductivity is enhanced due to the fact that aluminum oxide particles acquire a negative charge (mainly by electron attachment).

Liquid fuel

The purpose of this experiment was to study the effect of EF on flame stabilization at the atmospheric pressure in a combustion chamber of 70 mm by 70 mm cross section. A hydrocarbon fuel (96% vol. of ethylene alcohol) was sprayed into a chamber through a 0.7-mm diameter swirl injector. A frontal PMMA window 160 mm long and 70 mm wide provided the optical access into the test section. Air was used as the oxidizer. The flame front was stabilized on a conical holder (cone angle 90°, diameter 18 mm). Negative voltage 1.5 kV was applied to the bluff body, and the combustion chamber was grounded. The experiments have revealed that stable combustion occurs at distances between injector and holder not more than 60 mm. Thus, for the average flow velocity at the chamber inlet $V = 0.8$ m/s the equivalence ratio at the rich combustion stability limit was $\phi = 0.55$–0.6 (zero field), whereas with EF superposition, $\phi = 0.43$–0.45 (enhanced by about 23%). It is well known that flame stabilization limits depend on the intensity of heat and mass transfer between the recirculation zone (RZ) behind a bluff-body and the main flow. According to [3], positive ions were observed in RZ. Consequently, the ionic wind directed to the negative electrode-holder increases the RZ length and compensates for the decrease in combustion temperature in enriched fuel–air mixture.

In conclusion, it should be noted that the low required energy and the positive results suggest the use of EF for intensification of combustion processes in various engines.

References

[1] Lawton J., Weinberg F. J. *Electrical Aspects of combustion.* London, Clarendon Press Oxford, 1969.

[2] Shebeko Yu. N. *Fizika Goreniya Vzriva*, 1982, **18**, 4, 48 (in Russian).

[3] Reznik V. E., Tokarev V. V., Shaikin A. P. *Izv. VUZov. Aviatsionnaya Tekhnika*, 1977, **3**, 93 (in Russian).

SESSION 2. Ignition and Steady-State Flame Propagation

IGNITION THEORY FOR CONDENSED PROPELLANTS: DEVELOPMENT OF ZEL'DOVICH IDEAS

Igor G. Assovskii

Semenov Institute of Chemical Physics, Kosygin Str. 4, Moscow, 117977 Russia

Criteria for self-sustaining combustion process are the subject of current interest in combustion science and numerous applications.

The objective of this paper is to show how the ideas about ignition and extinction of gasifiable rocket propellants put forward by Zel'dovich are nowadays developed and used in theories of ignition process.

There are many similar features in ignition and extinction of condensed propellants, although both effects are usually caused by different sources. For example, the transient extinction of solid propellants due to fast pressure release in a combustion chamber is often accompanied by reignition [1], as the ignition under a high heat flux can be followed by propellant extinction [2]. So, advanced analysis of each of these effects is required to adequately understand the other one.

1. The principles of the modern theory of thermal ignition can be traced back to the classical work by Zel'dovich and Frank-Kamenetskii [3] on combustion wave propagation in gaseous mixtures. According to that work, the reaction proceeds at the maximum temperature in the combustion wave, and the propagation process can be viewed as a sequence of ignitions of fresh gas layers by hot combustion products.

   The next step was made in [4], where the initiation of exothermic reaction by hot surface was considered. The ignition was linked to the loss of stability of the steady-state temperature distribution in the reacting gas near the hot surface. It has been shown that the heat flux from the hot surface to the gas is zero under the critical conditions, and the heat flux from the gas reaction zone to the cold gas is equal to its minimum value.

   These results extended the thermal explosion theory of van't Hoff and Semenov to the cases where exothermic reaction takes place under nonuniform thermal conditions.

2. The application of the theory of [3, 4] to the problems of ignition and combustion of gasifiable condensed propellants [5, 6] has served as a basis for two approaches to ignition.

The first approach deals only with the initial stage of thermal decomposition of a condensed-phase propellant (the c-phase approach). The necessary condition for the thermal explosion of the reacting surface layer to occur is assumed to be the ignition criterion. In the c-phase approach, ignition is not affected by the characteristics of combustion wave propagation. The post-ignition behavior of the system is not considered because it is outside of the scope of the assumptions underlying this approach.

Comprehensive reviews of numerous works using this approach can be found in [7, 8].

The other approach to ignition is based on the phenomenological theory of non-steady combustion of condensed propellants [5] (the phenomenological approach). It postulates that ignition occurs when the criterion for combustion wave propagation is surpassed [9–11]. This ignition criterion disregards low-temperature thermal decomposition of propellant.

However, propellant ignition, as well as extinction, is close to the boundaries of the domains of both the existence of a combustion wave and the applicability of the theory of nonsteady combustion [11,12]. Therefore, the formulation of the ignition criterion requires invoking additional information concerning formation of the combustion wave.

3. The propellant ignition criteria are commonly used to determine ignition delay times. However, the ignition conditions can significantly influence the subsequent combustion rates and pressure histories in combustion chambers [13]. Thus an adequate description of the whole ignition process is required.

Such an integrated model of ignition, proposed in [14], combines the advantages of both the phenomenological approach (applied to the transient combustion following the initiation of the combustion wave) and the c-phase approach (applied to the propellant behavior prior to the flame propagation). This model takes into account the heat released in the reaction of propellant decomposition during the heating and the difference between the kinetics of low-temperature decomposition and the kinetics of the high-temperature combustion reactions.

The application of Zel'dovich phenomenological approach to the initial stage of combustion wave propagation makes it possible to effectively include complicated physico-chemical processes involved in the phenomenon.

Further developments in the ignition theory have been directed towards a more detailed characterization of both c-phase thermal decomposition [15–18] and formation of the gas–phase flame [19].

References

[1] Assovskii I. G., Istratov A. G., Leipunskii O. I. *Dokl. Akad. Nauk SSSR*, 1978, **239**, 3, 625 (in Russian).

[2] Assovskii I. G., Zakirov Z. G. *Sov. J. Chem. Phys.*, 1990, **6**, 11, 3122.

[3] Zel'dovich Ya. B., Frank-Kamenetskii D. A. *Zhurnal Fizicheskoi Khimii*, 1938, **12**, 1, 105 (in Russian).

[4] Zel'dovich Ya. B. *Zhurnal Experimentalnoi Teoreticheskoi Fiziki*, 1939, **9**, 12, 1530 (in Russian).

[5] Zel'dovich Ya. B. *ibid*, 1942, **12**, 11/12, 498.

[6] Zel'dovich Ya. B., Leipunskii O. I., Librovich V. B. *Theory of Nonsteady Combustion of Powder*, Moscow, Nauka, 1975 (in Russian).

[7] Merzhanov A. G., Averson A. E. *Comb. Flame*, 1971, **1?**, 89.

[8] Vilyunov V. N. *Theory of Ignition of Condensed Materials*, Novosibirsk, Nauka, 1984.

[9] Librovich V. B. *Zhurnal Prikladnoi Mekhaniki Tekhnicheskoi Fiziki*, 1963, **6**, 74 (in Russian).

[10] Gostintsev Yu. A. *Fizika Goreniya Vzriva*, 1971, **7**, 3 (in Russian).

[11] Novozhilov B. V. *Nonsteady Combustion of Solid Rocket Fuels*, Moscow, Nauka, 1973 (in Russian).

[12] De Luca L. *Proc. 18th Symp.(Int.) on Comb.*, The Combustion Institute, 1981, 1439.

[13] Assovskii I. G. *Dokl. Akad. Nauk SSSR*, 1987, **294**, 1, 103 (in Russian).

[14] Assovskii I. G., Zakirov Z. G., Leipunskii O. I. *Fizika Goreniya Vzriva*, 1983, **19**, 1, 41 (in Russian).

[15] Kumar M., *et al. AIAA J.*, 1984, **22**, 526.

[16] Glotov O. G., Zarko V. E. *Fizika Goreniya Vzriva*, 1984, **20**, 4, 3 (in Russian).

[17] Baklan S. I., Dik I. G., Vilyunov V. N. *ibid*, 1989, **25**, 1, 10 (in Russian).

[18] Zarko V. E., Knyazeva A. G. *Proc. 32nd Aerospace Sciences Meeting & Exhibit.*, AIAA, 1994.

[19] Assovskii I. G. *Proc. 30th Japanese Comb. Symp.*, 1992, 25.1.

BURN RATE AND SEM STUDIES ON METAL POWDER (Ti, Ni) BASED FUEL RICH PROPELLANTS

B. K. Athawale, S. N. Asthana, P. G. Shrotri, Haridwar Singh

Explosives Research & Development Laboratory, Pune 411 021, India

Introduction

Metallized fuel rich systems have emerged as an important class of rocket propellants with the resurgence of ramjet concept. These propellants offer much higher I_{sp} (> 400 s) in air breathing rocket ramjets than current solid propulsion systems (< 350 s) based on composite and composite modified double-base (CMDB) propellants. Ducted rockets and scramjets operating on the ramjet principle have a potential to meet the requirements of advanced futuristic tactical and standoff strategic missiles. Basically, fuel-rich propellants comprise metals in more than 20% proportion dispersed in a polybutadiene or double-base matrix. Recently, energetic polymers like glycidyl azide polymer (GAP) and bis-azidomethyl oxetane (BAMO) have also emerged as binder/plasticizer for fuel-rich propellants. A small quantity of oxidizer such as AP is added to ensure sustained combustion. Al, Be, B, Mg and Zr are the candidate metal fuels for this class of propellants. Both Al and Be have limitations as components of fuel rich propellants because the conditions required for their combustion are severe, due to the protective layer of metallic oxide. Furthermore, BeO, the main combustion product of Be, is toxic. B is a highly attractive fuel for ram rockets in view of its highest air/fuel ratio among the candidate metals. However, high melting and boiling points of B result in combustion inefficiency of fuel-rich propellants and its combustion product B_2O_3 is a solid or a highly viscous glassy liquid. Although Mg has limitations due to its relatively low air/fuel ratio (3.29), Mg-based fuel-rich propellants find wide applications owing to their easy ignition even at high metal loading.

Zr and Ti also have a potential to offer fuel-rich propellants with efficient combustion because of the advantage of solubility of their oxides in the molten metal and moderate ignition temperatures. Zr and Ti have the additional advantage of high density, as compared to Al and Mg, and hence offer high volumetric impulse. In view of high reactivity and density, Ni also appears to be a potential fuel for ramjet rockets. The information available on Zr-based formulations is limited and both Ti and Ni are almost unexplored as fuels. We have earlier reported the burn rate pattern of Zr-based propellants. The present study was undertaken to investigate in detail the burn rate behavior of Ti and Ni based fuel-rich systems in comparison to Al and Zr containing formulations with HTPB and double-base binder matrix in view of the promising results obtained during initial studies (initial work presented in VII National Seminar on High-Energy Materials, Feb'94). The potential of GAP as an energetic plasticizer has also

been evaluated in a double-base matrix. Scanning electron microscope (SEM) studies were undertaken to understand the combustion mechanism of fuel-rich propellants in condensed phase. The theoretical performance of Ti, Al and Zr based compositions in secondary chamber has been computed.

Experimental

Propellant compositions for the present work were prepared by a slurry cast technique. The basic composition of composite formulation was 20% binder [HTPB 12%, IDP + requisite DDI 8%] and 80% filler [20, 30, 40, 50, 60% metallic fuel and 60, 50, 40, 30, 20% AP]. CMDB compositions comprised 30% SNC (NC 27%, NG 2%, Carbamite 1%), 30% casting liquid (NG 24%, DEP 5.4%, 2–NDPA 0.6%) and 40% filler (20, 30, 40% metallic fuel and 20, 10, 0% AP). In the case of GAP-based compositions, DEP was replaced by GAP, while basic composition remained the same.

The burn rates were determined by acoustic emission technique at 10, 20, 35, 50, 70 and 90 KSC using a piezoelectric transducer with a resonance frequency of 200 kHz. The extinguished propellant samples were subjected to SEM (JEOL JSM J 200) studies. NASA CEC–71 code was adopted to theoretically predict the ballistic performance of fuel-rich compositions in the secondary chamber, except for the Ni-based formulations, since required thermochemical data on Ni was not easily available.

Results and Discussion

Composition containing 20% Al with 60% AP in the HTPB binder was taken as the control. In exhibited burn rates of 3.9–6.8 mm/s in the 10–90 KSC pressure range. On increase in Al content to 30–40% level at the cost of AP, stable combustion could not be achieved at 10 & 20 KSC and there was a drop in burn rates by 40–50% in the 35–90 KSC region. In the case of 20% Ti-based formulation, the burn rates were found to be comparable to those of corresponding aluminized formulation. Unlike aluminized composition with 30–40% metal content, the corresponding Ti-based formulations exhibited stable combustion even at lower pressures (10 & 20 KSC) and produced 30–60% higher burn rates in the 35–90 KSC region.

The fuel-rich propellant with 50% Al did not exhibit sustained stable combustion in the pressure range of 10–50 KSC and that with 60% Al in the pressure range of 10–90% KSC. However, the corresponding Ti-based fuel gave stable combustion in the entire pressure range of 10–90 KSC. As compared to Zr-based formulations, burn rates obtained for 20–40% Ti based compositions were relatively lower (5–20%). However, with 50–60% metal content Ti exhibited superior combustion behaviour. These results establish superior combustion efficiency of Ti-based propellants with high metal content at lower pressures.

Metallized double-base composition with 20% Al and 20% AP content was taken as the reference composition for comparative burn rate evaluation of fuel-rich formula-

tions in a double-base matrix. It yielded burn rates of 8.2–16.4 mm/s in the 35 -90 KSC region. On increase in Al content to the 30% level at the cost of AP, stable combustion could not be achieved at 35 & 50 KSC and burn rates recorded at 70 & 90 KSC were lowered by 40–50%. The formulation with 20% of Ti exhibited burn rates more or less similar to those for the aluminized propellant. Unlike the aluminized propellant, the 30% Ti-based formulation was characterized by stable combustion at 35 & 50 KSC and the burn rates obtained at 70 & 90 KSC were by 20–30% higher. 20–30% Ni-based propellants yielded burn rates comparable to those for the Ti formulation. However, unlike Ti, stable combustion could be achieved even at lower pressures (10 & 20 KSC) with Ni-based propellants, as in the case of Zr-based formulations. Burn rates recorded for both Ti and Ni containing compositions were relatively lower than those for Zr-based formulations. While the 40% Ti-based composition did not undergo stable combustion in the entire pressure range, 40% Zr-based formulations did not exhibit stable combustion in the pressure range of 10–20 KSC. However, the corresponding Ni-based fuel-rich propellant showed sustained combustion in the entire pressure range. Incorporation of GAP led to a remarkable (two to threefold) increase in burn rates for all the compositions and resulted in stable combustion even with 40% Ti as in the case of Al-based formulation in a double-base matrix.

Relatively poor combustion efficiency of aluminized propellants at low pressure and high metal loading can be attributed to the fact that aluminum combustion occurs at $\sim$ 2500 K, while the ignition temperature of Zr and Ti is $\sim$ 1200 K which can be achieved near the burning surface of the propellant. Supporting evidences were obtained by SEM. Thus, aluminized formations exhibited formulation of agglomerates of unburnt metal on the extinguished surface, while in the case of Ti- and Zr-based formulations expansion of metal particles followed by decomposition of overall surface was observed. Theoretical I_{sp} for Ti-based fuel-rich compositions was found to be $\sim$ 500 s at $A/F = 5$ as in the case of Al- and Zr-based formulations.

References

[1] Thomas A. N. Jr. *Astronautics and Aeronautics*, 1980, 38–41, 71.

[2] Kubota N., Yano Y., Miyata K., Kuwahara T., Mitsuno M., Nakagawa 1. *Propellants, Explosives, Pyrotechnics*, 1991, **16**, 287–292.

[3] Hsin W., Peretz A., Te Huang, Kuo K. *J. Propulsion*, 1991, **7**, 4, 497–504.

[4] King M. K. *Report No.TR–PL–5520*, Atlantic Research Corporation, Vergenia, 1976.

[5] Rastogi R. P., Deepak D. *JSIR*, 1977, **36**, 470–490.

[6] Mama H. P. *International Defense Review*, 1988, 291–295.

[7] Glassman I. *ARS Progress in Astronautics and Rocketry: Solid Propellant Rocket Research*, New York, Academic Press, 1960, I, 253–257.

[8] Langer H., Goedtke P. *Fr. Demande Fr 2*, 565, 583 (Cl. CO6 B21/00) 13 Dec 1985, DE Appl. 3, 321, 196, 11 June 1983, 9.

[9] Boyars C., Klager K. *Advances in Chemistry, Series 88*, American Chemical Society, Washington D. C., 1969.

[10] Bhat V. K. Singh H., Rao K. R. K. *Proc. 18th (Int.) Jahrestag Fraunhafer Inst. Treib Explosivst*, Karlsruhe, 1987, 18/1–18/10.

A METHOD OF REDUCTION OF TEMPERATURE SENSITIVITY OF BURNING RATE FOR HOMOGENEOUS CONDENSED SYSTEMS

Nikolai N. Bakhman, Igor N. Lobanov

Semenov Institute of Chemical Physics, Moscow, Russia

It is very important for certain types of solid propellants (SP) to ensure a sufficiently small temperature sensitivity of burning rate.

We consider a possible method of reducing this sensitivity. Let us take a basic system where the rate-controlling reaction occurs in the gas phase in the kinetic regime with sufficiently high activation energy and introduce into this system a certain amount of solid particles capable of reacting in the diffusion regime. A simple theoretical model was proposed in [1] for the case when both the gas and the particles react in the same zone. The following expression for the burning rate u was obtained: $u \sim (F_{hom} + F_{het})^{0.5}$, where F_{hom}, F_{het} is the heat release rate, J/cm^3s, due to homogeneous reaction in the gas phase and heterogeneous reaction on the surface of solid particles (or liquid droplets), respectively. A common expression was taken for F_{hom}, namely $F_{hom} = Ap^{2\nu} \exp(-E/RT_b)$, where T_b is the temperature in the reaction zone. The following expression was used for the value of F_{het} in the case of sufficiently small particles: $F_{het} = Bd^{-2}\rho_g Du/v = B_1 d^{-2}pT_b^{n-2}$, where d is the particle diameter, ρ_g is the gas density, D is the diffusivity of the gaseous component reacting on the particle surface, v is the gas velocity, and $2 - n = 0$–0.25. Thus, the theoretical dependence

of F_{het} on the temperature of the environment, T_e, (in this case $T_e = T_b$) is very weak. Therefore, addition of particles reacting in the diffusion regime can reduce the temperature sensitivity of systems reacting in the kinetic regime.

In the case of particles of heterogeneous catalysts, their content is commonly small (1–5% by mass) and the value T_b for the catalyzed system is close to that for the basic system ($T_b \simeq T_{b0}$); here, suffix 0 refers to the basic system. In this case, the following expression for the temperature exponent of the burning rate, $\beta = d\ln u/dT_{in}$, can be obtained: $\beta = \beta_0/Z^2$; here suffix *in* refers to the initial temperature of the system and $Z = u/u_0$. In the case of particles of aluminum or other metals with sufficiently high heat of combustion, $T_b > T_{b0}$ and $\beta = \beta_0 Z^{-2}(T_{b0}/T_b)\exp(E/R)(1/T_{b0} - 1/T_b)$.

It has been demonstrated in [2] that the equation $\beta = \beta_0/Z^2$ is consistent with the experimental data for AP + PMMA + 1% Fe_2O_3 mixtures:

oxidizer–fuel	$\beta_0 \cdot 10^3$	$\beta \cdot 10^3$, K^{-1}	
ratio	K^{-1}	calculated	experimental
0.5	6.2	2.1	2.3
0.6	3.7	2.0	2.0
0.7	2.9	1.6	1.8
1.0	1.8	1.2	1.4
1.6	2.2	1.4	1.6
3.4	8.5	2.1	2.3

However, it is interesting to consider not only the simple theoretical expression for F_{het} mentioned above but also the experimental data pertaining to the dependence of the burning rate of particles (or droplets) on T_e. The common equation for the variation of particle (or droplet) diameter in the course of burning is $d^2 = d_{in}^2 - Kt$, where K is a constant, t is time and $d_{in} = d_{t=0}$. In this case, we obtain $F_{het} = B_2 p d^{-2} K/T_e$.

The experimental data of [3–6] were plotted in the ($\ln K$, $1/T_e$) plane, and the following values of the effective activation energy E_{eff} were calculated:

Fuel	T_e range, K	E_{eff} kcal/mole	Ref.
Kerosene	$920 \div 1070$	5.5	[3]
Cetane	$870 \div 1170$	5.3	[3]
Kerosene	$850 \div 1150$	3.1	[4]
Coal	$1140 \div 1390$	8.4	[5]
Al–Mg alloy	$1150 \div 1350$	6.4	[6]

These values of E_{eff} are very small as compared to the common values of $E = 20$–40 kcal/mole for gaseous reactions typical for SP combustion. Of course, the range of T_e studied in [3–6] lies far below the common range of T_b for SP ($T_b = 2500$–3500 K). Nevertheless, the experimental data of [3–6] seem to be consistent with the idea (and

the experimental results of [2]) that the temperature sensitivity of the burning rate in homogeneous systems can be reduced by addition of particles (or droplets) reacting in the diffusion regime.

References

[1] Bakhman N. N., Kondrashkov Yu. A. *Dokl. Akad. Nauk SSSR*, 1966, **168**, 4, 844 (in Russian).

[2] Nikiforov V. S., Bakhman N. N. *Fizika Goreniya Vzriva*, 1969, **5**, 2, 270 (in Russian).

[3] Kobayasi K. *Proc. 5th Symp. (Int.) on Comb.*, The Combustion Institute, 1955, 141.

[4] Masdin E. G., Thring M. W. *J. Inst. Fuel*, 1962, **35**, 257, 251.

[5] Bukhman S. V. *Izvestiya Akademii Nauk Kaz. SSR, ser. Energet.* 1958, **1**, 68 (in Russian).

[6] Gnatovskii V. I. *Fizika Aerodispersnykh Sistem*, 1984 **26**, 30 (in Russian).

THE MODELLING OF THERMAL WAVES IN CATALYTIC SYSTEMS WITH CRITICAL PHENOMENA

V. I. Bykov*, T. I. Vishnevskaya*, K. G. Shkadinsky[†]

Krasnoyarsk State University, Krasnoyarsk, Russia
[†]*Institute of Structural Macrokinetics, Chernogolovka, Russia*

The wave phenomena in chemical systems currently attract considerable attention of investigators [1, 2]. Such nonlinear and transient effects have also been found in heterogeneous catalytic reactions. For example, the wave and self-oscillative regimes of CO oxidation reaction on a fine platinum filament have been found by Barelko [3].

In this work we consider a qualitative mathematical model of wave regimes in chemical systems of the type

$$\frac{\partial T}{\partial \tau} = \lambda \frac{\partial^2 T}{\partial \xi^2} + W(T, x) - \alpha(T - T_0), \tag{1}$$

$$\frac{\partial x}{\partial \tau} = F(T, x). \tag{2}$$

Here, the first equation governs the heat balance of the system, and the second equation is a kinetic submodel corresponding to a certain mechanism of chemical reaction.

At present the mathematical analysis of wave solutions for systems of type (1) and (2) is carried out only for particular cases. The application of numerical methods also requires some *a priori* information to construct an effective computational algorithm. However, if the characteristic times of chemical interaction are substantially shorter than those of heat relaxation one can invoke the quasistationarity principle and reduce the determination of concentration $X(t)$ to the solution of the transcendental equation(s)

$$F(T, x) = 0. \tag{3}$$

If X is unique and stable over the entire range of t, then, substituting $X(t)$ into the first equation, we obtain a single equation of the type of (1), the wave solutions of which have been thoroughly analyzed [4]. If Eq. (3) has a nonunique and stable solution X, or if Eq. (3) has a unique and unstable solution X for all t, then, substituting $X(t)$ into the first equation, we obtain a single equation of the type of (1) with hysteretic or oscillating sources of the form

$$f(T) = W(T, x) - \alpha(T - T_0).$$

In this paper, a general scheme of application of the mathematical model of wave phenomena in chemical systems will be proposed and two algorithms for constructing a wave solution will be formulated. The first algorithm, based on an analysis of the Semenov diagram, provides the wave existence conditions. In this algorithm, we go from a hysteretic dependence to a single-valued function. The second algorithm involves an analysis of the phase plane of the kinetic submodel and describes wave regimes in chemical systems with self-osciliations. To study wave relaxation to a steady state in terms of profile and propagation rate, it is nesessary to solve the whole set (1) and (2) by finite-difference methods.

The present general scheme for the analysis of wave phenomena in catalytic systems has been realized for the models of autocatalytic trigger, oscillator, and the model reaction of CO oxidation on Pt.

If Eq. (2) corresponds to the kinetic model of an autocatalytic trigger [5], it has the form

$$\frac{\partial x}{\partial \tau} = k_1 p z - k_{-1} x - k_2 x z^2, \qquad z = 1 - x, \tag{4}$$

where k_i are the reaction rates, and p is the partial pressure of the gaseous reactant. According to Bykov [5], in some parameter region the kinetic submodel (4) admits three steady states (two stable and one unstable). The knowledge of steady-state multiplicity region makes it possible to effectively use the algorithm for estimating the wave solutions for the hysteretic source proposed above. In this case, the initial conditions must lie in the neighbourhood of stable steady states in the (T, x) plane.

Suppose Eq. (2) corresponds to the kinetic model of autocatalytic oscillator [5], i.e., has the form

$$\frac{\partial x}{\partial \tau} = k_1 p z - k_{-1} x - k_2 x z^2,$$

$$\frac{\partial y}{\partial \tau} = k_3 z - k_{-3} y, \qquad z = 1 - x - y.$$

(5)

According to Bykov [5], in some parameter region kinetic submodel (5) admits one unstable steady state. In this case, we can find wave solutions by the second algorithm and obtain wave profiles and propagation rates.

If Eq. (2) corresponds to the kinetic model of the reaction of CO oxidation on Pt [5], i.e., has the form

$$\frac{\partial x}{\partial \tau} = 2k_1 p_1 (1 - x - y)^2 - 2k_{-1} x^2 - k_3 x y - k_4 p_2 x,$$

$$\frac{\partial y}{\partial \tau} = k_2 p_2 (1 - x - y) - k_{-2} y - k_{-3} x y,$$

(6)

where x, y, $1 - x - y$ are the concentrations of PtO, PtCO, Pt, and p_1, p_2 are the partial pressures of O_2, CO_2. In some parameter region, the kinetic submodel (4) admits three steady states (two stable and one unstable) [5]. According to the general scheme of (1) and (6), the conditions of reaction wave existence, wave profiles and propagation rates are obtained.

Conclusion

We have proposed a general scheme designed to apply the mathematical model of thermal waves in catalytic systems with critical phenomena and two efficient algorithms for constructing a wave solution based on the essential features of the phase plots of kinetic subsystems. These algorithms were realized for three model systems. In such situations, the criteria for reaction wave existence, the wave profiles and propagating rates have been obtained.

References

[1] Zel'dovich Ya. B., Barenblatt G. I., Librovich V. B., Makhviladze G. M. *The Mathematical Theory of Combustion and Explosion*. New York, Consultants Bureau, 1985.

[2] *Oscillations and Traveling Waves in Chemical Systems* (Field R., Burger M. Eds.) New York, Wiley, 1985.

[3] Barelko V. V. *Problems of Kinetics and Catalysis*, 1981, **18**, 61 (in Russian).

[4] Volpert A. I., Petrovsky I. G. *Selected Works*. Moscow, Nauka, 1987 (in Russian).

[5] Bykov V. I. *Modelling of Critical Phenomena in Chemical Kinetics*. Moscow, Nauka, 1988 (in Russian).

FLAMELET STRUCTURE OF RADIATING CH₄–AIR FLAMES

S. H. Chan, X. C. Pan, M. M. M. Abou-Ellail

Department of Mechanical Engineering, University of Wisconsin-Milwaukee, P.O.Box 784, Milwaukee, Wisconsin, 53201 USA

Introduction

Turbulent non-premixed (diffusion) flames can be described as a series of thin "flamelets" of different properties. The inner structure of these flamelets is controlled by molecular mass and heat transfer similar to the laminar diffusion flame [1]. Since the flamelet is very thin, it can be described by a one-dimensional set of transport equations [1]. A formal coordinate transformation, using the mixture fraction (a conserved property of the reacting flow) as an independent variable leads to a "universal description" of the flamelet properties [1]. This can be done by introducing a Lagrangian coordinate system attached to the maximum-reaction rate surface with the mixture fraction, f, taken as an independent variable [2]. Assuming equal molecular diffusivities of all species and unity Lewis number, it is possible to introduce general governing equations for energy and species concentrations [2,3]. As a result of the coordinate transformation, a new important parameter is introduced into the equations, namely,

the instantaneous scalar dissipation rate χ ($\equiv 2D\partial f/\partial x_k \partial f/\partial x_k$). The value of χ can be used as a measure of the instantaneous rate of molecular heat and mass transfer from the flamelet.

The objectives of this study are two-fold. First, the flamelet transport equations for non-premixed methane-air flames are solved at different values of χ to yield the structure of laminar flamelets, namely, the instantaneous temperature and the major species concentrations (CH_4, O_2, N_2, CO_2, CO, H_2O, H_2 and H) for mixture fractions ranging between zero and one. Flamelet structures are presented for adiabatic (no radiative heat loss) and nonadiabatic (with radiative heat loss) flamelets. Comparison is made with limited experimental data to show the accuracy of the prediction. Secondly, due to ultrasensitivity of thermal NO kinetics to temperature, the effect of thermal radiation on thermal NO formation over a wide range of flame stretch and mixture fraction is also investigated and results reveal how NO can be grossly overpredicted if thermal radiation from flamelets is ignored.

Flamelet Basic Equations

The species balance equation for steady-state diffusion flamelet is written as [2]

$$-\rho(\chi/2)\frac{\partial^2 X_i}{\partial f^2} = M_{N_2}\sum_{j=1}^{J} v_{ij}W_j \tag{1}$$

where ρ is the gas density, f is the mixture fraction (a passive scalar), W_j is the reaction rate of reaction j, J is the total number of a reduced reaction mechanism, v_{ij} are stoichiometric coefficients denoting the number of molecules of species i participating in reaction j, and χ and X_i are the instantaneous scalar dissipation rate and convenient mass concentration of species i, respectively.

The flamelet energy equation can be obtained from the energy balance equation for a non-premixed name by the same transformation technique used to obtain Eq. (1). We again assume unity Lewis number and apply the coordinate transformation to the Shvab–Zel'dovich energy equation to obtain the flamelet energy balance equation as

$$-\rho(\chi/2)\frac{\partial^2 h_s}{\partial f^2} = (-\Delta H)\sum_{j=1}^{J} Q_j W_j - \nabla \cdot \vec{q_r} \tag{2}$$

where $(-\Delta H)$ is the heat released from a one-step global irreversible stoichiometric reaction of the fuel; Q_j is the ratio of the heat released from reaction j to $(-\Delta H)$ and h_s is the sensible enthalpy; $\nabla \cdot \vec{q_r}$ is the thermal radiation source term modeled by the optically thin approximation. The needed mean absorption coefficient of the mixture is calculated on the basis of a narrow band model using RADCAL program [4]. The radiating species in the calculation includes CO_2, CO, H_2O and CH_4.

On the basis of steady-state, equilibrium and partial equilibrium assumptions, the full reaction mechanism of CH_4-air combustion has been reduced, by a good number
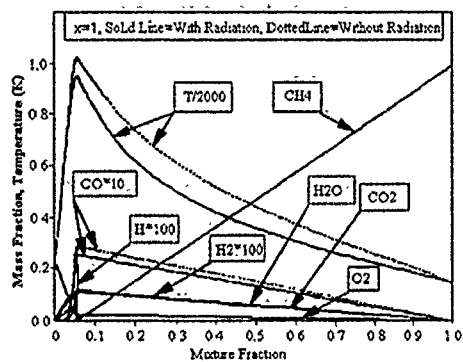
Figure 1: Flamelet properties state relationships of the CH_4–air non-premixed flame without radiation heat loss at $\chi = 1$ s^{-1}.
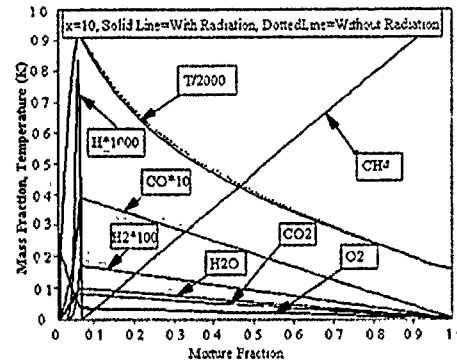
Figure 2: Flamelet properties state relationships of the CH_4–air non-premixed flame without radiation heat loss at $\chi = 10$ s^{-1}.

of investigators, to a four-step mechanism [1–2, 5–6] and subsequently to a three step mechanism. The present work adopts the latter, namely,

$$CH_4 + O_2 \rightarrow CO + H_2 + H_2O \tag{I}$$

$$CO + H_2O \rightleftharpoons CO_2 + H_2 \tag{II}$$

$$O_2 + 2H_2 \rightleftharpoons 2H_2O \tag{III}$$
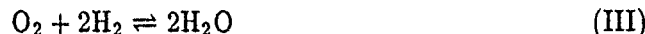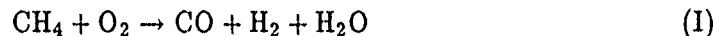
The reaction rates of the above chemical kinetic mechanism are used in Eq. (1) to evaluate the mass concentration profile of all species except NO, and in Eq. (2) to calculate flamelet temperature profile for a given value of χ. Then, without loss of generality, the simpler Zel'dovich mechanism [7] is used to investigate thermal radiation effects on NO formation.

Results and Discussion

The flamelet properties state relationships, of the methane–air non-premixed flame, with and without radiation heat loss, for a fixed scalar dissipation rate $\chi = 1$ s^{-1}, is depicted in Fig. 1 over the entire range of mixture fraction. It shows the temperature T and mass fractions of H_2, H, CO, CH_4, O_2, CO_2 and H_2O. Similar state relationships are shown in Fig. 2 for $\chi = 10$ s^{-1}. At $\chi = 1$ s^{-1} (Fig. 1), the maximum flame temperature is 2030 K, which is much lower than the adiabatic flame temperature under fast-chemistry assumption (2320 K [1]) or chemical equilibrium assumption (2250 K [8]). This is because the inner hot part of the flamelet loses heat to the outer colder part by conduction. The mass fractions of H_2, CO, CO_2, H_2O and H reach their

maximum values in the vicinity of $f = f_{st} = 0.055$, where the reaction rate reaches its maximum value as well; here, the mass fraction of CH_4 reaches its minimum value. The mass fractions of combustion products (except H) then decrease linearly to a zero value at $f = 1.0$, while the methane mass fraction increases to a unity value. However, the mass fraction of H drops sharply, after $f = f_{st}$ to a zero value. It should be mentioned here that the instantaneous equivalent reaction rate (W_e) varies with f, in a way similar to the variations of the atomic hydrogen mass fraction, i.e., W_e practically equals zero for $f \geq 0.057$ and $f \leq 0.03$. The combustion products, generated in the narrow reaction zone ($0.03 < f < 0.057$), are transferred to the outer non-reacting zone of the flamelet by molecular diffusion. It is interesting to notice that while the mass fraction of methane falls to zero near $f = 0.055$, the oxygen mass fraction reaches a non-zero value of about 0.02, and continues to decrease linearly for larger values of f. This is probably the explanation for the measured finite oxygen mass fractions, near the fuel nozzle at the centerline, as reported in [9-10].

The effect of thermal radiation on the flamelet properties is also shown in Fig. 1 for $\chi = 1.0$ s^{-1} and Fig. 2 for $\chi = 10.0$ s^{-1}. At low scalar dissipation rate ($\chi = 1.0$ s^{-1}), the effect of thermal radiation is important on flame temperature but not on mass fractions of major species. In this case, the radiation heat loss amounts to about 10% of the heat liberated by chemical reaction as shown in Fig. 3. At high flamelet stretching ($\chi = 10.0$ s^{-1}), the effect of radiation is not as important as the case for $\chi = 1.0$ s^{-1}, as can be seen from Fig. 2. In this case, the radiation loss is only about 1%. It should be noted here that the temperature difference (ΔT) between that with radiation and that without radiation cases is maximum around $f = 0.2$ and not $f = f_{st}$. This is because, at $f = f_{st}$, the high reaction rate can partially compensate for the radiation loss, while at $f = 0.2$, the reaction rate practically vanishes.

The effect of flame stretching is depicted in Fig. 3, where the maximum flamelet temperature (with and without radiation) is plotted versus χ^{-1}. The experimental data of Seshadri and Peters [2] are also included in Fig. 3. The data appear to agree well with the present predictions. Figure 3 clearly shows the existence of a critical value of $\chi = \chi_q$ at which flame extinction occurs. The extinction value of the scalar dissipation rate χ_q is about 15 s^{-1}, whether or not radiation is considered, as can be seen from Fig. 3; for $\chi > \chi_q$, the reaction is completely frozen and $T = 300$ K for all values of f.

Figure 4 shows the effect of thermal radiation on NO formation for a wide range of mixture fraction. It is seen that thermal radiation is extremely important at lower values of scalar dissipation rate. At $\chi = 1.667$ s^{-1}, for example, the maximum NO is grossly overpredicted by a factor of 5 if thermal radiation is ignored. Even at $\chi = 5$ s^{-1}, the deviation is still significant. As expected, the deviation diminishes as $f \to 0$ for all χ's since the temperature of flame is much too low to yield significant radiation. To show the flame stretch effect on NO formation, all the peak NO formations with and without radiation effects are plotted versus χ^{-1} in Fig. 5. It is clearly shown that radiation effects on NO formation indeed become increasingly important as the value of χ^{-1} increases. Of course, at the small χ^{-1} (i.e., large stretching), the flame approaches
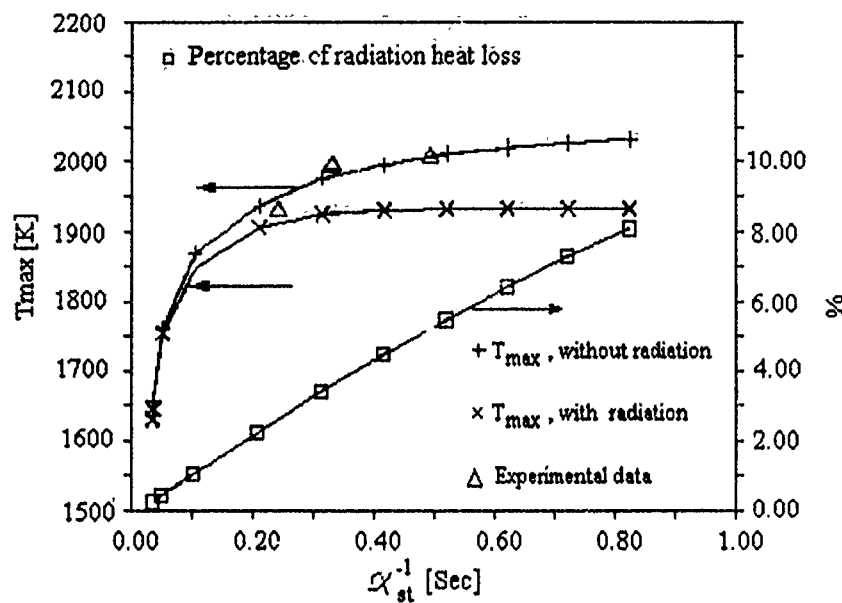
Figure 3: Variation of the maximum flamelet temperature and percentage of radiation heat loss versus χ^{-1}.
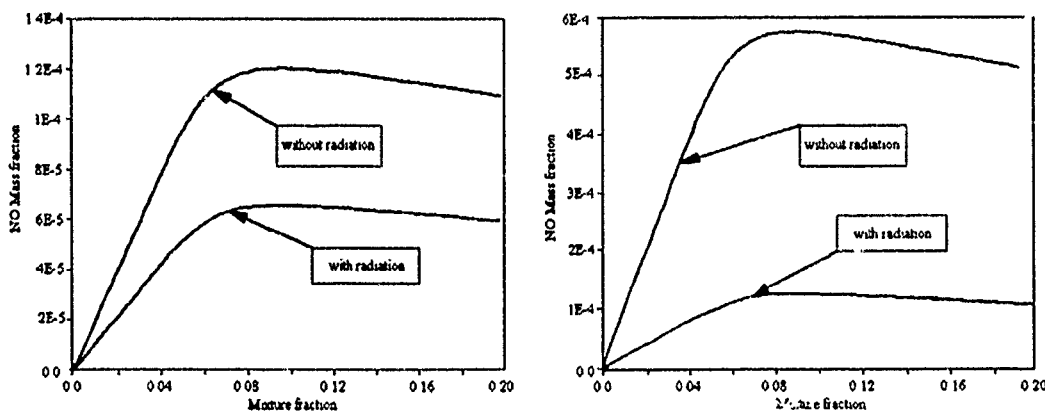

Figure 4: Thermal radiation effects on NO mass fraction at $\chi = 1.667$ and 5 s^{-1}.
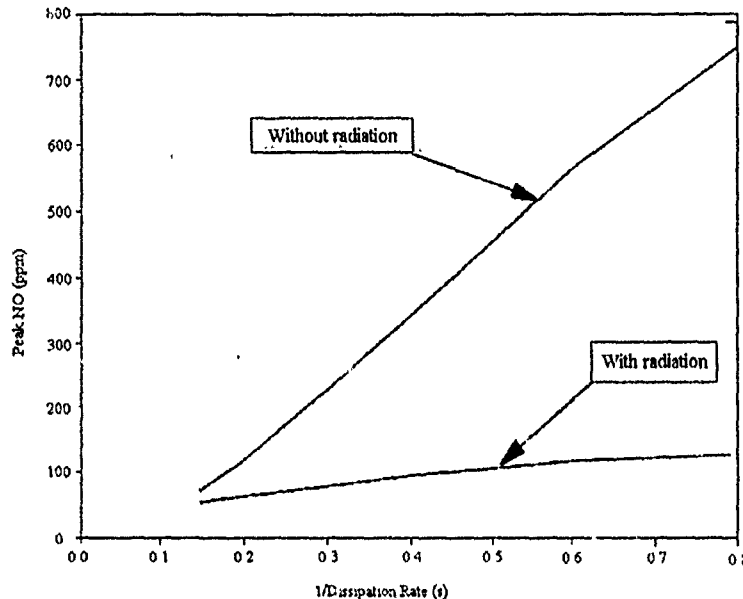
Figure 5: Variation of the peak NO formation with and without radiation versus χ^{-1}.

the extinction point where the flame temperature is again too low for NO formation to be affected by radiation as discussed above.

Conclusions

The present work describes a numerical and physical model for laminar non-premixed methane–air flames with and without the consideration of thermal radiation effects. The flamelet flame structure has been presented. The computed results clearly show a critical value of the scalar dissipation rate χ_q ($\simeq 15$ s^{-1}) above which chemical reaction is frozen. The effect of thermal radiation is high at low values of χ. Also, thermal radiation has more effect on the flamelet temperature at mixture fractions much larger than the stoichiometric value. It is also found that thermal radiation effects are even more profound on NO formation than other flamelet properties, except when flamelets are overly stretched. The obtained "flamelet library" can be used for turbulent non-premixed flame computations by the use of a two-dimensional probability density function $(P(f,\chi))$ which is a function of f and χ.

Acknowledgements

References

[1] Peters. N. *Proc. 21st Symp. (Int.) on Comb.*, The Combustion Institute, 1986, 1231–1250.

[2] Seshadri, K., Peters, N. *Comb. Flame*, 1988, **73**, 23–44.

[3] Peters, N., Kee, R. J. *Comb. Flame*, 1987, **65**, 17–29.

[4] Grosshandler, W. L. *Int. J. Heat Mass Transfer*, 1988, **23**, 1447–1459.

[5] Jones, W. P., Lindstedt, R. P. *Comb. Flame*, 1988, **73**, 233–249.

[6] Hautman, D. J., Dryer, F. L., Schug, K. P., Glassman, I. *Comb. Sci. Techn.*, **25**, 219–235.

[7] Bracco, F. V. *Proc. 14th Symp. (Int.) on Comb.*, The Combustion Institute, 1973, 831–842.

[8] Abou-Ellail, M. M. M., Salem, H. *J. Heat Transfer*, 1990, **112**, 1002–1007.

[9] Hassan, M. A., Lockwood, F. C., Moneib, H. A., presented at the Italian Flame Day, 1980, 357–372.

[10] Masri, A. R., Bilger, R. W., Dibble, R. W. *Comb. Flame*, 1988, **71**, 245–266.

ON AN ANALYTICAL SOLUTION TO THE PROBLEM OF NONTHERMAL FLAME PROPAGATION

V. I. Chernysh, N. M. Rubtsov, S. M. Temchin

Institute of Structural Macrokinetics, Chernogolovka, Russia

The phenomenon of nonthermal flame propagation has been predicted by Ya. B. Zel'dovich [1] and revealed in gas-phase chain branching processes such as CS_2 oxidation, NCl_3 decomposition, etc. [2, 3]. The nonthermal flame is an almost isothermic combustion wave occurring outside of the domain of self-ignition, due to the reactions of nonlinear chain branching [1–3].

The first solution to the problem of nonthermal flame propagation was obtained for the case of CS_2 oxidation [2], including the dependence of nonthermal flame velocity

on the initial conditions. Following to the ideas of [1, 4], it would be interesting to determine the conditions favoring self-ignition and nonthermal flame propagation, taking into account mixture consumption and the rate ω_0 of spontaneous chain origination.

The equation of diffusion and chemical kinetics in the single-center approximation is

$$\frac{dn}{dt} = D\frac{d^2n}{dx^2} + F(n), \tag{1}$$

where n is the concentration active centers, D is the diffusivity, and $F(n)$ is the kinetic polynomial,

$$F(n) = \frac{\omega_0}{a_0} + fa_0^2 n_0^2 (1 - n) - gn. \tag{2}$$

Here, a_0 is the initial fuel concentration, f is the kinetic factor of nonlinear chain branching, and g is the linear chain branching factor. In the simplest case,

$$\frac{dn}{dt} = F(n). \tag{3}$$

The steady states (s.s.) of Eq. (3) are the roots of the cubic equation $F(n) = 0$, which depend on the sign of the discriminant D_0, hence multiple s.s. (three real roots) exist at $D_0 < 0$, namely:

(a) the stable steady state with a low concentration of the active centers, n_1 (the initial mixture);

(b) the stable one with a high concentration of active centers, n_3 (the products of combustion);

(c) the unstable one, n_2, corresponding to the autocatalytic trigger [5].

$D_0 = 0$ is the condition at the multiple s.s. boundary, hence

$$\frac{g}{fa_0^2} = \frac{2}{9} + \frac{3\omega_0}{fa_0^3} \pm \frac{2}{9}\left(1 - \frac{3g}{fa_0^2}\right)^{\frac{3}{2}}. \tag{4}$$

Equation (4) with the minus sign determines the criterion for spontaneous explosion in a nonlinear chain branching system in the absence of diffusion flux (the case of equal roots n_1, n_2); Eq. (4) with the plus corresponds to flame suppression (the case of equal roots n_2, n_3).

The self-ignition criterion given by Eq. (4) differs from the one described in [2],

$$\frac{g}{fa_0^2} = 4\frac{\omega_0}{fa_0^3}, \tag{5}$$

by the existence of certain constraints on the domain of the kinetic parameters. It follows from Eq. (4) that

$$0 \leq \frac{g}{fa_0^2} \leq \frac{1}{3}, \qquad 0 \leq \frac{\omega_0}{fa_0^3} \leq \frac{1}{27}. \tag{6}$$

The equation of diffusion and chemical kinetics for nonthermal flame propagation at the velocity U_n is [5]

$$U_n \frac{dn}{dx} = D \frac{d_n^2}{dx^2} + \frac{\omega_0}{a_0} + f a_0^2 n^2 (1-n) - gn. \tag{7}$$

The boundary conditions are: $x = -\infty$, $n = n_1$; $x = +\infty$, $n = n_3$.
The solution to Eq. (7) is known [5]:

$$U_n = \sqrt{f a_0^2 \frac{D}{2}} |n_1 + n_3 - 2n_2| = 3\sqrt{f a_0^2 \frac{D}{2}} |\frac{1}{3} - n_2|. \tag{8}$$

The case of $n_2 > 1/3$ corresponds to a wave of increasing concentration of active centers, $n_2 < 1/3$ corresponds to a wave of decreasing concentration, and $n_2 = 1/3$ corresponds to $U_n = 0$, i.e.

$$\frac{g}{f a_0^2} = \frac{2}{9} + \frac{3\omega_0}{f a_0^3} \tag{9}$$

Equation (9) at $\omega_0 = 0$ coincides with the criterion for nonthermal flame propagation obtained by Ya. B. Zel'dovich [1].
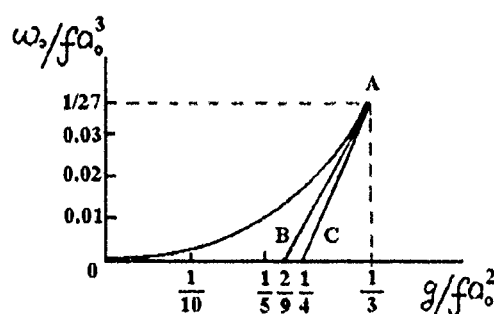
Figure 1: The domain of multiple steady states (OAC): propagation (OAB) and suppression of the wave of active centers concentration (BAC).

The domains of multiple s.s. corresponding to the propagation and suppression of active center concentration are shown in Fig. 1. Figure 1 shows that the flame propagation domain (OAB) is contained within the multiple s.s. domain (OAC) and limited from above by the self-ignition curve (OA) and from below by $U_n = 0$ (AB). The velocities of real nonthermal flames at the propagation limits are finite. This discrepancy is due to the use of single-center approximation, as explained theoretically in [6, 4] for nonthermal flame propagation in CS_2 oxidation. The finite values of U_n have been

obtained for $g/f a_0^2 = 0.0461$ and $\omega_0 = 0$. This implies that the real curve of the flame propagation ($U_n = 0$) is of finite width, in contrast to the predicted one (AB). Therefore, an area bounded by curves OA and AB can exist, wherein flame propagation is impossible but self-ignition occurs, in accordance with [7].

The work has been supported by the Russian Foundation for Fundamental Research.

References

[1] Zel'dovich Ya. B., Frank-Kamenetskii D. A. *Dokl. Akad. Nauk SSSR*, 1938, **19**, 693 (in Russian).

[2] Voronkov V. G., Semenov N. N. *Zhurnal Fizicheskoi Khimii*, 1939, **13**, 1695 (in Russian).

[3] Azatyan V. V., Borodulin R. R., Markevich E. A. *et al. Izvestiya Akad. Nauk SSSR, ser. Khim.*, 1976, **7**, 1459 (in Russian).

[4] Zel'dovich Ya. B., Barenblatt G. I., Librovich V. B. *et al. The Mathematical Theory of Combustion and Explosion.* Moscow, Nauka, 1980 (in Russian).

[5] Barelko V. V., Volodin Yu. E. *Kinetika Kataliz*, 1976, **17**, 683 (in Russian).

[6] Novozhilov B. V., Posvyanski V. S. *Fizika Goreniya Vzriva*, 1973, **9**, 225 (in Russian).

[7] Borodulin R. R., Rubtsov N. M., Saidkhanov S. S. *Khimicheskaya Fizika*, 1984, **3**, 521 (in Russian).

STEADY-STATE COMBUSTION OF SOLID PROPELLANTS

Aleksey D. Drozdov, Adir Pridor, Isaac R. Shreiber

Institute for Industrial Mathematics, Ben-Gurion University of the Negev, 22 Ha-histadrut Str, Beer-Sheva, Israel

Abstract

Based on the two-temperature and single-velocity theory of multiphase media, a new model is developed for the description of solid propellant combustion. For steady-state processes, the governing equations are simplified and reduced to a boundary problem for ordinary differential equations. Combustion of magnesium–tetrafluoroethylene propellants is analyzed numerically. The influence of the thermophysical and structural parameters of the propellant on the formation of the combustion and evaporation fronts is studied.

Introduction

In the past two decades the problem of solid propellant combustion has been the focus of numerous studies, see [1]. This can be explained by the rapid development of the rocket engines as well as by the growing tendency to replace liquid by solid jet propulsion. This tendency is limited for several reasons. One of them is the absence of simplified models which can be employed in engineering calculations. This is especially important for optimal design of engines, where only simple and "fast" models are used at the stage of preliminary investigation.

The goal of this paper is to derive a new mathematical model for solid propellant combustion, which allows to predict some new physical effects and to investigate the material parameters responsible for the thrust and to give some recommendations for their experimental study.

The Physics of Combustion

The combustion process consists of two main stages. First, the solid fuel is converted into the gas phase (vaporization), and, second, the gas burns in the flame (combustion). The vaporization process, in its turn, consists of two stages, which are treated here as an integral sublimation process.

We will study fuels with a non-negative oxygen balance, when the propellant contains an amount of oxygen sufficient for its stoichiometric combustion.

We restrict ourselves to the model of combustion which assumes that there exist two spatially separated zones of evaporation and burning. Experimental data show that for two-zone combustion, the characteristic length of the evaporation zone substantially exceeds the characteristic length of the combustion zone, see [2]. We will neglect the length of the burning region and treat it as a geometrical surface, where the thermodynamical parameters of the gas flow undergo finite jumps.

A fuel tank is modeled as an infinite tube of constant cross-sectional area filled with a granular medium having the initial porosity ϵ_0. The fuel particles are considered as rigid spheres with the initial radius a_0. Before burning, the propellant is contained in a closed fuel tank at the temperature Θ_0, which is lower than the evaporation temperature θ_ϵ, under the pressure p_0. At the initial moment $t = 0$, the propellant is ignited at the point $x = 0$. At the moment $t \geq 0$, the fuel tank volume consists of three main zones. The first one is the cold zone, where the vaporization process is negligible, the temperature of the solid particles coincides with the gas temperature and is less than θ_ϵ. The material porosity equals the initial porosity ϵ_0.

The second one is the evaporation zone, where the gas temperature differs from the temperature of the solid propellant. Due to this difference, the solid particles give off the gas. Since the gas density ρ is essentially lower than the density of the solid particles ρ_s, an additional pressure arises which causes the gas to move to the combustion surface. We restrict ourselves to the analysis of complete combustion. This means that
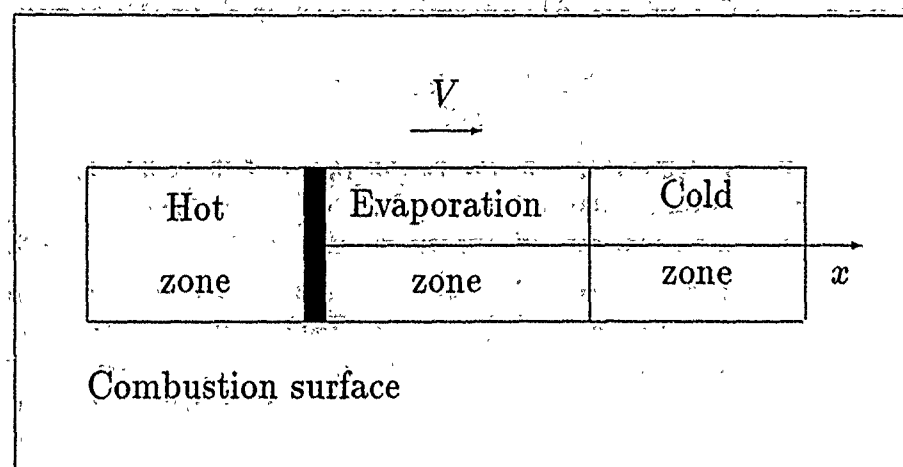
Figure 1: The basic structure of combustion.

(i) all particles of the solid propellant have evaporated;

(ii) all the gas produced in the evaporation zone burns in the flame.

These assumptions imply that the material porosity decreases in the evaporation zone from ϵ_0 at the interface with the cold zone to zero at the combustion surface, and the gas temperature Θ increases from the evaporation temperature θ_ϵ to the combustion temperature θ_c. The gas from the evaporation zone enters the hot zone through the combustion surface. At this surface, the gas burns and releases additional heat. A part of this heat warms the gas, and the other part returns into the evaporation zone and supports the evaporation process. We suppose that the velocity of the gas flow behind the combustion surface U_∞ coincides with the relative velocity of the exhaust gas. The thrust pressure $\mathcal{F}$ (the thrust force per unit area of the cross-section) can be calculated according to the Meschersky formula

$$\mathcal{F} = \Gamma U_\infty \tag{1}$$

where Γ is the burning rate (the mass of the gas burned per unit area of the combustion surface at the unit time).

Mathematical Model of Combustion

We consider the combustion process at three levels. At the microlevel, the gas evaporation on the surface of a single solid particle is analyzed. We assume that the gas flow is homogeneous, and the evaporation process depends only on the difference

113

of temperatures between the gas and solid particles. As a result, we derive the formula

$$\epsilon_{,t} = \frac{\beta_0 (1 - \epsilon)^{\frac{2}{3}} \Theta - \theta_\epsilon}{\rho_s \eta} \tag{2}$$

Here Θ is the gas temperature in the neighborhood of the solid particle, θ_ϵ is the evaporation temperature which is assumed to be a prescribed function of the gas pressure p, η is the latent heat of evaporation, β is the heat transfer coefficient, $\beta_0 = 3\beta \frac{[1-\epsilon(0)]^{\frac{1}{3}}}{\alpha_0}$, and the subscript after the comma denotes the differentiation with respect to the respective variable. Eq. (2) determines the material porosity ϵ at point x as a function of time and can be treated as a constitutive equation of a solid propellant.

At the macrolevel, a one-dimensional gas flow is studied through a porous medium with the porosity ϵ varying in time. The mechanical behavior of the gas obeys the constitutive equation

$$p = \rho R \theta \tag{3}$$

where ρ is mass density of the gas and R is the universal gas constant.

The constitutive equations of heat and mass transfer have been derived for a porous medium with phase transitions, including:

- the continuity equation

$$(p\epsilon\Theta^{-1})_{,t} + (p\epsilon U \Theta^{-1})_{,x} = \beta_0 R \eta - 1(1 - \epsilon)^{\frac{2}{3}}(\Theta - \theta_\epsilon) \tag{4}$$

- the momentum equation

$$p\epsilon(U_{,t} + UU_{,x})(R\Theta)^{-1} = -(p\epsilon)_{,x} - U[\rho\nu K^{-1}\epsilon + \beta_0\eta^{-1}(1 - \epsilon)^{\frac{2}{3}}(\Theta - \theta_\epsilon)] \tag{5}$$

- the heat balance equation

$$c_p p\epsilon(\Theta_{,t} + U\Theta_{,x}) - \epsilon(p_{,t} + Up_{,x})](R\Theta)^{-1} =$$
$$\Theta(\kappa\epsilon\Theta^{-1}\Theta_{,x}) - \beta_0(1 + \Theta\theta_\epsilon^{-1})(1 - \epsilon)^{\frac{2}{3}}(\Theta - \theta_\epsilon) \tag{6}$$

Here U is the gas velocity along the x axis, K is the permeability of the porous medium depending on the porosity coefficient $\epsilon = \epsilon/(1-\epsilon)$, ν is the kinematic viscosity, c_p is the specific heat at constant pressure, $\kappa = pc_p\delta$ is the heat conductivity, and δ is the thermal diffusivity of the gas.

Eqs. (4) and (5) are known, and Eq. (6) is new. In order to obtain these, we have used an approach similar to the approach used by Meschersky in the dynamics of material point of varying mass, the dependence of the material porosity on the gas temperature developing at the microlevel, and the Darcy law describing the interaction between the gas and the solid matrix.

114

The nonlinear partial differential equations (2)–(6) are too complicated for analytical solution. Since our purpose is to obtain explicit solutions for optimal design of jet propulsion, we restrict our consideration to the steady-state combustion regimes. We seek solutions of the governing equations in the form of travelling waves, when the functions ϵ, p, U and Θ depend only on the argument $\xi = t - x/V$.

The existence of steady-state combustion regimes imposes some limitations on the boundary conditions. At the interface between the evaporation zone and the cold zone, we have five boundary conditions. Two conditions determine the initial porosity of the propellant and the evaporation temperature. The other three describe the conservation laws for mass, momentum and energy. At the burning surface, we have six boundary conditions. Two of them determine the completeness of the combustion process, the third condition determines the flame temperature, and the other three describe the conservation laws. The latter equalities determine the gas flow after burning. The former three boundary conditions, together with the five conditions at the interface of contact with the cold zone, form an overdetermined boundary problem for a system of ordinary differential equations containing five unknown functions and two unknown parameters (the length of the evaporation zone l and its velocity relative to the fuel tank V). An additional boundary condition determines the initial porosity of a solid propellant which ensures the steady-state combustion regime. We solve this boundary problem numerically.

Numerical Analysis

The numerical analysis of steady-state combustion is carried out for $\rho_s = 1.5 \cdot 10^3$ kg/m^3, $c_s = 1.1$ kJ/(kg·K), $k_s = 0.3$ J/(m·s·K), $\eta = 44.0$ kJ/kg, $c_p = 1.0$ kJ/(kg·K), $\delta = 1.8 \cdot 10^{-5}$ m^2/s, $\gamma = 1.4$, $\gamma_\infty = 1.4$, $W = 16.8$ MJ/kg, $\theta_\epsilon = 400$ K, $\theta_c = 3000$ K, $\rho_\star = 1.2$ kg/m^3, $\Theta_\star = 400$ K, $l_\star = 0.01$ m, $V_\star = 409.88$ m/s. We neglect the characteristic heating time of solid particles and put $Nu = 2$. The evaporation temperature θ_ϵ, the combustion temperature θ_c and the burning rate Γ are assumed to be constant. All calculations are carried out for $Re = 1$.

The numerical analysis carried out for $Re = 0.1$ and $Re = 1000.0$ shows that the gas flow does not virtually depend on this parameter.

A detailed description of the numerical analysis is presented in [3]. Here we formulate only some results obtained.

The propellant porosity ϵ increases monotonically with the growth of $\xi_\star$, and tends unity at the burning surface. The gas pressure p, on the contrary, decreases but does not change significantly.

The growth of the initial radius of the propellant pellet a_0 leads to the decrease of the speed of the evaporation zone V, the gas velocity U_∞, the burning rate Γ and the thrust pressure $\mathcal{F}$, and to the increase of the evaporation zone length l. The interval 0.007 mm $< a_0 <$ 0.03 mm corresponds to the entire range of variation of the initial radius of solid particles.

The evaporation zone speed V and its length l increase monotonicaly with the

115
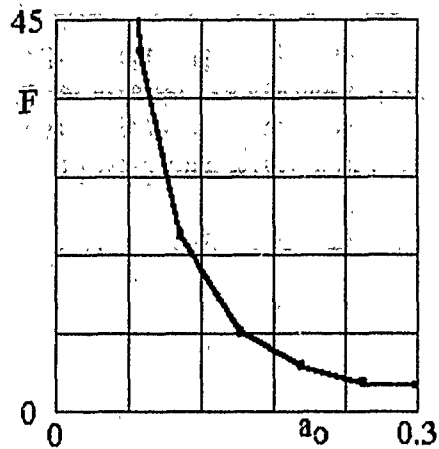
Figure 2: Thrust force $\mathcal{F}$ vs initial radius of fuel particles a_0.
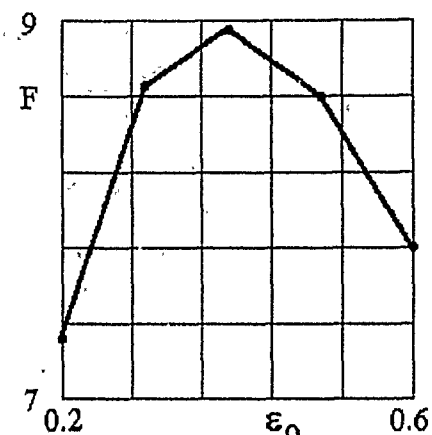
Figure 3: Thrust force $\mathcal{F}$ vs initial porosity of propellant ϵ_0.

growth of the initial porosity, but the gas velocity U_∞, the burning rate Γ and the pressure $\mathcal{F}$ demonstrate non-monotonic behavior. They increase for small and decrease for large initial porosities. This means that there exists the optimal initial porosity $\epsilon_0^{opt} \approx 0.35$ which maximizes the thrust pressure.

The numerical analysis of the effect of the burning temperature θ_{c^*} and the initial pressure p_{0*} shows that the growth of the combustion temperature leads to the increase of the thrust force, and growth of the initial pressure leads to its decrease.

Conclusion

A new model has been derived for solid propellant combustion. Governing equations derived have been simplified for the case of steady-state combustion and reduced to the overdetermined boundary problem for ordinary differential equations. The combustion of magnesium based propellants has been studied numerically. The results obtained are sufficiently close to experimental data.

It has been shown that the growth of the initial radius of propellant pellets leads to the decrease of the thrust pressure. The dependence of the thrust force on the initial porosity has nonmonotonic character. There exists the optimal initial porosity maximizing the thrust pressure. The growth of the initial pressure in the fuel tank causes the decrease, and the growth of the combustion temperature causes the increase of the thrust force.

References

[1] Zel'dovich, Ya. B., Leipunskij, O. I., Librovich, V. B. *Theory of Non-Stationary Combustion of Gun Powder*, Moscow, Nauka, 1975 (in Russian).

116

[2] Frolov, Yu. V., Korostelev, V. G. In: *Spreading of Thermal Waves in Heterogeneous Media*, (Matros, Yu. S. Ed.), Novosibirsk, Nauka, 1988 (in Russian).

[3] Drozdov, A. D., Pridor, A., Shreiber, I. R. *Int. Comm. Heat Mass Transfer*, 1994 (in press).

PREIGNITION PROCESSES IN LASER IGNITION OF PYROTECHNICS

A. S. Dudyrev, A. N. Golovchak, F. A. Chumak

Institute of Technology, 198013 St. Petersburg, Russia

Introduction

Recent investigations motivated by application of laser in pulse-transfer systems have shown a growing interest in creation of ignition chains by means of far infrared (FIR) lasers, primarily due to the appearance of useful FIR fiber optics. Prospects of using pyrotechnics in such systems are related to improvement of safety and thermal stability. However, one of the problems yet to be solved is the development of an adequate mathematical model of interaction of laser pulses with condensed systems. Pyrotechnic charges have been widely used in space technology, but the data on their laser ignition mechanism are still insufficient. An appropriate analysis must include numerous factors, the most important of which pertain to the optical properties of mixture components. The important role of optical characteristics of substances in their ignition mechanisms (as well as in modeling the process) has been demonstrated in [1]. The works conducted at the Institute of Technology have shown that the nature of changes in the absorption capacities of materials can be studied on irradiated samples.

Experimental Apparatus and Methods

A continuous CO_2 laser with a mechanical chopper was used in the experiments. The flux density range was 20-55 W/cm^2, and the beam diameter was 8 mm. Irradiation times amounted to 30-50% of the ignition times and were recorded by photocells. The following pressed pure pyrotechnic compounds were studied: $KClO_3$–B (85/15), $KClO_4$–B (78/22), $BaCrO_4$–B (95/5), Pb_3O_4–Si (55/45), $KClO_3$–Si (83/17), $K_2Cr_2O_7$–W (65/35). A method involving the analysis of IR spectra and DSC curves (in Ar)

117

was employed. The measurements were made by means of Fourier spectrometry and differential scanning calorimetry (DSC-7).

Experimental Results

The values of absorption coefficients at $\lambda = 10.6$ μm of pressed initial $(K\lambda)$ and irradiated samples $(K'\lambda)$, as well as their densities (ρ) are shown in Table 1.

Table 1.

Mixture	ρ, kg/m^3	$K\lambda$, m^{-1}	$K'\lambda$, m^{-1}
Pb_3O_4–Si	3150	0.18	0.16
$KClO_4$–B	2080	0.35	1.01
$KClO_3$–B	2080	6,12	10.01
$KClO_3$–Si	1850	6.29	8.32
$BaCrO_4$–B	3550	8.71	17.17

Table 2.

Compound	E, J	T, °C	$-\Delta H$, J/g	E_a, kJ/mol	$\ln K_0$	n
$KClO_4$–B	—	464–594	2840.5	501.2	68.8	1.5
	22.6	403–589	3472.5	198.6	23.5	0.6
$KClO_3$–B	—	360–569	1862.7	136.5	16.0	1.0
	7.2	435–539	1470.0	250.0	34.6	1.2
$KClO_3$–Si	—	357–478	947.6	277.0	43.4	1.1
	33.0	388–451	708.0	368.0	59.3	1.2
Pb_3O_4–Si	—	431–500	58.8	711.9	118.4	1.6
	11.5	444–488	62.9	707.1	111.6	1.4
$K_2Cr_2O_7$–W	—	396–423	237.4	861.2	150.6	2.1
	2.2	395–408	159.6	605.8	105.3	1.2

An analysis of IR spectra has shown that the difference in the absorption coefficients of the initial mixtures depends on the absorption properties of the oxidizers. For example, the oscillation frequency of radicals in $KClO_3$ coincides with the CO_2 laser frequency [2, 3]. It has been found that intense photochemical decay of oxidizer molecules can occur under the IR irradiation. This process is characterized by absorption of laser radiation by Cl(Cr)–O bonds, with an increased oxygen output and a significant decrease in laser ignition temperature and delay time for pyrotechnic compounds.

Significant changes in the characteristics of condensed-phase reactions in the irradiated samples were also recorded using the DSC method. Comparative characteristics of the initial and irradiated samples are shown in Table 2, where E_a is the activation energy, ΔH is the heat release of the reaction, ΔT is the temperature range of the

ignition reaction, $\ln K_0$ is the logarithm of the chemical reaction rate constant, n is the reaction order, and E is the absorbed laser energy.

The results obtained were analyzed simultaneously with the data on laser ignition of the mixtures studied. We have found a direct correlation between their sensitivity to a laser pulse, the optical properties of components and the character of the changes in the characteristics of solid-phase reactions in irradiated samples. These correlations, combined with experimental studies, can be successfully used to predict laser ignition mechanism of thermally stable heterogeneous systems.

References

[1] Ewick D. W. . *Proc. 15th (Int.) Pyr. Sem. of Boulder*, Colorado. USA, 1990.

[2] Nakamoto K. *IR Spectra and CE Spectra of Inorganic and Coordination Compositions*, Moscow, Mir, 1991 (in Russian).

[3] Ready J. F. *Industrial Applications of Lasers*, N. Y., Academic Press, 1978.

THE EFFECT OF GRAVITY ON THE DISTRIBUTION OF PRODUCTS AND INTERMEDIATE SPECIES IN THE LOW-TEMPERATURE ZONE OF METHANE BUNSEN FLAMES

I. V. D'yakov, A. A. Konnov, L. I. Kopylova, G. I. Ksandopulo

Institute for Problems in Combustion, Almaty, Kazahstan

The objective of this study was to investigate the structure of laminar bunsen methane–air flames at atmospheric pressure to provide an understanding of important differences between flat and conical flames. Experimental profiles of the distribution of stable species in slightly rich methane–oxygen–argon flames have been measured by the laser-induced fluorescence method for various orientations of the methane–air flames in the gravity field. These data were compared with the predictions of a one-dimensional model of flame structure.

Laminar CH_4–O_2–Ar flames with equivalence ratios 1.12 and 1.3 were stabilized over a 8-mm bunsen burner. Samples from the flame were taken by non-cooled conical quartz probes. Species concentration profiles were obtained along the horizontal axis

by moving the vertical bunsen burner relative to the fixed probe. The orifice diameters were 60–80 μm and the cone angle was 15–20 degrees. An analysis was carried out by means of modified MKh–1304 mass spectrometer in the flow regime. The profiles of CH_4, O_2, H_2O, CO_2, CO, H_2, CH_2O, C_2H_2, and C_2H_4 were detected. The sampling location was determined by KM–8 cathetometer with the error within of 10 μm. These coordinates were recalculated to the distances along the normal to the flame front surface. Temperature profiles were obtained using silica-coated Pt/Pt (10% Rd) П-shaped thermocouples with 30-μm wires.

Hydroxyl profiles were measured in the 10-mm burner using laser-induced fluorescence (LIF). The light source was a frequency-doubled computer-controlled custom-built tunable dye laser which was pumped by a frequency-doubled Nd:YAG laser. The output parameters of the probe laser were as follows: the spectral tuning covered the range from 295 to 330 nm, the bandwidth was 0.01 nm, the pulse energy was 0.03 mJ, the pulse duration was 10 ns, and the pulse frequency was 12.5 Hz. The laser light was focused by a lens which made a 100-mm diameter spot in the burner flame. The OH fluorescence was collected at a right angle to the exciting beam by a quartz lens and focused onto the slit of a monochromator equipped with a photomultiplier. The data were stored in a PC/XT computer after each laser shot.

The one-dimensional premixed flames were modeled using the codes (CHEMKIN, PREMIX) developed at Sandia National Laboratories by Kee and co-workers. The C1–C2 reaction mechanism used in the present work has been published previously [1] and updated on the basis of recent recommendations of European Evaluation Group [2]. This mechanism was successively validated against experimental results for oxidation, ignition and flame structure of hydrogen, carbon monoxide, formaldehyde and methanol. A largely good agreement was found between experimental data and simulation results.

The data of Bechtel et al. [3] for atmospheric pressure methane–air flame structure were used as the basis for the validation of the kinetic mechanism. The structure of freely propagating (adiabatic) lean, stoichiometric and rich flames was modelled. The temperature and species concentration profiles calculated are in a good agreement experimental profiles as concerns the shape and absolute values. It should be noted that these data were obtained using non-intrusive laser Raman scattering and LIF in horizontally stabilized flames.

We modeled the structure of CH_4–O_2–Ar freely propagating adiabatic flames and obtained a general disagreement with the data obtained for bunsen flames using mass-spectrometry. First of all, the experimental temperature profiles are smoother than the calculated ones. Evidently, this difference is caused by the nonuniformity of the flow in tubes and the flame front curvature in conical flames. The scaling of the coordinate in the one-dimensional model with the distance along the normal to the flame front is probably nonlinear. Also, the radial expansion of the hot gases reduces the velocity perpendicular to the flame front, increasing the diffusion back into the cool preflame zone.

The calculations using the experimental temperature profile (as for the case of burner-stabilized nonadiabatic flame) are in much better agreement with the concentration profiles for major species. Yet some distinctions between experimental results and model predictions are observed. The experimental species profiles are shifted upstream from the calculated profiles by about 200 μm. The gradients of the profiles measured are lower and the bell-shaped profiles of the intermediates, such as CH_2O, C_2H_2 and C_2H_4, are wider than the predicted ones. The nature of the distribution of the experimental profiles observed is twofold. It was shown in [4] and confirmed in subsequent studies that the sampling zone is wider than the calculated profile by two diameters of the probe orifice. In our case, the probe is 120-160 μm in diameter which is comparable with the flame front thickness.

The secondary flow instability of bunsen flame cones [5] also causes some spatial oscillations of the flame front. The influence of this instability on the concentration profiles observed was investigated by non-intrusive linear LIF method. It was found that, in a vertical bunsen burner, the profile of the OH radical concentration in the preflame cool zone has a flat portion. Similar flat portions were observed for bunsen flames with various front curvatures and this rules out the possibility of receiving the signal from the neighboring flame zone. The OH rotational temperatures in the preflame zone were also measured. These temperatures agree with thermocouple measurements within the limits of estimated error. Similar results were obtained for bunsen propane-air flames. Chemical reactions in the preflame zone cannot account for the observed effects due to the substantial difference between the kinetics of methane and propane.

A number of measurements of the OH radical profiles in horizontal flames were carried out in order to examine the potential hydrodynamic features of bunsen flames and the influence of gravity on the flame structure. In addition, the flame was located in a co-current flow of nitrogen to investigate the effect of surrounding air. The profile of the OH radical concentration in the preflame zone virtually did not change in this case. On the other hand, if a methane or propane flame had a horizontal luminous front, the profile of the OH concentration had a purely diffusional character, in agreement with the literature data [3] and calculations.

These structural differences between conical flames of other shapes and numerical calculation lead us to a conclusion about the effect of the stabilization mode on the flame hydrodynamics. In particular, in [3] a methane flame front was positioned horizontally in the gravity field. An analysis of two-dimensional Navie-Stokes equations showed that for a vertical or inclined flame in the gravity field a horizontal pressure gradient causing an added convection arises in the region of significant mixture density gradient. This pressure gradient, combined with the buoyancy of the hot layers, can give rise to an oscillatory mode of flow instability [5] and, therefore, some mixing in the cold region near the flame front.

Thus, the simultaneous analysis of the data obtained by mass-spectrometry, LIF, and numerical modeling revealed significant differences between flat and conical flames. It has been shown to what extent the experimental species concentration profiles can

121

be compared with the calculated ones. The effect of gravity on the intermediate species distribution in the low-temperature zone has been demonstrated and discussed.

References

[1] Dagaut P., Boettner J. C., Cathonnet M. *Comb. Sci. Technol.*, 1991, **77**, 127.

[2] Baulch D. L., Cobos C. J., Rox R. A., *et al. J. Phys. Chem. Ref. Data*, 1992, **21**, 411.

[3] Bechtel J. H., Blint R. J., Dash C. J., Weinberger D. A. *Comb. Flame*, 1981, **42**, 197.

[4] Miln T. A., Greene F. T., *Proc. 10th Symp.(Int.) on Comb.* The Combustion Institute, 1965, 153.

[5] Durox D., Baillot F., Scouflaire P., Prud'homme R. *Comb. Flame*, 1990, **82**, 66.

ON SOLID FUEL IGNITION AND FLAME SPREAD

A. Carlos Fernandez-Pello

Department of Mechanical Engineering, University of California at Berkeley, Berkeley, CA 94720, USA

The gas phase ignition of a solid and the subsequent spread of flames over its surface, are important processes in the combustion of solid fuels. In addition to the need of understanding theses processes fundamentally, there is a need for the development of predictive formulas for the ignition delay and flame spread rate that can used in practical applications, such as models of fire development and hybrid rocket fuel combustion. Those are the objectives of this work. Based on the available information on these processes, it is proposed to analyze the flame spread as a solid ignition problem where the flame acts both as the source of solid heating and gasification, and of ignition of the gas phase reaction (pilot). The flame spread rate is then given by the ratio of a solid heating length to the ignition time. An analysis of solid fuel ignition is developed that provides explicit expressions for the ignition delay, which is then used to obtain an
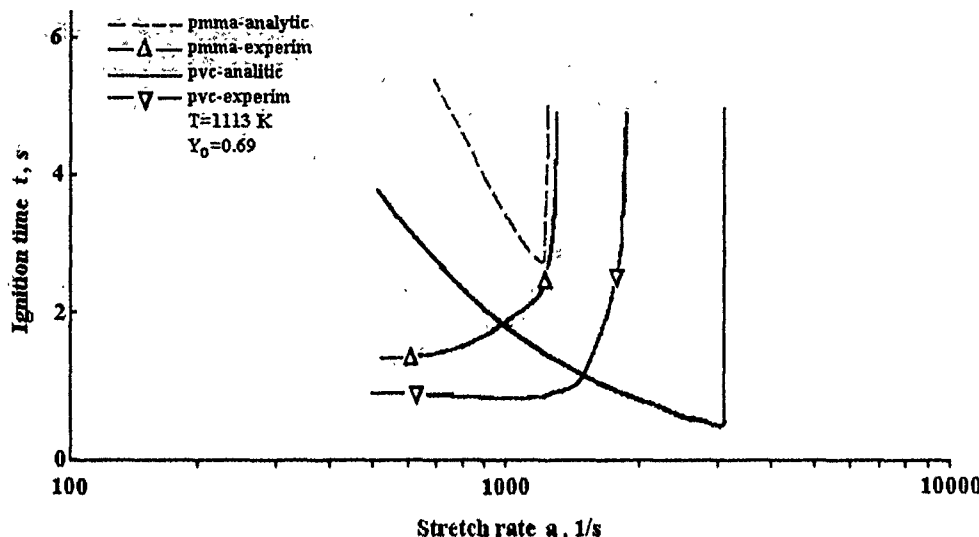
Figure 1: Variation of the ignition delay with the stagnation point flow stretch rate; comparison between experiments and theory.

explicit expression for the flame spread rate. This expression predicts well the available experimental flame spread rate data, including the fast and slow chemistry regimes, and the blow-off and surface heat losses extinction (no spread) limits.

Ignition

The gas phase ignition of a solid fuel is generally the combined result of an externally applied heat flux that causes the gasification of the solid, and the presence of thermochemical conditions that will lead to the onset of a sustained combustion reaction between the vaporized fuel and the oxidizer gas. Considerable work has been conducted on the ignition of solid fuels by Vilyunov and Zarko [1]. Particularly relevant for the present work is the experimental studies of Kashiwagi *et al.* [2], and Niioka *et al.* [3] of the spontaneous ignition of several polymers in a high temperature oxidizing gas flow. The former experiments were conducted in a flat plate flow and the latter in a stagnation point flow. The results from Niioka *et al.* [3] for the ignition delay are shown in Fig. 1. They suggest that two primary, competing mechanisms control the solid ignition process. One is the heating and gasification of the solid, and the other is the onset of the gas phase chemical reaction. The former one gives way to the definition of a "solid pyrolysis" time that decreases as the heat flux (stretch rate) is increased, and that is represented in the results of Fig. 1 by the descending branch in the ignition curves. The later one gives way to the definition of a gas phase "induction" time that increases as the stretch rate increases (convective cooling), and that is represented

by the ascending branch in the ignition curves. Explicit formulas for both times can be developed from analyses of the solid heating problem and the gas phase ignition problem (Niioka [4], August and Fernandez-Pello [5]). The results from such analysis is presented for comparison purposes in Fig. 1.

Flame Spread

For a flame to spread over the surface of a combustible material, enough heat must be transferred from the flame to the unburnt material ahead of the flame to pyrolyze it. The vaporized fuel is then diffused and convected away from the surface, mixing with the oxidizer and generating a flammable mixture ahead of the flame leading edge, which is then ignited by the flame. The rate of flame spread is therefore determined by the ability of the flame to transfer the necessary heat to pyrolyze the solid and to ignite the combustible mixture ahead of it. Considerable work has also been conducted on the spread of flames over a solid combustible surface (Fernandez-Pello and Hirano [6], Wichman [7]). Particularly relevant to the present work are the results of the experimental measurements of Fernandez-Pello et al. [8], of the rate of flame spread over the surface of thick PMMA sheets as a function of the velocity and oxygen concentration of a gas flowing parallel to the solid surface in the opposite direction of flame propagation. The results show that for high oxygen concentrations, as the flow velocity is increased the spread rate first increases, reaches a maximum, and then starts to decrease. For low oxygen concentrations, the spread rate decreases as the gas velocity is increased until the flame can no longer propagate against the opposed gas flow.

Through phenomenological arguments, the above authors postulated that the flame spread rate was controlled by the interaction between processes dominated by heat transfer from the flame to the solid and by gas phase chemical kinetics, and proposed correlating the flame spread rate data in terms of two non-dimensional parameters. One, a non-dimensional flame spread rate derived from a heat transfer flame spread analysis, and the other the Damkohler numbers.

The Relationship between Ignition and Flame Spread

An interesting aspect of the above studies is the similarity between the mechanisms controlling the ignition of the solid and the spread of the flames over its surface. In fact, by simply comparing the ignition data, and the flame spread data, it can be inferred that there is an inverse relationship between the ignition delay and the flame spread rate. This observation leads to the concept that the spread of the flame can be viewed as a solid ignition process where the flame acts both as a source of solid heating and a pilot for gas phase induction. Furthermore, it is possible to develop a simplified model of flame spread that is based on the analyses developed for the solid ignition.

To develop the analysis, it is convenient to describe the sequence of events that lead to the spread of the flame over the solid surface as those that a solid element, initially at the forward edge of the solid region heated by the flame, would undergo to its ignition. Since the time for the solid element to ignite is the same as for the flame

124
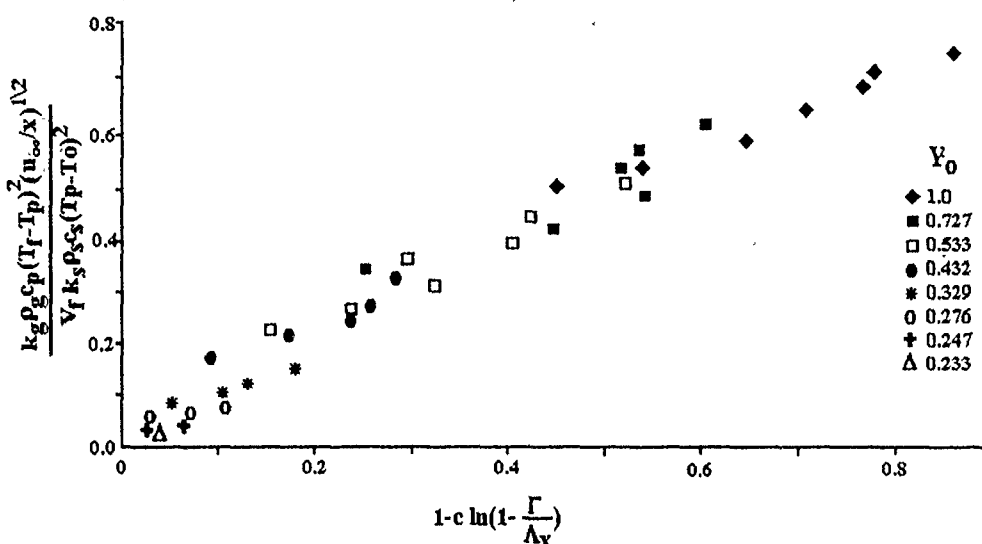
Figure 2: Correlation of opposed flow flame spread rate experimental data with theory.

to propagate to the solid element location, the flame spread rate would be given by the ratio of the length of the solid heated region n ahead of the pyrolysis front to the solid ignition time. Thus, for a specific flame spread problem, the analysis would consist of two sub-analyses: one that would give the solid ignition time, and another that would give the length of the solid region ahead of the flame (or pyrolysis) front. The flame spread rate would then be given by the ratio of the latter to the former values.

Such an analysis has been developed for the case of flame spread in an opposed forced flow, and used to correlate the data from Fernandez-Pello *et al.* [8]. The results of the correlation are presented in Fig. 2. It is seen that the correlation of the results is quite good except at low oxygen concentrations, where chemical kinetic effects are important and the ignition model falters somewhat due to the used simplified chemistry. Similar types of analyses can also be developed to predict flame spread under other flow conditions, i.e., downward and spread in natural convection, forward forced flow, etc.

References

[1] Vilyunov, V. N., Zarko, V. E. *Ignition of Solids*, Amsterdam, Elsevier, 1989.

[2] Kashiwagi, T., MacDonald, B. W., Isoda, H., Summerfield, M. *Proc. 13th Symp. (Int). on Comb.*, 1971, 1071.

[3] Niioka, T., Takahashi, M., Izumikawa, M. *Proc. 18th Symp. (Int.) on Comb.*, 1981, 741.

[4] Niioka, T. *Proc. 18th Symp. (Int.) on Comb.*, 1981, 1087.

[5] August M., Fernandez-Pello, A. C. *Proc. 14th Int. Coll. Dyn. Exp. and React. Syst.*, Coimbra, Portugal, 1993.

[6] Femandez-Pello, A. C., Hirano, T., *Comb. Sci. Techn.*, 1983, **32**, 1.

[7] Wichman, I. S., *Prog. Energy Comb. Sci.*, 1992, **18**, 6, 553.

[8] Fernandez-Pello, A. C., Ray, S. R., Glassman, I. *Proc. 18th Symp. (Int.) on Comb.*, 1980, 579.

THE CORRELATION BETWEEN IONS DISTRIBUTION AND TEMPERATURE FIELD IN A FLAME

B. S. Fialkov, I. A. Larionova, A. B. Fialkov

Chemical-Metallurgical Institute, Karaganda, Kazahstan

The principal trends in the formation of ionic composition of saturated and aromatic hydrocarbons, alcohols and ketones in low-pressure flames under different combustion conditions and their correlations with the temperature field were analyzed. Temperature was measured with chromel–alumel thermocouples with junction diameter 0.8 mm. To reduce the influence of systematic errors and for the sake of convenience, the values of temperature and ionic current were normalized by their maximum values, and the coordinate of the measurement location, y, was normalized by the coordinate of the internal boundary of chemiluminescence zone for each flame.

Four zones with different patterns of ion formation can be distinguished in flames:

(1) the preparation zone,

(2) the zone adjusted to the internal boundary of the front,

(3) the front, or chemiluminescence, zone, and

(4) the zone downstream of the front.

126
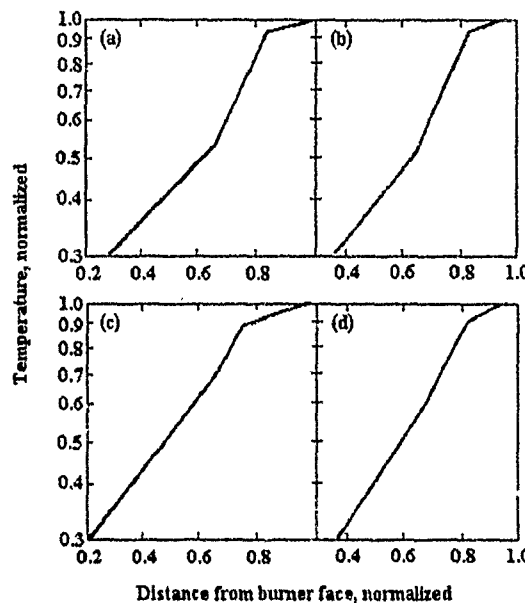
Figure 1. Temperature distribution in flames of ethanol (a), toluene (b), acetone (c), propane-butane (d).

The division of the front into structural zones is in agreement with the temperature distribution.

The differences in relative temperature distribution decrease toward the front ($y >$ 0.75). The latter value is consistent with the identity of ionic compositions in the front and downstream of it. In the preparation zone upstream of the first ions, the temperature distributions for different substances are described by exponentials parametrized mainly by thermophysical characteristics of the mixture. A more detailed analysis shows that the temperature distribution in the preparation zone can be described by functions of the form

$$T_{rel} = C \exp(by_{rel}) \tag{1}$$

differing for particular intervals.

If the temperature curve is presented in semilogarithmic coordinate plane (see Fig. 1), two junction points between the straight lines corresponding to different zones of flame are clearly seen. The values of y_{rel} at which the slope is changing, as well as coefficient of Eq. (1), are close for flames of different fuels. The last portions of the temperature curve are similar for all fuels (see Fig. 1). The coordinate of the last inflection point is close to the coordinate of the zone where polycyclic aromatic hydrocarbon (PAH) ions begin to form.

If the origin of coordinates is set at the maximum temperature points, all above-mentioned trends in the curve shape are preserved, but the number of the points of

127

slope discontinuity increases. In this case, the equation has the general form

$$\frac{T_1 - T_0}{T_{max}} = \frac{T_{max} - T_0}{T_{max}} \exp[b(a - y_{rel})], \tag{2}$$

where T_0 is the mixture temperature at the beginning of the preparation zone.

In this representation, the curves for toluene and acetone coincide. The values of temperatures as presented in semi-logarithmic coordinates, at which the slopes of straight lines change, become closer and for different substances, in terms of $(T_1 - T_0)/T_{max}$ are as follows: 0.26–0.3, 0.6, 0.8, and 0.95. The respective normalized coordinates of these points are 0.4–0.59, 0.65–0.76, 0.77–0.83, and 0.9 (the origin of coordinates is at the outlet plane of the burner). If the current temperature (of the difference between the current value and the inlet temperature) is normalized not by its maximum value, but by the temperature of the points of slope discontinuity, the graphs for different substances coincide, which indicates the similarity of heat exchange processes in the corresponding zones.

In all representations of temperature distribution in the preparation zone, its shape is similar to the Mikhelson profile, which suggests that the exponent is the function of average heat content.

The changes in temperature curves can be due to physicochemical processes at the corresponding locations in the preparation zone, accompanied by either heat release or heat absorption.

The correlation between the coordinates of singular points of temperature distributions in the preparation zones of flames of different substances premixed with air indicates that ionization and thermophysical phenomena are in agreement. The beginning of intense heat-release is observed at the values of the normalized coordinate where the first ions are detected.

In the colder region of the preparation zone the value of the coefficient in the exponential of Eq. (1) coincides with that obtained by dividing the mixture velocity by the value of its thermal diffusivity, i.e. Mikhelson type of the profile in the preheat zone is valid only at the beginning of the preparation zone.

Thus, the agreement of the thermophysical and ionization phenomena in the zones ahead of the front has been established. It has been shown that, in describing the temperature distribution in these zones, physicochemical processes occurring therein should be taken into consideration apart from thermal conductivity.

COMBUSTION OF 3-NITRO-1,2,4-TRIAZOL-5-ONE AND ITS SALTS

A. E. Fogelzang, V. P. Sinditskii, V. Y. Egorshev, V. V. Serushkin, V. I. Kolesov

Department of Chemical Engineering, Mendeleev University of Chemical Technology, Miusskaya Sq. 9, Moscow, 125820 Russia

Recently, 3-Nitro-1,2,4-triazol-5-one (NTO) was extensively investigated as one of the low-sensitivity explosives [1-3]. The salts of NTO are of interest as potentially promising ingredients for gun-propellant formulations [3-5]. Thus, it is important to investigate the combustion behavior of NTO and its salts.

NTO was obtained by the method described in [2]: the salts of NTO were prepared by mixing an aqueous solution of NTO with a proper base, except for the Pb salt, which was prepared by the exchange reaction between the Na salt of NTO obtained in situ and $Pb(NO_3)_2$ in an aqueous-alcohol solution. Flame temperatures were calculated using ASTRA thermodynamic code [6]. Steady-state combustion of NTO and its salts in the form of strands pressed into acrylic tubes was studied in a windowed constant-pressure bomb over the pressure range of 0.1-36 MPa. The temperature profiles of NTO were measured using 7 μm thick Π-shaped tungsten-rhenium thermocouples [7].

At 0.1 MPa, NTO can sustain combustion only when external heating is provided by an electrically heated nichrome wire. Decomposition reactions with gaseous products occurred, but no gas-phase flame was observed. The yellow-brown residue formed contained -NHCO- fragments in the compound, as shown by IR-spectroscopy.

The temperature profiles of NTO obtained at 0.5 MPa clearly indicate the presence of a thick molten reaction layer followed by a gas-phase reaction zone (Fig. 1). Redox reactions involving nitro group conversion appear to proceed only in the condensed phase, resulting in a temperature increase up to 1030 K. Keeping in mind the theoretical decomposition paths for the triazole ring, we expected that the N_2O molecule can be one of the possible products of NO_2 reduction. An analysis of the gaseous combustion products at 0.1-0.5 MPa has indeed revealed the presence of NO, N_2O, CO, and CO_2. The maximum combustion temperatures measured at 0.5 and 2 MPa were by about 700 and 300 K lower than the predicted values. The incomplete oxidation process during NTO combustion at low pressures appears to be responsible for the temperature discrepancy observed.

The heat released in the condensed phase at 0.5 MPa was calculated to be 190 cal/g, whereas the heat transferred back from the gas is five times lower. This suggests that combustion of NTO is essentially determined by the heat released in the condensed phase.
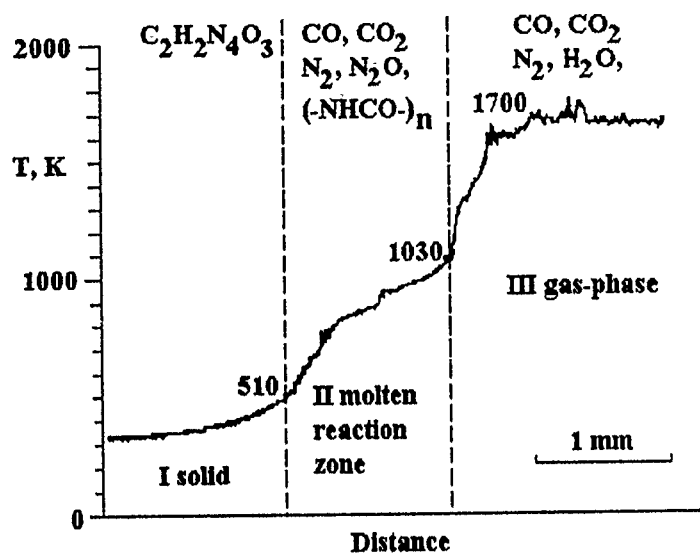
Figure 1: Temperature profile of NTO at 0.5 MPa.
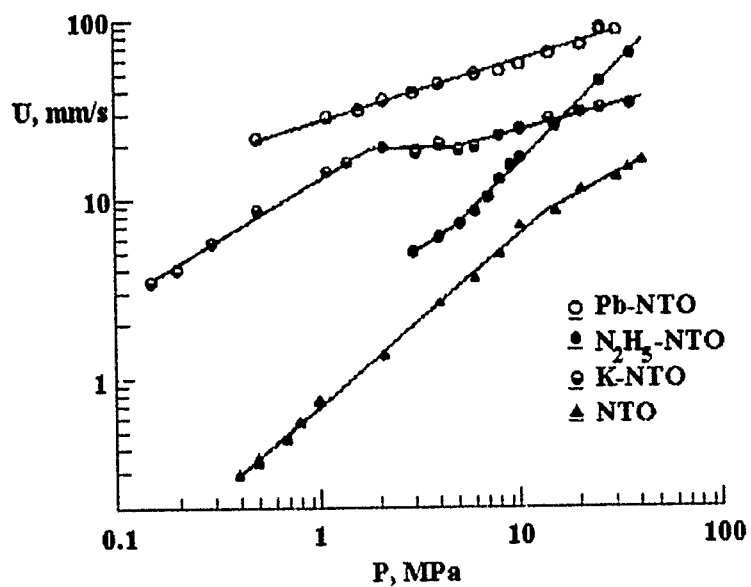
Figure 2: Burning rate versus pressure for NTO and its salts.

The burning rates measured for NTO and its salts are shown in Fig. 2 and Table 1. Comparing the combustion characteristics of NTO monopropellant with those of picric acid (PicH) [8] and methyleneamine-5-nitrotetrazole (MNTz), which exhibit similar combustion temperatures (2200 and 2368 K, respectively), one can note that, at 10 MPa, NTO burns at nearly the same rate as PicH (5.5 mm/s) and six times slower than MNTz. Here, the triazole ring, unlike the tetrazole derivatives [9], has a little effect on the value of the burning rate.

As shown in Fig. 2, all salts of NTO burn faster than NTO itself over the entire pressure range tested. This effect is expressed in terms of the burning rate ratio, Z, of salts to NTO at a fixed pressure. A comparison between the burning rates of NTO salts and picric acid salts shows that the values of Z for N_2H_5 and K salts are close. For Pb–Pic, the increase in the burning rate due to the catalytic effect of Pb is substantially higher than for Pb–NTO (42 and 9, respectively). This phenomenon is described to the abundant soot formation during Pb–Pic combustion that, in its turn, is known to strongly promote the catalytic activity of lead.

Table 1.

Substance	Enthalpy of formation, kcal/mole	Flame temperature, K	Strand density, g/cm^3	Burning rate ($P = 10$ MPa), mm/s
NTO	−25.8	2388	1.87	7
N_2H_5–NTO	−38	1200	1.40	17
K–NTO	−69	1965	1.60	26
Pb–NTO	−78	2040	2.34	63

References

[1] Lee, K. Y., Chapman, L. B., Coburn, M. D. *J. Energetic Materials*, 1987, **5**, 27.

[2] Becuwe, A., Delclos, P. *Propellants, Explos , Pyrotech.*, 1993, **18**, 1.

[3] Yi, X., Rongzu, H., Xiyoun, F., Xiayun, F. *Proc. 17th (Int.) Pyrotech. Sem.*, Beijing, 1991, **1**, 509.

[4] Lee, P., Stinecipher, M. M. *Propellants, Explos., Pyrotech.*, 1989, **14**, 241.

[5] Xiayun, F., Chunhua, Z., Jihua, Z. *Proc. 17th (Int.) Pyrotech. Sem.*, Beijing, 1991, **1**, 189.

[6] Trusov, B. G., *ASTRA: Chemistry and Phase Equilibrium at High Temperature*, Moscow, MSTU Publ., 1989.

[7] Fogelzang, A. E., Egorshev, V. Yu., Sinditskii, V. P., Dutov, M. D. *Comb. Flame*, 1991, **87**, 123.

[8] Fogelzang, A. E., Margolin, A. D., Koliasov, C. M. *et al. Fizika Goreniya Vzriva*, 1975, **6**, 844 (in Russian).

[9] Fogelzang, A. E., Egorshev, V. Yu., Sinditskii V. P. *Proc. 17th (Int.) Pyrotech. Sem.*, Beijing, 1991, **1**, 617.

THE GENERAL ANALYSIS OF THE ZONE STRUCTURE OF A GASLESS COMBUSTION WAVE

B. M. Khusid, O. S. Rabinovich

Luikov Heat and Mass Transfer Institute, Minsk 220072, Republic of Belarus

The first adequate analytical insight into the structure of a combustion wave was presented in one of the early works by Zel'dovich [1] for a premixed gas flame with a high activation energy. It has been shown that the combustion front consists of a wide preheat zone and a narrow reaction zone.

A number of unusual phenomena have been observed in combustion of condensed heterogeneous systems. Complicated physico chemical processes (the growth of a product layer, diffusion of reactants, melting, multi-step reactions, gas transport phenomena, etc.) lead to the formation of a multi-zone structure. Both the experimental observations [2] and the mathematical modeling [3, 4] have revealed the occurrence of a wide "post-reaction" ("after-burn") zone due to the strong self-inhibition of the reaction by the product formation. Combustion waves with two peaks of the heat release have been described, for example, in [5, 6].

The present work is aimed at the general mathematical analysis of the relationship between the structure of the steady-state gasless combustion wave, described by a gross reaction, and the properties of the local heat source function of this reaction.

Governing Equations. The general case, in terms of the kinetic model and temperature-dependent thermophysical properties of both reactants and products, is

considered. In nondimensional variables, the problem is governed by the following equations:

$$\frac{d\Theta}{d\eta} = \varepsilon\Phi(\eta,\Theta), \qquad \Phi(\eta,\Theta) = \frac{h(\eta,\Theta)}{K(\eta,\Theta)f(\eta,\Theta)}, \qquad (1)$$

with the boundary conditions $\Theta\,|_{\eta\to\eta_i}\to\Theta_i$, $\Theta\,|_{\eta\to 1}\to\Theta_e$, where Θ is the temperature, η is the conversion depth, h is the enthalpy, K is the thermal conductivity, f is the kinetic function, ε is the square of the dimensionless wave velocity. The kinetic function must satisfy the conditions $f(1,\Theta) = 0$ and $f(\eta \neq 1,\Theta) > 0$, and the "cut-off" constraint, $f(\eta,\Theta) = 0$, in the vicinity of the initial state.

The Classification of Zones in the steady-state combustion wave can be based on the parameter τF, where τ is the characteristic time scale of thermal phenomena, $\tau \sim a/U^2$ (a is the thermal diffusivity and U is the wave velocity), and $F(\eta,\Theta)$ is the dimensional reaction rate. In **the fast-reaction zone (FRZ)**, $\tau F \gg 1$; the heat released by the chemical reaction cannot heat the substance for the lack of time and is removed to another zone, so that $d\Theta/d\eta \ll 1$. In **the slow reaction zone (SRZ)**, $\tau F \ll 1$; the heating proceeds in a quasi-adiabatic regime ($d\Theta/d\eta \sim 1$, $\eta \approx \Theta$). In **the transition zone (TZ)** $\tau F \sim 1$; the heat release is negligible as compared to the heat flux across this zone, hence $d\Theta/d\eta \gg 1$.

The Critical Curve. From this classification, it follows that a change in the structure of a combustion wave can be directly related to the variation in the number of the extrema of the phase trajectory slope for the solution of the boundary problem (Eqs. 1). A simple consideration shows that this number changes upon crossing the curve in the phase plane for which $d^2\Theta/d\eta^2 = 0$ and $d^3\Theta/d\eta^3 = 0$. This curve, called **the critical curve (CC)**, is determined by the properties of the local heat source function $\Phi(\eta,\Theta)$, because, by invoking Eqs. 1, the relations determining the CC can be rewritten in the parametric form

$$\Phi_\theta' y + \Phi_\eta' = 0, \qquad \Phi_{\theta\theta}'' y^2 + 2\Phi_{\theta\eta}'' y + \Phi_{\eta\eta}'' = 0, \qquad y > 0, \qquad (2)$$

where the parameter y denotes the derivative $d\Theta/d\eta$ at the points of the CC corresponding to the trajectories that exhibit an extremum of the slope. The fulfillment of these conditions also depends on the global behavior of trajectories.

The Algorithm for the Investigation of the Phase Plane of Eqs. (1) is based on the analysis of the singular points of the CC and the global properties of the phase trajectories crossing the CC. This algorithm makes it possible to identify the domains in the phase plane that contain the starting points for the boundary problem solutions with different types of zones. Hence, the structure of a combustion wave can be altered by varying the initial temperature and conversion depth. The algorithm can also be used to solve the inverse problem in order to evaluate the parameters of a kinetic model for a known combustion wave structure.

Examples. To illustrate the analytical results, two kinetic models have been examined: a power law ($\phi_1(\eta)$) and an exponential law ($\phi_2(\eta)$) were chosen for the dependence of the reaction rate on the conversion depth. The Arrhenius law was used to
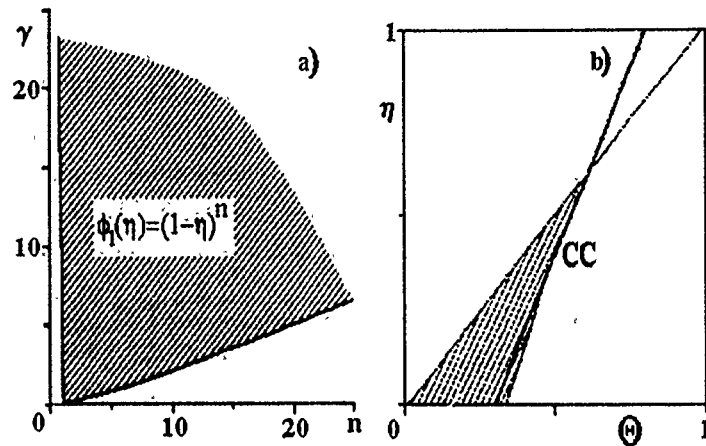
Figure 1: (a) Parameter plane ($\zeta = 0.4$) for the power-law kinetic model: $\gamma = E\Delta T_a/(RT_a^2)$, $T_a = T_0 + \Delta T_a$, $\zeta = \Delta T_a/T_a = 0.8$; E is the activation energy; T_0 is the initial temperature; ΔT_a is the adiabatic heating. The TZ–FRZ–SRZ sequence is possible in the hatched domain. (b) Phase plane for the power-law kinetic model. The TZ–FRZ–SRZ sequence occurs in the hatched domain; $\gamma = 5$, $n = 5$, $\zeta = 0.4$.

describe the temperature dependence of the reaction rate. The results of application of the above analysis to these cases are illustrated by Figs. 1 and 2. The division of the parameter plane in domains pertaining to different structures of the combustion wave is illustrated by Figs. 1a and 2a. Figures 1b and 2b illustrate the construction of the domain in the phase plane containing the starting points for the regimes where the TZ (i.e., preheat zone) is followed by the FRZ and then the SRZ. The solutions to the problem with the starting points lying on the right of the constructed domain (at higher Θ) correspond to the combustion regimes in which the SRZ begins just at the starting point.

The results obtained admit **a clear geometric interpretation**. For a chemical reaction with a weak dependence of the kinetic model on the conversion depth, a trajectory goes down along the $\Phi(\eta, \Theta)$ surface from the starting to the end point. In the combustion wave propagating in a system with a strong dependence of the reaction rate on the conversion depth, the descent of a trajectory along the $\Phi(\eta, \Theta)$ surface in both the FRZ and the TZ changes to an ascent in the SRZ.

The Asymptotic Analysis of the problem is based on the method of singular perturbation. Asymptotic solutions have been derived for the different zones of the combustion wave. These zones were characterized by the following relative length scales: $O(\varepsilon)$ for the SRZ, $O(1/\varepsilon)$ for the FRZ, and $O(1)$ for the TZ. A special second-order asymptotic analysis was performed in the heighborhood of the saddle point on the $\Phi(\eta, \Theta)$ surface. Matching conditions for the asymptotic expansions in the different
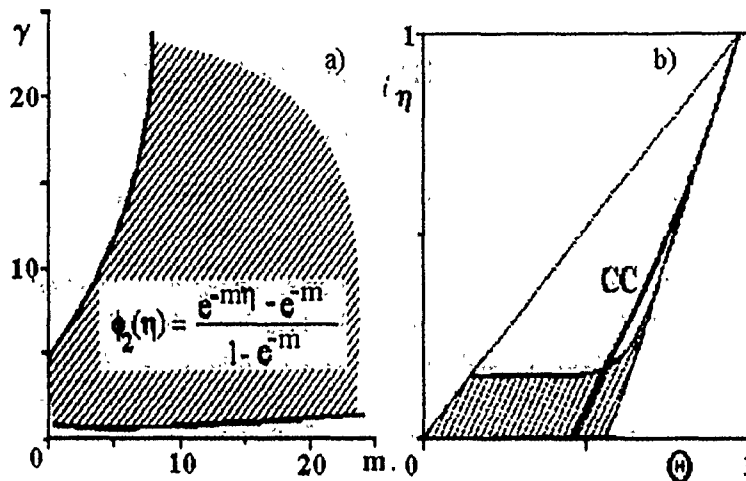
Figure 2: (a) Parameter plane ($\zeta = 0.8$) for the exponential-law kinetic model. (b) Phase plane for the exponential-law kinetic model: $\gamma = 10$, $m = 7.5$, $\zeta = 0.8$; notation as in Fig. 1.

reaction zones and near the saddle point were investigated.

References

[1] Zel'dovich Ya. B., Frank-Kamenetskii D. A. *Zhurnal Fizicheskoi Khimii*, 1938, **12**, 100–105 (in Russian).

[2] Shkiro V. M., Borovinskaya I. P. In: *Combustion Processes in Chemical Technology and Metallurgy*, Chernogolovka, Preprint of OIKhF Akad. Nauk SSSR, 1975, 253–257.

[3] Aldushin A. P., Martemianova T. M., Merzhanov A. G., Haikin B. I., Shkadinskii K. G. *Comb. Explos. Shock Waves*, 1972, **8**, 2, 202–212.

[4] Aldushin A. P., Merzhanov A. G., Haikin B. I. *Dokl. Akad. Nauk SSSR*, 1972, **204**, 5, 1139–1142.

[5] Novozhilov B. V. *Unsteady Combustion of Solid Rocket Fuels.* Moscow, Nauka, 1973 (in Russian).

[6] Merzhanov A. G., Rogachev A. S., Mukasian A. S., Khusid B. M. *Fizika Goreniya Vzriva*, 1990, **26**, 1, 5–13 (in Russian).

THE WAVE THEORY OF IGNITION

B. S. Seplyarskii

Institute of Structural Macrokinetics, Chernogolovka, 142432 Russia

The paper by Zel'dovich [1] has laid the grounds for the modern theory of condensed material ignition. Zel'dovich has evaluated the limiting value of the temperature gradient and shown that under the critical conditions the entire heat flux to the cold zone is due to the chemical reaction, i.e., the heat flux at the boundary is zero.

The numerical solution to the problem of condensed material ignition by a hot surface has shown that the temperature runaway always occurs at some distance from the surface, if the heated layer of the material is sufficiently deep. This implies that the heating of the material at the last stage of ignition is due to the chemical reaction. However, the approximate methods of calculation of the ignition delay time are based on the assumption that the stage of inert heating takes most of the ignition delay time, which conflicts the numerical results.

The first ignition theory for condensed materials dealing with the transition from heating by an external source to that by a chemical reaction was developed earlier [2]. It has been titled the wave theory, because it provided expressions for the durations of the main stages of the ignition process, τ_{in}, τ_0, and τ_{ig}, in terms of the parameters of the intermediate combustion wave, q_{st}, ω_{st}, and ξ_{st}. Here, τ_{in}, τ_0, and τ_{ig} are the times of inert heating, the onset of zero gradient at the material–heater boundary, and thermal explosion, respectively; q_{st}, ω_{st}, and ξ_{st} are the heat flux from the heat release zone, the velocity, and the width of the reaction zone, respectively. The intermediate combustion wave (ICW) is steady, with the maximum temperature in the heat release zone equal to the ignition temperature, T_{ig}.

The physical principle of this theory is as follows. The entire ignition process is divided in three stages: inert heating, thermal wave propagation into the material, and thermal explosion. At the first stage, a heated layer of the material is formed due to the energy flux from the external source. Equating the heat flux characteristic of the inert heating, $q = \theta_0/\sqrt{\pi\tau}$, to that from the heat release zone of the ICW, q_{st}, we obtain the following formula for the duration of the first stage:

$$\tau_{in} = \frac{\theta_0^2}{\pi q_{st}^2}. \tag{1}$$

At $\tau > \tau_{in}$, the heated layer moves into the material. It is assumed that the heat wave velocity is close to ω_{st}. The increase in the heat release by chemical reaction without a noticeable increase in the maximum temperature is considered as the sign of formation of the chemical reaction zone with a different quasi-steady temperature

distribution and zone width scaling linearly with time, $\xi_r = \omega_{st}(\tau - \tau_{in})$. When the width of the reaction zone is equal to that of the reaction zone of the ICW, $\xi_r = \xi_{st}$, the heating of the material is entirely due to the chemical reaction and the temperature gradient at the surface vanishes. The time of the onset of zero gradient is given by

$$\tau_0 = \tau_{in} + \frac{\xi_{st}}{\omega_{st}}. \tag{2}$$

The subsequent widening of the zone of chemical heat release at the velocity ω_{st} leads to the breakdown of the equilibrium between the chemical heat release and the heat transfer to the cold layers of the material. This results in a maximum in the temperature profile at the point of the lowest rate of heat removal from the reaction zone, i.e., close to the surface where the temperature gradient is zero. The temperature peak moves into the material at the same velocity, ω_{st}, increasing in amplitude. When it has moved over the length ξ_{st}, the heat fluxes to the heater and to the cold material become equal, and a drastic increase in temperature, i.e., a thermal explosion, occurs at the point of maximum temperature. Therefore, $\xi_{expl} = \xi_{st}$;

$$\tau_{ig} = \tau_0 + \frac{\xi_{st}}{\omega_{st}}. \tag{3}$$

Let us apply the suggested method to the evaluation of the ignition characteristics of the material where a zeroth-order reaction occurs.

The considered model of the process is standard for the thermal theory of ignition. At the boundary of a semi-infinite condensed material capable of exothermic conversion, at $t = 0$ the temperature instantaneously reaches the value T_{ig} $(T_{ig} > T_0)$ and is constant afterwards during the entire process. It is assumed that only condensed products are formed in the reaction, and the reaction rate is zero at the initial temperature, T_0. The ignition temperature is much lower than the adiabatic flame temperature. We start the evaluation of the ignition characteristics by calculating the ICW parameters. In accordance with the classification of combustion waves, the ICW is a combustion wave of the second type. The dependence of the combustion rate on the initial parameters and on the conversion depth for various kinetic functions has been determined by Merzhanov [3]. For a zeroth-order reaction, we have :

$$q_{st} = \sqrt{2}, \qquad \omega_{st} = \sqrt{2}, \qquad \xi_{st} = \sqrt{2}. \tag{4}$$

Substituting Eq. (4) in Eqs. (1)–(3), we obtain

$$\tau_{in} = \frac{\theta_0^2}{2\pi}, \qquad \tau_0 = \tau_{in} + \theta_0, \quad \tau_{ig} = \tau_0 + \theta_0. \tag{5}$$

Comparison of the estimated τ_0 and τ_{ig} with the numerical results [4] shows that the discrepancy does not exceed 10%.

The advantages of the wave theory of ignition are most conspicuous in the analysis of the condensed material ignition in the presence of heat loss from the side surface [5]. The wave theory makes it possible not only to calculate the temporal characteristics of the ignition process but also to find the dependence of the critical value of the heat loss coefficient on the basic parameters of the problem:

$$z_{cr} = (1 - \gamma\theta_0)\omega_{st}, \qquad \omega_{st} = \sqrt{2}\theta_0, \qquad (6)$$

where γ is the small parameter of combustion theory.

Within the framework of the wave theory, we can readily explain the nature of different regimes obtained by varying the heat loss coefficient z. At $z < z_{cr}$, the burnout time at the surface is $\tau_b = \gamma^{-1}$, exceeding the formation time of the reaction zone capable of self-propagation in the combustion regime, ξ_{st}. For this reason, the heating leads to ignition. At $z > z_{cr}$, $\tau_b < \tau_0$, the material at the surface burns out before the reaction zone of width ξ_{st} is formed. A further widening of the reaction zone becomes impossible, since the chemical heat release does not provide the heat flux into the cold layers that is required to support the ICW. The chemical heat release reaches its maximum at $\tau = \tau_b$ and then decreases. After the material in the surface layer of the sample has burned out, the temperature distribution and the heat flux on the surface tend to their steady values that are determined by the solution of the inert problem.

References

[1] Zel'dovich, Ya. B. *Zhurnal Experimentalnoi Teoreticheskoi Fiziki*, 1939, **9**, 12, 1530 (in Russian).

[2] Seplyarskii, B. S. *Dokl. Akad. Nauk SSSR*, 1988, **300**, 1, 96 (in Russian).

[3] Merzhanov, A. G. *Dokl. Akad. Nauk SSSR*, 1977, **233**, 6, 1130 (in Russian).

[4] Vilyunov, V. N. *Ignition Theory of Condensed Materials*. Novosibirsk, 1984 (in Russian).

[5] Seplyarskii, B. S. *Fizika Goreniya Vzriva*, 1990, **26**, 5, 3 (in Russian).

THE INFLUENCE OF A SUPERHEATED WATER AEROSOL ON A PREMIXED METHANE–AIR FLAME

Yu. N. Shebeko, A. Ya. Korolchenko, A. V. Trunev,
V. Yu. Navzenya, S. N. Papkov, A. A. Zaitsev

All-Russia Scientific Research Institute for Fire Protection
Balashiha-6, Moscow Region, 143900 Russia

The fine water aerosol formed by rapid evaporation of superheated water is widely used as an effective means of extinguishing of diffusive flames [1]. It is interesting to investigate the applicability of such aerosol for inertization of premixed combustible gas and oxidizer. This work is aimed at experimental elucidation of the influence of superheated water aerosol on combustion of methane–air mixtures in a closed vessel.
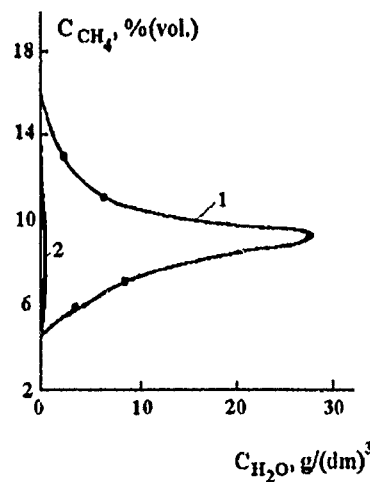
Figure 1: Methane flammability limits in air (c_{CH_4}) versus superheated water aerosol (1) [this work] and water vapor (2) [3] mass concentration c_{H_2O}.
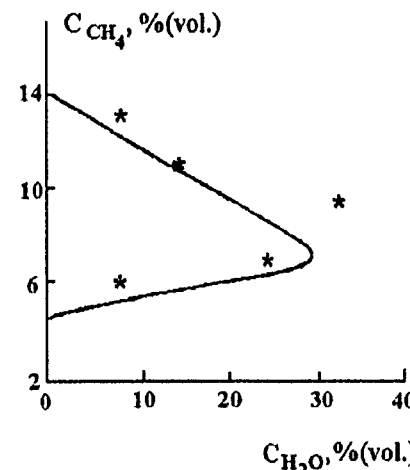
Figure 2: Methane flammability limits in air (c_{CH_4}) versus water vapor mass concentration c_{H_2O}. —— [3]; * this work.

Experiments were conducted in a spherical reaction vessel 20 dm^3 in volume, made of stainless steel. Combustible gaseous mixtures were prepared in the evacuated reaction vessel. Superheated water was introduced into the reaction vessel from a closed heated vessel. Superheated water temperature was 150 °C in all experiments. The heated vessel for superheated water preparation was positioned immediately above the reaction vessel and separated from it by a valve. A fused nichrome wire was used as

the ignition source. The ignition energy was about 10 J. Combustion of the premixed gas was monitored by a pressure transducer with a time constant $\sim 3 \cdot 10^{-3}$ s. The temperature of the combustible mixture in the reaction vessel before and after the introduction of superheated water was measured by a thermocouple.
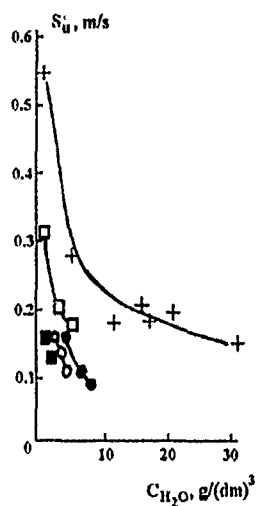
Figure 3: Dependence of laminar burning velocity S_u of methane–air mixture on superheated water aerosol mass concentration c_{H_2O}. Methane concentrations: 6(○), 7(●), 9.5(+), 11(□), 13(■) %(vol.).

The experimental procedure was as follows. A known amount of liquid was introduced into the vessel used for superheated water preparation, and then the vessel was sealed and heated to a required temperature. The combustible mixture was prepared in the reaction vessel. Then the heated vessel was connected with the reaction vessel for a short time (not longer than 1 s) and an aerosol–vapor–gas mixture was formed in the latter. The temperature of this mixture was about 60–80 °C. After some time (usually 5 s), the ignition source was activated. The pressure in the reaction vessel was recorded throughout the experiment (from the starting moment of water introduction to the pressure decrease due to the cooling of combustion products). The amount of superheated liquid introduced into the reaction vessel was determined as the difference between the initial water mass and the liquid mass remaining in this vessel after its cooling to the room temperature.

In the experiments, flammability limits (FL) and the laminar burning velocity S_u were determined. The value of each flammability limit was defined as the mean value of two concentrations, one of which corresponded to three ignitions obtained, the other corresponding to three non-ignitions. The values of S_u were found by the procedure described in [2].

The dependence of the FL for methane in air on superheated water aerosol mass concentration is presented in Fig. 1. In this figure, the inertization curve for methane–air mixture with water vapor is shown for comparison [3]. We can see that the value of inertizing concentration (the extremum point of the curve) for superheated water aerosol substantially exceeds the value for water vapor. This effect is probably due to the formation of relatively large water droplets in the reaction vessel volume, with mean droplet size within 10–50 μm [1]. These droplets do not evaporate to a sufficiently high extent in the narrow flame front, hence their influence on combustion characteristics is rather low. It can be conjectured that the efficiency of inertization by superheated

velocities. In the seminal papers on gene propagation (by Kolmogorov *et al.* [1]) and on premixed gas combustion (by Zel'dovich [2]) exact and approximate methods of determination of the wave velocity were proposed for reaction rate functions of diverse forms. Among later publications, the papers by Novozhilov [3], on condensed phase combustion, and Aldushin *et al.* [4, 5], on combustion of condensed mixtures with strong inhibition of the reaction by its products, should be mentioned.

It should be stressed that the conventional approximate methods developed for combustion waves invoke either the concept of "narrow reaction zone" [2, 3] or an analogy with the theory of thermal explosion [4, 5], and necessarily involve asymptotic solution in terms of a small parameter, constructed *ad hoc* for a particular form of source function. In the case of a nonlocal function of heat release $W(T, \eta)$, these methods fail to provide a satisfactory accuracy.

In this paper, a new general-purpose method is proposed for accurate evaluation of the propagation velocity and other characteristics of a combustion wave applicable to various forms of the source function W.

2 Problem Statement and Approximate Method

Dimensionless equation is considered in the phase plane (z, p), where z is the temperature, p is the conductive heat flux, and U is the combustion wave velocity:

$$p\frac{dp}{dz} = Up - W(z, \eta), \qquad p(0) = p(1) = 0, \tag{1}$$

$$W(z, \eta) = G(\eta) \cdot F(z), \qquad F(z) = \exp\left(\frac{z-1}{\varepsilon + \beta z}\right),$$

$$T_a = T_0 + \frac{Q}{c}, \qquad z = \frac{T - T_0}{T_a - T_0}, \qquad p(z) = \frac{dz}{d\xi},$$

$$\beta = \frac{RT_a}{E}, \qquad \gamma = \beta\frac{T_a}{T_a - T_0}, \qquad \varepsilon = \gamma - \beta,$$

Equation (1) describes:

(i) condensed combustion (in this case, the conversion depth is $\eta = z - p(z)/u$) for various forms of kinetic function $G(\eta)$, e.g. for the standard model

$$G(\eta) = (1 - \eta)^n, \tag{2}$$

or for the model of strong inhibition by reaction products [4]

$$G(\eta) = \exp(-m\eta) \tag{3}$$

(ii) gas combustion, with similarity, $\eta \equiv z$, and the kinetics modeled by (2).

water aerosol is mainly due to the presence of water vapor in it (see Fig. 2, where the dependence of FL for methane in air on the water vapor concentration [3] is presented together with the experimental results of our work). The water vapor concentrations in our work were computed using the measured partial pressure of water vapor in the reaction vessel at the ignition moment. The agreement between the results of [3] and the experimental results of our work is satisfactory.

In Fig. 3, the dependence of the laminar burning velocity S_u for the methane–air mixture on the superheated water aerosol mass concentration c_{H_2O} is presented. The rapid decrease in S_u with increasing c_{H_2O}, has an exponential character. This fact qualitatively agrees with the results of [4] for the influence of water vapor on the laminar burning velocity for hydrogen–air mixtures. This effect also confirms our conjecture concerning the primary role of water vapor in the inertization of gaseous mixtures by superheated water aerosol.

References

[1] Bezrodnyi I. F. *Fire Safety — Informatics and Techniques*, 1993, **1**, 72.

[2] Molkov V. V. *Fire and Explosion Safety*, 1992, **1**, 4, 3.

[3] Coward H. F., Jones G. W. *Limits of Flammability of Gases and Vapours*. Bulletin 503. Washington, Bureau of Mines, 1952.

[4] Lui D. D. S., MacFarlane R. *Comb. Flame*, 1983, **49**, 1–3, 59.

ON DETERMINATION OF COMBUSTION WAVE VELOCITY FOR VARIOUS FORMS OF SOURCE FUNCTION

B. V. Stepanov

Institute of Structural Macrokinetics, Chernogolovka, Russia

1 Introduction

One of the most important problems in the theory of nonlinear waves in parabolic systems, as well as in the combustion theory, is the determination of wave propagation

Based on certain general features of the source function W and assumptions concerning the behavior of the solutions to Eq. (1), the following relationships for the combustion wave velocity U and the temperature of peak heat flux z_m (at the transition from the preheat zone to the zone of the leading reaction stage) can be derived:

$$F(z_m) = 2\overline{W} \equiv 2 \int_0^1 W \, dz \qquad (4)$$

$$U^2 = \frac{F(z_m)}{z} \qquad (5)$$

Note that if the function W satisfies the criterion for "narrow reaction zone", i.e. W is localized in the vicinity of the adiabatic temperature T_a, Eqs. (4) and (5) yield the asymptotic result

$$z_m \Rightarrow 1, \qquad U^2 \Rightarrow 2\overline{W} \qquad (6)$$

obtained by Zel'dovich [2] for gas combustion and by Novozhilov [3] for condensed phase combustion.

3 Comparison with Numerical Results

To verify the proposed approximate method, Eq. (1) was solved numerically by a "shooting" technique using a highly accurate implicit self-adapting finite-difference scheme. Starting from the singular points (0,0) and (1,0) along the asymptotic solutions, two integral curves were computed toward each other, and the value of combustion velocity was found by matching these two curves at some "junction" point z_c.

As a first test, condensed combustion with the first-order kinetic law given by Eq. (2) was analyzed, and the dependence of combustion velocity U on the initial temperature T_0 was determined, all other parameters being fixed. In this case, the velocity U_n was found by numerically solving Eq. (1), and U was evaluated by Eqs. (4) and (5), for various pairs of β and γ, where $\gamma = \beta^2/\beta_0$ and β_0 is the value of β at $T_0 = 0$, taken 0.05. The computed results show that Eqs. (4) and (5) can be used to find the combustion wave velocity with a good accuracy.

As an another example, the dependence of combustion velocity on the inhibition degree m was considered for condensed phase combustion with the kinetic law of Eq. (3) (for this type of combustion, Eq. (4) has a more complicated form). The graphs of U/U_n and U_a/U_n as functions of m (where U_a is the approximate value of combustion velocity obtained in [4, 5]) demonstrate that the method proposed here provides a good accuracy of predicted combustion velocity in a broader range of m.

To test the potential accuracy of the new method, solution to Eq. (1) was found for the case of the kinetic law of Eq. (3) combined with the similarity between η and z: $\eta \equiv z$. In this case, the source function $W(z)$ belongs to the class of solitary impulse

functions, its shape being controlled by the values of m, γ, and β. Thus, we have shown that the proposed approach provides an accurate estimation of wave velocity for the source function $W(z)$ of solitary impulse type.

The author is happy to express his sincere gratitude to Prof. K. G. Shkadinsky for his interest in the problem and useful discussion of the results.

References

[1] Kolmogorov A. N., Petrovsky I. G., Piskunov N. S. *Bull. of Moscow State University, Section A*, 1937, **16**, 1 (in Russian).

[2] Zel'dovich Ya. B. Zhurnal Fizicheskoi Khimii, 1948, **22**, 57 (in Russian).

[3] Novozhilov B. V. *Dokl. Akad. Nauk SSSR*, 1961, **141**, 836 (in Russian).

[4] Aldushin A. P., Merzhanov A. G., Khaykin B. I. *Dokl. Akad. Nauk SSSR*, 1972, **204**, 5, 1139 (in Russian).

[5] Aldushin A. P., Martem'yanova T. M., Merzhanov A. G., Khaykin B. I. Shkadinsky K. G. *Fizika Goreniya Vzriva*, 1972, **2**, 202 (in Russian).

INFLUENCE OF TITANIUM SAMPLE DENSITY ON IGNITION AND STRUCTURE FORMATION IN ELECTROMAGNETIC FIELD

A. I. Trofimov, A. S. Mukasyan, I. P. Borovinskaya

Institute of Structural Microkinetics, Chernogolovka, Russia

The effect of electromagnetic field (EMF) on ignition and structure formation in the titanium–air system is investigated in the present work.

The experiments were carried out in a high-frequency generator with working frequency 440 kHz. The relative density of the pressed initial samples varied from 0.5 to 0.7. The pellet diameter $(2R)$ and its height were constant and equal to 1 cm. The anode voltage of the generator (V) was constant and equal to 3 kV.
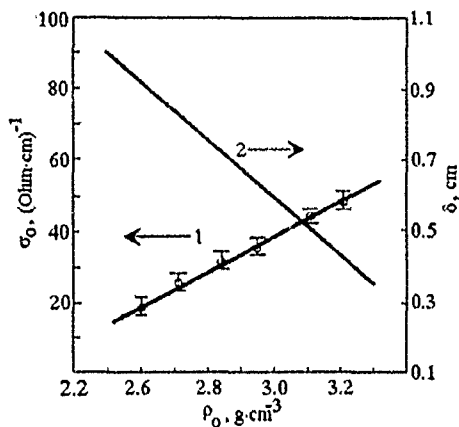
Figure 1: Dependencies of electrical conductivity (*1*) and skin layer thickness (*2*) on the initial sample density.
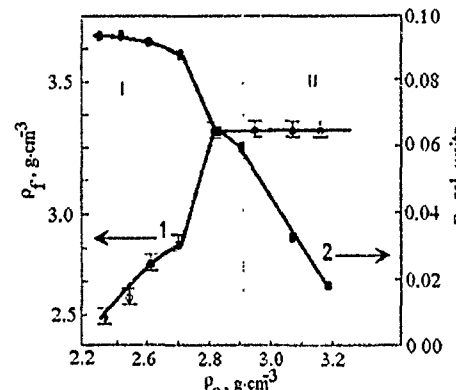
Figure 2: Dependencies of the final density (*1*) and degree of conversion (*2*) on the initial sample density.

The preheating of a porous titanium sample of cylindrical shape was shown to depend on the ratio of skin-layer width (δ) to sample density (ρ). Thermocouple measurements revealed two regimes: ignition at the side surface of the sample and at its center. In the case of $\delta \approx R$, depending on the initial sample density (ρ_0), various reaction modes related to sample filtration characteristics were possible. The value of δ can be approximately evaluated by the expression [1]: $\delta = c/\sqrt{2\pi\mu_0\sigma_0\omega}$, where c is the velocity of light; μ_0 and σ_0 are the magnetic permeability and specific electrical conductivity of titanium; ω is the frequency. Titanium is a paramagnetic, and $\mu_0 = 1$. To evaluate δ, we measured σ_0 versus sample density (Fig. 1, curve 1). The experimental dependence obtained allowed us to evaluate $\delta(\rho)$ (Fig. 1, curve 2).

The dependence of the final sample density (ρ_f) on the initial one (ρ_0) is shown in Fig. 2, curve 1. Two characteristic regions are present:

(i) with the linear scaling $\rho_f = F(\rho_0)$ and

(ii) with a virtually constant value of final density.

One can explain this result, invoking the relation ship between the initial and final densities, $\rho_f = \rho_0(1 + const \cdot \eta)$, where η is the final conversion depth. A chemical analysis shows (Fig. 2, curve 2) that in the case of the low ρ_0 (high porosity), the afterburn zone was wide due to the EMF effect, and η was essentially constant for every ρ_0, so that ρ_f was proportional to ρ_0. At high initial densities, in the surface regime of ignition, η decreased with increasing ρ_0.

Thermocouple measurements have proved that for the samples of $0.5 < \rho_{rel} < 0.6$ a mode of the volume reaction is realized in EMF, with gas infiltration from the outside being insignificant. Nitrogen and oxygen distributions over the sample radius were uniform. The microstructure was a porous crystallized frame of oxygen and nitrogen solid solution in titanium.

When $0.6 < \rho_{rel} < 0.7$, the ignition at the side surface was observed. The wave propagated to the sample centre. But the gas amount in pores was not sufficient to support intense chemical reaction, and the air access from the outside was difficult. In this case, the sharp decrease in the reaction depth was observed. In terms of structure and phase composition, product is a multilayer material with various components distributed along the radius. The sample edge consists of sintered particles of titanium oxide of 0.1 mm thick. Lying further beneath are regions of titanium nitride and solid solution of nitrogen in titanium of 3 mm thick, and the central layer is unreacted titanium.

References

[1] Landau L. D., Lifshits E. M. *Electrodynamics of Continua*, Moscow, Fizmatgiz, 1982 (in Russian).

UNIFIED DEPENDENCIES FOR TEMPERATURE SENSITIVITIES OF COMBUSTION RATE AND SURFACE TEMPERATURE OF DBP

A. A. Zenin, S. V. Finjakov

Semenov Institute of Chemical Physics, Kosygin Str. 4, Moscow, 117977 Russia

Introduction

The temperature sensitivities of the burning rate, $\beta = (\partial \ln m / \partial T_0)_p$, and of the surface temperature, $r = (\partial T_s / dT_0)_p$, are important characteristics of the burning process. (Here, m is the mass burning rate, T_s is the surface temperature, and T_0 is the propellant initial temperature.) These characteristics are of basic importance for the combustion theory and production of new propellants for rocket motors, guns etc. Nevertheless, the overviews of this problem (see, for example, [1] covering 36 articles) show

that the progress in this field is rather moderate, due to the absence of a combustion theory capable of explaining the gasification process in combustion waves. This paper presents a new equation for β and r, based on unified dependencies for the main parameters of combustion waves of double-base propellants (DBPs) [2]. The equations obtained can be used to calculate β and r in a very wide range of pressures (up to 1000 atm). The existence of the unified dependencies for β and r on pressure p ($p \geq 100$ atm) for DBPs under certain conditions have been proved.

Derivation of the Expressions for r and β

Two unified dependencies for the reaction zone parameters of DBPs are used. The first dependence (the gasification law) relates the mass burning rate, m, to the burning surface temperature, T_s, heat release Q in the combustion wave and pre-exponential factor $Q^* K_{01}$:

$$m^2 = \frac{\overline{k}\rho}{Q} \cdot \frac{RT_s^2}{E} \cdot Q^* K_{01} \exp\left(-\frac{E}{RT_s}\right), \tag{1}$$

where $\overline{k}$ is the thermal conductivity and ρ is the density of the solid. The experimental values of the macrokinetic parameters are: $E = (21 \pm 1)$ kcal/mol, $K_{01} = 8 \cdot 10^9 \text{s}^{-1}$, $Q^* = 0.17 Q_v$, where Q_v is the propellant caloric power at constant volume. The second dependence (the heat release law) relates heat release in the solid, Q, and the parameter Q_v to m and p:

$$\frac{Q}{Q_v} = 0.17 - 0.103 \exp\left(-0.0253 pm^{-\frac{1}{2}}\right), \tag{2}$$

where p is in atm, and m is in g·cm^{-2}s^{-1}.

Equations (1) and (2) are valid in a very wide range of pressures (1–1000 atm) [2].

The analysis shows that, to obtain the relationship between r and β, one can use, instead of Eq. (1), the expression $m \sim T_s/(T_s - T_0) \cdot \exp(-E/2RT_s)$, which yields

$$r = \frac{\beta - (T_s - T_0)^{-1}}{\frac{E}{2RT_s^2} - \frac{T_0}{T_s} \cdot (T_s - T_0)^{-1}}. \tag{3}$$

The unified dependence (2) was initially obtained for $T_0 = 20$ °C. Nevertheless, a special analysis shows that Eq. (2) is valid for T_0 varying from $+100$ °C to -100 °C. In this case, we can use a simplified form of Eq. (3):

$$\beta = \frac{E}{2RT_s^2} r. \tag{4}$$

The second equation relating β to r can be obtained by differentiating Eq. (2) with respect to T_0. The weak dependence of q on T_0 must be taken into account (*cf.* $Q = c_s(T_s - T_0) - q$, where q is the heat transfer from the gas to the solid). The final

equations for β and r are:

$$\beta = \left(\frac{2RT_s^2}{E} + \frac{1.3 \cdot 10^{-3} pQ_v}{c_s m^{1/2}} \right)^{-1}, \tag{5}$$

$$r = \left(1 + \frac{1.3 \cdot 10^{-3} pQ_v}{c_s m^{1/2}} \frac{E}{RT_s^2} \right)^{-1}. \tag{6}$$

Predictions. Unified Dependencies of β and r on p

The calculated parameters β and r are in a good agreement with the experimental β and r for many DBPs. This implies that Eqs. (5) and (6) can be used to predict these characteristics for DBPs under complicated conditions, such that β and r are difficult to obtain experimentally, for example, at high pressures. The parameters β and r were evaluated for a group of DBPs by Eqs. (5) and (6) for pressures up to 1000 atm ($T_0 = 20$ °C). In this group, the propellant caloric power Q_v varied from 600 cal/g to 1200 cal/g, whereas it varied within three times from propellant to propellant. The values of β and r, as well as the intervals of variation of these values at fixed pressures, have been shown to decrease as the pressure is increased. The following intervals of β have been obtained: $(2.2–2.7) \cdot 10^{-3}$ 1/°C at 130 atm, $(1.7–1.8) \cdot 10^{-3}$ 1/°C at 250 atm, $(1.1–1.3) \cdot 10^{-3}$ 1/°C at 500 atm, and $(0.75–0.82) \cdot 10^{-3}$ 1/°C at 1000 atm. The intervals of r are as follows: $(0.3–0.35)$ at 100 atm, $(0.14–0.17)$ at 500 atm, and $(0.11–0.14)$ at 1000 atm.

The variation in the values of Q_v covered a very wide group of DBPs. Thus, the obtained dependencies for r and β showing the slight variation in r and β at fixed pressures for $p \geq 100$ atm are acceptable as the unified dependencies of r and β on pressure for DBP.

References

[1] Cohen N. S., Flangan D. A. *AIAA Paper*, 1984, 286, 12.

[2] Zenin A. A. In: *Progress in Astronautics and Aeronautics*, **143**; N. Y., AIAA Inc., 1991.

SESSION 3. Diffusion and Heterogeneous Combustion

INTERACTION OF GASLESS AND FILTRATION COMBUSTION

A. P. Aldushin[*], B. J. Matkowsky[†], V. A. Volpert[†]

[*]*Institute of Structural Macrokinetics, Chernogolovka, 142432 Russia*
[†]*Department of Engineering Sciences and Applied Mathematics, Northwestern University, Evanston, IL 60208, USA*

We study the propagation of combustion waves through porous samples in which two reactions occur. The first is the gaseous solid–solid reaction between two solid species in the porous solid matrix to form a solid product, while the second is a solid–gas reaction in which the gas delivered to the reaction site through the pores of the sample reacts with one of the solid species to form both solid and gaseous products. We consider the case of coflow filtration, in which the direction of gas flow is the same as direction of propagation. The gas, consisting of both chemically active and inert components, filters to the reaction zone through the product region thus transferring heat from the high-temperature products to the unburned mixture [1].

Analysis of this problem, in which specific features of gasless and filtration combustion models are combined, is of particular interest from the point of view of the practical realization of SHS processes [2] involving weakly exothermic solid–solid reactions. It is known that the burning temperatures in coflow filtration combustion waves can significantly exceed the adiabatic value calculated for stoichiometric compositions. Thus, arranging for coflow filtration to occur in an otherwise gasless SHS process can enhance the exothermicity of the reaction which would otherwise the insufficient for the propagation of SHS waves. Examples of such systems are ceramic–oxide superconductors and silicon and tungsten carbides. The low heat release and, accordingly, the insufficiently high thermodynamic temperature are the principal difficulties in using the SHS method for these systems. A possible solution of this problem is to increase the temperature in the combustion wave by arranging for a parallel exothermic reaction between one of the solid components of the mixture and an active component of a gas which filters through the mixture. The possibility of generating high temperatures in the manner may, in fact, be important for the SHS process in general.

We study combustion waves with two reactions propagating through samples with a pre scribed constant incoming gas mass flux at the ignited end. In the coordinate system attached to the combustion wave which propagates from right to left at an unknown constant velocity u, the set of equations governing the energy and species balances is

$$u\frac{d\rho_0}{dx} = -W_1 - W_2, \tag{1}$$

$$u\frac{d\rho_1}{dx} = -\nu_1 W_1, \tag{2}$$

$$u\frac{d\rho_2}{dx} = -\frac{d(aG)}{dx} - \nu_2 W_2, \tag{3}$$

$$u\frac{d\rho_3}{dx} = \nu_3 W_1 \qquad (\nu_3 = 1 + \nu_1), \tag{4}$$

$$u\frac{d\rho_4}{dx} = \nu_4 z W_2 \qquad (\nu_4 = 1 + \nu_2), \tag{5}$$

$$u\frac{d\rho_5}{dx} = -\frac{d((1-a)G)}{dx} + (1-z)\nu_4 W_2, \tag{6}$$

$$C_u\frac{dT}{dx} = \frac{d}{dx}\left(\lambda\frac{dT}{dx}\right) + Q_1 W_1 + Q_2 W_2, \tag{7}$$

$$C_u \equiv u\sum_{i=0}^{6}\rho_i c_i + c_g G, \tag{8}$$

$$G = \rho v, \qquad v = -k_f\frac{dP}{dx}, \qquad P = \rho R T, \tag{9}$$

$$\rho = \rho_2 + \rho_5, \qquad a = \frac{\rho_2}{\rho}. \tag{10}$$

Here, $x = x' + ut$, where x' is the spatial variable and t is time, ρ_i $(i = 0\text{–}6)$ is the effective density of the component i, i.e. the mass of component i per unit volume of the mixture. The indices $i = 0, 1, 6$ correspond to the solid reactants A $(i = 0)$, S $(i = 1)$ and the inert solid I $(i = 6)$, the indices $i = 2, 5$ correspond to the gaseous reactant O $(i = 2)$ and the inert gas I_1 $(i = 5)$, and the indices $i = 3, 4$ correspond to the reaction products AS $(i = 3)$ and AO $(i = 4)$. Here, c_i is the specific heat of the i-th species, ρ is the effective density of the gas, a is the concentration of the gaseous reactant, T is the temperature, P is the pressure, v is the velocity of the filtering gas, G is the gas mass flux, m, k_f and λ are the porosity, filtration coefficient and the heat conductivity of the mixture, W_n and Q_n $(n = 1, 2)$ are the reaction rates and thermal effects of the two reactions, z is the fraction of solid in the product of the solid–gas reaction. The molecular weights and specific heats of all gaseous components are assumed to be equal $(c_2 = c_5 \equiv c_g$ is the gas specific heat).

The boundary conditions for Eqs. (1)–(7) are the initial state far ahead of the combustion wave

$$x = -\infty: \qquad T = T_0, \quad \rho_i = \rho_{i0}, \tag{11}$$

and the state at the right end of the sample behind the combustion wave, where the gas is forced into the sample and the complete consumption of the reactant A results in the termination of the reactions. Thus

$$x = 0: \qquad \begin{aligned} &\rho = \rho_{0b} = 0, \quad dT/dx = 0 \quad (W_1 = W_2 = 0)\\ &G = G_b = -g^0, \quad a = a_b = a^0. \end{aligned} \tag{12}$$

Here, ρ_{0b}, G_b and a_b are the values of the respective quantities behind the combustion wave. We prescribe the constant incoming gas mass flux g^0 and the constant incoming oxidizer concentration a^0.

We employ the simplest zeroth-order reaction scheme for the kinetics of both chemical reactions,

$$W_1 = \begin{cases} k_1(T) & \rho_1 > 0, \quad \rho_0 > 0 \\ 0 & \rho_1 \rho_0 = 0 \end{cases}$$

$$W_2 = \begin{cases} k_2(T) & \rho_1 > 0, \quad a > 0 \\ 0 & \rho_0 a = 0 \end{cases}$$

$$k_n(T) = k_{0n} \exp \left(-\frac{E_n}{RT} \right) \qquad (n = 1, 2).$$

Here, k_{0n} are the pre-exponential factors and E_n are the activation energies of the reactions. Both reactions accelerate with an increase in temperature. However, the degrees of acceleration can differ since the activation energies of the reactions are generally different. We emphasize the competition between the reactions: each consumes the reactant A, so that consumption of A in the reaction affects its availability for the other.

Using the method of infinitely narrow reaction zone [3, 4], we reduce the set of Eqs. (1)–(10) to the algebraic equations for the flame temperature, propagation velocity and the proportion of the reactant A consumed in each reaction. Analysis of these equations allows us to find, in particular, the composition of the product as depending on the controlling parameters of the problem such as the incoming gas mass flux and the concentration of the gaseous oxidizer.

Among other results obtained, there is the multiplicity of the stationary solutions in a certain range of parameter. It is not surprising since multiplicity of solutions has been found in simpler problems with competing reactions. [5, 6, 3]. However, unlike the case in simpler problems, the interaction between gasless and filtration combustion results, for certain values of parameters, in the absence of any stationary solutions. Another specific feature of such interaction is that, unlike pure coflow filtration combustion, the inverse structure of the combustion wave cannot occur in this problem.

References

[1] Aldushin A. P., Merzhanov A. G. In: *Propagation of Thermal Waves in Heterogeneous Media*, (Yu. Sh. Matros Ed.), Novosibirsk, Nauka, 1988, 9–52 (in Rusiian).

[2] Merzhanov A. G. In: *Combustion and Plasma Synthesis of High-Temperature Materials*, (Z. A. Munir, J. B. Holt Eds.), VCH, 1990, 1–53.

[3] Merzhanov A. G., Khaikin B. I. *Prog. Energy Comb. Sci.*, 1988, **14**, 1.

[4] Zel'dovich Ya. B., Barenblatt G. I., Librovich V. B., Makhviladze G. M., *The Mathematical Theory of Combustion and Explosions*, New York, Consultants Bureau, 1985.

[5] Aldushin A. P., Kasparyan S. G. *Khimicheskaya Fizika*, 1982, **10**, 1412 (in Rusiian).

[6] Khaikin B. I., Khudyaev S. I. *On the nonuniqueness of the uniformly propagating combustion waves with two parallel reactions*. Preprint of the Institute of Chemical Physics, Chernogolovka, 1978 (in Rusiian).

COMBUSTION OF ALUMINUM PARTICLES IN A FLOW OF SOLID PROPELLANT COMBUSTION PRODUCTS

V. A. Babuk, V. A. Vasilyev, O. Ya. Romanov

Baltic State Technical University, St. Petersburg, Russia

Introduction

Combustion of aluminized composite solid propellants (CSP) results in formation of a two phase flow containing Al/Al_2O_3 agglomerates. Modern CSP are characterized by a high (up to 60%) content of unburned metal in the flow of combustion products over the burning propellant surface. The flow evolves in a combustion chamber, and the parameters vary significantly. The metal combustion is the key process influencing the chamber performance. Combustion of Al droplets in gaseous media was studied quite successfully for a long time. However, the results do not provide the quantitative accuracy of predicted combustion parameters sufficient for practical application. In particular, this applies to the conditions in the combustion chamber. In this study, we developed a model of Al/Al_2O_3 agglomerate combustion in the flow of CSP combustion products. The model can be used to predict the characteristics of this process.

Model

The proposed diffusion model is based on the vapor-phase model of [1, 2], as illustrated in Fig. 1. The key points of the model are the following:

- the gas-phase flame zone is of finite thickness, and all reactions within the zone are at equilibrium;
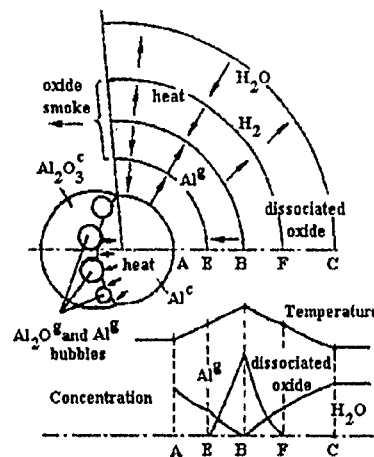
Figure 1: Schematic of the combustion model.

- the part of Al droplet surface covered by oxide does not take part in burning process;

- the chemical interaction between Al^c and $Al_2O_3^c$ resulting in gaseous products can take place in the agglomerate;

- the interaction between burning agglomerate and surrounding gas flow is analyzed in a boundary-layer approximation (zone AC in Fig. 1); within zone AC, heat transport is dominated by conduction and radiation, and mass transport occurs by diffusion.

The mathematical model of combustion includes 10 equations of heat and mass transfer in individual zones (AE, EB etc.).

In combination with the models of agglomerate structure [3] and chemical interaction between Al^c and $Al_2O_3^c$ in the agglomerate [3], this model makes it possible to calculate the following parameters of the process: the temperature field around agglomerate; the dimensions of individual zones; the Al burning rate; the rate of chemical interaction between Al^c and $Al_2O_3^c$.

Results and Discussion

The calculated temperatures of agglomerate and combustion zone are close to the experimental results of [4]. The predictions were compared with the results of the experimental study of the evolution of condensed-phase combustion products [3]. It has been found that the model predicts the total flux of vaporizing metal (J_m) within 10%. It should be noted here that the flux of metal reacting with oxide can amount to 30% of the flux of metal vaporizing from the free surface of Al agglomerate droplet.

Thus, the chemical interaction between Al^c and $Al_2O_3^c$ in the agglomerate has a quite substantial effect on the entire process.

For the practical purposes, a formal model was developed. It retains all the key relationships of the complete model and can be used to calculate the total flux of the vaporizing metal.
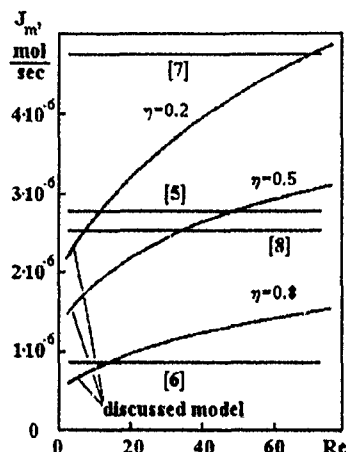
Figure 2: Dependence of J_m on Re and η.

Figure 2 compares the predictions of the model with the empirical laws currently employed in practice [5–8] at the following values of parameters: Al droplet diameter $D = 150\ \mu$m, gas-phase oxidizing potential $a_k = 0.2$, and pressure $P = 6$ MPa. Over the range of Reynolds numbers (Re) and oxide mass fractions in agglomerate (η) examined, the values of J_m calculated using the proposed model fall within the scatter in the predictions based on the relationships from [5–8]. This suggests that the scatter appeared because a number of factor (agglomerate structure, reaction of Al^c and $Al_2O_3^c$, etc.), which have a substantial effect on the combustion process, but were not taken in consideration.

Conclusion

The proposed model of aluminum agglomerate combustion in the flow of CSP combustion products is more universal and reliable as compared with the known approaches.

References

[1] Przustowski, T. A., Glassman, I. In: *Heterogeneous Combustion*, New York, Academic Press, 1964.

[2] Klyachko, L. A. *Fizika Goreniya Vzriva*, 1971, **7**, 2, 236 (in Russian).

[3] Babuk, V. A. *et al. ibid*, 1993, **29**, 3, 129 (in Russian).

[4] Pokhil, P. F. *et al.ibid*, 1970, **6**, 2, 143 (in Russian).

[5] Hermsen R. W. *AIAA Paper 81–0038*, 1981.

[6] Price, E. W. In: *Progress in Astronautics and Aeronautics*, N.Y., AIAA Inc. 1971, 479–513.

[7] Price, E. W., Park, C. J. *Proc. 18th JANNAF Combustion Meeting*, 1981.

[8] Pokhil, P. F., *et al. Combustion of Powdered Metals in Active Media.* Moscow, Nauka, 1972 (in Russian).

RANKING THE RELATIVE EFFECT OF FUEL PARAMETERS, SUBMODELS, AND AMBIENT CONDITIONS ON DEVOLATILIZATION TIME AND CHAR BURNOUT TIME FOR PULVERIZED BITUMINOUS COAL PARTICLES UNDER REALISTIC COMBUSTION CONDITIONS

Ole Biede

Laboratory of Heating and Air Conditioning, Technical University of Denmark, Building 402, DK-2800 Lyngby, Denmark

When designing experiments, deriving kinetic parameters and modelling pulverized-coal combustion, it is necessary to consider many different physical and chemical phenomena that might influence the results. To study the effect of these phenomena on devolatilization time and char burnout time, systematic variations have been made on coal type, char reactivity data, particle size, gas temperature, particle emissivity, wall temperature, oxygen partial pressure in the ambient gas, Nusselt number, blowing factor, thermal inertia, devolatilization model and rate, heat produced by carbon conversion the surface of particle, and heat consumed by devolatilization. The order of importance of the parameters, models, and ambient conditions is given in conclusion.

Theory

The energy conservation equation for a spherical particle is:

$$m_p c_{pp} \frac{dT_p}{dt} = A_p \frac{Nu\lambda}{d_p}(T_g - T_p)\left(\frac{B_\nu}{e^{B_\nu} - 1}\right)\left(\frac{B_c}{e^{B_c} - 1}\right) -$$

$$A_p \sigma \epsilon_p (T_p^4 - T_w^4) - \frac{dm_\nu}{dt}\Delta H_{d\nu} + \frac{dm_p}{dt}\Delta H_{eff}. \qquad (1)$$

The left-hand side Eq. (1) describes the thermal inertia of the particle while the right-hand side expresses (i) the convective heat transfer from the surrounding gas corrected for the high rates of mass transfer, during both devolatilization and char burnout, by the two blowing parameters B_ν and B_c, (ii) radiative heat transfer, (iii) heat loss during the endothermic devolatilization, and (iv) the heat released at the particle surface during char combustion.

The burning mode of the particles is described, as a function of burnout, by

$$\frac{\rho_c(t)}{\rho_{c,i}} = \left(\frac{m_c(t)}{m_{c,i}}\right)^\alpha, \tag{2}$$

$$\frac{d_c(t)}{d_{c,i}} = \left(\frac{m_c(t)}{m_{c,i}}\right)^\beta, \tag{3}$$

where $m_{c,i}$, $\rho_{c,i}$ and $d_{c,i}$ are the weight, the apparent density and the diameter of the initial char particle without ash. The apparent density of the particle, ρ_{ap}, is expressed, as a function of burnout, by

$$\frac{1}{\rho_{ap}} = \frac{X_a(t)}{\rho_a} + \frac{1 - X_a(t)}{\rho_c}, \tag{4}$$

where ρ_a is the ash density, and $X_a(t)$ is the fraction of ash at time t in a particle of char and ash only.

The char combustion is assumed to be zone 2 and zone 3 reactions, and oxygen is assumed to be the only oxidizer. In zone 2, the overall char burning rate per unit exterior surface area of the particle, q, is given by

$$q = k_s p_{O_2,s}^n = A_c \exp\left[-\frac{E_c}{RT_p}\right] p_{O_2,s}^n, \tag{5}$$

where $P_{O_2,s}$ is the oxygen partial pressure at the particle surface and A_c, E_c, and n are the coal type dependent pre-exponential factor, the apparent activation energy and the reaction order, respectively.

In zone 3, the overall char burning rate per unit exterior surface of the particle, q, and the oxygen mass transfer coefficient, k_d are given by

$$q = \frac{k_d}{\gamma} \ln\left(\frac{1 - \gamma p_{O_2,s}}{1 - \gamma p_{O_2,g}}\right), \tag{6}$$

$$k_d = \frac{M_c D_{ox} Sh}{d_p R T_m \nu_0}, \tag{7}$$

where $P_{O_2,g}$ is the oxygen partial pressure in the gas, D_{ox} is the diffusivity, M_c is the molar weight of carbon, Sh is the Sherwood number, ν_0 is the stoichiometric oxygen coefficient for the reaction at the particle surface, and γ is the change in volume during reaction per unit volume of oxygen.

The devolatilization is described by two different models: Distributed Activation Energy model (DAE–model) and the single first-order model. The release of individual species is described in the DAE–model by the number of independent first-order reactions:

$$\frac{dV_i}{dt} = (V_{0,i} - V_i) k_{\nu,0,i} \exp\left(\frac{-E_{\nu,i} \pm \sigma_i}{RT_p}\right), \tag{8}$$

where $V_{0,i}$ and V_i are the potential initial amount and the released amount, at time t, of the ith volatile species, and $k_{\nu,0,i}$, $E_{\nu,i}$ and σ_i are the frequency factor, activation energy and the standard deviation of activation energy for the i-th species. In the first-order reaction model, the volatiles are not divided into individual species but the entire devolatilization process is expressed by Eq. (8) without the standard deviation of activation energy.

Assumptions

- Gas temperature, oxygen partial pressure in the gas, and the ambient wa" t mperature are kept constant, e.g., homogeneous reactions in the gasphase are assumed to have no effect on the ambient conditions.

- There is no interaction between the particles.

- The initial particle temperature is 350 K, and the particles are assumed to be dry.

- Char combustion parameters from [1] are assumed to be applicable under all conditions considered.

- Parameters are varied within reasonable limits, e.g., within conditions representative of the pulverized-coal combustor conditions, and the parameters and models given and frequently used in the literature are employed.

- Devolatilization parameters are assumed to be independent of coal type.

- Char burnout time is defined as the burnout time for 99.5% of the char.

- Devolatilization time is the time by which 99% of the potential fraction of volatiles have been released.

Calculations

Standard case

A standard case was chosen: HVB bituminous Columbian Cerrejon coal, using the char reactivity data derived in 6% oxygen [1], at ambient gas temperatures of 1400, 1600, 1800 and 2000 K and the oxygen content of 3%, wall temperature of 500 K, timestep of 5 ms, particle sizes of 20, 50, 100, and 150 μm using a first-order devolatilization model with parameters from [2], emissivity described by the weighted mean of ash emissivity of 0.5 and coal type dependent char emissivity of 0.8–0.9, Nusselt number of 2, and the heat loss by endothermic devolatilization was 100 cal/g volatiles. Devolatilization and char burnout times for the standard case are shown in Table 1.

Table 1: Devolatilization and char burnout times [ms] as functions of the particle size and gas temperature for the standard case.

T_g	Devolatilization time [ms]				Char burnout time [ms]			
	d_p [μm]				d_p [μm]			
[K]	20	50	100	150	20	50	100	150
1400	5	15	35	70	365	1000	2370	4040
1600	5	10	25	50	95	245	565	1015
1800	5	10	20	40	35	95	320*	710*
2000	5	5	15	35	15	75*	295*	·660*

*Reaction rate limited by diffusion was defined as the effective reaction rate higher than 95% of the maximum diffusion rate.

In the sensitivity study, the ambient conditions, the fuel parameters and the submodels were varied within the limits described below.

Case variations (46 cases):
Ambient conditions:

- Gas temperature: 1400, 1600, 1800, and 2000 K.

- Oxygen partial pressure in gas: 0.01, 0.03, 0.06, and 0.12 atm.

- Wall temperature: 500, 1200, and 100 K below the gas temperature.

Fuel-dependent parameters:

- Particle size: 20, 50, 100, 150 μm.

- Devolatilization parameters: [2–5].

- Char reactivity parameters: parameters derived at 6 and 12% oxygen for Cerrejon [1].

- Coal types: Cerrejon, Columbia; Blair Atholl and Ulan, Australia; New Mexico Blue #1 (PSOC 1445), Pittsburgh #8 (PSOC 1451) and Illinois #6 (PSOC 1493), USA [1]. (The coal type dependent parameters are: the fractions of volatiles, ash and water; char reactivity parameters (A_c, E_C, and n); CO/CO_2 product ratio (influencing ν_0, γ, ΔH_{eff}, and B_c); burning mode constants (α and β); initial carbon density ($\rho_{c,i}$); char emissivity and swelling factor).

Submodels:

- Devolatilization model: single first order model, Distributed Activation Energy model.

- Particle emissivity: weighted mean of ash and char emissivities, or constant 0.6 and 0.9.

- Nusselt number: 2, 4.

- Heat produced at particle surface by heterogeneous reaction: $\Delta H(CO), \Delta H(CO_2)$.

- Heat loss by endothermic devolatilization: 0.100 cal/g volatiles.

- Blowing factors: included in calculations, neglected.

- Thermal inertia: weighted mean of heat capacities of ash, char and volatiles as function of burnout, multiplied by 0.5 and by 2.

Results

Devolatilization ranking		Burnout ranking	
1.	Devolatilization parameters (major)	1.	Particle size (major)
2.	Particle size (major)	2.	Gas temperature (major)
3.	Devolatilization model (major)	3.	Oxygen content in gas (major)
4.	Nusselt number (medium)	4.	Coal type (major)
5.	Gas temperature (medium)	5.	Char reactivity data (medium)
6.	Thermal inertia (medium)	6.	Ambient wall temperature (medium)
7.	Coal type (medium)	7.	Heat produced at surface (medium)
8.	Heat loss by devolatilization (medium)	8.	Nusselt number (medium)
9.	Blow factors (minor)	9.	Particle emissivity (medium)
10.	Ambient wall temperature (minor)	10.	Thermal inertia (medium)
11.	Particle emissivity (none)	11.	Heat loss by devolatilization (minor)
12.	Oxygen content in gas (none)	12.	Devolatilization parameters (minor)
13.	Char reactivity data (none)	13.	Blow factors (minor)
14.	Heat produced at surface (none)	14.	Devolatilization model (minor)

The results of this parametric study are presented as the ranking of the effect of each phenomenon on the devolatilization and burnout times, divided into four categories: major, medium, minor and none influence on the results. It must be kept in mind that the ranking is based only on the cases considered, e.g., within the limits of the parameter variations.

Among the *ambient conditions*, the gas temperature is important for devolatilization time and especially for char burnout time. The oxygen content in the gas is very important when studying char combustion, while it has no direct effect on devolatilization, and wall temperature has some effect on char combustion. As for the *fuel dependent parameters,* particle size is seen to be extremely important in both cases and also coal type is seen to be important, especially for burnout times. Char reactivity parameters have a significant influence on char burnout times, while devolatilization rate parameters have a significant influence on devolatilization time. As for the *submodels,* devolatilization models are important for devolatilization time, but have only a slight effect on char combustion. Neglecting heat loss by devolatilization and the blowing factors are seen to have some effect on devolatilization but almost no effect on char combustion. Models applied for emissivity and heat produced at the particle surface by heterogeneous reaction are seen to have some effect on char burnout times but no effect on devolatilization. Assumptions concerning Nusselt number and thermal inertia are seen to have some effect in both cases.

Acknowledgement

References

[1] Tørslev Jensen P., Mitchell R. E., *Energy Research Project No.1323/87–16*, Geological Survey of Denmark, 1993.

[2] Sørensen L. H., Biede O., Peck R. E., *Risø–R–669(EN)*, Denmark, 1993.

[3] Anthony D. B., Howard J. B., Hottel H. C., Meissner H. P., *Proc. 15th Symp. (Int.) on Comb.*, 1974, 1303.

[4] Kobayashi H., Howard J. B., Sarofim A. F., *Proc. 16th Symp. (Int.) on Comb.*, 1976, 411.

[5] Fletcher T. H., *Comb. Flame*, 1989, **78**, 223.

[6] Biede O., Sørensen L. H., Peck R. E., *Energy Research Project No.1323/88–23*, (mostly in Danish). Laboratory of Heating and Air Conditioning, Technical University of Denmark, 1992.

IGNITION AND COMBUSTION OF A SINGLE HYDROCARBON FUEL DROPLET IN MICROGRAVITY

V. N. Bloshenko

Institute of Structural Macrokinetics, Chernogolovka, 142143 Russia

The time-dependent theory of ignition and combustion of a hydrocarbon fuel droplet was proposed by Merzhanov and Peregudov with active participation of Khaikin in 1971–1974 [1–3]. It was a logical extension of the simplest nonpremixed combustion theory of Varshavsky (1945); Spalding, Godsave, Paleev, Gurevich, Klyachko, and Williams contributed much to its development later. The years that passed thereafter saw great progress in both computational and experimental hardware.

This paper highlights the most general physical ideas and further results of the time-dependent theory.

Quasi-steadiness of gas-phase processes is the main assumption made in the theory of diffusion-controlled combustion of a droplet. In other words, the processes of heat and mass transfer are assumed to instantaneously adjust to variations in the droplet surface state. The criterion for the quasi-steady approximation is

$$\left(\frac{r_f}{r_d}\right)^3 \ll \frac{\rho_d}{\rho},$$

where ρ_d and ρ are the droplet and gas densities, respectively; r_f and r_d are the combustion front and droplet radii, respectively. At ambient pressures, $(r_f/r_d) \ll 10$. At the same time, the value of (r_f/r_d) estimated for typical hydrocarbon fuels [3] appears to be within 9–27, i.e. the criterion for quasi-steady approximation does not hold true.

The basic result of the quasi-steady theory of diffusion-controlled combustion, the linear decrease in the squared droplet size with time, was verified in experiments on

combustion of a falling droplet ~ 1 mm in size. Although the main conclusions have been qualitatively confirmed, such an agreement is hardly to be expected and is likely to be caused by the effect of natural convection, which stabilizes the flame near the drop surface, where the temperature and concentration fields are quasi-steady. Thus, it can be concluded that the quasi-steady theory describes droplet combustion under the conditions of strong convection.

The time-dependent theory was developed for the case without natural convection. One of the most important conclusions this theory leads to is that the processes of ignition and combustion should not be considered independently. They can be divided into three interrelated stages (ignition, formation of a nonsteady diffusion front (a transitional regime), and nonstationary combustion), the duration of each stage being dependent on the deviation of its parameters from their critical values.

Ignition. As was mentioned above, the parameter characterizing the inertia of the gaseous environment is the ratio of the gas and droplet densities, $\pi = \rho/\rho_d$. Although at ambient atmospheric pressure its value is low, the inertia of the medium exerts a significant effect on the process. The point is that a sufficient amount of vapor formed by the droplet itself is necessary for the initiation of its combustion, because the chemical reaction rate cannot be high near the droplet because of its cooling effect. Saturation with vapor is the lowest among those providing ignition a maximum amount of vapor should fill the droplet environment. That is why under the critical conditions the droplet mass vanishes by the moment of its ignition. This major conclusion of the time-dependent theory of ignition agrees well with the experimental results obtained by Grigor'ev [4], Wood and Rosser [5], and Faeth *et al.* [6] and confirms the hypothesis put forward by Klyachko in 1960: the apparent decrease in the reaction order is the consequence of the nonsteadiness of heat and mass transfer in the gas phase. Thus, for a bimolecular reaction the dependence of the critical initial drop size η_{cr}, at which the drop ignition can occur at the given parameters of the environment, is $\eta_{cr} \sim 1/\sqrt{P}$, while the quasi-steady theory suggests $\eta_{cr} \sim 1/P$, where P is the pressure.

The Transitional Regime is a continuous process following ignition and resulting in the formation of a diffusion-controlled combustion front, the principles of which were formulated by Varshavsky in his theory. Near the critical conditions, the diffusion front forms at the expense of the burnout of the oxidant residue contained between the front and the droplet by the moment of ignition.

The Droplet Combustion. Diffusion combustion of a droplet is a nonsteady process, in which the ratio of the front radius to that of the droplet is increasing with time. This conclusion agrees well with the experimental data on combustion in zero gravity [7] and the theoretical studies of Kotaka and Okazaki [8]. The variability of the ratio of the front and drop radii is caused by two reasons. By the moment the droplet heats up, the front has travelled far enough for the nonsteady gas-phase processes to become a decisive factor. The linear dependence of the droplet size squared on time is also valid in the time-dependent theory to a sufficiently good accuracy, because the droplet surface temperature is close to the boiling point and the droplet evaporation

162

rate is mainly determined by the process of vapor diffusion.

In the above theory, convection was not taken into account and the droplet was supposed to be in a hot oxidizing medium which did not contain the droplet vapor at the initial moment. Thus, the theory was designed to describe droplet combustion in a 'pure' gaseous oxidant (the Grashof number is low and natural convection is immaterial for fine droplets). Droplet combustion is employed in various applications, for example, in internal combustion engines (ICE).

A study of droplet combustion in a gaseous oxidizing medium containing vaporized droplets should be a further step in the development of the theory under consideration. This case is closer to the processes in ICEs, particularly in fuel-injection engines. The process of ignition therein is a complex phenomenon. It is evident that, for some initial amount of the fuel vapor, the droplet size is nonzero under the critical conditions. Moreover, the concept of critical conditions seems to require reinterpretation in this case.

At present the conclusions of the theories developed previously and proposed herein are under experimental study. In particular, combustion of fine droplets can be simulated by burning large drops, aboard spacecraft on mission.

References

[1] Bloshenko V. N., Merzhanov A. G., Peregudov N. I., Khaikin B. I. In: *Combustion and Explosion*, Nauka, Moscow, 1972 (in Russian).

[2] Bloshenko V. N., Merzhanov A. G., Peregudov N. I., Khaikin B. I. *Fizika Goreniya Vzriva*, 1972, 2 (in Russian).

[3] Khaikin B. I. In: *Heat and Mass Transfer in Combustion Processes*, Chernogolovka, 1980 (in Russian).

[4] Grigor'ev Yu. M. In: *Combustion and Explosion*, Nauka, Moscow, 1972 (in Russian).

[5] Wood B., Rosser W. A., *AIAA J.*, 1968, **6**, 4, 70–76.

[6] Faeth G. M. *ei al. AIAA J.*, 1968, **6**, 4, 55–60.

[7] Isoda H. Kumagai S. *Proc. 7th Symp. (Int.) on Comb.*, The Combustion Institute, 1958, 523–531.

[8] Katane S., Okazaki T., *Int. J. Heat Mass Transfer*, 1969, 12.

TRANSITION DUALITY AND HYSTERESIS OF A
COMBUSTING DROPLET

H. H. Chiu, J. S. Hwang

Institute of Aeronautics and Astronautics, National Cheng Kung University, Republic of China, Taiwan

A central theme underlying all spray processes is the interface phenomena involving the mass, momentum and energy exchange driven by non-equilibrium which occurs between the dispersed droplet phase and the gaseous phase. The equilibration occurs in the presence or absence of hydrodynamic convective motion, time-dependent variations in flow variables, and finite rate chemical reactions in the droplet's environment. The latter consists of the mean flow of a gaseous mixture and a Stefan flow which originates at the droplet surface. In addition, the droplet interior motion induced by the relative motion enhances the interface exchange rate.

The gasification of a stationary droplet, with a fast chemical reaction rate, has been extensively studied by Godsave [1], Spalding [2] and others [3]. Analytical investigations of such a diffusion-controlled flame have been greatly facilitated by the mathematical procedure developed by Schvab and Zel'dovich [4,5] to aid in the determination of global flame configuration, field structure and burning rates. The combustion and vaporization of a convecting droplet in a general combustion environment has been studied extensively using empirical [6,7] and semi-empirical [8, 9] models, and by numerical simulations [10,11] for the prediction of the burning rate and flow behavior. However, there has been a lack of theoretical procedures which lend themselves to the determination of principal mechanisms to aid in the understanding and analytical determination of the laws of interface exchange. Moreover, little effort has been devoted to the determination of detailed configurations and their dependence on major environmental conditions such as temperature and Reynolds number of the relative motion.

The objectives of this paper are to present the recent results of theoretical developments of Canonical droplet theory [12] and the newly predicted phenomena of transition duality and hysteresis in steady and nonsteady environments. The first part of the paper covers the analytical development of the Canonical droplet theory.

The Canonical droplet theory provides a universal law by which the rates of the interface exchanges of scalar and vectorialproperties of an isolated droplet are analytically determined as the eigenvalues of the conservation laws represented by a set of nonlinear partial differential equations. Systematic studies entailing the principal mechanisms and parameters affecting the gasification and aerodynamic drag of a droplet in a general environment of steady and non-steady states are presented. The second part of the paper presents the phenomena of transition duality characterized by the existence
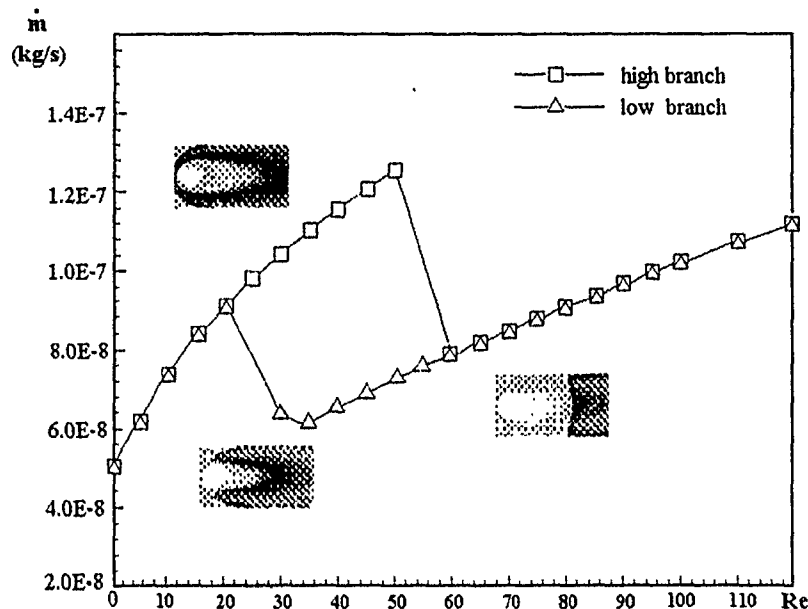
Figure 1: Droplet combustion rates versus Reynolds number and the respective upper and lower state flame configurations.

of two droplet states, the upper and lower branch state featured by an envelope flame and a wake flame, respectively. The transition duality is predicted to occur when the characteristic times of diffusion, chemical reaction and flow residence are approximately equal to each other. At the given environmental temperature of 1000 K and a droplet diameter of 100 μm, the transition duality is found to occur for $25 < Re < 50$, as shown in Fig. 1. The "upper state" is characterized by a higher burning rate than that of a "lower state". In addition, the wake of the upper state has a smaller axial extention than that of the lower state, as shown in Fig. 2. Additionally, structural, configurational and combustion properties of dual states and the hysteresis phenomena at a fixed Reynolds number are extensively examined by systematically varying the temperature of the environment. Furthermore, the effects of the droplet size on the nature and the excitation of the dual state are also scrutinized. The results of this analysis are used to construct a droplet configuration chart in which the excitations of the upper and lower states in the wide operational ranges of the Damkohler number and the Reynolds number are identified. A comprehensive system of universal droplet laws accounting for the upper and lower states is also proposed to aid in spray calculation.

The last section of the paper deals with the acoustic response of a combusting droplet to facilitate the identification of the potential mechanisms and factors affecting the onset of combusting droplet instability in a wide operating range, including the transition region. Analytical and numerical analysis reveals a striking dynamic response

Re=40, high branch   **Re=40, low branch**

Cold

Hot
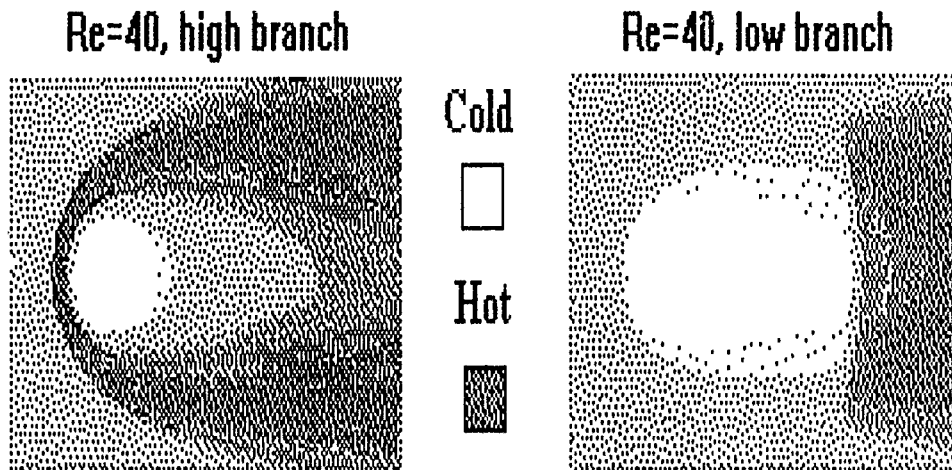
Figure 2: Flame configurations and wake structures of the upper and lower state at $Re = 40$.

characteristic of a combusting droplet under the excitation by an acoustic wave. When a combusting droplet in the lower state with, for example, $Re = 40$ is disturbed by an acoustic wave of 2000 Hz, which is characterized by a sinusoidal variation in Reynolds number, as shown in Fig. 3a, the timewise variation in the burning rate, Fig. 3a, behaves such that the Rayleigh integral, $\int wp\,dv$, remains to be a largely positive value throughout a cycle, Fig. 3b. This suggests that the combusting droplet in the lower combusting state is a potential source of combustion-driven oscillation [13]. An extensive study is also carried out to assess the acoustic response characteristics of a droplet in the various operating conditions represented by Reynolds number and Damkohler number under nonsteady excitations. These results are used to construct the instability criteria for a combusting droplet in a broad range of operating conditions.

The paper concludes with the identification of the broad area of unresolved issues and problems of isolated and interacting droplets. This is done to promote the progress in our understanding of droplet and spray combustion.

References

[1] Godsave G. A. *Proc. 4th Symp (Int.) on Comb.*, 1953, 818.

[2] Spalding D. B. *Proc. 4th Symp. (Int.) on Comb.*, 1953, 847.
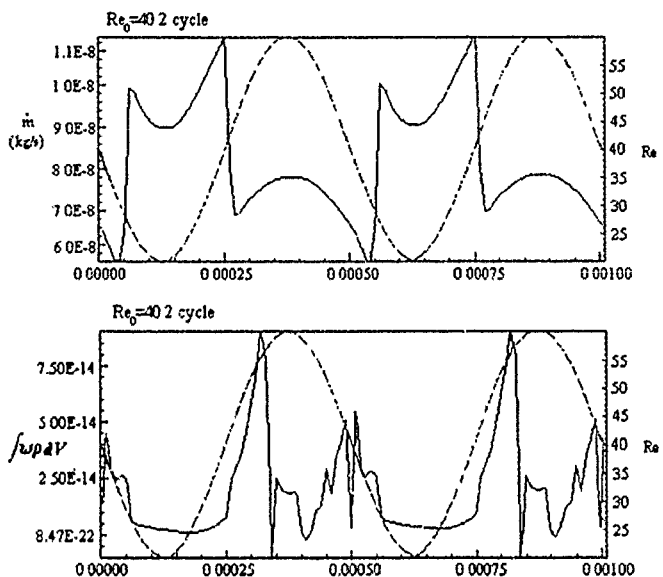
Figure 3: (a) (top) Time history of the burning rate in response to an acoustic velocity fluctuation. (b) (bottom) Time history of nondimensional Rayleigh integral in response to an acoustic velocity fluctuation.

[3] Williams F. A. *Combustion Theory*, Addison-Wesley, 1965.

[4] Shvab V. A. *Investigation of Combustion Processes of Natural Fuel*, Gosenergoizdat, Moscow–Leningrad, 1948 (in Russian).

[5] Zel'dovich Ya. B. *Zhurnal Tekhnicheskoi Fiziki*, 1949, **19**, 1199 (in Russian).

[6] Frossling N. *Gerlands Beitr. Geophys.* 1938, **52**, 170.

[7] Ranz W. E., Marshall W. R. *Chem. Eng. Prog.* 1952, **48**, 141.

[8] Sirignano W. A. *Prog. Energy Comb. Sci.* 1983, **9**, 291.

[9] Prakash S., Sirignano W. A. *Int. J. Heat Mass Transfer*, 1980, **23**, 253.

[10] Dwyer H. A., Sanders B. R. *Proc. 21st Symp. (Int.) on Comb.*, 1986, 663.

[11] Dwyer H. A., Sanders B. R. *Proc. 22nd Symp. (Intl.) on Comb.*, 1988, 1923.

[12] Chiu H. H. *Proc. Symp. on Transp. Phenomena and Applications*, Taipei, 1991.

[13] Lord Rayleigh. *The Theory of Sound.* N. Y., Dover, 1945.

ON THE INSTABILITY OF LAMINAR DIFFUSION FLAMES

I. F. Chuchalin

Mari Pedagogical Institute, Yoshkar-Ola, Russia

Diffusion flame is considerably influenced by the combustion products layer which is well seen in the interference photographs (Fig. 1). If the gas supply rate does not exceed a certain critical value, the flame is steady and the combustion products layer has the shape of rectilinear cylinder (Fig. 1a). With an increase in the gas supply rate, the combustion regime becomes oscillatory. The convexities and the concavities appear on the layer surface and propagate downstream with time (Fig. 1b).

The amplitude of the disturbances on the layer surface increases with the increase in gas supply rate. At the same time, the character of oscillations changes. When the oscillations become sufficiently strong, a bifurcation of the flame is observed, i.e. the fuel stream is burnt out. Until now, the nature of these oscillations and the flame shape have not been convincingly explained.

The flame oscillation mechanism is related to the changes in the thickness of the combustion products layer [1]. If the layer thickness increases, the oxygen supply to the reaction zone decreases. This is followed by an increase in the flame height. A decrease in the thickness leads to the opposite effect. This mechanism can also explain the bifurcation of the flame because the influx of the oxidizer is higher in the narrower cross sections of the combustion product layer, due to radial molecular diffusion, which should be the reason for the stream being burnt out. However, an attempt to theoretically explain the flame shape in terms of this mechanism did not lead to desirable results [2]. It has been shown by solving the diffusion equation that the flame boundary has a wavelike surface only. Furthermore, no burnout can be observed at any disturbance amplitude. Thus, molecular diffusion is not the only mechanism to be considered, and the most important factor has not been taken into account.

Some authors [3, 4] have noted that the oscillations in the oxygen supply are closely linked with hydrodynamic instability. Also, V. I. Blinov's data [3], obtained in line with the Zel'dovich theory [5], qualitatively explained certain trends.

In my opinion, however, the fact that the changes in the combustion product layer thickness along the flame height result in the pulsations of the flow velocity has not been taken into account in explaining the oscillations.

The velocity of the combustion product flow is greater in contractions, as compared to expansions. This must influence the radial molecular diffusion, which leads to additional suction of atmospheric oxygen into regions of higher flow velocity, where the pressure is lower.

A supporting evidence is provided by calculations of the flame shape as determined by velocity changes along its axis.
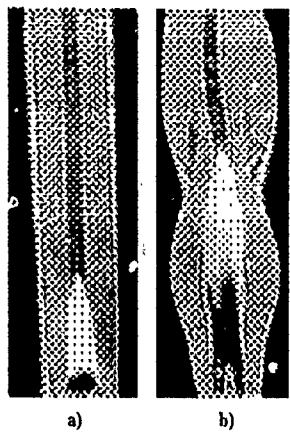
Figure 1.
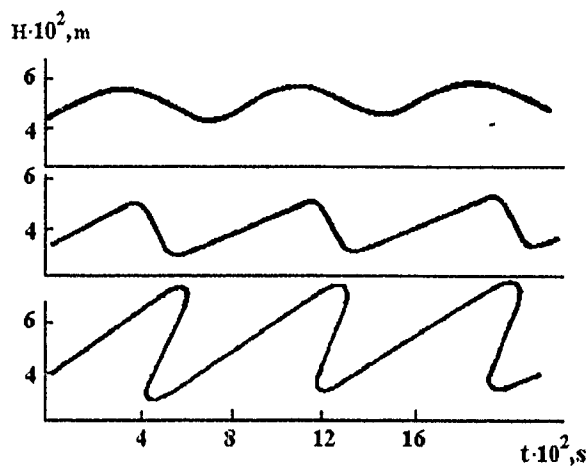
Figure 2.

Numerical calculations of the flame shape and height were performed using the diffusion equation

$$\frac{\partial c}{\partial t} = \mathfrak{D}\left(\frac{\partial^2 c}{\partial r^2} + \frac{1}{r}\frac{\partial c}{\partial r}\right).$$

It was assumed that the velocity changes along the flame axis by the harmonic law

$$u = u_0 + a\sin\frac{2\pi}{\lambda}(vt - z),$$

where u_0 is the nondisturbed flow velocity, a is the disturbance amplitude, λ is the disturbance wavelength, z is the coordinate, v is the velocity of the convexity and concavity displacement, and t is time.

The numerical results for both the shape and the height of the flame agree well with the experimental data.

Figure 2 shows the flame height histories for three disturbance amplitudes: 10^{-3} m/s, $3 \cdot 10^{-3}$ m/s, and $6 \cdot 10^{-3}$ m/s. The comparison between the predictions and the real scans of the oscillating flame shows a good agreement between the theoretical and experimental results.

Until now, the influence of flow velocity pulsations has not been taken into account. Qualitative coincidence of the numerical and experimental results suggests that this factor plays a major role in oxygen supply to diffusion flames. Perhaps, it should be taken into account for other configurations of burning fuel stream.

References

[1] Maklakov A. I. *Zhurnal Fizicheskoi Khimii*, 1956, **30**, 2 (in Russian).

[2] Chuchalin I. F. *Fizika Goreniya i Metody Issledovanii*, **2**, Cheboksary, Chuvash University Publ., 1972, 44–47 (in Russian).

[3] Blinov V. I. *Inzhenerno-Fizicheskii Zhurnal*, 1959, **2**, 8 (in Russian).

[4] Kimura Itsuro. *Proc. 10-th Symp. (Int.) Comb.*, The Combustion Institute, 1964.

[5] Zel'dovich Ya. B. *Zhurnal Eksperimentalnoi Teoreticheskoi Fiziki*, 1937, **7**, 12 (in Russian).

GROUP COMBUSTION OF CLOUDS OF CHAR/CARBON PARTICLES

Tov Elperin, Boris Krasovitov

The Pearlstone Center for Aeronautical Engineering Studies, Department of Mechanical Engineering, Ben-Gurion University of the Negev, P.O. Box 653, Beer-Sheva 84105, Israel

One of the major factors affecting combustion is the interaction between burning particles. The effect of group combustion is commonly estimated in terms of group combustion number $G = 3\sigma R_0^2/R_p^2$, where σ is the fuel volume fraction, R_0 is the cloud radius, R_p is the radius of a single char particle in the cloud [1]. The purpose of this study is to develop and validate an exact analytical model for the interaction between burning particles in the cloud.

1 Method of Irreducible Multipole Expansion for the Solution of Laplace Equation for N Spheres

The suggested theoretical quasi-steady model of group combustion of coal/char particles clouds is based on the expansion into irreducible multipoles proposed for the solution of boundary-value problems in low-Reynolds-number hydrodynamics in [2]. It was shown, that in the case of combustion of particle clusters in a hot stagnant atmosphere with large temperature gradients in the neighbourhood of burning particles,

the general set of nonlinear energy and mass conservation equations can be reduced to a Dirichlet boundary-value problem for the Laplace equation. The solution in the neighbourhood of the i-th droplet was obtained in the form

$$U = U_i^{(s)} x_i^{-1} + \sum_{n=0}^{\infty} B_{\nu_1 \ldots \nu_n}^i \left(1 - x_i^{-(2n+1)}\right) \overbrace{x_{\nu_1}^i \ldots x_{\nu_n}^i}, \tag{1}$$

where U is a conserved property of the continuous phase (concentration or temperature), $U_i^{(s)} x_i^{-1}$ is the field generated by the i-th droplet, $\overbrace{x_{\nu_1}^i \ldots x_{\nu_n}^i}$ is an n-th order irreducible tensor(see, e.g., [2]), and coefficients $B_{\nu_1 \ldots \nu_n}^i$ can be found from the set of linear equations:

$$B_{\nu_1 \ldots \nu_n}^i = B_{\nu_1 \ldots \nu_n}^{i(0)} - \sum_{\substack{j=1 \\ j \neq i}}^{N} \sum_{k=0}^{\infty} B_{\mu_1 \ldots \mu_L}^j \omega_{nk} \varepsilon_j^{k+1} \varepsilon_i^n \Omega_{\nu_1 \ldots \nu_n \mu_1 \ldots \mu_k}(\mathbf{L}_{ij}). \tag{2}$$

In the latter expression, $B_{\nu_1 \ldots \nu_n}^{i(0)} = \displaystyle\sum_{\substack{j=1 \\ j \neq i}}^{N} U_j^{(s)} \omega_{n0} \varepsilon_j \varepsilon_i^n \Omega_{\nu_1 \ldots \nu_n}(\mathbf{L}_{ij})$, $\varepsilon_i = \dfrac{R_i}{|\mathbf{L}_{ij}|}$, $\varepsilon_j = \dfrac{R_j}{|\mathbf{L}_{ij}|}$,

$$\Omega_{\nu_1 \ldots \nu_n \mu_1 \ldots \mu_L}(\mathbf{L}_{ij}) = \frac{(-1)^{k+n} \mathbf{L}_{ij}^{k+n+1}}{[2(n+k)-1]!!} \left[\nabla_{\nu_1}^{(i,j)} \ldots \nabla_{\nu_n}^{(i,j)} \nabla_{\mu_1}^{(i,j)} \ldots \nabla_{\mu_k}^{(i,j)} \left(\frac{1}{\mathbf{L}_{ij}}\right)\right],$$

$\omega_{kn} = \dfrac{(-1)^{k+n}[2(k+n)-1]!!}{k!(2n-1)!!}$, and $L_{\nu_k}^{(i,j)}$ are the Cartesian coordinates of L_{ij} and $\nabla_{\nu_k}^{(i,j)} = \dfrac{\partial}{\partial \mathbf{L}_{\nu_k}^{(i,j)}}$.

2 Combustion of Clouds of Char/Carbon Particles

Consider a system of N spherical char/carbon particles immersed in a K-component gaseous mixture containing oxidizer at temperature T_∞. It is assumed that the chemical reaction that occurs at the surface of the particles is of the first order and the chemical reaction rate is high. Since the characteristic rates of diffusion and heat relaxation are much less than the burning rate, a quasi-steady approximation for combustion model is used.

Under the above assumptions, in the case of power-law dependence of thermal conductivity and diffusivity on temperature and negligible effect of thermal radiation, the analytical expressions for the distributions of temperature T_g and dimensionless concentration C_ℓ and heat and mass fluxes are derived in the following closed analytical form:

$$C_\ell = C_{\ell,\infty} - (\nu_\ell D_{O,\infty}/\nu_O D_{\ell,\infty}) \frac{(1+\alpha-\beta_O)}{(1+\alpha-\beta_\ell)} \frac{(T_g/T_\infty)^{1+\alpha-\beta_\ell} - 1}{(T_s/T_\infty)^{1+\alpha-\beta_O} - 1}, \tag{3}$$
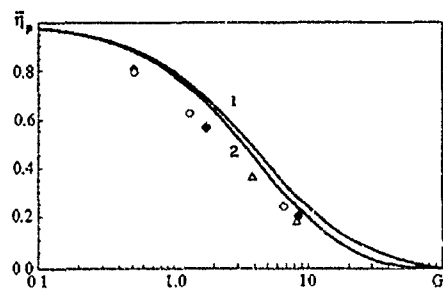
Figure 1: Average primary particle correction factor vs. G-number.
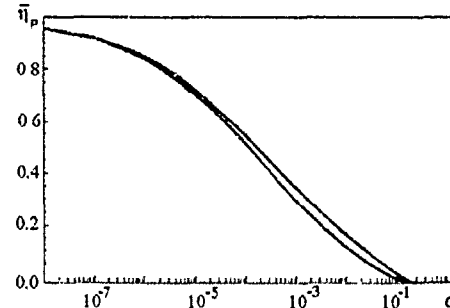
Figure 2: Average primary particle correction factor vs. volume fraction.

$$T_g = T_\infty \left\{ 1 + \left[\left(\frac{T_s}{T_\infty} \right)^{1+\alpha} - 1 \right] \left(\frac{1}{x_i} + \sum_{n=0}^{\infty} W^i_{\nu_1 \dots \nu_n} (1 - x_i^{-2n-1}) \overbrace{x^i_{\nu_1} \dots x^i_{\nu_n}} \right) \right\}^{\frac{1}{\alpha+1}}, \quad (4)$$

$$T_s = T_\infty \left[1 + (1 + \alpha - \beta_O) \frac{n_\infty D_\infty}{k_{g,\infty}} q m_O C_{O,\infty} \right]^{\frac{1}{\alpha+1-\beta_O}}, \quad (5)$$

$$Q_T^{(i)} = 4\pi R_i \int_{T_\infty}^{T_s} k_g \, dT \left[1 - \sum_{n=0}^{\infty} \frac{(-1)^n}{(2n-1)!!} (2n+1) W^i_{\nu_1 \dots \nu_n} \nabla^i_{\nu_1} \dots \nabla^i_{\nu_n} \left(\frac{1}{x_i} \right) \Big|_{x_i=1} \right], \quad (6)$$

$$Q_\ell^{(i)} = -C_{O,\infty} Q_T^{(i)} \left(\int_{T_\infty}^{T_s} \frac{k_g}{n D_O} \, dT \right)^{-1}, \quad (7)$$

where ℓ is the species number ("O" denotes oxidizer) and $C_\ell = n_\ell / n$, n and n_ℓ being the number densities of molecules of the gas mixture and molecules of the ℓ-th specie, D_ℓ is the binary diffusion coefficient, k_g is thermal conductivity of gas, T_g is the gas temperature, T_s is the temperature of the i-th particle, q is the heat of combustion, m_O is the mass of the oxidizer molecule, ν_O and ν_1 are stoichiometric coefficients, $Q_T^{(i)}$ and $Q_\ell^{(i)}$ are the heat and mass fluxes at the surface of the i-th particle, respectively, $W^i_{\nu_1 \dots \nu_n} = B^i_{\nu_1 \dots \nu_n} \Big|_{U_i^{(s)}}$, subscript "$\infty$" denotes the value at infinity.

The developed model was applied to the analysis of group combustion of spherical and cylindrical random clouds of particles. The results of calculation of the correction factor η_p, defined as the ratio of the single particle burning rate to the burning rate of a particle located at the center of a cluster of burning particles, versus G-number presented in Fig. 1 (curve 1 was plotted for a cylindrical cloud and curve 2 was plotted for a spherical cloud, both containing 100 particles) were compared with experimental data [3–5] obtained for the cylindrical cloud. As is seen from these plots, the suggested model of particle combustion agrees well with these experimental data.

172

The results of calculation of the correction factor η_p versus particle volume fraction for the spherical and cylindrical clouds containing $N = 100$ particles are shown in Fig. 2. Curve 1 was plotted for a cylindrical cloud and curve 2 was plotted for a spherical cloud. These calculations were performed for informly distributed coordinates and log-normally distributed radii of the particles.

The results of the analysis of burning of char/carbon particles clouds with cosine and exponential distribution of particle coordinates were also obtained. It was demonstrated that the rate of particle cloud combustion is determined by the rate of combustion of a primary (central) particle.

References

[1] Annamalai, K., Ryan, W. *Prog. Energy Comb. Sci.*, 1992, **18**, 221–295.

[2] Mazur P., Van Saarlos W. *Physica*, 1982, **115A**, 21–57.

[3] Auling, A. B., Smith, I. W. *Comb. Flame*, 1942, **18**, 173–184.

[4] Hamor, R. J., Smith, I. W., Taylor, R. J. *Comb. Flame*, 1973, **21**, 153-162.

[5] Kimber, G. M., Gray, M. D. *Proc. 3rd Conf. on Industrial Carbon and Graphite*, 1971, London, Imperial College Publ., 278–281.

COMBUSTION OF ALUMINIUM UPON LASER IRRADIATION

V. A. Ermakov, J. P. Zamyatina, A. A. Razdobreev

Research Institute of Applied Mathematics and Mechanics, Tomsk, Russia

The sintering of metal powder particles is an integral part of the process of combustion of metallized condensed systems (in rocket engines and MHD generators). The sinter formed consists primarily of the active metal and its oxide. The combustion of the sinter proceeds during its motion in a high-temperature gas flow. The study of the combustion dynamics under these conditions often presents substantial difficulties. Therefore, it is of interest to investigate experimentally some sinter specimens under model conditions. The use of laser heating offers some advantages in this case.

$V_{Al}, 10^{-12} m^3$
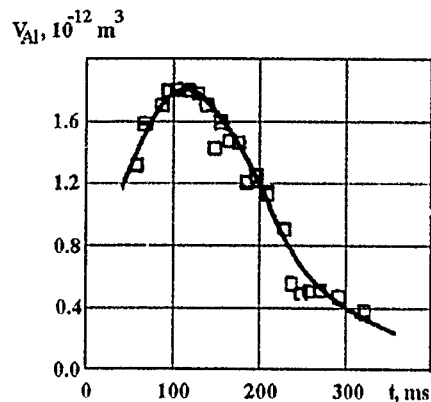
Figure 1: Aluminum volume evolution during agglomerate burning.
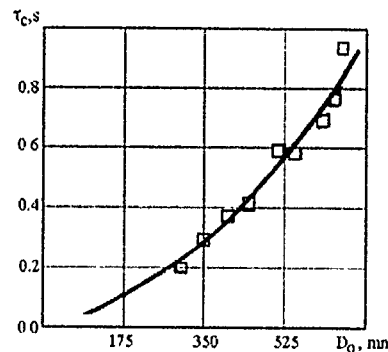
Figure 2: Variation of combustion time with size of agglomerate.

For the combustion and sintering studies, an experimental technique [1] based on the heating of a specimen by the radiation of a continuous IR laser and simultaneously recording the processes occurring in the specimen by a high-speed camera was developed. This technique was employed in our experiment on sinter combustion. The sinter specimens were ellipsoids consisting of two parts: an oxide hemisphere and a metallic hemisphere. The metal content varied from 16 to 40%. The experiments were carried out at atmospheric pressure and at 10 atm. The measured parameters of the sinters were the ignition delay time and the combustion time, the aluminum oxide and aluminum volumes varying in the process of combustion, as well as the limiting wetting angles. The aluminum and aluminum oxide volumes were found by solving the problem of the equilibrium for a composite drop.

Based on the experimental data obtained, the mechanism of sinter ignition and combustion has been proposed. The principal feature of sinter ignition and early combustion stage is the increasing amount of aluminum on the sinter surface. The ignition occurs, as a rule, over the surface of exposed metal. When the metal content is high (30 to 40%), the metal is liberated at the surface in the form of drop. After ignition, a hemispherical drop of aluminum forms at the top surface of the sinter, which is surrounded by a flame consisting of three zones (at atmospheric pressure) or a narrow bright luminous combustion zone which completely screens the sinter (at the pressure of 10 atm.). Subsequently, the combustion proceeds with a decrease in aluminum volume (Fig. 1: the radiation intensity is 1000 Wcm^{-2}, the sinter initial average size is 500 mm, at the atmospheric pressure).

The ignition delay and combustion times were measured for the sinters under investigation as functions of the sinter size. Figure 2 shows the size dependence of the combustion time for sinters containing 40% of metal, measured at the pressure of 10

174

atm. The data fit well the expression

$$\tau_c = \alpha D_0^{1.8}.$$

We estimated the effect of various factors, such as the varying surface area of the burning aluminum and the convective and radiative losses, on the character of the variation in aluminum volume in the process of sinter combustion. The effect of the quartz substrate on the accuracy of aluminum oxide volume measurements was investigated. It has been found that this effect is considerable only at low radiation intensities (and at the termination of the process of aluminum combustion under the conditions of our experiments), so it can be neglected here.

References

[1] Razdobreev A. A., Bukatyi V. J. *Izvestiya Vuzov SSSR, Ser. Fizika*, 1973, 4, 155 (in Russian).

STEAM GASIFICATION OF COKES OF NATURAL COALS

E. S. Golovina, V. G. Arabadzhiev, V. M. Kochan

Krzhizhanovsky Power Engineering Institute, Moscow, Russia

1. The present work reports the results of experimental studies of kinetics of cokes gasification for coals from the Irsha–Borodinsk and Kuznetsk deposits using the method of a thin fine-grained bed. Our expertise shows that a bed of moderate height, ~ 10 mm, provides conditions close to isothermic. Hydrodynamic mechanisms of gas flow through the bed are investigated. The papers by Ya. B. Zel'dovich [1], D. A. Frank-Kamenetskii [2], V. I. Blinow [3], L. N. Khitrin [4] etc., focused on the reactions in porous and powdered materials. The thin-bed method of studying ground coke is adequate for the process pattern presented by these authors.

2. The reactor was a quartz cylinder 38 mm in diameter, separated by a quartz grate with a 12-mm hight fill on it. It was placed into a graphite pipe heated by

a r.f. current. A flow of $H_2O + N_2$ mixture of prescribed concentrations, heated to 500 K, was fed from the top through the fill. At the bed outlet, residual moisture condensed, its amount was measured and the dry products were analyzed by means of a chromatograph. Also, the bed was weighed before and after the experiment. The temperature of the porous bed was measured by a thermocouple 0.3 mm in diameter in a quartz coating. Measurements of temperature distribution along the bed height and radius have shown that the temperature drop along 12 mm bed and 30 mm plateau amounts to $\sim$ 20–30 K. Experiments were conducted at 880–1500 K at the average steam volume fractions of 10%, 14.5%, 20%, and 27%; the flow velocity under these conditions was 0.3 m/s. Fuel grain sizes varied within 530–600 μm and 600–800 μm. The inner surface of the coke was measured by the BET method before and after the experiment. The inner surface substantially increased after pyrolysis from 12 m^2/g up to 123 m^2/g, and after reaction approximately 3 times more. It has been shown that the inner surface plays an active role in the reaction; the value of specific inner surface for particles of different diameters $\sim$ 550 and 800 μm, reacted under the same conditions, appeared to be close, thus pointing to the kinetics-controlled regime of reaction.

Figure 1 presents the yield of dry products for the Irsha–Borodinsk coal at various temperatures and steam concentrations. For the Kuznetsk coal, the results are similar. The decrease in hydrogen concentration with increasing bed temperature and excess of CO_2 over CO yield at $T < 1100$ K is of special interest, pointing to a noticeable role of the conversion reaction $CO + H_2O = CO_2 + H_2$ (I) and formation of CO_2 by the reaction $C + 2H_2O = CO_2 + 2H_2$ (II) at these temperatures. Calculations have shown that towards 1300 K the conversion reaction reaches an equilibrium and its role in the process tends to zero. The role of reaction (II) is proved by solving inverse kinetic problem.

Based on Fig. 1, gas analysis data and the measured change of bed weight due to the reaction, we obtained the values of specific reaction rate K_s ($g \cdot cm^{-2}s^{-1}$) for various temperatures and concentrations (the parameters are given above). The Arrhenius dependence on temperature and the first order of the reaction have been established only for concentrations of H_2O not exceeding 15–20% by weight.

It has been theoretically shown [1–4] that rate of chemical reaction in a porous bed is proportional to the square root of the rate constant K. The macroscopic rate of chemical reaction under these conditions, in the presence of oxidizer flow towards the bed surface, is known [2–4].

$$K_s = \frac{\beta C_0}{\frac{1}{\sqrt{D_i S_i K}} + \frac{1}{Nu_{dif} D/d}} \ \text{cm/s}, \tag{1}$$
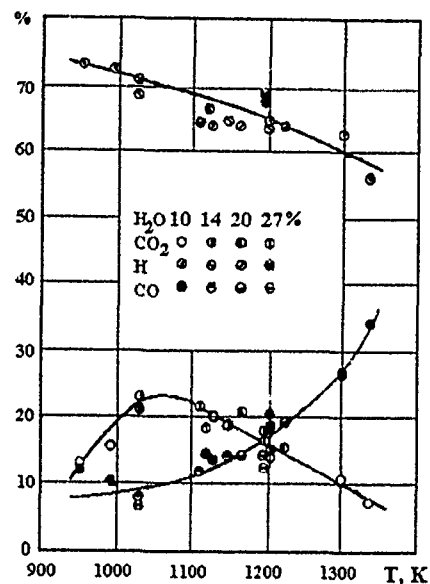
Figure 1: Dry products yield in gasification of the Irsha–Borodinsk coals.
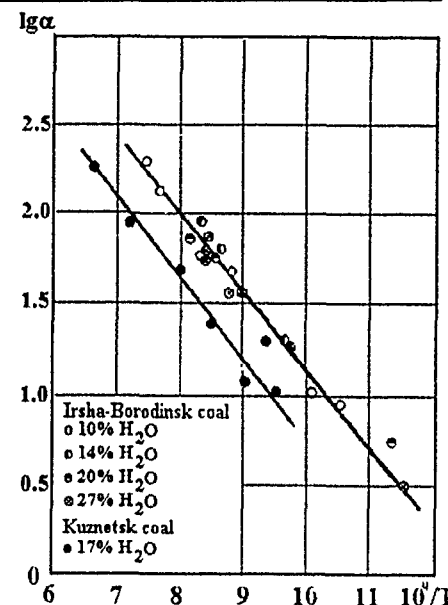
Figure 2: Dependence of reaction gas-exchange coefficient on temperature: (a) coke of the Irsha–Borodinsk coal; (b) coke of the Kuznetsk coal.

or, introducing the gas-exchange coefficient α [4],

$$K_s = \frac{\beta C_0}{\frac{1}{\alpha} + \frac{1}{\alpha_{dif}}}, \tag{2}$$

where α in general form is given by

$$\alpha = K + \lambda D_i \left(\coth \lambda R - \frac{1}{\lambda R} \right), \qquad \lambda = \sqrt{\frac{S_i K}{D_i}}. \tag{3}$$

Estimation of the denominators in Eqs. (1) and (2) has shown that, for the chosen conditions of gasification,

$$\frac{1}{\alpha} = \frac{1}{\sqrt{D_i S_i K}} \gg \frac{1}{Nu_{dif} D/d},$$

and, therefore,

$$\frac{K_s}{\beta C_0} = \alpha = \sqrt{S_i K D_i} \qquad \text{or} \qquad \log \left(\frac{K_s}{\beta C_0} \right) = \log(\alpha) = \log \left(\sqrt{S_i K_0 D_i} \right) + \log \left(e^{-\frac{E}{2RT}} \right).$$

Figure 2 presents the experimental data in the $(\log \alpha, (1/T) \cdot 10^4)$ plane. All the experimental points are close to the straight line $\log \alpha \sim T^{-1}$, in which case diffusional

177

resistance is not observed. The upper straight line "a" of Fig. 2 corresponds to the Irsha–Borodinsk deposit coal, and the lower one "b" to the Kuznetsk deposit coal. Using these experimental data, we obtained the value of the activation energy for the chemical reaction rate constant, $E = 42400$ cal/mol, for the Kuznetsk coal and $E = 39540$ cal/mol for the Irsha–Borodinsk coal. The upper cut off on the ordinate axis conforms to $\sqrt{D_i S_i K_0}$; its value is $2.34 \cdot 10^5$ cm/s for the Kuznetsk coal. Calculation of the preexponential K_0 is complicated by the difficulties in determining the reaction surface S. The surface measured by BET is not the reaction surface. The reaction surface has been determined experimentally [5, 6], which makes it possible to determine K_0 and find the constants K depending only on the temperature and not on other parameters, in particular, on the coke conversion depth. The latter fact explains the considerable discrepancies in the values of K obtained by different authors.

For the Irsha–Borodinsk coal, we present the calculated value of $\alpha = 2.93 \cdot 10^3 \exp(-39540/2RT)$ m/s.

For the Kuznetsk coal, according to the data of Fig. 2b,

$$\alpha = 2.34 \cdot 10^3 \cdot \exp(-42400/2RT) \text{ m/s}.$$

The activation energy for ι is obviously $E' = E/2 = 19770$ cal/mol for the Irsha–Borodinsk coal and $E' = E/2 = 21200$ cal/mol for the Kuznetsk coal .

The yield of useful products in experiment, $(CO + H_2)/CO_2$, is 2–2.5 m^3/kg.

References

[1] Zel'dovich Ya. B. *Zhurnal Fizicheskoi Khimii*, 1939, **13**, 2, 163 (in Russian).

[2] Frank-Kamenetsky D. A. *Diffusion and Heat Transfer in Chemical Kinetics.* Moscow, Nauka, 1967 (in Russian).

[3] Blinov V. I., Smirnov P. G. *Works of the Voronezh State Univ, Physics/Mathem.*, 1939, XI, 1 (in Russian).

[4] Predvoditelev A. S., Khitrin L. N., *et al. Combustion of Carbon.* Moscow, Nauka, 1954 (in Russian).

[5] Lizzo A., Yiang Hong, Radovic, *Carbon*, 1990, **28**, 1.

[6] Zibin Zu, Changfang Zang, *J. of Chem. Ind. and Ener.*, 1992, **43**, 4.

NONSTEADY HETEROGENEOUS FLAME PROPAGATION: A DEVELOPMENT OF TODES AND ZEL'DOVICH SCALING IDEAS IN 1969-1994

A. Goltsiker, S. Chivilikhin, A. Belikov

St. Petersburg Institute of Fine Mechanics and Optics St. Petersburg, Russia

The principal feature of the classical combustion theory developed in the glorious 30s was an early and intuitive usage of spatial (in Ya. Zel'dovich's famous "narrow heat release zone" approximation in the theory of laminar flame propagation and dynamic temporal (in O. Todes general time-dependent theory of thermal explosion) scaling and self-similarity ideas. The more complex and realistic subsequent models of combustion phenomena dealt with more sophisticated spectrum of scales and therefore met with difficulties in using the scaling techniques. This is correct with regard to heterogeneous systems, especially such as gas–particle mixtures.

Without depreciating the role of some pioneering contributions made in 20s through 50s, it should be stressed that it was L. Klyachko who put forward in the 60s a program of reformulation of the classical model combustion problems of ignition and flame propagation for such heterogeneous systems, with their specific scales of heat release and transfer phenomena. Many analytical and numerical but few experimental (especially "experimentum crucis" style) works were conducted to fulfil this program: they tried to find an adequate energy transfer mechanism (and the corresponding scale) to explain why flame propagation velocities for heterogeneous systems remain of the same order of magnitude as in gas despite the appreciably lower rate of energy release. The disadvantage of standard gas-conduction models, as well as the apparent turbulence suppression in a particle-laden gas, spurred the development of the Nusselt–Cassel–Essenhigh idea of preignition heating due to radiative energy transfer.

We tried to highlight the importance and influence of spatial and temporal scales, based on physical factors; a similar approach was later used by Ogle *et al.* The most interesting result of such an approximation (with fixed, independent kinetics) was the comparative analysis of competing energy transfer scales, conductive and radiative, leading to problems of boundary-layer type. Furthermore, Bhadury, Rumanov and Khaikin, Stepanov, Vainshtein, Gouling, Krazinski and many others tried to investigate radiative or radiative-conductive models of propagating dust–air flames with various types of diffusion kinetics, most of these works, including those by the Odessa University group (Zolotko, Shevchuk, Goroshin *et al.*) and ours, used numerical approaches. They realized the proposed radiation mechanism for numerous metals. It is interesting that Joulin *et al.* named the governing dimensionless parameter, relating competing scales in the problem, the "Zel'dovich number". These principal modelling investigations are mainly of qualitative use because of the extreme degree of uncertainty in the great many of physicochemical parameters, their distributing as well as even in

their mean values. That is why the most interesting experiments have been realized not for direct verification of numerical results (those provided only qualitative estimates, trends in the correlations between variables, etc.), but to assess the accuracy of the basic assumptions e.g., that of the leading role of transferred and absorbed radiation. Such sophisticated spectral experiments were conducted at the US Bureau of Mines to measure the intensity of light emitted and absorbed by coal particles radiation in ultraviolet, visible and especially infrared spectral regions.

The second specific scale feature of dust–air flames is their rather large (as compared to other scales, e.g., particle diameter, interparticle distances, and even the conductive length in gas, $\sqrt{\alpha \tau_p}$, etc.) radiative zone depth, which includes the reaction zone $\nu \tau_p$, followed by the zone of hot and radiating reaction products. This broad radiating zone leads to some nonsteady effects, which were negligible for the classic Zel'dovich-type flames with narrow reaction zone. This nonsteadiness was first mentioned by Cassel and later experimentally studied by Ionnshas in our laboratory in the 70s. At the same time, we proposed a radiation-induced mechanism of the nonsteady flame propagation in air–dust systems consisting of the previously formed preignited finite zone with distinct forward and backward front surfaces. An adequate technique for such a confined evolving energy source must employ integral differential equations, which yields "jumping" propagation with smoothing derivatives. Some criteria for the asymptotic (stationary) propagation have also been formulated, as well as the parametric correlations for the limits of such regimes. This radiative mechanism of nonsteady flame propagation was also applied to the spherical case.

Later on, the nonsteady dust–air flame propagation was experimentally investigated by Shevchuk, Ozerov and others for various particulate substances. At the end of the 80s some authors attempted numerical solutions for the more complex case, including both conductive and radiative energy transfer scales and using the kinetic model of chemical reaction. Ivanischeva and Stepanov failed to observe the transition to steady radiation-driven propagation because of specific (rather weak and narrow) ignition source. Furthermore, Rumanov, Shkadinsky and others introduced a thick source and computed the acceleration regime as well as determined the negligible role of conductive energy transfer. Recently, Yuen *et al.* made a similar effort and claimed that the nonsteadiness is an intrinsic feature of such flames.

It should be noted that the aforementioned "jumps" with nonmonotonic evolution of velocity in the direction of propagation were computed, with different explanations, by all these authors.

Thus, we can conclude that flame propagation in a dusty gas is a more complex problem than homogeneous flame propagation, because of the complexity of the spatial scales of energy transfer spectra and especially the great influence of the instantly (spontaneously) formed burning source. However, in general they are governed by the scaling laws discovered about 60 years ago by Ya. Zel'dovich and O. Todes.

References

[1] Klyachko L. *Proc. 2nd All-Union Symp. on Comb. and Explosion* Moscow, 1969 (in Russian).

[2] Todes O., Ionushas K., *et al. Fizika Goreniya Vzriva*, 1973, **9**, 2 (in Russian).

[3] Todes O., Goltsiker A., Ionushas K. *Fizika Goreniya Vzriva*, 1974, **10**, 1, 83 (in Russian).

[4] Todes O., Goltsiker A., Chivilikhin S. *Dokl. Akad. Nauk SSSR*, 1973, **213**, 2, 321 (in Russian).

[5] Goltsiker A., Todes O., Chivilikhin S. In: *Gorenie i Vzryv*, Moscow, Nauka, 1977, 300 (in Russian).

[6] Todes O., Goltsiker A., Chivilikhin S. In: *Gorenie gasov*, Chernogolovka, Akad. Nauk SSSR Publ., 1980, 106 (in Russian).

[7] Yuen W., Zhu S. *Proc. 8th Int. Conf. Heat Transf.*, San-Francisco, 1986, 833.

[8] Ogle R., Beddow J., Vetter A. *Comb. Flame*, 1984, **58**, 77.

[9] Krazinsky K. *Prog. Energ. Comb. Sci*, 1979, **5**, 31.

[10] Deshaies B., Joulin G. *SIAM Journ. of Appl Math.*, 1986, **46**, 561.

[11] Klyachko L., Goroshin S. *Inzhenerno-Fizicheskii Zhurnal*, 1988, **54**, 2, 330 (in Russian).

THE MODEL OF A POROUS COAL CHAR PARTICLE COMBUSTION

V. M. Gremyachkin, A. N. Buyanov

Institute for Problems in Mechanics, pr. Vernadskogo, 101, Moscow, 117526 Russia

The kinetic data of coal char particles combustion [1–4] obtained in different experimental investigations are very different due to the difference in both experimental

procedures and data analyses employed. The methods employed in the analysis of experimental data are usually based on the simplest models disregarding the mechanism of coal char particle combustion and such factors as radiative heat losses.

A model of combustion of coal char particles must include the equations of heat and mass transfer in the gas phase and into the porous char and the kinetics of both homogeneous chemical reactions in the gas phase and heterogeneous reactions in the porous coal char. The equations of heat and mass transfer can be written in the form of the balance of atoms involved in process (carbon and oxygen) and heat conservation, thus eliminating the rates of homogeneous chemical reactions.

$$\text{div} \sum \frac{m_j I_j}{\mu_j} = \frac{\Phi_c}{\mu_c}, \tag{1}$$

$$\text{div} \sum \frac{n_j I_j}{\mu_j} = 0, \tag{2}$$

$$\text{div} \sum (I_j h_j + I_h) = \Phi_c h_c - I_R \delta(r - r_0). \tag{3}$$

Here, m_j and n_j are the numbers of carbon and oxygen atoms in $C_{m_j} O_{n_j} H_{l_j}$ molecules of molecular mass μ_j, Φ_c is the rate of carbon consumption in heterogeneous reactions, h_j and h_c are the enthalpies of gaseous substances and solid carbon, I_r is the radiative heat flux from coal char surface, $I_j = m z_j - \rho D \text{grad} z_j$ and $I_h = m c T - \lambda \text{grad} T$ are the diffusive flux of substances and the heat flux, respectively.

We also consider the equations

$$\sum z_j + z_{in} = 1, \tag{4}$$

$$\text{div} \, m = \Phi_c, \tag{5}$$

$$m = -\rho K \text{grad} P. \tag{6}$$

The latter equation is the Darcy law, which relates the mass flux of the gas to the pressure gradient in the porous coal char.

Equations (1) to (6) govern flow dynamics and heat and mass transfer. It is also necessary to consider the chemical processes. The rates heterogeneous chemical reactions in the coal char can be written as

$$\Phi_c = \rho S[\gamma_1(z_1 - z_{e1}) + \gamma_2(z_2 - z_{e2})], \tag{7}$$

where γ_1 and γ_2 are the rate constants of chemical reactions of coal char with carbon dioxide and oxygen; z_i and z_{e_i} are the concentrations and the equilibrium concentrations of gaseous reactants; S is the internal surface of coal char.

The rates of homogeneous reactions are generally higher than the rates of heterogeneous reactions. The homogeneous reactions can be assumed to proceed in the

diffusion-controlled regime [5] if the size of coal char particles is greater than a few microns. In this case, the gas phase is in chemical equilibrium. The equations of chemical equilibrium in the gas phase are [6]

$$P_j = \frac{P_C^{m_j} P_O^{n_j} P_H^{l_j}}{K_j},$$ (8)

where P_j, P_C and P_O and P_H are the partial pressures of gaseous species, carbon vapor, oxygen and hydrogen atoms, respectively, K_j is the equilibrium constants.

The boundary conditions in environment are $r = \delta$, $T = T_0$, $z_j = z_j^0$, $P = P_e$, and, at the center of coal char particle, $I_j = I_h = m = 0$.

The solution of this task allows to determine, as functions of composition, ambient temperature and pressure, intensity of heat losses by radiation, and the gas-flow parameter δ, the following characteristics:

(1) the rates of coal char combustion and gasification;

(2) the distributions of temperature and concentrations in the gas phase and the porous coal char;

(3) the distribution of pressure in porous coal char;

(4) the temperature of coal char surface;

(5) the composition of the resulting gaseous products.

The example of temperature, pressure and gaseous species distributions in the gas phase and a porous coal char particle of size $2 \cdot 10^{-4}$ m is shown in Fig. 1. In this case, the particle burns out in the absence of both radiative heat losses and the effect of gas flow.

The kinetic parameters of heterogeneous chemical reactions of carbon interaction with carbon dioxide and oxygen were taken in the form $\gamma_1 = 760 \exp(-30214/T)$ [7], $\gamma_2 = 1.11 \cdot 10^2 \exp(-17614/T)$ [4], and $S = 3.78 \cdot 10^7$. It should be noted that the kinetics of chemical reactions of carbon with carbon dioxide may be considered as determined, but the kinetics of chemical reaction of carbon with oxygen strongly differs in different experiments. An analysis of experimental data based on this theoretical model can help to elucidate this kinetics.

Figure 1 shows that the oxygen is consumed almost completely in the gas-phase homogeneous chemical reaction $CO + O_2$. In the porous coal char, the reactions $C + CO_2$ and $C + O_2$ take place. However, the intensity of the chemical reaction of carbon with oxygen is low in comparison with the intensity of its reaction with carbon dioxide. As a result, the pressure in the porous structure of coal char increases up to 18 atmosphere. The kinetics of heterogeneous chemical reactions in the porous coal char also depends on temperature and pressure.

183
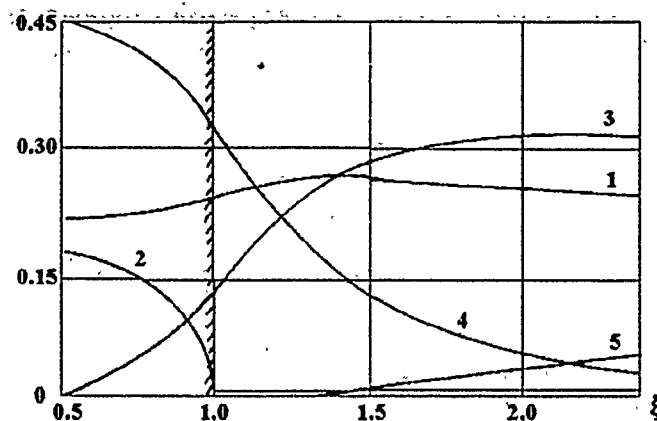
Figure 1: The distributions of (1) temperature ($T \cdot 10^{-4}$ K); (2) pressure ($P_e \cdot 10^{-2}$ atm), and relative mass concentrations of substances (3) z_{CO_2}, (4) z_{CO}, and (5) z_{O_2} in the gas phase and porous coal char particle along the dimensionless coordinate $\xi = r/R$ for a coal char particle burning at $T_0 = 1000$ K, $P_e = 1$ atm, $P_{CO_2} = 0.1$ atm, $P_{CO} = 0$, $P_{O_2} = 0.2$ atm.

References

[1] Golovina E. S. *High-Temperature Combustion and Gasification of Carbon.* Moscow, Energoatomizdat, 1983 (in Russian).

[2] Laurendau N. M. *Prog. Energy Comb. Sci.*, 1978, **4**, 221.

[3] Smith I. W. *Comb. Flame*, 1979, **14**, 237.

[4] Vilenskii T. V., Khzmalyan D. M. *The Dynamics of Dust Fuel Combustion,* Moscow, Energiya, 1978 (in Russian).

[5] Gremyachkin V. M., Schiborin F. B. *Fizika Goreniya Vzriva*, 1991, **27**, 5, 67 (in Russian).

[6] *Thermodynamic properties of Individual Substances* (Glushko V. P. Ed.), Moscow, Nauka, 1978 (in Russian).

[7] Lee S., Angus J. C., Edwards R. V., Gardner N. C. *AIChE J.*, 1984, **30**, 583.

THE UNSTEADY REGIMES OF POWDER COMBUSTION IN THE ROCKET CHAMBERS

A. G. Istratov, V. N. Marshakov, G. V. Melik-Gaikazov

Semenov Institute of Chemical Physics, Moscow, Russia

The unsteady combustion of powder in a combustion chamber occurs if the pressure varies over times comparable to the relaxation time of the heated layer of burning powder. In small engines with short combustor emptying time, the possibility of unsteady combustion allows for the instability of steady combustion below the limit determined by the ratio of the characteristic relaxation times of the chamber and the powder, which is called "apparatus constant" or stability criterion χ.

In this work the powder combustion was experimentally investigated under conditions close to this limit as well as in transitional regimes when the pressure in the chamber varied due to the sharp increase in the nozzle critical section area.

The engine model load used for this study was a set of pipes with their ends inserted into the engine bottom (so called "brush" load). This load provides a large area of combustion surface in a small volume and relatively high pressures near the stability limits to preclude extinction of powder at low pressures. Also, the powder pipes are long enough for erosive combustion to appear. This shape of the load makes it possible to independently vary the conditions leading to erosive combustion, the pipe length/inner diameter ratio (Pobedonostsev criterion, Π) and the ratio of the combustion surface to the nozzle critical section area which determines the pressure in the engine. The value of Pobedonostsev criterion reached 180.

At the initial time, the engine nozzle was closed by a metal membrane, which broke at the pressure close to that of the steady regime.

The combustion characteristics and pressure histories differed, depending on the apparatus constant χ and Pobedonostsev criterion Π.

At $\chi > 2$, the powder burns up and there are regions in the pressure histories which correspond to the steady regime. However, there are peaks in the pressure history characterized by pressures higher than the steady level. The peak amplitude does not correlate with the value of Pobedonostsev criterion.

These peaks may be due to the acoustic oscillations in the combustor. They are not visible in the pressure history and require high-frequency recording. It has been found that the initial conditions for the longitudinal acoustic waves in the engine are close to those determining the stability limit in terms of the parameter χ. The shape of the extinction surface was different along the pipes, while the shape pattern corresponded to the acoustic mode of oscillations. We cannot rule out the possibility that the peaks result from non-acoustic oscillations of combustion rate, related to the possibility of
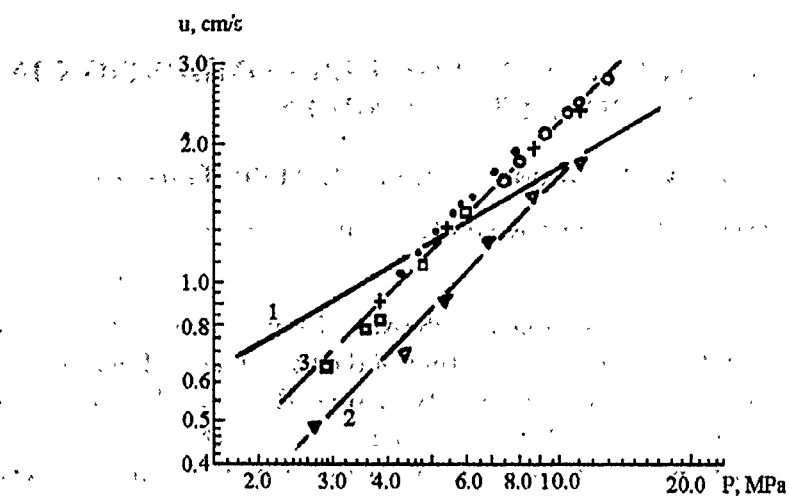
Figure 1: Combustion rates versus pressure for double-base powder: 1 — steady state with pressure exponent $\nu = 0.54$; 2, 3 — nonsteady combustion rates calculated from pressure histories for model engine with nonsteady pressure exceeding predicted steady-state value (2) and close to it, with $\nu \simeq 0.9$ (3).

nonsteady oscillatory combustion. Moreover, the membrane breakage at the initial time of engine operation gives rise to major disturbances capable of initiating the auto-oscillations.

For short loads ($\Pi < 50$), extinction was observed at $\chi < 2$.

For long loads ($\Pi > 50$), the combustion regimes were observed with pressures significantly lower than those characteristic of the steady regime. It is logical to relate the explanation of the low pressure levels to the acoustic oscillations, so that different parts of the load burn at different rates, and the average load combustion rate is lower than the steady-state value. The load always extincts at $\chi < 0.5$.

The combustion rate was calculated using the pressure histories and the equation of mass balance. Its dependence on pressure is stronger than the respective steady-state value. We obtained similar results for regimes with the pressure peak (see Fig. 1). The stronger dependence of the combustion rate on pressure is typical for nonsteady powder combustion regimes.

The engine employed in the study of the transition regimes had two opposite nozzles and a single thick-wall channel load.

For this engine, the steady regime was obtained at $\chi \geq 0.84$. With a further increase of the nozzle area ($\chi < 0.4$), combustion ceased immediately after the ignition.

The transition regime was obtained in this engine by opening the second nozzle after the steady regime had established at the first nozzle. After the opening of the

186

second nozzle, the steady regime with the lower pressure level occurred at $\chi \geq 1.16$. An increase in the second nozzle area led to a pressure decrease down to atmospheric and to extinction of the load. In these cases, the maximum χ was equal to 0.7. Thus, the critical value χ_{cr} is within $0.7 < \chi_{cr} < 1.16$.

The investigations of the powder combustion in the engine close to the limit of its stable operation have revealed a wide variety of phenomena, which affect the pressure level, the steadiness of engine operation and the possibility of powder extinction.

INVESTIGATION OF THE CATALYTIC HETEROGENEOUS IGNITION AND THE AUTOTHERMAL BEHAVIOR OF HYDROCARBONS AND ALTERNATIVE FUELS IN THE AIR

J. Jarosinski, R. Lapucha, J. Mazurkiewicz, M. Szrajer

Institute of Aviation
Al.Krakowska 110/114, 02-256 Warsaw, Poland

The experimental results presented in [1–4] show that flow of a gaseous air–fuel mixture over a heated catalyst surface changes its temperature not only because of external energy supply but also as a result of heterogeneous chemical reaction between fuel and oxygen on the surface.

Two kinds of characteristic functions of catalyst surface temperature can be observed [3, 4]:

- S-shaped curve;

- S-shaped curve with jump-like change.

An analysis of the above S-curves reveals three characteristic points:

- the local maximum of power, referred to as the heterogeneous ignition temperature t_{HI};

- the local minimum of power, referred to as heterogeneous extinction temperature t_{HE};

- the jump-like change in the autothermal temperature t_{AT}.
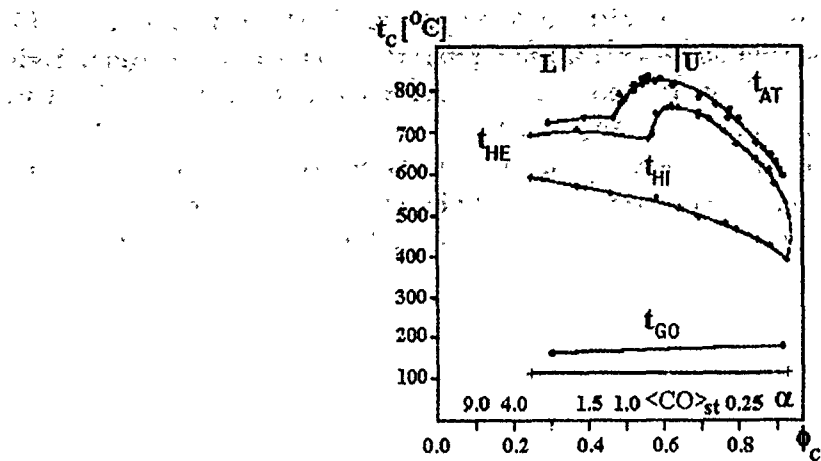
Figure 1: Temperature of the catalyst versus excess air coefficient α for technical methane; pellet Pt/MgO; temperature of the fuel–air mixture: $+ \, t_{GO} = 115\text{--}125 \, ^\circ C$; $* \, t_{GO} = 165\text{--}185 \, ^\circ C$.

Knowing the results of a sufficient number of measurements, we can draw a bifurcation diagram for the catalyst temperature versus the excess air coefficient α or the comparative coefficient $\phi_c = 1/\alpha + 1$ [3].

In order to determine catalyst temperature relationships for the hydrocarbon gases and the vapors of liquid fuels in mixtures with air, a special test stand was built [4]. The experimental setup consisted of a test chamber 20 mm in diameter and 1200 mm long with two heating sections and a temperature regulator in each section. A catalytic probe in the form of a pellet about 0.5 mm in diameter was fixed on a platinum wire stretched between two small posts on the axis of the chamber just before the outlet. The pellet made of magnesium oxide is covered with a thin layer of the catalyst. Technical methane and the vapors of unleaded gasoline, diesel oil, ethyl alcohol and rape oil ester in mixtures with air were investigated. Figures 1 to 3 present bifurcation diagrams of the catalyst temperature for the technical methane and the vapor of the unleaded gasoline and ethyl alcohol.

The test results in the following:

1. The maximum value of the autothermal temperature for mixtures of technical methane and the vapors of unleaded gasoline, diesel oil and rape oil with air occurs in the fuel-rich region adjacent to the stoichiometric mixture for CO production.

2. The maximum value of the autothermal temperature for mixtures of ethyl alcohol with air occurs in the vicinity of the stoichiometric mixture for CO_2 production.

3. The lean limit of the autothermal temperature for mixtures of the vapor of liquid fuels with air is leaner than the lower flammability limit at the ambient tem-
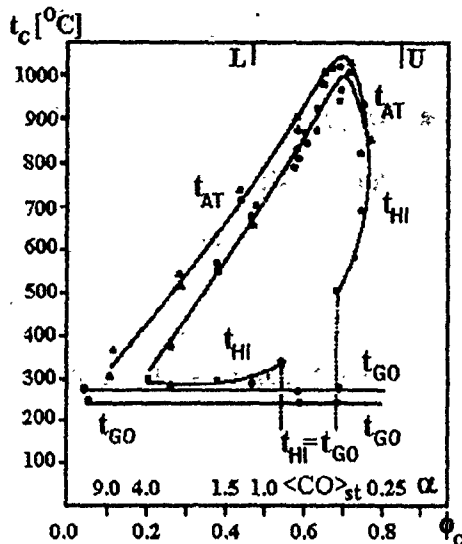
Figure 2: Temperature of the catalyst versus excess air coefficient α for unleaded gasoline; pellet Pt/MgO; temperature of the fuel–air mixture: o $t_{GO} = 250$ °C; Δ $t_{GO} = 280$ °C.
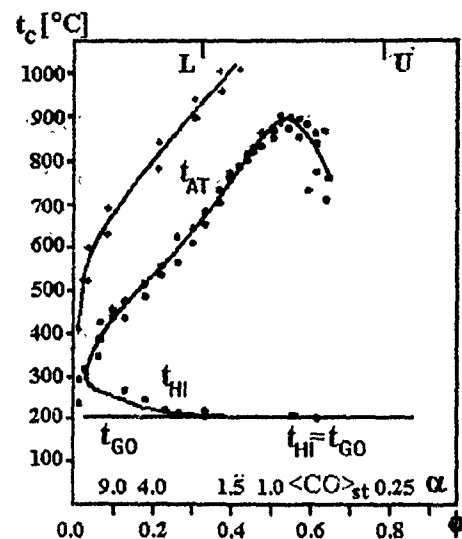
Figure 3: Temperature of the catalyst versus excess air coefficient α for ethyl alcohol; pellet Pt/MgO: temperature of the fuel–air mixture: o $t_{GO} = 200$ °C; + $t_{GO} = 320$ °C.

perature. This is probably due to the preheating of fuel up to the evaporation temperature.

4. The lean limit of the autothermal temperature for the gaseous hydrocarbons is richer than the lower flammability limit at the ambient temperature.

5. Increasing preheating of the fuel–air mixtures expands the autothermal lean region and increases the autothermal temperature.

6. The temperature of fuel–air mixture or the catalyst temperature must exceed the temperature of heterogeneous ignition (by a certain value for a given fuel), so that the catalyst surface temperature could jump to autothermal temperatures.

7. For a flow of the mixture of vapors of unleaded gasoline with air and vapors of ethyl alcohol with air over the catalyst (Pt/MgO), direct transition is possible from heterogeneous ignition on the catalyst surface to homogeneous ignition of mixture near the catalyst if mixture composition is with the range of $\alpha = 0.8-1.25$.

The test results presented in this paper may serve as a basis for studies of a catalytic prechamber for a lean-burn internal combustion engine under conditions of a higher compression ratio.

References

[1] Cho P., Law C. K. *Comb. Flame*, 1986, **66**, 159–170.

[2] Griffin T. A., Pfefferle L. D. *AIChE J.*, 1990, **36**, 861–869.

[3] Williams W. R., Stenzel M. T., Song X., Schmidt L. D. *Comb. Flame*, 1991, **84**, 277–291.

[4] Jarosinski J., Lapucha R., Mazurkiewicz J., Szrajer M. *Proc. 14th Int. Colloquium on Dynamics of Explosives and Reactive Systems*, University of Coimbra, 1993, C11.8.1.

BURNING CHARACTERISTICS AND IGNITION DELAY OF THE WASTE TIRE CHIPS IN HIGH-TEMPERATURE ENVIRONMENTS

Jongsoo Jurng, Eun-Sung Park, Jong Won Park, Gyo Woo Lee

Division of Mechanical Engineering
Korea Institute of Science and Technology, Korea

Recently, with the number of cars in Korea rapidly increasing, the issue of waste car tire treatment has been raised as a new problem. There are largely three categories of technology for waste tire: raw tire itself, retreatment, and the thermal energy of waste tires. Burning and using the thermal energy of waste tires has been highlighted because other methods lack the capability for large consumption. The direct burning of waste tires as a secondary fuel in energy-consuming industries, for example, cement kilns has turned out to be an economically viable method.

One of the major problems with the utilization waste tire in cement kilns will be the effect of tire burning on kiln emission. The combustion characteristics of tire materials in cement kilns are also very important for the design of the tire-burning system. Chemical reactions in cement kilns are very complicated and the quality of limestone used in Korea is known to be not as good as that in foreign cement companies. This should make it difficult to burn waste tires without further detailed research.

Experiments were carried out to investigate the burning characteristics of waste tires in high temperature environments. The main purpose of this research was not

190

only to design the supply system of waste tires to the kiln, but also to investigate what happens to the tires when they are thrown into the hot low-oxygen environment inside the kiln.

In the experiments, the flame structure and the combustion reactions involved in waste tire burning were mainly investigated. A ceramic matrix combustor simulating the conditions of waste tire burning in the cement kiln, for example the average temperature of 1100 °C and the oxygen content of 1–2%, was used. Commercial grade propane was used as the fuel for the burner. The diameter of the combustor was 90 mm, and the typical size of the tire chips in the experiments was $10 \times 10 \times 3$ mm. The size ratio of a tire chip to the combustor is approximately 1 to 10 which is similar to that of a whole tire to the real kiln.

The burning of waste-tire chips includes four stages: evaporation of volatile substances, ignition, burning of the volatile substances, and burning of solid carbon.

The experiments have shown that the total burning time of waste tire chips depends on the temperature of the environment and the initial weight of the chip. However, the ignition delay for tire chips depends not only on the temperature but also on the oxygen content in the environment. When the radiative heat transfer to the ceramic radiation shield increases, the burning time of the waste tire chips becomes shorter. This is mainly due to the increase in the radiative heat transfer to the tire chips from the ceramic burner plate and also the decrease in the radiation loss from the flame.

SPHERICAL WAVES OF FILTRATIONAL GAS COMBUSTION

N. A. Kakutkina, I. V. Borovykh, Yu. M. Laevskii, V. S. Babkin

Institute of Chemical Kinetics & Combustion, Computer Cent r SB RAS, Novosibirsk, 630090 Russia

The laws of filtrational gas combustion (FGC) have been considered in [1], and the essential role of interfacial heat exchange has been shown. In addition to the parameters of porous medium and premixed gas, the gas filtration velocity (v_0) is a key parameter controlling combustion wave characteristics, such as propagation direction, wave velocity, thermal wave structure and equilibrium temperature. A typical FGC wave propagates in a steady gas flow in a tube of constant cross section at a velocity of gas filtration independent of the coordinate, which defines the steady-state regime of wave propagation. In a spherical FGC wave, with a steady gas flow rate (G_0), filtration

velocity varies with the wave coordinate. Thus, new phenomena can be expected to occur. Consider the set of one-dimensional equations for a spherical FGC wave:

$$c_\theta \rho_\theta \frac{\partial \theta}{\partial t} = \frac{1}{r^2} \frac{\partial}{\partial r} \left(\lambda_\theta r^2 \frac{\partial \theta}{\partial r} \right) + \frac{\alpha_0 S_c}{1-m}(T-\theta),$$

$$c_T \rho_T \frac{\partial T}{\partial t} = \frac{1}{r^2} \frac{\partial}{\partial r} \left(\lambda_T r^2 \frac{\partial T}{\partial r} \right) - \frac{\alpha_0 S_c}{m}(T-\theta) -$$

$$\frac{1}{r^2} \frac{\partial}{\partial r}(c_T \rho_T v r^2 T) + Q\rho_T W(\eta,T), \tag{1}$$

$$\rho_T \frac{\partial \eta}{\partial t} = \frac{1}{r^2} \frac{\partial}{\partial r} \left(r^2 \rho_T D \frac{\partial T}{\partial r} \right) - \frac{1}{r^2} \frac{\partial}{\partial r} \left(r^2 \rho_T v \eta \right) - \rho_T W(\eta,T),$$

$$\frac{\partial \rho_T}{\partial t} = -\frac{1}{r^2} \frac{\partial}{\partial r}(r^2 \rho_T v).$$

Here, θ and T are the temperatures of inert porous medium and gas, η is the relative mass concentration of the deficient reactant, v is the filtration velocity, ρ_θ and ρ_T are the densities of inert medium and gas, λ_θ and λ_T are their heat conductivities, D is the diffusivity, m is the porosity, α_0 is the heat exchange coefficient, S_c is the specific area of porous medium, Q is the heat release and $W(\eta,T)$ is the rate of chemical reaction:

$$W(\eta,T) = k_0 \eta \exp \left(-\frac{E}{RT} \right),$$

where E is the activation energy, R is the universal gas constant, k_0 is the preexponential factor. For the diverging gas flow, the boundary conditions are

$$r = 0: \qquad \theta = T = T_0, \quad \eta = 1;$$

$$r = \infty: \qquad r^2 \frac{\partial \theta}{\partial r} = r^2 \frac{\partial T}{\partial r} = 0, \quad \eta = 0.$$

We will consider the steady-state regimes for a static combustion wave and determine static wave characteristics in the case of strong interfacial thermal interaction, which corresponds to the low-velocity regime (LVR) [1] with $\lambda_T = 0$ and $D = 0$. Substituting these into Eqs. (1) and rearranging gives a set of steady-state equations:

$$\frac{1-m}{m} \frac{\lambda_\theta}{c_T G} \left(r^2 \frac{\partial \theta}{\partial r} \right) - (T - T_0) + \frac{Q}{c_T}(1-\eta) = 0,$$

$$\frac{G}{\rho_T} \frac{1}{r^2} \frac{\partial T}{\partial r} + \frac{\alpha_0 S_c}{m c_T \rho_T}(T-\theta) - \frac{Q}{c_T} W(\eta,T) = 0, \tag{2}$$

$$\frac{G}{\rho_T} \frac{1}{r^2} \frac{\partial \eta}{\partial r} + W(\eta,T) = 0.$$

Here, $G = const = \rho_T v r^2$. It was additionally assumed that $\alpha_0 = \infty$. Let the narrow zone of chemical reaction be located at $r = r^*$. Then the preheat zone is at $r < r^*$, and the heat relaxation zone is at $r > r^*$. Solving Eqs. (2) with boundary conditions, we obtain the temperature distribution

$$T = T_0 + (T^* - T_0)\exp\left[-\frac{m}{1-m}\frac{c_T G}{\lambda_\theta}\left(\frac{1}{r} - \frac{1}{r^*}\right)\right] \qquad \text{at} \quad r < r^*,$$

$$T = T^* \qquad \text{at} \quad r > r^*,$$

$$\theta \equiv T \qquad \text{at} \quad \text{any} \quad r,$$

T^* is the adiabatic flame temperature for premixed combustion. Using the method of matching [2] for the chemical reaction zone, we obtain the relationship for r^*:

$$k_0 \rho_T^0 \frac{T_0}{T^*}\exp\left(-\frac{1}{\beta}\right)\frac{r^{*4}}{2q}\left[1 - \frac{2r^*}{q} + \frac{2r^{*2}}{q^2}\left(1 - \exp\left(-\frac{q}{r^*}\right)\right)\right] = G, \qquad (3)$$

where ρ_T^0 is the gas mixture density at the initial temperature,

$$\beta = \frac{RT^*}{E}, \qquad q = \sigma\frac{T^* - T_0}{2\beta T^*}, \qquad \sigma = \frac{m}{1-m}\frac{c_T G}{\lambda_\theta}.$$

An analysis shows that a unique real positive r^* value satisfying Eq. (3) exists for any set of realistic parameter values, implying that a spherical FGC wave in a diverging gas flow will move to the coordinate $r = r^*$ no matter what the coordinate of wave initiation is. It follows from Eq. (3) that r^* increases with increasing gas flow rate G and decreasing reactivity of the gas mixture.

To validate the theoretical conclusions, spherical FGC waves were initiated in a steel frustum of a cone, filled by porous material. The bottom diameter of the vertical cone was 2 cm, its height was 40 cm, and cone angle was 14°. The cone was filled with SiC grains of mean size $d = 3$ mm and porosity $m = 0.5$. Combustible hydrogen–air mixture was fed through the bottom (narrow) cone end and ignited at its top end.

A combustion wave initiated at the top of the cone propagated through the porous medium with gradually decreasing velocity and stopped at a certain $r = r^*$, depending on the gas mixture composition and flow rate. The attempts to reach the same equilibrium position in a downstream direction, as the theory predicts, failed. This is due to two reasons. First, the downstream FGC wave is not stable, and normally breaks down before reaching the equilibrium position. Secondly, downstream wave propagation is hampered by the influence of the metal walls of the cone.

The measured value of r^* increases with gas flow rate, as predicted by the theory (Fig. 1). Quantitative discrepancy between the predicted and measured r^* values is due to the modeling assumption of infinite rate of heat exchange.
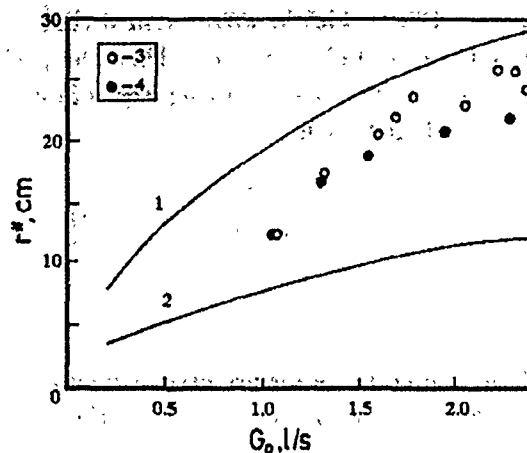
Figure 1: Predicted (curves) and measured (points) r^* values vs gas flow rate. Gas mixtures: $1 — 10\%$ H_2+ air, $2, 3 — 15\%$, $4 — 16\%$.

References

[1] Laevskii Ju. M., Babkin V. S. In: *Thermal Wave Propagation in Heterogeneous Media.* Novosibirsk, Nauka, 1988, 108 (in Russian).

[2] Laevskii Ju. M., Babkin V. S., Drobyshevich V. I., Potytnyakov S. I. *Fizika Goreniya Vzriva*, 1984, **20**, 6, 3 (in Russian).

A STOCHASTIC MODEL FOR MULTI-STAGE HETEROGENEOUS COMBUSTION

B. M. Khusid*, B. B. Khina*, E. P. Podvoiski[†], I. S. Chebotko[†]

*A. V. Luikov Heat & Mass Transfer Institute, Byelorussian Academy of Sciences, 15 P.Brovka Str., Minsk 220730, Republic of Byelarus

[†]Physico-Technical Institute, Byelorussian Academy of Sciences, 4 Zhodinskaya Str., Minsk 220730, Republic of Byelarus

The stochasticity of chemical reactions, associated with nonuniformities of physical and chemical properties of reactants is inherent in the combustion of condensed heterogeneous systems. In particular, it has a pronounced effect on unstable regimes of

combustion-driven synthesis, or the so-called self-propagating high-temperature synthesis (SHS) of refractory compounds and composite materials, because in the reaction zone of SHS wave, which has a width of 1–100 μm, only a small number of solid particles can react simultaneously. Reactions in SHS waves are of complex multi-stage nature. In this work, a stochastic model of combustion in gasless systems is developed for the case of multi-stage reaction $A_0 \to A_1 \to A_2 \to \ldots \to A_m$.

A two-dimensional region is assumed to consist of square cells with the side h; each cell is characterized by the random temperature T and state η. The latter can take on $M+1$ values from 0 (initial) to M (final). During a short time interval τ, the cell can undergo only one transformation (from the i-th to $i+1$-th state). At small τ, the transformation probability is proportional to τ: $p_i = p(T, i) = \tau k_{i+1} \exp[-E_{i+1}/(RT)]$. At the $n+1$-th time step, the temperature of the cell with coordinates (k, l) is determined by the heat release due to reaction in this cell and conductive heat transfer from the neighboring cells:

$$\theta(k, l, n+1) = \theta(k, l, n) + \delta\theta(k, l, n+1) + \frac{a\tau}{h^2}[\theta(k-1, l, n)+$$

$$\theta(k+1, l, n) + \theta(k, l-1, n) + \theta(k, l+1, n) - 4\theta(k, l, n),$$

$$\delta\theta(k, l, n+1) = q_i[\eta(k, l, n+1) - \eta(k, l, n)], \qquad i = \eta(k, l, n+1),$$

with the probability of cell transformation

$$p_\eta = p(\theta, \eta(k, l, n)) = \tau k_i \exp\left(-\frac{E_i}{RT_s(\theta + \theta_0)}\right), \qquad i = \eta(k, l, n+1), \qquad p_M = 0.$$

Here, $\theta = (T - T_0)/T_s$, $q_i = Q_i/(pcT_s)$, and $\theta_0 = T_0/T_s$, where T_0 is the initial temperature and T_s is the temperature scale. This model extends the previously developed one [1] to the case of sequential reactions in the SHS wave. An analysis has shown that the stochastic model reduces to the deterministic one [2], if we neglect the correlation between $\eta(k, l, n)$ and $\theta(k, l, n)$. The latter is responsible for the continuous generation of two-dimensional perturbations, which results in spontaneous development of spin combustion and chaotic regimes in the respective ranges of dimensionless parameters $\beta = RT_a/E$ and $\gamma = pcRT_a^2/(EQ)$, where $T_a = Q/(pc) + T_0$, as was demonstrated for a one-stage reaction [1].

Computer simulation was performed for the two-stage reaction $A_0 \to A_1 \to A_2$ for three typical cases [2, 3]: (1) the so-called "separation regime" ($0 < \sigma_E < \phi$, where $\sigma_E = E_1/(E_1 + E_2)$, $\phi = (\sigma_Q + \sigma)/(1 + \sigma_Q + 2\sigma)$, $\sigma_Q = Q_1/(Q_1 + Q_2)$, and $\sigma = pcT_0/(Q_1 + Q_2)$), in which the reaction waves are independent and the SHS is controlled by the first reactions; (2) the "control regime" ($\phi < \sigma_E < 0.5$), where the first reaction has the lower activation energy, and the heat release is controlled by the heat flux from the second reaction front, and (3) the "merged regime" ($0.5 \leq \sigma_E < 1$) when the reaction fronts nearly coincide.
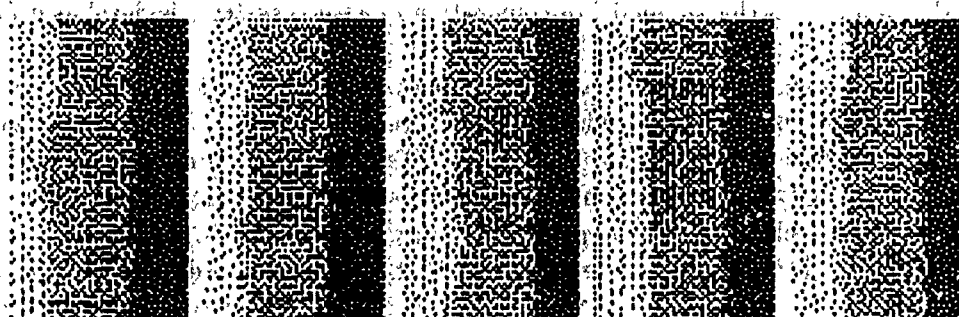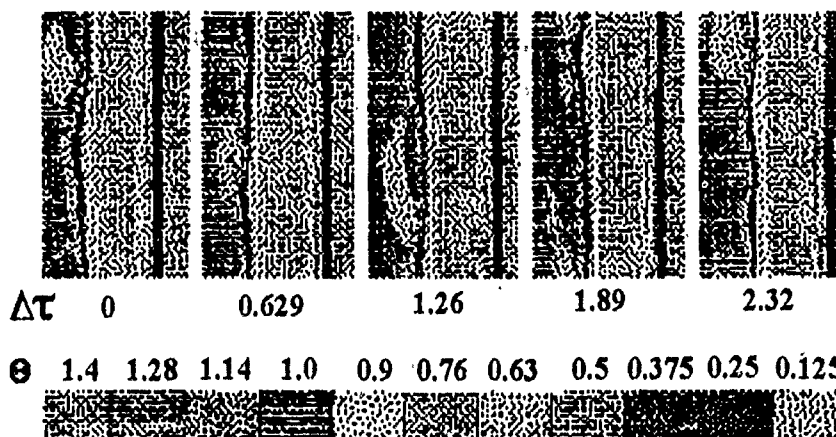
Figure 1: Developed cylinder with the maps of state (a) and dimensionless temperature (b) for the "separation regime" with $\sigma_0 = 0.533$, $\sigma_E = 0.14$, $\sigma_k = k_1/(k_1 + k_2) = 1.75 \cdot 10^{-8}$ $(0 < \sigma_E < \phi = 0.37)$.

The characteristics of stable combustion (the wave velocity, the temperature field, and the degree of conversion) are similar in the stochastic and deterministic models. The effects due to stochasticity are very conspicuous under the conditions of plane wave front instabilities. In these cases, the stochastic model demonstrates diverse patterns of dynamic behavior, e.g., spinning combustion or chaotization of reaction fronts.

In the "separation regime", the reaction waves demonstrate various dynamic behaviors. For example, either one of the combustion waves is plane and the other propagates

in the spin mode (see Fig. 1 which shows a development of a cylinder with the maps of temperature and state at a number of dimensionless times $\delta\tau$), or both exhibit spinning combustion. In the "control regime", the patterns of SHS wave dynamic behavior are rather complex and diversified. This is due to the existence of the heat flux from the zone of the second reaction to the first reaction front, on the one hand, and the possibility of occasional formation of the final product at certain locations ahead of the second reaction front, on the other hand. In the "merged regime", when the reaction fronts nearly coincide, the SHS wave of a two-stage reaction behaves as a one-stage reaction wave.

The results obtained within the framework of the stochastic model qualitatively agree with experimental data for a number of SHS reactions [4, 5].

References

[1] Astapchik A. S., Podvoiski E. P., Chebotko I. S., Khusid B. M., Merzhanov A. G., Khina B. B. *Phys. Rev. E.*, 1993, **47**, 1, 319.

[2] Khaikin B. M., Filonenko A. K., Khudyaev S. I. *Fizika Goreniya Vzriva*, 1968, **4**, 4, 591 (in Russian).

[3] Berman V. S., Ryazantsev Yu. S. *Zhurnal Prikladnoi Mekhaniki Tekhnicheskoi Fiziki*, 1973, **1**, 75 (in Russian).

[4] Strunina A. G., Dvoryankin A. V., Merzhanov A. G. *Fizika Goreniya Vzriva*, 1983, **19**, 2, 30 (in Russian).

[5] Maksimov Yu. M., Merzhanov A. G., Pak A. T., Kuchkin M. N. *Fizika Goreniya Vzriva*, 1981, **17**, 4, 51 (in Russian).

DIFFUSION FLAME PROPAGATION IN AN INERT POROUS MEDIUM WETTED WITH FUEL

A. A. Korzhavin, V. A. Bunev, V. S. Babkin

Institute of Chemical Kinetics & Combustion, Novosibirsk, Russia

The scientific interest in the problem of propagation of combustion waves in porous media wetted with fuel is due to the fact that the propagation mechanism of these waves involves coupling between chemical reaction and mixing processes. It has been shown in [1] that in an inert porous medium with liquid hydrocarbon fuel films on its surface and a gas-phase oxidizer, chemical reaction waves can propagate in detonation (400–1200 m/s) and subsonic regimes (80–300 m/s). It was concluded that under such conditions combustion regimes with lower velocities do not exist. In this paper, we present the experimental data demonstrating that steady-state combustion waves can propagate in porous medium wetted with fuel at 4–10 cm/s.

The experiments were carried out in a closed vertical steel tube of cross section 48 mm × 48 mm and height 2 m filled with a porous medium of density 36.5 kg/m^3 wetted with n-octane. The porous medium consisted of stacked separate elements 48×48 mm^2 in cross-sectional dimensions and 0.085 mm in thickness each, produced by stretching aluminum foil cuts.

Prior to a run, the tube was filled with the fuel and thermostatted. Then the fuel was discharged, the tube was filled with air to certain pressure, and closed. Ignition was provided by an electric discharge pulse heating a fuel-wetted wire spiral in a free space at the top of the tube. Flame propagation velocities were measured by an array of photodiodes. Pressure rise was recorded by a tensimeter-type transducer. Experiments have shown that, after an initial period, the flame propagates steadily. The r.m.s deviation of velocity from its mean value was 6–10%.

Under thermodynamic equilibrium, the correlation between the initial pressure and gas composition is consistent with the temperature-dependent vapor pressure of liquid fuel. In our experiments, the thermodynamic temperature of the system was maintained at 27 °C. Figure 1 shows flammability limits under different conditions. Line A is a hyperbola corresponding to the saturated vapor condition of the fuel shown in the fuel concentration (c, % vol.) — initial pressure coordinates. The closed circles pertain to the flammability region and the open circles represent nonflammable conditions. Line B is deduced from the experimental flammability line for propane–air flames in this porous medium using the assumption of identical flammability conditions for n-octane–air and propane–air flames. Line C is the lean flammability limit for n-octane–air flames in a free space [2].

It is evident that there are two combustion regimes in the porous medium. The one known as the high-velocity regime (HVR) [3] occurs in the initial pressure range of
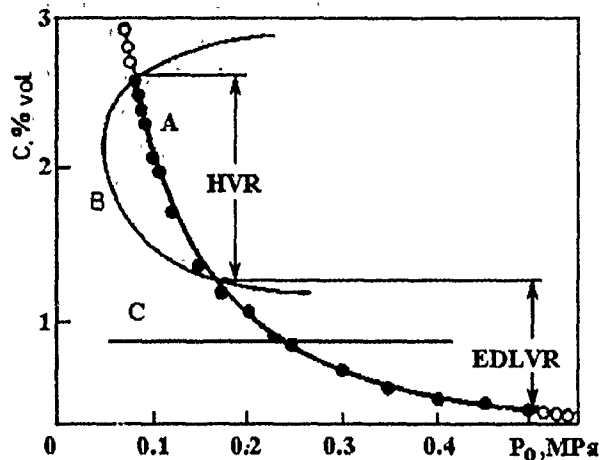
Figure 1: Flammability regions in the porous medium wetted with n-octane.

0.08–0.17 MPa and the previously unknown low-velocity regime in the range of 0.17–0.5 MPa. The latter exists not only outside the HVR flammability limits ($P > 0.17$ MPa), but also beyond lean flammability limit observed in a free space ($c = 0.9\%$) down to $c = 0.43\%$. In this regime, flame propagation velocities are by one or two orders of magnitude lower than in HVR and range from 4 to 10 cm/s. The dependence of flame propagation velocity on initial pressure is weak and tends to decrease with increasing initial pressure. Based on this tendency, one can speculate that an upper pressure limit P^* may exist. However, its occurrence remains an open question, because the observed "limit" ($P^* = 0.5$ MPa) may be due not to the criticality conditions, but, rather to ignition problems.

The fact that the regime under consideration is observed in the parametric region that rules out the possibility of premixed gas combustion suggests that the gaseous mixture is formed during combustion as a result of evaporation of the liquid fuel and its mixing with air in the flame zone. This is a principal distinction of this regime as compared to the conventional filtrational combustion of homogeneous gas mixtures. However, in contrast to the regimes analyzed in [1], when the strong hydrodynamic interaction of a high-speed flow with fuel films and droplets is essential, the evaporative diffusive low-velocity regime (EDLVR) under consideration does not necessarily involve such an interaction. It is due to the fact that heat release under the EDLVR conditions is sufficient not only for evaporation of the amount of fuel required for combustion, but also for the heating of the porous medium, owing to its low specific heat.

The coupling between the mixing and chemical reaction is responsible not only for the existence of EDLVR, but also for the mechanism of flame velocity stabilization. Increasing the flame velocity suppresses fuel evaporation in the flame zone, lowers its concentration in the gas phase and hence the flame velocity. Conversely, decreasing the

flame velocity extends the disposable time for evaporation, increases the concentration of fuel vapor and results in increased flame velocity. There is an indirect evidence corroborating this conclusion. At high flame velocities in HVR under the conditions of large excess of liquid fuel (30 kg/m^3), evaporation in the flame zone has little or no effect on flame velocity (the flame velocity maximum is close to that expected for the homogeneous n-octane–air mixture) or the rich limit observed at relatively high velocity (0.6 m/s).

References

[1] Lyamin G. A., Pinaev A. V. *Combust., Explosion and Shock Waves*, 1992, **28**, 5, 102.

[2] *Fire-hazardous properties of materials and methods of fire suppression.* (A. N. Baratov Ed.) Moscow, Khimiya, 1990 (in Russian).

[3] Babkin V. S. *Pure and Applied Chemistry*, 1993, **65**, 2, 335.

HETEROGENEOUS REACTIONS AND THE DYNAMICS OF THIN SURFACE FILMS

Dirk Meinkohn

Institut für Chemische Antriebe
Deutsche Forschungsanstalt für Luft- und Raumfahrt (DLR)
D–71239 Hardthausen, Germany

For a variety of heterogeneous processes, condensed–phase surface layers are found to play an important role. Examples include:

- layer formation by chemical vapour deposition (CVD),

- formation of surface deposits covering the walls or combustion machinery of heat exchangers,

- surface layers covering condensed–phase reactants, with layers either consisting of reaction products as in the case of metal or boron combustion, or consisting of impurities which build up on the reaction surface while it regresses during the reaction, as it often found in the case of coal combustion,

- fouling of catalytic surfaces.

In each of these examples, the surface of a condensed–phase body represents the site of a reaction while being partly or entirely covered by a surface layer which exerts a controlling influence on the evolution of the surface reaction. The surface layer is classified as "inert", implying that its influence on the surface reaction is only via its thickness which may vary over the surface in space and time.

Heterogeneous reactions differ from their homogeneous counterparts in that a reaction surface exists which influences the reaction by its geometry, morphology, accessibility and uniformity. The present work is concerned with the consequences of nonuniformity of the conditions at the reaction surface. Therefore, as to its geometry, morphology and accessibility, the reaction surface is assumed to be as simple as possible: a model is presented based on a flat, smooth, equiaccessible reaction surface, for which nonuniformity arises due to the varying thickness of the surface layer. A layer substance may be formed (by chemical reaction, vapour deposition, forming impurities) and it may be removed (by evaporation).However, due to its contact with the vapour atmosphere, the substrate surface will never be entirely devoid of layer molecules. A representative system is in the form of a solid fuel in an oxidizing vapour atmosphere, with reaction products forming a liquid layer or an adsorption layer, depending on the surface temperature.

The processes contributing to the evolution of the reaction may be classified as to their direction with respect to the surface: there are transversal processes which are directed in the normal direction, and lateral ones which act in a tangential direction to the surface. As it turns out, transversal and lateral processes are coupled nonlineary via thermal and mechanical effects. Since surface forces are found to be extremely strong for thin layers (disjoining/conjoining pressure effects), the mechanical coupling between the lateral and transversal processes is of primary importance, particularly in the case of film spreading involving the propagation of a film edge over the surface of the body, the edge comprising film thickness ranging from microscopic to macroscopic values. Such a propagation edge arises for spreading ruptures in a macroscopic film, leading to the appearance and growth of film areas covered by remnant adsorbed layers of microscopic thickness, or alternatively for a spreading macroscopic "cap" on a "moist" surface, leading eventually to a film cover of macroscopic thickness. Here, "moist" designates a remnant microscopic coverage of the substrate surface.

In the context of a reacting fuel surface covered by an inert liquid layer, spreading of film ruptures will be associated with ignition, whereas spreading of caps corresponds to extinction.

201

Since film spreading is in tangential directions, it corresponds to a lateral process. Propagation of an edge therefore represents a surface wave. These waves are described by the solutions of an appropriate surface transport equation, the film evolution equation. It will be shown that two kinds of self-similar surface waves arise. There are waves basically associated with an initial value problem for the case of the transport equation being weakly parabolic, the so-called "Barenblatt waves". They closely correspond to the phenomenon of wave-like spinodal decomposition observed during equilibrium phase transitions. However, due to the transversal processes of film formation (due to surface reaction) and film evaporation, self-similar surface waves also exist for strongly parabolic (i.e. non-degenerately parabolic) film equations. These waves correspond to transitions between metastable states by means of a nucleation phenomenon, i.e. nucleation of ruptures or caps. Consequently, they resemble the nucleation waves which may also occur for phase transitions in equilibrium systems.

The mechanical coupling between transversal and lateral processes is due to the thermodynamical relation between the disjoining pressure and the vapor pressure. Designating the internal pressure of a film of thickness h by p_h and the vapour pressure above such a film by p_h^v, the relation is found, similar to the Kelvin equation for curved surfaces:

$$p_h - p_\infty = -\Pi(h) = \frac{kT}{\bar{V}} \ln \left(\frac{p_h^v}{p_\infty^v} \right). \tag{1}$$

p_∞ represents the internal pressure and p_∞^v the vapour pressure for macroscopic values of the thickness h. Consequently, the disjoining pressure $\Pi(h)$ represents the effect of the film thickness being non-macroscopic, k designates the Boltzmann constant, T is the temperature, $\bar{V}$ is the volume of a molecule. The film thickness h is determined by the vapour pressure p_h^v and the temperature T:

$$h = h(p_h^v, T). \tag{2}$$

Here, $T = const$ gives the adsorption isotherms, whereas $p_h^v = const$ defines the adsorption isobars. The relationship $h = h(p_h^v, T)$ will be shown to provide the equation of state for a thin film, viewed as a surface phase. For a particular equation of state, various distinct surface phases may exist, taking the form of a surface gas or a surface liquid, for instance, with surface phase transitions between them. The appearance of critical points leads to second–order surface phase transitions known as "wetting transitions".

It will be shown that certain geometrical properties of the state surface, i. e. its vertical tangents with $\partial p_h^v / \partial h = 0$ are associated with the weak parabolicity of the film equation and thus lead to the occurrence of Barenblatt waves.

Thin films are defined to have thicknesses in the microscopic and mesoscopic range, with thin film properties determining the shape and the evolution of the so-called "precursor" at the edge of the macroscopic film. It will be shown that, due to large gradients in the internal pressure of the film, thermal and mechanical phenomena may

be decoupled. Thus, as to the spreading phenomena for film precursors, the surface temperature distribution is assumed to be given (that is, independently derived). It will be shown that the partial derivative $\partial h/\partial p_h^v$ is geometrically similar to the precursor profile. For a one-dimensional surface, an invariant profile is thus found to propagate on the surface, which is given as follows:

$$\frac{\partial h}{\partial p_h^v} \sim -\frac{\partial h}{\partial x}. \tag{3}$$

Consequently, the precursor profiles may be classified according to the well-known growth modes for films on condensed-phase substrates. Examples comprise growth modes according to Volmer–Weber, Frank-van der Merwe, Stranski–Krastanov.

In order to derive film profiles pertaining to microscopic as well as macroscopic thicknesses, wetting processes for "moist" surfaces are investigated. On account of the surface reaction persisting unabated for any thickness of the coverage, surface portions entirely devoid of layer molecules will not occur.

A moist surface with an adsorption layer of thickness h which is in contact with the ambient vapour atmosphere is assigned a surface tension $\gamma_{sv}(h)$. The adsorption layer being of microscopic thickness, it is viewed as a two-dimensional thermodynamic phase, so that $\gamma_{sv}(h)$ is a property of the interface. Consequently, $\gamma_{sv}(0)$ corresponds to an ordinary "dry" interface. It will be shown that the spreading coefficient $S(h)$ for a macroscopic layer spreading over a moist surface may be found in terms of the disjoining pressure $\Pi(h)$. For static wetting, a macroscopic "apparent" contact angle θ characterizes the film profile at the edge where the leading edge of the macroscopic film intersects the "moist" surface.

Negative values of the spreading coefficient S correspond to contact angles θ with $0 < \theta < \pi$ (partial wetting), whereas a vanishing S corresponds to complete wetting. As with "dry" surfaces, large positive values of S favour the dynamic spreading of the film on the moist surface.

The interplay of film formation (i.e., chemical reaction) and film removal (i.e. evaporation) may lead to a stabilization of films which are mechanically unstable, or, vice versa, to a destabilization of mechanically stable films. If film formation exactly balances film removal, uniform metastable stationary states are possible on infinite substrate surfaces. It will be shown that a boundary layer approximation for thin films (the so-called "lubrication approximation") leads to a unified description of precursor spreading in terms of a generalized diffusion equation given in terms of a generalized transport coefficient. This equation describes the evolution of the layer thickness h, under the combined influences of the lateral spreading forces due to gradients in the disjoining pressure, and the transversal processes of layer formation and evaporation. In the case of a strictly nonvanishing transport coefficient, this evolution equation is nondegenerate. For this case, planar and circular self-similar surface waves are derived which are shown to represent the nucleation and spreading of ruptures and caps and thus describe ignition and extinction processes.

References

[1] P. G. De Gennes, *Rev. Mod. Phys.*, 1985, **57**, 827–863.

[2] Meinkohn D., Mikhailov A.S., *Physica*, 1993, **A198**, 25–45.

[3] Meinkohn D., Mikhailov A.S., *Phys. Lett.*, 1993, **A178**, 143–149.

[4] Meinkohn D., Paper submitted to *Comb. Sci. Techn.*

HETEROGENEOUS SOLID MIXTURES COMBUSTION: INFLUENCE OF MICROSTRUCTURE

A. Pivkina, Yu. Frolov

Semenov Institute of Chemical Physics, Kosygin Str. 4, Moscow, 117977 Russia

A substantial and continuously growing research effort has been invested in the field of heterogeneous combustion of solid mixtures, especially lately. This phenomenon underlies the processes in solid rocket motors, pyrotechnical devices, and self-propagating high-temperature synthesis [1].

Combustion of composite solid mixtures involves a variety of physicochemical processes combined with the geometrical heterogeneity of the internal microstructure. Thus, this process is difficult for modeling and analyzing [2].

The fractal and percolation theories have recently aroused a great interest [3] as the means of description of critical behavior of disordered systems. The most attractive ussue to be addressed is the relationship between the structural parameters and properties of the system, e.g., combustion characteristics.

Scher and Zallen [4] have found that the conducting volume fraction necessary for the onset of percolation is about 16% of the total volume (SZ criterion).

Table 1 shows some literature data of concentration combustion limits. For systems under consideration, components react on the contact surface, so that the area and "connectivity" of the reaction surface play a critical role in the initiation and propagation of the process. The network of particles of each component must not be disconnected for the reaction to come to completion.

As presented in Table 1, for gasless and small-gas-content systems it is possible to predict concentration limits with acceptable accuracy using the SZ criterion.

Table 1: Concentration limits of composition combustion.

NN	System	Mass content of the second component at combustion limits, $M/\%$	Volume content of components at combustion limits, $V/\%$	
1.	Ta–Si	4.4–31.7	16.1	15.1
2.	Hf–Si	7.3–38.6	19.9	14.3
3.	Nb–Si	7.0–47.6	14.1	15.0
4.	Mo–Si	22.7–41.7	33.0	14.5
5.	Zr–Si	12.1–43.2	16.7	19.2
6.	Ti–Si	14.9–57.0	15.2	16.8
7.	Nb–Al	6.8–48.6	11.3	15.9
8.	Nb–Ge	14.6–70.0	12.9	12.7
9.	Ni–Al	13.3–58.0	20.0	10.8
10.	Zr–Al	15.4–62.6	18.3	12.0
11.	Ti–Al	15.8–62.8	14.3	15.7
12.	Ti–Ni	28.5–87.6	10.1	13.6
13.	Ti–Co	32.5–76.3	11.8	22.5
14.	Hf–B	4.6–23.2	14.4	18.2
15.	Nb–B	7.2–23.2	15.0	19.9
16.	Mn–B	11.6–20.7	17.4	23.8
17.	Zr–B	7.4–37.0	13.9	18.7
18.	Ti–B	8.3–56.0	11.4	15.1
19.	Mg–B	25.0–71.0	17.1	17.3
20.	Zr–C	7.4–43.0	14.0	15.8
21.	Ti–C	8.1–57.0	11.7	14.2
22.	PbO_2–Wo_2	31.0–73.0	13.2	15.8
			$V = 15.5 \pm 3.1\%$	

The model of solid composites has been developed: the percolating and isolated clusters of particles play a crucial role in system properties. The outer fractal surface and critical parameters were calculated by the methods of probability theory.

The use of percolation theory combined with the fractal concept is a fruitful approach to the qualitative analysis of the spatiotemporal correlations between process characteristics such as the reaction front velocity, conversion depth, and physicochemical parameters of the system.

The model developed is also important for the determination of the group of components which defines the velocity of the reaction front (U). Also, the analysis of the calculated fractal surface of the components (S) and dependence $U(S)$ provides the opportunity to predict combustion limits and the value of U for composite solid mixtures containing an unlimited number of chaotically packed components with irregular

particle shape.

These concepts were previously proposed [5] as a method of obtaining solutions to the problem of concentration limits. We believe that this approach can be used more extensively to model combustion wave propagation.

References

[1] Merzhanov A. G. In: *Combustion and Plasma Synthesis of High-Temperature Materials*, (Munir, Holt Eds.), N.Y., VCH Publishers, 1990.

[2] Varma A., Lebrat J.-P., *Chem. Eng. Sci.*, 1992, **47**, 9–11, 2179–94.

[3] Bunde A., Halvin S. *Fractal and Disordered Systems.* Heidelberg, Springer–Verlag, 1993.

[4] Sher H., Zallen R., *J. Chem. Phys.*, 1970, **53**, 3759.

[5] Frolov Yu., Nikolsky B. *Proc. Joint Meeting of Soviet and Italian Sections of the Combustion Institute*, Pisa, 1990.

PROPAGATION OF A FLUIDIZING COMBUSTION WAVE

G. P. Pron, L. K. Gusachenko, V. E. Zarko, B. M. Malkin

Institute of Chemical Kinetics & Combustion, Novosibirsk, Russia

Experiments on ignition of a fluidized bed with 1–1.6 mm chamotte particles were conducted in a laboratory setup 125 mm in diameter. The height of the stationary bed was 160–170 mm, the inlet air temperature was 50 °C and the blow-through gas flow velocity was $V < V_2$ (V_2 is the fluidizing blow-through velocity). Coal-particle feeding to the bed surface started simultaneously with the blow-through flow and was performed at a constant flow rate. Ignition was initiated by burning wood bars on the bed surface. Thermocouples mounted above and in the bulk of the bed at different distances from the gas distribution grating were used to record the thermal profiles (Fig. 1).

In Fig. 1, one can see a pronounced heating wave with a steep front propagating from the top to the bottom of the bed. The fluidization occurs in the wave front, where
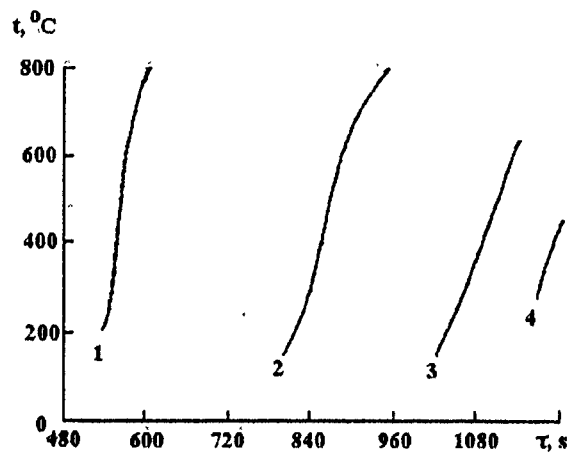
Figure 1: Thermocouple records at different distances from the gas distribution grating: *1* — 16 cm, *2* — 10 cm, *3* — 4 cm, *4* — 0.5 cm. Wave velocity averaged between positions: *(1–2)* $v = 0.02$ cm/s; *(2–3)* $v = 0.027$ cm/s; *(3–4)* $v = 0.035$ cm/s. The temperature above the bed is about 800 °C; $N = 0.87$.
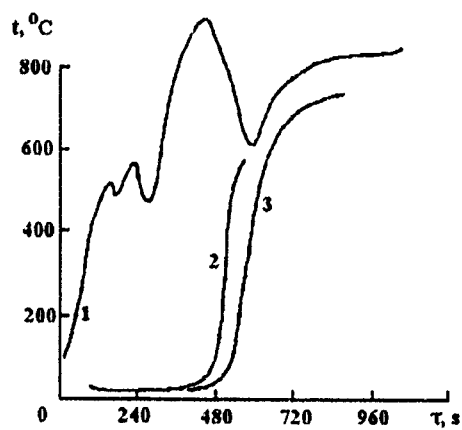
Figure 2: Thermocouple readings: *1* — above the bed, *2*, *3* — inside the bed at the distances 12 cm and 2 cm from the grating, respectively. The averaged wave velocity is 0.2 cm/s; $N = 0.9$.
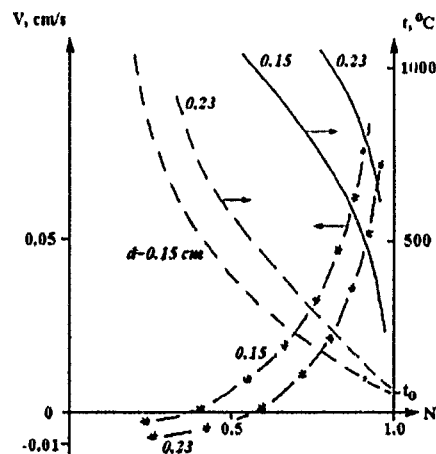
Figure 3: Results of calculations for particles with $d = 0.15$, 0.23 and 0.31 cm. Fluidized part temperature, °C; quiescent part surface temperature, °C; interface temperature difference on the same surface.

the linear flow velocity exceeds the critical level necessary for fluidizing the bed with the chosen particles size and air heated to 800 °C. Figure 1 can also be used to calculate the wave propagation speed.

An elementary model of the process has been proposed. The heat flux from the fluidized part to the quiescent part of the bed was calculated, based on known empirical correlations for heat exchangers. The dependences of fluidized bed temperature and fluidization wave propagation speed calculated versus the normalized blow-through velocity , $N = V/V_2$, (Fig. 3) qualitatively agree with the experimental results (Figs. 1 and 2). The model predicts the narrowing of the range of acceptable values of N with increasing particle size. The model cannot reflect the wave acceleration effect observed in the experiments because it does not take into account the mechanical influence of the fluidized part on the quiescent part of the bed (due to the impact by particles and vibration).

A method for the bed ignition by "forced" fluidization wave propagation has been proposed. The wave propagation is induced by creating a vibration zone traveling from the top to the bottom of the bed. The necessary fluidized layer temperature can be obtained with N not too close to unity, which ensures fairly good stabili·· of the process.

ON THE ROLE OF SURFACE FILMS IN THE IGNITION AND COMBUSTION OF METAL PARTICLES

E. Ya. Shafirovich, U. I. Goldshleger

Institute of Structural Macrokinetics, Chernogolovka, 142432 Russia

New interest in metal combustion has arisen recently due to the plans of using *in-situ* propellants in lunar and Mars missions. Recent research have yielded new experimental results which cannot be explained by the available theories of metal ignition and combustion.

This paper presents experimental results on magnesium particle combustion in the atmosphere of carbon dioxide or monoxide. Particular consideration is given to the effect of surface films on the ignition and combustion behavior of particles.

The experiments were performed in a flow reactor and a closed chamber in a controlled environment. The mass and temperature of samples, as well as the flame temperature, were measured throughout the experiment.

Figure 1 shows the observed regions of combustion regimes for Mg with CO_2 and CO in the scale of ambient gas temperatures.

Combustion of Magnesium in Carbon Dioxide

When the ambient temperature is lower than the Mg melting point (923 K), the heterogeneous reaction does not initiate ignition, the oxidation law is close to paralinear, and there is no overheating of particles above the gas temperature. In the range of temperatures from 923 to 964 K, we observed the breakdown of thermal equilibrium resulting in steady heterogeneous combustion with the particle overheat of about 10 K. This transition is associated with the surface film cracking observed with a microscope. In the heterogeneous combustion regime, the oxidation law is similar to autocatalytic.

At temperatures above 964 K, the transition to vapor-phase burning is observed. In this regime, the particle temperature is close to the Mg boiling point ($\sim$ 1370 K at 1 atm), and the maximum flame temperature is 2600–2800 K. It should be noted that, at the lower limit of the vapor-phase regime (964 K), the ignition occurs when the metal has been almost completely consumed in the heterogeneous reaction.

Our analysis shows that the observed "heterogeneous" combustion is caused by the metal vapor–oxidizer reaction inside the porous layer of combustion products. Due to the capillary flow of metal in the pores, the effective surface of evaporation increases, resulting in an autocatalytic-like law of mass variation. By the end of the heterogeneous combustion, the rest of the metal does not cover the entire inner surface of the product layer. Therefore, both the effective surface of evaporation and the rate of sample mass variation decrease. The breakdown of the quasi-steady heterogeneous combustion regime, i.e., the transition to the vapor-phase combustion, occurs at a mass variation rate close to its maximum.

Combustion of Magnesium in Carbon Monoxide

The behavior of Mg oxidation and combustion in CO at lower temperatures is similar to that in CO_2. In the range of temperatures from 923 to 947 K, we observed the heterogeneous combustion with the particle overheating by 20–30 K.

When the ambient temperature exceeds 947 K, the vapor-phase combustion occurs, the particle temperature is close to the boiling point of Mg, and the flame temperature is $\sim$ 1800 K (the adiabatic flame temperature calculated fo. Mg with CO is about 2000 K). Estimates show that, in contrast to the case of CO_2, the heat flux from the flame zone to the particle is not sufficient for its heating to the measured values of temperature. This points to the substantial role played by the heterogeneous reaction in the vapor-phase combustion of Mg in CO.

The increase in the ambient temperature reduces the measured mass increment for the time until the inflammation. The effective surface of evaporation decreases and the role of the "heterogeneous" reaction increases. As a result, pulsating combustion is observed in a wide range of temperatures (985–1230 K). Vapor-phase flashes against the background of vigorous heterogeneous reaction occur in this regime. Figure 2 presents a
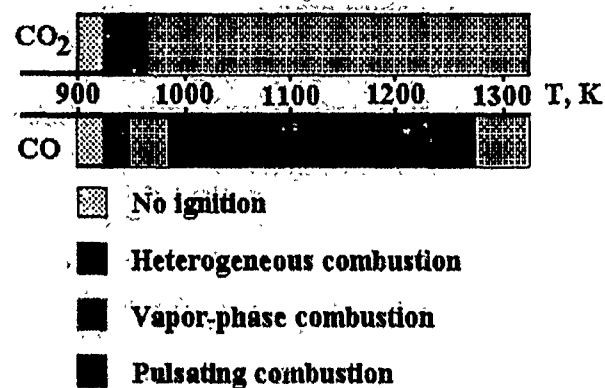
Figure 1: Combustion regimes for 2-mm magnesium samples in the atmospheres of carbon dioxide and monoxide.
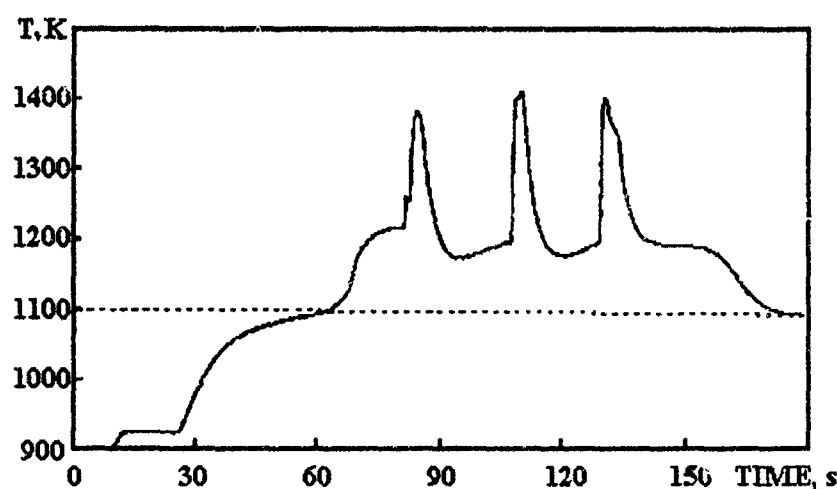
Figure 2: Variation of temperature for Mg sample in CO atmosphere at the ambient gas temperature of 1098 K (shown by the broken line) and the gas flow rate of 1 cm/s.

typical temporal variation of temperature for particles burned in the pulsating regime. The heterogeneous reaction results, on the one hand, in the loss of the protective properties of the film (due to the cracking), and, on the other hand, in the heating of the formed cracks These concurrent effects give rise to the pulsations.

It should be noted that the pulsating combustion is not observed in the case of CO_2, because the powerful heat release in the gas phase leads to high rates of evaporation and reduces the role of the heterogeneous reaction.

In both CO_2 and CO, the increase in the density of the surface coating is observed with increasing ambient temperature. In the case of CO, this results in the onset of the second regime of heterogeneous combustion in the range of temperatures from 1230 to 1272 K. Furthermore, when the temperature exceeds 1272 K, vapor-phase combustion is observed again. This high-temperature vapor-phase regime is characterized by vigorous ejection of metal vapor through ruptures in the surface coating.

Concluding Remarks

The available theoretical models consider the ignition of a metal particle as either the breakdown of thermal equilibrium with a constant kinetic law of oxidation or the loss of the protective properties of the film. Little attention has been paid to the mechanism of heterogeneous reaction. In a new theory of metal ignition and combustion, one should take into consideration the metal vapor–oxidizer reaction in the pores of the surface film, the capillary flow of liquid metal, the growth and structural variations (healing) of the film, and therefore, the change in the kinetic law during oxidation and combustion. Allowing for these factors would make it possible to develop a new model of metal particle ignition and combustion reflecting adequately the observed multiplicity of combustion regimes, including the pulsating regime.

COMBUSTION OF DUST

V. G. Shevchuk, A. V. Florko

Odessa State University, Odessa, Ukraine

Dust–air mixtures of solid combustible particles, as well as gaseous mixtures, represent typical examples of chemical active media, i.e. the media with distributed nonlinear sources of energy and diffusive interaction between the elements of the media (in general, the diffusive interaction is realized by heat conduction and diffusion). Depending

on the proportion between nonlinear kinetic and diffusive factors the following asymptotic regimes of conversion are possible: the induction (distributed) regime when the kinetics limits the process; diffusion-controlled regime characterized by the inverse proportion of the factors; autowave regime when both factors are comparable. As regards autowave combustion, the nonlinearity of hydrodynamic rather than thermokinetic type plays the dominant role. This determines the existence of the various hydrodynamic regimes of flame propagation, including laminar, oscillatory, turbulent and intermediate between these.

Odessa State University has long been conducting investigations of the distinctive features of dust-air premixed combustion in comparison with gas combustion. In dusts, the intrinsic scales are related to the particle size and the average distance between particles together with the external geometrical scale of combustion system. As regards the phenomena pertaining to the external scale, a profound similarity between ignition and combustion processes in dusts and gases exists in terms of the techniques employed in studying dust and gas self-ignition, the existence of nonadiabatic lean flammability limits (quenching in narrow channels), the conditions of realization and mechanisms of laminar, oscillatory, turbulent and intermediate regimes of autowave combustion, the criteria of free-convection instability of the flame front, the characteristics of single- and two-phase diffusive bunsen flames, etc.

In dusts, the components are mixed on the macroscopic level, in contrast to gases, where the mixing occurs on the molecular level. This leads to the dependence of all ignition and combustion characteristics on the intrinsic parameters of a dust, the particle size r_0 and the distance between particles l_0, expressed in terms of ignition temperatures, ignition delay times and combustion times as functions of r_0 and l_0. In Bunsen diffusive flames, the disperse phase strongly affects the temperature and concentration fields as well as the integral characteristics (the length and shape of the flame brush).

As regards autowave regimes of combustion, the addition of a disperse phase to a combustible mixture of given chemical combustion makes it possible, in contrast to gases, to considerably change the rate of flame propagation and its stability and even obtain the hydrodynamic regime of combustion by varying fuel dispersion. In particular this is evidenced by the existence of the adiabatic lean flammability limit and its dependence on the particle size, the direct and inverse cascades of transitions "laminar ↔ I-type oscillatory ↔ II-type oscillatory ↔ turbulent flame", the instability of laminar flames with respect to gravity-induced stratification in tubes, etc.

Another distinctive feature of dust–air mixtures (particularly disperse metals) is the formation of disperse condensed combustion products, which generates additional space and time scales determined by the product particle size and spacing. These phenomena give rise to a number of specific features of two-phase combustion. In the first place, this concerns radiative characteristics, which have been studied using well-developed optical techniques for simultaneous measurements of atomic, molecular and continuous spectra over the wave length range 0.25-6 μm with high spectral ($\sim 2 \cdot 10^4$), spatial

212

($\sim 50\,\mu$m) and temporal (to 10^2 sp/s) resolution. These studies involved diagnostics of both individual emitters (single oxide particles and the flame zone as a whole (integral flame characteristics)). It has been shown that spectral characteristics of individual emitter are related to the structure of the crystalline lattice, the nonstoichiometry of the oxide, the presence of additives, and the geometric limitations in terms of the emitter size ($\leq 0.1\,\mu$m). In particular, the attenuation of radiation by particles is strongly influenced by temperature, in contrast to scattering. For solid particles (such as MgO), the scattering depends on the wavelength. Radiative parameters of liquid drops (Al_2O_3, ZrO_2, and TiO_2) exhibit no specific trends and agree with those predicted by the Mie theory for high temperatures (~ 3000 K). Such information can serve as a basis for estimating integral radiative parameters of burnt dust. The integral emission coefficients obtained are: $\varepsilon_{Mg} = 0.05$, $\varepsilon_{Al} = 0.03$, $\varepsilon_{Zr} = 0.01$, and $\varepsilon_{Fe} = 0.3$.

The studies of the dispersion of Al, Mg, Zr, Ti, Fe dust-air combustion products have revealed a slight sensitivity of dispersion (0.05–$1.0\,\mu$m) to the combustion conditions and fuel type. It was experimentally shown that the electrophysical phenomena form the basis of such stability. The burnt dust–air mixture is a low-temperature plasma with condensed disperse phase. Negative ions O_2^- are the oxide condensation centres. The average distance between the positively charged oxide particles ($Z \approx 20$–$100|e|$) was found to be close to the Debye radius of the electron component. There is a deep feedback between the generation rate of particles and their concentration. Its essence lies in the following. The molecular ions O_2^- and small negatively charged particles of radius smaller than the critical one ($r_k \leq 0.5$–1.0 nm) are affected by "destructions" at c-particles concentration $N \sim 10^{17}$–10^{18} m^{-3} (depending on metal type). This leads to the asymptotic concentration N. The first process is due to the "destructions" O_2^- as result of their interaction with large positive c-particles, the second one is due to the coagulation of unlike charges (negative subcritical and positive stable c-particles). As a result of the steady-state concentration N and spatially homogeneous distribution of c-particles due to their repulsive interaction, the final size r_c of oxide particles is weakly influenced by the combustion conditions, for instance $r_c \sim (B)^{1/3}$ (where B is the fuel concentration).

Thus, the hydrodynamic, electrophysical and optical phenomena are all closely linked, and constitute a single method base for investigating the dust combustion process.

References

[1] Shevchuk V. G., Goroshin S. B., Klyachko L. A., Ageev N. D., Kondratyev E. N., Zolotko A. N. *Fizika Goreniya Vzriva*, 1980, **16**, 1, 57–63 (in Russian).

[2] Kondratyev E. N., Shevchuk V. G., Polishcuk D. J. *ibid*, 1981, **17**, 5, 125–127 (in Russian).

[3] Shevchuk V. G., Kondratyev E. N., Zolotko A. N., Smirnov V. V. *ibid*, 1982, **18**, 5, 70 (in Russian).

[4] Shevchuk V. G., Bezrodnukh A. K., Boichuk L. V., Kondratyev E. N. *ibid*, 1988, **24**, 2, 85-90 (in Russian).

DETERMINATION OF REACTIVITY PARAMETERS ON MODEL CARBONS, COKES AND FLAME-CHARS

Lasse Holst Sørensen, Erik Gjernes, Thomas Jessen

Department of Combustion Research, Risø National Laboratory, DK-4000 Roskilde, Denmark

Abstract

Reactivity profiles have been defined and measured using thermogravimetry for dense metallurgical Longyear coke, polymer-derived Carboxen 1000 porous active carbon, and three flame-chars [1], Illinois #6, Pittsburgh #8, and Blue #1. For each sample, it has been found that the reactivity profile can be split into a chemical kinetics factor and a structural profile describing reactivity evolution. Determination of the structural profiles has been performed for reaction rates varying over 2 orders of magnitude and for burn-out depths between 20% and 80%. The apparent reaction order and activation energy in oxygen have been estimated over a 100 K temperature range (cases vary from 573 K to 773 K) and the maximum oxygen partial pressure range of 0.01–1 atm. For different samples, the reaction orders vary between 0.65 and 0.90 and the activation energies between 119 and 146 kJ/mole. Over the pressure–temperature domain considered, the reactivity varies considerably, but the structural profile is approximately invariant, i.e., each sample consistently exhibits the same structural evolution over a broad span of kinetic conditions. The structural profile is different for each sample. In the 20% to 80% burn-out range, Carboxen undergoes a four times increase in reactivity, while for coal-derived chars the reactivity decreases by a factor of two to five. These results emphasize the importance of a rational understanding of the structural evolution of a given sample in evaluating kinetic parameters. Our method of obtaining kinetic parameters is discussed, and, after isolating the structural effects, these are described in terms of generalized unipore/unigrain models [2]. It is further described how a comparison of structure-dependent sample reactivity can be performed and used for

ranking char reactivity. The measured reactivity and the derived reactivity indices of the coal-derived chars are found to compare well with high-temperature data found in literature [3].

Theory

The *reactivity* R_M of a char is defined in terms of conversion rate as

$$R_M = -\frac{1}{M}\frac{dM}{dt},\tag{1}$$

where M denotes the mass of the organic part of the sample. In general, R_M is a function of temperature, oxygen partial pressure, total pressure and the burn-out depth $X = (M_0 - M)/M_0$. At a fixed total pressure, it may be advantageous to split the functional dependence into the chemical kinetics term r_c and the structural profile $f(X)$, hence

$$R_M = r_c(T, P_{O_2})f(X).\tag{2}$$

Reactivity vs. burn-out depth at fixed temperature and O_2 partial pressure, $R_M(X)|_{T,P_{O_2}}$, yields a *reactivity profile* (RP) summarizing the effect of internal surface, active/reactive sites, and pore evolution.

The present work emphasizes the importance of a reliable estimation of the structural profile, prior to the evaluation of kinetic parameters. Since the RP is often a directly measured quantity, the kinetic term r_c can only be obtained when the structural profile is known.

The RP was obtained by continuously monitoring the reactivity R_M over a broad burn-out range at fixed temperature, total and O_2 partial pressure. The validity of Eq. (1) was tested by repeatedly observing the structural profile at various temperatures and pressures. If the structural profile is invariant over a sufficiently broad T–P domain of interest, the effects of 'structure' and 'kinetics' can be dealt with separately. One may then attempt a theoretical prediction of the RP, based on structural confederations and pore evolution models.

Studying the three flame-chars, the metallurgical coke and the synthetic active carbon over a 100 K temperature range and O_2 partial pressures ranging from 0.01 atm to 1 atm, we have found that the structural profiles are essentially constant, i.e., each sample undergoes the same evolution in terms of reactivity, regardless of the reaction rate. However, pronounced variations exist between different samples. While the coal-derived chars show a two to five times decrease in reactivity with burn-out depth increasing from 20% to 80%, Carboxen active carbon exhibits a four times increase over the same burn-out range. Thus, the relative reactivity may change by as much as a factor of 20 during the process, due to the difference in structural evolution. These results indicate that due attention should be paid to the RPs, when deriving and comparing kinetic parameters.

A random pore/grain model, recently generalized by the authors, will be used to fit, discuss and compare the RPs. The generalized models describe the evolution of available reactive sites rather than the pore surface area.
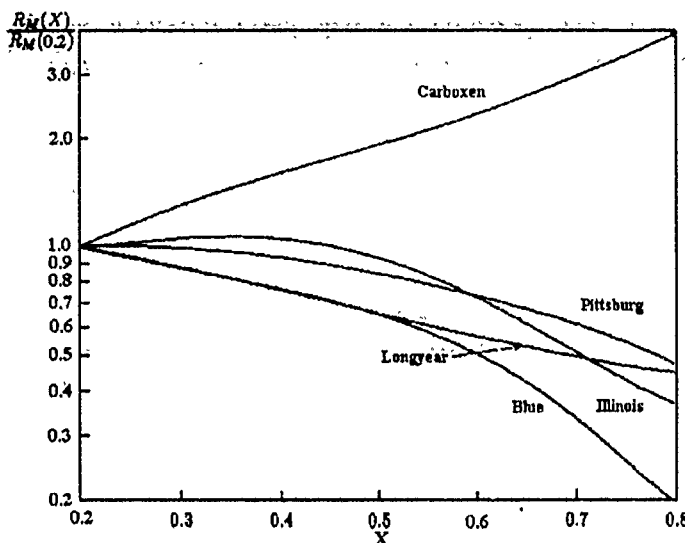
Figure 1: Reference reactivity profiles for Carboxen, Pittsburgh #8, Illinois #6, Blue #1 and Longyear cokes normalized by R_m at $X = 0.2$.

Finally, the knowledge of the RP for a given sample allows one to parametrize the burn-out dependence of the reactivity in order to obtain a reactivity measure incorporating structural effects. Thus, the possibilities for obtaining a reactivity index and carrying out a fuel ranking program will be discussed.

Experimental

A dense metallurgical coke prepared by coking highly volatile Longyear coal for approximately 30 hours in a coke oven, Carboxen 1000 porous active carbon, and three selected flat-flame-burner chars, Pittsburg'. #8, Illinois #6 and Blue #1 pyrolyzed at 1500–1700 K have been characterized by thermogravimetric analysis. A 'SDT 2960 Simultaneous TGA–DTA' from TA–Instruments was used in the experiments. The samples were heated in oxygen to the final temperature and then weighed under isothermal conditions during burn-out. Only the experiments where the measured sa nple temperature was within ±1 K of the preset value were used in the data interpretation. The oxygen concentration was varied from 1 to 100% in nitrogen at atmospheric pressure using two calibrated Bronkhurst HI–TEC flow meters and a manifold. In a single experiment (100% O_2 at 773 K), the flow was varied from 50 to 500 ml/min, and in another experiment the oxygen concentration was varied in situ.

Method and Results

For each carbon, the RPs at three temperature levels and various fixed oxygen partial pressures were measured. For each fuel, all RPs were normalized with respect to a reference RP, in order to obtain the average reactivity over the 20–80% burn-out
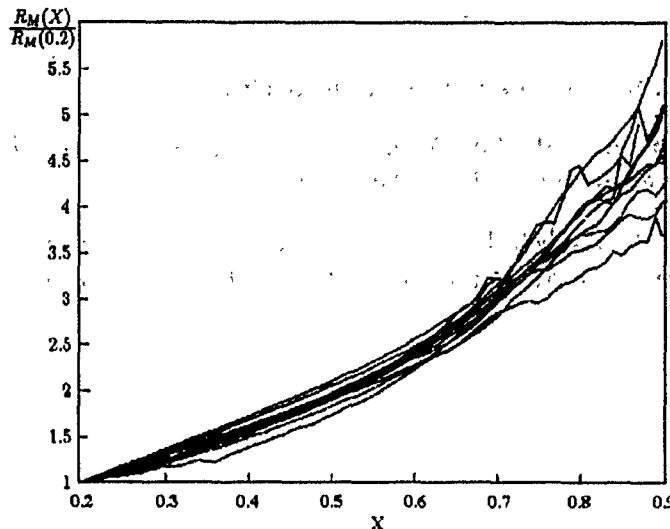
Figure 2: Normalized structural profiles for all Carboxen cases investigated (673–773 K and 1% to 100% O_2). The value of R_M varies by the order of 100.

range relative to the reference value. The estimated values can then be used to derive the kinetic parameters, i.e., the activation energy and the reaction order.

Figure 1 shows representative structural profiles for various samples. The three chars and the coke show reactivities decreasing with increasing burn-out depth, while Carboxen exhibits the opposite trend. Attention should be paid to the pronounced variations in relative reactivity over the burn-out range considered.

Figure 2 shows the structural profiles measured for Carboxen. They were obtained in the temperature range of 673 K to 73 K, with oxygen concentration varying from 1% up to 100%. In the 20% to 80% burn-out interval, the profiles have the same shape, which justifies the use of the reference RP. The diverging trend in the last portion of the burn-out is due to the uncertainty in determining the residual mass. The residual mass M enters Eq. (1) as the denominator and thus magnifies any uncertainties as M goes to zero.

Conclusion

Pittsburgh #8, Illinois #6, and Blue #1 chars, as well as Longyear coke and Carboxen 1000 porous active carbon, can all be described in terms of reactivity profiles (RP) which parametrize their structural behavior with respect to burn-out. These structural effects must be taken into account when deriving kinetic data. The physical interpretation of the RPs is given in terms of unipore/unigrain models.

References

[1] Sørensen, L. H., Bide, O., Peck, R. E. To be published.

[2] Jessen, T., Sørensen, L. H. *Proc. Nord. Seminar on Comb. and Gasification Reactivities of Solid Fuels.* Jyväskylä, Finland, 1993.

[3] Tørslev Jensen, P., Mitchell, R. E. *Energy Research Project No.1323/87–16.* Laboratory of Heating and Air Conditioning, Technical University of Denmark, 1993.

THE COMBUSTION MECHANISM OF AMMONIUM NITRATE AND ITS MIXTURES

V. A. Strunin, A. P. Dyakov, L. B. Petukhova, G. B. Manelis

Institute of Chemical Physics in Chernogolovka, Chernogolovka, Russia

Ammonium nitrate (AN) is of interest as an oxidizer in various compositions (explosives, solid propellants) and as a representative of ammonium salts, of which ammonium perchlorate (AP) has been examined in detail.

AN in its pure state is incapable of deflagration differing from AP in this respect. From the book by A. P. Glaskova [1], it follows that AN can burn only with additives such as compounds of metals of variable valency, the salts of alkaline metals or organometallic compounds. Most of the mixtures begin to burn at 50 atm, but some of them, e.g., with potassium chromate, are capable of deflagration at atmospheric pressure.

We consider at first the chemistry of the processes occurring in the combustion wave. Thermal decomposition of this salt proceeds in two modes: dissociation to ammonia and nitric acid, their evaporation and decay to nitrogen oxides, water, nitrogen and oxygen. The main features, as compared to AP, are:

1. The salt decomposes during combustion in the liquid phase.

2. The concentration of the acid formed in the liquid phase, as a result of equilibrium dissociation, is greater, since nitric acid and is a weaker acid than perchloric acid.

3. The volatility of A I is higher and, respectively, the temperature of the burning surface is lower.

Table 1: Combustion characteristics of AN at 70 atm.

	v, cm/s	T_s	f	Q, cal/g	n	k
theory	0.34	790	0.51	150	1.04	3.4
experiment	0.3–0.6*	—	—	—	0.8–0.9	unstable

*with 5% additives of NaCl, BaCl$_2$, Cr$_2$O$_3$ [1]

4. The oxidizing ability of AN decomposition products, as compared to ammonia, hydrocarbon and other fuels, is weaker.

Taking into consideration these features, we calculated the combustion characteristics of AN using the model of condensed-phase combustion of the low-volatile substances [2] employing the ideas of Ya. B. Zel'dovich [3].

An essential feature of this model is that the surface temperature and the thermal effect in the condensed phase, which are very important parameters in this mechanism, can be obtained from the mathematical equations involving the rate constants of decomposition and evaporation without using any arbitrary assumptions such as those brought forward in some combustion models. In our calculations, we used the kinetic [4] and thermodynamic [5] constants of AN. The results obtained and experimental data are presented in the Table 1. Here v is the burning rate, T_s is the temperature of the surface, f is the fraction of evaporation, Q is the thermal effect in the condensed phase, n is the pressure exponent, k is the stability criterion, which is > 1 in the unstable region [6, 7].

It is seen that there is a rather good agreement between theory and experiment.

The dependence of the burning rate on the pressure of AN composition has been investigated over a wide pressure region [1]. To obtain an additional information about the mechanism of AN combustion we used the method of smoothing of experimental points (spline method) with subsequent computation of the pressure exponent in any narrow pressure interval [8]: $n = p(v_2 - v_1)/v(p_2 - p_1)$.

The results are shown in the Fig. 1. The exponent n first decreases from ~ 1 to 0.1–0.4 in the range of 50–400 atm, then the curve exhibits a minimum which may be explained by the reduction of AN evaporation fraction and the transfer of combustion to the instability region. The increase in n at high pressures is apparently caused by the gas-phase oxidation reactions involving nitrogen oxides, oxygen and the organic components of the mixture. The general pattern of the $n(p)$ dependencies is similar to that for perchlorate compositions [9], which validates the same mechanism of their combustion.

A remarkable feature of AN combustion is the paradoxically strong effect of alkaline metal salts (chlorides, nitrates) which do not practically catalyze the decomposition of AN. However, similar effects have also been revealed for other ammonium salts,
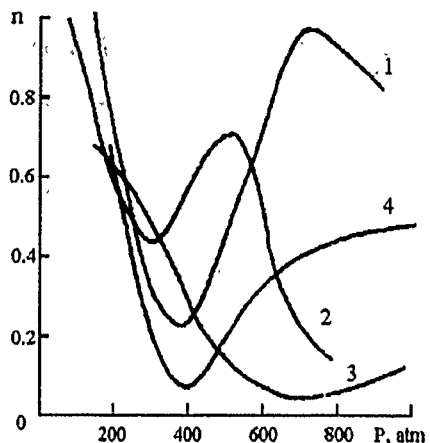
Figure 1: Dependence of the pressure exponent on pressure. *1* — AN (76.2%), urea (19.5%), copper oxinate (4.3%); *2* — AN (85%), vinyl polymer (15%); *3* — AN (95.2%), boronsalicylic acid (4.8%); *4* — AN (95%), ferric chloride (5%).

especially for hydrazine nitrate [10]. The mechanism of this influence, proved by the chemical analysis of the surface layer of extinguished samples and by the appropriate modelling, is simple and consists in the accumulation of the additive at the burning surface, a decrease in evaporation of the main component, an increase in the surface temperature and a respective increase in the burning rate.

We also studied combustion of several compositions based on AN. The mixture of AN, rubber and aluminium exhibits rates $\sim$ 3 times lower than those of similar AP propellants. At 100 atm, the rate is equal to 0.34 cm/s. The $n(p)$ treated by the spline method is characterized by a significant decrease in n with p, but addition of some catalysts improves the dependence: brings down the value of n and makes it nearly constant in this pressure range. Ferrocenyl copper acetylide turned out the best catalyst among the additives examined because it contains two catalyzing elements and an active unsaturated bond.

Consequently, it may be concluded that the combustion laws of AN compositions are explained in terms of the mechanism in which the decomposition in the condensed phase plays the main role together with an additional influence of the gas phase reactions during combustion and it is characteristic for most ammonium salts compositions.

References

[1] Glaskova A. P. *Catalysis of Explosives Burning.* Moscow, Nauka, 1976 (in Russian).

[2] Manelis G. B., Strunin V. A. *Comb. Flame*, 1971, **17**, 69.

[3] Zel'dovich Ya. B. *Zhurnal Experimentalnoi Teoreticheskoi Fiziki*, 1942, **12**, 498 (in Russian).

[4] Rubtzov Yu. I., *et al. Kinetic Laws of Thermal Decomposition of Ammonium Nitre.* Preprint of IChPh, Chernogolovka, 1990 (in Russian).

[5] Feick G. *J. Am. Chem. Soc.*, 1954, **76**, 5858.

[6] Novozhilov B. V. *Zhurnal Prikladnoi Mekhaniki Tekhnicheskoi Fiziki*, 1965, **4**, 157 (in Russian).

[7] Strunin V. A., Manelis G. B. *Fizika Goreniya Vzriva*, 1971, **4**, 498 (in Russian).

[8] Petukhova L. B. *et al. ibid*, 1989, **3**, 36 (in Russian).

[9] Strunin V. A. *et al. ibid*, 1993, **2**, 68 (in Russian).

[10] Zhevlakov A. F. *et al. ibid*, 1976, **12**, 185 (in Russian).

IGNITION OF MAGNESIUM IN VARIOUS OXIDIZING MEDIA AT REDUCED PRESSURES

A. E. Valov, E. I. Gusachenko, V. I. Shevtsov

Institute of Chemical Physics in Chernogolovka, Chernogolovka, Russia

The effect of pressure on ignition of metal particles is very important for the understanding of high-temperature oxidation. According to the theory of vapor-phase ignition and combustion of metal particles, an increase in pressure results in increasing particle heating [1]. However, according to experimental results, the induction time actually does not depend on pressure for the particles of aluminum [2] and magnesium [3]. To this date, there have been very few experimental studies of the effect of gas pressure and oxidizer concentration in the gas on the ignition of metals.

Therefore, in our work we studied the effect of (a) the pressure of the oxidizing medium, (b) the oxidizer concentration and (c) the chemical composition of the oxidizing medium, on the ignition of magnesium particles. In addition, we explored the possibility of the description of magnesium ignition at various pressures of the medium and various concentrations of the oxidizer by the vapor-phase oxidation model.

All experiments on single particle ignition were carried out using the device described in detail in [4].

Figure 1 shows the effect of air pressure on the dependence of the critical ignition temperature on particle sizes. The curves shift to the right with decreasing pressure. The ignition temperature of relatively small particles (smaller than 100–120 μm) decreases with a increase in pressure, whereas large particles (larger than 120 μm) ignite, within the experimental accuracy, at the same temperature for all pressures.

The effect of oxygen concentration on the ignition (Fig. 2) was studied at the total pressure 1 atm and the content of oxygen in nitrogen 20%, 5% and 1%. At the oxygen content lower than 1%, the flash was not observed. It can be seen that decreasing oxygen concentration in oxidizing media leads to the same results as decreasing total gas pressure at a constant concentration of oxygen, namely to higher ignition temperature for small particles (smaller than 150 μm).
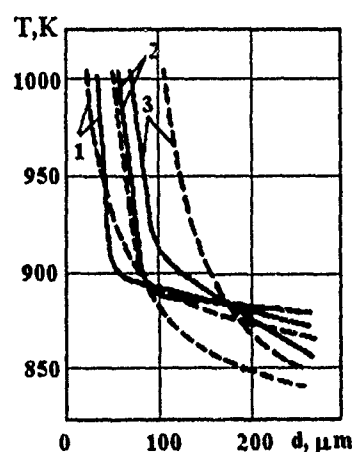
Figure 1: Dependencies of the critical temperature of ignition of magnesium in air on the particle size. Solid curves are the experimental data, dashed curves are the calculated results: (1) 10^5 Pa, (2) $5.3 \cdot 10^3$ Pa, (3) $5.3 \cdot 10^2$ Pa.
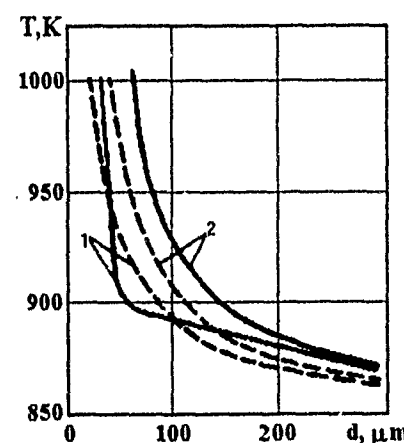
Figure 2: Effect of oxygen content on the critical ignition temperature for magnesium particles. Solid curves are the experimental data, dashed curves are the calculated results: (1) 20% of oxygen in nitrogen, (2) 5% of oxygen in nitrogen.

Taking into account the published data, we can take as reliable the fact that the contribution of metal vapour oxidation to the high-temperature magnesium oxidation becomes substantial at temperatures lower than the experimental ignition temperatures. Therefore, in our work we calculated the critical ignition temperatures by the

model of vapor-phase oxidation. The model takes into account evaporation of the metal and oxidation of its vapour in the process of ignition. Comparison of the predicted and experimental dependences shows that this model correctly describes the dependence of the magnesium ignition limit on the particle size at all air pressures and oxidizer concentrations in the mixture of oxygen and nitrogen.

We studied the ignition of single particles of magnesium in carbon dioxide. The dependences of the critical temperature of ignition on the size of initial metal particles at various pressures of carbon dioxide (Fig. 3) show that the critical temperature decreases with increasing particle size at all gas pressures studied. In addition, the ignition temperatures decrease with a decrease in pressure, whereas in air the temperature rises.

The experimental dependences of the critical ignition temperature on the particle size at various concentrations of carbon dioxide in argon (Fig. 4) show that a decrease in carbon dioxide concentration leads to an increase in critical temperature.
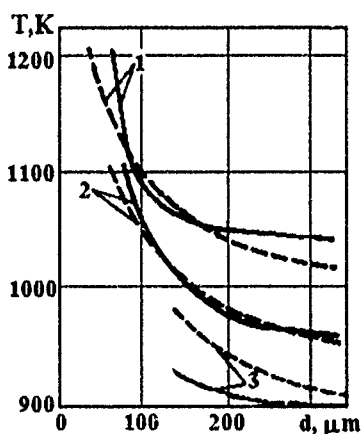
Figure 3: The dependencies of the critical temperature of ignition of magnesium on the size particle in carbon dioxide. Solid curves are the experimental data, dashed curves are the calculated results: (1) 10^5 Pa, (2) $5.3 \cdot 10^3$ Pa, (3) $5.3 \cdot 10^2$ Pa.
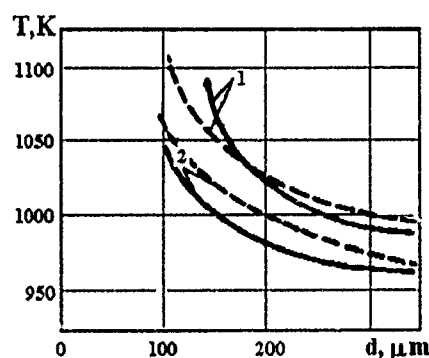
Figure 4: The dependences of the critical temperature of ignition of magnesium on the size of particles. Solid curves are the experimental data, dashed curves are the calculated results: (1) 2.6% of carbon dioxide in argon, (2) 5.3% of carbon dioxide in argon. The total pressure is 10^5 Pa.

The critical temperatures of ignition, calculated by the model of vapor-phase oxidation at various carbon dioxide pressures and concentrations in mixtures with argon, agree satisfactorily with the experimental results (Figs. 3 and 4).

References

[1] Lukin A. Ya., Stepanov A. M. *Fizika Goreniya Vzriva*, 1983, **19**, 3, 41 (in Russian).

[2] Belyaev A. F., Frolov Yu. V., Korotkov A. I. *ibid*, 1968, **4**, 3, 323 (in Russian).

[3] Shafirovich E. Ya., In: *Chemical Physics of the Processes of Combustion and Explosion. Combustion of Heterogeneous and Gaseous systems*, (Novozhilov B. V. Ed.), Chernogolovka, 1986, 62 (in Russian).

[4] Valov A. E., Gusachenko E. I., Shevtsov V. I. *Fizika Goreniya Vzriva*, 1991, **27**, 4, 3 (in Russian).

NUMERICAL SIMULATION OF ETHANE–AIR DIFFUSION FLAMES STABILIZED OVER A FLAT PLATE BURNER: COMPARISON WITH NORMAL AND MICROGRAVITY EXPERIMENTS

H. Y. Wang, J. L. Torero, L. Bonneau, P. Joulain

Laboratoire de Chimie Physique de la Combustion
Universite de Poitiers — UA 872 au CNRS
Domaine du Deffend, 86550 Mignaloux-Beauvoir, France

Abstract

A laminar diffusion flame is established over a horizontal flat plate burner when ethane is injected into a stream of air flowing parallel to burner. The geometric configuration corresponds to that of a wind tunnel with a test section 270 mm long and a rectangular cross section 120 mm wide and 90 mm in height. A 50 mm by 200 mm sintered-bronze porous burner is mounted on the floor of the wind tunnel symmetrically with respect to the flow direction at the distance of 35 mm from the air inlet [1]. This geometric configuration is used to carry out a numerical simulation with the aim of better understanding the effect of buoyancy on this type of flame. The results obtained by numerical simulation are compared with experiments conducted under normal gravity and microgravity conditions. The parameters studied are the velocity and temperature profiles, as well as the flame geometry. Numerical simulations and experiments have

been conducted for different air and gas forced flow velocities under both normal and microgravity conditions.

Description of the Numerical Model

A three-dimensional stationary numerical solution is obtained for the temperature and velocity fields corresponding to a laminar flame established in the wind tunnel such as the one described above. The chemical reaction is described by the flame sheet approximation, therefore, fuel, oxidizer, inert gases and products are assumed to undergo a single-step global reaction at an infinitely fast rate. The three-dimensional Navier–Stokes equations are used to describe the flow field. The coupling of momentum, energy and species equations is obtained using the Shvab–Zel'dovich formulation, where a linear combination of the partial differential equations corresponding to temperature, fuel (Y_F) and oxygen (Y_O) results in a mixture fraction equation without a source term.

The resulting equations that will be solved numerically are as follows:
For mass:

$$\frac{\partial(\rho u)}{\partial x} + \frac{\partial(\rho v)}{\partial y} + \frac{\partial(\rho w)}{\partial z} = 0$$

For momentum and mixture fraction:

$$\frac{\partial(\rho u\phi)}{\partial x} + \frac{\partial(\rho v\phi)}{\partial y} + \frac{\partial(\rho w\phi)}{\partial z} = \frac{\partial}{\partial x}\left(\Gamma_\phi \frac{\partial\phi}{\partial x}\right) + \frac{\partial}{\partial y}\left(\Gamma_\phi \frac{\partial\phi}{\partial y}\right) + \frac{\partial}{\partial z}\left(\Gamma_\phi \frac{\partial\phi}{\partial z}\right) + S_\phi$$

Here, Γ_ϕ is the transport coefficient and S_ϕ is the source term. Both of these are specific with respect to the variables u, v and w. The effects of gravity are incorporated through the momentum equation and S_ϕ is equal to zero for the mixture fraction equation.

Experimental Results

A series of experiments were conducted under normal and micro-gravity conditions where the parameters varied were the fuel and air forced flow velocities. Temperature measurements and video images were recorded. Microgravity experiments were carried out in a 5 s drop tower (ZARM, Germany) and on board of an aircraft performing Keplerian parabolas (CNES, Caravelle Aircraft). Under normal gravity conditions, the flame can be divided in two well-determined regions, the boundary layer region (where inertia dominates), and the plume region (where buoyancy dominates). In the boundary layer region, the air entrainment induced by the plume adds to the forced flow, resulting in flames stabilized closer to the burner and premature extinction. When gravity is eliminated, the plume region disappears; therefore, the overall air flow velocity is reduced to that of the forced flow, hence the stand-off distance increases and higher air forced flow velocities are necessary for extinction to occur. In microgravity, the flame stabilized along an almost straight line and periodically expanding reactive

225
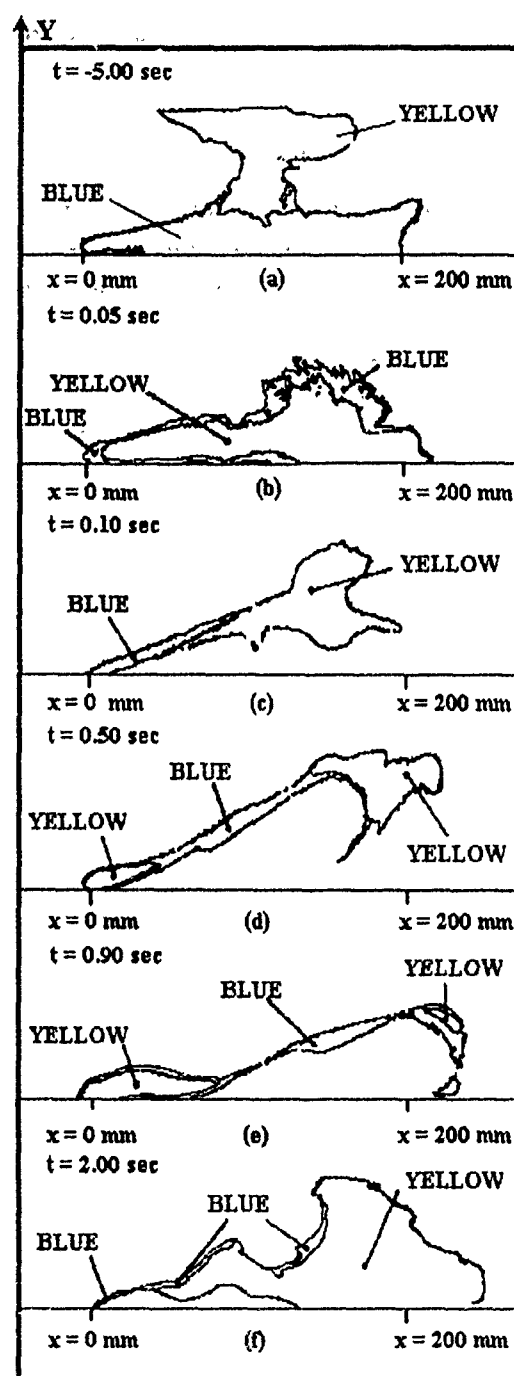
Figure 1: Processed images of a boundary layer diffusion flame in normal and micro-gravity.

Champ de temperature, K

Champ de temperature, K
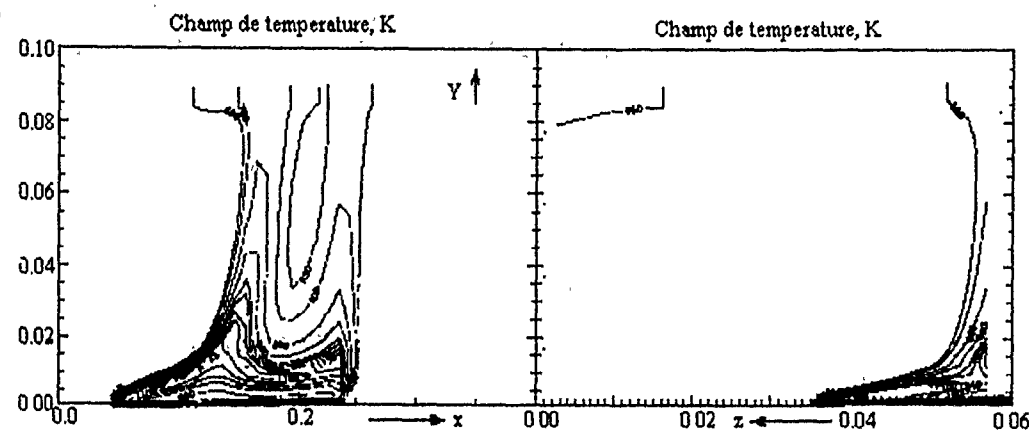
Figure 2: Temperature field obtained by a numerical simulation of a diffusion flame under normal gravity conditions.

Champ de temperature, K

Champ de temperature, K
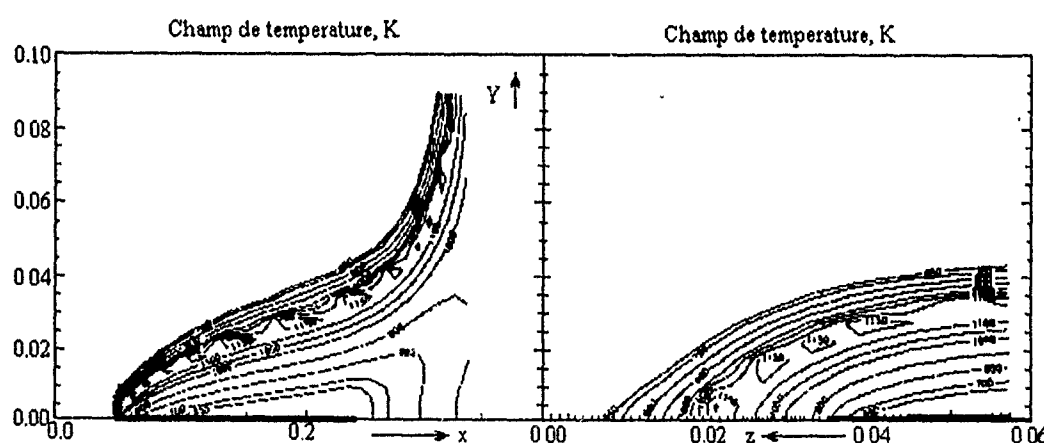
Figure 3: Temperature field obtained by a numerical simulation of a diffusion flame under micro-gravity conditions.

227

zones are observed. The reactive zones appear at the leading edge of the flame and enlarge as they propagate downstream and towards the walls of the wind tunnel in the direction perpendicular to the forced flow. A processed image of the first period after the disappearance of the gravitational acceleration is presented in Fig. 1. The images correspond to the flame developing at the air flow velocity 0.115 m/s and fuel injection velocity 0.0052 m/s, but its characteristics are similar to most of the other conditions studied.

Comparison and Conclusions

The temperature field presented in Fig. 1 was numerically obtained and presented in Fig. 2 for normal gravity and in Fig. 3 for microgravity conditions. It can be observed that the numerical simulation describes very well the geometry of the flame in the presence of gravity. On the contrary, in microgravity, the stationary model is not capable of describing neither the geometry of the flame nor the periodic development of reactive zones in the direction perpendicular to the forced flow plane. A simple scaling analysis, with diffusion neglected, seems to predict better the nature of the flame in microgravity [2]. By comparing the analysis to the numerical solution and experimental results, the limitations of the model are identified. It is clear that the model properly describes the structure of the buoyancy-induced flow and that the effect of buoyancy dominates the physical structure of the flame, which the numerical model is incapable of describing. Buoyancy is therefore the controlling factor determining the geometry of the flame in normal gravity, and, in its absence, a time-dependent interaction between a finite-rate chemical reaction and the species equations seems to be necessary to properly describe the geometry and structure of the flame.

References

[1] Bonneau L., Joulain P., Most J. M., Fernandez–Pello A. C. *AIAA–93–0826.* 1993.

[2] Torero J. L., Bonneau L., Most J. M., Joulain P. *Proc. 25th Symp (Int.) on Comb.,* The Combustion Institute, 1994 (submitted).

MECHANISM OF FLAME PROPAGATION IN FOAMS

V. V. Zamashchikov, N. A. Kakutkina, V. S. Babkin

Institute of Chemical Kinetics & Combustion, Novosibirsk, 630090 Russia
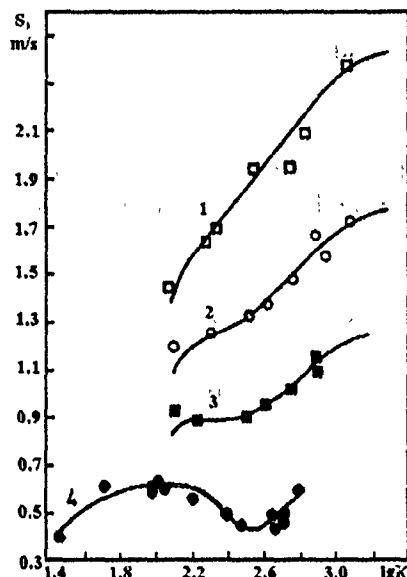
Figure 1: Dependencies of flame speed on expansion ratio. Points — experiment, curves — calculation: 1 — 15% H_2+air, $\chi = 2.8$, $\beta = 2.8 \cdot 10^{-3}$; 2 — 13% H_2+air, $\chi = 2.8$, $\beta = 2 \cdot 10^{-3}$; 3 — 11.6% H_2+air, $\chi = 2.8$, $\beta = 1.3 \cdot 10^{-3}$; 4 — 10% H_2+air, $\chi = 2.8$, $\beta = 4 \cdot 10^{-4}$.

Foam combustion is a complex physicochemical phenomenon involving such elementary phenomena as foam destruction, formation of liquid aerosol, combustion of the gas released from the foam etc. A number of processes accompanying foam combustion is responsible for the distinctive features of combustion wave propagation [1, 2].

One feature of combustion of water-based foams is nonmonotonic dependence of the flame speed S on the expansion ratio K including the range of K where increase in K results in a decrease in S (Fig. 1). This has been shown to be due to the effects of heat transfer from the gas to foam films and aerosol droplets forming upon the destruction of foam by the flame as described by the model developed in this work.

Foam combustion is modeled as a steady-state gas combustion with additional heat flux to liquid films and droplets. Let us make the following simplifying assumptions.

1. The heat consumed by droplets and films is consumed by their evaporation. The energy consumed by heating of droplets and films is insignificant for the total heat balance.

2. Relatively large droplets are considered, so that their evaporation in the flame front does not noticeably change their size.

3. The increase in the mass of gas due to the evaporation of droplets and films is inconsequential for the total balance of gas mass.

229

4. The flame front in each region is considered to be plane and laminar. The total increase in combustion surface area due to the burn out of gas bubbles is taken into account by the empirical turbulization factor χ.

5. Discrete foam films are replaced by an imaginary continuous film, the heat transfer to which equals the volume-averaged heat transfer to real films.

6. Three flame zones are introduced:

   - the preheat zone $(x < 0)$,
   - the narrow chemical reaction zone $(x = 0)$, and
   - the heat relaxation zone $(x > 0)$.

After the films have been destroyed, they are spontaneously dispersed to form an aerosol. Starting from the coordinate $-x_L$, foam combustion is considered as gas combustion with distributed water droplets.

The equations of energy and mass balances for the system under study are

$$\rho_0 u_n c \frac{dT}{dx} = \frac{d}{dx}\left(\lambda \frac{dT}{dx}\right) - Q_1 - Q_2 - Q_3 - Q_4 + QW$$

$$Q_1 = \frac{\chi u_n \rho_1 \beta c_w}{K}\frac{dT}{dx} \qquad Q_2 = \pi\lambda Nu d_1 n(T - T_a)$$

$$Q_3 = \pi\lambda Nu d_1 n c_w \frac{(T - T_a)^2}{H} \tag{1}$$

$$Q_4 = \pi\lambda Nu d_1 n \frac{c_w}{H}\frac{dT}{dx}\int_{-x_L}^{x}(T - T_a)\,dx$$

$$\rho_0 u_n \frac{da}{dx} = \frac{d}{dx}\left(\rho D \frac{da}{dx}\right) - W$$

where ρ_0, c, λ, and D are the density, specific heat, heat conductivity and diffusivity of the gas, a is the relative mass concentration of the fuel, Nu is the Nusselt number, c_w is the specific heat of water vapor, Q and W are the heat release and chemical reaction rate, respectively, n is the droplet number density, d_1 is the mean droplet diameter, ρ_1 is the density of detergent solution, β is the coefficient that takes into account a part of film liquid to be evaporated due to film destruction, u_n is the burning velocity of foam, H is the heat of evaporation. Term Q_1 pertains to the heating of the water vapor formed by evaporated foam films, and term Q_4 to that from evaporated droplets. Term Q_2 is the heat transfer to droplets, and term Q_3 is due to the heating of the

vapor, resulting from droplets, from the temperature of droplet surface T_a to the gas temperature T. The boundary conditions are

$$x = -x_L: \qquad T = T_1, \quad \lambda \frac{dT}{dx} = \frac{\chi u_n H \rho_1 \beta}{K}, \quad a = a_0, \quad \frac{da}{dx} = 0$$

$$x = 0 + 0: \qquad T = T_b, \quad \lambda_b \frac{dT}{dx} = q_p, \qquad a = 0, \quad \frac{da}{dx} = 0,$$

where q_p is the heat flux from the chemical reaction zone to the heat relaxation zone (q_p is obtained as a result of calculation), λ_b is the heat conductivity at $T = T_b$.

Assuming the Arrhenius dependence of W on temperature and the similarity of the profiles of fuel temperature and concentration and integrating Eq. (1), we get the expressions for the flame maximum temperature T_b and the flame speed S:

$$(T_b^0 - T_b) = \left[1 + \frac{(T_b - T_0)c_w}{H}\right] \left[\frac{\beta \chi \rho_1 H}{K \rho_0 c} + \frac{6 d_1 (T_b - T_0) \lambda (Nu\kappa^2 - Nu_1 \kappa_b^2)}{K d_3^3 u_n^2 (1 + F)}\right]$$

$$S = \chi u_n^0 \exp\left[\frac{E(T_b - T_b^0)}{2R(T_b^0)^2}\right] \qquad F = \frac{\chi \beta \rho_1 c_w}{K \rho_0 c} \tag{2}$$

Here, T_b^0 and u_n^0 are the flame temperature and the burning velocity of gas filling foam bubbles, Nu and κ are the Nusselt number and heat conductivity in the preheat zone, Nu_1 and κ_b are those in the combustion products, E is the activation energy, d_3 is the mean cubed droplet diameter.

Set of Eqs. (2) was solved numerically and the results were compared with the measured dependencies of the flame speed on expansion ratio for various foams. Parameters χ and β were chosen by the best agreement with experimental dependencies. The numerical results for $S(K)$ are shown in Fig. 1 by lines. We notice from Fig. 1 that the proposed model adequately describes all the basic features of flame speed dependencies on expansion ratio.

References

[1] Zamashchikov V. V., Kakutkina N. A., Pleslov A. A., Babkin V. S. In: *Problems of Combustion and Explosion*. Chernogolovka, 1989, 62 (in Russian).

[2] Zamashchikov V. V., Kakutkina N. A. *Fizika Goreniya Vzriva*, 1993, **29**, 3, 15 (in Russian).

SESSION 4. Turbulent Combustion

ON THE COMPUTATION OF THE VARIANCE OF TEMPERATURE FLUCTUATIONS AND ITS INFLUENCE ON NO PREDICTIONS FOR A GAS FLAME

A. Beretta*, N. Mancini*, F. Podenzani*, L. Vigevano[†]

*ENTRICERCHE, 20097 S. Donato Milanese (Milan), Italy

[†] Dipartimento di Ingegneria Aerospaziale, Politecnico di Milan, Via Golgi 40, 20133 Milan, Italy

An experimental and theoretical study has been carried out to investigate the influence that the statistical description of temperature fluctuations has on the total NO emission predictions in a non-premixed gas flame. A small-scale cylindrical combustor has been simulated, using an existing CFD code which describes the flow and combustion processes, supplemented with a decoupled NO kinetics model that solves the transport equation for the average NO mass fraction. The computed results are then compared with in-flame measurements of temperature and species concentrations.

The combustion model integrates the transport equations for the Favre-averaged values of the mass fraction of all but one of the chemical species included in the assumed kinetic mechanism. In the present study, a two-step global oxidation reaction mechanism was considered. The average rate of formation/destruction of the i-th species due to the two reaction steps was controlled either by an Arrhenius kinetic rate expression or by the mixing of turbulent eddies related to fluctuating species concentrations [1].

The formation of thermal NO was represented by the classical extended Zel'dovich mechanism, with an additional equilibrium hypothesis, in order to express the O atom concentration in terms of molecular oxygen concentration. This assumption is usually introduces in simulations of complex turbulent flames, when the simple combustion model employed precludes the knowledge of the radical pool. Prompt NO was governed by the global mechanism proposed by De Soete. The average production term $\overline{S}_{NO}$ was computed using the instantaneous NO formation rate and taking into account the effect of turbulent fluctuations of temperature. Using a statistical approach and assuming the gas temperature, suitably normalized, to be the independent variable, the mean turbulent reaction rate $\overline{S}_{NO}$ was computed as follows:

$$\overline{S}_{NO} = \int_{0}^{1} \frac{d[NO]}{dt} \frac{\overline{\rho}}{\rho(\theta)} \tilde{P}(\theta)\, d\theta$$

The assumed shape for the density-weighted pdf $\widetilde{P}(\theta)$ is a beta-function with coefficients related to the mean value $\overline{\theta}$ and to the variance $\widetilde{\theta''^2}$ of the normalized temperature.

Various approaches to computing the second moment $\widetilde{\theta''^2}$ were employed. The first two lead to algebraic expressions obtained by either simply taking the variance equal to a constant fraction of its maximum local value or assuming equilibrium between the production and the dissipation terms in the second moment transport equation [2]. The third, more rigorous, approach is based on the solution of the transport equation for the second moment of the sensible enthalpy [3], which is then related to the temperature variance.

Special care had to be taken of the source term $\overline{h''S_h}$ in the enthalpy variance equation, resulting from the source term S_h in the enthalpy conservation equation; S_h is the sum of two contributions, $S_h = S_c + S_r$. The S_r term is responsible for radiation, $S_r = Q_A - k_a\sigma T^4$, where Q_A is the absorbed radiant energy, in the radiation model; a flux model was applied in this study. The S_c term is due to combustion, $S_c = f\Sigma_j R_j\Delta h_{R,j}$, where R_j is the rate of the j-th combustion reaction considered, expressed in the Arrhenius form, and $\Delta h_{R,j}$ is the corresponding thermal effect of reaction. The factor f reflects the influence of turbulent mixing on the combustion process. In a previous investigation of premixed combustion [2], f was chosen to represent the fraction of turbulent fine structures in the total gas mass. In the present work on diffusion flames, the latter choice in the computation leads to abnormally high values of the temperature variance. An indication of the influence of turbulence on combustion can be, however, derived from the combustion model itself, where the reaction rate is considered to be the lower one of the kinetics-controlled rate R_k and the diffusion-controlled rate R_d. The factor f is then computed as $f = R_d/R_k$.

Since the high values of the temperature fluctuations that characterize the combustion region make a linear approximation rather inaccurate, the exact forms for S_c and S_r are retained, and the source term $\overline{h''S_h}$ is computed iteratively by convolution with the density-weighted pdf.

The temperature and NO distributions computed with the above models are compared with experimental data. The experiments were performed in a cylindrical water-cooled furnace, 0.6 m in diameter and 2.0 m long. The furnace was operated with a gas burner, designed by IFRF, at the heat input of 450 kW. Methane was injected through a circumferential array of holes in the central bluff body perpendicularly to the swirling air stream. The swirl number was set equal to 0.5 and the air excess to 5%. Temperature and species (O_2, CO_2, CO, NO, NO_x) concentration data were obtained using suction probes and standard instrumentation.

The computed stream function and temperature fields are shown in Figs. 1 and 2, where strong expansion of the swirling jet and a large axial recirculation region can be observed. Figure 3 compares the computed and measured temperature distributions at two different locations of the furnace. The comparison with experimental data also allows us to ascertain the influence of the temperature variance calculation procedure on the emission predictions. For the sake of brevity, only the results obtained using the modified differential approach are shown in Fig. 4.

233
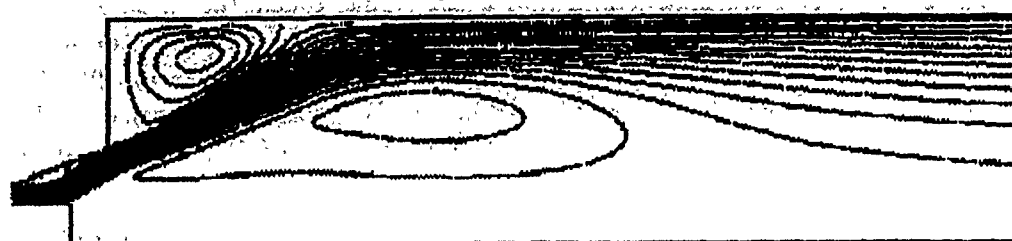
Figure 1: Computed streamlines inside the furnace.
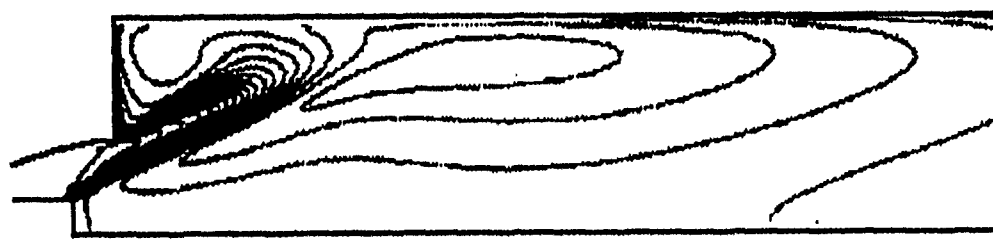
Figure 2: Temperature distribution inside the furnace.
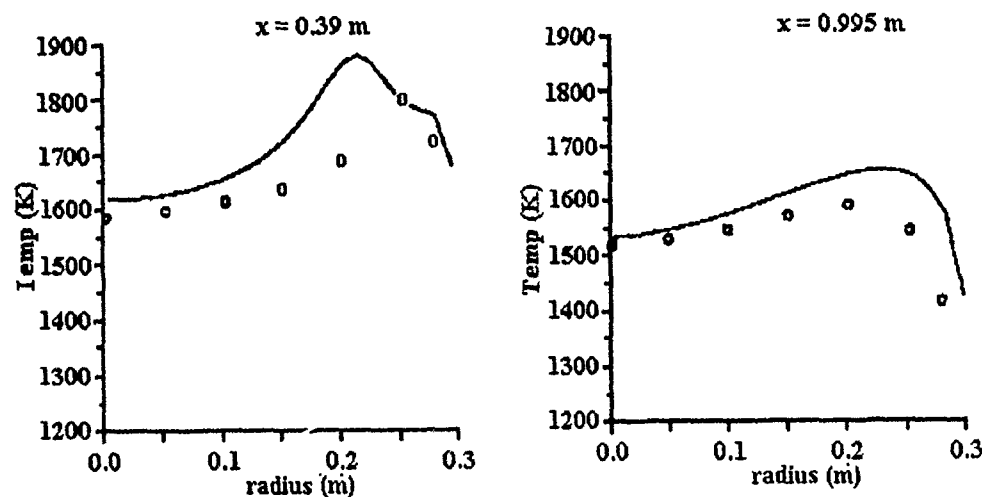
Figure 3: Temperature distributions at two locations in the furnace (symbols: experiments, solid line: computation).

234
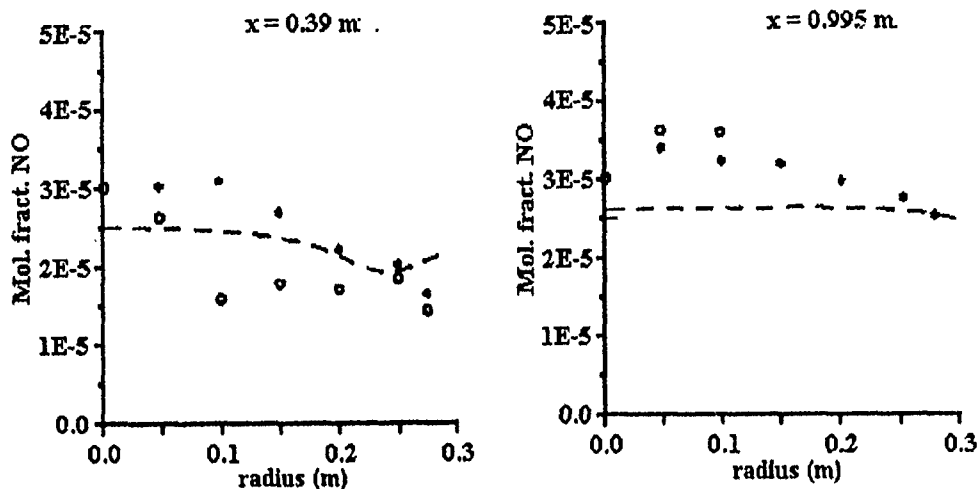
Figure 4: NO concentration distributions at two locations in the furnace (symbols: experiments, solid line: computation).

We conclude that modeling of the variance transport equation is required to obtain correct NO predictions, and computed results are sensitive to the method by which the combustion contribution to the variance source term is handled.

References

[1] Magnussen B. F., Hjertager B. H. *Proc. 16th Symp. (Int.) on Comb.*, The Combustion Institute, 1977, 719–727.

[2] Mancini N., Podenzani F., Vigevano L. *Proc 2nd Int. Conf. on Combustion Technologies for a Clean Environment*, Lisbon, 1993.

[3] Zinser W., Schnell U., In: *Fundamentals of the Physical–Chemistry of Pulverized Coal Combustion*, (Lahaye J., Prado G. Eds.), NATO ASI Series, Martinus Nijhoff Publ., Dordecht, 1987.

THE HELICAL STRUCTURE OF A FLAME IN A SWIRL FLOW

A. A. Borissov, P. A. Kuibin, V. L. Okulov

Institute of Thermophysics, Novosibirsk, Russia

One way to stabilize a flame is to swirl the flow of a mixture. A theoretical model providing a means to describe the flame shapes arising in this case is presented here.

The statement of the combustion problem here is similar to the kinematic statement put forward by Ya. B. Zel'dovich [1]. Suppose the flow is steady, and combustion proceeds at the flame front to be determined. The flame propagation does not change the gas properties. The flame surface moves relative to the gas along the normal to its own surface at a certain normal burning velocity.

In contrast to Ya. B. Zel'dovich, let us consider the combustion of swirling gas in a cylindrical tube. A very simplified hydrodynamic model, namely Rankine vortex, was used to approximate the swirl flow in the preceding works [2]. Indeed, the flow with a strong swirl and non-zero axial velocity must have a helical structure, which was not taken into consideration previously. Here, the investigation is based on a new analytical solution derived by the authors for the problem of the swirl flow induced by the helical vortex in the cylindrical tube [3]. The problem was solved within the framework of the theory of inviscid incompressible flows. The authors have derived new analytical formulas for all components of the velocity induced by an infinitely thin helical vortex filament in the tube. The exact solution was written out as infinite series in terms of the modified Bessel functions. The leading terms of the series were collected, and original expressions in terms of elementary functions, approximating the exact solution very well, were found. The next step in [3] was to extend the results obtained to a vortex with uniform core of finite cross section. The azimuthal average velocities were only derived for this case. Nonetheless, these showed excellent agreement with experimental data.

Here, we restrict our analysis to the case of a rectilinear vortex, taking into account the helical structure of the flow. This implies that the transverse velocity profile is the same as for the Rankine vortex. However, the axial velocity profile is parabolic inside the vortex core and uniform outside it.

This velocity distribution allows us to consider two combustion regimes: translational propagation of the flame front along the tube axis (termed here the normal combustion) and helical propagation (the helical combustion). In the first case, the flame surface propagates along the tube axis and does not depend on the transverse coordinate. In the second case, the flame propagates along helical lines with the same pitch as that of the helical flow structure. The flame front shape is governed by a known equation of surface evolution including kinematic addition of velocities and the Huygens' principle.

236

Let us investigate the flame shape for the case of normal combustion, assuming that the direction of the flame front motion coincides with the flow direction. If the axial velocity reaches a maximum value at the tube axis (which corresponds to positive swirling direction), the flame shape is qualitatively similar to that determined by Zel'dovich [1]. Otherwise, when the swirl is negative, we obtain a flame surface in the form of cone. The protruding part of the flame has the shape of a flat ring occupying the area of the vortex exterior. The cone height is proportional to the vortex core size.

In the case of helical combustion, the flame surface is of helical shape with the same pitch as mentioned above. The theory developed here can also explain the occurrence of flames in the shape of hollow cylinders [4]. We used the paper [4] to validate our models since it contained data on the measured flow angle. Calculation of the steady-state flame shape, based on the model of normal combustion, resulted in a frustum of a cone surface adjoining the tube wall. This contradicts the experimental data.

Using the model of helical combustion in calculations yields a flame not adjoining the tube walls. In this case, the flame shape is a part of a helical surface with a small angle of deviation from the axis. One can interpret the flame shape as the hollow cylinder here, because of the large pitch of the helical surface and the small inclination.

In practice, the overlapping sections of the helical surface, where the burning is physically impossible, are not visible. Thus the flame shape seems to be a thin and narrow ribbon screwed into heli-like surface. The "corrugated flame" in [5] can be explained in terms of the model constructed here. Our model of the helical combustion is also in complete agreement with the flame surface in the shape of screwed ribbon, obtained in experiments [6, 7].

Thus, new models describing the velocity field and flame shape for the normal and helical propagation of a flame front have been constructed. It has been shown for the first time that the steady-state helical combustion, contrary to normal one, yields extraordinary flame shapes, such as the helical surface or the hollow cylinder observed in experiments.

References

[1] Zel'dovich, Ya. B. *Zhurnal Tekhnicheskoi Fiziki*, 1947, **17**, 3, 3 (in Russian).

[2] Gupta A. K., Lilley D. G., Svred N. *Swirl Flows*. N.Y., Abacus Press, 1984.

[3] Borissov A. A., Kuibin P. A., Okulov V. L. *Acta Mechanica*, 1994 [Suppl], 4, 289.

[4] Albright L. F., Alexander L. G. *Proc. 6th Symp. (Int.) on Comb.*, The Combustion Institute, 1957, 464.

[5] Sakai Y., Ishizuka S. *JSME, Ser. II*, 1991, **34**, 2, 234.

[6] Ishizuka S. *Comb. Flame*, 1989, **75**, 3–4, 367.

[7] Ishizuka S. *Comb. Flame*, 1990, **82**, 1, 176.

THERMOCHEMICAL MODEL OF A TWO-STAGE COMBUSTION PROCESS IN THE CONCEPT OF PULSED JET COMBUSTION

D. A. Detkovskii*, S. M. Frolov*, P. Furmanski[†], P. Wolanski[†]

Semenov Institute of Chemical Physics, Moscow, Russia
[†]*Politechnika Warszawska, Warszawa, Poland*

Introduction

The concept of Pulsed Jet Combustion (PJC) proposed by Oppenheim [1] for internal combustion engines, refines the open chamber — direct injection — stratified charge concept. The combustion process, once started in prechamber, is then extinguished at efflux from the orifice between the prechamber and the cylinder head space. Later on, combustion revives in the turbulent vortices created by the high-speed jet. The PJC concept implies that active radicals in the burning vortices maintain a sufficiently high temperature during mixing with the fresh gas and give rise to multiple ignition sources. The latter fact is of essential significance, since the combustion process becomes apparently distributed rather than propagating in the mode of a turbulent diffusion flame.

Thus, the PJC concept is based on the idea of a two-step combustion process:

- the first step provides a high-speed turbulent jet of combustion products containing active radicals;

- the second step is reignition followed by sustained formation of multiple ignition sites in vortices.

The paper describes an idealized (i.e., adiabatic) zero-dimensional thermochemical model for the two-step combustion in the PJC system.

Formulation

The combustion system under study consists of the main chamber of volume V° and the prechamber of volume V_p. Prior to ignition, the former is filled with a homogeneous

fuel–air mixture with specified molar concentrations of components, y_{0k}, while the latter is filled with a homogeneous mixture of different composition with concentrations y_{pk}. Initial temperature and pressure in the system are T° and p°.

The diameter of the orifice between the prechamber and the main chamber is D°. After ignition in the prechamber, a turbulent plume is created in the main chamber by the jet of combustion products. The plume is composed of multiple vortices of various sizes. Combustion is resumed in the vortices due to the mixing of the high-temperature combustion products with the cold fresh mixture. The vortices grow in size by engulfing new portions of fresh mixture and thermal expansion due to the chemical reaction. The combustion process terminates when the entire mixture has burned out.

To model the combustion process in the system, the following simplifying assumptions have been adopted:

- the prechamber mixture burns under constant volume conditions;

- combustion products have a thermodynamically equilibrium composition;

- expansion of prechamber combustion products is isentropic;

- both fuel–air mixture and combustion products obey the equation of state of a perfect gas;

- pressure is uniform throughout the system;

- heat losses to the walls are negligible;

- mixing and reaction of the fresh mixture with combustion products proceed simultaneously;

- vortices are spherical and similar in size;

- vortices, once having appeared, do not disappear or multiply;

- chemical reaction is of one-step Arrhenius type.

The j-th vortex is characterized by the following properties: the vortex diameter d_j (or volume v_j), the entrainment velocity across the vortex boundary u_j, the vortex mass m_j, the vortex temperature T_j, and the molar concentration of the k-th component. The process of engulfing the fresh mixture is modelled by the equation

$$dm_j = \dot{m}_j dt = \chi \pi d_j^2 \rho_0 u_{j0} dt. \tag{1}$$

Henceforth, the suffix 0 denotes unburned mixture properties, t is time, ρ is the density, χ is the coefficient introduced here for taking into account the engulfing of burned gas from neighbouring vortices. For a set of similar vortices we assume that $\chi = (V^\circ - V_b)/V^\circ$, where V_b is the volume of burned gas.

Chemical conversion in a vortex is governed by the net reaction rate of Arrhenius type with the rate constant k_A.

Within the framework of the assumptions adopted, the equations for pressure, volume and average temperature of the j-th vortex are:

$$dp = D_0^{-1} \left[\frac{R_0 T_0}{p} \sum_j dm_j - \sum_j \frac{h_0\, dm_j}{C_j} \right.$$

$$\left. + \sum_j \sum_{k=1}^{n_f} \frac{\mu_k N_j h_{jk} dy_{jk}}{C_j} + \sum_j \sum_{k=1}^{n_f} \frac{\mu_k y_{jk}(h_{jk} - C_{pk}T_j)dN_j}{C_j} \right],$$

$$dv_j = C_j^{-1} \left[- \left(\sum_{k=1}^{n_f} \frac{\mu_k y_{jk} C_{pk}}{R} - 1 \right) v_j\, dp - \sum_{k=1}^{n_f} \mu_k N_j h_{jk} dy_{jk} \right. \tag{2}$$

$$\left. - \sum_{k=1}^{nf} \mu_k y_{jk}(h_{jk} - C_{pk}T_j)dN_j + h_0\, dm_j \right],$$

$$dT_j = \frac{v_j dp}{R N_j} + \frac{p\, dv_j}{R N_j} - \frac{T_j dN_j}{N_j},$$

where

$$C_j = p \sum_{k=1}^{n_f} \frac{\mu_k y_{jk} C_{pk}}{R}, \quad h_{jk} = h_k^o + C_{pk}(T_j - 298), \quad T_0 = \left(\frac{p}{p_0} \right)^\xi T^o$$

$$D_0 = \frac{(\xi - 1)m_0 R_0 T_0}{p^2} - \sum_j \left(\frac{\sum_{k=1}^{n_f} \mu_k y_{jk} C_{pk}}{R} - 1 \right) \frac{v_j}{C_j}.$$

In the above equations, R is the gas constant, h is the enthalphy, m is the mass, n_f is the number of components in the gas, μ_k is the molecular mass, C_{pk} is the specific heat at constant pressure, h_k^o is the component formation enthalpy, N_j is the number of moles in the j-th vortex, $\xi = (\gamma - 1)/\gamma$ with γ being the specific heat ratio of the unburnt gas.

Results and Discussion

As an example, combustion of a stoichiometric methane–air mixture is considered under the following conditions: $p^o = 10^5$ Pa, $V^o = 3 \cdot 10^{-4}$ m^3, $V_p = 3 \cdot 10^{-6}$ m^3, $T^o = 332$ K. The entrainment velocity u_{0j} was assumed constant $u_{0j} = u_0$, the initial size of vortices $d_j(t = 0) = d(t = 0) = D^o$.

The reaction equation is taken in the form [2]

$$\frac{d[CH_4]}{dt} = -k_A[CH_4][O_2]^{0.5} \tag{3}$$

where

$$k_A = 4.8 \cdot 10^6 T(p \cdot 0.987 \cdot 10^{-5})^{0.2} \exp\left(-\frac{12200}{T}\right),$$

$[CH_4]$ and $[O_2]$ are the concentrations of methane and oxygen in $mole/(cm^3 \cdot K)$.

To close the set of governing equations the following equations of balance for CH_4, O_2, N_2, CO_2, and H_2O concentrations are used:

$$dN_j = Adm_j,$$

$$dy_{CH_4 j} = \left(\frac{x_{CH_4}}{\mu_{CH_4}} - y_{CH_4 j}A\right)\frac{dm_j}{N_j} - k_A M_j^{1/2} y_{CH_4 j} y_{O_2 j}^{\frac{1}{2}} dt,$$

$$dy_{O_2 j} = \left(\frac{x_{O_2}}{\mu_{O_2}} - y_{O_2 j}A\right)\frac{dm_j}{N_j} - 2k_A M_j^{1/2} y_{CH_4 j} y_{O_2 j}^{\frac{1}{2}} dt,$$

$$dy_{N_2 j} = \left(\frac{x_{N_2}}{\mu_{N_2}} - y_{N_2 j}A\right)\frac{dm_j}{N_j}, \tag{4}$$

$$dy_{CO_2 j} = -\frac{y_{CO_2 j}Adm_j}{N_j} + k_A M_j^{1/2} y_{CH_4 j} y_{O_2 j}^{\frac{1}{2}} dt,$$

$$dy_{H_2O j} = -\frac{y_{H_2O j}Adm_j}{N_j} + 2k_A M_j^{1/2} y_{CH_4 j} y_{O_2 j}^{\frac{1}{2}} dt,$$

$$A = \frac{x_{CH_4}}{\mu_{CH_4}} + \frac{x_{O_2}}{\mu_{O_2}} + \frac{x_{N_2}}{\mu_{N_2}},$$

where $M_j = 10^3 N_j/V_j$ is the molar concentration of mixture in the j-th vortex, x_k denotes the mass concentration of the k-th component in the burned mixture. The balance equations (4) indicate that species concentrations in the j-th vortex vary due to mixing and chemical conversion.

The set of governing equations was solved numerically using the standard Runge–Kutta method. The STANJAN code [3] was used to estimate equilibrium compositions and thermochemical parameters.

At fixed geometry and thermodynamic initial conditions, for a specified fuel–air mixture, the solution of Eqs. (1) to (4) contain a single dimensionless governing parameter $\alpha = t_{ch}/(D^\circ/u_0)$, where $t_{ch} = (k_A M_j(0)^{0.5})^{-1}$ is the characteristic chemical time, D°/u_0 is the characteristic time of turbulent mixing. Our calculations revealed that the dependence of pressure p/p° on the dimensionless time tu_0/d shows a bifurcation behavior at $\alpha = \alpha_* = 1.9 \cdot 10^{-3}$. At $\alpha < \alpha_*$ the solution of the problem is represented with a good approximation by a unique curve 1 in Fig. 1, whereas at $\alpha > \alpha_*$ mixture ignition fails, and $p/p^\circ = 1$ (curve 2 in Fig. 1). Curve 3 in Fig. 1 corresponds to the almost
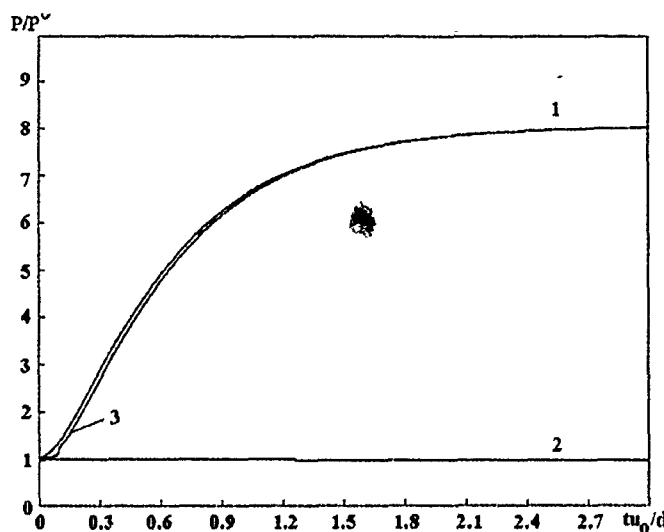
Figure 1: Predicted pressure histories in the constant-volume adiabatic PJC system depending on the dimensionless parameter $\alpha = t_{ch}(D^\circ/u_0)^{-1}$. Curve 1 represents solutions with $\alpha < \alpha_*$, curve 2 with $\alpha > \alpha_*$, curve 3 with $\alpha = 0.995\alpha_*$, where $\alpha_* = 1.9 \cdot 10^{-3}$ is the critical value of α.

critical case, $\alpha = 0.995\alpha_*$. The absence of heat loss in the model results in monotonous pressure increase to the thermodynamic value. Qualitatively, the predicted pressure vs time dependence corresponds with the experimental findings of [1]. The model allows to study the effect of turbulence and mixture composition on pressure history in the PJC system as well as NO_x formation.

Conclusion

A zero-dimensional thermochemical model of PJC system has been proposed. The model yields the rate of pressure rise depending on the parameters of the turbulent jet plume. Further improvement of the model with due regard for vortices size distribution and heat loss is projected to better represent the real conditions. The model is planned to be used for studying NO_x formation in PJC system.

Acknowledgement

References

[1] Oppenheim A. K. Proc. Conf. (Int.) on Comb. in Engines, IMechE, London, 1992.

[2] Edelman R. B. *Proc. of NSF (RANN) Workshop on Numerical Simulation of Combustion for Appl. to Spark and Compres. Ign. Engines*, SAI, La Jolla, Calif., 1975.

[3] Reinolds W. C. *STANJAN Interactive Computer Programs for Chemical Equilibrium Analysis*, Stanford Univ., 1986.

3D MODELING OF PULSED JET COMBUSTION

S. M. Frolov*, M. Suffa†, R. Tatschl‡, P. Wolanski§

* *Semenov Institute of Chemical Physics, Moscow, Russia*
† *Hochschule fur Wirtschaft und Technik, Dresden, Germany*
‡ *AVL LIST GmbH, Graz, Austria*
§ *Politechnika Warszawska, Warszawa, Poland*

Introduction

The concept of Pulsed Jet Combustion (PJC), proposed by Oppenheim [1] as an alternative mode of energy release in stratified-charge internal combustion engines, shows a number of practical advantages. Based on the fundamental ideas of Gussak, Semenov and Zel'dovich concerning the role of active radicals in the torch mechanism of ignition and flame propagation, the PJC concept implies a staged combustion process:

- the flame generated in a prechamber is extinguished by shear at efflux from the orifice between the prechamber and the main chamber;

- combustion is spontaneously reinitiated in the main chamber in the core of the hot turbulent jet.

According to [1], further chemical transformations in the main chamber occur in a fireball, i.e. via distributed combustion sustained by multiple pockets of high concentration of active radicals. Of prime importance are the entrainment processes resulting in the fireball growth.

It should be emphasized that the fireball mode of combustion differs in principle from turbulent propagating flame mode. The latter is characterized by laminar-like average structure with certain characteristic thickness of the turbulent reaction zone. The turbulent propagating flame mode is assumed in the most stratified charge concepts.

243

This paper reports a 3D computer modeling of the PJC system behavior, focusing on the evolution of exothermic processes.

PJC System Geometry

The PJC system is assumed to consist of the main combustion chamber and two identical opposed jet prechambers. The main combustion chamber is a cylinder of 8.26 cm bore, 10 cm in height, and total volume $\approx$ 536 cm^3. The prechamber is of the same design as reported in [1]. It consists of a cylindrical cavity $\approx$ 1 cm^3 in volume and a co-axial tubular electrode perforated (32 orifices) for charge inlet. The orifice plates between the prechambers and the main combustion chamber are 2.5 mm in diameter. The orifices are sharp-edged, 0.5 mm thick. The prechambers are affixed to the main chamber at height 9 cm. Initially, the PJC system is filled with propane–air mixture of equivalence ratio 0.6 at pressure 5 bar and temperature 60 °C.

At $t > 0$, propane-air mixture of equivalence ratio 1.5 is injected through the perforations in the prechambers. The injection persists for 10 ms at the mass flow rate 0.332 kg/s. At $t = t_{ign} = 10$ ms, the rich mixture remaining in the prechambers is ignited by a spark. The ignition point is located at the outlet orifice inside the prechamber.

Modeling

A set of 3D conservation equations of mass, momentum and thermal energy serves as the basis of the mathematical model.

The variables in the governing equations are expressed in terms of mean and fluctuating components. The subsequent averaging process generates unknown correlations of the products of the fluctuating components. The unknown correlations are modeled within the framework of the standard k–ε model. The k–ε model involves additional partial differential equations for the turbulent kinetic energy k and its dissipation rate $\varepsilon = C_\mu^{3/4} k^{3/2}/l_t$, where $C_\mu = 0.09$ is an empirical constant and l_t is the turbulence length scale. The initial conditions for the turbulence model in the present case are: $l_t = 1$ mm, $k = 1$ m^2/s^2. Appropriate boundary conditions are also imposed. Semi-empirical "laws of the wall" are invoked for the dependent variables in the near wall region.

Turbulence-Controlled Combustion Model

The combustion model employed is the turbulence-controlled model proposed in [2]. This model assumes that, in premixed turbulent flames, the reactants (fuel and oxygen) are contained in the same eddies and are separated from the eddies containing hot combustion products. Since the chemical time scales are very short, as compared with those of turbulent transport processes, it can be assumed that the rate of combustion is determined by molecular mixing of the eddies containing reactants with those containing hot products, in other words, by the rate of dissipation of these eddies.

The mean reaction rate can thus be written, in accordance with [2], as

$$\overline{\rho \dot{r}_{fu}} = \frac{C_{fu}\bar{\rho}}{\tau_R} \min\left(\bar{y}_{fu}, \frac{\bar{y}_{Ox}}{S}, \frac{C_{Pr}\bar{y}_{Pr}}{1+S}\right)$$

The first two terms of the 'minimum value of' operator $\min(\bar{y}_{fu}, \bar{y}_{Ox}/S, (C_{Pr}\bar{y}_{Pr})/(1+S))$ simply determine whether fuel or oxygen is the limiting reactant, and the third is a reaction probability which ensures that the flame does not exist in the absence of hot products. C_{fu} and C_{Pr} are empirical coefficients and τ_R is the turbulent mixing time-scale. The calculations were made for the following values: $C_{fu} = 20$, $C_{Pr} = 0.5$, $\tau_R = 5 \cdot 10^{-3}$ s.

The ignition event was modeled by introducing a kernel of hot combustion products of fixed size at a certain location.

Numerical Solution

The FIRE code developed by AVL was used to solve the governing equations. FIRE rewrites all the equations in a general curvilinear non-orthogonal coordinate system. The individual terms of partial differential equations are replaced by algebraic expressions obtained by integration over a control volume of finite size. The finite volume discretization leads to a set of nonlinear algebraic equations for the values of dependent variables, such as velocities, pressure etc.. at the centre of the computational mesh

Results and Discussion

The computational grid contained about 16,000 spatial cells. The predicted density distributions were compared directly to the schlieren records of jet plumes obtained by means of the dual PJC system of [1], similar to the one used in our study. A comparison between the predicted and measured data have shown a good quantitative agreement until $t = 15$ ms, which is an indication of satisfactory simulation.

Figure 1 shows the predicted spatial profile of the reaction rate at $t = 12.5$ ms. It is evident that the exothermic process in the main combustion chamber occurs over the entire core of the turbulent jet (i.e., in the fireball mode). In contrast to the combustion process in the main chamber, the process in the prechamber exhibits features of a turbulent flame. The maximum outflow velocity from the prechamber is about 57 m/s at $t = 12.5$ ms.

Figure 2 shows the spatial profile of the reaction rate at $t = 15$ ms. Apparently, the distributed exothermic process typical for $t = 12.5$ ms is replaced now by a distinctly propagating mode of combustion. Flame extinction is apparent at the exit of the high-speed jet. In the prechamber, the flame propagates counter to the mass flow. Therefore, the apparent flame velocity is substantially lower than in the main chamber, despite the fuel-rich mixture composition in the former. Note that the thickness of the turbulent flame in the main chamber is affected by the computational mesh size which grows towards the periphery of the chamber.
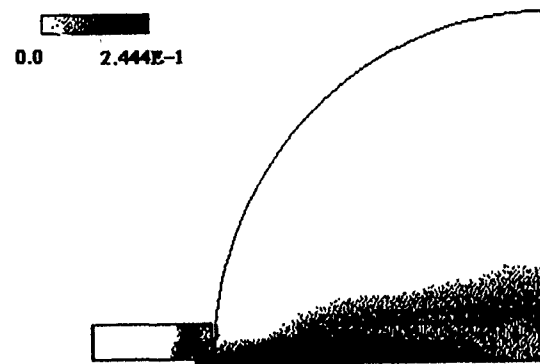
Figure 1: Predicted reaction rate distribution in a single-orifice dual PJC system at 2.5 ms after ignition.
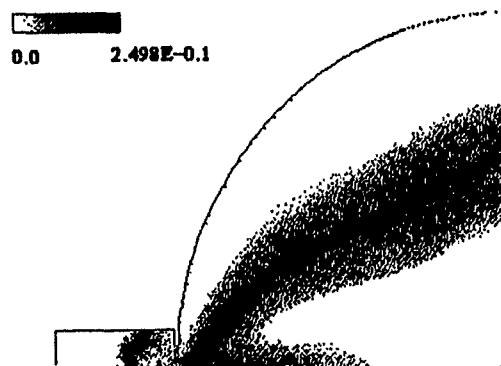
Figure 2: Predicted reaction rate distribution in a single-orifice dual PJC system at 5 ms after ignition.

Conclusion

As a result of 3D numerical simulation of the PJC system, it has been found that turbulent combustion in the main chamber exhibits two distinct modes, namely the fireball mode and the turbulent diffusion flame mode. The fireball mode is characteristic of the initial stage of the process, while the turbulent flame dominates at later stages. Further studies are planned with the view of improving the combustion model.

References

[1] D. M. Hensinger, J. A. Maxson, K. Hom, A. K. Oppenheim. *SAE Paper 920414*, 1992.

[2] B. F. Magnussen, B. H. Hjertager. *Proc. 16th Symp. (Int.) on Comb.*, Pittsburgh, Pennsylvania, 1977.

TURBULENT DIFFUSION FLAME WITH A MEAN STREAMWISE PRESSURE GRADIENT

V. Frost*, M. Gorokhovski†, Yu. Vladimirov*

Institute for Problems in Mechanics, Russian Academy of Science, Russia
† *Universite' de Rouen — U.R.A. C.N.R.S. 230 CORIA, France*

I. The strong nonlinearity of chemical reaction rates as the main problem of turbulent combustion theory was first emphasized by Ya. Zel'dovich (1949): the mean reaction rate cannot be correctly evaluated in terms of mean flow properties. After the advent of probability density function (PDF) methods, the problem of reaction rate averaging in turbulent combustion modelling appears to be simplified. Over the last 30 years, the transport equations for the PDF of temperature and concentrations have been obtained [1–3] with the view of turbulent combustion applications.

Combustion–flow interactions related to the flame present a similar problem: due to the strongly nonmonotonic form of density function, an additional density — velocity correlation must be calculated. The latter arises as a direct effect of mean streamwise pressure gradient on the turbulent variable-density flow through selective acceleration of low and high density fluids. This problem, known as the one of flame-generated

turbulence, has prompted both numerical and experimental studies of diffusion flames [4–7]. Recently [8–10], a method designed to predict turbulent mass fluxes in the presence oi ̄ng density variation was proposed. It has been shown that a fluctuating density field coupled with a mean pressure gradient (due to either bouyancy or Eulerian inertial forces) leads to self-turbulence in diffusion flames. All the papers mentioned above rely on different assumptions concerning the expression for conditionally averaged velocities (CAV).

Alternatively, the transport equation for CAV can be derived in the following form:

$$\frac{\partial \langle u_i \rangle_c}{\partial t} + \frac{\partial \langle u_i u_\gamma \rangle_c}{\partial x_\gamma} + (\langle u_i u_\gamma \rangle_c - \langle u_i \rangle_c \langle u_\gamma \rangle_c) \frac{\partial \ln P}{\partial x_\gamma} - \langle u_i \rangle_c \frac{\partial \langle u_\gamma \rangle_c}{\partial x_\gamma} =$$

$$-\frac{\alpha}{\rho}(\langle u_i \rangle_c - \langle u_i \rangle) - \frac{\beta_\rho}{\rho}(c - \langle c \rangle)\frac{\partial \langle u_i \rangle_c}{\partial c} - \frac{1}{\rho}\frac{\partial p}{\partial x_i}, \tag{1}$$

where ρ is the density, $\langle u_i \rangle_c$ are CAV, P is the PDF, p is the mean pressure, α and β_ρ are micromixing rates.

To obtain a continuous distribution of intermediate concentrations, we can further express the second micromixing term in the form proposed by Kaminsky for the PDF equation derived in [1]:

$$-\beta \left[\int\limits_0^c dc' \int\limits_c^1 dc'' \cdot P(c')P(c'') \left(\frac{\langle u \rangle_{c'} + \langle u \rangle_{c''}}{2} \right) \right.$$

$$\left. -\langle u \rangle_c \frac{P(c)}{2} \{ \int\limits_0^c P(c')(c - c')\,dc' + \int\limits_c^1 P(c'')(c'' - c)\,dc'' \} \right] \tag{2}$$

Finally, the values of $P(c)$ and $\langle u \rangle_c$ calculated from transport equations are used to find the flame-generated turbulence defined as

$$\left\langle \frac{u'}{\rho} \right\rangle = \int \frac{\langle u \rangle_c}{\rho(c)} P(c)\,dc. \tag{3}$$

II. The numerical analysis of a simple-geometry diffusion flame was conducted to simulate the effects of flame-generated turbulence using Eqs. (1)–(3). We considered a fuel jet in a co-current flow of oxidizer, such that the streamwise negative mean-pressure gradient is constant. It was assumed that a one-step irreversible chemical reaction proceeded at an infinitely high rate; the molecular heat and mass transfer was described by a single diffusivity and $Le = 1$. In this case, the thermochemical state of the gaseous mixture is completely described by the normalized Shvab–Zel'dovich function c and the density can be taken in a simple form,

$$0 < c < c_f : \qquad \rho = \rho_0 + (\rho_f - \rho_0)\frac{c}{c_f}; \tag{4}$$

248
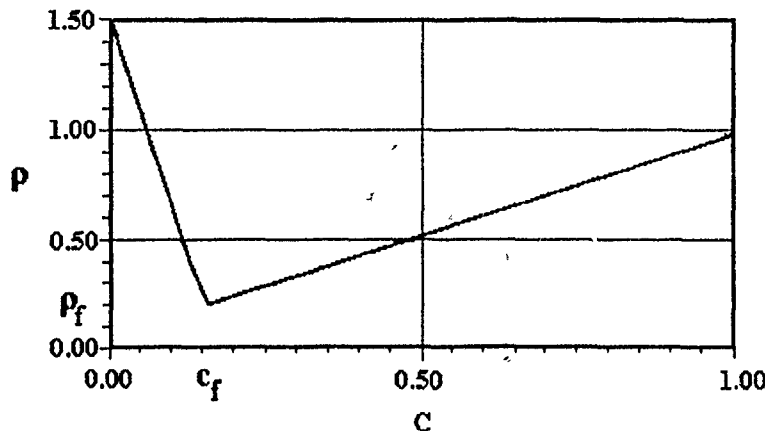
Figure 1.

$$c_f < c < 1: \qquad \rho = \rho_f + (\rho_1 - \rho_f)\frac{c - c_f}{1 - c_f}; \qquad (5)$$

The boundary conditions for the computational domain of $x \geq 0$, $y \in [0, h]$ are

$$
\begin{aligned}
x = 0, \quad & y < h: \quad & c = 1, \quad & \rho \equiv \rho_1 = 1; \\
x = 0, \quad & y > h: \quad & c = 0, \quad & \rho \equiv \rho_0 = 1.5;
\end{aligned}
\qquad (6)
$$

the mixture parameters are chosen as $\rho_f = 0.2$, $c_f = 0.15$, with $\mathrm{grad}\, p = 0.02$. A typical example of density distribution is given in Fig. 1.
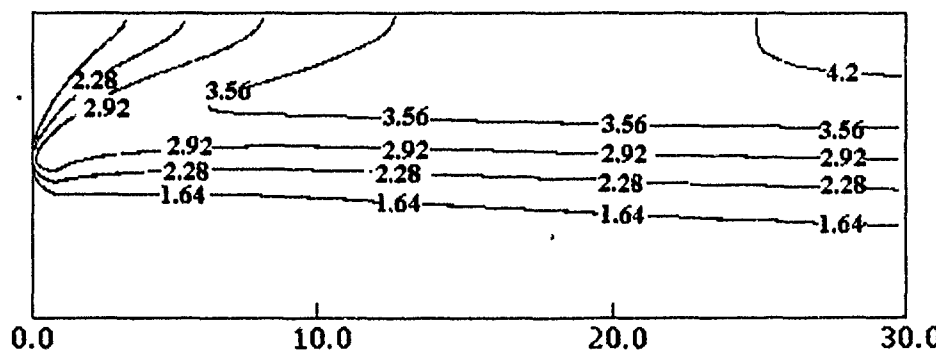
Figure 2.

The governing equations were formulated without boundary layer and without any gradient approximation. The transport equations for $\langle u \rangle$, $\langle v \rangle$, $P(c)$, $\langle u'^2 \rangle$, $\langle v'^2 \rangle$, $\langle w'^2 \rangle$, $\langle u'v' \rangle$ were solved first, with the third-order moments taken to be zero. Equation

249

(3) was then used to obtain $\langle u \rangle_c$ and the flame-generated turbulence intensity. The tridiagonal matrix algebra combined with Seidel iterations was used as the numerical algorithm.

As an illustration of the computed flame characteristics, Fig. 2 shows the mean temperature distributions related to the starting temperature (the fuel and coflow starting temperatures were taken to be equal). Note that the maximum temperature is lower than the adiabatic flame temperature, which equals 5 here.

We have compared turbulence intensities in the diffusion flame to those calculated for the case of nonreactive jet mixing with monotonic density distribution.

Figure 3 illustrates the effect of self-turbulization by the distributions of

$$\langle u'^2 \rangle = \langle u'^2 \rangle_f - \langle u'^2 \rangle_{in},$$

normalized by the starting velocity squared. We can see the longitudinal turbulence intensity generated in the zone of maximum temperatures increase in the downstream direction.
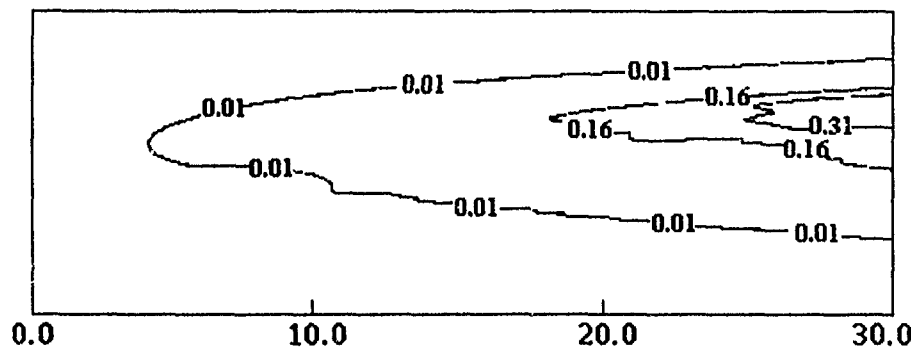
Figure 3.
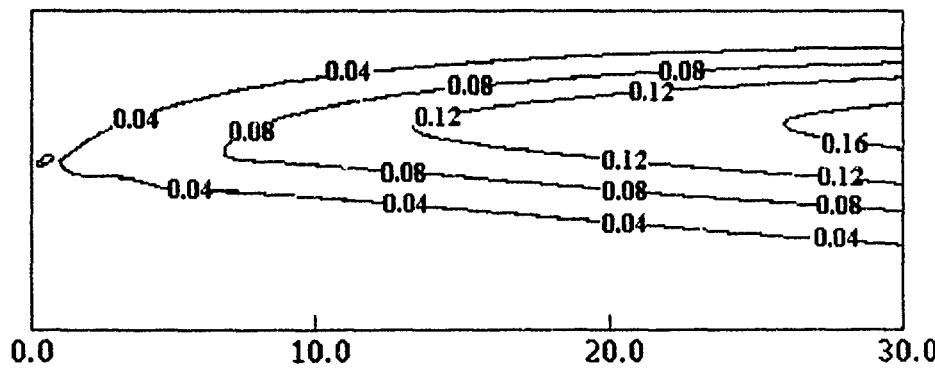
Figure 4.

Figure 4 shows the distribution of intensity due to the flame-generated turbulence only, calculated by

$$\langle u' \rangle_c = \int |\langle u \rangle_c - \langle u \rangle| P(c) \, dc, \tag{7}$$

normalized by the starting velocity. Note that the selective acceleration of the low and high density fluids by the streamwise mean pressure gradient plays a significant role in the process of turbulence generation; in the example considered here, we see that the flame-generated intensity of turbulence is as high as 30% (Fig. 4).

References

[1] Frost V. *J. Fluid Mech., Sov. Res.*, 1975, **4**, 124.

[2] Chang P. *AIAA J.*, 1962, **7**, 1982.

[3] Kuznetsov V., Sabelnikov V. *Turbulence and Combustion*, 1990, Hemisphere Publ.

[4] Starner S. H., Bilger R. W. *AIAA Pap., No.80-0205*, 1980.

[5] Driscoll J., Schefer R., Dibble R. *Proc. 19th Symp. (Int.) on Comb.*, The Combustion Institute, 4 1982, 59–467.

[6] Borghi R., Escudie D. *Comb. Flame*, 1984, **56**, 149–164.

[7] Kolbe W., Kollman W. *Acta Astron.*, 1980, **7**, 91.

[8] Baev V., Gorokhovski M., Spilberg I., *Fizika Gogeniya Vzriva*, 1987, **23**, 3, 21–33.

[9] Baev V., Gorokhovski M., Ribakov S. *ibid*, 1989, **57**, 2, 285–291.

[10] Emelianov V., Frost V., Nedoroob S., *Proc. 24th Symp. (Int.) on Comb.* The Combustion Institute, 1992, 435–442.

AERODYNAMICS AND COMBUSTION PRODUCTS TRANSFER IN LARGE AREA FIRES

Yu. A. Gostintsev[*], N. P. Kopylov[†], I. R. Khasanov[†]

[*]*Semenov Institute of Chemical Physics, Moscow, Russia*
[†]*All-Russia Scientific Research Institute for Fire Protection, Balashiha, Russia*

The plumes generated by large-area fires can cause major local perturbations of the atmosphere. The spread of significant amounts of smoke produced in the fire may have climatic and environmental consequences [1].

The dynamics of turbulent convective flows of viscous compressible heat-conducting gas in the stratified moist atmosphere above big fires is simulated within the framework of an axisymmetric finite-difference field model based on the Navie–Stokes equations [2]. The transfer of combustion products (smoke, water vapour and condensed moisture) is considered with the dispersion fluid model and described by the equations of turbulent diffusion. The turbulent transport coefficients are calculated according to the algebraic model [3] which includes local shear and stratification effects. The fire is simulated by a distributed heat release Q_1 and smoke source S_c with arbitrary flame envelope and heat and smoke generation rates. The volumetric heat source Q_2 is introduced to calculate the heat release due to phase transition in condensation centres.

The computations were based on a micro-control volume finite-difference approach using primitive variables [4].

The smoke plume evolution was studied by modeling smoke cloud formation above the large fires of various areas (of radii 2, 4, 5, 8 and 10 km) and fire intensities. Results include smoke concentrations, distributions of condensed water and temperature, as well as the velocity, density, and pressure fields.

Figure 1 shows the initial smoke concentration and velocity fields above the 5-km radius fire with the heat release rate $q_m = 4.7 \cdot 10^4$ W/m^2. The heating rate q increases linearly from $q = 0$ to its prescribed value q_m at $t = 1800$ s.

Initially, the fire generates several rotating cells in the source region. The continued, constant production of buoyancy generates an increasing inflow which gradually imposes a radially directed flow in the fire region. The rotating cells increase in dimensions and rise together with the convective column. The condensed water released in the form of drops, snow, or ice is transferred by the convective flows, forming a moisture cloud of shape close to that of the smoke particles cloud. The isolines of smoke aerosol concentrations $C = 0.5 \cdot 10^{-5}, 1.5 \cdot 10^{-5}, 2.5 \cdot 10^{-5}$ kg/kg are shown at successive moments of time.
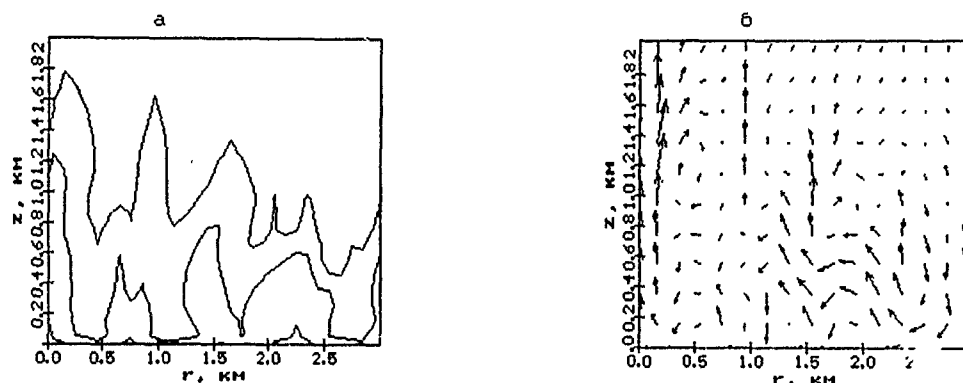
Figure 1: Smoke concentration (a) and velocity (b) fields above 5-km radius fire after 520 s.
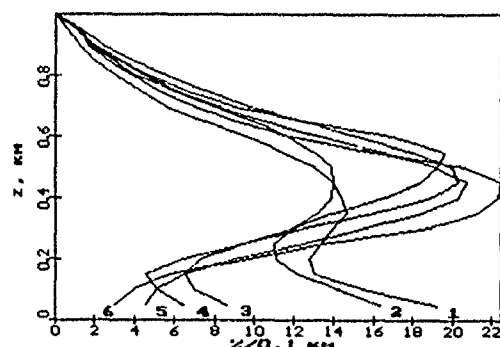
Figure 2: Normalized smoke injection profiles above large-area fires in dry atmosphere; τ: 1 — 3.44; 2 — 5.16; 3 — 8.9; 4 — 13.4; 5 — 26.7; 6 — 40.

Using the calculations the criterion X, which determines the difference between the flows above a massive fire with compact heat release and a large-area massive fire, is obtained [5]. This criterion characterizes the ratio of the heat release rate q_m (W/m^2) to the area of fire ($X = q_m/R_0^2$, where R_0 is the radius of fire). The aerodynamics above a compact massive fire corresponds to the laws of flow above a point source ($X > 0.002$). In the case of large fire, unsteady vortex motions are formed above the fire region. The dynamics of convective flows above large-area fires ($X < 0.002$) is consistent with the laws of flow above a distributed source known from the plume rise theory.

The development of a vertical distribution of smoke aerosol above a large-area fire is presented in Fig. 2. The smoke injection profiles at different dimensionless times τ of the combustion process are given. The dimensionless time is defined as $\tau = t/t_a$, where t_a is the time of thermal relaxation of the atmosphere, $t_a = (\pi R_0^4/\Pi_0)^{1/3}$ and Π_0 is the integral of the buoyancy flux.

The results obtained in this paper can be used to predict and evaluate the characteristics of atmospheric pollution by combustion products above big fires.

References

[1] Pittock A. B. *et al. Environmental Consequences of Nuclear War. SCOPE 28.* **1**: *Physical and Atmospheric Effects.* Chichester, John Wiley & Sons, 1986.

[2] Gostintsev Yu. A., Kopylov N. P., Ryzhov A. M., Khasanov I. R. *Fizika Goreniya Vzriva,* 1991, **27**, 6, 10 (in Russian).

[3] Yang K. T., Lloyd J. R., Kanury A. M., Satoh K. *Comb. Sci. Techn.,* 1984, **39**, 107.

[4] Patankar S. V. *Numerical Heat Transfer and Fluid Flow.* Washington, DC, Hemisphere, 1980.

[5] Kopylov N. P, Gostintsev Yu. A., Ryzhov A. M., Khasanov I. R. *ASME Transactions Scientific Siberian,* Series A, ASME Press, France, 1992, **3**, 11.

ABOUT ONE APPARENT PARADOX OF PREMIXED TURBULENT COMBUSTION

V. P. Karpov*, A. N. Lipatnikov†, V. L. Zimont†

Semenov Institute of Chemical Physics, Moscow, Russia
†*Moscow Institute of Physics and Technology, Dolgoprudnyi, Moscow Region, Russia*

Since with the first investigations, it is generally believed that the greater the laminar burning velocity U_l, the greater is the rate, S_t, of turbulent combustion of this mixture at constant turbulent parameters. The currently accepted correlations (for example, those using the product $Ka \cdot Le$ as the only characteristic of the local changes of the burning velocity in strained flamelets [1, 2]) have the same feature. Here, $Ka \simeq u'/U_l \cdot (u'\tau_c/L)^{1/2}$ and $Le = \kappa/D$ are Karlovitz and Lewis numbers, respectively, where $\tau_c = \kappa/U_l^2$ the chemical time scale, κ and D denote molecular diffusivities of heat and the deficient reactant, u' and L are turbulent velocity and length scale. Typically, an increase in turbulent burning rate results from increasing U_l or combustion temperature T_b or decreasing τ_c or $Ka \cdot Le$.

A scrutiny of the measurements made in stirred bombs [3–6] has revealed that these correlations fail for the specially composed mixtures. Some of these experimental data
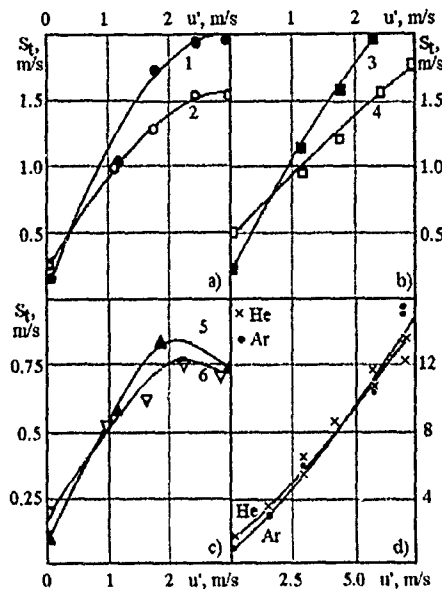
Figure 1: Dependencies of turbulent consumption rate S_t, characterizing the pressure rise in the bomb, and turbulent burning velocity U_l, measured by the leading edge of the flame, on turbulence intensity u'. Symbols are explained in Table 1.

are shown in Fig. 1 and the estimates of the above physicochemical parameters based on $u' = 1$ m/s, $L = 10$ mm, and U_l measured in the same bomb are presented in Table 1. These pairs of the burning mixtures have been selected thanks to the absence of the correlations referred to: for each pair $U_{li} > U_{lj}$ the slopes, dS_t/du', of the rising branches of the curves and the values of S_t at moderately large u' correlated inversely. These apparently paradoxical results are likely to be an important test for any model of turbulent combustion.

To describe these and similar data [3–6], we made an attempt to incorporate a sub-model of local thermodiffusional phenomena occurring in premixed turbulent flames into the closure of the averaged heat release rate, which yielded encouraging quantitative results for ordinary burning mixtures [7] and corresponded to

$$S_t = Au' \left[\frac{L}{u'\tau_c} \right]^{\frac{1}{4}}, \tag{1}$$

where A is a constant. For this purpose, we used the concept of leading points developed in [8], where the formulas for local values of T_b and relative air/fuel ratio, α, were derived for flamelets under critical stretching. The authors [8] recommended to use $U' = U_l(\alpha')$ corresponding to this critical local composition determined by α' instead of $U_l(\alpha_0)$ for premixed turbulent combustion modeling, where α_0 characterized the initial mixture.

The values of α' computed according to [8] and the burning velocities U_l' measured

Table 1: Parameters of burning mixtures (U_l in cm/s, τ_c in ms).

N	Mixture	T_b, K	U_l	τ_c	$Ka \cdot Le$	U_l'	τ_c'	T_b', K	T_b'', K	U_l''	τ_c''	Symb
1	H_2/air, $\alpha = 4.5$	987	16	1.12	0.90	33	0.29	1310	1288	30	0.36	●
2	$2H_2 + O_2 + 12N_2$	1356	26	0.48	1.07	32	0.35	1277	1147	18	1.10	○
3	$2H_2 + 2O_2 + 17Ar$	1339	21	0.68	0.56	62	0.09	1863	1745	49	0.14	■
4	$2H_2 + 2O_2 + 17He$	1339	51	0.57	0.32	56	0.47	1535	1326	29	1.76	□
5	C_3H_8/air, $\alpha = 0.6$	1852	10	2.11	4.45	25	0.32	2062	2071	25	0.31	▲
6	CH_4/air, $\alpha = 1.4$	1859	19	0.61	1.16	22	0.47	1902	1934	24	0.39	▽

Table 2.

N $(i:j)$	estimates			measurements
	$(\tau_{cj}/\tau_{ci})^{1/4}$	$(\tau_{cj}'/\tau_{ci}')^{1/4}$	$(\tau_{cj}''/\tau_{ci}'')^{1/4}$	$(dS_t/du')_i/(dS_t/du')_j$
1:2	1.24	0.95	0.76	0.80
3:4	1.05	0.66	0.53	0.54
5:6	1.36	0.91	0.94	0.70

in the bomb, are presented in Table 1 together with the estimated $\tau_c' = \kappa(\alpha')/U_l'^2$ and computed $T_b' = T_b(\alpha')$. Moreover, using the formulas [8] for T_b'' and the known values of U_l', we estimated $U_l'' = U_l(\alpha', T_b'')$ and $\tau_c'' = \kappa(\alpha')/U_l''^2$ (see Table 1), assuming that $U_l \approx \exp(-T_a/2T_b)$, where $T_a = 13000$ K for H_2 and $T_a = 20000$ K for CH_4 had been obtained using U_l measured for various types and amounts of the diluent in the same bomb. We also used $T_a = 20000$ K for C_3H_8.

Analyzing Table 1, one can easily show that for each pair of the mixtures the greater U' or U'' and the smaller τ_c' or τ_c'', the greater is the measured slope dS_t/du'. This fact is in a qualitative agreement with EQ. (1), as is demonstrated by Table 2, where the experimental slopes correspond to $u' = 1$ m/s. If we want to quantitatively model the experimental data presented in Fig. 1 as a whole, we must increase the constant A for lean hydrogen-air mixtures 1, 3, and 4, as compared to its optimum value for ordinary burning mixtures [7]. This tendency should be analyzed in future.

According to Eq. (1), turbulent burning velocity is controlled by the chemical time scale rather than laminar flame speed, which is apparently supported by the experimental data [3] (see Fig. 1d). For these mixtures ($C_3H_8 + 5O_2 + 21Ar$ or $21He$),

$U_l(\text{Ar}) = 0.8$ m/s, $U_l(\text{He}) = 1.4$ m/s, but $\alpha'(\text{Ar}) = 1.23$ and $\alpha'(\text{He}) = 1.26$ are closely related, hence $U_l'(\text{He})$ is likely to remain much greater than $U_l'(\text{Ar})$. Our estimation resulted in $\tau_c'(\text{Ar})$ being just above $\tau_c'(\text{He})$, but $\tau_c''(\text{Ar}) \cong \tau_c''(\text{He})$, and the experimental curves match almost exactly.

Thus, the paradox under consideration can be qualitatively explained in terms of the concept of leading points [8] and Eq. (1). Further studies of thermodiffusional phenomena in premixed turbulent flames are required, as well as more accurate and consistent use of the submodels of these phenomena in the predictions of premixed turbulent combustion.

Acknowledgement

References

[1] Bradley D., Lau A., Lawes M. *Phil. Trans. R. Soc. Lond.*, 1992, *A338*, 359.

[2] Bray K. N. C., Peters N. *Turbulent Reacting Flows* (P. A. Libby and F. A. Williams Eds.), New York, Springer-Verlag, 1993.

[3] Sokolik A. S., Karpov V. P., Semenov E. S. *Fizika Goreniya Vzriva*, 1967, 1, 62 (in Russian).

[4] Karpov V. P., Severin E. S. *Dokl. Acad. Nauk SSSR*, 1978, **239**, 1, 123 (in Russian).

[5] Karpov V. P., Severin E. S. *Fizika Goreniya Vzriva*, 1980, **16**, 1, 45 (in Russian).

[6] Karpov V. P., Severin E. S. *ibid*, 1981, **17**, 1, 137 (in Russian).

[7] Lipatnikov A. N., Zimont V. L. *Proc. Russian–Japanese Seminar on Combustion*, Chernogolovka, 1993, 67.

[8] Kuznetsov V. R., Sabel'nikov A. A. *Turbulence and Combustion*. New York, Hemisphere Publ., 1990.

EVOLUTION OF TURBULENT FIELDS IN EXPLOSIONS

A. L. Kuhl[*], J. B. Bell[*], R. E. Ferguson[†], K.-Y. Chien[†], J. P. Collins[†], M.-L. Lyons[†]

[*]*Lawrence Livermore National Laboratory, EL Segundo, CA, USA*
[†]*Naval Surface Warfare Center, White Oak Detachment, Silver Spring, MD, USA*

Explosions always contain turbulent mixing regions, e.g.: boundary layers, shear layers, wall jets and unstable interfaces. The inherent unsteadiness of turbulent mixing in explosions, and the lack of sufficient data, pose insurmountable difficulties for turbulence modeling of such flows.
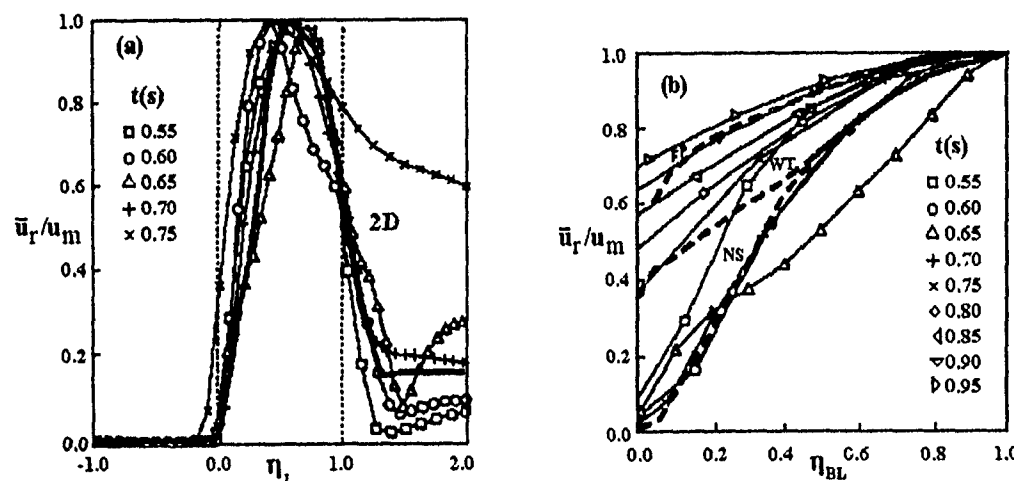
Figure 1: Evolution of the mean radial velocity profiles at 600 m: (a) wall jet profiles; (b) boundary layer profiles. Curves labeled NS and WT represent dusty boundary layer profiles measured behind a normal shock and in a wind tunnel; FP denotes flat plate profile.

Proposed in this paper is a direct numerical simulation approach — where the three-dimensional (3-D) conservation laws are integrated via a high-order Godunov method. Adaptive Mesh Refinement (AMR) is used to capture the convective mixing processes on the computational grid. Then, an azimuthal-averaging operator is applied to the 3-D solution — in order to extract the instantaneous mean and fluctuating components of the turbulent field. As an illustration, this methodology is applied to
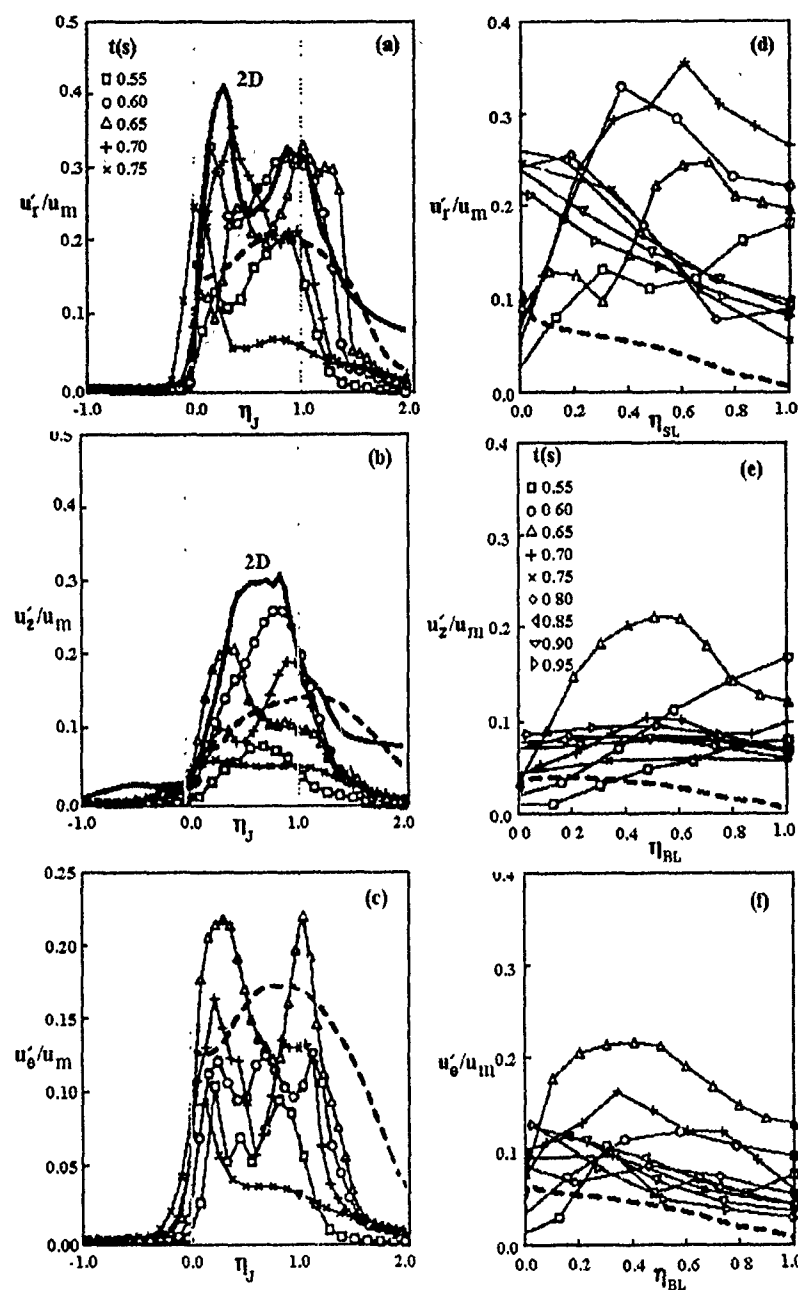
Figure 2: Evolution of the velocity fluctuation profiles at 600 m in the wall jet (a — radial, b — vertical, c — azimuthal) and boundary layer (d, e, f). Solid lines denote previous 2-D calculation, while dashed lines denote measurements.

the numerical simulation of the turbulent wall jet and dusty boundary layer flow induced by a point explosion above a ground surface (Figs. 1–2). During the wall jet phase, the mean profiles (Fig. 1a) resemble our previous two-dimensional calculations, while the velocity fluctuation profiles and Reynolds stress profiles are qualitatively similar to measurements of self-preserving wall jets. During the boundary layer phase (Fig. 1b), the mean velocity profile evolved with time, e.g.: initially it agreed with measurements of a dusty boundary layer behind a shock; at intermediate times it resembled the dusty boundary layer profiles measured in a wind tunnel; while at late times, it approached a 1/7 power-law profile. Velocity fluctuation profiles (Fig. 2) were qualitatively similar to those measured for a turbulent boundary layer on a flat plate. The methodology can be used to predict the evolution of other turbulent fields such as dust clouds, axisymmmetric jets, fireball instabilities, and dusty boundary layers in shock tube and wind tunnel flows.

NUMERICAL SIMULATION OF AUTOIGNITION OF NONUNIFORM UNBURNED MIXTURE AHEAD OF A PREMIXED TURBULENT FLAME FRONT

Andrei N. Lipatnikov

Moscow Institute of Physics and Technology, Dolgoprudnyi, Russia

A model of the influence of turbulence on the autoignition of the unburned gas mixture ahead of a premixed turbulent flame spreading in a combustion chamber of variable volume has been proposed in [1]. Some results of numerical investigations of this influence have been presented in [1, 2]. The goal of this paper is to continue these investigations and simulate the interaction between the turbulence and the unburned mixture temperature nonuniformities due to heat losses through the walls of the combustion chamber.

A cylindrical vessel of variable height is filled with a hydrocarbon–air mixture at the bottom dead center (BDC). Then the height is decreased and the gas is compressed. During the compression phase the chemical reactions are ignored and the mean (over the vessel) pressure and temperature are calculated using the adiabatic compression law. At $t = 0$, the mixture is ignited by a spark located at the center, and a flame spreads to the walls. The turbulence intensity u' and length scale L corresponding to the initial moment are the input parameters of the model, as well as the integral heat

flux $\dot{q}_w$ through the walls, which is assumed to be constant during the process of flame spread. The combustion stage is modeled by a set of time-dependent one-dimensional equations including the k–ε submodel of turbulence, Bray–Moss submodel of flame propagation [3], the balance of enthalpy, and the Shell kinetic scheme [4] for the chemical reactions in the unburned mixture resulting in the autoignition. The minimum value T^{cr}_{BDC} of the mean (over the vessel) gas temperature at the BDC, for which the autoignition can occur before the flame front reaches the walls, is of special importance.
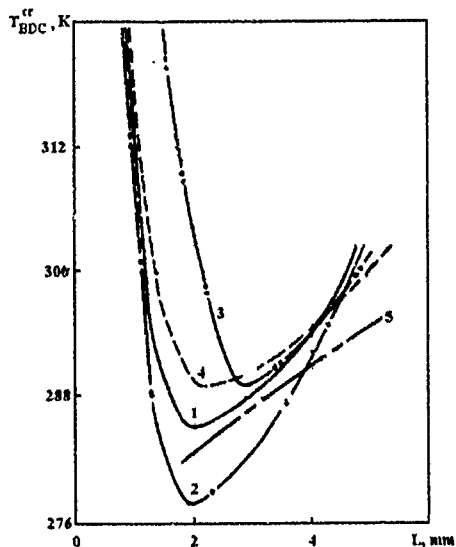
Figure 1: The influence of the initial temperature distribution and the wall heat losses q_w on the critical temperature T^{cr}_{BDC}. 1 — $T_w = 500$ K, $n = 6$, q_w; 2 — 600 K, 6, q_w; 3 — 500 K, 4, q_w; 4 — 500 K, 6, $2q_w$; 5 — as 1 with taking into account turbulent pulsations.
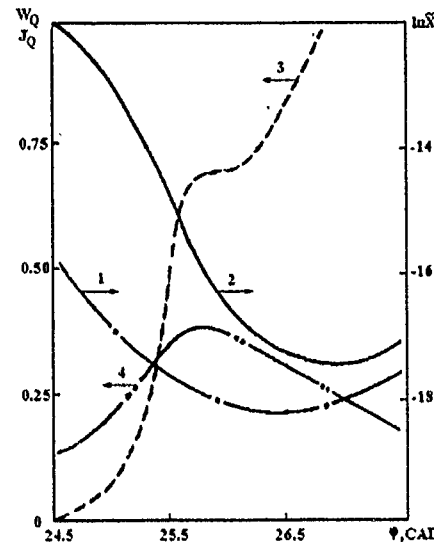
Figure 2: A plot, showing that increase in the wall heat losses is able to accelerate the autoignition due to turbulent diffusion of autocatalytic products from the center of the combustion chamber to the wall. $u' = 2$ m/s, $L = 5$ mm. 1 — $q_w/2$; 2, 3 — W_Q, 4 — J_Q with $2/3 \cdot q_w$. W_Q is the averaged dimensionless rate of autocatalytic products formation; J_Q is the dimensionless turbulent diffusion flux.

Shown in Fig. 1 are the dependencies of T^{cr}_{BDC} on L, computed for various temperature distributions in the near-wall zone. Curve 1 corresponds to $u' = 3.2$ m/s, compression ratio $E = 8$, engine speed $N = 600$ rpm, pressure at the BDC $P_{BDC} = 1$ atm, spark advance $\varphi_0 = 13$ degrees of crank angle (DCA), the exponent of the power-law

near-wall temperature profile at the ignition moment $n = 6$, and the wall temperature $T_{\dot{w}} = 500$ K. According to the Bray–Moss submodel, a decrease in L results in increasing mean rate of products creation and accelerates flame propagation. At small turbulence length scales, this effect is dominant, and the decrease in L suppresses the autoignition. At the larger L, this effect compensates for the widening of the averaged combustion zone, and the increase in T_{BDC}^{cr} with L results from the slower compression of the unburned mixture, whereas the intensification of heat and mass transfer promotes autoignition under these conditions. Owing to the competition between the mechanisms considered, there is a range of the turbulence scales where the autoignition can occur at a lower initial temperature.

Curve 5 has been calculated by taking into account the influence of temperature and concentration fluctuations on the averaged rates of the Shell-reactions. To this end, the model has been modified by expanding these rates in Taylor series before averaging and solving the balance equations for the second-order correlations between the main species and temperature. One can see that the turbulent fluctuations in the unburned mixture promote autoignition.

According to Fig. 1, the increase in T_w promotes autoignition. If the turbulence length scale L is small, the decrease in q_w and the exponent n of the initial temperature distribution will lead to similar effects. When T_{BDC} is close to T_{BDC}^{cr}, the higher is the initial temperature, the shorter the autoignition delay is, and the effect of variations in T_w, or n, or q_w (see Fig. 1) is caused by the respective variations of mean local temperature of the unburned mixture in the near-wall zone. However, when L is larger, an increase in wall heat losses can promote autoignition, as illustrated by the intersection of curves 1 and 4 in Fig. 1.

This effect is elucidated in Fig. 2. According to the Shell scheme, after the cool flame is quenched, the Favre-averaged mole fraction $\tilde{X}_B$ of the branching agents, B, falls to a small value. For larger q_w, this value is greater. As a result, after the cool flames have been quenched everywhere in the unburned mixture, the concentration of B is the highest near the walls. Such a distribution, together with the turbulent diffusion of autocatalytic product, Q, from the center of the vessel to the walls (see Fig. 2) can promote the autoignition in the near-wall zone, when q_w is increased.

References

[1] Lipatnikov A. N. *Khimicheskaya Fizika*, 1992, **11**, 12, 1665 (in Russian).

[2] Lipatnikov A. N. *Proc. Int. Scientific Conf. on Internal Combustion Engines.* Gdansk, 1993, 285.

[3] *Turbulent reacting flows*, (P. A. Libby, F. A. Williams Eds.), N. Y., Springer–Verlag, 1980.

[4] Halstead M. P., Kirsch L. J., Quinn C. P. *Comb. Flame*, 1977, **30**, 45.

TURBULENCE MODELLING OF FOUR DIFFERENT TYPES OF CONFINED SWIRLING FLOWS USING THE k–ε MODEL AND REYNOLDS STRESS MODEL

C. M. Trinh

Laboratory of Heating and Air Conditioning, Technical University of Denmark
Building 402, DK-2800 Lyngby, Denmark

Turbulent swirling flow is very important in combustion. It is used to stabilize the flame in furnaces. In this study, isothermic swirling flows were computed by means of a commercial computer code FLOW3D (release 2.4) from Harwell Laboratory. The "standard" wall reflection term (WRT) proposed by Gibson & Launder [3] in FLOW3D for simple geometries (e.g. pipe or plane) was extended to complex geometries. This term is used in Reynolds Stress Models in order to improve the results. Experience and recommendations are described in this paper.

Four test cases with four different types of confined swirling flows were used for the testing. These cases were called A (Kitoh [5]), B (So *et al.* [6]), C (IFRF [4]) and D (Risø [1]). The geometries of cases A and B were long pipes called "simple", whilst the geometries of cases C and D were called "complex" because they have inlet, divergent (quarl) and outlet sections. After the quarl, there was an expansion region (field) and before the outlet section there was a contraction region. These regions make the flow very complex. The flows of cases A and C were simple flows, which have only one flow at their inlets and the flows in cases B and D were called complex, because they had more than one flow at inlet. The diameters in test cases C and D (0.640 m and 1.200 m) were larger than the diameters in cases A and B (0.150 m and 0.125 m).

All the cases were computed using k–ε model (KEM) and Reynold Stress Model (RSM). The velocities calculated using RSM were much closer to experimental data than those calculated using KEM. However, the agreement of tangential velocities with the data was still poor. The tangential velocity profiles computed using KEM evolved too rapidly to a solid body rotation (forced vortex) and therefore they were quite different from experimental data.

The RSM with WRT was also used to compute the flows. C_μ is the empirical constant that appears both in KEM and RSM. In KEM, C_μ is the constant (having only one value) in the expression for turbulent viscosity ($\mu_T = C_\mu \cdot k^2/\epsilon$, where $C_\mu = 0.09$). However, in RSM the "constant" C_μ appearing in the WRT varies with different flow types, and its optimum value seems to be case-dependent.

The WRT term was very difficult to implement in flows with complex geometries, e.g., a geometry with divergent walls (cases C and D), because at the divergent wall the normal vectors in WRT must be divided into two vectors: one parallel and one normal to the wall. They are indistinct at the boundary between inlet and divergent section

and, therefore, give poor results. The *WRT* without the influence of the divergent wall ($C_\mu = 0.00$ at divergent wall) was also used for examination in cases C and D. The results obtained with *RSM* with and without *WRT* are quite different. However, the difference is small, and the choice of the empirical constant C_μ is still somewhat doubtful, due to the inaccuracy of experimental data.

Case A is a simple swirling flow, and case D is a very complex swirling flow. Apart from various turbulence models, *RSM* with and without *WRT*, these cases were also tested with various difference schemes and grid resolution. Four difference schemes, Upwind-Difference Scheme (UDS), Higher-Order Upwind Difference Scheme (HUDS), Quadratic Upstream Interpolation for Convective Kinematics Schemes (QUICK) and Curvature Compensated Convective Transport Scheme (CCCT), were used for testing. For case A, there were no significant differences between them, which may be due to the fine grid ($NI \times NJ = 60 \times 35$) and a very uniform flow. However, in case D, with the $NI \times NJ = 75 \times 51$ grid, the UDS (first-order accurate) was not good for computations.

A number of tests of the sensitivity to the grid density were performed. In case A, the calculations were performed with the grid densities $NI \times NJ = 40 \times 23$, 60×35, 60×48, 80×35 and 80×48 (RSM was employed in all calculations). In case D, the grid densities used in RSM were $NI \times NJ = 50 \times 51$, 75×51, 100×51, 75×38 and 75×76 and in KEM were 75×51 and 75×76. The grid densities 60×35 in case A and 75×51 in case D are sufficient for the computations.

Some of the conclusions of this paper are:

- Most of the experiments involved only a few measurement points in the radial direction, which may present problems with the specification of the inlet. Interpolation is a poor method for swirling flows when the velocity profiles are not linear.

- The *RSM* is much better, with regard to computing the swirling flows, than *KEM* (Figs. 1 and 2). In general, the mean flow properties are predicted better than the turbulence properties.

- It is very difficult to specify the *WRT* at the boundary between the inlet and divergent sections in cases C and D. However, the *WRT* without the influence of divergent wall can be instrumental. $C_\mu = 0.065$ can be used in turbulent parallel flows [7] (it has also been recommended by Harwell Laboratory) but $C_\mu = 0.090$ may be the best for swirling flows.

- The strong central jet (case B) can reduce the influence of *WRT*.

- For axisymmetric flows, the influence of *WRT* should be due to the presence of two walls. However, the difference between the effects of one and two walls is small.

264
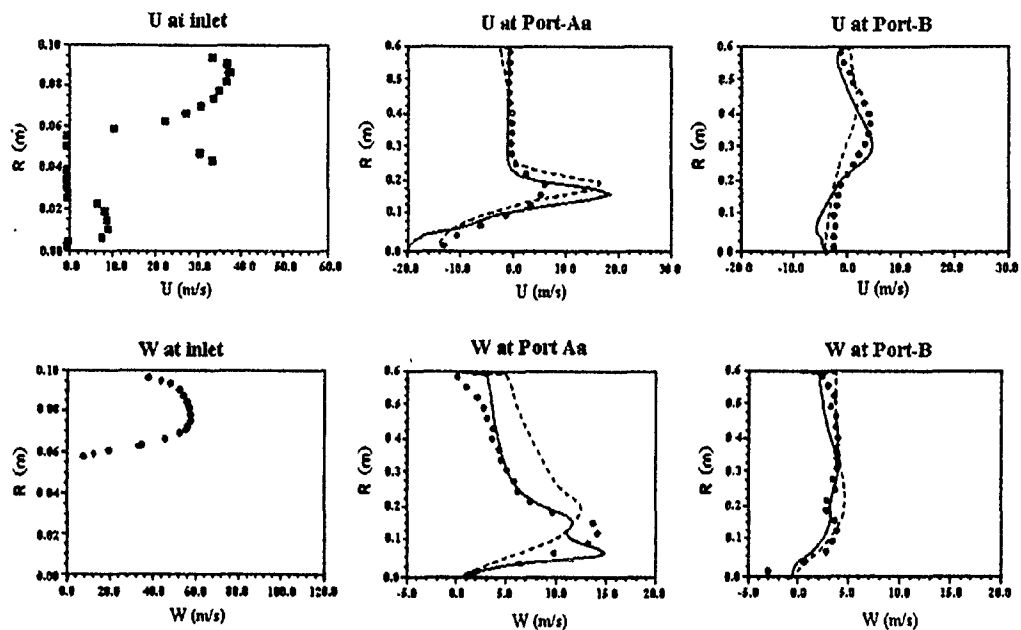
Figure 1: U — axial velocity profile, W — tangential velocity profile; Risø's test case. o experiment; —— RSM (without WRT); - - - KEM.
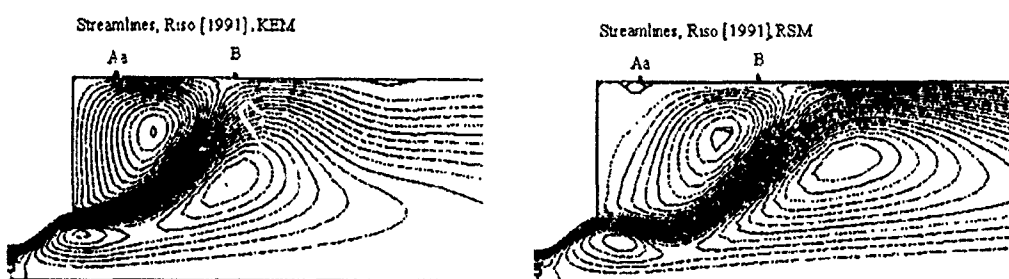
Figure 2: Streamlines; Risø's test case. KEM: k–ε Model, RSM: Reynolds Stress Model

265

- Computations using RSM with WRT required a CPU time by about 8% longer than for the computations using RSM without WRT.

- The difference schemes have a significant effect on the complex flow (case D) and almost no effect on more uniform flows, such as the flow in case A.

- The grid density in the radial direction is very critical as compared with that in the axial direction. The KEM is more sensitive to grid density than the RSM.

References

[1] Bak J., Clausen S., Astrup P. *LDA measurements of burner inlet conditions and cold flow in furnace room*. Report for Fase 1 of Project 02259. Department of Combustion Research, Risø National Laboratory, Denmark, 1991.

[2] Beér J. M., Chigier N. A. *Combustion Aerodynamics*. London, Applied Science Publ. Ltd., 1972.

[3] Gibson M. M., Launder B. E. *J. Fluid Mech.*, 1978, **86, 3**, 491–511.

[4] Hagiwara A., Bortz S., Weber R. *IFRF doc. No. F259/a/3*, International Flame Research Foundation, 1986.

[5] Kitoh O. *J. Fluid Mech.*, 1991, **225**, 445–479.

[6] So R. M. C., Ahmed S. A., Monjia H. C. *NASA CR–3832*, 1984.

[7] Trinh M. C. *Ph.D. Thesis*. Risø-R–647(EN) Department of Combustion Research, Risø National Laboratory, Denmark, 1993.

SESSION 5. Unsteady Combustion

THE EXCITATION CONDITIONS OF A KINETIC SINGING FLAME

V. V. Afanas'iev, S. A. Abrukov, A. K. Kuz'min, A. I. Kitaev

Chuvash State University, Moskovskii prosp. 15, Cheboksary, Russia

Many researchers studied oscillatory combustion over the last few decades. However, no unified explanation of the development mechanism of vibrational combustion has been established. In particular, not much is known about kinetic singing flames (KSF), despite the fact that they provide a convenient model unobstructed by such phenomena as atomization, evaporation and mixing of the fuel components and hence useful for determination of the role played by combustion *per se* plays in the nature of the phenomenon in question. In [1], KSF excitation and silence concentration ranges were first reported to depend on propane–air mixture composition (in the range of 3–15%), without the physical mechanism of the observed phenomena being discussed.

The objective of the present work was to examine the mechanism of the influence of fuel mixture composition on the KSF excitation and silence concentration ranges. Experiments were made using tubes 35 mm in diameter and 1.2 to 1.8 m in length. The fuel mixture was prepared dynamically, and its composition and flow rate were monitored by a Rayleigh interferometer and rotameters. The burners used were made of copper and stainless steel. Visualization was provided by schlieren optics with a slit-and-thread technique. As part of the experiments, the acoustic pressure level and the phase difference between the pressure oscillations and the heat release rate were measured. Following [2], the heat release rate was determined from the CH intermediate radical radiation intensity at wavelength 431.5 nm recorded by a photomultiplier. This is also evidenced by the in-phase variation in the optical radiation and the flame surface calculated from the cine film frames containing schlieren images and oscilloscope records of the radiation. The authors believe that the normal rate of combustion is unaffected by the acoustic oscillations observed. Figure 1 shows plots of (1) the level of the acoustic pressure recorded by the microphone installed at the lower end of the tube resonator; (2) the level of the integral (over the flame volume) light emission flux; and (3) the phase shift between the pressure oscillations and radiation versus the propane–air mixture composition. The vertical lines in Fig. 1 represent the limits of flame excitation.

The results of numerous experiments conducted by the present authors suggest that the number of the excitation zones and their locations depend on the tube resonator length, whereas the excitation zone width and the intensity of acoustic oscillations are functions of the tube resonator Q-factor. Also, it should be noted that the zone width
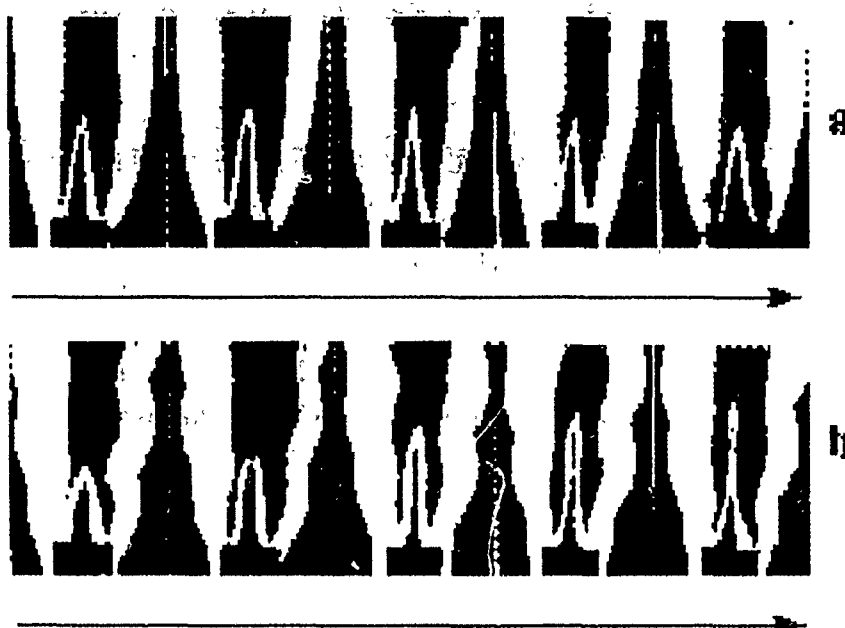
Figure 1: Parameters of the singing flame versus the fuel mixture composition.

and its location depend only slightly on the fuel mixture flow rate, when other parameters are equal. As suggested by Fig. 1, the acoustic pressure level and the optical radiation intensity have a dome shape depending on the fuel mixture composition, and the phase shift in each zone is different in character and is less then 90% in magnitude. Moreover, the pressure oscillations are advanced in phase with respect to the optical radiation, and, formally, the pressure oscillations occurring in all the three areas can be intensified through periodic heat release due to variation in the flame surface area, according to the Rayleigh criterion. However, if one, strictly adheres to the Rayleigh criterion, the pressure maximum should correspond to zero phase shift, which is at variance with the experimental evidence. In order to provide an explanation for this discrepancy, special experiments were made to determine the pressure oscillations — optical radiation phase shift selected by means of a horizontal slit moved vertically relative to the flame height for different fuel mixture compositions. The experiments indicated that the phase shift did vary with the flame height from 0 to 2, with the maximum and minimum phase shifts occurring in the third and the first excitation areas, respectively. In addition, the zero phase shift and maximum optical radiation intensity for mixtures developing maximum pressure oscillations are observed at the coordinate which corresponds to the cone tip of the undisturbed flame or to the middle position of the oscillating flame tip. When the fuel mixture composition is made richer or leaner, the phase shift increases, i.e. the conditions of pressure oscillation excitation deteriorate and reach the laboratory noise level at the self-excitation limits. As suggested by the
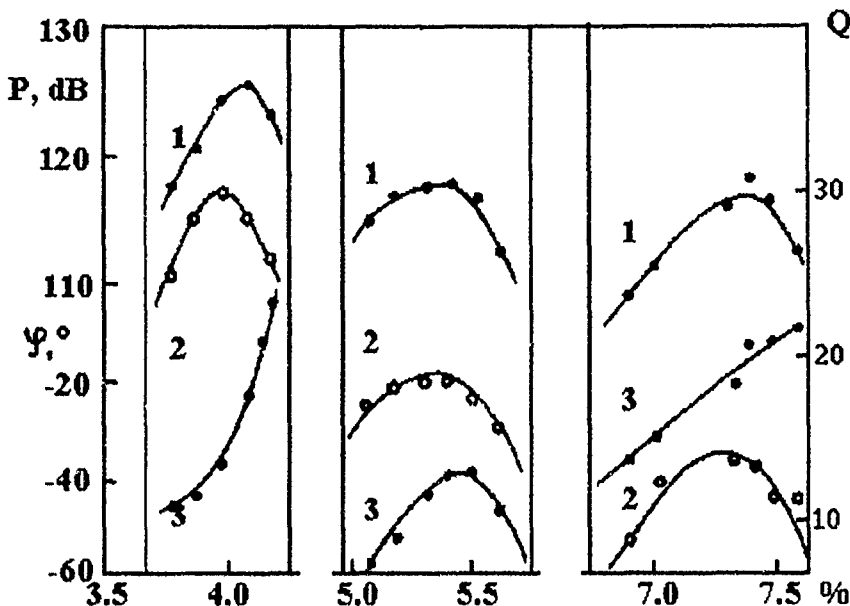
Figure 2: Cine film frames representing the singing flame excitation process: (a) the starting moment (b) "mature" oscillations.

cine film images (Fig. 2) and optical radiation intensity analysis, it is at the apex of the cone that the heat release varies most, i.e. the apex of the flame cone is responsible for maintaining the existing pressure oscillations. Thus, the appearance of KSF excitation and silence zones is linked to the deterioration of the phase relationships deteriorating between the pressure oscillations and heat release rate at the apex of the flame cone, which is the case when the fuel mixture composition is varied.

In summary, the occurrence of KSF self-excitation and silence areas, varying with the fuel mixture composition, is due to the changes in the phase relationship between the pressure oscillations and heat release rate.

References

[1] Afanas'iev V. V., Kuz'min A. K., Abrukov S. A. *Combustion and Electrodynamic Phenomena*, Cheboksary, 1990, 14-19 (in Russian).

[2] John R. R., Summerfield M. *Jet Propulsion*, 1957, **27**, 169-178.

UNSTEADY EFFECTS IN PROPELLANT COMBUSTION AT HIGH PRESSURES

V. N. Alexandrov, B. D. Dinovetsky, A. V. Kostochko,
V. N. Marshakov*

Semenov Institute of Chemical Physics, Moscow, Russia

Due to the fact that experimental studies of unsteady propellant combustion have been carried out only at low pressures [1–3], and the results of theoretical works [4, 5] are contradictory, there is currently no common view with regard to the occurrence of unsteady effects at high pressures.

In this report, we present experimental evidence of the occurrence of unsteady effects at high pressures and estimate the limits of their existence.

In the experiments, the variation of propellant sample sizes during combustion with pressure increase or decrease was recorded by means of high-speed filming. The burn rate was determined by the results of streak recording. Simultaneously with the filming, pressure was measured in the combustion chamber.

Three series of experiments with an NDT type ballistite propellant have been carried out: in the first series, the propellant burn rate was determined at increasing pressure; in the second series, the propellant burn rate in going from one pressure level to another higher one was determined; in the third series, the propellant burn rate at increasing pressure was determined by its extinction due to pressure drop [6].

The results of the first series have shown that the mean values of burn rates measured at the pressure increase rates of 450, 1120 and 1510 MPa/s virtually coincide with the steady burn rates. At the pressure increase rates of 2122 and 9720 MPa/s, the mean values of burning rates agree with the steady values up to pressures $\sim$ 60 MPa and at higher pressures become considerably lower than the steady ones.

At pressure increase rates up to 1510 MPa/s, the propellant combustion proceeded in a steady regime, and at pressure increase rates greater than 2125 MPa/s, unsteady combustion was observed. The rates of pressure increase corresponding to the transition from the steady to unsteady conditions of propellant combustion are within 1510–2125 MPa/s.

In the second series of experiments, after ignition, the propellant combustion proceeded after ignition at increasing pressure and then at almost constant pressure.

In all the experiments (with pressure increase rates ranging from 2400 to 21500 MPa/s), the experimental propellant burn rate at increasing pressure was lower than the steady burn rate, continued to increase at constant pressure and later reached the steady value corresponding to the final pressure level. During propellant combustion at constant pressure, one can observe the variation of burn rates which points to the unsteadiness of propellant combustion under these conditions.

It should be noted that the results of the second series of experiments agree with the unsteady combustion theory, the variability of propellant surface temperature [7] and the results of experimental studies at low pressures [3] being taken into account.

In the third series of experiments, combustion was interrupted by a sharp pressure drop, and the propellant extinction time was determined, which depended on pressure increase rate at constant parameters of the pressure drop. Moreover, it was concluded that, if the extinction time did not vary with the pressure increase rate, the propellant combustion was steady at increasing pressure and unsteady otherwise.

The results obtained have shown that the extinction time depends on the pressure increase rate, which makes it possible to determine the value of pressure increase rate dividing the steady and unsteady combustion modes. For pressures ~ 60 MPa, the value of this pressure increase rate is about ~ 1500 MPa/s, which agrees well with the results of the two previous series of experiments.

The results of numerous experiments with propellant extinction point to the unsteadiness of propellant combustion at pressure drop, as evidenced by rather high values of pressures at which it is completed (up to 48 MPa), the variable influence of initial temperature, the use of catalysts and combustion stabilizers for extinction at drops from high to low initial pressures.

To estimate the limits of unsteady effects due to the pressure drop in the first approximation, one can assume the value of the critical rate of pressure drop. These values divide not only different combustion modes but also the ranges of propellant burn rates where they are quite different.

A negligible increase in the rate of pressure drop near its critical value leads to extinction and a decrease in the average combustion rate by approximately 2 times, without any variation with a further increase in the rate of pressure drop. The value of critical rate of pressure drop for an NDT type ballistite propellant at pressure of ~ 60 MPa is 2500 MPa/s.

In summary, the results of the study point to the occurrence of unsteady effects in propellant combustion at high pressures.

References

[1] Marshakov V. N., Leipunsky O. N. *Fizika Gorenija Vzriva*, 1967, **3**, 2, 231 (in Russian).

[2] Ivashchenko Yu. S., Komarov A. S. *ibid*, 1978, *14*, 1, 151 (in Russian).

[3] Zhernosekov G. I., Karatigin N. A., Marchenko V. V., Romanov O. Ya., Ulitin V. D., Zheltuhin P. P. *Proc.2nd All-Union Symposium on Combustion and Explosion*. Collected Papers. Chernogolovka, 1969, 13 (in Russian).

[4] Cooker D. E., Nelson C. W. *Trans. ASME: J. Heat Transf.*, 1979, **101**, 2, 359.

[5] Cohen Norman S., Strand Leon D. *AIAA J.*, 1980, **18**, 8, 968.

[6] Alexandrov V. N., Dinovetsky B. D., Kostochko A. V. *Chemical Physics of Combustion and Explosion Processes. Combustion of Condensed Systems.* Chernogolovka, 1989, 51 (in Russian).

[7] Novozhilov B. V. *Unsteady Combustion of Solid Propellants.* Moscow, Nauka, 1973 (in Russian).

CONTROLLABLE REGIMES OF NONSTEADY COMBUSTION OF SOLID PROPELLANTS

V. A. Arkhipov

Institute of Applied Mathematics and Mechanics, Tomsk, Russia

Active control of a burning solid propellant charges important from both technological and scientific perspectives. Controlled thrust termination of a solid-propellant rocket motor largely improves its flexibility in operations; the lack of flexibility is indeed one of the main disadvantages of the solid-propellant as compared to liquid-propellant motors. The purpose of this presentation is to propose three concepts for controlling solid propellant combustion rate and discuss some experimental results concerning this subject.

The characteristic property of combusting gas-permeable systems is that the convective mechanism of combusting wave propagation essentially prevails, as compared with the conductive one. As a result, the mass combustion rate can lead to an increase in the rate of layer-by-layer combustion of a monolith block by several orders of magnitude. Such a regime has been known in literature as convective combustion (CC).

Perhaps, the creators of the first specimen of a firearm who filled a liner with black powder were the first to have used the convective combustion regime. At present, the combustion of a fill charge is widely applied in guns of various types.

In combustion of condensed systems, this regime commonly plays a negative role. The initiation and development of CC in the cracks and pores of the charge, which under certain conditions develops into detonation, can result in damaging of the block. Combustion in fill charges and single pores has long attracted physicists' attention.

The essential progress in understanding these processes has been achieved due to the works by K. K. Andreev, A. F. Belyaev, B. S. Ermolaev, A. I. Korotkov, N. N. Smirnov, A. A. Sulimov, Godai, S. M. Kovachich, M. Kumar, K. Kuo, A. Chen and others.

In this study, we made an attempt to find a means of controlling the CC regime and thus to obtain useful effects. With this aim in view, we proposed to create ordered porous structures in the bulk of the charge. As an example, consider a "sandwich", consisting of stacked plane parallel plates, with network of capillary channels on the end surfaces. The combustion of the "sandwich" is characterized by a number of interesting effects, the most important of which are:

- initiation and development of the CC in the capillary network,

- nonsteady two-sided after-burning of individual plates.

In this work, a detailed study of the CC initiation and development in plane capillary networks and the location of ignition spots at the channel walls was performed using high-speed filming. The steady-state ignition conditions have been experimentally obtained and the quantitative characteristics of the process have been found.

During the two-sided afterburning of the symmetrical elements (plates), an interesting type of a nonsteady combustion associated with the temperature field evolution inside a plate (superposition of Mikhelson profiles), rather than with the variable external conditions, takes place. A. D. Margolin and Yu. A. Gostintsev (1964) were the first to propose a theory of this regime.

Here, analytical and experimental results concerning the plate afterburning in a half-closed volume at increasing pressure are discussed. An expression for the amplitude of a pressure shock well correlating with numerical results and test data has been obtained by the method of integral relations. In order to find out the "net" effect of the heating of a central part of the plate, control tests of lateral afterburning of the plates were carried out over a wide range of thermal diffusivities.

As applications of the above phenomenon, two schemes of gas generators with program and command control of product consumption were considered. In the first scheme, the preset cyclogram of combustion is provided by the "sandwich" assembly of solid and gas-permeable plates. In the second scheme, the gas inlet control is operationally realized by means of an electric arc fuse positioned along the "sandwich". The burnout rate determines the velocity of the combustion wave along the charge.

The presented test results for the gas generators have proved the practicability of the regime controlled by convective combustion with a significant positive effect (30-fold consumption control).

An active control of a burning solid propellant charge could be achieved by forcing cones around the areas of faster burning rate. A general concept of active control of cone burning is presented based on the principles implicit in metal wire technology. We discuss a new approach employing metal elements made of shape-memorizing alloys. The shape-memorization phenomenon in metals can be used to increase the extent of

burning rate control. This concept combines the use of thermal mechanism, mechanical destruction of channels and convective combustion in pores.

Erosive burning is usually due to the increase in the propellant burning rate caused by high-velocity combustion gases flowing over the propellant surface. The turbulent nature of the flow field over the propellant surface contributes in two ways to the erosive burning behavior. First, it enhances diffusive mixing of the fuel and oxidizer gases, bring the gas-phase reaction zone and heat release zone closer to the surface as the free stream velocity increases. Secondly, the rate of heat transfer to the propellant is increased because turbulence increases the transport coefficients of the gas phase. The overall effect of turbulence, therefore, is to enhance thermal feedback, which, in turn, increases the burning rate of a propellant.

These effects are more important in swirling flows. A concept of active control of solid propellant burning rate has been developed, which makes use of the influence of swirl intensity on the erosive burning. The effect of the swirl intensity in the gas flow blowing along the propellant surface of a charge of channel–tube shape, was studied experimentally. Criterial expressions for the erosion factor have been obtained for two orientations of the burning surface with respect to the vector of mass forces. The expressions obtained have been reformulated in terms of modified Vilyunov parameter.

PARAMETRIC ANALYSIS OF THE ZEL'DOVICH–SEMENOV MODEL

V. I. Bykov, T. P. Pushkaryeva

Computer Center, 660036 Krasnoyarsk, Russia

Model. For one chemical reaction of the n-th order $nA \longrightarrow B$, where A is hydrocarbon and B is the combustion product, the nondimensionalized mathematical model of continuous stirred-tank reactor is

$$\dot{x} = f(x)\exp\left(\frac{\theta}{1+\beta\theta}\right) - \frac{x}{Da} = f_1(x,\theta),$$

$$\gamma\dot{\theta} = f(x)\exp\left(\frac{\theta}{1+\beta\theta}\right) - \frac{\theta}{Se} = f_2(x,\theta), \tag{1}$$

$$f(x) = (1-x)^n.$$

The steady states of the system (1) are the solutions to the equations

$$f_1(x, \theta) = 0,$$
$$f_2(x, \theta) = 0, \tag{2}$$

which can be reduced by elementary transformations to

$$F(\theta) = P(\theta). \tag{3}$$

Here, $F(\theta)$ is the heat production function and $P(\theta)$ is the heat loss function under steady-state conditions. The solutions to Eqs. (2) are considered in the region

$$\Omega = \{x, \theta : 0 \le x \le 1, \ 1 \le \theta \le \theta^\infty\}.$$

Equations (2) have one or several steady-state points. These points are analyzed using Semenov diagram, where the dependencies of the heat production and heat loss rates under the steady-state conditions on the substance temperature in the reactor are plotted.

The points of the intersection of $F(\theta)$ and $P(\theta)$ are the steady state temperature. For the steady-state to be unique it is necessary and sufficient that the heat loss rate in the steady state be greater than the heat production rate, i.e.

$$P' > F'. \tag{4}$$

Stability of steady states. The type of stability is known to be determined by the roots of the characteristic equation

$$\lambda^2 + \sigma\lambda + \Delta = 0,$$

where the coefficients σ, Δ are defined in terms of the elements of Jacobi matrix of the right-hand sides of Eqs. (2) in the steady-state:

$$\sigma = -(a_{11} + a_{22}), \qquad \Delta = a_{11}a_{22} - a_{12}a_{21},$$

The steady-state is stable if the inequalities $\Delta > 0$ and $\sigma > 0$ are satisfied.

Parameter dependencies. The steady states are the solutions to Eq. (3) or the equation

$$G(\theta) = F(\theta) - P(\theta). \tag{5}$$

Let us rewrite Eq. (5) as

$$G(\theta, Da, Se) = 0, \tag{6}$$

where, apart from θ, two parameters, Se and Da, are resolved. By virtue of the specificity of the system (2), Eq. (6) is linear in Se and Da, and (6) can be represented as

$$Da\, g_1(\theta) = g_2(\theta) \quad \text{or} \quad Da = Da(\theta) = \frac{g_2(\theta)}{g_1(\theta)}.$$

By constructing the dependence $Da(\theta)$, we obtain a function which is inverse to the unknown parametric dependence $\theta(Da)$. Knowing $\theta(Da)$ and using Eqs. (2), we can construct the dependence $x(Da)$.

Thus, the dependence of the steady state on parameters can be constructed without iteratively solving the algebraic equation (3).

Multiplicity curve. The set (2) involves four parameters: Da, β, γ and Se. Let us construct the multiplicity curve in the plane of two parameters, for example, Da and Se. We need to solve the equations

$$G(\theta,\, Da,\, Se) = 0. \tag{7}$$

$$\Delta(\theta,\, Da,\, Se) = 0. \tag{8}$$

Substituting the explicit expression for $Se(\theta, Da)$, obtained from Eq. (7), into Eq. (8), one can write out the equation for the boundary of the steady state multiplicity region L_Δ in the parameter plane $(Da,\, Se)$:

$$L_\Delta(\theta,\, Da(\theta),\, Se(\theta,\, Da)) = 0 \tag{9}$$

Neutrality curve. When $\Delta > 0$, the stability is determined by the sign of σ: if $\sigma > 0$, the steady state is stable, and if $\sigma < 0$, it is unstable. This the curve L_σ: $\sigma = 0$ corresponds to the bifurcation points of parameters and can be used to analyze the change in the steady state stability. The curve L_σ is defined by the equations

$$G(\theta,\, Da,\, Se) = 0 \tag{10}$$

$$\sigma(\theta,\, Da,\, Se) = 0 \tag{11}$$

By substituting the explicit expression for $Da(\theta)$, obtained from Eq. (10), into Eq. (11), one can arrive at the explicit form of the equation for the curve L_σ.

The mutual configuration of the multiplicity and neutrality curves in various parameter planes is most interesting, because it provides a basis for a comprehensive classification of steady states. The explicit form of the local bifurcation curves L_Δ and L_σ in various planes of dimensionless parameters also makes it possible to construct these curves in various planes of actual dimensional parameters. In this work, the curves L_Δ and L_σ are constructed in the $(T^\circ,\, C_0)$ plane, where C_0 is the concentration of oxygen in the fuel–air mixture of hydrocarbons (for $n = 1$).

Phase portraits. The bifurcation curves L_Δ and L_σ divide the parameter plane into six regions which are distinguished by the number and stability type of the steady states. For a fixed set of parameters, each phase portrait was constructed by integrating the set of the two ordinary differential equations (1) with various initial conditions. The values of $(x(0),\, \theta(0))$ were taken on the boundary of the reaction simplex Ω.

Time dependencies. When Eqs. (1) have a single stable steady state, the solution $(x(\tau),\, \theta(\tau))$ tends to it as $\tau \longrightarrow \infty$ with any initial conditions. If the equations have

276

three steady state solutions (one unstable and two stable), $x(\tau)$ and $\theta(\tau)$ tend to one of the stable steady states. The temporal self-oscillations of the dimensionless temperature and concentration are of relaxational nature.

Conclusion. The developed method can be applied to other parameter-dependent models of CSTR. For example, the model reaction $O_2 + nA \rightarrow B$ in some cases is similar to the Zel'dovich–Semenov model. Thus, its parametric analysis can follow the demonstrated scheme. The mutual configuration of bifurcation curves makes it possible to predict the ignition conditions and dynamic behavior of a combustion process.

MEAN DYNAMICS OF FORCED WRINKLED FLAMES

Pierre Cambray, Karl Joulain, Guy Joulin

Laboratoire d'Energétique et Détonique, URA 193 CNRS, ENSMA
Site du Futuroscope, B.P. 109, 86960 FUTUROSCOPE (Poitiers — France)

In the absence of significant body forces, premixed flames propagating in quiescent gases are subject to the Landau [1] — Darrieus [2] instability: the long-wave, harmonic ($\sim \Gamma(t)\exp(ik.X)$) infinitesimal disturbances of a planar front have an amplitude governed by $\dot{\Gamma}/\Gamma = S_L\Omega|k|$ (with $|k| = (k \cdot k)^{1/2}$, S_L = laminar flame speed, Ω = known positive dimensionless function of the density contrast $\gamma = (\rho_u - \rho_b)/\rho_u$). Local changes in the burning speed due to curvature and stretch modify the dynamics to $\dot{\Gamma}/\Gamma = S_L\Omega|k|(1 - |k|/K_{neutral})$ with the net result that only the modes with k below the neutral wavenumber $K_{neutral}$ lead to exponentially growing amplitudes. The minimum of $\dot{\Gamma}/\Gamma$, attained at $|k| = K_{neutral}/2$, defines the characteristic time $t_{LD} = (4/\Omega S_L)K_{neutral}$. If the fresh gases are *weakly turbulent* (RMS intensity $u' \leq O(S_L)$) the above mechanisms of wrinkling still exist but must compete with the incoming velocity fluctuation and, of course, with nonlinearity. To analyze such situations we studied the forced Michelson–Sivashinsky equation [3]

$$\dot{\phi} + \frac{S_L}{2}(a\phi_{X^2} + (1-a)\langle\phi_{X^2}\rangle) = S_L\Omega\left(\frac{\phi_{XX}}{K_{neutral}} + I(\phi, X)\right) + u(t, X) \qquad (1)$$

where $a(\gamma) \geq 1$ is known, the linear operator $I(\phi, X)$ is defined by $I(e^{ikX}, X) = |k|e^{ikX}$ and $\langle \cdot \rangle$ denotes a transverse average. In the absence of forcing ($u' \equiv 0$), Eq. (1) was recently shown to yield fair quantitative predictions [4] for the shape(s) and speed(s) of spontaneously-grown wrinkles.
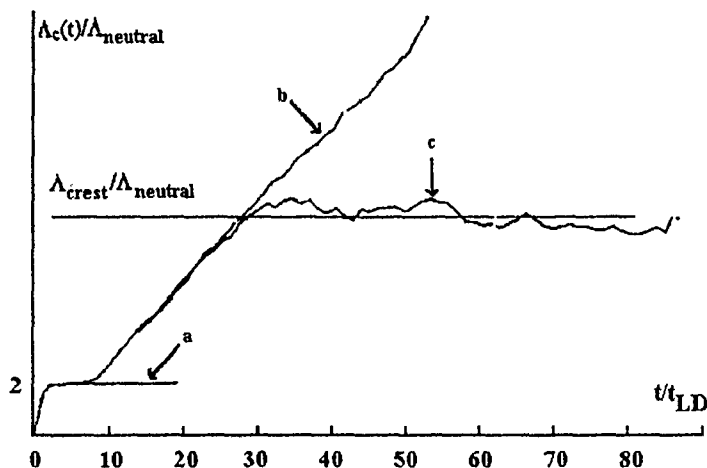
Figure 1: Sample time–evolutions of $\Lambda_c(t)$. Curve a: linearized version of Eq. (1); Curve b: from Eq. (1) with noise cut-off for $t > 8t_{LD}$; Curve c: Regular case, with noise from $t = 0$ onward. All curves correspond to 50 realizations of $u(t, X)$.

The forcing function $u(t, X)$, meant to represent propagationwise turbulent velocity fluctuations, is a two-dimensional superposition of "square eddies" at the mean flame location $Z = \langle Z_f \rangle \equiv -S_L t + \langle \phi \rangle$ (hence $\langle \dot{Z}_f \rangle = -S_L(1 + \langle \phi_{X^2} \rangle /2)$), viz:

$$u(t, X, Z) = u' \sum_{n \geq 1} \sigma_n \cos(n K_{box} X + X_n) \cos(n K_{box} Z + Z_n + \bar{\omega}_n t) \qquad (2)$$

Apart from u', Eq. (2) involves the phases $X_n = r_n 2\pi$ and $Z_n = r'_n 2\pi$ and turnover frequencies $\omega_n \sim \sigma_n u' n K_{box}(2r''_n - 1)$ defined in terms of independent random variables (r_n, r'_n, r''_n) which are sampled uniformly over $[0, 1]$; the weights σ_n determine the spectral energy of $u(t, X)$ and are defined by

$$\sigma_n \sim S\left(\frac{n K_{box}}{K_{int}}\right), \qquad \sum_{n \geq 1} \sigma_n^2 = 1 \qquad (3)$$

in terms of the integral length of forcing, $L_{int} = 2\pi/K_{int}$, and of the imposed spectrum $S(\cdot)$.

Assuming $\phi(0, X) \equiv 0$ and $2\pi/K_{box}$–periodicity in X, we studied Eq. (1) numerically and analytically, focusing on the mean, ensemble-averaged spacing $\Lambda_c(t)$ between flame crests (local maxima of ϕ). Examination of many histories $\Lambda_c(t)$ such as that labelled "c" in Fig. 1 led us to distinguish among three consecutive stages.

Linear stage: While ϕ_X is still small, one can linearize and solve Eq. (1) to show that the corresponding $\Lambda_c(t)$ approaches $2\Lambda_{neutral}$, as shown by curve "a" in Fig. 1.

This lasts until ϕ_{X^2} ceases to be negligible, i.e. for $t \leq t_*$ with [5]

$$\left(\frac{t_*}{t_{LD}}\right)^{\frac{1}{4}} \exp\left(-\frac{t_*}{t_{LD}}\right) \Omega \sqrt{\Omega^2 + 4} \sim \frac{u'}{S_L}\left(\lambda S \frac{\lambda}{2}\right)^{\frac{1}{2}}, \quad \lambda \equiv \frac{L_{int}}{\Lambda_{neutral}}. \tag{4}$$

For $u'\langle\langle S_L, t_*\rangle\rangle t_{LD}$, and an analysis shows that the influence of $u(t,X)$ is then felt at early times only ($t \sim t_{LD}$).

When $t = t_* + O(t_{LD})$, approximately equidistributed and mature cells have been born; they are about $2\Lambda_{neutral}$ in wavelength, hence $\pi/K_{box}\Lambda_{neutral}$ in number, and have $O(\Omega/aK_{neutral})$ amplitudes. At $t \sim t_*$, they begin to enter a coalescence stage during which $\Lambda_c(t)$ increases linearly; curve "b" in Fig. 1, obtained numerically from Eq. (1) by setting $u'/S_L = 0$ for $t > O(t_{LD})$, shows that the coalescence is unaffected by the noise [5], because the corresponding cell troughs are too highly curved [6]. An inspection of the exact solutions of the unforced MS equation that are provided by the pole-decomposition method [7] confirmed that the coalescence stage is governed by the free-flame dynamics with $d\Lambda_c/dt = const \cong 0.3\Lambda_{neutral}/t_{LD}$. The latter statement is also confirmed by an approximate, mean-field analysis of the collective crest dynamics; which is reduced to a nonlinear recursion for the pdf of finding the crests about evenly spaced location and turned out to be statistically self-similar asymptotically.

Finally, when the cells become wide enough to be sensitive to the external disturbances despite the stretch effect induced by the curvature of their troughs [6], they can break and ultimately reach an equilibrium stage during which noise-induced crest implants balance coalescence. The corresponding value Λ_{crest} of Λ_c can be computed [5–8], upon adapting ideas from [6, 9], as

$$\xi^{\frac{5}{4}} e^{-\frac{\pi}{2}\xi\left(1-\frac{1}{\xi}\right)^2} = c\frac{u'_{eff}}{S_L}, \quad \frac{u'_{eff}}{S_L} = \frac{u'}{S_T}\frac{a}{\Omega}\left(\frac{\lambda S(\lambda)}{S(l)}\right)^{\frac{1}{2}} \tag{5}$$

where c is a constant and $\xi \equiv \Lambda_{crest}/\Lambda_{neutral}$. The values of ξ implied by Eq. (5) are such that the small subwrinkles generated by forcing at the mean-cell troughs reach finite amplitudes comparable to Λ_{crest} itself after (Lagrangian) amplification by the LD instability in presence of the curvature effect and geometry–induced stretch. At least for sufficiently small intensities of forcing, we successfully checked (e.g., see Fig. 2) all the functional dependencies implied by Eq. (4), [5, 8], including the effects of the shape of the spectrum $S(\cdot)$ and of L_{int} upon Λ_{crest}; more details are given on the posters.

Acknowledgement
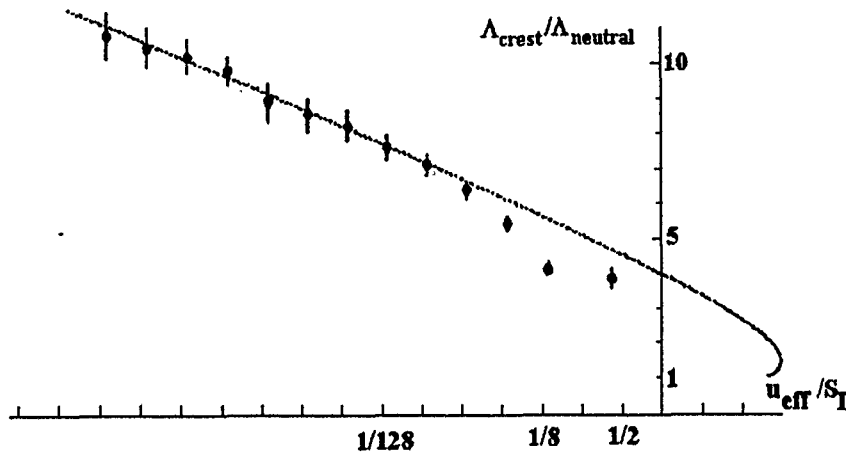
Figure 2: Reduced mean spacing between crests, the reduced intensity of forcing (Eq. (5)) for a Lorentz spectrum $(S(x) \equiv 1/(1 + x^2))$. *Symbols*: from Eq. (1), after averaging over 50 realizations of $u(t, X)$; *Solid line*: analytical prediction of Eq. (5).

References

[1] Landau L. D. *Acta Physicochim*, USSR, 1944, **19**, 77.

[2] Darrieus G. *Unpublished work presented at "La Technique Moderne"*, Paris, 1938.

[3] Sivashinsky G. I. *Acta Astronautica*, 1977, **4**, 1177.

[4] Joulin G., Cambray P. *Combust. Sci. Techn.*, 1992, **81**, 243.

[5] Cambray P., Joulain K., Joulin G. 1944 (submitted).

[6] Zel'dovich Ya. B., Istratov A. G., Kidin N. I., Librovich V. B. *Combust. Sci. Tech.*, 1980, **24**, 1.

[7] Thual O., Frisch U., Henon M., *J. Physique*, 1985, **46**, 1485 (in French).

[8] Cambray P., Joulin G. *Comb. Sci. Techn.*, 1994 (in press).

[9] Clavin P. In: *Disorder and Mixing, NATO ASI E125*, (Guyon *et al.* Eds.), 1988, 293.

IONIZATION DIAGNOSTICS OF OSCILLATION REGIMES IN THE CYLINDER OF AN INTERNAL COMBUSTION ENGINE

J.-O. Chae*, V. M. Shmelev†, K. M. Lee‡, C. S. Chung*

*Mech Eng Dept, Inha University, Inchon, Korea
†Semenov Institute of Chemical Physics, Moscow, Russia
‡Fluid and Climate Control Research Lab, KATECH, Korea

Measurement of ionization current (IC) in an internal combustion engine (ICE) cylinder is a prospective method of combustion diagnostics. The spark plug can be used as an ionization probe in a spark ignition engine (SIE), as well as the glow plug in a diesel engine (DE). The combustion processes and the motion of combustion products in the cylinder are frequently accompanied by oscillation phenomena. In this paper, the nature of these oscillations is analyzed by comparing pressure and IC measurements. It is shown that oscillations of regular type, such as entropy waves, acoustic oscillations, and relaxation oscillations, occur in the cylinder when the gas flows out of half-closed volumes (for example from DE prechamber).

The investigations were conducted for different ICE types. The experiments showed that the strongest IC mode was the oscillation at the frequency of 1–2 kHz in normal combustion regimes for each type of the tested engines of similar dimensions (Fig. 1). The oscillations appear when the engine speed exceeds a critical value or in transient regimes, which points to a rough excitation mechanism. The oscillations were almost nondetectable by a pressure sensor and could appear when the pressure increased or decreased. The nature of these oscillations can be attributed to entropy waves.

In a DE with prechamber, the amplification of relaxation oscillations can occur when the gas flows from the prechamber to the main chamber. In this case, the resonance mode appears at the frequency $F = SC/V_p$. Here, V_p is the prechamber volume, S is the cross section of the prechamber orifice and C is the sound velocity. The experiments showed that the oscillations of this particular frequency develop in the chamber when the instability develops.

The experiments in a model setup were carried out to investigate these phenomena in more detail. The setup was a 0.25-l bomb with a prechamber of variable volume V_p ($V_p = 10$–20 cm^3) separated from the main chamber by a diaphragm with an orifice of cross section $S = 0.2$–0.8 cm^2. The volume was first evacuated and then filled to the atmospheric pressure by a mixture of natural gas of volumetric concentration ψ and air. The mixture in the prechamber was ignited by a conventional spark plug. The spark plug was used as an ionization probe. The experimental results showed that, in the absence of the diaphragm, combustion of the mixture could proceed in the laminar regime within its flammability limits. The typical records of pressure and IC histories show that the probe detects a magnitude of IC during the first several milliseconds after
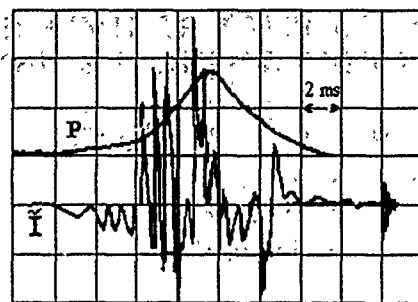
Figure 1: Typical pressure (P) and ionization current (I) record for laboratory single-cylinder SIE (A1), volume is $0.3l$, 1000 rpm, 3 kgm torque. The scales are 20 atm and 0.5 μA per division.
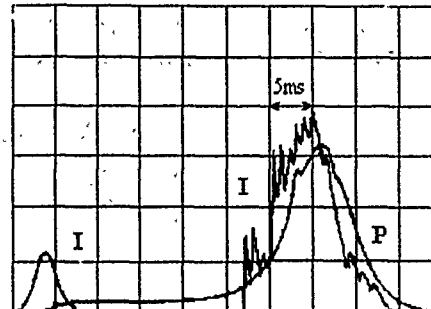
Figure 2: Typical pressure (P) and ionization current (I) records for model setup. The scales are 2 atm and 20 μA per division.
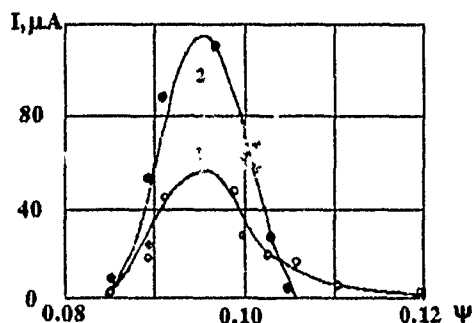
Figure 3: The amplitudes of first (1) and second (2) pulses of IC in model setup for $V_p = 10$ cm^3, $S = 0.2$ cm^2.
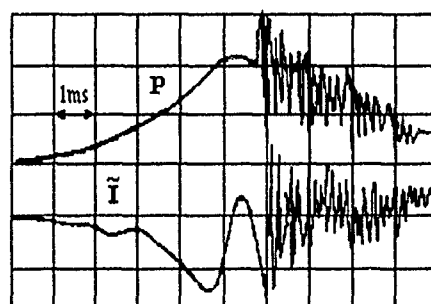
Figure 4: Typical pressure (P) and ionization current (I) records for abnormal combustion regime in SIE (A1) at 1000 rpm. The scales are 20 atm and 0.5 mA per division.

ignition. Then the IC signal falls off sharply. This is due to the cooling of combustion products by the plug electrodes and chamber walls.

The records of pressure and IC are different if the diaphragm is installed. A second, more powerful, pulse of IC is observed after the first pulse corresponding to the laminar combustion of the prechamber mixture. The pressure also increases (Fig. 2). The ratio of the second to the first pulse amplitudes depends on the concentration ψ (Fig. 3) and reaches 2 at its maximum. In the rich mixtures with $\psi > 0.105$, the second IC pulse disappears. These pressure and IC records show that during the combustion of prechamber mixture the combustion products flow through the diaphragm orifice into the main chamber with subsequent flame jet ignition and turbulent combustion. The relaxation oscillations are excited after a rapid increase in pressure. The frequency of these oscillations changed in accordance with the relationship $F = SC/V_p$ in the range of 0.5–2 KHz when the parameters V_p and S were varied.

When the knock appears in the ICE cylinder, the oscillation frequency is within 5–6 KHz. The knocking acoustic wave frequency is determined by the cylinder bore L: $F = C/L$, and the amplitude of the ionization signal is very sensitive to the pressure oscillation amplitude.

A MODEL SOLUTION FOR REACTIVE FLOW IN POLYTROPIC MEDIA

M. Cowperthwaite

SRI International, 333 Ravenswood Avenue, MenloPark, California, 94025 USA

Introduction

An explicit solution for an idealized reactive flow problem is presented to provide a better understanding of reactive flow and its dependence on the characteristic times associated with the hydrodynamic and energy release rate processes.

The Solution for an Idealized Reactive Problem

Our idealized, reactive flow problem is based on Lagrange's problem in interior ballistics [1, 2]. We consider a length (l_0) of polytropic explosive contained in a tube of

unit cross section between a rigid wall and a piston denoted, respectively, by the subscripts w and p. The piston is withdrawn at time, $t = 0$, but in contrast to Lagrange's problem, the explosive is allowed to react at a finite rate.

Our explicit solution to the one-dimensional conservation equations governing the inviscid, adiabatic flow produced in the tube as chemical energy is liberated in the expanding polytropic material can be written as:

$$\frac{v}{v_i} = \frac{x_p}{l_0} = \left(1 + \frac{t}{\beta}\right) \tag{1}$$

$$u = \left(\frac{u_p}{l_0}\right) \frac{x}{(1 + t/\beta)} \tag{2}$$

$$\frac{p}{p_i} = \left(\frac{v_i}{v}\right)^k \left[1 + \frac{(k-1)Q}{p_i v_i} \int_0^t \left(\frac{v}{v_i}\right)^{\kappa-1} \left(\frac{d\lambda}{dt}\right) dt\right] \tag{3}$$

where t, x, v, u, p and k denote, respectively, time, distance, specific volume, particle velocity, pressure and polytropic index, λ and Q denote the extent and heat of decomposition of the explosive, i denotes the initial condition when $\lambda = 0$, and the characteristic hydrodynamic time $\beta = (l_0/u_p)$.

This solution is based on (a) Lagrange's approximation that the flow between the rigid wall, where $x_w = u_w = 0$, and the piston satisfies the condition $(\partial v/\partial x)_t = 0$, and (b) the condition that the flow, on the one hand, must satisfy the isentropic constraint, $pv^k = p_i v_i^k$ when $Q = 0$, and on the other hand, must satisfy the isentropic constraint, $pv^k = p_f v_f^k$ after the decomposition rate terminates, $d\lambda/dt = 0$, at the pressure p_f and the volume v_f.

Particular Solutions for our Idealized Reactive Flow Problem

Particular solutions, constructed for different decomposition rates will be presented in the paper, but because of space limitations only the solution for the rate,

$$\frac{d\lambda}{dt} = \frac{2}{\alpha}(1-\lambda)^{1/2} = \frac{2}{\alpha}\left(1 - \frac{t}{\alpha}\right) \tag{4}$$

will be considered here. Using Eq. (4) to perform the integration in Equation (3) leads to the following equation for the pressure,

$$\frac{p}{p_i}\left(\frac{v}{v_i}\right)^k = 1 + \frac{2(k-1)Q}{k(k+1)p_i v_i}\frac{\beta}{\alpha}\left\{(k+1)\left[\left(\frac{v}{v_i}\right)^k (1-\lambda)^{1/2} - 1\right] + \frac{\beta}{\alpha}\left[\left(\frac{v}{v_i}\right)^{k+l} - 1\right]\right\} \tag{5}$$

with the (v/v_i) terms and the $(1 - \lambda)^{1/2}$ term known functions of t from Eqs. (1) and (4). Equation (5) shows the explicit dependence of the pressure on the ratio of the characteristic hydrodynamic time β to the characteristic decomposition time α.

Because $dp/dt < 0$ when the decomposition ends at $\lambda = 1$, the condition for the pressure history to exhibit a maximum is that $dp/dt > 0$ when the decomposition begins at $\lambda = 0$. Formulating this condition with the energy equation shows that the pressure will attain a maximum ($\hat{p}$) when

$$\frac{kp_iv_i}{2(k-1)Q}\left(\frac{\alpha}{\beta}\right) < 1 \tag{6}$$

Differentiating Eq. (5) with respect to t and setting $dp/dt = 0$ gives the equations for the volume $\hat{v}$ and the time $\hat{t}$ when $p = \hat{p}$ as

$$\frac{\hat{v}}{v_i} = \left\{1 + (k+1)\frac{\alpha}{\beta}\left[1 - \frac{kp_iv_i\alpha}{2(k-1)Q\beta}\right]\right\}^{1/k+1} \tag{7}$$

$$\frac{\hat{t}}{\alpha} = \frac{\beta}{\alpha}\left(\frac{\hat{v}}{v_i} - 1\right) \tag{8}$$

Examination of Eqs. (7) and (8) shows that:

- $\hat{v}/v_i = 1$ and $\hat{t}/\alpha = 0$ when $\alpha/\beta = 2(k-1)Q/kp_iv_i$;

- $\hat{v}/v_i \approx 1 + \alpha/\beta$ and $\hat{t}/\alpha \approx 1$ when $kp_iv_i/2(k+1)Q \le 1$ and $(\alpha/\beta)^2 \ll 1$.

Thus, when $kp_iv_i/2(k-1)Q \le 1$, the maximum in the pressure history moves from $\hat{t}/\alpha = 0$ to $\hat{t}/\alpha \approx 1 + \alpha/\beta$ as α/β decreases from the value $2(k-1)Q/kp_iv_i$ to values of α/β for which $(\alpha/\beta)^2$ and higher terms can be neglected.

Nondimensional pressure versus time profiles for the polytropic explosive, with $k = 3$, $(k-1)Q/p_iv_i = 2$, and different values of α/β are shown in Fig. 1 to provide a more illustrative description of the influence of chemical reaction on hydrodynamic flow. Because the reaction terminates when $t/\alpha = 1$, the entropy increases along these profiles until $t/\alpha = 1$ but thereafter remains constant. The relative positions of these isentropes in the nondimensional (p/p_i–v/v_i) plane is governed by the following equation for the pressure and volume at the end of the reaction zone,

$$\frac{p_f}{p_i}\left(\frac{v_f}{v_i}\right)^3 = 1 + \frac{\beta}{3\alpha}\left[\frac{\beta}{\alpha}\left\{\left(1 + \frac{\alpha}{\beta}\right)^4 - 1\right\} - 4\right] \tag{9}$$

that is obtained from Eq. (5), by setting $k = 3$, $(k-1)Q/p_iv_i = 2$, $\lambda = 1$ and $t = \alpha$. Differentiating Eq. (9) with respect to α/β gives the equation

$$\frac{d(p_fv_f^3/p_iv_i^3)}{d(\alpha/\beta)} = \frac{4}{3}\left(1 + \frac{\alpha}{2\beta}\right) \tag{10}$$

which shows that $p_fv_f^3$ increases as α/β increases. Thus, in the (p/p_i–v/v_i) plane, an isentrope with a given value of α/β lies to the right of an isentrope with a lower value
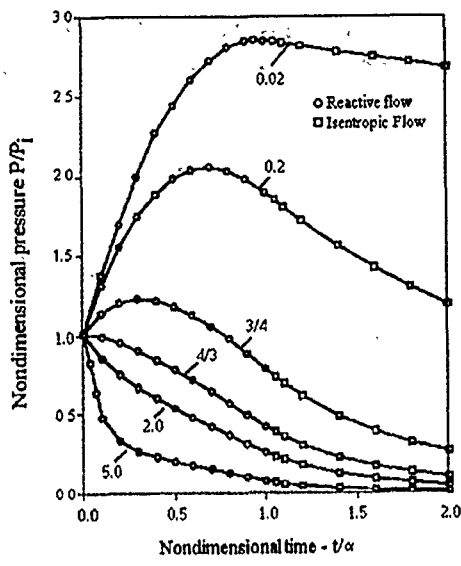
CM-314571-86

Figure 1: Nondimensional pressure (p/p_i) versus nondimensional time (t/α) profiles for the polytropic explosive with $k = 3$, $(k-1)Q/p_iv_i = 2$, and different values of the ratio of the characteristic chemical time (α) to the characteristic hydrodynamic time (β).

of α/β and to the left of an isentrope with a higher value of α/β. In addition, for the pressure histories shown in Fig. 1, the entropy produced by the reaction increases as α/β increases.

Conclusions

A solution to an idealized, reactive, flow problem, based on Lagrange's approximation for interior ballistics, was constructed and its particular solutions were used to provide an insight into the influence of chemical reaction on hydrodynamic flow. The pressure histories, with different values for the ratio of the characteristic chemical time to the characteristic hydrodynamic time, presented in this abstract, illustrate different types of Lagrange pressure histories that are observed during the shock-initiation process in heterogeneous explosives.

References

[1] Lagrange J. L.: *J École Polytech (Paris)*, 1832, **21**, 13.

[2] Corner J., *Theory of the Interior Ballistics of Guns*, New York, John Wiley and Sons, Inc., 1950.

AN ELECTROMAGNETIC FIELD EFFECT ON SPIN COMBUSTION

I. A. Filimonov*, N. I. Kidin†

*Institute of Structural Macrokinetics, Chernogolovka, Russia
†Institute for Problems in Mechanics, Moscow, Russia

Recent experimental investigations raised problem of theoretical treatment of possible electromagnetic effects on combustion of SHS systems, the thermal effect being the simplest among them. It can be due to additional Joule energy dissipation in different manner in different zones of an SHS wave, thus affecting the wave front stability and propagation mode. Extensive theoretical analysis of the thermal mechanism in the case of an electric current passing through the burning sample [1–3] showed (see [3]) that under the limit of SHS wave propagation the combustion modes could be changes in the simplest way. However, at the limit of combustion many SHS systems are known to burn in the spinning mode. Therefore, investigation of the effect of electromagnetic energy absorption on the spinning mode of SHS is of special interest.

Figure 1: The conductivity parameters for systems Mo + B (1), Ti + C (2) (adaptation of results obtained by Bloshenko et al. [6, 7]).

The model presented is based on the spin propagation theory [4]. Usual assumptions concerning homogeneity of the reacting medium with respect to the diffusion processes and high activation energies of the chemical reaction (Zel'dovich number $Ze \gg 1$, $Ze = E[T_b - T_0]/RT_b^2$) were made there. Moreover, the characteristic scales of temperature distribution in the spin mode were indirectly assumed to be much smaller than the diameter of burning cylindrical sample [4]. Under these assumptions, the heat transport equation in general form with due to regard for the absorption of electromagnetic energy in the skin layer of the sample is used in the present study.

An external electromagnetic field of the limited frequency ω at which the quasi-stationary energy absorption occurs [5] is considered. In view of the strong nonlinear dependence of electric conductivity on temperature in most SHS systems, such as Mo + B, Ti + C (see [6, 7], Fig. 1), we can consider the dissipation of electromagnetic energy as an additional competing process of thermal wave propagation in the system.

287
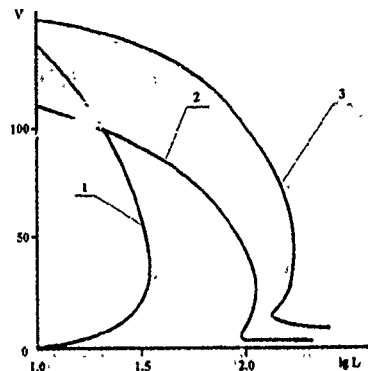
Figure 2: Region of the spin mode existence without electromagnetic field. $RT_b/E = 0.1$, $\Theta_a = 0$, $f = 0$, $\gamma = 3.5$. $1 - H = 4.62$, $2 - 7.31$, $3 - 11.58$, $4 - 23$.
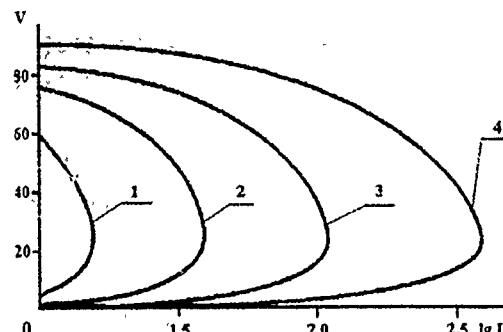
Figure 3: Region of the spin mode existence in electromagnetic field. $RT_b/E = 0.1$, $RT_b/A = 0.2$, $\Theta_a = 0$, $EA^{-1}(\sigma_0|E_0|^2/Qk) = 1$, $\gamma = 3.5$, $f = 1$: $1 - H = 4.62$, $3 - 11.58$; $f = 0.3$: $2 - H = 11.58$.

Nevertheless, it is associated not with chemical conversion but, for example, with the removal of the oxide films in the green mixture (their dissolution or evaporation) or with a phase transition.

Calculation shows that the conditions favoring the existence of the spinning mode are determined by the rate of heat transfer to the center of the sample, rather than that to the products or the green mixture. Increasing heat transfer to the center (with the decrease in H) reduces the region of the spin existence. At sufficiently high rates of heat transfer the spin does not exist (see Fig. 2). The parameters selected yield the value of the critical characteristic length of temperature distribution $H \cong 3.67$. The same takes place with the increase in the sample diameter $\propto L$ (see Fig. 2). The trends observed correspond to the conclusions made in [4].

The pattern is different with absorption of electromagnetic energy. In the case corresponding to the absence of the electromagnetic wave at sufficiently high rates of heat transfer to the sample core, the region of existence of the spinning mode expands due to the effect of electromagnetic energy absorption (cf. Figs. 2, 3). Figure 3: Region of the spin mode existence in electromagnetic field. $RT_b/E = 0.1$, $RT_b/A = 0.2$, $\Theta_a = 0$, $EA^{-1}(\sigma_0|E_0|^2/Qk) = 1$, $\gamma = 3.5$, $f = 1$: $1 - H = 4.62$, $3 - 11.58$; $f = 0.3$: $2 - H = 11.58$.

While in the case of moderate heat transfer to the center of a thick sample or weak electromagnetic energy dissipation, the chemical reaction front degenerates to a spinning thermal wave in the mode of oxide films removal or phase transition (see Fig. 3 (2, 3)). There is no chemical conversion in such a wave. With increasing efficiency or intensity of the electromagnetic energy absorption, the mode of oxide films removal develops

into chemical reaction with a high-temperature front characterized by a propagation velocity (see Fig. 3 (2, 3)).

Thus, at sufficiently large heat removal and limited absorption of the electromagnetic energy, the reaction front cannot exist, and a heat wave propagates across the sample in the mode of oxide film removal without chemical conversion. In contrast, at limited heat removal and sufficiently efficient dissipation of Joule energy in the area of the spin head, the removal of the oxide films is accompanied by chemical reactions with intense product formation in the front.

References

[1] Filimonov I. A, Kidin N. I. In: *Flame Structure*, Ed. Korobeinichev O. P., Novosibirsk, Nauka, 1991, 290-293.

[2] Kidin N. I., Filimonov I. A. *Int. J. SHS*, 1992, **1**, 4, 513.

[3] Filimonov I. A., Kidin N. I. *Proc. 24 Symp. (Int.) on Comb.*, The Combustion Institute, 1992, 1893.

[4] Novozhilov B. V. *Dokl. Akad. Nauk SSSR*, 1992, **326**, 3, 485 (in Russian).

[5] Landau L. D., Lifshits E. M. *Electrodynamics of continuous media.* Moscow, Nauka, 1982 (in Russian).

[6] Bloshenko V. N. *et al. Fizika Goreniya Vzriva*, 1984, **20**, 6, 87 (in Russian).

[7] Bloshenko V. N. *et al. ibid*, 1988, **24**, 2, 102 (in Russian).

STABILITY OF REACTION FRONTS IN LIQUIDS

M. Garbey, A. Taik, V. Volpert

Laboratoire d'Analyse Numérique
Université Lyon-1, France

1 Mathematical Formulation

The experiments show that propagation of reaction fronts in liquids can be strongly influenced by hydrodynamics [1, 2, 6]. On the one hand, the exothermic reaction can

cause convection of a liquid, which can even lead to the extinction of reaction front. On the other hand, hydrodynamic perturbations can influence the thermal stability of the reaction front.

To study the stability of reaction fronts in liquids, we consider a model which includes the heat equation, equation for concentration, and the Navier–Stokes equations in the Boussinesq approximation:

$$\frac{\partial T}{\partial t} + u\nabla T = \kappa\Delta T + qK(T)\phi(\alpha) \tag{1.1}$$

$$\frac{\partial \alpha}{\partial t} + u\nabla \alpha = K(T)\phi(\alpha) \tag{1.2}$$

$$\frac{\partial u}{\partial t} + (u\nabla)u = -(\frac{1}{\rho}\nabla p + \nu\Delta u + \gamma\beta g(T - T_0) \tag{1.3}$$

$$div\ u = 0 \tag{1.4}$$

Here T is the temperature, α is the concentration of the reaction product, u is the velocity of the medium, p is the pressure, κ is the thermal diffusivity, q is the adiabatic heat of the reaction, ρ is the density, ν is the viscosity, γ is the unit vector in the vertical direction, β is the coefficient of thermal expansion, g is the gravitational acceleration, T_0 is the average value of temperature,

$$K(T) = k_0 e^{-E/RT}$$

k_0 is the pre-exponential factor, E is the activation energy, R is the gas constant, $\phi(\alpha)$ is a kinetic function which we assume to correspond to a zero-order reaction. In the equation for the concentration we neglect the diffusion term since the diffusivity for liquids is usually much smaller than the thermal diffusivity, and the characteristic time of mass diffusion is much shorter than that of heat diffusion. The stability of a gas combustion wave was studied in the Boussinesq approximation in [4].

We perform a linear stability analysis of the model (1.1–1.4) and find cellular and oscillatory stability boundaries. We consider the fronts propagating upward and downward and study the cases in which the product of the reaction is solid or liquid. Both of them are possible in experiments on frontal polymerization, which provides an interesting example of reaction fronts in liquids. The boundary conditions at the infinities depend on the direction of the front propagation and have the usual form. We neglect the influence of the side walls of the reactor.

The results of the analysis are discussed briefly below.

2 Reaction Fronts with a Solid Products

To study the problem analytically, we apply the infinitely narrow reaction zone method suggested by Zel'dovich and Frank-Kamenetskii for gas combustion [7] and

developed by Novozhilov for reaction fronts in condensed media [5]. This approach allows us to reduce the system of Eqs. (1.1–1.4) to a singular perturbation problem with the reaction zone localized on a surface $z = \zeta(x, y, t)$. The assumption that the product of the reaction is solid implies that the velocity of the medium is zero behind the reaction zone.

Thus, in front of the interface we have the set of equations:

$$\frac{\partial T}{\partial t} + u\nabla T = \kappa \Delta T, \qquad \alpha = 0 \tag{2.1}$$

$$\frac{\partial u}{\partial t} + (u\nabla)u = -\frac{1}{\rho}\nabla p + \nu\Delta u + \gamma\beta g(T - T_0) \tag{2.2}$$

$$div\ u = 0. \tag{2.3}$$

Behind the interface, we have

$$\frac{\partial T}{\partial t} = \kappa\Delta T, \qquad \alpha = 1, \qquad u = 0. \tag{2.4}$$

The jump conditions at the interface have the form:

$$[T] = 0, \qquad [T'] = \frac{q}{\kappa}\frac{\partial \zeta}{\partial t}, \qquad [T'^2] = -2\frac{q}{\kappa}\int^{T_b} K(T)\,dT, \qquad u = 0 \tag{2.5}$$

Here $[\cdot]$ denotes the jump of a function across the reaction zone, $T' = \partial T/\partial \zeta$.

The problem (2.1–2.5) has a travelling-wave solution for which $u = 0$ and which coincides with that for a front propagating in a quiescent medium. To study the stability of this solution, we linearize the problem about it. The linearization of the jump conditions (2.5) gives the dispersion relation

$$\sigma = -\frac{Z + \frac{d-1}{2} + \omega Z}{Z + \frac{d-1}{2} + \omega}$$

where ω is an eigenvalue of the linearized problem, $d = \sqrt{1 + k^2 + 4\omega}$, k is the wavenumber, $Z = qE/2RT_b^2$ is the Zel'dovich number, T_b the temperature in the reaction zone for the steady-state propagating front,

$$\sigma = \frac{1}{u_0}\frac{\theta'(0)}{\theta(0)},$$

u_0 is the dimensionless velocity of the front propagation, θ is the amplitude of the dimensionless perturbation of the liquid temperature. The function σ should be found from the equations for the amplitudes of the perturbations:

$$Pv'''' + u_0 v''' - (2Pk^2 + \omega)v'' - u_0 k^2 v' + k^2(Pk^2 + \omega)v = Qk^2\theta$$

$$\theta'' + u_0\theta' - (k^2 + \omega)\theta = v\theta'_s$$

Here P is the Prandtl number, $Q = PR$, R is the Rayleigh number, θ_s the dimensionless temperature profile for the steady-state propagating front.

From the equations for perturbations and the boundary conditions

$$v(0) = v'(0) = 0,$$

we find the function $\sigma(R, P, u, k, \omega)$. In the case of small R, it has the form

$$\sigma = -\frac{1+d}{2} - \frac{4P^2R}{u^3} \frac{k^2}{(1+d)(1+d+k)^2(1+\tilde{d}+P(1+d))(1-\tilde{d}-P(1+d))} + o(R)$$

$$(2.6)$$

where $d = \sqrt{1 + k^2 + 4\omega}$, $\tilde{d} = \sqrt{1 + k^2P^2 + 4\omega P}$. To find the cellular stability boundary, we put $\omega = 0$. In this case, the dispersion relation has the form $\sigma = -1$. For $R = 0$ it has a solution only for $k = 0$. This solution pertains not to the stability boundary but to the invariance of solutions with respect to translation. It is easily seen from Eq. (2.6) that, for negative R, σ decreases and the dispersion relation cannot have solutions for positive k. This means that, for the front propagating downward, the cellular instability cannot occur. For positive R, σ increases, the dispersion relation can have solutions for nonzero wavenumbers, and, consequently, the cellular instability can arise.

From Eq. (2.6), we find the critical value of the Rayleigh number:

$$R_c = \frac{u^3}{16P^2}(1+d)(1+d+k)^2[1+\tilde{d}+P(1+d)][-1+\tilde{d}+P(1+d)] \qquad (2.7)$$

Thus, the critical value of the Rayleigh number is an increasing function of the wavenumber. It tends to a finite limit (as $k \to 0$), which can be easy calculated from Eq. (2.7).

In the case of an arbitrary value of the Rayleigh number, the expression for σ is more complicated, and the dispersion relation should be analyzed numerically [3]. The analysis shows that, similar to the case of small R, for the front propagating upward, a cellular instability can occur but for the descending front it cannot. This is somewhat similar to the Rayleigh–Bénard convection in a liquid layer heated from below or from above. We note that for the Rayleigh–Bénard problem the critical value of the Rayleigh number tends to infinity as k goes to zero. This difference from the problem considered here is probably due to the unboundedness of the liquid layer in the problem of front propagation. The criterion for the cellular instability does not depend on the Zel'dovich number, and the perturbation of the temperature behind the reaction zone in this case is zero.

The oscillatory instability can occur for ascending as well as descending fronts. The criteria for the stability with respect to multidimensional perturbation are different in these two cases. The hydrodynamics makes the front propagating upward more stable and the front propagating downward less stable. This explains why the spinning

modes were observed experimentally for the values of the parameters such that the front should be stable in the case of solid phase combustion. We note that in all experiments where the spinning modes were observed the descending fronts were considered. Moreover, the experimental results show that elimination of convection also eliminates the instability [6].

3 Reaction Fronts with a Liquid Product

We make here some remarks concerning the case of a liquid product. The velocity of the medium behind the reaction zone may be nonzero in this case. Applying the matching of asymptotic expansions, we obtain that the first term of the external expansion of the velocity is continuous at the interface, together with its derivatives:

$$[u_z] = [u_z'] = [u_z''] = [u_z'''] = 0 \tag{3.1}$$

In this case, the dispersion relation is similar to the previous one but also includes the normalized velocity σ_z:

$$\sigma = -\frac{Z + \frac{d-1}{2} + \omega Z + \sigma_z}{Z + \frac{d-1}{2} + \omega + \sigma_z}, \qquad \sigma_z = \frac{1}{u_0} \frac{u_z(0)}{\theta(0)}$$

As above, from the equations for the perturbations and the boundary conditions, which in this case have the form of Eq. (3.1), we can find the function σ and the stability boundaries.

References

[1] Begishev V. P., Volpert V. A., Davtyan S. P., Malkin A. Y. *Dokl. Akad. Nauk SSSR,* 1984, **290,** 4, 1057 (in Russian).

[2] Chechilo N. M., Khvilivitsky R. Y., Enikolopyan N. S. *ibid*, 1972, **204, 4-6,** 512 (in Russian).

[3] Garbey M., Taik A., Volpert V. *Quart. Appl. Math.* (in press).

[4] Matkowsky B. J., Sivashinsky G. I. *SIAM J. Appl. Math.*, 1979, **37, 3,** 669.

[5] Novozhilov B. V. *Dokl. Akad. Nauk SSSR*, 1961, **141,** 836 (in Russian).

[6] Pojman J. A., Graven R., Khan A., West W. *J. Phys. Chem.*, 1992, **96,** 7466.

[7] Zel'dovich Ya. B., Frank-Kamenetsky D. A. *Zhurnal Fizicheskoi Khimii*, 1938, **12,** 100 (in Russian).

ON THE FRACTAL FLAME BALL STRUCTURE

Yu. A. Gostintsev, A. G. Istratov

Semenov Institute of Chemical Physics, Moscow, Russia

The fractal scaling of a flame ball is obtained from experimental data on spherical flame propagation in sufficiently large volumes of combustible mixture using an appropriate theoretical treatment [1]. The accuracy of the resulting fractal dimension depends on the interpolation procedure applied to the burning velocity data. This approach is usually based on the assumption that the flame ball fractalization and combustion acceleration are caused by a spontaneous instability only.

The presented detailed analysis of experimental data involves examination of the flow pattern arising due to the buoyancy-driven upward motion of the flame ball and its influence on the tangential drift of surface perturbations. The rather low velocities of the ball motion are essential for the drift and the consequent flame deceleration. These phenomena are most evident at the final stage of the combustion process.

The theoretical analysis can rely on competing treatments. One of these is the cascade model of flame surface perturbations growth [1], and the other refers to the turbulence inside the flame sphere. It is difficult to discriminate between the two alternative approaches within the scope of the burning velocity data processing.

Another problem of interest is the spectrum of flame surface perturbations.

References

[1] Gostintsev Yu. A., Istratov A. G., Shulenin Y. V. *Fizika Goreniya Vzriva*, 1988, 5 (in Russian).

DYNAMICS OF FIRE STORMS OF FULL-SCALE ATMOSPHERIC FIRES

Yu. A. Gostintsev*, A. M. Ryzhov[†]

*Semenov Institute of Chemical Physics, Moscow, Russia
[†] All-Russia Research Institute of Fire Protection, Balashikha, Russia

In this work, a fire storm originating in mass fires under the effect of a prior extraneous vertical vortex has been numerically realized. The data on the real large fire in Hamburg during World War II were used to investigate the dynamics of fire storms.

Mathematical models were developed, based on full Navier–Stokes equations for viscous compressible flows, including the angular momentum conservation equation. Turbulent nature of transport processes was taken into account using an algebraic turbulence model. Allowance for combustion was made, based on a diffusive vortex model. The details of the mathematical model, the numerical method and algorithm have been presented in [1, 2].

Fire storm modeling was performed in the computational area (12.0 × 15.0 km) having an equivalent fire radius, r_1. The maximum burning rate of a combustible wood load, m_1, was in agreement with the condition for maximum heat release, Q_1, attained linearly in the first half-hour since fire initiation. According to such a scenario, $m_1 = Q_1/Q_{fu}$, where the heat of burned wood $Q_{fu} = 18.6$ J/kg.

Background distribution of the extraneous vertical vortex with atmosphere height was preset at a distance, r_2 from the fire center, corresponding to weak circulation Γ at the earth surface in a prior background vortex.

The atmospheric temperature distribution was set to be standard up to the tropopause height 11.0 km, above which the temperature was considered to be constant.

Modeling of the fire in Hamburg was performed at the following values of parameters: $r_1 = 2.0$ km, $r_2 = 8.0$ km, $Q_1 = 1.7 \cdot 10^{12}$ W, $\Gamma = \Gamma_0 = 3.2 \cdot 10^4$ m^2/s.

As a result of numerical experiments the agreement between the computed and real fire characteristics was achieved for the situation modeled. It was found that in the fire storm within 1.5–2 hours an eddy flow with the maximum tangential velocity $v = 45$ m/s developed, in contrast to conventional convective columns having the maximum horizontal radial velocity 14 m/s. The maximum rise of combustion products amounted to 11.8 km.

Using a fire with a similar area as an example, the influence of fire severity on the intensity of rotation was studied at the external circulation Γ_0, specified above. It has been shown that a fire storm with high vertical velocities w_1 and an intense rotation at the maximum velocity $v_1 = 15$ m/s can occur at $Q > 0.4Q_1$.

The rotation of the fire core at the velocity of 10 m/s occurred at $Q = 0.2Q_1$. Due to the considerable decrease in vertical velocities stemming from the decrease in
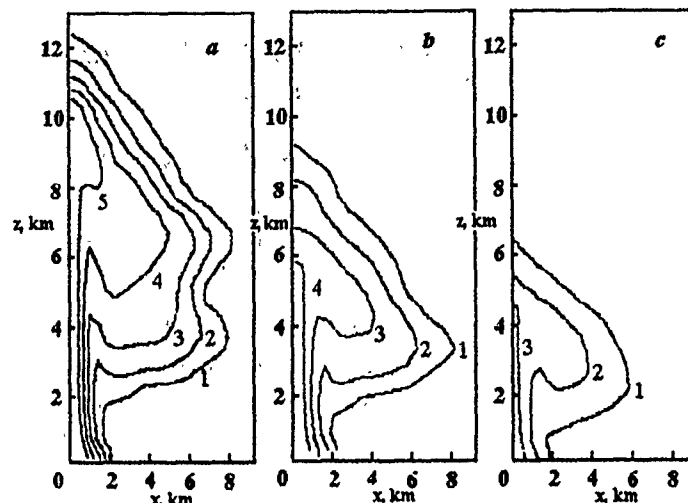
Figure 1.

fire severity, an increase in the vortex extent S of the fire storm core $S = G/(2 - G)$ was observed, where the quantity G, unlike than in [3], was defined as the ratio of maximum velocities in the flow, $G = v_1/w_1$. In this case, the elevation of combustion products, dropped to 4.5. Isolines of combustion products mass concentration at the moments of maximum rotation ($C \cdot 10^2$kg/kg) for the fires with $Q = Q_1$, $0.5Q_1$ and $0.25Q_1$ are presented in Fig. 1a–c (isolines 1–5 correspond to the values from 0.03 to 0.23 with step 0.05).

The impact of extraneous circulation on maximum tangential velocities and the flow vortex extent for a fire seat of intensity $Q = Q_1$ were investigated. The rotational motion at the tangential velocity, $v_1 = 10$ m/scan occur at the extraneous circulation $\Gamma = 0.20\Gamma_0$. The extent of the vortex core of such a flow is $S = 0.085$.

As compared to earlier works [4], the results obtained lead to a conclusion regarding the possibility of fire storms occurring in large-scale fires based on a wider range of governing parameters, such as the overall intensity of heat release and the extraneous background circulation in the fire region.

References

[1] Gostintsev Yu. A., Ryzhov A. M. *Proc. Rus.-Jap. Sem. Comb.*, Moscow, 1993, 83.

[2] Ryzhov A. M., Gostintsev Yu. A. *Fire and Explosion.* 1993. **1**, 3–16.

[3] Gupta ., Lilley D., Syred N. *Whirled flow.* oscow, Mir, 1987 (Russian translation).

[4] Carrier G. F., Fendell F. E., Feldman P. S. *J. Heat Transfer*, 1985, 107, 19–26.

EXACT SOLUTION FOR ZEL'DOVICH EQUATION AND FOR SYSTEMS OF THE TYPE "REACTION–DIFFUSION"

O. V. Kaptsov, V. I. Bykov

Computing Center, Krasnoyarsk, 660036 Russia

Examples of exact solutions to the Zel'dovich equation are well known [1–4]. However, the mathematical technique developed in [4, 5] also provides exact solutions to the sets of equations of "reaction + diffusion" type.

The equations

$$
\begin{aligned}
u_t &= u_{xx} + F(u, v), \\
v_t &= dv_{xx} + G(u, v), \quad d > 0,
\end{aligned}
\tag{1}
$$

which admit the differential substitution of the first order,

$$
u = f(v, v_x),
\tag{2}
$$

are considered.

Definitions. Equations (1) admit the differential substitution (2), if the first equation is satisfied identically on substituting (2) (such that satisfies the second equation).

Lemma 1. *Equations (1) admit the first-order differential substitution (2) if and only if*

$$
\begin{aligned}
u_t &= u_{xx} + q_2 u^2 + q_1 u + q_0 \\
v_t &= v_{xx} + \frac{a_v}{a^3} u^2 - \frac{2a_v b}{a^3} u + c,
\end{aligned}
\tag{3}
$$

where a, b, c are arbitrary functions of v; q_i $(i = 1, 2, 3)$ are given by

$$
q_2 = \frac{a_v b_v}{a^3} - \frac{b_{vv}}{a^2},
$$

$$
q_1 = \frac{1}{a^4} \left(-a_{vv} ab^2 - 2a_v^2 b^2 + a_v a^3 c - 4a_v a b_v b + a^4 c_v + 2a^2 b b_{vv} \right),
\tag{4}
$$

$$
q_0 = \frac{1}{a^4} \left(a_{vv} ab^3 - 2a_v^2 b^3 - a_v a^3 bc + 2a_v b_v ab^2 - a^4 bc_v + a^4 b_v c - a^2 b_{vv} b^2 \right)
$$

and differential substitution (2) is linear in v_x:

$$
u = av_x + b.
\tag{5}
$$

Lemma 2. *The set*

$$
\begin{aligned}
u_t &= u_{xx} + q_2 (u - b)^2 \\
u_t &= v_{xx} + \frac{a_v (u - b)^2}{a^3}
\end{aligned}
\tag{6}
$$

297

with arbitrary function a, b and $q_2 = a_v b_v / a^3 - b_{vv}/a^2$ admits a reduction to the equation of heat conduction

$$w_t = w_{xx} + h(w). \tag{7}$$

Using Eq. (5), we obtain from Eq. (6) an equation containing only v:

$$v_t = v_{xx} + \frac{a_v}{a} v_x^2 + c - \frac{a_v b^2}{a^3} \tag{8}$$

If $c = a_v b^2 / a^3$, Eq. (8) can be rewritten in the form of Eq. (7) using the simple substitution $v = \mu(w)$.

The Zel'dovich equation [2]

$$w_t = v_{xx} + 2w^2(1 - w) \tag{9}$$

has the exact solution [4]

$$w_* = \frac{k \exp(t - x) - 1}{2t \div x + m + k \exp(t - x)} \tag{10}$$

For any fixed $t \geq 0$, $w_* \to 0$ as $x \to \infty$, and $w_* \to 1$ as $x \to -\infty$. For sufficiently large values of t, the function w_* is similar to the travelling wave with the rate $\omega = 1$.

In conclusion, let us demonstrate an example of a system which is reduced to Eq. (9):

$$\begin{aligned} u_t &= u_{xx} + uv P_v(\ln v) \\ v_t &= v_{xx} - vu^2 + v P(\ln v) \end{aligned}$$

where $P(w) = 2w^2(1 - w)$. The functions $v_* = \exp(w_*)$ and $u_* = w_{*x}$ are obviously the solutions to Eq. (11).

References

[1] Zel'dovich Ya. B., Barenblatt G. I., Librovich V. B., Makhviladze G. M. *Mathematical Theory of Combustion and Explosion*. Moscow, Nauka, 1980 (in Russian).

[2] Maslov V. P., Danilov V. G., Volosov K. A. *Mathematical Simulation of Processes of Heat and Mass Transfer*. Moscow, Nauka, 1987 (in Russian).

[3] Galaktionov V. A., Dorodnitsyn V. A., Elenin G. G., Kurdyumov S. P., Samarskii A. A. *Modern Probl. Mathem. New Achievements*, Moscow, VINITI Publ., 1986, **28**, 95 (in Russian).

[4] Kaptsov O. V. *Matem. Modelirovanie*, 1992, **4**, 8, 31 (in Russian).

[5] Kaptsov O. V. *Nonlinear Analysis. Theory. Methods and Appl.*, 1992, **19**, 8, 753.

ASYNCHRONOUS EXCITATION OF UNSTEADY COMBUSTION

Yaroslav A. Lissotchkin

State Institute of Applied Chemistry, St.Petersburg, Russia

In the sixties, we discovered that the combustion process in rocket engines may become unstable when a small periodical disturbance of pressure in the chamber is excited with a frequency different from the resonance. In the theory of non-linear oscillations this phenomenon is termed asynchronous excitation The existing literature does not consider this type of combustion instability. Analytic approach to the problem of the asynchronous excitation should start with some hypothetical simple model of the combustion chamber process,

$$\frac{\partial^2 P}{\partial t^2} - a^2 \frac{\partial^2 P}{\partial x^2} = \frac{a^2}{C_p T}\frac{\partial Q}{\partial t} - a^2 \sigma \frac{\partial P}{\partial t} \tag{1}$$

where P is the pressure perturbation, t is time, x is the axial distance from injector end, a is the speed of sound, T is temperature, C_p is the specific heat at constant pressure, Q is the heat release rate per unit volume, σ is the bulk viscosity coefficient.

Suppose

$$Q = J(P)\Phi(x) \tag{2}$$

and assume that Q depends on P so that

$$J(P) = K_1 P + K_2 P^2 + K_3 P^3 + K_4 P^4 + K_5 P^5$$

The boundary conditions are:

$$x = 0: \quad \frac{\partial P}{\partial x} = 0; \qquad x = l : P = P_0 \cos \nu t, \tag{3}$$

where P_0, ν are the amplitude and frequency of the external perturbation.

The solution of Eq.(1) is given by [1]

$$P(x,t) = \Psi(x)\tau(t) + \eta(x)\cos \nu t \tag{4}$$

where $\Psi(x)$, $\eta(x)$ are given by the equation

$$\frac{\partial^2 P}{\partial t^2} - a^2 \frac{\partial^2 P}{\partial x^2} = 0 \tag{5}$$

and boundary conditions (3).

Hence,

$$\Psi(x) = \cos\frac{\omega x}{a};$$

$$\omega = \frac{\pi a}{2l},$$

$$\eta(x) = \frac{P_0 \cos\frac{\nu x}{a}}{\cos\frac{\nu l}{a}}. \tag{6}$$

This solution is obtained on the assumption that only the fundamental acoustic mode takes place. Substituting Eq. (4) into Eq. (1), multiplying by $\Psi(x)dx$, and integrating from 0 to l, we obtain the non-linear equation

$$\tau''(t) + \omega^2\tau(t) = F(\tau, \tau', \theta), \tag{7}$$

where $\theta = \nu t$; $\omega = (\pi a)/(2l)$, and

$$F(\tau, \tau', \theta) = \frac{4\omega^2}{\pi C_p T}\int_0^l \Psi(x)\frac{\partial\theta}{\partial t}\,dx - \frac{4\omega^2\sigma}{\pi}\int_0^l \Psi(x)\frac{\partial P}{\partial t}\,dx. \tag{8}$$

Equation (7) can be solved by the asymptotic method of [2].

If $\omega \neq (P/q)\nu$, where P, q are integers, then the result of the first interation can by written as

$$\tau = b\cos\varphi, \tag{9}$$

$$\frac{db}{dt} = A_1(b); \qquad \frac{d\varphi}{dt} = \omega + B_1(b), \tag{10}$$

where

$$A_1(b) = -\frac{1}{4\pi^2\omega}\int_0^{2\pi}\int_0^{2\pi} F_0(a, \varphi, \theta)\sin\varphi\,d\varphi d\theta,$$

$$B_1(b) = -\frac{1}{4\pi^2\omega}\int_0^{2\pi}\int_0^{2\pi} F_0(a, \varphi, \theta)\cos\varphi\,d\varphi d\theta, \tag{11}$$

$$F_0(a, \varphi, \theta) = F(\tau, \tau', \theta) \quad \text{with} \quad \tau = b\cos\varphi; \quad \tau' = -\omega b\sin\varphi.$$

The integration in Eq. (11) yields

$$A_1(b) = (\lambda_1 + \lambda_4 + \lambda_7 - \lambda_2)b + (\lambda_3 + \lambda_6)b^3 + \lambda_5 b^5, \tag{12}$$

where

$$\lambda_1 = \frac{2\omega^2 K_1}{\pi C_p T}\int_0^l \Psi^2(x)\phi(x)\,dx, \qquad \lambda_2 = \frac{2\omega^2\sigma l^2}{\pi^2},$$
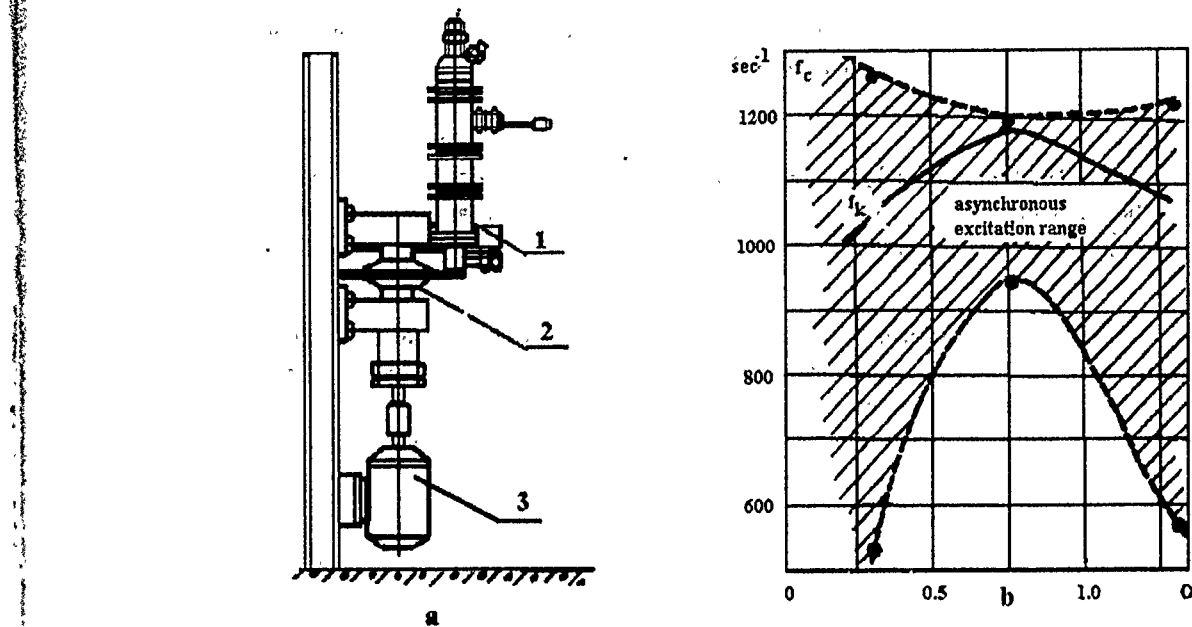
Figure 1: (a) Schematic of experimental apparatus. *1* — small-scale combustor, *2* — device for periodic variation of sonic throat area, *3* — electric motor. (b) The effect of propellant equivalence ratio on the range of asynchronous excitation; f_c is the frequency of periodical area variation of the sonic throat, f_k is the fundamental acoustic mode of combustion chamber.

$$\lambda_3 = \frac{3\omega^2 K_3}{2\pi C_p T} \int_0^l \Psi^4(x)\phi(x)\,dx, \qquad \lambda_4 = \frac{3\omega^2 K_3}{\pi C_p T} \int_0^l \Psi^2(x)\phi(x)\eta^2(x)\,dx,$$

$$\lambda_5 = \frac{5\omega^2 K_5}{4\pi C_p T} \int_0^l \Psi^6(x)\phi(x)\,dx, \qquad \lambda_6 = \frac{5\omega^2 K_5}{\pi C_p T} \int_0^l \Psi^4(x)\phi(x)\eta^2(x)\,dx, \qquad (13)$$

$$\lambda_7 = \frac{15\omega^2 K_5}{4\pi C_p T} \int_0^l \Psi^2(x)\phi(x)\eta^4(x)\,dx,$$

$$B_1(b) = 0.$$

The assumption of stationary amplitude of self-sustained oscillations is

$$A_1(b_*) = 0. \qquad (14)$$

The stability criterion for the amplitude of the self-sustained oscillations has the form

$$\left. \frac{\partial A_1(b)}{\partial b} \right|_{b=b_*} = 0. \qquad (15)$$

301

From Eqs. (12)–(15) one can obtain that the criterion for the self-amplification of the resonant oscillations in the chamber is

$$\gamma_* = \lambda_1 - \lambda_2 + \lambda_4 + \lambda_7 > 0. \tag{16}$$

If $P_0 = 0$, then $\gamma_0 = \lambda_1 - \lambda_2 < 0$ is the criterion of stable combustion when the externally applied disturbance is absent. Thus, the criteria for the asynchronous excitation of unsteady combustion are

$$\gamma_* > 0, \qquad \gamma_0 < 0. \tag{17}$$

The investigation of asynchronous excitation of unsteady combustion was tested by using a small-scale double-based liquid propellant rocket. The hypergolic propellants UDMH + N_2O_4 were used as the fuel.

The oscillation excitation in the rocket was performed using a special device for periodic variation of the sonic throat cross-section area (see Fig. 1a). Tests on a small-scale combustor showed that the range of frequencies of the externally applied disturbances exciting the self-sustained oscillations depend on propellant mixture composition (Fig. 1b), combustor pressure, and propellant line.

References

[1] Kauderer K. *Nonlinear mechanics*, Moscow, Izd. Inostr. Lit., 1961 (in Russian).

[2] Bogolyubov N. N., Mitropolskii Ju. A. *Asymptotic Methods of Theory Nonlinear Oscillations*, Moscow, Izd. Fiz.-Mat. Lit., 1958 (in Russian).

THEORETICAL ANALYSIS OF NONLINEAR EFFECTS IN HYDRODYNAMIC INSTABILITY OF PREMIXED FLAMES

S. S. Minaev

Institute of Chemical Kinetics & Combustion, Novosibirsk, Russia

Within the framework of the Darrieus–Landau hydrodynamic approximation, the flame is treated as a surface of density discontinuity. A nonlinear flame stability analysis carried out by Sivashinsky [1] has shown that in a suitable asymptotic regime the dynamics of a slightly perturbed flame front is governed by a nonlinear integro-differential equation. In the 1D case, the equation for a slightly perturbed plane front is

$$\frac{\partial f}{\partial t} - \frac{\varepsilon}{2}\{Kf\} - \frac{\partial^2 f}{\partial x^2} - \frac{1}{2}\left(\frac{\partial f}{\partial x}\right)^2 = 0. \tag{1}$$

Here, $f(x, t) = z$ is a small perturbation of the plane front, $\varepsilon \ll 1$ is a small parameter in the case of weak thermal expansion. It also reflects the physicochemical characteristics of the combustible mixture. In Eq. (1), $\{Kf\}$ is a linear operator defined in terms of spatial Fourier transform:

$$\{Kf(x,t)\} = \frac{1}{2\pi} \int\limits_{-\infty}^{\infty} |k| \cos(kx) \hat{f}(k,t)\, dk,$$

where the cap denotes the cosine Fourier transform of f.

For an outward propagating hydrodynamically unstable flame front, the evolution equation takes the form:

$$\frac{\partial R_0}{\partial t} + \frac{\partial f}{\partial t} - \frac{\varepsilon}{2R_0}\{Kf\} - \frac{1}{2R_0^2}\left(\frac{\partial f}{\partial \varphi}\right)^2 - \frac{1}{R_0^2}\left(\frac{\partial^2 f}{\partial \varphi^2}\right) - 1 = 0, \qquad (2)$$

Used in Eq. (2) are the polar coordinates ρ, φ, where $\rho = R_0 + f(\varphi, t)$ the perturbed flame front, R_0 is the effective radius of the wrinkled flame. Operator $\{Kf\}$ is defined as

$$\{Kf\} = \frac{1}{\pi} \sum_{n=1}^{\infty} n \int\limits_{0}^{2\pi} \cos[n(\varphi - \varphi^*)] f(\varphi^*, t)\, d\varphi^*.$$

Equations (1), (2) can be solved by a method similar to pole decomposition.

Let $\Phi(x, z)$ be the hydrodynamic potential due to several sources and sinks located in the burnt gas. For example a single source located at $x = 0$, $z = -a$ generates the potential Φ of the form:

$$\Phi = 2\ln[x^2 + (z + a)^2]. \qquad (3)$$

It turns out that $\Phi(x, z)$ due to a source located on the unperturbed flame surface is an exact solution to Eqs. (1), (2). For the plane flame ($z = 0$) the solution corresponding to a single sink is

$$\Phi\Big|_{z=0} = f(x, t) = 2\ln[x^2 + a^2(t)],$$

and

$$a\frac{\partial a}{\partial t} = \frac{\varepsilon}{2} - a.$$

At $t \to \infty$, the equation for a yields a stable equilibrium configuration with $a = \varepsilon/2$. Solutions corresponding to several sinks on the normal to the plane flame front also exist. In [2, 3], a nonlinear dynamic model describing the flame surface for this case was developed using the method of pole decomposition. In the periodic case, Eq. (1) admits the following solutions [4]:

$$f(x, t) = 4\Re\left\{\ln(\alpha_0 + \alpha_1 e^{-i\kappa x} + \ldots + \alpha_N e^{-iN\kappa x})\right\},$$

where $\Re$ denotes the real part operator, and the real coefficients α_0, α_1, ..., α_N satisfy the set of ordinary differential equations:

$$\frac{\partial}{\partial t} \sum_{l=0}^{N-n} (\alpha_l \alpha_{n+l}) - \omega_{n+l,l} \alpha_l \alpha_{n+l} = 0,$$

and

$$\omega_{n+l,l} = \frac{\varepsilon}{2}(2l+n)\kappa - n^2\kappa^2.$$

For $\alpha_l \sim \exp\left(\frac{1}{2}\omega_{N,0}t\right)$, we obtain particular solutions modelling the steady-state configuration of a flame propagating at a constant velocity $2\omega_{N,0}$.

It should be emphasized that all these solutions can be obtained from Eq. (3) by a simple superposition. In the case of outward propagating cylindrical flame, by placing source at and sinks around the center of symmetry, we can reduce the solution to the following:

$$f(\varphi,t) = 2\ln\left[1 + a^2 + 2a\cos(N\varphi)\right].$$

Effective radius R_0 and amplitude of flame wrinkles, in this case, are related by

$$\begin{cases} \dfrac{\partial a}{\partial t} &= \left(\dfrac{\varepsilon N}{2R_0} - \left(\dfrac{1+2a^2}{1-a^2}\right)\dfrac{N^2}{R_0^2}\right)a \\ \dfrac{\partial R_0}{\partial t} &= 1 + \dfrac{4N^2 a^2}{(1-a^2)R_0^2} \end{cases}$$

The amplitude of the nonlinear harmonic increases after effective radius has reached the critical value $R_{cr} = 2N/\varepsilon$. At $t \to \infty$, both the amplitude of the wrinkles, defined as $\ln(1 + a/(1-a))$, and the flame radius R_0 tend to infinity.

References

[1] Sivashinsky G. I. *Acta Astrounautica*, 1977, **4**, 1177–1206.

[2] Thual O., Frisch U., Henon M. *J. Phys. (Paris)*, 1985, **46**, 1485.

[3] Joulin G. *J. Phys. (Paris)*, 1989, **50**, 1069.

[4] Minaev S. S., Pirogov E. A., Sharipov O. V. *Fizika Goreniya Vzriva*, 1993, 6 (in Russian).

ZERO-RANGE POTENTIALS AND THE FLAME FRONT EQUATION

I. Yu. Popov

Institute of Fine Mechanics and Optics, St.-Petersburg, Russia

As early as in the mid-1940s, Zel'dovich [1] has proposed a qualitative explanation for the fact that cellular flames tend to form in mixtures deficient in the light reactant. In the framework of this model, a linear analysis of the stability of a plane flame front with respect to long-wave disturbances yields the following dispersion relation [2]

$$\sigma = D_{th}[2^{-1}\beta(1 - Le) - 1]k^2,$$

where $\beta = E(T_b - T_u)/RT_b^2$, $Le = D_{th}/D_{mol}$ is the Lewis number of the limiting reactant, which is assumed to be highly deficient, σ is the rate-of-instability parameter, $\vec{k}$ is the wave vector of the disturbance of the flame front, $F \simeq \exp(\sigma t + i\vec{k} \cdot \vec{r})$, E is a constant, specific to the reaction and called its activation energy, R is the universal gas constant, T_u is the temperature of the unburned cold mixture, at which the reaction rate is negligibly small, T_b is the temperature of the burned gas, usually 5 to 10 times T_u, D_{mol} is the molecular diffusivity, and D_{th} is the thermal diffusivity of the mixture. The flame is stable only if the mobility of the limiting reactant is sufficiently low ($Le > Le_c = 1 - 2/\beta$). At $Le < Le_c$, the flame is unstable. In a typical flame, $\beta \simeq 15$, hence $Le_c = 0.87$.

However, as was pointed out later [3], a flame, although potentially unstable with respect to long-wave disturbances, is nevertheless always stable with respect to short-wave disturbances. At $Le \simeq Le_c$, the dispersion relation incorporating the damping effect of short-wave disturbances is

$$\sigma = D_{th}[2^{-1}\beta(1 - Le) - 1]k^2 - 4D_{th}L_{th}^2 k^4,$$

where L_{th} is the thermal thickness of the flame defined as D_{th}/U_u, where U_u is the propagation speed of the flame relative to the unburned gas. Hence, we obtain the following equation (in a nondimensional parameter-free form) for the function $z = F(x, y, t)$ describing a curved flame front [4]:

$$\sigma F + \Delta F + 4\Delta^2 F = 0. \tag{1}$$

Remark. This equation can be obtained from the Kuramoto–Sivashinsky equation [4, 5]

$$\sigma F + 2^{-1}(\nabla F)^2 + \Delta F + 4\Delta^2 F = 0,$$

if the nonlinear term is omitted.

[2] Gelfand B. E. In: *Chemical Physics of Combustion and Explosion (Detonation)*, Chernogolovka, Akad. Nauk SSSR Publ., 1977, 28 (in Russian).

[3] Aslanov S. K. *Jour. Aerosol. Sc.*, 1993, **24**, S1, 123.

[4] Aslanov S. K., Girin A. G. *Dokl. Akad. Nauk SSSR*, 1985, **282**, 1, 72 (in Russian).

ON THE FLOW ASSOCIATED WITH CO DETONATION COMBUSTION IN AN EXPERIMENTAL FACILITY WITH A SHOCK TUBE

V. A. Bityurin*, V. A. Ivanov*, A. Veefkind[†], V. S. Bajovic[†]

Institute of High Temperature, Russian Academy of Sciences, Izhorskaya str. 13/19, Moscow, 127412 Russia

[†]*Eindhoven University of Technology, PO Box 513, 5600 MB Eindhoven, The Netherlands*

A combustible mixture of carbon oxide and oxygen is used as a working body in the Eindhoven Shock Tunnel Facility (EUT STF). EUT STF consists of a shock tube, a supersonic nozzle with a channel and a dump tank. The driver section and diaphragm section of the shock tube are filled with helium at pressure 11 and 5.5 bar, respectively. The test section of the shock tube and the remaining part of the EUT STF were filled with CO and O_2 at partial pressures 74 and 37 mbar, respectively. Ignition of the combustible mixture was performed by shock-wave compression after the rupture of diaphragms [1].

Pressure transducers were located at several positions in the test section of the shock tube and in the channel to record pressure during the run. Moreover, a line profile measurement was carried out at the resonance line of Cs at a wavelength of 852.11 nm in the middle of the channel. The temperature was determined experimentally by fitting the self-reversed spectral line profile.

The experimental studies were accompanied by a numerical simulation of the gas flow and CO combustion in the experimental facility. The nonsteady flow of premixed atomic and molecular gases was described within the framework of a one-dimensional approach by the Euler equations including chemical reaction sources. The considered gas components were CO, CO_2, He, H_2O, O and O_2. The dependence of the temperature of the molecular components of the mixture on the thermodynamic properties was taken into account.

References

[1] Zel'dovich Ya. B. *Theory of Combustion and Detonation of Gases.* Moscow, Akad. Nauk SSSR Publ., 1944 (in Russian).

[2] Barenblatt G. I., Zel'dovich Ya. B., Istratov A. G. *Zhurnal Prikladnoi Mekhaniki Tekhnicheskoi Fiziki*, 1962, 4, 21 (in Russian).

[3] Sivashinsky G. I. *Comb. Sci. Techn.*, 1977, **15**, 137.

[4] Sivashinsky G. I. *Ann. Rev. Fluid Mech.*, 1983, **15**, 179.

[5] Buckmaster J. *ibid*, 1993, **25**, 21.

[6] Demkov Yu. N., Ostrovski V. N. *Zero-range Potentials in Atomic Physics.* Leningrad, LGU Publ., 1975 (in Russian).

[7] Albeverio S., Gesztezy F., Hoegh-Kron R., Holden H. *Solvable Models in Quantum Mechanics.* Berlin, Springer, 1988.

[8] Pavlov B. S. *Uspekhi Matematicheskikh Nauk*, 1987, **42**, 6, 99 (in Russian).

[9] Popov I. Yu. *J. Math. Phys.*, 1992, **33**, 11, 3794.

[10] Popov I. Yu. *Physica Scripta*, 1993, **47**, 682.

[11] Karpeshina Yu. E., Pavlov B. S. *Matemat. Zametki*, 1986, **40**, 1, 49 (in Russian).

A SIMPLE MODEL FOR THE FRONT SELF-OSCILLATIONS

E. Rumanov

Institute of Structural Macrokinetics, Chernogolovka, Russia

According to Zel'dovich analysis [1], the combustion front instability is "physically one-dimensional" in the case of low diffusivity (as compared to heat diffusivity). The origin of instability is the heat accumulated by the preheat zone. Since the minimal

respectively. The term spin implies that one or more hot spots move in a helical fashion on the surface of the specimen. Fig. 1 is consistent with the analogous graph of [4] and thereby with the data of [5]. Indeed, during the experiments, a number of specimens made of mixtures providing various values of T_b has been used. A decrease in T_b results in a decrease in α and an increase in ν. This is equivalent to a downward displacement along the lines shown in the Fig. 1 (the lower one corresponds to the larger diameter). The details of plotting the lines are described in [4]. As we move along them, we pass multispot regimes before reaching the one-head spin-wave regime. The same change of regimes was observed in [5]. We also examined the case of essentially nonzero heat loss by introducing the respective term into the energy equation. We have found that the representing points occupy qualitatively the same relative positions as in the above case. The difference is that the points shift to the right and upward, and the plane oscillations disappear.

These results, combined with the conclusion of [7] concerning the chaotic planar oscillations at $\alpha \ll 1$ and zero heat loss, allow us to speculate on the existence of an interesting self-organization phenomenon. Let us consider the case of zero heat loss. The planar chaotic oscillations will occur at zero diameter under strong instability conditions ($\nu \to \infty$, $\alpha \ll 1$). In the opposite limit of large diameters ($\nu \to 0$), multiple hot spots must appear on the front. It seems natural to expect that their interaction should result in a new chaotic regime. Thus, the domain of periodic one-head spin regime turns out to be covered by chaotic regime domains. In other words, the domain of periodic regime deeply intrudes into the region of instability. We intend to verify this statement in our forthcoming studies.

References

[1] Makhviladze G. M., Novozhilov B. V. *Zhurnal Prikladnoi Mekhaniki Tekhnicheskoi Fiziki*, 1971, **5**, 51 (in Russian).

[2] Barenblatt G. I., Zel'dovich Ya. B., Istratov A. G. *ibid*, 1962, **4**, 21 (in Russian).

[3] Shkadinsky K. G., Khaikin B. I., Merzhanov A. G. *Fizika Goreniya Vzriva*, 1971, **7**, 15 (in Russian).

[4] Strunin D. V. *ibid*, 1993, **29**, 4, 42 (in Russian).

[5] Strunina A. G., Dvoryankin A. V. *Dokl. Akad. Nauk SSSR*, 1981, **260**, 1185 (in Russian).

[6] Ivleva T. P., Merzhanov A. G., Shkadinsky K. G. *Fizika Goreniya Vzriva*, 1980, **2**, 3 (in Russian).

[7] Bayliss A., Matkowsky B. J. *SIAM J. Appl. Math.*, 1990, **50**, 437.

We will show that the instability at frequencies given by Eq. (6) results in a soft onset of the self-oscillations. For this purpose, consider the behavior of phase trajectories as determined by the equation

$$\frac{d\theta}{d\xi} = b^{-1}[\exp(z\theta) - (1+\theta)(1+\xi)^{-1} - \theta\alpha^{-1}][1 - \exp(z\theta)]^{-1} \tag{7}$$

in the neighborhood of the focus $(0, 0)$. Assuming g to be small, we expand the right-hand side of Eq. (7) in powers of ξ and θ:

$$\frac{d\theta}{d\xi} = -(bz)^{-1}\frac{\xi}{\theta}[1 + f(\xi, \theta)],$$

$$f = -\xi + \left(1 - \frac{z_c}{2}\right)\theta + z_c^2\frac{\theta^2}{2\xi} + g\frac{\theta}{\xi} + \xi^2 - \left(1 - \frac{z_c}{2}\right)\xi\theta -$$

$$\frac{z_c}{2}\left(1 - \frac{z_c}{6}\right)\theta^2 - z_c^3\frac{\theta^3}{12\xi} + \dots$$

Using the polar co-ordinates $\xi(bz_c)^{-1} = r\cos\varphi$ and $\theta = r\sin\varphi$, we have, instead of Eq. (7),

$$\frac{dr}{d\varphi} = f(r, \varphi)r\cos\varphi\sin\varphi. \tag{8}$$

If the small value of f is neglected, the trajectories will be circles. Actually, they are spirals diverging from the unstable focus, but the spiral pitch is small as compared to its radius. After integrating Eq. (8) over φ from 0 to 2π, the pitch Δr is obtained on the left-hand side. On the right-hand side we can approximately treat r as a constant. Let the stable limit cycle be at the origin. The cycle radius is given by $\Delta r = 0$. The expansion terms of f odd in powers of either ξ or θ contribute to Δr only. In particular, the first powers ξ, θ, and $\theta^2\xi^{-1}$ vanish after integration. Retaining the terms up to the second order only, we find the amplitudes of self-oscillations of l and T:

$$A_l = r_0\kappa\sqrt{bz_c}(\rho c u_c)^{-1}, \quad A_T = (T_b - T_0)r_0, \quad r^2 = 16z_c(z_c^2 - 2bz_c + 4b)^{-1}g.$$

It should be emphasized that the condensed products have a stabilizing influence [5]. Without such an influence, which is described by the last term of Eq. (2), the stationary combustion wave would be unstable at any real z. When the supercriticality g is not small, the oscillations are seen as sequence of short flashes and long depressions. However, this model (with constant a and b) cannot describe, of course, the remarkable period doubling [6] that served as the basis for the Barenblatt's prediction of the chaotic behavior of the front at increased z.

References

[1] Zel'dovich Ya. B. *Comb. Flame*, 1981, **40**, 225.

[2] Andronow A. A. *Compt. Rend.*, 1929, **189**, 15.

[3] Andronow A. A., Leontovich-Andronowa E. A. *Sci. Notes of Gorkii Univ.*, 1939, 6, 3 (in Russian).

[4] Hopf E. *Berichte Math.-Phys. Klasse Sachischen Acad. Wiss. zu Leipzig*, 1942, **94**, 1.

[5] Merzhanov A. G. *Archivum Combustionis*, 1981, **191**, 23.

[6] Shkadinsky K. G., Khaikin B. I., Merzhanov A. G. *Combust. Explos. Shock Waves*, 1971, **7**, 15.

DYNAMICS OF THE REACTION FRONT ACCOMPANIED BY A SHARP INCREASE IN VISCOSITY

A. S. Segal

Department of Computer Technologies, Institute of Fine Mechanics and Optics, 14 Sablinskaya str., St.Petersburg, 197101 Russia

A sharp increase in fluid viscosity due to certain reactions can result in a substantial bending of their propagating fronts in flows and lead to formation of jets of the initial low-viscosity substance bounded by stagnation zones of the final high-viscosity product [1]. In mathematical terms, this phenomenon is due to the existence of a small parameter, namely the ratio of viscosities at the front, which introduces a singular perturbation into the initial problem. The stiffness of the equations of the problem hampers its direct numerical solution for this case and suggests that alternative approaches should be sought. One of them is developed in this paper. A version of the method of matched asymptotic expansions (MMAE) is proposed here for a "jump" model of the front. A numerical technique for front movement simulation within the framework of this model is developed, based on the method of boundary-integral equation (MBIE) [2]. The dynamics of arbitrary finite perturbations of a steady front is studied numerically.

The transfer processes associated with a reaction front are characterized by at least two spatial scales, the thickness of front preheat zone Δ and its curvature radius R. The front is distinct when $\Delta \ll R$, so that we have the small parameters $\varepsilon = \Delta/R = \kappa/UR = 1/Pe$ (κ is the thermal diffusivity), U is the front propagation velocity, and Pe is the Peclet number). In this case, the front can be treated as an object of boundary-layer type and analyzed by means of MMAE. Since this "boundary layer" is curved and travelling, the internal expansion (on the scale of Δ) is carried out in the specific moving curvilinear frame of reference tied to the front. The main result of this asymptotic analysis is that an the external scale, R, the front may be considered as a surface of discontinuity of the variables, which moves in the direction of its normal n at the velocity W_n determined, in the zeroth and first orders, by

$$W_n = V_n + U, \qquad W_n = V_n + U + \kappa Z \left(\frac{1}{R} + \frac{1}{U} \frac{\partial V_n}{\partial n} \bigg|_F \right). \tag{1}$$

Here, V is the local fluid velocity, Z is the Zel'dovich number, and F is the front surface. It is interesting that the first-order correction is a sum of that introduced by Markstein and that due to stretch effect [3]. Moreover, it can be shown that fluid dynamics in the regions ahead of and behind the front is described by the Stokes equations (convective terms are neglected in both regions) with conditions of continuity of velocity and stress vectors at F.

The problem in the above reduced form still remains rather complicated since it contains a free surface F. Its further simplification relies on MBIE, which makes it possible to reduce the Stokes equations, with the respective boundary conditions, to one integral equation for the velocity vector at all boundaries. We consider here the particular planar case when a closed front envelopes source or sink points, and there are no other boundaries. In the case of a source, an integral equation is obtained in the following form:

$$V(i) - \frac{\alpha - 1}{\alpha + 1} \int_F \Gamma(i,j) V(j) \, F_j = \frac{2\alpha}{\alpha + 1} \frac{r(i)}{r^2(i)}. \tag{2}$$

Here, i is the "fixed" point at the front surface, j is the "current" one, α is the ratio of fluid viscosities at the front, Γ is the fundamental tensor (see [2]), r is the radius vector. The right-hand side describes the velocity field of the source, while the integral term is responsible for the distortion of this field by the viscosity jump (it vanishes at $\alpha = 1$).

The problem (1), (2) was studied numerically. Equation (2) was solved at each time step by a direct method [2] while step-by-step front propagation was implemented using an explicit finite-difference scheme. Some results of the computations are given in Figs. 1 and 2.

Figure 1 shows the distribution of flow velocity vector along the elliptic front for the case of a source located at its center for $\alpha = 1$ and $\alpha = 0.01$ (arrows 1 and 2
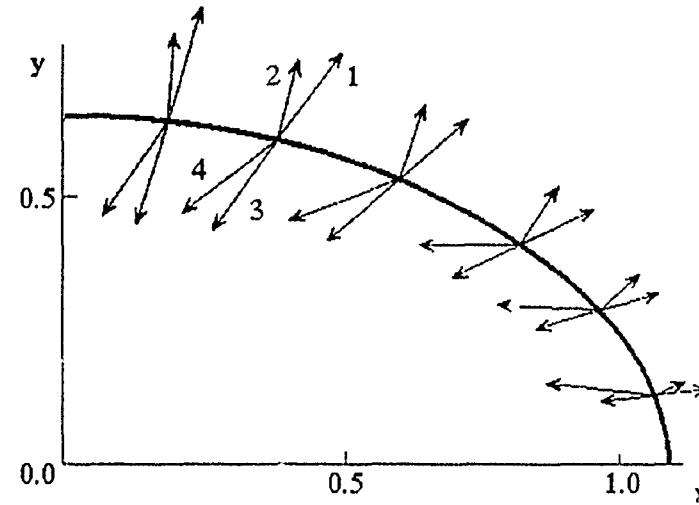
Figure 1: Distributions of velocity vector along the elliptic front for different values of the ratio of fluid viscosities α.
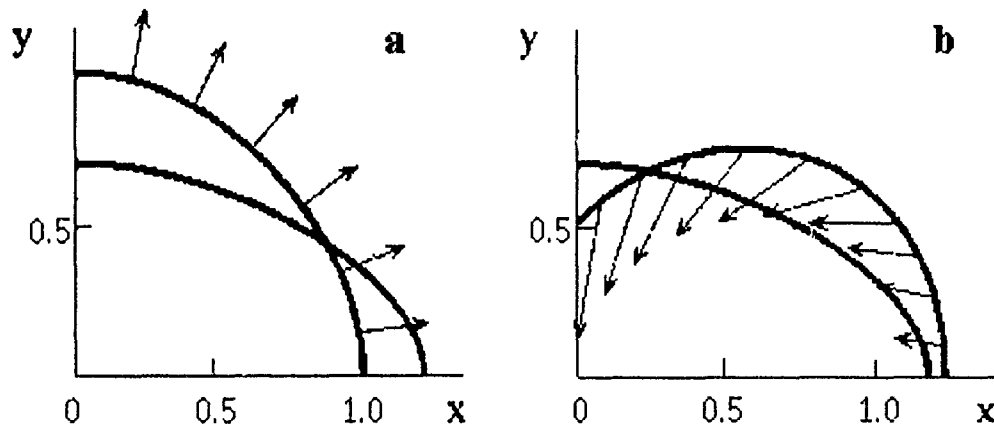
Figure 2: Unsteady behavior of the initially elliptic front for the cases of a source and a sink in its center.

respectively) and for the case of a sink for the same values of α (arrows 3 and 4, respectively). In the case of a source, the velocity vector turns toward the normal direction and simultaneously decreases in its value with decreasing parameter α, while its behavior in the case of a sink is just the converse. The unsteady behavior of an initially similar elliptic front for $\alpha = 0.01$ is presented in Fig. 2. The front is stable in the case of a source and tends to a steady circular shape (Fig. 2a). In the case of a sink, the front is unstable, its curvature increasing and jets of initial substance growing toward the center at same locations (Fig. 2b). The variation of parameter α has a weak effect on this process.

References

[1] Malkin A. Ya., Zhirkov P. V. *Adv. Polym. Sci.*, 1990, **95**, 111.

[2] *Boundary-Integral Equation Method* (Cruze T. A., Rizzo F. J. Eds.), N. Y., Troy, 1975.

[3] Zel'dovich Ya. B., Barenblatt G. I., Librovich V. B., Makhviladze G. M. *Mathematical Theory of Combustion and Explosion*. New York, Consultant Bureau, 1985.

ON THE THERMAL INSTABILITY OF ELECTRICAL HEATING OF CERAMIC MATERIALS

A. Stolin*, **L. Stelmakh**[†]

Institute of Structural Macrokinetics, Russian Academy of Sciences, 142432 Chernogolovka, Moscow Region, Russia

[†]*Institute of Chemical Physics in Chernogolovka, Russian Academy of Sciences, 142432 Chernogolovka, Moscow Region, Russia*

Thermal instability due to the nonlinearity of heat release rate as a function of temperature is characteristic of many processes in chemistry and mechanics [1–2]. However, it can be observed in the presence of a strongly nonlinear heat sink as well. This possibility with regard to boiling processes was discussed in [3], where a nonlinear form was chosen for the temperature dependence of heat release coefficient, which should be, strictly speaking, determined while solving the problem. Similar critical phenomena

can occur during heating in materials characterized by a falling or nonmonotonic dependence of thermal conductivity on temperature. Many ceramic materials have this character of heat conductivity variation.

Theoretical analysis of heat instability for the system consisting of the rod heater surrounded by a cylindric ceramic layer was performed within the framework of the analytical model proposed in the paper. The possibility of nonunique steady states in the thermal instability domain was shown. The number of stable and unstable regimes was determined, and the criteria for transitions between the regimes were found.

Based on the numerical analysis of the problem taking into account the temperature distributions along the radius of the heater and in the ceramics, the following characteristics of the thermal instability have been defined: the time of thermal stability, the induction period, and the dynamics of temperature variation in the heater and ceramics. The possibility of analytical solution of the simplified problem with temperature averaged over the heater was studied.

The practical realization of the thermal instability and real existence of critical parameters are illustrated. Some conclusions concerning practical calculations of heat isolation of thermal equipment are made, based on the results obtained.

References

[1] Zeldovich Ya. B., Barenblatt G. I., Librovich V. E., Makhviladze G. M. *Mathematical Theory of Combustion and Explosion*, Moscow, Nauka, 1980 (in Russian).

[2] Frank-Kamenetski D. A. *Diffusion and Heat Transfer in Chemical Kinetics*, Moscow, Nauka, 1967 (in Russian).

[3] Zhukov S. A., Barelko V. V. Merzhanov A. G. *Dokl. Akad. Nauk SSSR*, 1978, **242**, 1064 (in Russian).

THE EVOLUTION OF A DISTRIBUTED COMBUSTION FRONT OF STRONG THERMAL INSTABILITY

D. V. Strunin, T. P. Ivleva, K. G. Shkadinsky

Institute of Structural Macrokinetics, Chernogolovka, Russia

The thermal instability of a combustion wave has been revealed by means of linear stability analysis [1] based on the approach developed by Zel'dovich with co-authors
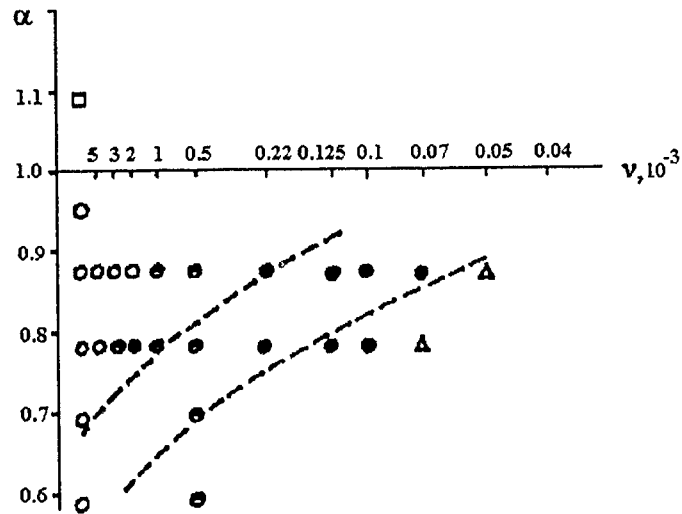
Figure 1: Combustion regimes in the plane of control parameters (α, ν).

[2]. A similar result has been obtained simultaneously in numerical experiments [3]. Strictly speaking, the linear analysis allows one to establish only the fact of stability or instability of a plane steady wave but not the developing pattern of wave propagation. However, one can try to use such analysis to qualitatively predict the wave behavior due to the instability. Such an attempt has been made in [4] to explain the experimentally observed change in the pattern of gasless combustion wave propagation [5] as the system moves away from a stable state. Below, we present numerical results confirming the conclusions of [4].

We examined the simplest model, in which the wave propagates along an empty cylinder of circular cross section. We analyzed the standard set of partial differential equations [6] describing the release and diffusion of heat and the consumption of the limiting reactant. In the first series of computations, heat loss was neglected, in which case the number of control parameters is reduced to two:

$$\alpha = 9.1\gamma - 2.5\beta \quad \text{with} \quad \gamma = \frac{cRT_b^2}{QE}, \quad \beta = \frac{RT_b}{E},$$

$$\nu = \frac{\lambda RT_b^2}{\pi^2 d^2 QEa} \exp\left(\frac{E}{RT_b}\right),$$

where Q is the heat of reaction, E is the activation energy, c is the specific heat, R is the gas constant, T_b is the temperature of reaction products, a is the pre-exponential factor in the Arrhenius law, d is the diameter of the cylinder, λ is the thermal conductivity.

The numerical results are shown in the (α, ν) plane in the Fig. 1. The open square corresponds to the steady plane wave, open circles, half-closed circles, closed circles, and triangles represent planar oscillations, two-head spin wave, and three-head spin wave,

respectively. The term spin implies that one or more hot spots move in a helical fashion on the surface of the specimen. Fig. 1 is consistent with the analogous graph of [4] and thereby with the data of [5]. Indeed, during the experiments, a number of specimens made of mixtures providing various values of T_b has been used. A decrease in T_b results in a decrease in α and an increase in ν. This is equivalent to a downward displacement along the lines shown in the Fig. 1 (the lower one corresponds to the larger diameter). The details of plotting the lines are described in [4]. As we move along them, we pass multispot regimes before reaching the one-head spin-wave regime. The same change of regimes was observed in [5]. We also examined the case of essentially nonzero heat loss by introducing the respective term into the energy equation. We have found that the representing points occupy qualitatively the same relative positions as in the above case. The difference is that the points shift to the right and upward, and the plane oscillations disappear.

These results, combined with the conclusion of [7] concerning the chaotic planar oscillations at $\alpha \ll 1$ and zero heat loss, allow us to speculate on the existence of an interesting self-organization phenomenon. Let us consider the case of zero heat loss. The planar chaotic oscillations will occur at zero diameter under strong instability conditions ($\nu \to \infty$, $\alpha \ll 1$). In the opposite limit of large diameters ($\nu \to 0$), multiple hot spots must appear on the front. It seems natural to expect that their interaction should result in a new chaotic regime. Thus, the domain of periodic one-head spin regime turns out to be covered by chaotic regime domains. In other words, the domain of periodic regime deeply intrudes into the region of instability. We intend to verify this statement in our forthcoming studies.

References

[1] Makhviladze G. M., Novozhilov B. V. *Zhurnal Prikladnoi Mekhaniki Tekhnicheskoi Fiziki*, 1971, **5**, 51 (in Russian).

[2] Barenblatt G. I., Zel'dovich Ya. B., Istratov A. G. *ibid*, 1962, **4**, 21 (in Russian).

[3] Shkadinsky K. G., Khaikin B. I., Merzhanov A. G. *Fizika Goreniya Vzriva*, 1971, **7**, 15 (in Russian).

[4] Strunin D. V. *ibid*, 1993, **29**, 4, 42 (in Russian).

[5] Strunina A. G., Dvoryankin A. V. *Dokl. Akad. Nauk SSSR*, 1981, **260**, 1185 (in Russian).

[6] Ivleva T. P., Merzhanov A. G., Shkadinsky K. G. *Fizika Goreniya Vzriva*, 1980, **2**, 3 (in Russian).

[7] Bayliss A., Matkowsky B. J. *SIAM J. Appl. Math.*, 1990, **50**, 437.

SESSION 6. Detonation

THE SPRAY DETONATION THEORY AND THE KINETIC EQUATION FOR DISPERSION OF A DROP IN A FLOW

S. K. Aslanov

Odessa State University, Petra Velikogo 2, Odessa, 270057 Ukraine

The kinetics for the breakup of combustible drops in the high-velocity gas flow behind the moving shock wave, plays an important role in the construction of the theory of detonation in gas–liquid systems. This process, determining the sizes and intensity of the shedding of small droplets off the surface of the starting drops, controls the formation of the secondary dispersion and defines the intensity of the subsequent evaporation, mixing and combustion. A comprehensive theoretical study of detonation propagation in such systems requires, as a first step, derivation of an adequate equation governing the kinetics of breakup of drops by the incoming gas flow. The present work attempts to construct a closed theory of steady detonation, which includes the release of the self-sustaining regime using the conditions proposed by Ya. B. Zel'dovich [1].

The mechanism of the rapidly developing dynamic instability of the surface layer is used as the basis of theoretical explanation of the drop breakup process by the aerodynamical effects of the flow and acceleration. It manifests itself in the progressive development of spontaneous wave formation at the front edge of the drop. For a disturbance of the form $\sim \exp \omega t$ the counteracting factors including drop viscosity and inertia as well as the effects of the surrounding flow and surface tension are taken into account. The conjugated problem for perturbations is solved using the power asymptotics for the eigenvalue ω parametrized by viscosity. The probable size of the resulting droplets is estimated (within the accuracy of the leading-order term) as determined by the range of the wave spectrum scales corresponding to the highest increase of the inertial forces is

$$\delta \simeq \left\{ \left(36 \div \frac{225}{16} \right) \frac{\mu^2}{\rho^2 W} \right\}^{\frac{1}{3}},$$

where W is the drop acceleration μ and ρ are the viscosity and density of the fluid, respectively, upon reaching a sufficiently high value, those forces induce the breakaway of liquid droplets from the crests of surface waves. The breakup delay time for the drop is estimated by the increment of wave formation:

$$\Delta t \sim \frac{1}{\mathrm{Re}\,\omega} \simeq \left(\frac{\mu}{\rho W^2} \right)^{\frac{1}{3}}.$$

This model of the drop breakup explains the dependence of Δt on viscosity contrary to the result $\mu^{-1/3}$ predicted by the model of boundary layer separation [2].

The kinetic equation for the breakup process is based on the estimate of mass decrease for a single spherical drop $m(t)$,

$$\frac{dm}{dt} = -A(t)\frac{\Delta m}{\Delta t}$$

with the factor $A(t)$ reflecting the existence of the breakup delay time. The incremental mass decrease Δm is found from the simplest model of layer-by-layer breakaway of secondary particles off the drop surface. As a result, a differential kinetic equation with the undefined breakup constant A_1 of order unity [3] is obtained. Its integration yields

$$\frac{m}{m_0} = 1 - \tau^2(3 - 2\tau), \quad \tau = \frac{t}{t_k}, \quad t_k = 2\frac{\Delta t d_0}{A_1 \delta}, \tag{1}$$

where m_0 is the starting mass of the drop of diameter d_0, t_k is the total breakup time. This theoretical result agrees well with the known empirical cosine law [2].

The thermogasdynamic computational scheme [4] is used to model the two-phase flow inside the detonation zone. This scheme has been constructed for a five-component, two-speed medium with inertiafree dispersion of the secondary particles. Equation (1) is introduced into this scheme together with appropriate equations of drop evaporation with constant rate of decrease in the surface area and Arrhenius combustion chemistry. The set of equations of motion is integrated from the leading shock front to the Jouguet plane, where the Mach number of the gas phase reaches unity. As a result, the possibility of existence of a family of steady detonation zones described by a two-valued dependence of the propagation velocity D on the zone length, is established for every composition and dispersability. The breakup constant A_1 is an additional parameter. The problem of practical realization is solved by selecting a self-sustaining regime satisfying the conditions of [1] at the of Jouguet plane, thus ensuring the subsonic to supersonic flow transition. This can occur only at the maximum detonation velocity (with complete combustion) and close to the regime with the minimum width of zone (with incomplete combustion). In the latter case, the agreement of the calculated values with the known experimental data makes it possible to appropriately fit the value of the undefined constant A_1.

Computations were performed for the monodisperse suspension of kerosene in oxygen. At stoichiometric composition $d_0 = 0.29, 0.90, 2.60$ mm. Accordingly, the values $D = 1890, 1700, 1610$ m/s are obtained. Thus, decreasing character of the function $D(d_0)$ is explained.

References

[1] Zel'dovich Ya. B. *Zhurnal Experimentalnoi Teoreticheskoi Fiziki*, 1940, 10, 5, 542 (in Russian).

[2] Gelfand B. E. In: *Chemical Physics of Combustion and Explosion (Detonation)*, Chernogolovka, Akad. Nauk SSSR Publ., 1977, 28 (in Russian).

[3] Aslanov S. K. *Jour. Aerosol. Sc.*, 1993, **24**, S1, 123.

[4] Aslanov S. K., Girin A. G. *Dokl. Akad. Nauk SSSR*, 1985, **282**, 1, 72 (in Russian).

ON THE FLOW ASSOCIATED WITH CO DETONATION COMBUSTION IN AN EXPERIMENTAL FACILITY WITH A SHOCK TUBE

V. A. Bityurin*, V. A. Ivanov*, A. Veefkind[†], V. S. Bajovic[†]

Institute of High Temperature, Russian Academy of Sciences, Izhorskaya str. 13/19, Moscow, 127412 Russia

[†]*Eindhoven University of Technology, PO Box 513, 5600 MB Eindhoven, The Netherlands*

A combustible mixture of carbon oxide and oxygen is used as a working body in the Eindhoven Shock Tunnel Facility (EUT STF). EUT STF consists of a shock tube, a supersonic nozzle with a channel and a dump tank. The driver section and diaphragm section of the shock tube are filled with helium at pressure 11 and 5.5 bar, respectively. The test section of the shock tube and the remaining part of the EUT STF were filled with CO and O_2 at partial pressures 74 and 37 mbar, respectively. Ignition of the combustible mixture was performed by shock-wave compression after the rupture of diaphragms [1].

Pressure transducers were located at several positions in the test section of the shock tube and in the channel to record pressure during the run. Moreover, a line profile measurement was carried out at the resonance line of Cs at a wavelength of 852.11 nm in the middle of the channel. The temperature was determined experimentally by fitting the self-reversed spectral line profile.

The experimental studies were accompanied by a numerical simulation of the gas flow and CO combustion in the experimental facility. The nonsteady flow of premixed atomic and molecular gases was described within the framework of a one-dimensional approach by the Euler equations including chemical reaction sources. The considered gas components were CO, CO_2, He, H_2O, O and O_2. The dependence of the temperature of the molecular components of the mixture on the thermodynamic properties was taken into account.

Figure 1: Pressure versus time in the stagnation region of the shock tube.

The complex chain mechanism of CO and O_2 combustion in the presence of H_2O vapor is described by a single equation of overall kinetics. The combustion rate was taken from [2]. Also, oxygen dissociation was taken into consideration at high temperatures. The backward reaction rates are derived using chemical equilibrium constants.

An incident shock generated by the rupture of the diaphragms moves in the test section and the gas is heated above the ignition temperature behind the incident shock [3]. The chemical reaction starts and the ignition of the combustible mixture occurs at 3 ms after the rupture of the diaphragms. The time interval of 3 ms is the ignition period of the mixture after its interaction with the incident shock wave. The combustion leads to formation of two detonation waves propagating in opposite directions from the ignition point. The first detonation wave overtakes the incident shock wave, and the incident shock wave is taken up in the detonation wave. After the passage of the detonation wave, thermodynamic equilibrium is reached. The product gas is stopped in the region between the two detonation waves.

The computed pressure histories are compared with measured pressures in Figs. 1 ai ـ 2. Solid line denotes the computational results, points are experimental data for different runs. The locations are 0.1 m upstream of the shock tube end plate (stagnation region) (Fig. 1) and 1.115 m downstream of the end plate (Fig. 2). For the cases presented, the time starts at the 4th ms after the run start. The trough in the pressure signal between 2 and 5 ms is due to the passage of the reflected shock wave through the region of quiescent product gas. The pressure plateau is observed in this region in the experiments with nonreacting gas. The product gas is collected in the dump tank.

320
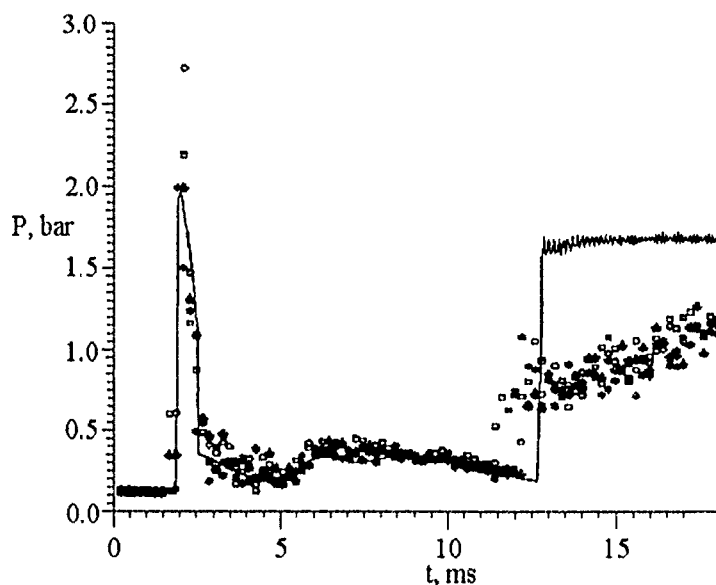
Figure 2: Pressure versus time in the channel.

Pressure in the tank increases and a shock wave begins to propagate upstream in the channel. This shock has been observed both theoretically and experimentally in Fig. 2 at 12 ms.

The temperature determined by fitting the self-reversed spectral line profile is 2600 K. The same average value of temperature has been obtained numerically at this observation point for the time interval when stagnation region appears in the shock tube.

References

[1] Veefkind A., Merck W. F. H., Bajovic V. C., van Buuren M. A., Ivanov V. A., Bityurin V. A. *Proc. 31st SEAM*, Montana, 1993, 3.4.1–3.4.11.

[2] Vilenskii T. V., Khzmalian D. M. *Dynamics of dust fuel combustion.* Moscow, Energiya, 1978 (in Russian).

[3] Zel'dovich Ya. B., Raizer Yu. P. *Physics of shock waves and high-temperature hydrodynamic phenomena.* Moscow, Nauka, 1966 (in Russian).

321

ON THE NATURE OF DETONATION PROPAGATION IN BLASTING EXPLOSIVE MIXTURES WITH INERT ADDITIVES SUCH AS POLYSALT

I. F. Bondarenko, A. T. Vedin

Yakutniproalmaz, Mirnyi, Russia

Unstable propagation of the detonation process along the charge is characteristic for blasting explosives with intergrain space filled with inert additives [1]. The loss of stability of a detonation waveh with a steady front leads to generation of a detonation waveh with a pulsating front [2, 3]. It is assumed that the pulsating process is one of the forms of propagation of explosive chemical coversion near the detonation limits [3].

The paper presents some results on the nature of detonation waves in charges consisting of a heavily diluted TNT/polysalt mixture.

Cylindrical charges of bulk density contained in a glass shell of diameter 8 mm and length 120 mm were used in the experiments to determine the velocity D and the character of the detonation wave propagation. The initiation of the charges was performed by a weighted amount of PETN and a drop of lead azide. In order to study detonation, we used trotyl powders with mass content of particles of size below 10 μm 96.3%, of size 10-20 μm 3.2% and of size 20-30 μm 0.5%. A multicomponent salt predominantly consisting of calcium chloride component (86% mass) evaporated from a salt drine was used as the inert additive to the mixture.

The character of the detonation propagation along the charge length was judged by the luminosity photoscan as viewed from the lateral face of the specimen and by the front velocity measurements using an SFR–2M photographic recorder, as well as by the impression traces on the side walls of copper cylinder channel.

Stable detonation was observed for charge mixtures containing not more than 50% of additives (C). A more complex detonation pattern was recorded for TNT/polysalt mixtures (50/50). Figure 1 shows a typical recorded high-speed photograph of detonation in such a mixture. It has been found that, although the detonation wave front on the photoscan is a staight line, its luminosity is inhomogeneous and contains internal disturbances varying along the charge length down to the discontinuity of the luminosity line. The detonation velocity for the chosen mixtures is determined by relationship $D(C)$.

The characteristic detonation property of TNT/polysalt mixtures containing 50% and more of additives is the existence of an unstable detonation wave propagation regime. The transition to the unstable detonation in the studied mixtures occurs at the distance of 5 charge diameters (d) from the initiation point. The continuous luminosity scan is observed over the region ranging from the onset of the unstable detonation
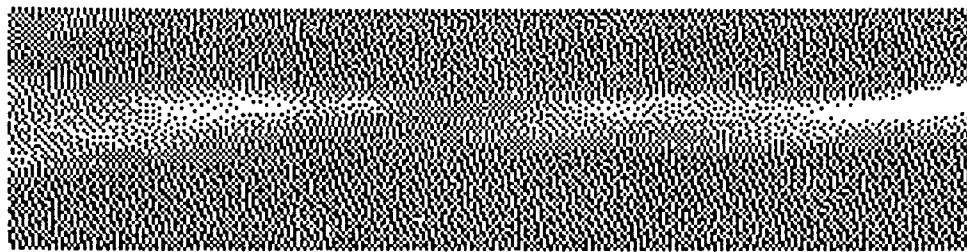
Figure 1: A fragment of the recorded high speed photograph.

regime up to $8d$, and further to the end of the charge the luminosity is intermittently discontinued. The characteristic impression traces of cellular structure are left on the channel walls after detonating the 50/50 mixture of TNT/polysalt in a massive copper shell with side walls thickness 18 mm. The severity of exposure to the detonation wave front across the section of the channel is irregular. The coincidence of the reduced luminosity detonation trace areas with the cells of coarsened structure is noticeable. The regularity of areas with such a structure has a pronounced wave character. The frequency of the cellular structure, as well as character of the detonation wave front luminosity involving generation of pulsations, suggest that the observed regime is a limiting case of detonation transition in blasting explosives mixtures.

Thus, the existence of the pulsating detonation is characteristic not only of charges of diameter less than critical [3] but also of mixtures with a large amount of the inert component such as polysalt.

References

[1] Danilenko V. A., Afanasiev A. N. *Dokl. Akad. Nauk SSSR*, 1981, **256**, 6, 1409–1411 (in Russian).

[2] Dremin A. N. *Fizika Goreniya Vzriva*, 1983, **19**, 4, 159–169 (in Russian).

[3] Shvedov K. K., Dremin A. N. *ibid,*, 1985, **21**, 6, 123–125 (in Russian).

INITIATION OF DETONATION RESULTING FROM A COLLISION OF A SHOCK WAVE WITH AN ORIFICE

C. K. Chan, A. Guerrero, F. Torchia

AECL Research Whiteshell Laboratories Pinawa, Manitoba, ROE 1LO Canada

It has been demonstrated [1] that collision of a shock wave a 2-dimensional reentrant corner in a combustible mixture can cause local strengthening or focussing of the shock wave. Depending on the incident shock strength (expressed in terms of shock Mach number, M_s) and mixture sensitivity, such a collision can create local hot spots capable of causing ignition or direct initiation of detonation in the mixture. It was also observed that shock focussing is a transient phenomenon and the local high pressure decays rapidly due to 3-dimensional gasdynamic expansion. It is well known that ignition and detonation initiation result from competition between various characteristic time and length scales. In order for the onset of detonation (a local explosion) to occur, the gasdynamic decay time must be longer than the characteristic chemical induction time of the mixture. Furthermore, the exploding "kernel" must also be sufficiently large for a self-sustained detonation wave to develop. As a result, the shock focussing phenomena are scale dependent. However, the gasdynamic effect in the above mentioned study [1] is two-dimensional in nature and there is no variation of the exploding kernel size in the z-direction. As a result, the scale effects of the phenomenon could not be determined quantitatively.

This paper describes the results of a quantitative investigation of 3-dimensional scale effects on the initiation of detonation by shock focussing. Since orifices are often found in flow processing systems, experiments were performed to examine collisions of a shock wave with orifices of various diameters, D_0. Moreover, this geometry allows not only the examination of 3-dimensional shock focussing and gasdynamic expansion effects, but also modelling of the phenomena using a 2-dimensional (axisymmetric) computer code.

The experiments were performed in a 9 cm × 9 cm, 4-m long, shock tube consisting of a driver section filled with helium and a test section filled with a sub-atmospheric stoichiometric H_2–O_2 mixture (see Fig. 1). This tube was equipped with glass windows allowing direct photographic observation of the shock reflection and ignition processes. A shock wave created by breaking the diaphragm, separating the two sections, with a plunger. Various shock strengths were achieved by varying the initial pressure of the helium in the driver section. An orifice mounted downstream in the test section was thus subjected to normal incident shocks of various strengths. It was observed that, if the incident shock was sufficiently strong, the compound reflections resulted in ignition of the gas mixture (leading to deflagration). With even stronger incident shocks, direct initiation of detonation resulted.

324
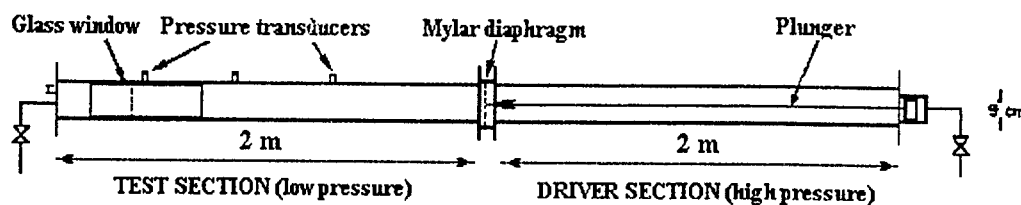
Figure 1: A schematic of the experimental apparatus.

Figure 2 shows the critical shock strength for initiation of detonation as a function of the orifice diameter. The initial pressure of the mixture was 7.9 kPa. The critical incident shock Mach numbers for initiation of detonation were found to vary from about 2.55 (for 1 cm dia. orifice) to about 2.4 (for 5 cm dia. orifice), respectively. The trend of the data suggests that these critical incident shock Mach numbers will eventually reach an asymptotic value of 2.4. It is interesting to point out that the critical shock Mach number is about 2.6 for collision of a shock wave with a plate with no hole [2].

In order to understand the dynamic processes involved in the experiment, a series of two-dimensional calculations was performed using an explicit gas dynamics code (SPLIT2D developed by Combustion Dynamics Ltd.) This code employs the Flux Corrected Transport Algorithm [3] and assumes the gas mixture to be inviscid. A 2-step model similar to the one adopted by Taki and Fujiwara [4] was used to describe the reaction process. The first step describes the induction time and the second step describes the energy release rate. Figure 3 shows the predicted critical conditions (in terms of the incident shock Mach numbers) for the initiation of detonations resulting from collisions of a shock wave with orifices of various diameters. The solid and the open symbols represent detonation and no detonation cases, respectively. The predicted scale dependence of the phenomenon is similar to that observed experimentally. These calculations show, in agreement with the experiments, that it is easier to achieve detonation for larger orifices, although the critical incident shock Mach number reaches an asymptotic value. The above calculations employed about 10,000 grid points with the uniform grid spacing of 0.5 mm. Schlieren photographs reveal that the hot region created by shock focussing is very localized and transient. To simulate initiation of detonation, the grid spacing has to be sufficiently fine to ensure reliable results. Calculations using different grid spacings showed that further reducing the grid spacing below 0.5 mm does not significantly change the results.

The present experiment with stoichiometric H_2–O_2 mixtures shows that a collision of a shock wave with an orifice can create local hot spots that are capable of causing initiation of detonation in the mixture. The critical incident shock strength required for
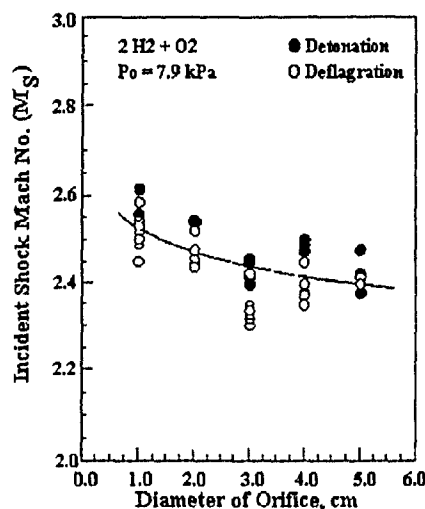
Figure 2: The critical incident shock Mach numbers for initiation of detonation resulting from collision of a shock wave with orifices of various diameters.
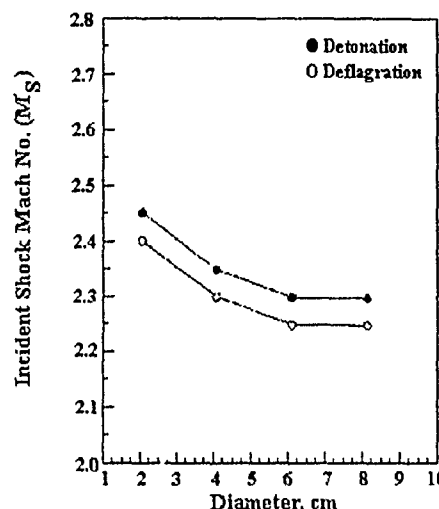
Figure 3: The predicted critical incident shock Mach numbers for initiation of detonation resulting from collision of a shock wave with orifices of various diameters.

initiation of detonation is found to be sensitive to the size (diameter) of the orifice. It is easier (in terms of lower incident shock Mach number) to achieve initiation of detonation with larger orifices. The critical conditions will eventually reach an asymptotic value. Using a 2-step chemical kinetic model, the calculated critical conditions as well as the scale dependence of the phenomenon agree with the experimental observation.

References

[1] Chan C. K., Lau D., Thibault P., Penrose J. D. *Proc. 17th Symp. (Int.) on Shock Tubes and Shock Waves*, AIP Conference Proc., 1990, **208**, 161.

[2] Meyer J. W., Oppenheim A. K., *Proc. 13th Symp. (Int.) on Comb.*, The Combustion Institute, 1971, 1153.

[3] Boris J. P., *Naval Research Lab. Memorandum Report No.3237*, 1976.

[4] Taki S., Fujiwara T. *Proc. 18th Symp. (Int.) on Comb.*, The Combustion Institute, 1981, 1671–1681.

A SIMPLIFIED MODEL FOR THE DETONATION SHOCK DYNAMICS

Sun Chengwei, Gao Wen

Laboratory for Shock Wave and Detonation Physics Research, Southwest Institute of Fluid Physics, P.O. Box 523 Chengdu, Sichuan, 610003, China

A generalized geometrical optics model has been proposed to describe two-dimensional detonation wave propagation. As compared with other equations of the detonation shock dynamics proposed by Bdzil, *et al.* [1, 2], a similar evolution equation for the detonation front can be deduced from this model. The corresponding boundary conditions are discussed with the shock polar for partly reacted detonation products.

Basic Equations for the Detonation Shock Dynamics (DSD)

Based on Bzdil's work [3], Stewart [2, 4] obtained a parabolic evolution equation for weakly curved detonation fronts,

$$\frac{\partial Z}{\partial \tau} = a \cdot \nabla^2 Z + \frac{D_J}{2} \cdot |\nabla Z|^2 - \Delta D \varepsilon^{-2} \tag{1}$$

where $Z(x, y, \tau)$ is the detonation front shape in the frame attached to the front and moving along the z-direction at velocity D_J, the small parameter ε is the ratio of reaction zone length to the mean curvature radius $1/\kappa$ of the front, $\tau = \varepsilon^2 t$, t is time, ∇ is the gradient operator in (x, y) plane. The deficit in detonation velocity is $\Delta D = D - D_J$, D_J and D are CJ and steady detonation velocities, respectively. The parameter $a = -(dD_n/d\kappa)$ is usually considered to be a constant, D_n is the normal velocity of detonation front.

Equation (1) can be rewritten as follows:

$$\frac{\partial \Phi}{\partial t} = a \frac{\partial^2 \Phi}{\partial s^2} - D_J \sin \Phi \frac{\partial \Phi}{\partial s}, \tag{2}$$

where Φ is the angle between the front normal and fixed direction, s is the arc length along curve representing the front.

Lambourn [5] modified the Whitham's shock dynamics with the assumption $D_n = D_n(\kappa)$, and his result can be rewritten as

$$\frac{\partial \phi}{\partial t} = a \frac{\partial^2 \Phi}{\partial s^2}. \tag{3}$$

Also, we rewrite the Bzdil's DSD equation as

$$\frac{\partial \Phi}{\partial t} = a \frac{\partial^2 \Phi}{\partial s^2} - [(\Phi - \Phi_e)\overline{D}_n + D_{ne} \tan \Phi] \frac{\partial \Phi}{\partial s} \tag{4}$$

where $\overline{D}_n$ is some average of D_n over the interval $[\Phi,\ \Phi_e]$, subscript e means the end of the front. It is concluded that Eqs. (2), (3) and (4) are similar in the principal terms and differ only in the terms involving $\partial\Phi/\partial s$, i.e., the transverse wave and end effect terms.

The Generalized Geometrical Optics (GGO) Model

The detonation front in an isotropic heterogeneous medium can be described by the eikonal equation:

$$F(x, y, z) = t. \tag{5}$$

Because of the dependence of D_n on the front curvature κ, Eq. (5) yields the equation for the detonation shock dynamics

$$|\mathrm{grad}F|^2 = D_n^{-2}(\kappa). \tag{6}$$

Equation (6) is a complex nonlinear differential equation. We consider special cases of Eq. (6) in the cylindrical and spherical coordinates. Let r be the radial or transverse coordinate. For the detonation front symmetrical about the z axis or two dimensional in (z, r) coordinates, Eq. (6) has the following form

$$\frac{\partial Z}{\partial t} = (1 + Z'^2)^{1/2} D_n - D_J, \tag{7}$$

where $Z' = \partial Z/\partial r$. A linear dependence of D_n on κ is assumed, so that

$$D_n = D_J - a\kappa, \tag{8}$$

where

$$\kappa = \kappa_1 + N\kappa_2 = -\left\{ \frac{Z''}{[1 + Z'^2]^{3/2}} + \frac{NZ'}{r[1 + Z'^2]^{1/2}} \right\}. \tag{9}$$

$N = 0, 1$ correspond to planar and cylindrical 2-D geometries, respectively. Substituting Eqs. (8) and (9) into Eq. (7) and neglecting small quantities of higher order, we obtain an evolution equation similar to Stewart's Eq. (1),

$$\frac{\partial Z}{\partial t} = aZ'' + \frac{D_J}{2}Z'^2 + \frac{aN}{r}Z' - \Delta D, \tag{10}$$

where the detonation velocity deficit $\Delta D = aZ''(Z')^2$. As t approaches infinity, $\partial Z/\partial t \approx 0$, we have a quasisteady 2-D detonation front in an explosive stick or bar,

$$Z = \begin{cases} \dfrac{2a}{D_J} \ln \left| \dfrac{\cos\left(\dfrac{r}{a}\sqrt{\dfrac{-D_J\Delta D}{2}}\right)}{\cos\left(\dfrac{r_e}{a}\sqrt{\dfrac{-D_J\Delta D}{2}}\right)} \right|, & N = 0 \\[30pt] \dfrac{2a}{D_J} \ln \left| \dfrac{J_0\left(\dfrac{r}{a}\sqrt{\dfrac{-D_J\Delta D}{2}}\right)}{J_0\left(\dfrac{r_e}{a}\sqrt{\dfrac{-D_J\Delta D}{2}}\right)} \right|, & N = 1 \end{cases} \tag{11}$$

where r_c is the radius or half-thickness of the explosive bar, J_0 is the Bessel function of zero order. It should be noted that the solution (11) is essentially the same as that obtained by Bdzil [3], except for the coefficients.

The expression for this model in polar coordinates has been deduced, but it seems that there is no simple analytical solution.

Boundary Conditions for the DSD Equation

The energy Q during detonation is assumed to release in two stages, i.e., $(1 - \delta^2)Q$ is released immediately in the front, then $\delta^2 Q$ is released in the reaction zone. Furthermore, we take $D^2 = 2(\gamma^2 - 1)Q$, where γ is the polytropic index of detonation products. In the front frame, the particle velocity just behind the front has the components u and v respectively, along the z and r directions. We have

$$\begin{cases} u = \dfrac{-D}{\gamma + 1}\left[\gamma + \sin^2\psi - \cos\psi\sqrt{\delta^2 - \sin^2\psi}\right] \\ v = (D + u)\tan\psi \end{cases} \tag{12}$$

where ψ is the angle between normal to the front end and boundary tangent.

The corresponding density ρ and pressure p of detonation products are

$$\begin{cases} \dfrac{\rho_0}{\rho} = \dfrac{1}{\gamma + 1}\left[\gamma - \dfrac{1}{\cos\psi}\sqrt{\delta^2 - \sin^2\psi}\right] \\ p = \dfrac{\rho_0 D^2\cos^2\psi}{\gamma + 1}\left[1 + \dfrac{1}{\cos\psi}\sqrt{\delta^2 - \sin^2\psi}\right] \end{cases} \tag{13}$$

where ρ_0 is the density of the original explosive. Thus,

$$\cos^2\psi = \dfrac{(\gamma + 1)p^2}{\rho_0 D^2\left[2p - \frac{(1 - \delta^2)\rho_0 D^2}{\gamma + 1}\right]} \tag{14}$$

Since the refraction angle for a streamline crossing the front is $\theta = -\arctan(u/v)$, Eqs. (12) and (14) determine the detonation shock polar in (p, θ) plane for the partly reacted system.

The sound speed c can be calculated using the Bernoulli theorem:

$$c^2 = \dfrac{\gamma^2 - \delta^2}{2(\gamma + 1)}D^2 - \dfrac{\gamma - 1}{2}(u^2 - v^2) \tag{15}$$

Finally, we derive the following equation for the boundary or end condition of front

$$c^2 - (u^2 + v^2) = D^2\cos^2\psi\left[\dfrac{\gamma}{\gamma + 1}\dfrac{\sqrt{\delta^2 - \sin^2\psi}}{\cos\psi} - \dfrac{1}{\gamma + 1}\dfrac{\delta^2 - \sin^2\psi}{\cos^2\psi} - \tan^2\psi\right] \tag{16}$$

Assuming that the detonation products at the front end leave the front at the sound speed, from Eq. (16) we obtain

$$\tan\psi = \frac{\delta(\gamma^2 - \delta^2)^{1/2}}{\gamma^2 + \delta^2} \tag{17}$$

In a calculation of DSD coupling with hydrodynamic code, δ is given by Eq. (12) from p and ψ. Then, Eq. (16) is employed to determinate whether the flow is supersonic. If so, Eq. (17) will be used to adjust the boundary angle ψ. When the flow becomes sonic, ψ becomes constant henceforth.

According to the generalized geometrical optics model and the above boundary conditions, a computer code has been developed. It works well in reproducing measured detonation wave propagation in insensitive explosives [6].

References

[1] Bdzil J. B., Steward D. S. *Phys. Fluids A*, 1989, **1**, 7, 1261.

[2] Steward D. S., Bdzil J. B. *T and AM Report No.481*, Univ. of Illinois, Urbana, Dept. of Theoretical and Applied Mechanics, 1986.

[3] Bdzil J. B. *J. Fluid Mech.* 1981, **16**, 2, 195.

[4] Steward D. S., Bdzil J. B. *Proc. 9th Symp. (Int.) on Detonation*, 1989, 773.

[5] Lambourn B. D., Swift D. C. *ibid.* 784.

[6] Gao Wen *et al.* (to be published).

ELECTRIC STRENGTH AND ELECTRIC CONDUCTIVITY OF DETONATION PRODUCTS, FOLLOWING DETONATION WAVE FRONT IN A SOLID HIGH EXPLOSIVE

V. K. Chernyshev, V. A. Ivanov

All-Russia Scientific Research Institute of Experimental Physics, Arzamas 16, Nizhni Novgorod Region, Russia

Recent years have shown the growing interest in studying electric properties of high explosive (HE) detonation products. This is due to the fact that in the number of cases

only HE allow solution of complex applied problems. For example, the application of HE in designs of magaamper opening switches allows one to enhance their fast operation, to increase electric strength, and to use electromagnetic energy more efficiently (in electroexplosive current opening switches a part of energy is lost due to conductor transition from solid to gaseous state) [1, 2].

The basic parameters, characterizing a current opening switch, are the resistance, introduced into an electric contour during its opening, and the electric field strength along an opening switch (i.e., electric strength). To a significant degree, these parameters are specified by the electric conductivity and electric strength of detonation products of HE used in an opening switch.

The task of the present work was to study electric conductivity and electric strength of detonation products of the HE charge composed of 30% trotyl and 70% hexogen). In our experiments, the density of the HE charge was 1.7 g/cm^3. For estimating experimentally the detonation product (DP) conductivity, we have conducted two sets of experiments by using electrocontact measuring technique [3] with flat and annular electrodes. Experimental results have shown that the effective thickness of the DP conductivity zone in the vicinity of detonation wave front is $\leq$ 1 mm, and the resistance is within the range from 0.2 to 0.3 Ohm·cm.

The electric strength of DP has been measured by using two measuring techniques. In the first, the electric strength has been estimated on the basis of the break down voltage of a gap between electrodes. In the second, the electric strength of DP was determined by using the voltage which develops at the ends of a gap arising as a result of conductor break by HE charge at the dielectric ribbed barrier. The size of gap in a conductor was determined in earlier experiments [4, 5]. The both measuring techniques gave the value of DP electric strength of about 40 kV/cm.

References

[1] Chernyshev V. K., Volkov G. I., Ivanov V. A., Vakhrushev V. V. In: *Megagauss Physics and Technology*, N. Y., Plenum Press, 1980, 663–675.

[2] Chernyshev V. K. *et al.* In: *Megagauss Fields and Pulsed Power Systems*, N. Y., Nove Science Publishers, 1990, 465–470.

[3] Brish A. A., Tarasov M. S., Tsukerman V. A. *Zhurnal Tekhnicheskoi Fiziki*, 1950, **37**, 6 (12), 1542–1550 (in Russian).

[4] Chernyshev V. K. *et al. Mechanical Conductor Disruption Character in Explosive Current Commutators.* Ref.2, 533–537 (in Russian).

[5] Chernyshev V. K. *et al. Time Dependence of Switching Delay upon the Broken Foil Thickness.* Ref.2, 481–484 (in Russian).

EXCITATION OF SECONDARY EXPLOSIVE SUBSTANCE DETONATION USING ELECTRIC EXPLOSION OF CONDUCTORS

V. K. Chernyshev, E. I. Zharinov, V. V. Vakhrushev

All-Russia Scientific Institute of Experimental Physics, Arzamas-16, Nizhni Novgorod Region, Russia

Despite the numerous investigations of excitation of secondary high explosive (HE) detonation using electrical explosions of conductors [1, 2, 3], the issue has remained open what is the optimum bridge length and can the HE explode with the bridge length being fractions of millimetre.

The goal of the present work was to investigate the reliability of detonation excitation in a fine crystalline PETN, using electroexplosion of a constantan bridge 0.03 mm in diameter, as depending on a bridge length and the amount of energy put into the bridge. A cylinder 10 mm in diameter and 15 mm in height was used as the experimental model chamber (see Fig. 1).

The cylinder included a block (1) made of an insulating material with two 1-mm wire electrodes (2) pressed into it and a bridge (3); a casing made of an insulating material (4) with a bulk of fine crystalline PETN (5) of density 0.8 g/cm^3 and weight of 0.2 g and a pellet (6) made of plastic HE of diameter 8 mm and height 5 mm.

To study the process of HE detonation excitation by the conductor explosion, a capacitor bank was used as the source of electric energy with the maximum voltage of 10 kV and the following parameters: 0.15 μF capacity and discharge circuit inductance $\sim$ 1 μH. During experiments, the following characteristics were measured: the wire current, the voltage applied to the electrodes, and the time of explosive facility operation .

The experiments were conducted with the electrode gap width varied from 0.4 mm to 3.5 mm and 7 kV voltage in a capacitor bank. The current and voltage histories are given in Fig. 2, and the power and resistance histories are given, respectively, in Figs. 3 and 4. For comparison, we also show the power and resistance histories (dotted lines) for chambers not charged by HE.

Analysis of the experimental data shows that the peak of power history coincides with that of resistance, i.e. corresponds to the moment of maximum voltage. When the bridge length is decreased, the peak resistance decreases in a lesser proportion: for l_{bridge} = 3.5 mm, R_{max} = 7 Ohm, and R_{max}/l_{bridge} = 2 Ohm/mm, whereas for l_{bridge} = 0.4 mm, R_{max} = 1.5 Ohm, and R_{max}/l_{bridge} = 3.7 Ohm/mm. It is interesting to note that, with a decrease in bridge length, the maximum power per unit length also increases (for l_{bridge} = 3.5 mm, P_{max}/l_{bridge} = 1.4 MW/mm, and for l_{bridge} = 0.4 mm, P_{max}/l_{bridge} = 4 MW/mm). When the bridge explodes without HE (in the air), the
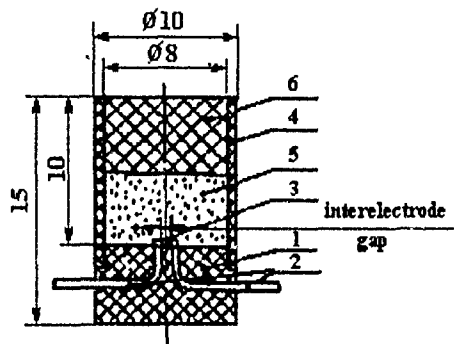
Figure 1.
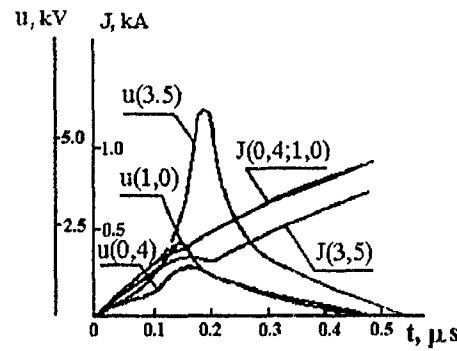
Figure 2.
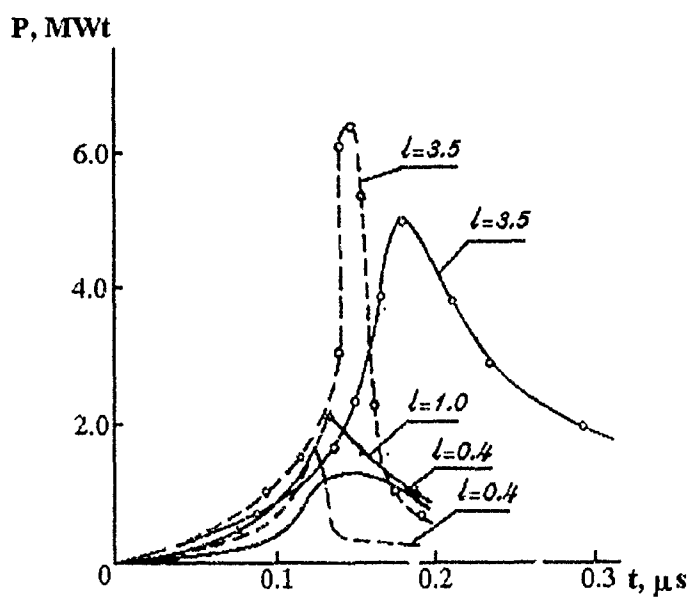
Figure 3.
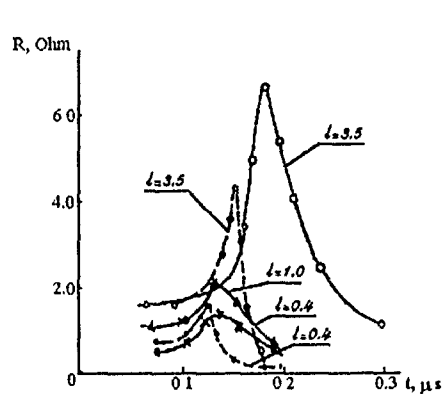
Figure 4.
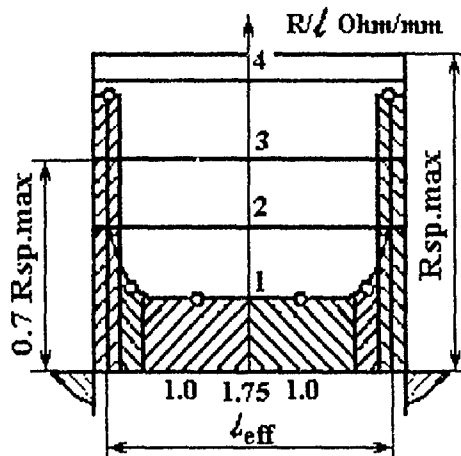
Figure 5.

peak resistance per unit length is lower, but the maximum power is higher than with HE. In this case the bridge explodes noticeably earlier, and the power and resistance rise substantially sharper. The given dependences correspond well to the trends in wire explosion behavior, observed by a number of authors. In particular, Tucker and Nelson [4], in analyzing the dependence of the energy input into the wire prior to its explosion on the wire length have come to the conclusion that "the curve extrapolation of energy dependence on the length to zero length does not give zero energy value" and speculate that end effects may lead to extensive branching of the current-conducting paths at the gap ends. F. Webb and N. Chase observed branching of this type of the final stage of wire explosion [5]. Evidently, this can be the physical reason for the growth of resistance per unit length with decreasing gap width. Figure 5 shows the resistance dependence of the bridge unit length versus the location of the portion under consideration in the gap, plotted on the basis of the oscilloscope records.

The graph reflects the sharp increase in the resistance of the portions of conducting paths adjoining the electrodes. The resistance per unit length of these portions is approximately four times higher than that in the middle of the gap.

If according to a total quantity of the interelectrode gap we assume the energy released by the bridge of length 3.5 mm as the reference value, then the energy of the bridge of 1 mm length is 2.4 times and that of the bridge of 0.3 mm or 0.4 mm length is 3.1 times lower, respectively.

Thus, in terms of energy, bridges of length 0.3 or 0.4 mm are optimum.

References

[1] Herlach F. In: *Exploding Wires*, N. Y., Plenum Press, 1968, 4, 281–298.

[2] Tucker T. J. *ibid*, 211–232.

[3] Howard S. L. *ibid*, 319–332.

[4] Tucker T. J., Neilson F. In: *Vzryvayuschiesya Provolochki*, Izd. Inostr. Liter., Moscow, 1963, 67–74 (in Russian).

[5] Webb F., Chase N., Ernstin M., Tallestrup A. *ibid*, 34–55 (in Russian).

NUMERICAL SIMULATION FOR MECHANICAL FRACTURE AND THERMAL INITIATION IN SOLID EXPLOSIVES BY IMPACT

A. V. Dubovik

Due to the labor content and high costs of the studies of the determination of high explosives (HE) sensitivity to mechanical actions, there is a need in numerical simulation of the process of explosion initiation by an impact [1–3]. Successful development of this project will allow us to advance in the investigation of the mechanism of initiation of fast chemical reactions during the mechanical activation in solids.

Mathematical models describing the mechanical behavior are presented where initiation of HE is based on the experimental data obtained during the investigations of solid organic HE sensitivity to impact [4–5]:

(1) explosion initiation occurs via the failure of the HE charge;

(2) the HE failure is the result of thermal unstrengthening (softening) of the explosive;

(3) the HE heating at the contact boundaries between the fragments (slipbands) resulting from the charge failure bring the HE to its melting point;

(4) until the moment of charge failure, the HE compression occurs in a quasisteady regime.

335

Within the framework of the models under consideration the following assumptions are introduced:

- the mechanical behavior of the HE during the impact is described in terms of the visco-plastic model for solids;

- the quasisteady character of the HE compression persists during the charge failure as well;

- the heat release in the slipbands is due to:

  a) the sliding friction with specific force equal to the limit shear strength (the friction F-model);

  b) the viscous dissipation in the liquid interlayer between the fragments (visco-plastic VP-model);

- the HE decomposition reaction is high-activated and is high-exothermic, the explosion initiation time t_b is determined by

$$f = \int\limits_0^{t_b} \tau_a^{-1}(T(t))\, dt = 1,$$

where $\tau_a(T)$ is the adiabatic induction time.

The goal of calculations was to determine the criterion for the initiation of explosion in the HE, as defined by the equality of the charge failure time t_p and the explosion time t_b. In the axially symmetric presentation, the HE charge is characterized by its radius R and thickness h. With decreasing h, t_p increases as h^{-k} ($k \simeq 1$), due to the growing resistance of the charge failure (determined by dissipative and inertial forces). At the same time, the dissipated energy increases as $h^{-1/2}$ and, as a result, t_b decreases as $\exp(Hh^{1/2})$, where $H \simeq E/\mathcal{R}T_0$ (E is the activation energy, $\mathcal{R}$ is the gas constant). The critical thickness of the charge h_k, as determined from the equation $t_b = t_p$, correlates to the critical pressure initiation, $p_k \sim h_k^{-1}$ (the pressure created in the HE charge prior to its failure for the critical conditions of the impact). The parameter p_k characterizes the HE sensitivity to impact and hazard in handling.

The numerical procedure of determination of p_k is as follows. Initially, the temperature distribution along the charge radius R is found. Next, the value of radius, r_k, at which T is maximum is determined. Next, the value of h is varied and the value of f is calculated. The process is continued until $f = 1$ is reached. At this moment, $h = h_k$ and $p = p_k$.

The predicted and measured critical parameters at initiation for PETN obtained under moderate impact conditions (energy being 25 J) are given in the Table 1. The

Table 1.

models	p_k, GPa	h_k, mm	T_k, K	t_b, μs	r_k, mm
F	0.489	0.281	682	11.5	1.00
VP	0.489	0.270	656	14.3	1.38
Exper	0.49	0.27	—	—	—

calculations were made by the friction (F) and visco-plastic (VP) models. The experiments were carried out in a drop-weight machine (weight 10 kg, impact velocity 2.2 m/s) with roll units (the roll diameter $2R = 1$ cm).

Despite the difference in mathematical representations of heat release in HE during the impact (planar in the F-model and volumetric in the VP-model), the calculations of p_k using these models are similar. The estimates show that the liquid interlayer thickness in HE is smaller than the fragment size ($\sim h$). This situation allows us to consider the liquid interlayer as a plane source of heat release.

The calculations show that p_k weakly depends on the impact velocity and the HE shear strength, decreasing with increasing R and initial temperature T_0, but strongly depends on the activation parameters of HE thermal decomposition. All these results agree with the available experimental data on the HE sensitivity to impact [4–6].

References

[1] Dubovik A. V., Lisanov M. V. *Fizika Goreniya Vzriva*, 1985, **21**, 4, 211 (in Russian).

[2] Dubovik A. V., Lisanov M. V., Avdeev E. A. *Khimicheskaya Fizika*, 1986, **5**, 4, 539 (in Russian).

[3] Dubovik A. V. *Fizika Goreniya Vzriva*, 1993, **29**, 2, 78 (in Russian).

[4] Afanas'ev G. T., Bobolev V. K. *et al. ibid*, 1975, **11**, 3, 467.

[5] Winter R.E., Field J. E. *Proc. Roy. Sec. London*, 1975, **A 343**, 1634, 399.

[6] Avdeev E. A., Dubovik A. V. *Khimicheskaya Fizika*, 1988, **7**, 5, 688 (in Russian).

DEFLAGRATION-TO-EXPLOSION TRANSITION OF PELLETIZED EXPLOSIVE MATERIALS

B. S. Ermolaev, V. A. Foteenkov, B. A. Khasainov, A. A. Sulimov

Institute of Chemical Physics, Russian Academy of Sciences
Kosygin street 4, Moscow, 117977 Russia

Spontaneous transition from deflagration to explosion or detonation during accidents remains an urgent problem of safety in manufacturing, transportation and storage of explosive materials (EM). The main feature of accidental large-scale explosions of EM is that the initial center of combustion (the burning kernel) is subjected to the strong effect of expansion due to the scattering of EM layers already in the earliest stage of the process. The conventional methods of DDT investigation do not take into account this phenomenon. The new approach suggested here makes it possible. The method was named "EM column critical height test". According to it, an EM sample contained in a thin-walled steel tube with the open upper end is ignited by a hot wire at the bottom, and the combustion wave spreads initially as a conductive layer-by-layer process. The final result of the combustion process depends on the EM column height. The experiments revealed the existence of a critical height (H_{cr}): below it, combustion resulted in ejection of the EM column from the tube and its slow burn-out without explosion, while above it an explosion occurred. The critical height and the critical pressure P_{cr}, which is observed in the burning kernel under the critical conditions, could be used as reliable measures of the tendency of large masses of EM to deflagration-to-explosion transition under emergency conditions.

The critical values of H_{cr} and P_{cr} for HMX, single-base propellants (with and without a combustion inhibitor), and double-base propellants were determined. The pressure in the burning kernel was measured by a piezoelectric gauge in the bottom flange of the tube near the ignition location. The diagnostics also included high-speed photography and evaluation of TNT equivalent by standard methods. In order to find the critical conditions, we performed a series of tests with gradually increased heights of the EM column. The effect of the tube diameter (up to 100 cm) on the critical conditions was examined. The typical dependence of H_{cr} on the tube diameter included two regions: at small diameters (up to 30–40 cm) H_{cr} increases sharply with the diameter; at large diameters (above 40 cm) the dependence levels off. Besides, the effects of pellet size, the presence of an inhibitor, and tube wall roughness were studied.

A one-dimensional mathematical model of the process has been developed, including the transition from layer-by-layer combustion to convective combustion driven by the pressure rise in the burning kernel and the competing expansion due to filtration of the combustion products through the EM column and ejection of the EM from the tube, which results in a pressure drop. If the expansion dominates, the EM burns out

slowly without a marked pressure rise in the burning kernel. If the expansion is not fast enough to suppress the pressure rise, rapid acceleration of the burning rate and the pressure rise will result in explosion.

The convective burning is treated using the simplified model developed earlier [1]. Before the onset of convective combustion, the HE ignited at the bottom surface initially burns in the conductive regime at a rate specified by the normal combustion law of the EM. A delay in the onset of convective combustion is defined as the moment at which the combustion products penetrating into the EM column heat the surface of the particles ahead of the conductive flame front to the ignition temperature. The convective flame front is treated as a plane separating the filtration zone and the combustion zone. The preheat zone is thin as compared with these zones. The EM particles behind the flame front burn over their entire surface at the regression rate of conductive combustion.

The pressure rise in the burning kernel moves the EM column as a whole along the tube and ejects it from the confinement. The threshold pressure at which the EM movement starts and the friction force which impedes the movement are taken into account.

The set of governing equations of the model was solved numerically. The results show a good agreement with the experimental pressure–time histories measured in the burning kernel, the existence of the critical height of the EM column separating the explosive and slow combustion modes, and the dependencies of H_{cr} on the tube diameter and the particle size. Moreover, we were able to predict numerically the effects of the initial temperature and the presence of a combustion inhibitor.

Conclusions

A new approach to the problem of deflagration-to-explosion transition based on the EM column critical height test has been developed. Criteria discriminating between the explosion and the burn-out without explosion have been examined. A theoretical model of the test has been developed. The test and characteristics measured under the critical conditions (the critical height of the EM column ignited at the bottom of a steel tube with the open upper end, and the critical pressure measured in the burning kernel when the height of the HE column is critical) will be undoubtedly useful for realistic assessment and elimination of the explosion hazard.

References

[1] Ermolaev B. S., Posvyansky V. S., Sulimov A. A., Khasainov B. A. *Fizika Goreniya Vzriva*, 1983, **19**, 4, 190 (in Russian).

ISOTHERMAL DETONATION

A. P. Ershov

Lavrent'ev Institute of Hydrodynamics,
Lavrent'ev Prosp. 15, Novosibirsk, 630090 Russia

In this paper, detonation with very high frictional losses is investigated. At this limit, the $P - V$ diagram retains its usual form but assumes a new meaning.

Let us consider low-velocity detonation in a porous medium consisting of fixed solid combustible particles. The thickness of the evaporated reacting layers enveloping the surface of particles is negligible as compared to the particle size. Conversely, the reaction zone thickness in the direction of wave propagation is comparatively large. The burnt layer is thin and the gas can be treated as ideal. Such a picture is an idealization of the experiments of [1, 2, 3] and the assumptions made thus far are close to those of [4].

The gas density and pressure sharply increase across the reaction zone. However, temperature variations occur within a rather narrow range, which is roughly corroborated by the correlation $T \sim P/\rho$. Indeed, in the case of the classical single-phase detonation, heat release gives rise to a temperature increase. Conversely, in the system under consideration the heating primarily occurs in thin burning boundary layers, which are ignored in the classical analysis. The pore space is filled with the final "ready-to-use" combustion products. This process gives rise to conditions similar to those of a thermostat in the reaction zone. Because of high friction in the porous medium, internal energy cannot be converted into kinetic energy, either. The internal energy of the gas equals the reaction heat release Q, because combustion takes place in a virtually constant volume. This determines the actual value of temperature.

The accuracy of this approximation was analyzed in [5]. The temperature variations have been found to amount to a few percent.

One-dimensional flow equations take the form (the notation is standard)

$$\frac{\partial \rho}{\partial t} + \frac{\partial(\rho u)}{\partial x} = j, \qquad \frac{\partial(\rho u)}{\partial t} + \frac{\partial(\rho u^2 + P)}{\partial x} = -f. \tag{1}$$

Here, j is the incoming mass flux and f is the friction force. Instead of the energy equation, in this approximation the isothermal equation of state is used, $P = c^2 \rho$, where c is the isothermal sound velocity, $c^2 = RT/\mu = (\gamma - 1)Q$. In so far as the burnt layer is thin, the porosity is constant and drops out of the equations.

For a steady wave, all quantities depend on $\xi = x - Dt$, where D is the wave

velocity. Integration of Eq. (1) from an arbitrary $\xi < 0$ to the shock ($\xi = 0$) gives

$$\rho(D - u) = \rho_0 D + J, \qquad\qquad J = \int_{\xi}^{0} j\, dx,$$
$$P = P_0 + F + \rho u(D - u), \qquad F = \int_{\xi}^{0} f\, dx. \tag{2}$$

Here, ρ_0 is the initial gas density in pores, $P_0 = c_0^2 \rho_0$ (the initial sound velocity c_0 is generally lower than c); $J, F > 0$. From Eq. (2), one obtains

$$P = P_0 + F + D(\frac{D}{V_0} + J) - V(\frac{D}{V_0} + J)^2, \tag{3}$$

V being the specific volume. The closing equation takes the form

$$P = \frac{c^2}{V}. \tag{4}$$

Equation (3) is independent of the isothermal approximation. Given D, J, and F, it defines a straight line with a negative slope on the (P, V) plane, which, for F not too large, has two intersection points with the hyperbola given by Eq. (4) (Fig. 1).

The resemblance between Fig. 1 and the classical picture is partly superficial. The straight line given by Eq. (3) is not the Rayleigh line in the usual sense, because during the mass release the state of gas does not move along it. More likely, Eq. (3) is an analog of the reacted (in general partially) Hugoniot adiabat. The point of state belongs to it after certain values of J and F have been reached. During the evolution, the points representing the state of gas move along the hyperbola (4). This line, though curved, is obviously not analogous to Hugoniot (nor to Rayleigh) line. Every possible state belongs to Eq. (4), including those outside the stationary zone.

Nevertheless, physically, the problem is similar to a classical one. The mass influx J that supports the wave propagation is analogous to the reaction heat release. This is natural, because all the mass released carries its chemical energy.

In the case of Hugoniot (3) being tangent to the state curve (4), it is easy to show that $D - u = c$. Thus, inside the wave a Chapman–Jouguet point separating sub- and supersonic flows exists. In the practically interesting case $J \gg c/V_0$ (the mass of products exceeds the initial gas mass). If, in addition, friction is the dominant factor, then u is small, and $D \approx c$.

To qualitatively examine the structure of the reaction zone, Eqs. (1) were solved numerically. The flow approaches the steady regime. The corresponding steady-state wave structure is shown in Fig. 2. The Chapman–Jouguet point is generally inside the reaction zone. In the variant shown, the shock, to make it visible, is comparable to the subsequent pressure rise. Actually, the shock is relatively small and is needed only to initiate combustion.
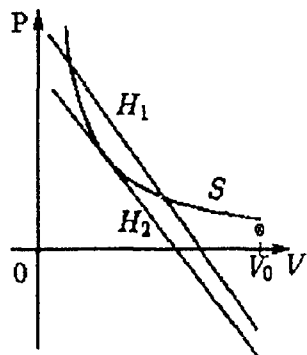
Figure 1: *P–V* diagram. H_1 — Hugoniot intersecting the state hyperbola S. H_2 — Hugoniot tangent to S. The initial state (marked by ⊗) lies generally below S and above H.
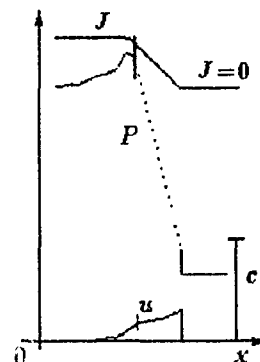
Figure 2: Computed wave structure. $f = \rho u^2 / d$ — force, d — characteristic internal length scale, e.g., particle diameter. Mass input $j(x, t)$ is defined so that it lasts a certain reaction time after shock arrival at given point x. P, u — pressure and velocity profiles, J — mass influx. The J curve is raised to show it more clearly. The vertical bar denotes the Chapman-Jouguet point. The bar at the right shows the scale of sound velocity.

The model predicts the detonation velocity $D \approx \sqrt{(\gamma - 1)Q}$. This limiting value for high friction was reported by Mitrofanov [6]. A much simpler analysis follows from the isothermal approximation. The experimental data [1, 2, 3] scatter around the theoretical value (about 1 km/s) which is no surprise in view of the idealizations made. High friction implies low gas velocity, which makes the ignition questionable. Experiments [1, 2, 3] apparently show that the present theory is in line with reality.

Author is grateful to V. V. Mitrofanov and L. A. Luk'yanchikov for useful discussions.

References

[1] Andreev, V. V., Luk'yanchikov, L. A. *Fizika Goreniya Vzriva*, 1974, **10**, 6, 912 (in Russian).

[2] Andreev, V. V., Ershov, A. P., Luk'yanchikov, L. A. *ibid*, 1984, **20**, 3, 89 (in Russian).

[3] Pinaev, A. V., Lyamin, G. A. *Dokl. Akad. Nauk SSSR*, 1992, **325**, 3, 498 (in Russian).

[4] Kuo, K. K., Summerfield, M. *AIAA J.*, 1974, **12**, 1, 49.

[5] Ershov, A. P. *Fizika Gorenia Vzriva*, 1994, **30**, 2, 177 (in Russian).

[6] Mitrofanov, V. V. *ibid*, 1983, **19**, 4, 169 (in Russian).

THE MODEL OF VASIL'EV AND NIKOLAEV APPLIED TO THE CALCULATION OF THE DETONATION CELL IN UDMH/OXYGEN MIXTURES

V. P. Fokeev*, S. Abid†, G. Dupre†, C. Paillard†

Institute of High Temperatures (IVTAN), Moscow, 127412 Russia
†*Laboratory of Combustion and Reactive Systems (LCSR) and University Centre National de la Recherche Scientifique, 45071 Orleans Cedax 2, France*

The one-dimentional model proposed by Zel'dovich [1, 2], von Neumann [3] and Döring [4], known as ZND model, has made it possible to take into consideration the chemical kinetics and heat losses from the induction and reaction zones. It has contributed to stimulate numerous studies in this field of research. However, the structure of the detonation front is three-dimensional, with transverse waves and nonhomogeneous regions leading to the complex pattern of cells visible on smoked records.

A closed two-dimensional model (called VN model) with a regular cell structure has been proposed by Vasil'ev and Nikolaev [5–6] for gaseous detonation propagation in a flat channel. The calculated cell dimensions correspond satisfactorily to the experimental values for hydrogen or light hydrocarbon mixtures with oxygen [5–7].

In the present work, a theoretical study of gas detonation in unsymmetrical dimethylhydrazine (UDMH)/oxygen/argon mixtures was carried out to calculate the cell size, using the VN model. The results were compared with experimental data.

In the VN model, the processes inside the cell originate from cylindrical explosion of diameter τ, similarly to a point cylindrical explosion (Fig. 1). They manifest themselves by a velocity decrease from the apex to the cell end, as shown by Dormal *et al.* [8]. The detonation velocity D along the cell length depends on the gas density ρ_0 and energy E_l per unit length:

$$D = \frac{dr}{dt} = \frac{1}{2r}\sqrt{\frac{E_l}{\rho_0}} \quad \text{with} \quad E_l = \frac{E_c}{\alpha} + \beta\rho_0 q\pi\left(r^2 - \frac{\tau^2}{4}\right),$$
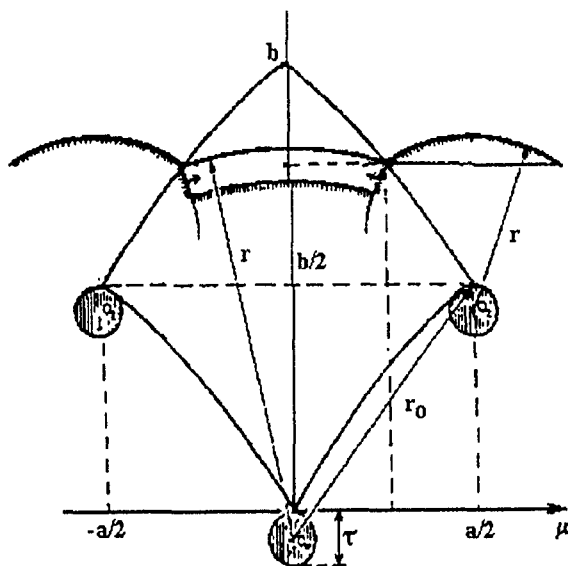
Figure 1: Schematic of an elementary detonation cell [6].

where r is the distance from the explosion point. The first term of E_l is the energy released by the microexplosion (E_0/α) where $\alpha \approx 1$ and $E_0 = P_3\pi\tau^2/4(\gamma_e - 1)$, where P_3 and γ_e are the pressure and the specific heat ratio of the detonation products in the microexplosion cylinder of diameter τ. The second term is the energy released during the shock/reaction zone coupling, with q being the specific reaction heat release and $\beta = 4D_{CJ}^2/q\pi$. The third one is the energy that is not released because of the shock – reaction zone decoupling.

In order to calculate the nondimensional characteristics of the detonation cell, we have to introduce some nondimensional variables and parameters (normalized by the cell length b, the period of the cell $t_2 = b/D_{CJ}$, or the Chapman–Jouguet velocity D_{CJ}):

$$z = \frac{r}{b}, \quad y = \frac{\tau}{2b}, \quad e = \frac{E_0}{4D_{CJ}^2\rho_0 b^2\alpha}, \quad t_a = \frac{t}{t_2}, \quad D_a = \frac{D}{D_{CJ}}.$$

Thus,

$$D_a = \frac{dz}{dt_a} = \frac{\sqrt{e + z^2 - y^2}}{z} \tag{1}$$

The integration of Eq. (1) leads to the following expression, where $x = r_x/b$ and r_x is the distance at time t_x between the explosion and the decoupling:

$$\frac{(1+y)^2 - x^2}{2\sqrt{e + x^2 - y^2}} + \sqrt{e + x^2 - y^2} - \sqrt{e} - t_2 = 0, \tag{2}$$
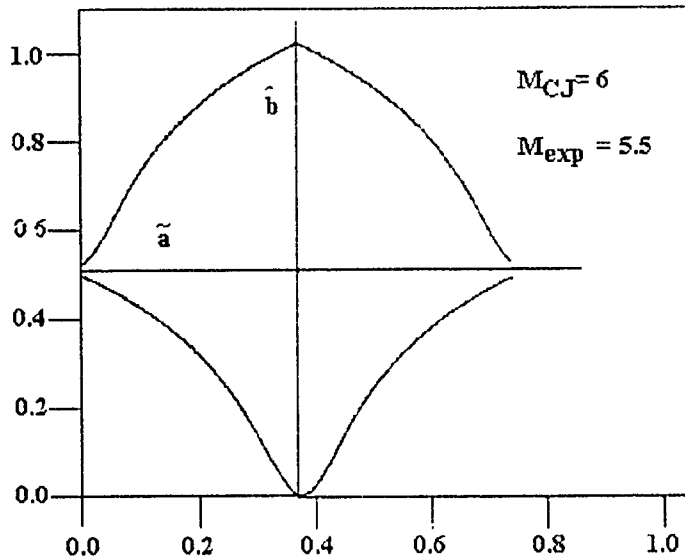
Figure 2: Calculated cell shape for CJ detonation Mach number $M_{CJ} = 6$ and average experimental Mach number $M_{exp} = 5.5$ ($\tilde{a}$ and $\tilde{b}$ are the nondimensional width and length of the cell).

$$\frac{P_3 \pi y^2}{4 D_{CJ}^2 \rho_0 \alpha (\gamma_e - 1)} - e = 0. \tag{3}$$

To calculate the nondimensional characteristics of the detonation cell, Eq. (2) has to be solved for various values of x ($0 < x < 1$) using Newton's method and the values of D_{CJ}, D_{exp}, γ, and γ_e to find out x, y, and e. Using these values, one can calculate all the cell characteristics and verify Eq. (3). A software program was written in the laboratory to solve Eqs. (2) and (3) and calculate the variation of the nondimensional velocity D/D_{CJ} along the cell. Using the triple point coordinates (μ, η) and the transverse shock velocity $D_l = d\mu/dt$, it is also possible to determine the trajectories of triple points and the ratio $\tilde{a} = a/b$ of the width to the length of cell, as shown in Fig. 2.

The **dimensional parameters of the detonation cell** are calculated using the following expression given by Vasil'ev and Nikolaev from the decoupling point:

$$1 = \int_{t_x}^{t_2} \frac{dt}{t_i} = \int_{r_x}^{b+\frac{\tau}{2}} \frac{dr}{Dt_i} = \int_x^{1+y} \frac{b\,dz}{Dt_i},$$

where t_i is the delay time of the explosion reaction.

By analogy with Vasil'ev–Nikolaev formula, b can be written as $b = 1/\int_x^{1+y} \frac{dz}{Dt_i}$,

$$b \approx \frac{D_{exp}}{(1+y-x)} \frac{\theta}{T} t_i.$$
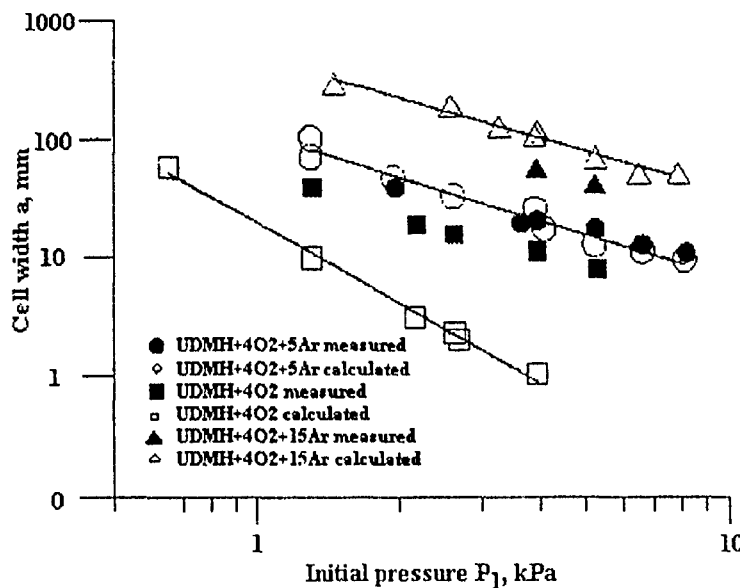
Figure 3: Detonation cell width for different $UDMH/4O_2/Ar$ mixtures versus initial pressure. Closed symbols correspond to experiments, open symbols to calculations by VN model.

If the temperature and density are assumed to be constant in the induction zone, then the delay time, determined from shock tube data [9], is

$$t_i = A[\text{UDMH}]^m [O_2]^n [\text{Ar}]^p \exp\left(\frac{\theta}{T}\right).$$

It follows that

$$b \approx \frac{D_{exp}}{(1+y-x)} \frac{12900}{T} 10^{-9} X^{0.06} Y^{-1\,44} Z^{0.94} \left(\frac{P}{RT}\right)^{-0\,44} \exp\left(\frac{12900}{T}\right),$$

where D_{exp} is the experimental detonation velocity, m, n, and p are coefficients, $\theta = 12960$ K is the activation temperature, $A \approx 10^{-9}$ $(\text{mol·m}^{-3})^{0.44}\text{s}^{-1}$ is a constant, [...] are the reactant concentrations, X, Y, Z are the reactant molar fractions, and P and T are the von Neumann pressure and temperature. All the terms are given in SI units

Figure 3 shows a comparison between the cell width as measured by soot records and its value determined from the above expression, with $a = b\tilde{a}$. A better agreement is obtained for the mixtures diluted with argon.

The theoretical method of Vasil'ev and Nikolaev provides an interesting means of calculating the detonation cell size of a given mixture, providing that the overall kinetics of the explosive reaction is known.

References

[1] Zel'dovich Ya. B. *Zhurnal Experimentalnoi Theoreticheskoi Fiziki*, 1940, **10**, 5, 542 (in Russian).

[2] Zel'dovich Ya. B., Kompaneets A. S. *Theory of Detonation*. Moscow, Gostekhteorizdat, 1955 (in Russian).

[3] von Newmann J. *Theory of Detonation Waves*. OSRD Report No.549, 1942.

[4] Döring W. *Ann. Phys. Lpz.*, 1943, **43**, 5, 421.

[5] Vasil'ev A. A., Nikolaev Yu. A. *Fizika Goreniya Vzriva*, 1976, **5**, 744 (in Russian). Translated in *Comb. Expl. Shock Waves*, 1976, **5**, 682.

[6] Vasil'ev A. A., Nikolaev Yu. A. *Acta Astronautica*, 1978, **5**, 983.

[7] Vasil'ev A. A., Nikolaev Yu. A., Ul'yanitskii V. Yu. *Fizika Goreniya Vzriva*, 1977, **3**, 404 (in Russian). Translated in *Comb. Expl. Shock Waves*, 1977, **3**, 338.

[8] Dormal M., Libouton J.-C., van Tiggelen P. J. *Acta Astronautica*, 1979, **6**, 7-8, 875.

[9] Abid S., Dupré G., Paillard C. In: *Prog. Astron. Aeron.*, 1991, **153**, 162.

ON PLANE DETONATION WAVE INITIATION AND PROPAGATION IN SOLID HIGH EXPLOSIVES: THE RESULTS OF ELECTRICAL MEASUREMENTS

L. A. Gatilov, V. M. Gerasimov, A. V. Kudashov, G. S. Smirnov

RENC-VNIIEF, Arzamas-16, Russia

This paper presents measurement results for shock initiation and propagation of a plane detonation wave (DW) in cast TNT and four highly compacted formulations: HE1 (70% RDX plus a TNT-based explosive), HE2 (90% HMX plus a TNT-based explosive), HE3 (94% HMX plus an inert teflon-based additive), and HE4 (90% TATB plus an inert teflon-based additive).
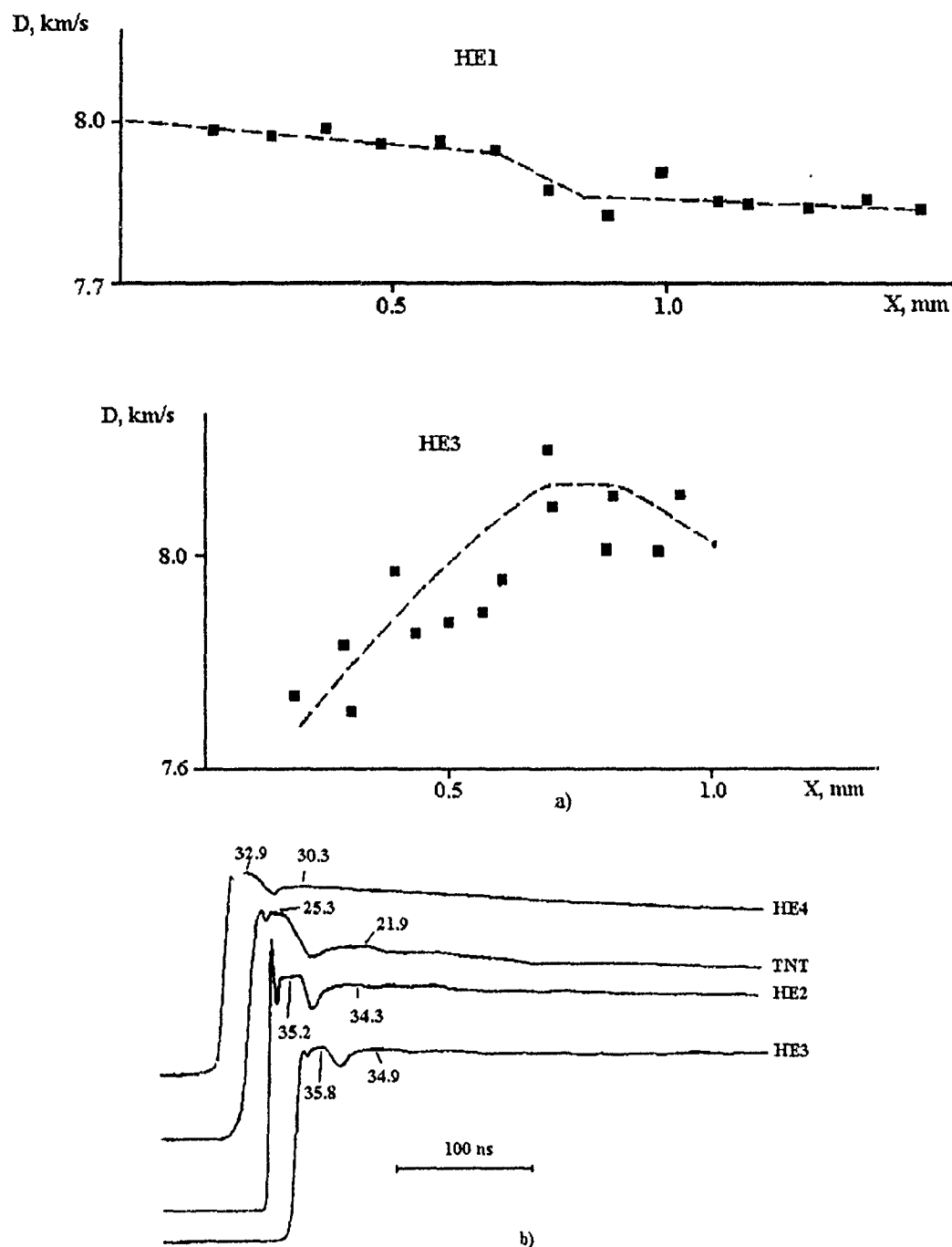
Figure 1: (a) — Shock velocity in aluminum plates. (b) — Manganin gage oscilloscope records. The pressure values in oscilloscope records are given in GPa.
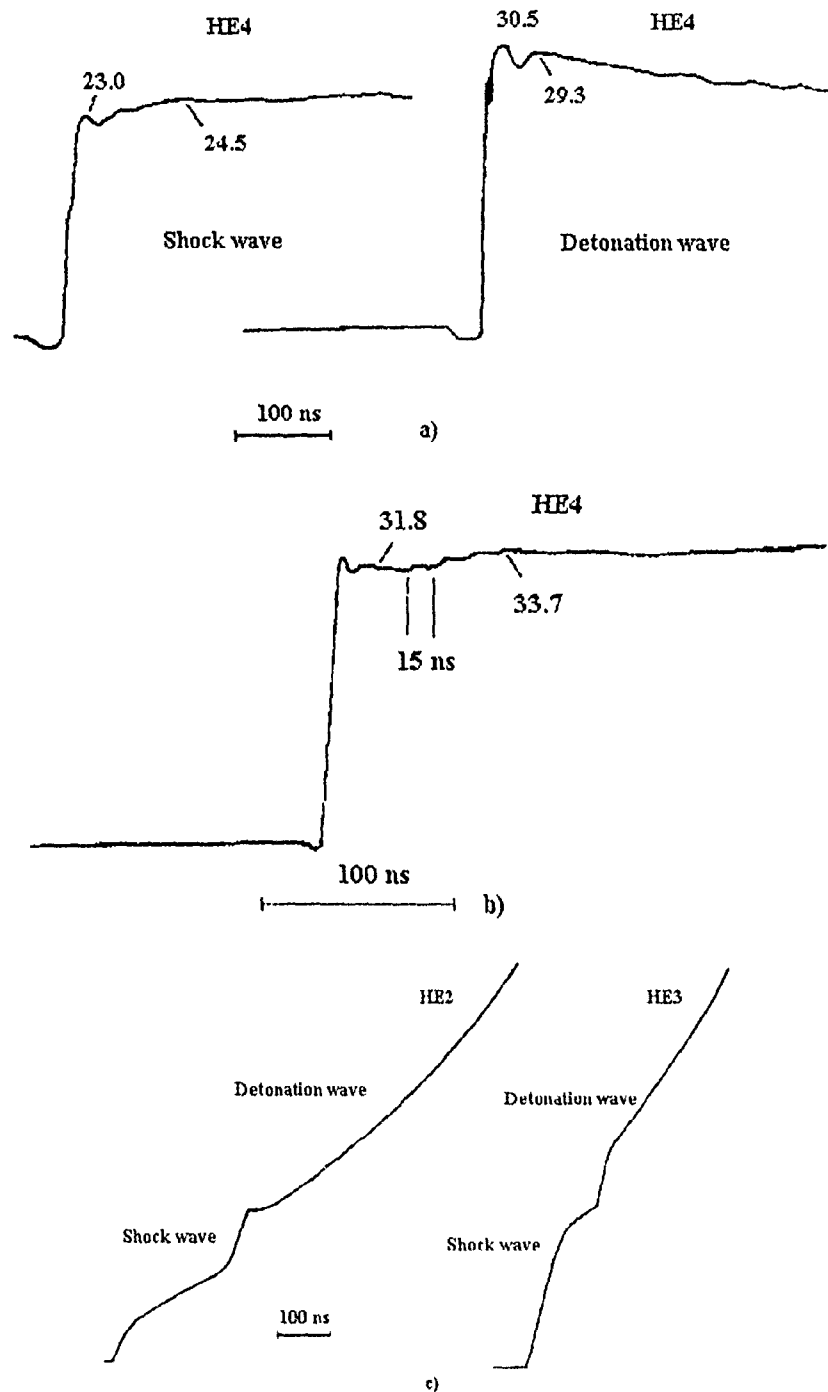
Figure 2: The oscilloscope records of manganin gage (a), (b) and capacitive gage (c). The pressure values in oscilloscope records are given in GPa.

In a nanosecond-resolution study of DW pressure profiles, the shock velocity through the HE-package (a stack of 10 mm × 10 mm × 0.1 mm aluminium plates and HE) was measured within 1 to 2% accuracy [1].

Figure 1a shows the shock velocity as a function of the distance X to the HE-package where the self-sustained DW emerged.

Figure 1b presents the oscilloscope records of DW pressure profiles obtained using a manganin gage introduced into teflon at the distance from HE 0.2 mm [2].

The DW front tilting in HE3 and HE4 containing inert additives is indicated by the underrated reverberation peak of the gage signal. For cast TNT and HE4 having large critical diameters, a further pressure decrease behind the DW front starting at about ~ 100 ns is observed.

The rarefaction pulse as shown by the oscilloscope records results from the gap around the gage, which is filled with a low-density material.

No marked pressure decrease within about ~ 10 ns behind the DW front and tilted DW front in HE having inert additives indicate the HE decomposition in the DW front in about ~ 1 ns or less.

Figure 2a shows oscilloscope records of the pressure profiles of the initial shock wave (SW) and the preceding DW generated in 5 mm and 6 mm thick HE4 plates, respectively, with the SW entering these at pressure $P_0 = 19.3$ GPa. The gage was introduced into teflon at the distance from HE 0.2 mm.

The HE decomposition rate and shock compressibility are determined using the gage positioned on the side of the HE plate through which the shock enters. The relevant oscilloscope record for HE4 experiment at $P_0 = 31.8$ GPa is given in Fig. 2b. The delay in HE decomposition is observed to be 15 ns, and the teflon and HE4 shock compressibilities at $P_0 = 31.8$ GPa are nearly equal to one another. As suggested by this experimental observations, the HE conditions behind the shock and DW fronts differ in terms of pressure vs. volume dependence.

The capacitive gage technique [3] was first used to measure the velocities of initial SW and then DW in the HE plate serving as the gage dielectric. The oscilloscope records for two HE2 experiments are given in Fig. 2c. Clearly, at the time the DW is generated, the wave amplitude increases abruptly, as in the case of homogeneous HE. This is an evidence against significant "hot-spot" contribution to the DW propagation.

References

[1] Gatilov L. A., Ibragimov R. A., Kudashov A. V. *Fizika Goreniya Vzriva*, 1989, **25**, 2, 82 (in Russian).

[2] Gatilov L. A. *et al. Proc. 4th All-Union Meeting on Detonation*, Chernogolovka, 1988, **1**, 172 (in Russian).

[3] Ivanov A. G., Novikov S. A. *PTE J.*, 1963, **1**, 135 (in Russian).

ON CREEPING DETONATION IN FILTRATION COMBUSTION

Vladimir Gol'dshtein*, Isaak Shreiber†, Gregory Sivashinsky‡

*Department of Mathematics and Computer Sciences
†Institute for Industrial Mathematics, Ben Gurion University of the Negev Beer Sheva, Israel
‡School of Mathematical Sciences, Tel Aviv University Tel Aviv, Israel

1 Introduction

The objective of this communication is to demonstrate the possibility of self sustaining combustion waves in porous media, whose propagation is controlled not by heat and mass diffusivities but rather by the adiabatic compression. The latter is in turn maintained by the energy release provided by the chemical reaction. The phenomenon is quite analogous to the classical detonation occurring in gaseous combustion in open system. In contrast to the conventional detonation, however, in the case of porous medium the reaction wave spreads at a subsonic speed controlled by the viscous friction.

2 Mathematical Model

In studies of premixed gas flames in an open space one usually disregards the pressure perturbations, since the flame propagation speed is significantly lower then the speed of sound. From the modelling aspect this is straighforward consequence of the fact that the pressure waves are governed by the acoustic wave equations, whilst combustion waves are discribed by parabolic equation for thermal diffusion. In porous media, on the contrary, the pressure waves are governed by the parabolic equation for barodiffusion associated with low Reynolds number creeping flows.

The porous media hydrodynamics is generally described in the framework of the two-temperature model. However, if the relaxation time of pressure is much longer then that of temperature the two-phase media may be safely described by a single-temperature model. These conditions indeed hold in many realistic gas–solid system such as soils, sponges, foams [1].

For modelling purpose the porous media may be loosely regarded as a bundle of capillaries that are fused together or a honeycomb of holes. Due to the quasi-periodic nature of such a system each of capillaries may well be regarded as thermally insulated from its neighbours. In 'nis sense the filtration combustion may be modeled as a flame propagation through an adiabatic capillary.

Let ρ, ρ_g, ρ_s, be densities of the porous media and its gaseous and solid phases, correspondingly. Similarly λ, λ_g, λ_s are the heat conductivities; c, c_g, c_s are the heat capacities (specific heats), α_g, α_s are volumetric fractions of gaseous and solid phases. Hence

$$\rho c = \alpha_g \rho_g c_g + \alpha_s \rho_s c_s, \tag{1}$$

$$\lambda = \alpha_g \lambda_g + \alpha_\varepsilon \lambda_s. \tag{2}$$

If the skeleton (solid phase) has a low heat capacity and a low volumetric fraction the relations (1), (2) are simplified to

$$\rho c \simeq \alpha_g \rho_g c_g, \qquad \lambda \simeq \alpha_g \lambda_g, \qquad \rho \simeq \alpha_g \rho_g. \tag{3}$$

In order to elucidate the impact of barodiffusion the thermal and molecular diffusivities D_{th}, D_{mol} are regarded as negligibly small compared to the barodiffusivity D_b. This limit is quite consistent with numerical estimates (see 4.2).

In light of the above assumptions the system of governing equations reads as follows. Energy equation:

$$c\rho \left(\frac{\partial T}{\partial t} + u \frac{\partial T}{\partial x} \right) = QW. \tag{4}$$

Concentration equation:

$$\rho \left(\frac{\partial C}{\partial t} + u \frac{\partial C}{\partial x} \right) = -W. \tag{5}$$

Momentum equation:

$$\rho u = -\frac{K}{\nu} \frac{\partial P}{\partial x}. \tag{6}$$

Continuity equation:

$$\frac{\partial \rho}{\partial t} + \frac{\partial \rho u}{\partial x} = 0. \tag{7}$$

State equation:

$$P = (c_p - c_v)\rho T. \tag{8}$$

Chemical kinetics equation:

$$W = Z\rho C \exp \left(-\frac{E}{RT} \right). \tag{9}$$

Equations (4)–(7) are written in the frame of references attached to the skeleton. u is the gas velocity relative to the skeleton. C is the concentration of the deficient reactant controlling the termination of the reaction, W is the chemical reaction rate, v is the kinematic viscosity of the gas, K is the permeability of the porous medium, Z is the frequency factor, E is the activation energy, R is the universal gas constant, Q is the heat release. Other notations are conventional .

The model (4)–(9) is similar to that discussed in [2], [3] where, however, effects due to central to the present study, were omitted.

3 Travelling wave solution

The solution of the system (4)–(9) is sought in the form of a travelling wave moving at a speed V from left to right.

Introduce the following reference parameters: $a = \sqrt{\gamma(c_p - c_v)T_0}$, (here $\gamma = c_p/c_v$, a — speed of sound in fresh mixture); $D_b = Ka^2/\gamma\nu$ — barodiffusivity; $T_b = T(-\infty)$ — the adiabatic temperature of combustion products.

Similar to the classical theory of Zel'dovich and Frank-Kamenetsky, the flame speed appears to be proportional to the square root of the transport coefficient. In the present situation it is barodiffusivity rather then thermal diffusivity as happens in freely propagation flame [4], i.e.

$$V \sim \sqrt{D_b Z \exp\left(-\frac{E}{RT_b}\right)}. \tag{10}$$

The relation (10) permits making a quantative estimate of the filtration combustion speed V compared with that of a freely propagating flame V_0 of the same premixture and initial conditions

$$\frac{V}{V_0} \sim \sqrt{\frac{D_b}{D_{th}} \exp\left[\frac{E}{RT_b^*}\left(1 - \frac{T_b^*}{T_b}\right)\right]}. \tag{11}$$

Since $D_b \gg D_{th}$ and $T_b > T_b^*$ ($\alpha > \Delta + 1$) the enhancement of the flame speed due to viscous friction may be rather significant. For a typical set of parameters: $\gamma = 1.4$; $\alpha = 300$ m/s; $T_0 = 300$ K; $T_b^* = 1500$ K ($\alpha = 5.65$, $T_b = 1695$ K); $D_{th} = \nu = 2.5 \cdot 10^{-5}$ m^2/s; $K = 10^{-12}$–10^{-9} (clean sand [6]) one obtains

$$D_b = 3.2 \cdot 10^{-3} - 3.2 \text{ m}^2/\text{s}, \qquad V/V_b \sim 35\text{--}1131. \tag{12}$$

Thus, depending on the permeability of the skeleton the filtration combustion speed may well reach the level of sound speed in open space a.

Laevsky and Babkin report [3] an increase in the methane–air flame speed from 0.3 m/ec for open space to 3 m/s in porous media. High flame speeds in the range 400 m/s – 1.100 m/s were observed by Mitrofanov [6] in filtration combustion through sand and sandstone.

References

[1] Nigmatullin R. I. *Dynamics of Multiphase Media*. New York – Washington – Philadelphia – London, Hemisphere Publishing Corp., 1990.

[2] Aldushin A. P., Merzhanov A. G. In: *Propagation of Thermal Waves in Heterogeneous Media* (Matros Yu. Sh. Ed.), Novosibirsk, Nauka, 1988, 9–15 (in Russian).

[3] Laevsky Yu. M., Babkin V. S. *ibid*, 108–144 (in Russian).

[4] Frank-Kamenetsky D. A. *Diffusion and Heat Transfer in Chemical Kinetics*. N. Y., Plenum, 1969.

[5] Nield D. A., Bejan A. *Convection in Porous Media.* N. Y., Springer–Verlag, 1992.

[6] Mitrofanov V. V. In: *Mechanics and Scientific-Technological Progress. 2: Mechanics of Liquids and Gases* (Sedov S. I., Cherny G. G., Lubimov G. A. Eds.), Mocow, Nauka, 1987, 226–243 (in Russian).

CAN DETONATION WAVES PROPAGATE IN ONE-DIMENSION?

Longting He*, John H. S. Lee[†]

**Laboratoire de Recherche en Combustion, URA 1117 CNRS & Université d'Aix-Marseille I, Service 252, Centre St-Jérôme,13397 Marseille CEDEX 20 France*
[†]*Department of Mechanical Engineering, McGill University, Montreal, H3A 2K6 Canada*

The planar steady detonation postulated by Zel'dovich, von Neumann and Doering consists of an inert shock wave followed by a reaction zone. This classical model is based on the fact that a rapid chemical reaction can take place in the reactive mixture heated and compressed by the leading shock wave [1]. For ordinary reactive mixtures, the Mach number of the detonation front ranges from 4 to 6, the leading shock is strong enough to heat the initial mixture to a high temperature (1200 - 2000 K) and cause rapid self-ignition. The one-dimensional ZND structure seems to be perfectly self-sufficient in the sense that it provides the propagation mechanism of auto-ignition via adiabatic shock heating.

Although the propagating planar detonation becomes unstable when the activation energy E is larger than a critical value E_{c1}, direct numerical simulations of planar time-dependent detonations presented in the literature also seem to support the auto-ignition mechanism. Typically, two types of planar detonation propagation modes have been reported ([2–4] and the references given therein):

(i) when $E < E_{c1}$, a steady planar ZND detonation is obtained,

(ii) when $E > E_{c1}$, periodic oscillations appear in the propagation of detonations.

The existing numerical results show that, even in case (ii), the average velocity is equal to that given by ZND model and the chemical reaction is essentially due to the auto-ignition caused by the leading shock.

However, the existing numerical simulations have been limited to a range of moderate values of activation energy $10 < E/RT_0 < 30$, where T_0 is the temperature of the initial reactive mixture and R is the gas constant. These values are only representative of a very few sensitive reactive mixtures such as C_2H_2–O_2 or H_2–O_2 mixtures highly diluted with argon. For fuel–air mixtures, the parameter E/RT_0 characterizing the global sensitivity of the chemical reaction to temperature is much larger, in particular, when the detonability conditions are approached. One important problem is to know how the planar detonation propagates when the chemical reaction rate strongly depends on temperature. Understanding of the propagation mechanism of the planar detonation will undoubtedly help us to elucidate the propagation mechanism of the multidimensional detonation front and the mechanism controlling the direct initiation of detonation.

In this short paper, a theoretical study is reported on the propagation of the planar detonation with relatively large values of activation energy to answer the basic question regarding whether transverse waves are absolutely essential to the propagation of detonation [5]. It will be shown that there exists a second critical value for the reduced activation energy E_{c2} ($> E_{c1}$) above which the propagation of planar detonation via auto-ignition becomes impossible.

In order to demonstrate the basic mechanisms of the new phenomenon, we limited our attention to the planar geometry and to a minimum model based on a one-step chemical reaction governed by the Arrhenius law. A stability analysis was first performed. The results obtained show that in the unstable case ($E > E_{c1}$) the frequency of the first mode decreases when E increases and is equal to zero at the second critical value E_{c2}.

Numerical simulations were then performed for three typical modes of for the propagation of planar detonations: piston-supported overdriven detonations, piston-supported Chapman–Jouguet (CJ) detonation and the direct initiation of detonations by a strong blast wave. All numerical results obtained for these three different situations show a common feature: due to the hydrodynamic instability effect, the one-dimensional detonation cannot propagate via auto-ignition mechanism when the activation energy is larger than a critical value.

Only the results on piston-supported CJ detonations are presented here. Figures 1a–d show the pressure history at the Neumann spike for four different values of the reduced activation energy: $E/RT_0 = 25$, 27, 31 and 35; the specific heat ratio and the heat release parameter Q are fixed ($\gamma = 1.2$ and $Q/RT_0 = 50$). The numerical simulation started with the corresponding steady ZND profiles. For the sake of comparison, the exact solution for the steady ZND detonation is also shown in these figures. These numerical results show four typical cases of the propagation of the planar detonation:

- The propagating detonation is stable (Fig. 1a), which is the case when $E < E_{c1}$;

- Regular oscillations appear in the propagation of detonation when E is slightly above the stability limit (Fig. 1b);
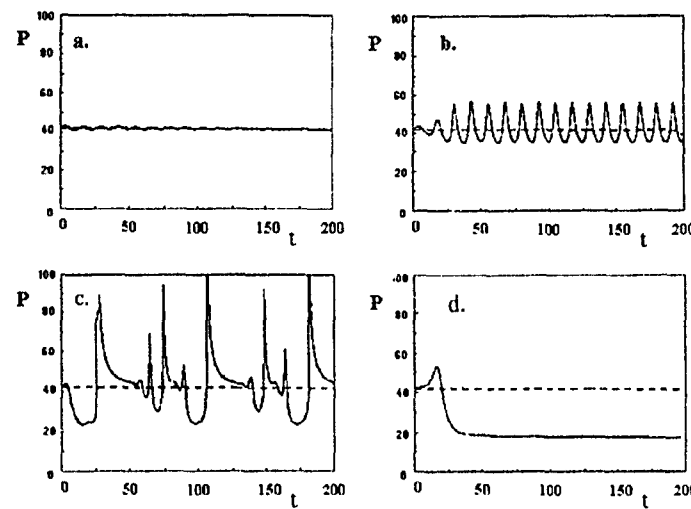
Figure 1: Pressure at the Neumann spike as a function of time. a. $E/RT_0 = 25$, b. $E/RT_0 = 27$, c. $E/RT_0 = 31$, d. $E/RT_0 = 35$.

- Irregular oscillations appear in the propagation of detonation when E is slightly below the second critical value E_{c2} (Fig. 1c). Note that the amplitude of the oscillations increases when the activation energy increases. In Fig. 1c the minimum pressure is about 23, which is much lower than the Neumann pressure of the steady CJ detonation, which is 42;

- The planar detonation cannot propagate and a self-extinction phenomenon can be observed when $E > E_{c2}$ (Fig. 1d). The pressure first increases until $t = 7.5$ and then the pressure decreases suddenly to $p = 17.9$. The temperature in the mixture just behind the shock is 2.53. The chemical induction time immediately behind the leading shock is about 500 times larger than that in the steady CJ detonation. Figure 2 shows the trajectories of the leading shock and the "reaction zone" for this case. Since the velocity of the leading shock is larger than the velocity of the reaction front, the distance between the leading shock and the reaction zone becomes larger and larger. In fact, the velocity of the reaction front is equal to the local gas velocity, and the reaction interface is only convected passively by the gas flow behind the shock. The intensity of the propagating shock is supported by the gas flow behind the front, while the slow chemical reaction does not contribute to the propagation of the shock. It should be pointed out that, in our numerical simulations, the molecular transport effects were neglected. If the molecular transport effects were taken into account, we would have been able to observe diffusion-controlled laminar flame propagation, but the slow laminar flame could not have strengthened the leading shock.
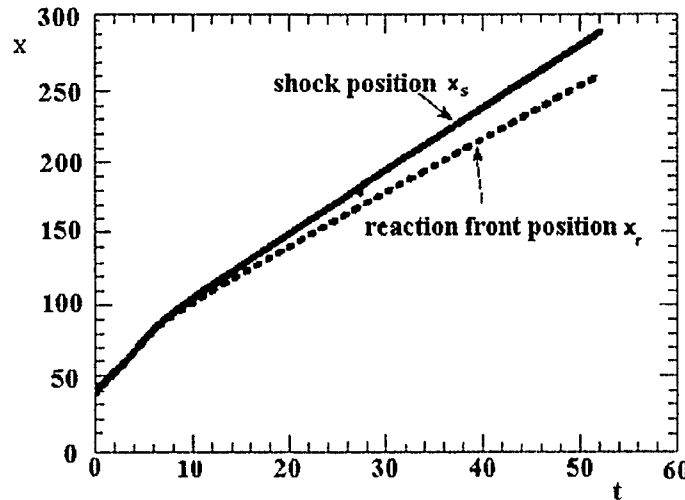
Figure 2: Trajectories of the shock and of the reaction front for $E/RT_0 = 35$.

In conclusion, this study demonstrates clearly that, due to the hydrodynamic instability effect, the planar detonation cannot propagate via the auto-ignition mechanism when the activation energy is larger than the critical value. In a tube, transverse waves are necessary for the successful propagation of detonation [5]. Future investigations using a two-dimensional model are needed to deal with the re-ignition problem and to identify the mechanism of propagation of detonations in a tube.

References

[1] Zel'dovich Ya. B. *On the Theory of Detonation Propagation in Gaseous Systems.* 1940. In: *Selected Works of Yakov Borisovich Zel'dovich*, **1**, *Chemical Physics and Hydrodynamics,* (Ostriker J. P., Barenblatt G. I., Sunyaev R. A. Eds.), Princeton University Press, 1992, 411–451.

[2] Ficket N., Davis W. C. *Detonation,* Berkeley, University of California Press, 1979.

[3] Abousieff G. E., Toong T. Y. *Comb. Flame,* 1982, **45**, 67.

[4] He L. T., Larrouturou B. Submitted to *J. Comput. Phys.*, 1994.

[5] Lee J. H. S. In: *Dynamic structure of detonation in gaseous and dispersed media* (A. A. Borissov Ed.), Kluwer Academic Publishers, 1991, 1–26.

TRANSFORMATION OF DETONATION MODES IN HYBRID TWO-PHASE MIXTURES

B. A. Khasainov*, B. Veyssiere†

Semenov Institute of Chemical Physics, Moscow, Russia
†*L.E.D., U.R.A.C.N.R.S. 193, E.N.S.M.A., Poitiers, France*

_ʌ explosive systems with nonmonotonic in time heat release, multiple detonation regimes may exist [1–3]. The total number of possible detonation regimes is odd. If the detonation mode is unique, it is stable. If there exist several detonation modes, the odd ones are stable with respect to infinitesimal perturbations (these regimes correspond to local maxima of heat release) and the intermediate even ones are unstable. As a result, detonation waves propagating at the highest and lowest velocities are stable. Namely, in the case of one maximum of heat release downstream of the shock front, this theory predicts the existence of stable "normal" and "low" velocity detonations along with unstable intermediate detonation regime.

Heat release in two-phase hybrid mixtures is generally nonmonotonic because it is due to fast decomposition of gaseous explosive and slower burning of particles or droplets. However, for mixtures of this kind a discrepancy in the number of solutions with the predictions of theory of nonideal detonations has been demonstrated recently [4]. In particular, in some particle concentration ranges two stable detonation modes were found but without the intermediate unstable one (stability being considered with respect to infinitesimal perturbations). The same problem exists for detonations of cryogenic hydrogen–oxygen mixtures [5]. The analysis of steady detonation problem for two-phase hybrid mixtures shows that the detonation mode with higher velocity corresponds to the case when both gaseous explosive and particles contribute their chemical energy to the detonation wave (below this velocity, regime is referred to as single-front detonation, SFD, to distinguish it from the double-front detonation structure). The solution with lower velocity describes the so-called pseudo-gas detonation (PGD) wave in which particles remain inert upstream of the Chapman–Jouguet plane.

Here, we used unsteady one-dimensional code to analyze detonation development and stability of detonation waves in the hybrid mixtures studied previously using the steady ZND model [4]. In the numerical experiments, a point explosion was used to initiate the hybrid mixture filling a shock tube.

The PGD wave formed quite rapidly due to the high reactivity of the gaseous explosive and propagated steadily over long distances. Secondary compression waves are formed behind the PGD wave, due to the reaction between aluminum particles and gaseous detonation products. In the same particle concentration range where the steady analysis [4] had predicted the existence of two stable detonation modes, the evolution of the compression waves led to the formation of a secondary shock

358

that rapidly overtakes the leading PGD wave, and then the transition to steady SFD occured, i.e., the PGD wave cannot propagate steadily over infinitely large distances when both detonation regimes are possible. Thus, the PGD is not stable because it is influenced by finite perturbations. However, this effect cannot be predicted on the basis of the classical steady ZND model. From an other point of view, if the PGD is recognized as unsteady detonation mode, then the aforementioned problem concerning the multiplicity of detonation regimes in two-phase mixtures is eliminated.

The run distance to the point x_{tr} where the transition from PGD to SFD occurs depends on the reactivity of particles and increases with the particle size. The dependence of x_{tr} on the particle concentration goes through a minimum near the stoichiometric concentration of aluminum particles in the hybrid mixture. Besides, x_{tr} decreases as the point explosion energy increases.

The mechanism and hazard of low-velocity detonations predicted by the unsteady model is also discussed.

References

[1] Zel'dovich Ya. B., Kompaneets A. S. *Theory of Detonations.* N. Y., Academic Press, 1960.

[2] Kuznetsov N. M. *Soviet Physics JETP*, 1967, **25**, 1, 199–204.

[3] Kuznetsov N. M. *Zhurnal Prikladnoi Mekhaniki Tekhnicheskoi Fiziki*, 1968, **9**, 1, 45–55 (in Russian).

[4] Veyssiere B., Khasainov B. A. *J. Shock Waves*, 1993 (in press).

[5] Voronin D. V., Zhdan S. A. *Fizika Goreniya Vzriva*, 1984, **20**, 4, 461–465 (in Russian).

PROPAGATION OF NITROMETHANE DETONATIONS IN POROUS MEDIA

J. J. Lee*, D. L. Frost†, M. Brouillette*, J. H. S. Lee†, A. N. Dremin‡

*Department of Mechanical Engineering, University of Sherbrooke, Sherbrooke, Quebec, J1K
2R1 Canada
†Department of Mechanical Engineering, McGill University, Montreal, Quebec, H3A 2K6
Canada
‡Institute of Chemical Physics in Chernogolovka, Chernogolovka, Russia

Critical diameter measurements were performed on unconfined cylindrical charges of nitromethane (NM) sensitized with 15%, 10%, and 5% diethylenetriamine (DETA) which was then introduced into a porous medium consisting of a packed bed of glass beads [1,2]. The bead diameter was systematically varied from 66 μm to 2.4 mm, and the volume fraction of the liquid inside the explosive mixture remained constant at approximately 40%. The variation of the critical diameter with bead size shows three regions of behavior (Fig. 1). For bead sizes above approximately 1 mm, the critical diameter decreases with increasing bead size. For bead sizes below approximately 0.7 mm, the trend is reversed and the critical diameter decreases with decreasing bead size. In the region between 0.7 mm and 1 mm where the changeover occurs, there appears to be a sharp increase in the mixture sensitivity, as indicated by the increase in critical diameter. Velocity measurements of the detonation propagation along the charge show different velocities in the region above 1 mm and the region below 0.7 mm, further lending support to the proposition of different propagation mechanisms for larger beads and for smaller beads [1]. Reducing the amount of DETA in the explosive to 10% was found to have a different effect in the large bead region (above 1 mm), as compared with the small bead region (below 0.7 mm). The sensitivity of a homogeneous mixture of NM and DETA decreases only slightly from 15% to 10% [2–4]. In the glass bead mixture, however, the critical diameter increases by more than two times near the changeover region ($\approx$ 1.5 mm) but remains almost the same for the largest bead size tried (2.4 mm) (Fig. 2). In the small bead region, reducing the amount of DETA causes an increase in the sensitivity of the heterogeneous mixture, as can be seen by the decrease in the critical diameter.

In previous studies involving glass micro-balloons (GMB) and solid particles in pure NM [5–8], the principal effect of the inert particles was the sensitization of the micron range and the volume fraction of the particles was generally low, except the GMB study [5]. In the present work, the critical diameter of the sensitized NM and the diameter of the beads overlap, thus revealing a different set of propagation mechanisms. In the large beads, the increase of the critical diameter with decreasing bead size may be

360
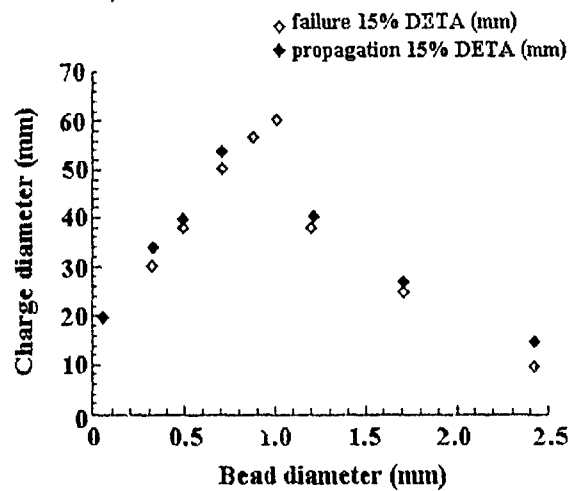
Figure 1: The propagation or failure of detonations for cylindrical unconfined charges of different diameter with an explosive mixture of NM sensitized with 15% DETA (by weight) in packed glass beads of various sizes. The critical diameter dependence on bead size is shown.
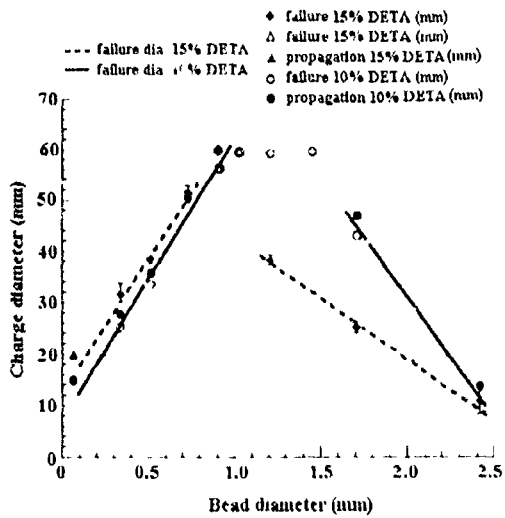
Figure 2: The dependence of critical or failure diameter on bead size for mixtures of NM with 10% and 15% DETA (by weight) inside packed glass beads of different sizes.

explained by the stronger local diffraction of the detonation around the beads as their size decreases. This local cooling by diffraction facilitates the overall failure of the detonation wave, hence the increase of the critical diameter with decreasing bead size. In the small beads, local propagation of the detonation through the inter-bead pores is no longer possible and the propagation shifts to a global mechanism through the bead–liquid mixture. The failure might thus depend on shock attenuation through the porous medium resulting in an increase in the induction zone and the curvature of the front.

References

[1] Lee J. J., Frost D. L., Dremin A. N., Lee J. H. S. *Presented at the 14th Int. Colloq. on Detonations and Reactive Mixtures*, Coimbra, Portugal, 1993.

[2] Lee J. J., Brouillette M., Frost D. L., Lee J. H. S. *Submitted to the 25th Symp. (Int.) Comb.*, 1993.

[3] Trocino J. L. *et al. Bulletin JLTN-2, 15233 Ventura Blvd.* Penthouse 8, Sherman Oaks, CA, 1974.

[4] Walker F. E. *Acta Astronautica*, 1979, **6**, 807–813.

[5] Presles H. N., Campos J., Heuze O., Bauer P. *Proc. 9th Symp. (Int.) on Detonation*, 1989, **1**, 362–365.

[6] Engelke R. *Phys. Fluids*, 1983, **26–9**, 2420–2424.

[7] Kato Y., Brochet C. *Proc. 6th Symp. (Int.) on Detonation*, 1976, 124–132.

[8] Kurbangalina R. Kh. *Zhurnal Prikladnoi Mekhaniki Tekhnicheskoi Fiziki*, 1969, **10–4**, 133–136.

DIRECT INITIATION OF DETONATION IN A HYROGEN–AIR MIXTURE

V. A. Levin*, S. F. Osinkin*, V. V. Markov†

Institute of Mechanics, Moscow State University, Moscow, Russia
†*Steklov Mathematics Institute, Moscow, Russia*

The initiation of detonation requires the presence of a rather strong shock wave by which the combustible gas mixture is heated to the ignition point, after which it burns in a narrow zone adjacent to the shock. One of the means of shock wave initiation is a point energy release [1]. For example, a shock ware can be obtained by setting off a condensed explosive charge, by means of an electric discharge [2], a laser spark, an exploding wire, a moving piston, etc. No matter how the energy is supplied, if it is too low, detonation will not be possible. In a gas, detonation will be impossible if conditions favoring ignition of the gas are not created immediately behind the shock wave. Moreover, even if the wave is sufficiently strong to ignite the gas behind it, detonation will not necessarily be initiated. Whether detonation should take place or not will depend on the structure of the gas flow behind the shock wave and its effect on the mechanism of the chemical reactions, as well as on the effect of the heat release on the flow dynamics. Thus, when the externally supplied energy is relatively small, the induction period sharply increases and the ignition zone rapidly falls behind the shock wave, due to the presence of a strong rarefaction wave behind the shock wave. Starting from some critical value of the energy released, detonation is observed.

This paper presents some results on direct initiation of plane and cylindrical detonation waves in a hydrogen–oxygen mixture diluted with nitrogen, using an exploding copper wire or a moving piston, and in a hydrogen–air mixture, using a spherical charge of condensed explosive. Also, the onset of detonation in subcritical case due to a finite-time interaction of a decaying wave with a hard cover is investigated.

1 Initiation of Detonation by a Moving Piston

In a quiescent homogeneous hydrogen–oxygen mixture, starting from the moment $t = 0$, let a piston travels at the constant velocity V_p for time T, after which it stops. If V_p and T are large enough, then the strong shock wave formed in front of the piston will ignite the combustible mixture and a flow with a detonation wave will be formed. Otherwise, detonation will not take place, and after the piston stops the shock wave will decay with time.

The set of equations for a perfect gas flow with plane, cylindrical, and spherical waves was used. Nine reversible elementary reactions were used to model hydrogen oxidation [3].

The equations of gas dynamics were solved simultaneously with the equations of chemical kinetics by a finite-difference method based on the Godunov scheme with a moving difference grid and explicit separation of the forward shock from the contact surface between the vapor and the gaseous combustion products for the case of initiation by an exploding wire or by a condensed explosive.

Computations for the initial values $P = 10^5$ Pa, $T = 300$ K and the molar fractions $r_{H_2} = 0.232$, $r_{O_2} = 0.116$ and $r_{N_2} = 0.652$ showed that a piston travelling at a velocity greater than the velocity of the gas behind the leading shock, which propagated at the Chapman–Jouguet velocity, initiated a pulsating detonation wave. The numerical results show that the sharp changes in the parameters and the explosive growth of pressure and temperature behind the shock front occur in a time much shorter than the mean period of the oscillations, and the process as a whole is similar to the experimentally observed "an explosion within an explosion" effect. This effect is associated with the process of formation, propagation and interaction of the secondary shock wave, formed in induction zone, and the lead shock. It is interesting that the induction zone length varies by several orders of magnitude during the oscillation period. The observed dependence of the critical work E done by the piston on its velocity V_p shows that E reaches a minimum value when V_p equals the gas velocity behind the forward shock in the Chapman–Jouguet detonation and increases sharply as the piston velocity decreases.

2 Initiation of Detonation by an Exploding Wire (Lamella)

In the case of detonation initiated by a copper wire (lamella) of thickness d, it is assumed that at $t = 0$ the wire evaporates instantaneously, and the high values of the resulting vapor pressure, temperature and density are related by complicated equations of state. The computations were performed for the aforementioned initial state of combustible mixture and the copper density $\rho = 8.9$ g/cm^3 and the specific energy of copper vapor $e = 24830$ kJ/kg. The energy E released during the explosion was determined by the thickness of the wire d, which was varied in the computations. The calculations showed that, if d exceeds a certain minimum critical value, then the explosion gives rise to a flow with a detonation wave. This value for the wire is within the interval $0.58 < d < 0.78$ mm and the corresponding critical energy is within the interval $6.0 < E < 10.5$ kJ/m. In addition, a comparison of the results showed that in determining the critical energy the equation of state of a perfect gas is valid for the copper vapor, if the value of the specific heat ratio lies within 1.5–1.8.

3 Initiation of Detonation by a TNT Charge

It is assumed that at $t = 0$ a charge of TNT evaporates instantaneously and the values of pressure and density of the resulting vapor are related by an equation of state of complicated form. Computations were performed for the molar fractions $r_{H_2} = 0.286$,

$r_{O_2} = 0.143$ and $r_{N_2} = 0.571$, which correspond to a hydrogen–air mixture, and a fixed value of the specific heat release of TNT, $Q = 1000$ kcal/kg. The predicted intervals for the critical values of diameter D, mass M and energy E at three values of explosive density ρ_{TNT} are as follows:

$\rho_{TNT} = 1.60$ g/cm^3: $0.014 < D < 0.016$ m, $2.30 < M < 3.43$ g, $9.61 < E < 14.34$ kJ
$\rho_{TNT} = 1.29$ g/cm^3: $0.016 < D < 0.018$ m, $2.77 < M < 3.94$ g, $11.57 < E < 16.47$ kJ
$\rho_{TNT} = 0.90$ g/cm^3: $0.018 < D < 0.020$ m, $3.39 < M < 4.65$ g, $14.18 < E < 19.45$ kJ

For subcritical cases, the problem of finite-time interaction of a decaying detonation wave with a hard spherical cover surrounding the charge was considered. It appears that for some intervals of the cover radius there exists an interval of interaction times when a detonation is restored. For example, for $D = 0.005$ m, when the radius is 0.1 m, the time is within 10–30 μs.

References

[1] Sedov L. I. *Similariry and Dimensional Methods.* London, 1959.

[2] Zel'dovich Ya. B., Kogarko S. M., Simonov N. N. *Zhurnal Tekhicheskoi Fiziki*, 1956, **26**, 1744 (in Russian).

[3] Levin V. A., Markov V. V., Osinkin S. F. *Mekhanika Zhidkosti Gaza*, 1992, **6**, 151 (in Russian).

ON THE EXPERIMENTAL EVIDENCE FOR SPONTANEOUS DETONATION ONSET

S. P. Medvedev, A. N. Polenov, B. E. Gelfand

Semenov Institute of Chemical Physics, Moscow, Russia

The concept of spontaneous detonation onset in system with appropriate distribution of the gradients of ignition delay time was proposed by Zel'dovich *et al.* [1, 2]. The experimental data of [3–5] corroborate the gradient mechanism (SWACER [3, 4]). Nevertheless, the results of [3–5] are not conclusive as to whether the observed onset of detonation is due to the gradient of ignition delay time only. In particular, it appears

to be rather difficult to distinguish between the cases of jet initiation and critical tube diameter problem [5]. This is no surprise since even the most sophisticated experimental methods provide no means to determine the distribution of the ignition delay times, prior to the onset of detonation over very short distances under transient and essentially non-onedimensional conditions. Thus, the long since spoken words of Oppenheim et al. [6] about "the mysteries still surrounding the formation of detonation" in smooth tubes apply to the current status of the problem. Further elucidation of the problem of shockless initiation of detonation could be based on the additional experimental data which would be difficult to interpret otherwise than in terms of the gradient mechanism. To illustrate this point, we present here a more comprehensive study of the phenomenon of detonation onset induced by the venting of gaseous explosion [7].

The schematic of the 4-liter cylindrical explosion chamber [7] wherein the tests have been performed, is shown in Fig. 1. Without going into detail, we merely note that the experimental procedure originates from the well-known principle of venting the gaseous explosion in a vessel initially plugged with a bursting diaphragm. As has been shown in [7], the presence of a short duct connected to the vent opening inevitably gives rise to the onset of detonation propagating into the explosion chamber. Since this took place shortly after the penetration of the flame into the duct, the present work has been focused on the photographic study of the pre-detonation processes inside the duct. To facilitate the high-speed schlieren recording, we used a rectangular duct (35×54 mm^2) of 170 mm in length.

Figure 1 (pressure profiles and the upper sequence of frames) gives an example of successful initiation of detonation in the stoichiometric acetone–oxygen mixture diluted by nitrogen (33% vol.). The initial pressure of the mixture ignited by an electrical spark was 2 bar. The membrane was designed to burst at 3.5 bar. As evident from the pressure and streak camera records, up stream-directed detonation is initiated shortly after the flame arrival at the vent opening. Simultaneously, another detonation wave propagates downstream. It is pertinent to note that in spite of the obvious similarity of the observed phenomenon to the process of deflagration to detonation transition in smooth tubes, there are good reasons to believe that the upstream-directed wave is a detonation rather than retonation wave. This is evident from the violent pressure buildup inside the explosion chamber and the smoked-plate records presented in [7]. The location of the origin of the detonations is inside the duct.

The upper frame sequence provides some information concerning the pre-detonation flow field. Apparently, the combustion products (CP) flow into the duct at a relatively high velocity (about 700 m/s). The unburned mixture (UM) is ejected into the duct in parallel with CP. By geometrical reasoning, the UM fills the vicinity of the walls, whereas CP show up as the central jet. The turbulent mixing between the hot CP and the UM gives rise to the local explosion (self-ignition) at the wall surface (see the last frame) and the subsequent onset detonation.

Another trend takes place in a partially confined duct (without side walls), as illustrated by the bottom frame sequence of Fig. 1. The CP emerge at the lowest velocity

Spontaneous detonation onset $\Delta t = 50\,\mu s$

No detonation $\Delta t = 100\,\mu s$
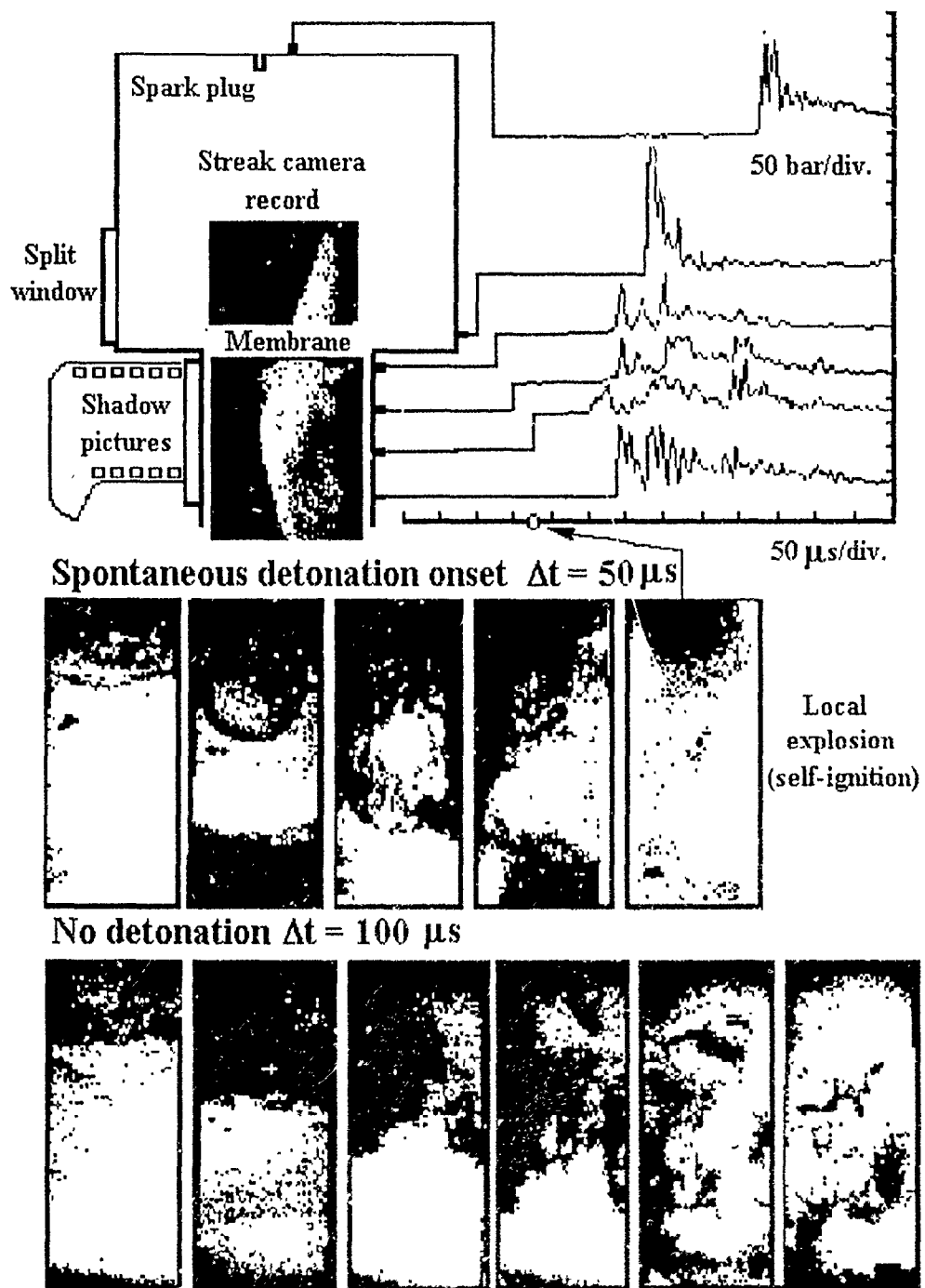
Figure 1: Schematic of the experimental setup and the results of successful (pressure records and upper frame sequence) and unsuccessful (bottom shadow sequence) spontaneous detonation onset.

(about 250 m/s). As a result, no detonation was observed both inside and outside the explosion chamber. Thus, the presence of, at least, short confined duct plays a crucial role in the spontaneous detonation onset. On the one hand, the ducting promotes intense turbulent mixing between CP and UM. On the other hand, it can provide a gain in the outflow velocity. Without considering all the details of the phenomenon in question, we focus below on an attempt to elucidate the importance of the value of the velocity of CP within the framework of the gradient mechanism of spontaneous detonation onset. The following simplified analysis concerns the criterion for the upstream-directed detonation onset since this phenomenon is of great practical importance in the problem of vented explosions.

Consider the parallel outflow of hot combustion products (CP) and cold unburned mixture (UM) under the following assumptions:

(1) there is an intense turbulent mixing between CP and UM;

(2) the co-current motion begins at $t = 0$ and $x = 0$;

(3) the outflow velocity a_f is constant.

Thus, the ignition delay time τ of a certain small volume of the UM will decrease due to the turbulent mixing. Simultaneously, this volume will move downstream. Thus, at any time there exists a distribution of ignition delay time of UM along the duct ($\tau \to \infty$ at $t = 0$, $x = 0$). The simplest relationship describing the variation in the induction time along the path of the outflow is a power law: $\tau(x) = Ax^{-p}$ ($p > 0$, $A > 0$). The ignition delay under transient conditions is governed by the integral [4]

$$\int_0^{t_s} \frac{dt}{\tau(t)} = 1.$$

Taking into account the obvious relationship $x = a_f t$, one can rewrite the integral in terms of x. Thus, one can determine the location of the self-ignition event: $x_s = (A(p + 1)a_f)^{\frac{1}{p+1}}$. Using the criterion of [2] for the onset of strong shock wave and detonation $|d\tau/dx|^{-1} \approx a_p$ (a_p is the speed of sound in CP), one can find the coordinate of the point x_d at which detonation will start: $x_d = (Apa_p)^{\frac{1}{p+1}}$. Therefore, detonation can arise and propagate upstream if $x_s \geq x_d$. It is surprising that this imposes a simple condition on the outflow velocity, which is expressed in terms of only a_p and p: $a_f \geq a_p p/(p + 1)$. If $a_f < a_p$, the self-ignition wave can propagate upstream. To summarize, the condition for the onset upstream-directed spontaneous detonation is

$$\frac{p}{p + 1} \leq \frac{a_f}{a_p} < 1.$$

Setting $a_p \approx 10^3$ m/s and taking into account the experimental results, one can roughly estimate the range of p: $p = 0.3$–2.

References

[1] Zel'dovich Ya. B. *et al. Acta Astronaut.*, 1970, **15**, 313.

[2] Zel'dovich Ya. B. *et al.* In: *Progress in Astronaut. and Aeronaut.*, 1988, **114**, 99.

[3] Lee J. H. S. *et al. Acta Astronaut.*, 1978, **5**, 971.

[4] Knystautas R. *et al. Proc. 17th Symp. (Int.) on Combustion*, The Combustion Institute, 1979, 1235.

[5] Inada M. et al. In: *Prog. Astron. Aeron.*, 1992, **153**, 253.

[6] Oppenheim A. K. *et al. Comb. Flame*, 1962, **6**, 2, 193.

[7] Medvedev S. P. *et al. Proc. Russian–Japanese Seminar on Combustion*, 1993, 180.

INCREASED SHOCK-WAVE SENSITIVITY OF A TATB-BASED EXPLOSIVE TO DOUBLE SHOCK-WAVE LOADING WITH INTERMEDIATE RAREFACTION: EXPERIMENT, PHENOMENOLOGICAL MODEL, NUMERICAL SIMULATION

V. G. Morozov, I. I. Karpenko, S. E. Kuratov, V. N. Shamrayev,
S. S. Sokolov, L. V. Dmitriyeva, T. L. Grebennikova,
A. A. Evstigneyev, A. D. Kovtun, V. A. Komrachkov, I. E. Plaksin,
V. F. Gerasimenko, A. N. Shuykin, Yu. M. Makarov,
V. M. Gerasimov, V. I. Shutov

Russian Federal Nuclear Centre, All-Russian Scientific Research Institute of Experimental Physics (VNIIEF), 607200 Arzamas-16, Nizhni Novgorod Region, Russia

Using TATB-based explosive as an example, increased heterogeneous explosive sensitivity to a preliminary shock wave followed by a rarefaction wave was studied.

Experiments with weak planar loading and rarefaction of explosive samples followed by shock-wave initiation of detonation were performed.

Within the framework of the "hot spot" concept, a phenomenological model of explosive decomposition kinetics was proposed. The model accounts the effect of explosive density variation prior the shock wave on the shock-wave sensitivity.

Earlier, this model was used to describe explosive sensitivity to preliminary shock-wave compression.

Using hydrodynamic computer codes, experiments for plane geometry were simulated to refine and verify the model.

An X-ray test was performed to demonstrate the increased TATB-based shock-wave sensitivity of the explosive in the context of two-dimensional interaction of a shock and a rarefaction wave. A computational simulation of the test reproduced sufficiently well the experimental picture.

THE EFFECT OF NON-ISENTROPIC PROCESSES ON DEFLAGRATION TO DETONATION TRANSITION IN GASEOUS COMBUSTIBLE MIXTURES

M. A. Noskov*, S. M. Frolov*, P. Wolanski[†]

Semenov Institute of Chemical Physics, Moscow, Russia
[†]*Politechnika Warszawska, Warszawa, Poland*

Introduction

Deflagration to detonation transition (DDT) in most gaseous combustible mixtures is known to take place in sufficiently long ducts. Despite extensive studies of the DDT phenomenon, universal theory is still lacking. Zel'dovich [1] was one of the pioneers in explaining DDT by shock-flame interaction. Manson [2] reported the results of thermodynamic calculations of flame and shock velocities pertaining to DDT. The limits of DDT were calculated within the framework of a simplified one-dimensional model ignoring the non-isentropic processes behind the shock wave [3].

Oppenheim [4] has demonstrated experimentally that the detonation wave arises suddenly after 'explosion in explosion' somewhere between the flame and the sequence of shock waves. So far, there has been no adequate quantitative explanation for the phenomenon of 'explosion in explosion'. Experimental observations show that a localized explosion, if occurs, does not necessarily give rise to detonation. What conditions are then required for the onset of detonation? Oppenheim analyzed the thermodynamic parameters of the shock-compressed gas in multiple shocks under conditions pertaining to DDT. It has been found that the pressure p and temperature T of the *critical particle* (fluid particle located in the centre of 'explosion in explosion', [4]) appear to be outside

the explosion limits. Moreover, the delay time integral for the critical fluid particle

$$I = \int\limits_{t_0}^{t} \frac{dt}{\tau(p,T)} \tag{1}$$

has been found to vary from $5 \cdot 10^{-4}$ to $4 \cdot 10^{-2}$, depending on the empirical formula used for steady state induction time $\tau(p,T)$. This implies that shock compression itself does not provide conditions favoring autoignition of the *critical particle*.

Wolanski [5] has suggested possible explanation of *'explosion in explosion'* based on the analysis of non-isentropic processes behind the lead shock. Kinetic energy dissipation at the duct wall can result in local temperature increase thus locally enhancing chemical energy release.

This paper reports a detailed study of the effect of the non-isentropic processes on mixture autoignition behind a shock wave. As a starting point, the laminar boundary layer behind a single shock wave is considered.

Formulation

Consider propagation of a single plane shock wave in a duct filled with a combustible gas mixture. The shock velocity is assumed to be constant. Fluid particles entering the wall boundary layer decelerate, and their temperature increases. Based on the known velocity distribution in the boundary layer, one can estimate the temperature profile using the energy conservation equation. Depending on the thermal boundary conditions at the duct wall, the temperature maximum can be reached at a finite distance from the wall, or at the wall itself if adiabatic conditions are specified. The difference in gas temperature drastically affects the autoignition time delay for fluid particles. The time delay is expected to depend on the distance from a fluid particle to the wall and differs considerably from the value found for the *critical particle* in [4].

The mathematical model for the effect under study is based on the following simplifying assumptions:

(1) plane shock wave;

(2) two-dimensional planar steady flow;

(3) laminar boundary layer;

(4) constant thermophysical properties;

(5) adiabatic confinement;

(6) negligible pre-ignition self-heating of combustible mixture, as compared with the temperature increase due to kinetic energy dissipation;

(7) single-step chemical reaction.

371

In the coordinates attached to the shock, the gas velocity ahead of the shock is D, while behind the shock the free stream has the constant longitudinal velocity U_∞ and a variable transverse velocity component. The latter arises due to the curvature of a realistic shock wave and can be determined from the solution of the shock wave – boundary layer interaction problem [6]. The corresponding gas temperatures in the undisturbed and shocked free-stream gas are T_0 and T_∞ where subscripts '0' and '∞' denote the conditions prior and after shock arrival, respectively.

The profile of the longitudinal velocity u has been found in [7] for a range of the shock Mach numbers. For a shock wave of moderate intensity, it can be approximated with a good accuracy, using the solutions obtained in [7], as a piece-linear function of coordinates: $u = u(x, y)$.

Then, the mass conservation equation

$$\frac{\partial}{\partial x}(\rho u) + \frac{\partial}{\partial x}(\rho v) = 0, \tag{2}$$

yields the transversal velocity component v. The procedure outlined was used to calculate the flow velocity distribution.

Temperature was estimated using the Crocco integral for a compressible boundary layer. Under the conditions

$$\frac{dp}{dx} = 0, \qquad Pr = 1, \qquad \gamma = const, \qquad v^2 \ll u^2,$$

the gas temperature at the wall is [8]

$$T = T_\infty \eta \left(1 + r_c M^2 \frac{\gamma - 1}{2} \frac{1 - w^2}{U^2} \right), \tag{3}$$

where U and w denote the longitudinal velocity components of particle in the free stream and in the boundary layer, respectively, in the laboratory coordinate system, M is the local Mach number of the shock-compressed gas, γ is the specific heat ratio, r is the temperature recovery coefficient, η is the coefficient introduced for taking into account thermal boundary conditions at the duct wall, Pr is the Prandtl number.

A 7% decrease in initial reactant concentration is introduced as a criterion for autoignition. This was found to correspond approximately to condition $I \approx 1$ (see Eq. (1)) for the kinetic parameters specified below. The equation for the reaction rate with the initial condition is

$$\frac{da}{dt} = -ka^2 \exp\left(-\frac{E}{RT} \right), \qquad a(0) = 1, \tag{4}$$

where $a = [A]/[A]_0$ denotes the dimensionless reactant concentration (e.g., the oxidizer), k is the pre-exponential factor, E is the activation energy, R is the gas constant.

Table 1: Properties of particles entering the boundary layer.

Particle No.	y/m	τ/s	x_{ign}/m	T_{ign}/K	$a_s/(\text{m/s})$	$I(\tau)$	$u_{sp}/(\text{m/s})$
1	free stream	$7.48 \cdot 10^{-3}$	3.19	966	952.7	1	—
2	$12 \cdot 10^{-5}$	$198 \cdot 10^{-6}$	0.141	1278	1096	0.87	419
3	$11 \cdot 10^{-5}$	$171 \cdot 10^{-6}$	0.126	1288	1100	0.88	556
4	$10 \cdot 10^{-5}$	$149 \cdot 10^{-6}$	0.113	1297	1104	0 89	591
5	$9 \cdot 10^{-5}$	$128 \cdot 10^{-6}$	0.100	1302	1106	0.88	619
6	$8 \cdot 10^{-5}$	$109 \cdot 10^{-6}$	0.088	1310	1109	0.88	631
7	$7 \cdot 10^{-5}$	$91 \cdot 10^{-6}$	0.078	1320	1113	0.89	556
8	$6 \cdot 10^{-5}$	$74 \cdot 10^{-6}$	0.068	1328	1117	0.89	588
9	$5 \cdot 10^{-5}$	$59 \cdot 10^{-6}$	0.057	1339	1121	0.88	733
10	$4 \cdot 10^{-5}$	$46 \cdot 10^{-6}$	0.049	1349	1126	0.89	615
11	$3 \cdot 10^{-5}$	$35 \cdot 10^{-6}$	0.041	1357	1129	0.89	727

If the initial and boundary conditions are specified, one can obtain the histories of gas variables along the trajectory of a fixed gas particle and, finally, find the ignition location and delay time.

Results

The problem formulated above was solved numerically for a model combustible mixture with the following properties:

$$\gamma = 1.36, \quad \nu = 10^{-5} \text{ m}^2/\text{s}, \quad E = 40 \text{ kcal/mole}, \quad k = 10^{10} \text{ s}^{-1}, \quad \eta = 1, \quad r_c = 1,$$

$$p_0 = 10^5 \text{ Pa}, \quad T_0 = 300 \text{ K}, \quad a_0 = 538.5 \text{ m/s},$$

$$M_s = 3.5, \quad U_\infty = 427 \text{ m/s}, D = 1885 \text{ m/s}, \quad M = 1.53,$$

$$p_1 = 14.3 \cdot 10^5 \text{ Pa}, \rho_1 = 2.15 \text{ kg/m}^3.$$

Ten particles (Particles 2 to 11) entering the boundary layer and a single particle (Particle 1) moving in a free stream were examined. Table 1 shows the predicted particle parameters. Particle trajectories are shown in Fig. 1, with particle ignition time and position marked by dark circles. Clearly, the delay time for Particle 1 is larger than for Particles 2–11. Note, that the transverse velocity in the post-shock gas affects considerably the particle ignition delay time, despite the fact that $v \ll u$.

The predicted value of the delay time integral (1) for Particle 1, taken at the moment of ignition of Particle 10, is $5 \cdot 10^{-3}$. It correlates, by the order of magnitude, with the respective data of [4] for a *critical particle* at the moment of its explosion. Thus, the boundary layer effect explains the discrepancy between the predictions of [4] and experimental findings.

The predicted values of induction integral (1) for Particles 2 to 11, taken at the moments of their ignition, are close to unity.
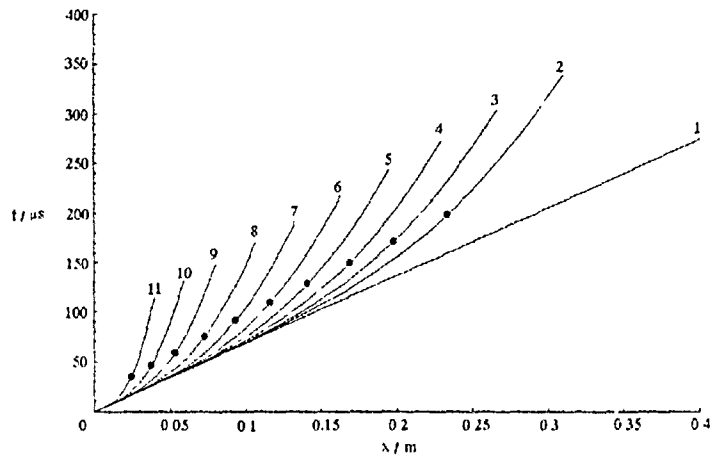
Figure 1: The predicted time–distance diagram for 11 fluid particles moving behind a shock wave of $M = 3.5$. Particle 1 represents free stream conditions. Particles 2 to 11 enter the near-wall laminar boundary layer at different height. Dark circles show time and position of particle ignition. Ignition site of particle 1 is located outside the plot scale.

Let us estimate the ratio u_{sp}/a_s, where u_{sp} is the spontaneous flame velocity [8] and a_s is the local sound velocity. The value of u_{sp} can be approximated as

$$u_{sp} = \frac{1}{|\mathrm{grag}\tau|} \approx \left(\frac{\Delta\tau}{\Delta x}\right)^{-1}. \tag{5}$$

It follows from Table 1 that u_{sp}/a_s is of the order of unity. This fact indicates that the amplification of pressure waves initiated by ignition events inside the boundary layer can occur by the Zel'dovich mechanism [9]. The Zel'dovich mechanism provides an explanation of the nature of strong shock or detonation waves onset [10] and, therefore, could be the reason for 'explosion in explosion'.

Discussion

A further improvement of the model should take into account the effects of transport processes on the fluid particle ignition, turbulent fluctuations in the boundary layer, and multiple shock compression.

Under non-adiabatic conditions, instead of Eq. (3) one can use the similarity relation [2]

$$\frac{T_* - T_W}{T_{*\infty} - T_W} = \frac{w}{U} \tag{5}$$

where T_* and T_W are, respectively, the stagnation and wall temperature. The exact solution of [7] for the laminar boundary layer can be replaced by the "1/7"th power

low for velocity distribution in the turbulent boundary layer (TBL), i.e.

$$\frac{w}{U} = \left(\frac{y}{\delta}\right)^{\frac{1}{7}} \tag{6}$$

where δ is the boundary layer thickness. The combination of Eqs. (5) and (6) allows one to obtain the profile of average static temperature in TBL, replacing Eq. (3). It can be shown that at $M > \sqrt{\frac{2}{\gamma-1}(1 - T_W/T_\infty)}$ the static temperature attains a maximum value inside TBL, which is dependent of M, γ, and T_W. Hence, non-isentropic processes are expected to effect ignition in TBL under non-adiabatic conditions

The account of multiple shock compression of reactive mixture will evidently decrease the characteristic Mach number at which the effects under consideration become significant.

Conclusion

Kinetic energy dissipation in a compressible boundary layer behind a shock wave is shown to considerably affect autoignition of a reactive mixture. The particles entering a boundary layer have been shown to exhibit substantially shorter ignition delay time than in the free stream, which provides the explanation for the discrepancies between simplified 1D simulations and experimental findings. The predicted spontaneous flame velocity has been shown to be close to the local sound velocity. According to the Zel'dovich mechanism, in this case one can expect the strong coupling between the localized chemical energy release and the accompanying pressure waves which can be used as a basis for the further studies of the *'explosion in explosion'* phenomenon

Acknowledgement

References

[1] Zel'dovich Ya. B., Kompaneetz A. S. *Detonation Theory*, Moscow, Gostehteorizdat, 1955 (in Russian).

[2] *Fundamentals of Gas Dynamics* (H W Emmons Ed), Princeton Univ. Press, 1958.

[3] Lee C O , Sichel M *Proc Meeting of the Eastern Section of the Combustion Institute*, Orlando, Florida, 1990

[4] Meyer J V., Urtiew P. A., Oppenheim A. K. *Comb Flame*, 1970, **14**, 13–20.

[5] Wolanski P. *Archivum Combustionis*, 1991, **11**, 3-4, 143–149

[6] Hartunian R. A. *Phys. Fluids,* 1961, **4**, 9, 1059–1063.

[7] Loitzyanski L. G. *Laminar Boundary Layer.* Moscow, Fizmatgiz, 1962 (in Russian).

[8] Schlichting H. *Die Grenzschicht–Theorie.* Karlsruhe, 1951.

[9] Zel'dovich Ya. B. *Comb. Flame,* 1980, **39**, 211–214.

[10] Frolov S. M., Gelfand B. E., Tsyganov S. A. *Fizika Goreniya Vzriva,* 1992, 5, 111–123 (in Russian).

PRACTICAL APPLICATION OF RANEFACTION SHOCK-WAVE EFFECT PREDICATED BY YA. B. ZEL'DOVICH

S. A. Novikov

Russian Federal Nuclear Center, Arzamaz–16, Russia

In 1946, Zel'dovich has suggested for the first time an idea of rarefaction waves with abruptly decreasing pressure, i.e. rarefaction shock waves (RSW), likely to exist in a medium under certain conditions [1].

The possibility of RSW occurrence could be conditioned by the Poisson adiabat having a portion with the negative second pressure derivative over volume, i.e. $\partial^2 P / \partial V^2 < 0$. As an example, Zel'dovich considered a medium with its state near the critical point where there is no distinction between vapor and liquid phases.

Experimentally, RSW were initially observed in iron and steel, with first-order phase transition (αFe–ϵFe) occurring at pressure 130 Kbar [2]. The bend point of iron adiabat represents a particular limiting case for abnormal adiabat portion having negative second derivative.

In 1956, during VNIIEF experiments on iron and steel specimens fracture, an original kind of spall fracture, i.e. smooth spalling, was observed. That appeared to be the earliest experimental evidence of RSW existing [3, 4, 5]. Later in [6], a profile record of a shock pulse involving RSW has been obtained

Novosibirsk scientists were the first who have shown experimentally the RSW existing in the region near the critical "liquid–vapor" point as suggested by Zel'dovich [7]. In 1986, the RSW effect co-authored with Zel'dovich was registered as the discovery [8].

376

Currently, there are experimental indications ol RSW for a large variety of solid materials.

With RSW taken into account in numerical calculations, the accuracy could be significantly improved in predicting the responses of materials and critical structures to shock loading.

RSW effects were used to account for some structural changes in metals, such as the formation of a vigorous twinning region in steel [9]. During spall fracture, metals would have negative pressures in a very narrow region with its size dependent on the RSW front width. Under these conditions, real metals are likely to achieve theoretical or near-theoretical strength. An attractive and somewhat unexpected application of this affect is the comparative brisance evaluation of high explosives [10].

Of great practical importance is the use of RSW collision technique blast fragmentation of thick-wall structures. With this technique, solid many-tons steel structures can be cut using high explosives, their amount being a factor of 100 as small as the value predicted by standard relationships. This is quite essential for operations in an aquatic environment, including disassembly of sea-based oil platforms, ets.

References

[1] Zel'dovich 'a. B. *The Theory of Shock Waves and Fundamentals of Gasdynamics.* Izd. AN SSSR, 1946 (in Russian).

[2] Bankroft D., Peterson E., Minshall S *J Appl Phys.*, **27**, 291, 1956.

[3] Ivanov A. G., Novikov S. A. *Zhurnal Tekhicheskoi Fiziki,* 1961, **40**, 6, 1879 (in Russian).

[4] Ivanov A. G., Novikov S. A., Tarasov Yu 1. *Fizika Tverdogo Tela,* 1962, IV, 1, 249 (in Russian).

[5] Ivanov A. G., Novikov S. A. *Fizika Goreniya Vzriva,* 1986, **3**, 91 (in Russian).

[6] Bat'kov Yu. V., Ivanov A. G., Novikov S. A. *Zhurnal Prikladnoi Mekhaniki Tekhnicheskoi Fiziki,* 1985, **6**, 142 (in Russian).

[7] Borisov M. A., Borisov A A., Kutateladze S. S., Nakoryakov S. S. *Dokl. Akad. Nauk SSSR*, 1980, 3, 3 (in Russian).

[8] Ivanov A. G., Novikov S. A., Borisov M A, Borisov A. A, Zel'dovich Ya. B, Nakoryakov V E. *Diplom No.321, Vestnik AN SSSR,* 1987, 8, 139 (in Russian).

[9] Ivanov A G., Divnov I. I, Novikov S. A. *FMM,* 1965, **20**, 1 (in Russian).

[10] Novikov S. A., Pogorelov A. P., Sinitsyna L. M. *Patent No.1184359, ot 8.06.85* (in Russian).

"VACUUM" DETONATION IN A POROUS MEDIUM

A. V. Pinaev

Lavrent'ev Institute of Hydrodynamics, Siberian Division Russian Academy of Sciences,
Novosibirsk, 630090 Russia

The detonation of monofuels in an evacuated porous medium was for first time experimentally obtained in [1]. The detonation of high explosive (HE) particles suspended in an evacuated channel and tossed up from its bottom was reported in [2].

The study of detonation of RDX and TNT powders covering with a uniform thin layer the particles of an inert porous medium is reported in the paper. The influence of the initial gas pressure p_0 on the limits and characteristics of detonation is considered in detail, and the wave structure and the ignition and propagation mechanisms of detonation are described.

The experiments were performed in thick-walled cylinders of length $L = 200$ and 300 mm, with inner diameter $d = 20$ mm and steel balls of diameter $\delta = 2.5$ mm inside. The detonation was initiated in the working section from the top, using a supplementary section ($L = 150$ mm, $d = 10$ mm) by igniting $2H_2 + O_2$ mixture at the initial pressure 0.25–0.4 MPa.

The detonation velocity D, the pressure p, and luminescence were measured at the gauge length 50 mm by two tourmaline transducers (of crystal size 1 5 mm and eigenfrequency 300 kHz) with quartz light guides ($d = 0.3$ mm) inserted close to the piezoelements. The detonation velocity was also measured at two gauge lengths 50 mm each by thin quartz light guides. The self-luminescence process was photographed in an optical section ($I = 500$ mm, $d = 35$ mm) with the balls 2.5 mm, 5 mm, and 11.5 mm in diameter through a slit 250 mm long and 1 mm wide. The covered particles of HE were μm in size. It had been preliminarily proved by firing in the porous medium without HE that error due to the initiating pressure impulse was negligible: at a distance $\sim 20\delta$, the pressure decreases to 0 05 MPa, while its delay with respect to the detonation wave is over 250 μs

A distinctive feature of "vacuum" detonation is the smooth rise of the leading front and luminescence, their peaks being usually coincident, the pressure rise was 3–10 μs ahead of the luminescence. The basic characteristics of steady-state detonation include the rise length $\lambda_1 = \tau_1 D$ (τ_1 is the time of pressure increase in the wave), the duration of pressure decrease τ_2, and the luminescence time τ_l. For RDX, $\lambda_1 \sim 18 \pm 1$ mm at $\rho = 5 \div 40$ mg/cm^3, which amounts to $(7\text{-}8)\delta$.

The reaction zone was conventionally subdivided into an active zone (up to the Chapman Jouguet surface), where the gas moves forward, and a passive one, where the HE particles ignite over a long time ($\tau \leq \tau_l \sim 250$ 350 μs) in the presence of a
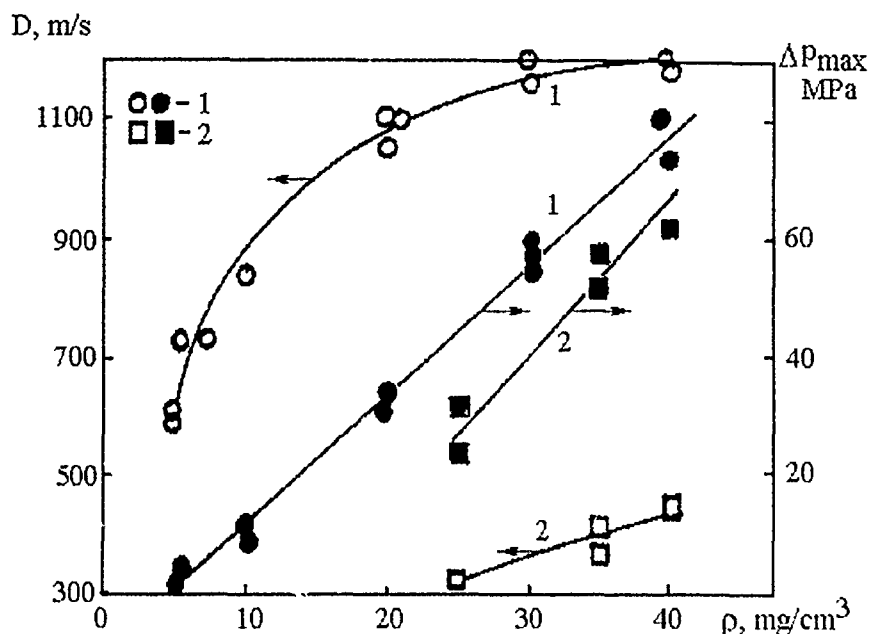
Figure 1.

slow ($\simeq 10$ m/s) reverse motion of the reaction products due to the negative pressure gradient in the wave. The analysis of the scanning have shown that the active zone thickness is close to λ_1. The value τ_l is determined more precisely from the scanning of the process. The characteristic value of τ_2 is only by 50–100 μs greater than that of τ_l, which may be due to the fast cooling of the ignited gas in the pores.

The experimental dependencies of velocity and maximum pressure Δp_{max} on ρ in the steady detonation waves are shown in Fig. 1 for RDX (*1*) and TNT (*2*). The extreme left points correspond to the critical values ρ^*, D^*, and Δp_{max}^* determined with an error of 10–15%. The negligible change in the value of ρ near the limit has the most significant effect on Δp_{max}. Thus, for RDX $\Delta p_{max}^* \simeq 3.5$–$4$ MPa at $\rho^* = 4.6$ mg/cm^3, and $\Delta p_{max} \simeq 7.5$ MPa at $\rho \simeq 5$ mg/cm^3, for TNT $\Delta p_{max}^* \simeq 25$–$35$ MPa at $\rho^* \simeq 25$ mg/cm^3. The reduced detonability of TNT is due to its higher ignition temperature, as compared to RDX. The experiments were not conducted at $\rho > 40$ mg/cm^3 because of the shedding of HE off the particles of porous medium. The experimental curve of $\Delta p_{max}(\rho)$ is close to a straight line, and the growth of D is slower.

Experimental data were consistent within the measurement error, if p_0 was increased from 0.1 to 10^2–10^3 Pa. The influence of p_0 is most significant in the vicinity of ρ^*, because the wave is rather weak. The results for RDX are presented in Fig. 2. It has been found that both lower and upper limiting values of p_0 exist. With a decrease in ρ, the zone of detonation was observed to narrow. At $\rho \simeq 4.0$ mg/cm^3, pure "vacuum" detonation cannot exist. Its occurrence starts at $p_0 \simeq 0.05$ MPa and ceases when
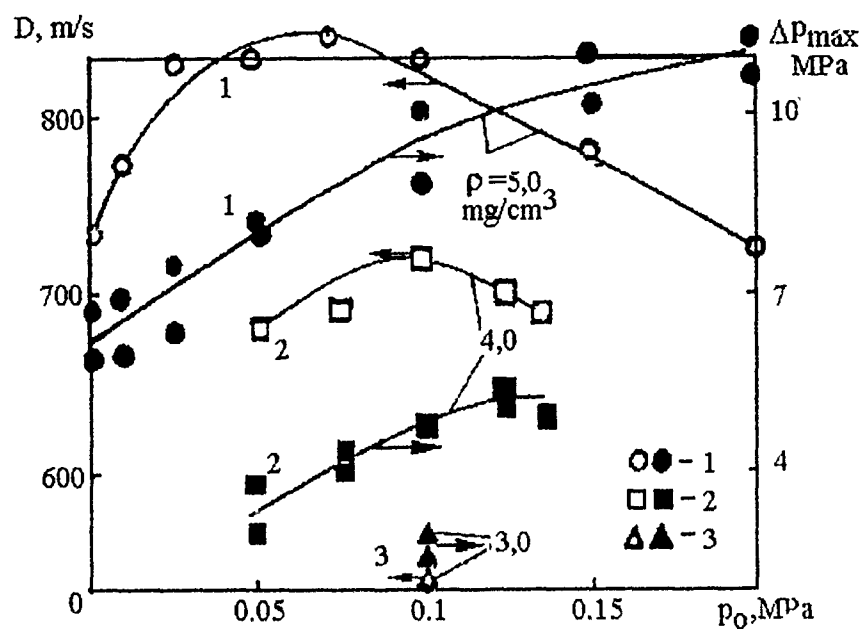
Figure 2.

$p_0 \geq 0.136$ MPa. The highest values of D were observed in the interval between the limits. The nature of the upper density limit is attributable to the quenching action of the inert gas component, whereas a moderate addition of gas to the system promotes detonation, which explains the nature of the lower limit. At $\rho \simeq 3$ mg/cm^3, the detonation occurs only in a narrow vicinity of $p_0 = 0.1$ MPa, and at lower densities detonation is absent.

The existence of a purely jet mechanism of ignition and propagation of "vacuum" detonation has been established in optical studies. Hot gas jets flow out of the high-pressure region and ignite the HE particles. The peak apparent velocity of the jets at the leading front, measured by the tracks at the detonation scanning, is close to D and in some pores exceeds it by 100–200 m/s. With an increase in p_0 at low ρ, the gas in pores ahead of the wave cools down, decelerates the jets, and inhibits the detonation.

The mean free path length for molecules in a porous medium does not exceed δ. Therefore, the steady-state detonation velocity and a non-spreading pressure profile establish rapidly. For this reason, the porous medium is more suitable for the studies of "vacuum" detonation, as compared to drops or dusts.

References

[1] Pinaev A. V., Lyamin G. A. *Dokl. Akad. Nauk SSSR*, 1992, **325**, 1, 498 (in Russian).

[2] Mitrofanov V. V., Bakirov I. T. *Fizika Goreniyr Vzriva*, 1994, **30**, 2 (in Russian).

EVOLUTION OF EXPLOSION IN TATB HIGH EXPLOSIVE IN THE PROCESS OF ITS EXPANSION INTO A FREE SPACE FOLLOWED BY AN IMPACT AGAINST HARD BARRIER

I. E. Plaksin, V. I. Shutov, V. M. Gerasimov, V. F. Gerasimenko

RFNC-VNIIEF, Arzamas-16, Russia

It is well known that a high explosive (HE), shock-compressed at sub-threshold intensity, becomes less sensitive to a subsequent shock-wave loading. HE shock de sensitization is primarily caused by the change of its rheological properties involving pore destruction and heterogeneity smoothing, so that HE approaches the state of solid homogeneous matter. Desensitization is most pronounced for low-sensitive HE TATB compositions.

Later experiments revealed another remarkable feature of these high explosives, namely their post-shock resensitization. When a HE unloads and expands into a free space after having been shock-compressed, its shock-wave sensitivity rises again and becomes higher as compared to that of the starting HE.

This feature of HE is related to one poorly investigated phenomenon.

This phenomenon can potentially result in expanding fragments of the **damaged HE** that can be caused by incomplete explosion of the HE-containing facility. In this connect: on they should be considered as a serious effect.

Three runs of experiments were carried out, wherein three thin HE samples (TATB plus 10% of plastic binder, $\rho_0 = 1.88$–1.89 g/cm^3) were accelerated, using shock-wave generators, and hit barriers made of materials of various hardness (shock impedance) such as magnesium, aluminum and steel.

In all cases, when we analyzed the acceleration of HE specimens after the. hitting magnesium, aluminum and steel barriers, the initial amplitudes of the resulting pressures were lower than the starting HE initiation threshold: $P_{Fe} = 4$ GPa, $P_{Mg} = 6$

GPa, $P_{Al} = 3.5$ GPa. Evolution of explosion initiated by pulses of these amplitudes shows that, during implosion and expansion, the starting low-sensitive HE changes its structure greatly and becomes close to RDX and HMX compounds in terms of sensitivity.

The results obtained should be taken into account in developing the models of detonation initiation and evolution.

A thorough structural analysis of a HE, which has undergone rheological changes during shock compression followed by unloading, is required to elucidate the mechanism of initiation and evolution of the explosive.

The estimation of the increased content of defects and changes in phase state, heat conduction, strength and viscosity of a TATB-based HE, which has been repeatedly shock-compressed during intermediate unloading, is apparently a promising research target in this field.

DETONATION IN NITROMETHANE AND NITROMETHANE–OXYGEN GASEOUS MIXTURES

H. N. Presles, D. Desbordes, M. Guirard

Laboratoire d'Energétique et de Détonique — URA 193 CNRS, ENSMA - BP 109 –
Chasseneuil du Poitou, 86960 Futuroscope Cédex, France

Detonation in pure gaseous nitromethane (NM) and in gaseous mixtures NM/O_2 has been studied. NM is liquid under the normal temperature and pressure conditions, so experiments were performed in a preheated steel tube (5 m long and 52 mm inner diameter (d)). The initial temperature T_0 could be varied up to 400 K $\pm$ 2 K; however all the experiments have been made at 390 K.

Detonations were monitored by means of ionization probes, pressure gages and the smoked foil technique.

Initiation of detonation was provided by a cap surrounded by 1 g of high explosive (PETN composition).

Detonation in Pure NM

Detonation was obtained in the range of initial pressure $0.05 \leq p_0 \leq 1.7$ bar. Different modes of detonation propagation depending on p_0 were observed:

- For $p_0 \geq 1.2$ bar, a multi-headed mode of propagation was observed with a velocity close to the CJ predictions. This detonation regime exhibits a double

5 cm
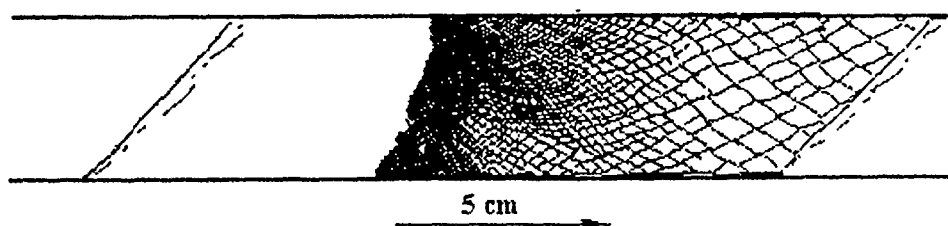
Direction of detonation propagation

Figure 1: Spinning detonation in gaseous NM: $T_0 = 390$ K, $p_0 = 0.3$ bar.

cellular structure with two different characteristic sizes. A fine structure of size λ_1 grows inside the main structure of size λ_0 up to the end of these main cells. In classical gaseous explosive mixtures, a fine structure sometimes exists in the first part of the main cells.

- For $1.2 \geq p_0 \geq 0.3$ bar, that is, over a wide pressure range, spinning detonation could be observed with a classical spin pitch P (*i.e.*, $P = 15$ cm $\cong \pi d$).

The velocity deficit of the detonation, with respect to the CJ predictions, increases when p_0 decreases and is about 6% for $p_0 = 0.5$ bar.

Here, the double cellular structure also exists: the main cell corresponds to the single spin, and we can observe the fine structure between two successive turns of the helix along the tube (Fig. 1). This structure is oriented along the axis of the detonation tube. It appears at a distance of about $P/3$ from a helix trace, its size increasing progressively towards the next helix path.

In other words, this structure does not vanish as it happens in the case of classical C_nH_m/O_2 or Air gaseous explosive mixtures.

- For $0.3 > p_0 > 0.05$, the spinning regime turns progressively into a periodic mechanism of period P larger than the classical spin pitch· for $p_0 = 0.05$ bar, $P = 22$ cm. This periodic mechanism is due to successive detonation initiations and extinctions and could tend, with p_0 decreasing, towards the "galloping" regime.

In that regime, only this substructure remains. Its cell size increases along the periodic zone until a new reinitiation occurs. At that point, the cell size is about 0.25 to 0.3d.

Detonation in NM/O$_2$ Mixtures

For slight dilution with O_2 (corresponding to the global equivalence ratio ϕ ranging from $\phi = 1.76$ (pure NM) to about $\phi \cong \phi^* = 1.4$), the detonation in NM/O$_2$ mixtures
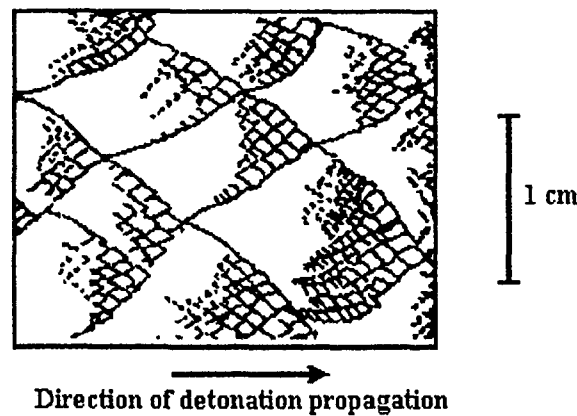
Figure 2: Typical cellular structure of the detonation of NM/O_2 mixture $\phi = 1.4$, $T_0 = 390$ K, $p_0 = 0.5$ bar.
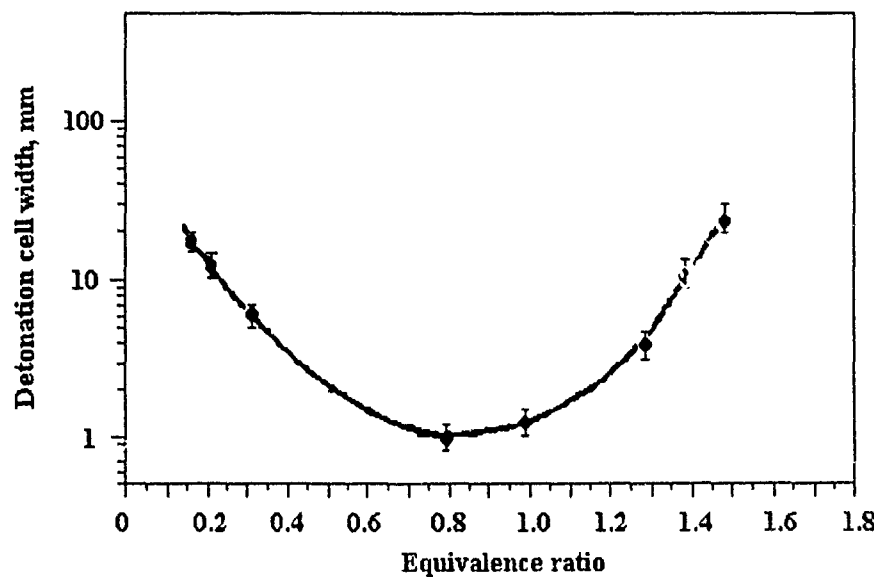
Figure 3: Variation of the size λ_0 of the main cells in NM/O_2 mixtures versus the equivalence ratio ϕ for $T_0 = 390$ K and $p_0 = 0.5$ bar.

shows the same behavior as the detonation in pure NM, that is, the existence of a double cellular structure (Fig. 2).

For $\phi < \phi^*$, the fine cellular structure inside the main cells progressively disappears. In the spinning regime ($\phi \leq 0.1$) the fine cellular pattern looks like that observed in the classical $C_n H_m / O_2$ or Air mixtures. The classical U-shaped $\lambda_0(\phi)$ curve is given in Fig. 3. Its minimum corresponds to a lean mixture ($\phi = 0.8$).

Conclusion

The detonation in gaseous NM and NM/O_2 mixtures exhibits some special features, as compared with classical gaseous explosive mixtures, mainly by the existence of a double cellular system, which could be related to a nonclassical law of energy release rate.

THE INITIATION OF DETONATION IN A COVERED EXPLOSIVE CHARGE PENETRATED BY A PROJECTILE

Fang Qing, Wei Yuzhang, Gao Wen

Laboratory for Shock Wave and Detonation Physics Research, Southwest Institute of Fluid Physics, P.O. Box 523, Chengdu, Sichuan, 610003 China

Using a two-stage light gas gun, we conducted experiments on the initiation behavior of covered explosive charges penetrated by a projectile. The projectile launched by the gas gun induced EM pulse signals while flying through inductive transducers, then triggered a high-resolution streak camera to record the flash signal as the detonation wave emerged on the surface of explosive charge.

The experimental set-up is shown in Fig. 1. On one side of the RHT–901 (TNT/RDX = 40/60) charge, a stripe of explosive was attached. If the charge detonated or a high pressure pulse appeared, an outward-propagating detonation wave in the explosive stripe would be induced, punching the blind hole at the cover. The cylindrical projectile was of diameter 16.2 mm, with the conical head with cone angle 83°. The thickness of the steel cover was 6 mm. An experimental record corresponding to the projectile velocity of 3.0 km/s is shown in Fig. 2.

The experimental results show that the cylindrical steel projectiles of mass 26 g can initiate the RHT–901 charge covered with a 6 mm thick steel plate, if its velocity is greater than 1.66 km/s. The experiments have demonstrated that the initiation
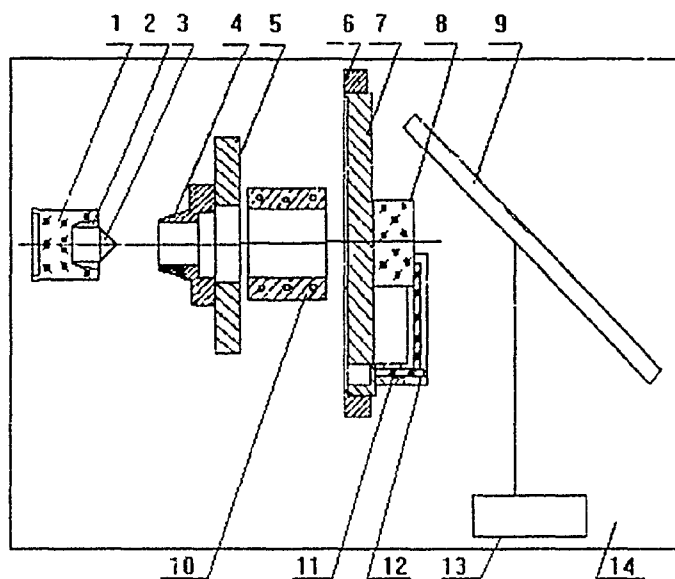
Figure 1: Experimental set-up: *1* projectile sabot; *2* paraffin wax; *3* projectile; *4* sabot separator; *5* flange plate; *6* mount; *7* steel cover; *8* RHT–901 charge; *9* mirror; *10* inductive transducer; *11* explosive stripe; *12* vacuum mire; *13* window to camera; *14* target chamber.

Figure 2: The optical record of the experiment with a sharp-headed projectile at velocity 3.0 km/s.

behavior of covered RHT–901 charges impacted by flat-head cylindrical projectiles can be described by the Jacob's initiation criteria [1].
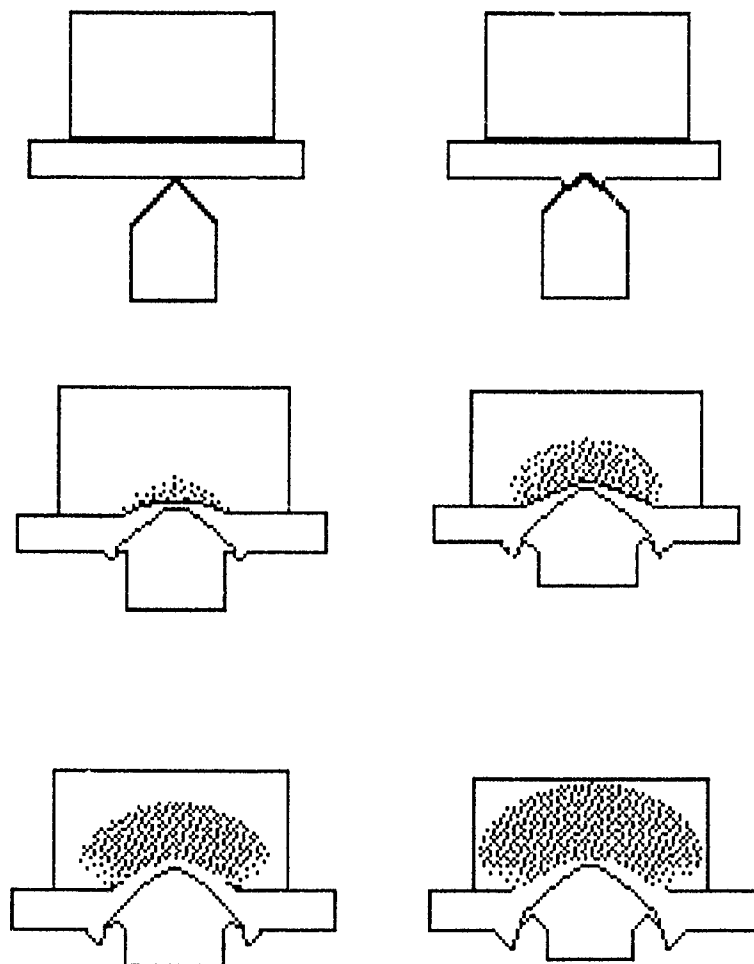
Figure 3: The numerical simulation of the initiation process of covered explosive charge penetrated by a sharp-headed cylindrical projectile at 3.0 km/s.

The numerical calculation was carried out by the HELP hydrodynamic code, where the forest-fire reaction rate and linear mixing assumptions were employed for the reactive flow modeling, the ``WL or HOM equation of state was used for the detonation

Table 1: Critical velocity of projectile for initiating the covered explosive charge.

projectile size/mm	the steel cover thickness/mm	projectile velocity/(km/s)		calculated and observed results
		calculation	experiment	
$\phi 16.2 \times 16.2$ flat head	14	2.14	2.14	initiation
$\phi 16.2 \times 16.2$ flat head	14	1.96	1.97	no reaction
$\phi 16.2 \times 16.2$ flat head	6	1.3	1.66	initiation
$\phi 16.2 \times 16.2$ flat head	6	1.2	no	no reaction
$\phi 16.2$ cone angle $83°$	6	3.0	3.0	initiation
$\phi 16.2$ cone angle $83°$	6	2.9	2.3	no reaction
spherical $R9.247$	6	2.4	no	initiation
spherical $R9.247$	6	2.3	no	no reaction

products, and so were the Grüneisen equation caiibrated with respect to the shock adiabat for the unreacted explosive and the Tillotson equation of state for metals. Note that we employ the parameters of explosive Comp.B in the following calculation instead of that of RHT–901.

The results of numerically simulated initiation process of Comp.B explosive charge impacted by a sharp-headed cylindrical projectile at the velocity of 3.0 km/s are shown in Fig. 3. They coincide with the experimental observations.

Table 1 shows the calculated critical velocities for steel projectiles with different heads compared with the experimental data. It is concluded that, because of the lateral rarefaction wave, the impact pressure incident onto the charge is much lower for the projectile with a sharper head, so that a much higher critical velocity is required.

References

[1] Bahl K. L. *et al.*, *Proc. 7th Symp. (Int.) on Detonation*, 1981.

[2] Mader C. L. *Numerical Modeling of Detonation*, Berkeley, Univ. Cal. Press, 1978.

EXCITATION OF THE EXPLOSION OF INITIATING EXPLOSIVES BY PULSES OF FAST ELECTRONS

S. M. Ryabykh, V. P. Zhulanova, V. G. Shakhovalov, N. V. Holodkovskaya

Kemerovo State University, Kemerovo, Russia

Excitation of explosions in a number of initiating explosives (azides of lead, silver and cadmium, lead styphnate, mercury fulminate) by pulses of fast electrons has been studied. Two accelerators generating electron pulses of two types were used: single pulse of controlled duration $(5-25) \cdot 10^{-9}$ s and a sequence of pulses of duration $5 \cdot 10^{-6}$ s and frequency 200 s⁻1. The energies of fast electrons were 0.3 MeV and 2.5 MeV, the integral energies of pulses were within 0.01–1 J/cm^2 and $(0.3-8) \cdot 10$ J/cm^2, respectively. Pressed tablets of initiating explosives of height exceeding ·he electron mean free path were used. Ignition delay times were determined by measuring the kinetic and optical absorption during the explosive decomposition.

The results obtained are as follows:

1. With electron pulses of 10^{-9} s duration, heavy metal azides (HMA) were excited to produce an explosion, while all the rest of the initiating explosives failed to explode. The ignition delay time was 10^{-7}–10^{-6} s. With electron pulses of 10^{-6} s duration, all the tested materials exploded. By their degrees of stability, they ranked conversely to the previous test results, e.g., mercury fulminate and lead styphnate were found to be less stable, while silver azide is the most stable (Fig. 1). The ignition delay times were within 5–80 μs.

2. The critical parameter for excitation by 10^{-9} s pulses is the integral energy of pulse, while for excitation with 10^{-6} s it is the radiation power $I = E/\tau$ (τ is the pulse duration).

3. Two critical values, E_1 and E_2, were found to exist. For pulse energies $E \leq E_1$, the explosion was not initiated irrespective of the number of pulses, while for $E \geq E_2$ the explosion was always initiated by the very first pulse. In the range $E_1 \leq E \leq E_2$, under irradiation by successive pulses, the explosion could be initiated by any pulse at random, its probability increasing with the pulse energy.

4. When the temperature of the irradiated samples was lowered to 77 K at fixed integral energy of the pulse, the ignition delay time did not change significantly (Fig. 2).

The experimental data obtained allowed us to conclude that in the latter case the process of explosion excitation is of nonthermal nature. First, both calculations in the
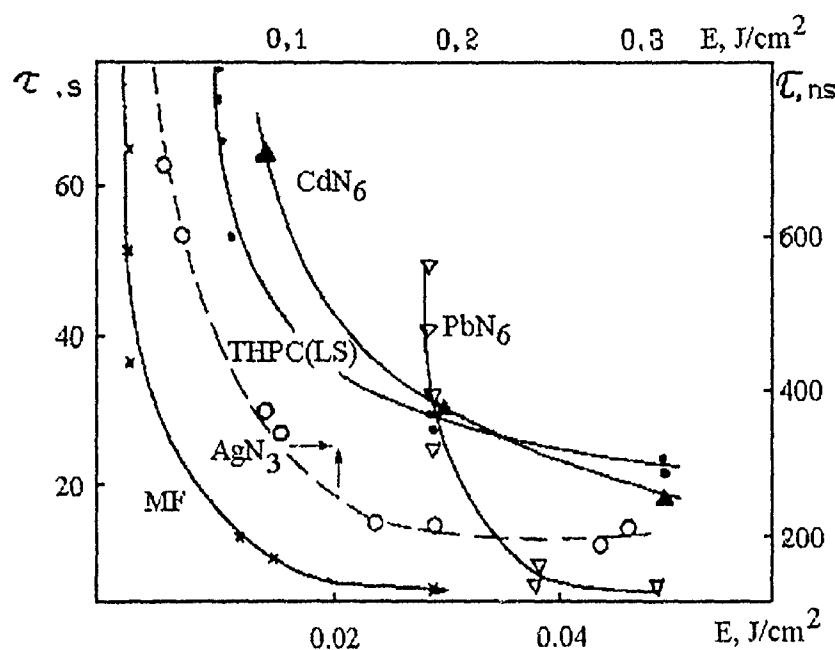
Figure 1: Effect of pulse energy on the ignition delay time.
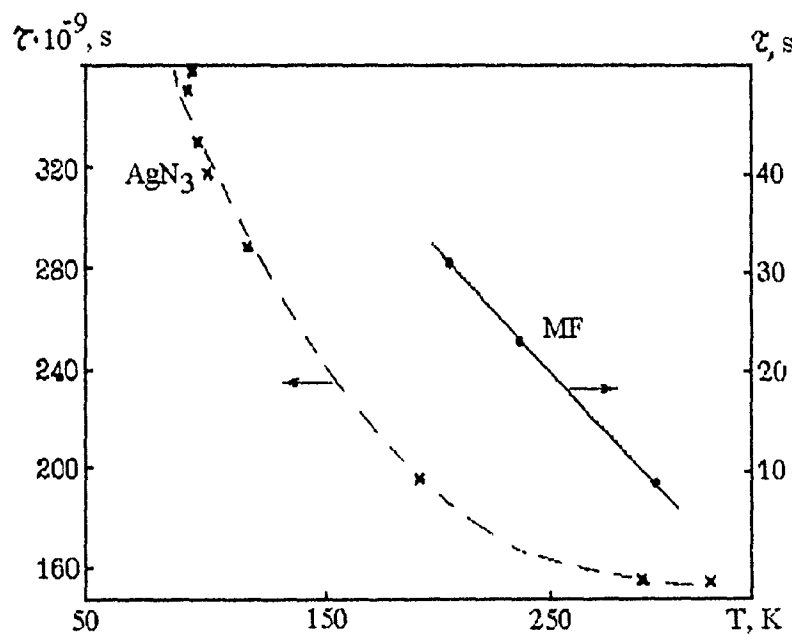
Figure 2: Effect of irradiation temperature on the ignition delay time.

adiabatic approximation and direct measurements showed that the temperature rise in the irradiated samples did not exceed 10–50 K, and, secondly, the decrease of the temperature to 77 K did not significantly change the ignition delay time.

Based on these observations, the region of increased concentration of electron excitations generated by irradiation of an almost unexcited atom subsystem has been suggested as a model of initiation site. It may be viewed as an analog of electron–hole droplets in semiconductors.

To create such regions via homogeneous generation of electron excitations in the bulk of the crystal of initiating explosives, the excitations must have a sufficiently long life time, be mobile enough, and have appreciable mutual binding energy For azides, all these above requirements are fulfilled. The electron excitations are the thermalized zone electrons and holes generated by irradiation. At their effective masses 0.5 and 3.5 and lifetimes ca 10^{-6} s, their free paths are large enough for them to contribute to the formation of the initiation site by their successive attachment to a growing site. The mutual binding energy of excitons in an electron–hole droplet is close to the dissociation energy of excitons, which is of the order of 0.1 eV in HMA. Therefore, the above process is likely to take place in HMA. Since there is no experimental data for the other explosives studied, our suggestion is true only when the above requirements are satisfied. Further, we assume that a region of increased concentration of electron-zone excitations becomes an initiation site when this concentration exceeds a critical value.

Based on the experimental data on the changes in the degree of stability due to irradiation by pulses of various durations, we conclude that the formation of excited states and the growth of initiation sites in azides proceeds faster than in other tested materials but they have a short life time. Hence, the higher stability of silver azide with respect to pulsed irradiation can be attributed to the weak intensity of a single pulse and the decomposition of excited states by the beginning of the next one. As for lead styphnate, mercury fulminate, and potassium picrate the generation and growth of an initiation site proceeds slower, which explains why there is no explosion under irradiation by 10^{-9} s pulses.

The characteristic parameters (rate constants of certain reactions, the critical values of E and I, the concentration of excitations) were determined by numerical simulation.

THEORETICAL AND EXPERIMENTAL INVESTIGATION OF DEFLAGRATION TO DETONATION TRANSITION IN REACTIVE GAS MIXTURES IN CLOSED VESSELS AND LAYERS WITH FREE BOUNDARIES

N. N. Smirnov, I. I. Panfilov, M. V. Tyurnikov, A. G. Berdyuguin

Department of Mechanics and Mathematics, Moscow State University, Moscow, 119899 Russia

Experimental and theoretical investigations of the onset of detonation were conducted by many authors [1–11] and great progress has already been achieved. This paper presents the results of numerical and experimental investigation of the process of deflagration to detonation transition. It is shown that both regimes of deflagration to detonation transition and regimes including deflagration waves lagging behind the shock waves are possible. Several types of flow patterns of deflagration to detonation transitions are determined theoretically and experimentally. Stability of one- and two-dimensional detonation waves is investigated. It is shown that one-dimensional pulsations in the symmetrical case with free boundaries cause strong transverse pulsations.

Mathematical Model

Here, we model the evolution of an initially quiescent combustible mixture inside a tube, bounded by plane, rigid, noncatalytic walls. Our study is based on the standard mathematical model of nonsteady flow of a reactive viscous heat-conducting gas. The governing set of equations has the form

$$\frac{\partial \rho}{\partial t} + \mathrm{div}\rho\vec{u} = 0, \tag{1}$$

$$\frac{\partial \rho\delta}{\partial t} + \mathrm{div}\rho\delta\vec{u} = \mathrm{div}(\rho D\mathrm{grad}\delta) - \dot{w}_\delta, \tag{2}$$

$$\frac{\partial \rho Y_1}{\partial t} + \mathrm{div}\rho Y_1\vec{u} = \mathrm{div}(\rho D\mathrm{grad}Y_1) - \dot{w}, \tag{3}$$

$$\frac{\partial \rho\vec{u}}{\partial t} + \mathrm{div}\rho\vec{u}\cdot\vec{u} = -\mathrm{grad}p + \mathrm{div}J, \tag{4}$$

and

$$\frac{\partial \rho h}{\partial t} + \mathrm{div}\rho h\vec{u} = \Delta H\dot{w} + \mathrm{div}(J\vec{u} + \lambda\mathrm{grad}T + \rho TD\sum_{j=1}^{2}c_{pj}\mathrm{grad}Y_j) + \frac{\partial p}{\partial t}, \tag{5}$$

where ρ, u, p, T are the density, velocity, pressure, and temperature of gas mixture, respectively; Y_i, m_i, c_{pi} ($i = 1,2$ are the mass concentration, molar mass, and specific

heat at constant pressure of the i-th component; $h = \sum_{i=1}^{2} c_{pi} Y_i T + u^2/2$ is the total mixture enthalpy per unit mass; μ, λ, D are the transport coefficients (viscosity, thermal conductivity and diffusivity, respectively); ΔH is the heat release; J is the viscous stress tensor with components $\| \tau^{ik} \|$, $\mathrm{div} J$ is the vector with components $\sum_{i=1}^{3} \nabla_i \tau^{ik}$, $k = 1, 2, 3$; $\mathrm{div} \rho \vec{u} \cdot \vec{u}$ is the vector with components $\sum_{i=1}^{3} \nabla_i \rho v^k v^i$, $k = 1, 2, 3$.

Parameter δ characterizes the part of the induction period left before the explosion.

The chemical kinetics is modelled by a two-stage mechanism involving an induction period, when δ changes from 1 to 0 at the rate $\dot{w}_\delta = K_\delta \rho \cdot \exp(-E_\delta/RT)$ and an exothermic stage with the rate of reaction $\dot{w} = K \rho Y_1 p \chi(-\delta) \cdot \exp(-E_a/RT)$, where E_a, E_δ are the activation energies, and

$$\chi(z) = \begin{cases} 0, & \text{if } z < 0; \\ 1, & \text{if } z \geq 0. \end{cases}$$

The assumption that each component of the combustible mixture has the molar mass m_i and obeys the ideal gas equation of state

$$p = \rho RT \sum_{j=1}^{2} \frac{Y_j}{m_j}, \tag{6}$$

combined with $\sum_{j=1}^{2} Y_j = 1$, closes the set of Eqs. (1) to (5).

One-Dimensional Model

We consider a one-dimensional planar flow of a reactive viscous heat-conducting gas mixture bounded by plane solid noncatalytic walls at $x = 0$ and $x = L$. It is more convenient to study the set of Eqs. (1) to (5) in Lagrangian coordinates $q(x, t) = \int_0^x \rho(r, t) \, dr$. The coordinates (q, t) are particularly useful in the zone of large density gradients.

Note that we can introduce several characteristic times of the process: the acoustic time $t_a = L/a_1$, the conduction time $t_c = L^2 (\lambda_1/\rho_1 c_{p1})^{-1}$, the induction time $t_i = (K_\delta \rho)^{-1} \exp(E_\delta/RT)$, and the characteristic time of heat release $t_e = (K\rho)^{-1} \exp(E_a/RT)$.

The scaling parameters of the system are the following:

$$\mathrm{Re} = \frac{\rho_1 a_1 L}{\mu_1}, \quad \mathrm{Pr} = \frac{\mu_1 c_{p1}}{\lambda_1}, \quad \mathrm{Sc} = \frac{\mu_1}{\rho_1 D_1}, \quad \theta_\delta = \frac{E_\delta}{R_{un} T_1},$$

$$\theta_a = \frac{E_a}{R_{un} T_1}, \quad \frac{\Delta H}{c_{p1} T_1}, \quad \frac{c_{p2}}{c_{p1}}, \quad \frac{m_2}{m_1}, \quad \mathrm{Da}_i = \frac{t_a}{t_{i1}}, \quad \mathrm{Da}_e = \frac{t_a}{t_{e1}}. \tag{7}$$

The dimensionless initial and boundary conditions for the case of forced ignition are:

$$t = 0: \quad 0 \leq q \leq q_0: \quad u = 0, \quad \rho = 1, \quad T = r_T, \quad Y_1 = 0, \quad \delta = 0,$$

$$q_0 < q \leq 1: \quad u = 0, \quad \rho = 1, \quad T = 1, \quad Y_1 = 1, \quad \delta = 1. \tag{8}$$

$$q = 0, \quad q = 1: \quad u = 0, \quad \frac{\partial Y_1}{\partial q} = 0, \quad \frac{\partial \delta}{\partial q} = 0, \quad \frac{\partial T}{\partial q} = 0. \tag{9}$$

Numerical Results

The results are displayed in terms of the nondimensional variables

$$X = \frac{x}{L}, \quad \bar{t} = \frac{tc_1}{L}, \quad \bar{p} = \frac{p}{\rho_1 c_1^2}, \quad \bar{T} = \frac{T}{T_1}, \quad \bar{u} = \frac{u}{c_1}, \quad \rho = \frac{\rho}{\rho_1},$$

where the suffix 1 pertains to the parameters of unreacted combustible mixture. The values of the parameters are as follows:

$$\gamma_1 = 1.4, \quad \frac{c_{p2}}{c_{p1}} = 1.2, \quad \frac{m_1}{m_2} = 0.8, \quad Re_1 = 10^6, \quad Pr_1 = Sc_1 = 0.72,$$

$$\frac{\Delta H}{c_{p1} T_1} = 10: \quad \mathrm{Da}_i \exp \theta_\delta = \mathrm{Da}_e \exp \theta_e = 10^9.$$

Figure 1 corresponds to a transition where the detonation forms at the contact surface that forms in the zone of compressed gas between the leading shock and flame front. This contact surface may result from the shock collision in front of the flame zone, when the ignited zone of gas is located at some distance from the closed end of the tube and the weak shock wave reflected from the wall ($x = 0$) overtakes the leading shock. Figure 3 shows the pressure and temperature profiles for various times. The sharp temperature rise (dashed curve) up to $T \sim 10$ takes place in the flame zone. A contact surface, clearly seen on the temperature profiles, exists between the flame zone and the leading shock at times $t \geq t_3$. The zone between the leading shock and the contact surface has a higher temperature. Thus, the induction period in this zone is shorter than between the flame front and the contact surface. The first explosion takes place in the layer of gas that has been at the higher temperature for the longest time, i.e. in the gas layer adjoining the contact surface. This gives rise to two detonation waves propagating in opposite directions. The intensity of the retonation (reverse detonation) wave drops on entering the reaction products afterwards. The leading forward detonation wave propagates towards the leading shock. After it interacts with the leading shock, an overdriven detonation enters the "cold" mixture. This wave decelerates to the Chapman–Jouguet speed. Our numerical experiments show that the kinetic parameters and the initial preignition state determines where the contact surface between the reaction front and the leading shock is located at the moment of explosion. Thus, the onset of detonation may be located either in the vicinity of the flame front or close to the leading shock.

394
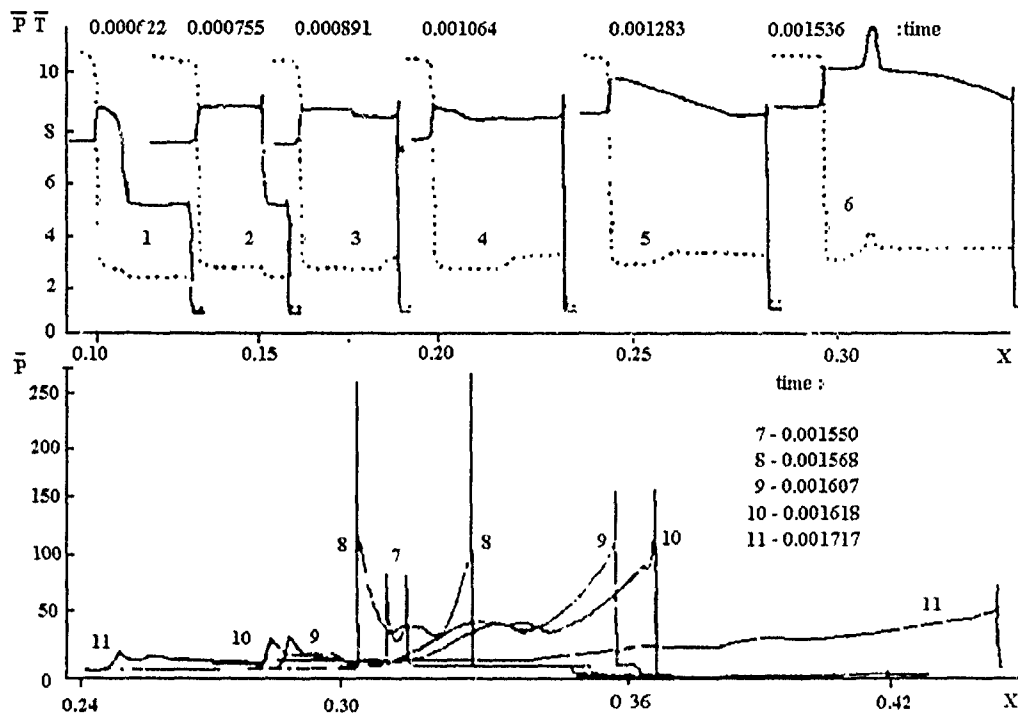
Figure 1: Computed pressure and temperature profiles at different times for the case of deflagration to detonation transition.

Two-Dimensional Model

Although one-dimensional models are very helpful in describing detonation phenomena there exist some peculiarities such as transverse pulsations, wave curvature and lateral expansion in explosions with free boundaries, that can be simulated only within the framework of multidimensional models. In this part of the paper we deal with the detonation in the layer of finite thickness with free boundaries. The plane detonation wave formed in a duct with fixed boundaries at $t = 0$ enters the layer of the same gas mixture with free boundaries. In this case the mathematical model (1)–(5) can be simplified by neglecting the effects of molecular transport. The set of equations was solved using the modified Godunov scheme [12], which provides sufficient accuracy in solving the problems of multidimensional reactive flows [13, 14]. Two groups of ki-

395

netic parameters E_a, E_α, k, k_α were chosen for two types of self-sustaining wave flow patterns: 1) the induction zone is substantially narrower than the reaction zone; 2) the induction zone behind the leading shock is much wider than the reaction zone.
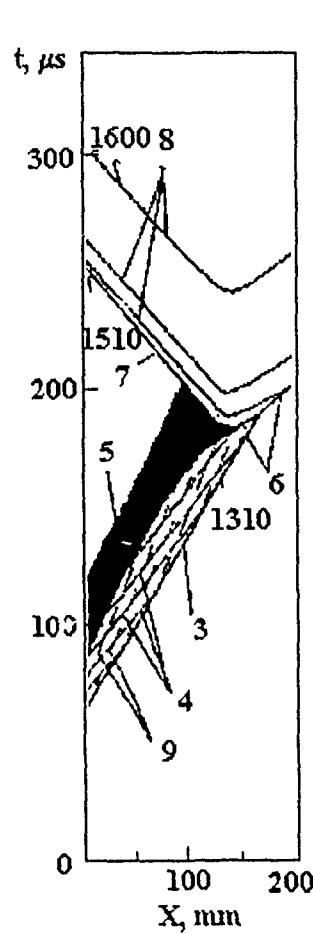
Figure 2.
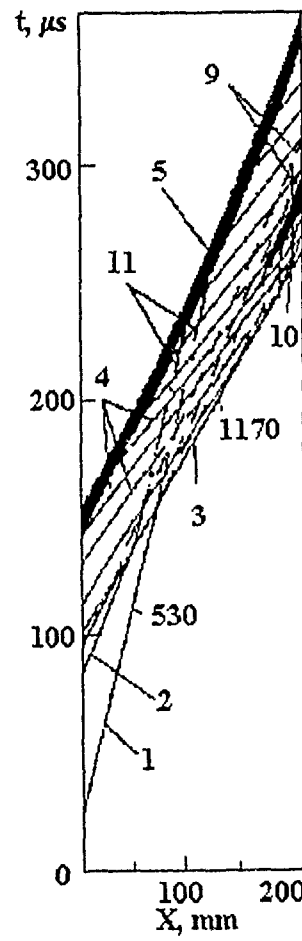
Figure 3.

The self-sustaining detonation velocity depends on the half-thickness of the combustible layer for both types of detonation. For the layers of smaller thickness than the first critical value (H^*), the detonation wave slows down. If the layer thickness H exceeds the second critical value (H^{**}), the detonation wave breaks into a shock wave and a combustion zone lagging behind the shock. It is seen, that for the detonation wave with kinetics of type II the breaking occurs earlier ($H^{**}_{II} > H^{**}_I$).
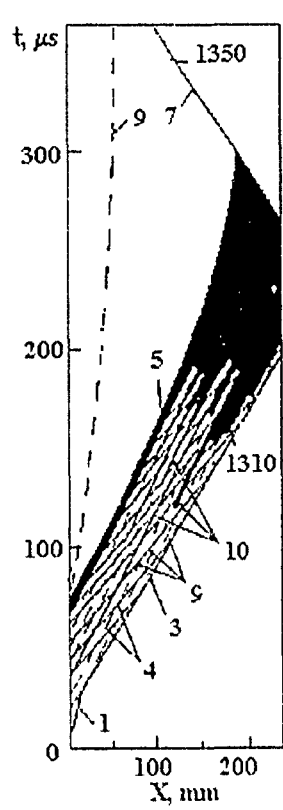
Figure 4.
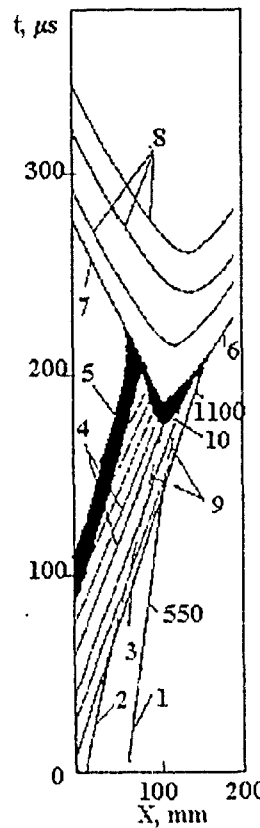
Figure 5.

The flow pattern for the detonation with kinetic parameters of type II turns out to be unstable and exhibits strong transverse pulsations originating in the symmetrical flow as a result of one-dimensional pulsations of the initial plane detonation wave in the bounded duct.

Experimental Results Experimental investigations of deflagration to detonation transition in a hydrocarbon–air mixture were carried out in a square duct of cross section 25 mm × 25 mm. The flow was visualized by a laser schlieren method.

In the end part of the transition section ($L = 1690$ mm), a variety of deflagration-to-detonation transitions occurs. Figures 2 to 5 illustrate different types of flow patterns in the windowed sections. The following nomenclature is used in the figures:

1, 2, 3 are the primary shock waves; 4 is the compression wave; 5 is the flame zone; 6 is the detonation wave; 7 is the retonation wave; 8 are the waves resulting from the reflection of the detonation wave from the tube walls; 9 are the contact surfaces resulting from shock wave interactions, 10 are the spontaneous flames, originating at the contact surfaces; 11 are the first characteristics of rarefaction waves resulting from shock wave interaction; the velocities of waves in meters per second are printed in the figures parallel to the wave trajectories.

It has been shown experimentally that several types of transition processes are possible. The first type (Fig. 2) is as follows: the detonation wave originates in the flame zone, rapidly accelerates and, after the interaction with the leading shock, forms a strong detonation wave which slows down to the Chapman–Jouget regime. In the second type (Fig. 3), the detonation originates at the contact surface located between the leading shock and the flame. This local explosion gives rise to the detonation and retonation waves. The third type (Fig. 4) starts with ignition at the contact surface between the flame zone and the leading shock. Turbulent combustion leads to the onset of detonation and retonation waves. The fourth type (Fig. 5) involves rapid ignition at several locations ahead of the flame zone leading to the onset of the detonation wave. In the latter case, the flow pattern is similar to bulk explosion or spontaneous flame.

References

[1] Oppenheim A. K., Soloukhin R. I. *Ann. Rev. Fluid Mech.*, 1973, **5**, 31.

[2] Salamandra G. D. *et al. Some Methods of Investigation of Highly Transient Processes and their Application to Detonation Wave Formation.* Izd. Akad. Nauk SSSR, Moscow, 1960 (in Russian).

[3] Soloukhin R. I. *Measurement Techniques and Main Results of Experiments in Shock Tubes.* Novosibirsk, Izd. Novosibirsk. Univ., 1969

[4] Zeldovich Ya. B., Librovich V. B., Makhviladze G. M., Sivashinsky G. I. *Zhurnal Prikladnoi Mekhaniki Teknicheskoi Fiziki*, 1970, 2, 76 (in Russian).

[5] Gelfand B. E., Makhviladze G. M., Rogatykh D. I., Frolov S. M. *Spontaneous Forming of Explosive Regimes of Reaction in the Regions with Non-Uniformities of Temperature and Concentration.* Preprint No.358, Moscow, Institute for Problems in Mechanics, 1988 (in Russian).

[6] Clarke J. F., Kassoy D. R., Riley N. *Proc. Roy'al Soc., Lond.*, 1986, **A408**: 129–148.

[7] Smirnov N. N., Demyanov An. Yu., Panfilov I. I. *Khimicheskaya Fizika Protsessov Goreniya Vzriva: Detonatsiya.* Chernogolovka, Izd. Akad. Nauk SSSR, 1989, 52–56 (in Russian).

[8] Urtiew P. A., Oppenheim A. K. *Proc. Roy. Soc., Lond.,* 1966, **A295**, 13.

[9] Urtiew P. A., Oppenheim A. K. *ibid,* 1968, **A304**, 379.

[10] Oran E. S., Boris J. P. *Prog. Energy Comb. Sci.,* 1981, **7**, 1–71.

[11] Smirnov N. N. Panfilov I. I. *Proc. Sci. Conf. (Int.) on Internal Combustion Engines,* Gdansk, 1993, 545–552.

[12] Korobeinikov V. P. *Problems of Point–Blast Theory.* N. Y., American Institute of Physics, 1991, 382.

[13] Levin V. A., Markov V. V., Osinkin S. F. *Dokl. Akad. Nauk SSSR,* 1990, **313**, 2.

[14] Levin V. A , Markov V. V. *Izvestiya Akad. Nauk SSSR. Mekchanika Zhidkosti Gaza,* 1974, 5, 89—93.

THE NON-UNIFORMITY OF CONCENTRATION AS A CAUSE OF DETONABILITY IN A GASEOUS MIXTURE

I. Sochet, A. Reboux, J. Brossard

Laboratoire de recherche Universitaire — Université d'Orléans, 63 Avenue de Lattre de Tassigny, 18020 Bourges Cedex, France

The basic objective of this paper is to define and anticipate the detonability conditions of a nonstationary concentration gradient of an explosive gaseous mixture diluted with air. Following the well-known paper of Zel'dovich et al. (1970), the Russian research team has strongly contributed to the knowledge of the DDT of spatially nonuniform explosive mixtures. Several co-workers including Gelfand, Frolov, Makhviladze, Tsyganov [2, 3, 4] have proposed and validated criteria based upon the Zel'dovich criterion. Numerous important calculated results have confirmed the main idea. Unfortunately, the experimental results are not so numerous because it is difficult to create a well-defined spatial nonuniformity especially that of the gaseous explosive mixture
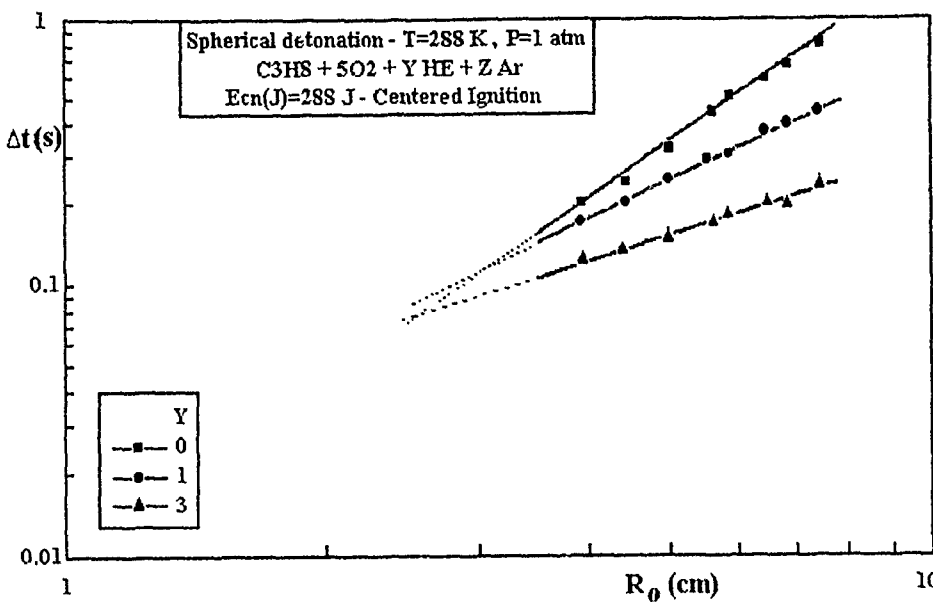
Figure 1: Critical time delay versus initial charge radius for a spatially nonuniform mixture.

concentration. Recent experimental results are briefly presented and similarity relationships are deduced for the case of propane–oxygen–helium mixture diffusing in air. All the results are justified by means of an advection–diffusion model. This paper outlines a criterion which establishes the conditions required for the transition to detonation in a spatially nonuniform gaseous mixture.

The laboratory-scale experiments were conducted at room temperature and atmospheric pressure. The explosive gaseous mixture was introduced into a hemispherical soap bubble confinement. The diffusion of the initially uniform mixture followed until the rupture of the confinement. The stoichiometric propane–oxygen–helium composition ($C_3H_8 + 5O_2 + YHe$, $Y = 0, 1, 3$) diffused in the surrounding quiescent air yielding a spatially nonuniform and nonstationary explosive mixture. After the rupture of the confinement, the time delay Δt during which the detonation was not observed, was investigated. The detonation was initiated by means of a bursting wire located on a plane surface. Figure 1 shows the critical time delay Δt for the initiation, which corresponds to the domains of deflagration and detonation as functions of the charge radius R_0. In this case, the critical energy equals to 288 J for a spherical geometry, was released at the center of the initial charge. The symmetrical propagation of the initial perturbation occured along the negative gradient of reactivity. Further experiments were conducted with an off-center igniter location [5] and confirmed the effect of the gradient of reactivity on the detonability. Two similarity relationships follow directly

400
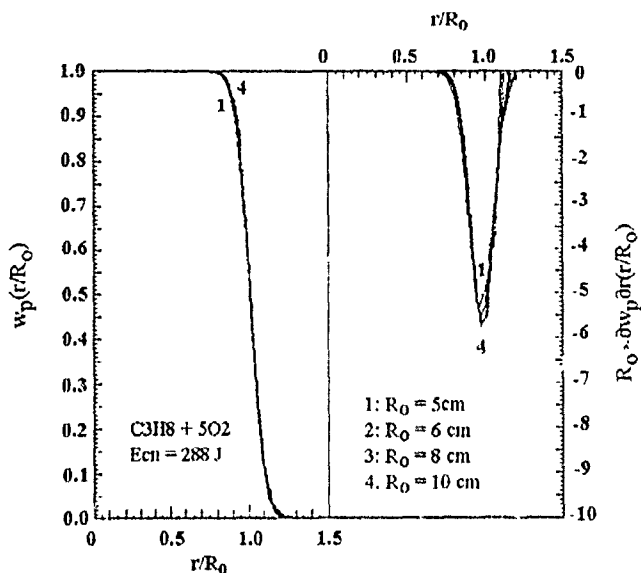
Figure 2: Calculated a) mass fraction and b) nondimensional derivative of mass fraction with respect to radial distance of explosive mixture in air versus nondimensional radial distance at critical time delay.

from these experimental results. The first similarity relationship allowed us to predict the initiation delay as a function of the initial charge radius for a given gaseous mixture and for a given critical energy $\Delta t_2 = \Delta t_1 (R_{02}/R_{01})^\alpha$ where $\alpha(Y)$ is a function of the helium fraction Y. The second similarity relationship was used to predict the initiation delay as a function of the helium fraction Y in the explosive mixture for a given critical energy and an initial charge radius: $\Delta t_{(Y')} = a R_0^b \Delta t_{(Y)}$.

If we assume that the critical time delay determines the spatial dilution distribution of the reactive medium, the same similarity relationships are clearly confirmed by the advection–diffusion model [6], which yields the distributions of concentration ω_p and gradient $\partial \omega_p / \partial r$ at the time Δt just before the explosion. Such a similarity is reported in Fig. 2. We represent the mass distribution of the fraction of stoichiometric propane-oxygen mixture diluted in air on the plane versus the nondimensional radial distance for various initial charge radii and, consequently, for various critical time delays. All the curves $\omega_p(r/R_0)$ and $\partial \omega_p(r/R_0)/\partial(r/R_0)$ merge into one. The possibility to create the detonation of the nonuniform gaseous mixture is directly linked to the concentration gradient. If the time of the explosive mixture dilution is greater than the critical time delay Δt, the local gradient of reactivity is not sufficient for a DDT: the burnt gas expansion cannot intensify the shock wave. The nondimensional derivative of the mass fraction versus the radial distance, $R_0 \partial \omega_p / \partial r$, (Fig. 2) shows a maximum located near the initial charge radius. The peak abscissa is close to the critical radius R_c of

detonation [5] which is defined by $E_c = 4\pi \int_{R_c-\Delta}^{R_c} E_v(r)r^2\,dr \approx 4\pi E_v(R_c)R_c^2\Delta$, where the energy of reaction E_v per unit volume varies as a function of ω_p at any point and any time. In fact, the experiment matches the three fundamental initial parameters R_0, E_c and Δt (or the initial reactivity distribution), so that the critical radius $R_c < R_0$.

Zel'dovich showed clearly the existence of three possible regimes of the development of chemical reaction in a nonuniformly preheated gas. The nonuniformity was characterized by a linear temperature [1, 7] or concentration [8, 4] distribution. These regimes were defined by the propagation velocity of the intensive reaction zone, calculated in terms of the inverse gradient of the induction period. In other words, the shock strength was directly linked to the slope of the temperature distribution. The expressions of detonation and spontaneous flame velocities [2, 3, 4] were based on the initial conditions and particularly on the initial temperature which was of the order of 1000 K. This temperature is very different of the temperature used in our experiments ($\sim$ 300 K) and the strong ignition modified the upstream flow field. Consequently, the spontaneous flame velocity suggested by Makhviladze *et al.* [4] could not be used. So, our local criteria of detonation differ from that proposed by Zel'dovich *et al.* [1–3, 7, 8] and Makhviladze *et al.* [4].

The first approach, to define a detonation criteria of a spatially nonuniform concentration gaseous mixture, based upon the similarity of experimental and theoretical results, leads to the following fundamental remarks:

i) the existence of the critical concentration gradient as defined by the Zel'dovich criteria has been clearly confirmed,

ii) the formulation in terms of the spontaneous flame velocity cannot be directly applied in the case of nonpreheated gas;

iii) the critical radius of detonation seems to be close to the point where $R_0 \partial \omega_p / \partial r$ is maximum.

References

[1] Zel'dovich Ya. B., Librovich V. B., Makhviladze G. M., Sivashinsky G. I. *Acta Astronautica*, 1970, **15**, 313.

[2] Gelfand B. E., Frolov S. M., Polenov A. N., Tsyganov S. A. *Khimicheskaya Fizika*, 1986, **5**, 1277 (in Russian).

[3] Gelfand B. E., Polenov A. N., Frolov S. M., Tsyganov S. A. *Fizika Goreniya Vzriva*, 1985, **21**, 118 (in Russian).

[4] Makhviladze G. M., Rogatykh D. I. *Comb. Flame*, 1991, **87**, 347.

[5] Sochet I., Reboux A., Brossard J. *Proc. 14th ICDERS*, Coimbra, 1993.

[6] Sochet I. *PhD Thesis*, University of Orleans, France, 14 Octobre 1993.

[7] Zel'dovich Ya. B. *Comb. Flame,* 1980, **39**, 211.

[8] Zel'dovich Ya. B., Gelfand B. E., Tsyganov S. A., Frolov S.M. *et al. Prog. Astron. Aeron., Dynamics of Explosions,* 1988, **114**, 99.

THE PHYSICAL FACTORS FAVORING THE DEVELOPMENT OF EXPLOSION IN THE REACTION PRODUCTS – UNBURNED GAS SYSTEM

V. A. Subbotin

Lavrent'uev Institute of Hydrodynamics, Novosibirsk, 630090 Russia

Most studies of shockless (weak or "soft") development of explosion and detonation in gaseous combustible mixtures deal with the flow of hot reaction products out of tube (of a prechamber) into a volume of cold gas. The turbulent mixing and SWACER mechanisms have been proposed, based on such experiments [1]. The two factors required to activate these mechanisms are of physical and chemical nature. Here, the physical factor is formation of large-scale eddies in the unburned gas. The chemical factor is the positive radial field of gradient of the ignition delay time, $\text{grad}\,\tau$, in the vortices generated in the process of mixing of the hot and cold gases. Ya. B. Zel'dovich et. al. [2] were the first to point to the possibility of fast development of detonation in the direction of $\text{grad}\,\tau$ under certain conditions. This phenomenon has been extensively investigated [3], being known as "the gradient mechanism", "selfignition wave", "spontaneous", or "induction" flame.

The peculiarity of the reaction products – unburned gas system is the substantial difference in the densities of its components. In the two-fluid model of [4], this physical factor is included, and the possibility of generating an explosion in the mixture of fragments of the hot and cold gases is demonstrated. Experimentally, the mixture of fragments (MF) may be produced by turbulence. Two other efficient methods for the preparation of MF are:

(1) the above method using a hot gas flow out of a prechamber, and

(2) the mixture ignition by the efflux of hot reaction products into the volume from the periphery of the detonation wave after its passing through a crevice.
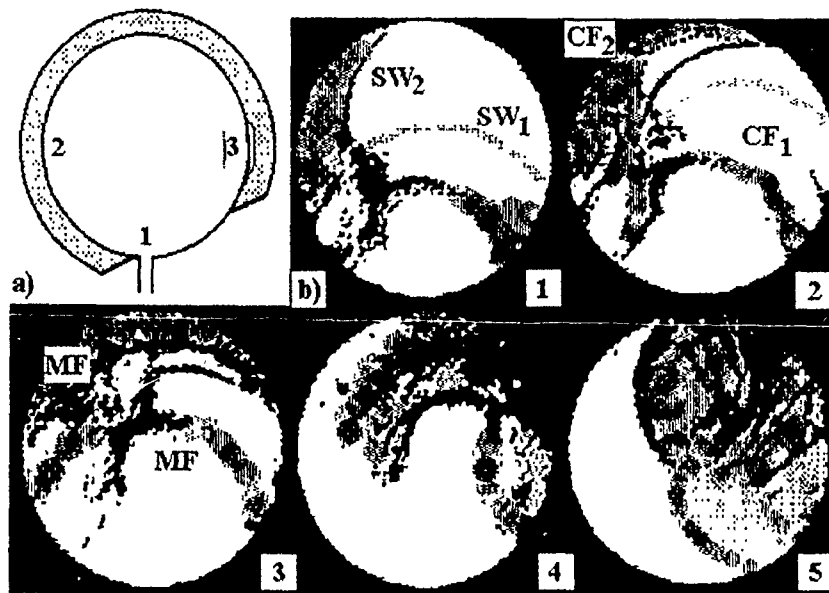
Figure 1: a) Shape of the crevice; *1* — orifice, *2* — crevice, *3* — baffle between crevice and volume. b) SW_1, CF_1 — primary complex: shock wave – combustion front, SW_2, CF_2 — secondary complex, MF — mixture of fragments.

Method 2 was first applied in [5, 6].

Experiments using the second method of mixture preparation were conducted in a dist chamber with a crevice at its periphery. The chamber was made of two rings, 90 mm in inner diameter, glued together. One ring was 9.5 mm thick plexiglass, and the other was 0.7 mm thick rubber. The crevice of outer radius equal to 54 mm was formed by taking rubber off the plexiglass. The crevice shape is shown in Fig. 1a. This sandwich (plexiglass + rubber) was clamped between two cylindrical glass plates 120 mm in diameter.

The process in the chamber was initiated by the entry of a detonation wave through a 3.5 mm diameter orifice drilled in the plexiglass ring. In the vicinity of the outlet, the detonation wave decayed into the primary complex consisting of a shock wave (SW) and a combustion front (CF). High-speed schlieren photographs of the process in the $2H_2 + O_2$ mixture at $p_0 = 0.28$ MPa are presented in Fig. 1b. The detonation in the crevice developed in $t = 40$ μs after its entering the chamber. Its characteristics were as follows: the angular velocity $\omega = 5600$ rad/s, the tangential velocities $V_1 = 2500$ m/s and $V_2 = 3000$ m/s at the inner and outer boundaries of the clearance, and the theoretical $D_{C-J} = 2800$ m/s. The detonation wave in the crevice is not visible and its existence is registered due to the secondary SW–CF complex diverging from the clearance. Their velocities were $V_{sw} \approx 0.34$, $V_1 \approx 850$ m/s, and $V_{cf} \approx 450$ m/s. Frame 1 in Fig. 1b corresponds to $t = 72$ μs, and the time interval between frames is

$\Delta t = 16\ \mu s$. As evident from frames 1 and 2, the secondary SW propagates ahead of the primary one and its origin is not related to the autoignition wave [3]. MF are located near the primary CF and between the chamber wall and the secondary CF. Frame 3 represents the instant when a detonation wave is passing through the crevice section, which is separated from the chamber volume, so that SW and CF are decoupled near the chamber wall. Frame 4 illustrates detonation wave propagation from the crevice into MF and an oval wave propagating into the burned gas. The propagation velocities at the periphery of the wave are close to V_1, whereas middle section has a velocity about 1900 m/s. In the last frame, one can see a semicircular wave which arises in secondary MF and propagates outward at the velocity 2800 m/s. Note that, after the passage of this wave, the MF are not completely burnt and only after being affected by several waves reflected from the walls, the inhomogeneities indicating a fragmentary structure disappear.

The above observations, together with the experiments performed in planar ducts, where the MF was obtained by the first method, indicate that the detonation regimes can arise with out the factors required for the development of detonation via the turbulent mixing mechanism. In the case of the initiation of detonation by a hot gas jet, the key factors providing the appropriate mixing of gases have been found to include:

(1) a supersonic flow of an unburned gas in the volume and

(2) the piston action of reaction products.

The self-ignition of gas in individual isolated volumes ("hot spots") has been shown to affect the process not directly but rather through an increase in the burning rate of MF.

The results presented corroborate the mechanism of explosion initiation by mixing [6]. In the theory, a similar approach to the problem has been employed in the work [4] only. As regards applications, the process shown in Fig. 1b may be considered as a physical model of developing detonation in internal combustion engines ("knock") where squish volumes between the cylinder and the piston always exist. In accident explosions one more mechanism for production of MF may be realized, such as mechanical mixing by fans, propeller blades of helicopters, moving vehicles (such as a railway train), and so on.

References

[1] Knystautas R. *et al. Proc. 17th Symposium (Int.) on Comb.*, The Combustion Intitute, 1979, 1235.

[2] Zel'dovich Ya. B. *et al.*, *Zhurnal Prikladnoi Mekhaniki Tekhnicheskoi Fiziki*, 1970, **2**, 76 (in Russian).

[3] Frolov S. M., Gelfand B. E., Tsyganov S. A. *Fizika Goreniya Vzriva*, 1992, **28**, 5, 13 (in Russian).

[4] Spalding D. B. *AIAA J.*, 1986, **24**, 6, 876.

[5] Subbotin V. A., Mosunov O. B *Dokl. Rus. Akad. Nauk*, 1993, **328**, 3, 352 (in Russian).

[6] Subbotin V. A. *Fizika Goreniya Vzriva*, 1993, **29**, 3, 154 (in Russian).

EXPERIMENTAL INVESTIGATION OF DIFFRACTION OF DETONATION WAVES IN CONDENSED EXPLOSIVES

Zhao Tonghu, Yu Chuan, Sun Chengwei

Laboratory for Shock Wave and Detonation Physics Research, Southwest Institute of Fluid Physics, P.O.Box 523 Chengdu, Sichuan, 610003 China

The experimental investigation of the diffraction of detonation waves in condensed explosives is presented in this paper. The results show that the diffraction pattern of detonation waves varies with the explosive sensitivity and boundary condition. The chemical reaction rate in the vicinity of a convex angle is low and increases gradually with the departure from the convex angle.

1 Introduction

Diffraction is a phenomenon frequently occurring in detonation propagation. It is important for the investigation and practical application of detonations. A number of studies has been dedicated to diffraction of detonation waves. Gibb [1] observed the diffraction of detonation waves passing round a right angle and a circular arch in nitromenthane. Dick [2] observed the diffraction of detonation waves passing round a right angle in the bare explosives X-0290 and X-0219.

In our experiments, we studied the diffraction of detonation waves passing round a right angle in condensed explosives RHT-901 (TNT/RDX = 40/60) and TA01 (TATB/ F2311 = 95/5) and showed that the diffraction pattern of detonation waves varies with the explosive sensitivity and the boundary condition. The chemical reaction rate in the vicinity of a convex angle is small and it increases gradually with the departure from the convex angle.
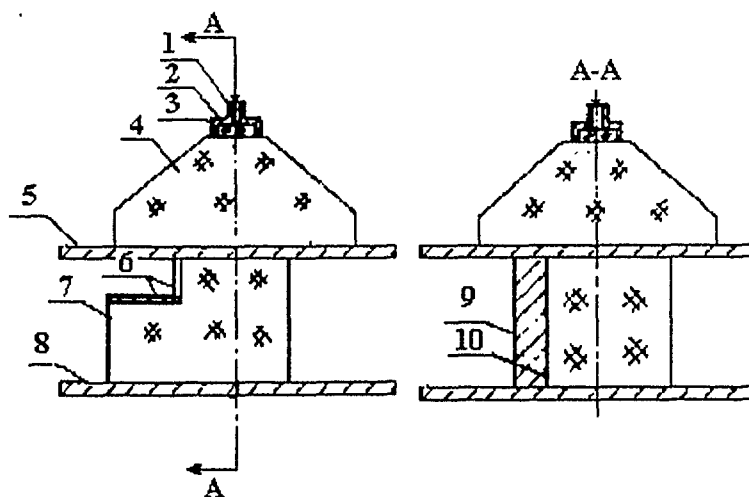
Figure 1: Experimental geometry of the diffraction of detonation wave in condensed explosives. *1.* Detonator; *2.* Case of the detonator; *3.* Booster; *4.* Lens and explosive column; *5.* Al plate; *6.* Steel plate; *7.* Explosive studied; *8.* Al base plate; *9.* PMMA; *10.* Adhesive plaster.

2 Experimental Technique

The experimental geometry is shown in Fig. 1. The initiation system consisted of 100-mm diameter explosive lens, explosive column and Al plate. The rigid wall at convex angle consists of a steel plate of thickness 5 mm. The observation window made of PMMA reduced the effect of lateral rarefaction waves on the detonation wave. The height of the explosives studied was 100 mm and the width was 150 mm. The density of TA01 is 1.888 g/cm^3.

The flow patterns were recorded by a high-speed framing camera at 10^6 f/s. The experimental error was about ±0.5 mm.

3 Results and Discussion

The recorded patterns of detonation fronts are shown in Figs. 2 and 3. The mean curvatures of detonation fronts are given in Table 1.

3.1. It is seen from Figs. 2 and 3 that although all diffractive fronts are in contact with the rigid wall, the details of patterns are different in these two kinds of explosives. There is a zone of weak waves of partial reaction nearby convex angle in TA01 explosive. There is no zone of weak waves in RHT–901 explosive. It can be seen from Table 1 that the curvatures of detonation fronts are also different for these two explosives. The curvatures of detonation fronts in TA01 are larger than that in RHT–901. TA01 is an insensitive explosive whose basic component is TATB and the reactive zone in TA01 is wider than that in RHT–901. The
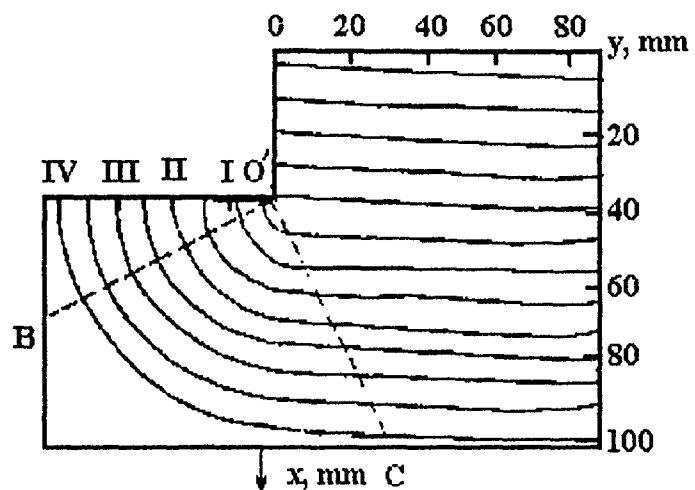
Figure 2: Diffraction pattern of a detonation wave in RHT–901; 1 μs between waves.
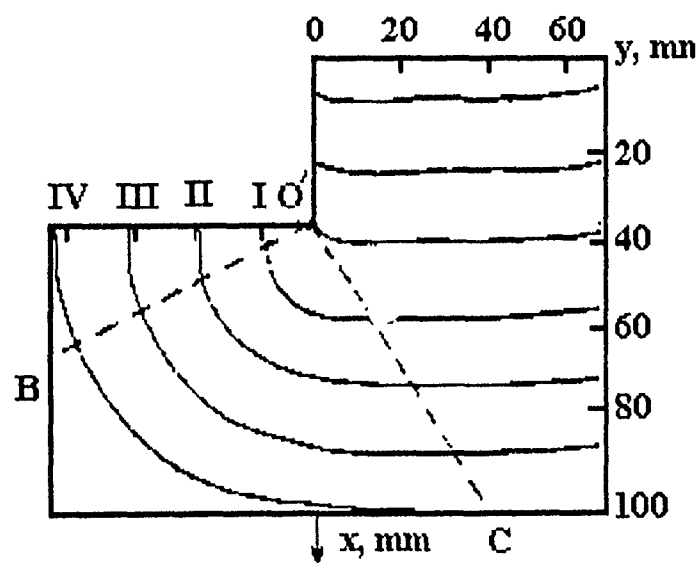
Figure 3: Diffraction pattern of detonation wave in TA01; 2 μs between waves; $-\cdots-$ denotes a weak wave.

Table 1: Mean curvatures (K) of detonation front.

explosive	n	I	II	III	IV
PHT–901	R (mm)	9	26	41	56
	K (1/mm)	0.067	0.029	0.020	0.016
TA01	R (mm)	7	28	44	60
	K (1/mm)	0.07	0.034	0.020	0.017

Note: n are the numbers of detonation fronts in Figs. 2 and 3.
R is the distance from detonation front to vertex of convex
angle along the rigid wall

effect of rarefaction waves which propagate from the vertex of convex angle into the explosive along the detonation front on the patterns of reactive zone and detonation front is different for the two explosives. It is concluded that the performance of diffraction wave pattern varies with explosive sensitivity.

3.2. Dick [2] observed the diffractive pattern of detonation waves in the bare explosive X–0290 (TATB/Kel–F = 95/5), which is similar to TA01, and found a dead zone of no reaction in the pattern. Comparing with our experimental results, we conclude that the boundary condition has an effect on the pattern of diffraction.

3.3. When detonation wave diffracts, the flow includes three zones, according to Whitham's theory [3]: (I) undisturbed zone, (II) disturbed zone, and (III) constant zone. Their boundaries are expressed as lines $O'C$ and $O'B$ respectively in Figs. 2 and 3. The line $O'C$ is related to the points where the larger gradient variation along the experimental wave begins. The fronts of diffracting waves are basically perpendicular to the rigid wall in Figs. 2 and 3. Our analysis shows that Whitham's theory can be used to approximately describe the diffraction of detonation waves.

3.4. Bdzil [4] has proposed the relationship between the depletion of the reaction rate and the normal velocity and the curvature of diverging detonation waves. The normal velocity and the curvature of detonation fronts were measured using Figs. 2 and 3. Then depletions were found from the relationship given by Bdzil. From those depletions, we conclude that the rate of chemical reaction in the vicinity of the convex angle is small and it increases gradually with the departure from the convex angle.

References

[1] Gibb A. W. *PB90–221409*, 1986.

[2] Dick R. D. *LA–UR–76–1425*, 1976.

[3] Whitham G. B. *et al. J. Fluid Mech.*, 1957, **5**, 2, 171.

[4] Bdzil J. B *et al. Proc. 9th Symp. (Int.) on Detonation*, 1989, **1**, 730.

INITIATION OF GASEOUS DETONATION BY A HIGH-VELOCITY BODY

A. A. Vasiljev

Lavrentyev Institute of Hydrodynamics, Siberian Division of the Russian Academy of Sciences, Novosibirsk, 630090 Russia

Professor Jakov B. Zel'dovich, to the memory of whom this International Conference is dedicated, was the one of the pioneers in application of high-velocity blunt-bodies (HVB) to experimental investigation of combustion initiation in explosive gaseous mixtures [1]. The theoretical aspects of the HVB flying in chemically active mixtures are widely investigated in the Institute of Mechanics of the Moscow State University. HVB may be successfully used for supersonic combustion modelling, e.g. in RAM accelerators.

The criterion for detonation initiation by HVB may be formulated as follows: the work of aerodynamic drag force per unit length, when the body moves through an explosive mixture, must exceed the minimum energy of cylindrical initiation of multi-headed detonation:

$$c_x \rho_0 w^2 \pi \frac{d^2}{8} \geq 0.22 \beta n_* \rho_0 D_0^2 b^2, \tag{1}$$

where c_x is the aerodynamic drag coefficient of HVB, ρ_0 is the initial density of the mixture, w is the relative velocity of gas in respect to HVB, d is the effective diameter of HVB, $\beta < 1$ is the efficiency parameter (among distributed and point initiators [2], D_0 is the ideal Chapman–Jouguet detonation velocity for the specified mixture, b is the longitudinal size of an elementary cell of a detonation wave, n_* is the number of
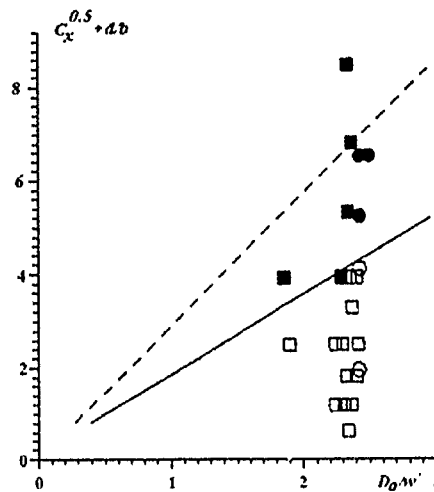
Figure 1.

microexplosions sufficient for initiation of the detonation wave (the model of multi-point initiation geometry [3]).

Equation (1) yields the following relationship between the aerodynamic characteristics of the high-velocity body and the physicochemical parameters of the gaseous explosive gaseous mixture:

$$\frac{d}{b} \geq 0.75 \left(\frac{\beta n_*}{c_x}\right)^{1/2} \frac{D_0}{w}. \tag{2}$$

For a fixed initial pressure of explosive mixture, the values of D_0, n_* and b are constant; therefore, if the shape of HVB does not vary during its flight, c_x is also constant and the criterion for detonation initiation (2) may be represented as follows:

$$dw \geq const. \tag{3}$$

In laboratory investigations of detonation initiation by HVB, it is reasonable to choose the most active media (because of the decrease in the critical initiation energy E_{2*}), to increase the work of aerodynamic drag by increasing c_x (using poorly streamlined bodies), w and the transverse dimension d of the HVB.

A cylindrical projectile ($d = 7.62$ mm) with a hemispherical or plane bow edge was used as a high-velocity body in these experimental studies. The HVB velocity ranged from 800 to 1400 m/s, that is 2 or 3 times lower than the detonation velocity D_0. The experimental data for $C_2H_2 + 2.5\ O_2$ mixture are shown in Fig. 1: the dashed line corresponds to $\beta = 1.0$ in Eq. (2) and the solid line to $\beta = 0.4$ (a distributed initiator exhibits a higher efficiency as compared to point initiation). The value of $\beta = 1$ may serve to predict the body parameters reasonably sufficient for initiation of self-sustained detonation.
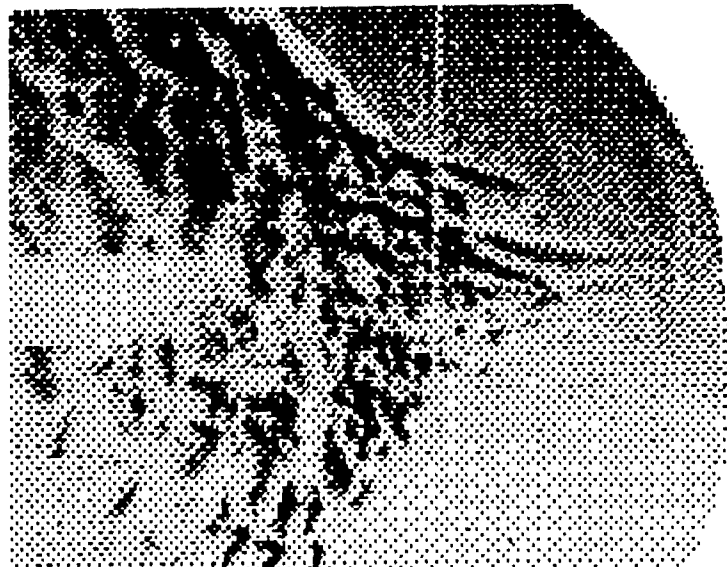
Figure 2.

The analysis of the experimental data for other explosive mixtures with $\beta = 0.4$ shows that they are in good agreement with the initiation criterion (2).

The critical parameters of HVB for detonation initiation are listed in the Table for some stoichiometric explosive mixtures at $p_0 = 1.0$ atm and $w = D_0$:

Mixture			D_0, m/s	b, mm	d, mm
C_2H_2	$+$	$2.5\,O_2$	2424	0 3	0.8
$2H_2$	$+$	O_2	2837	2.6	7.3
CH_4	$+$	$2O_2$	2391	4.7	13.2
C_2H_2	$+$	air	1864	13.6	38
H_2	$+$	air	1966	15.9	45
C_2H_4O	$+$	air	1850	22	62
MAPP	$+$	air	1800	47	132
C3H8	$+$	air	1797	77	216
CH_4	$+$	air	1801	330	920

The new mechanism of ballistic wave transformation to detonation is observed (Fig. 2) at the low-velocity ($w < D_0$) regime of the body flight: high-velocity micro-jets of combustion products, accelerated by the body as a piston, overtake the leading ballistic wave and ignite the initial explosive mixture as a multi-point source, thus forming a multi-front detonation.

References

[1] Zel'dovich Ya. B., Shljapintoh I. Y. *Dokl. Akad. Nauk SSSR*, 1949, **115**, 6, 871 (in Russian).

[2] Vasiljev A. A. *Fizika Goreniya Vzriva*, 1989, **25**, 1, 113 (in Russian).

[3] Vasiljev A. A., Nikolaev Y. A., Uljanitsky V. Y. *Fizika Goreniya Vzriva*, 1979, **15**, 6, 94 (in Russian).

ON THE THEORETICAL ANALYSIS OF A PARTICULAR BOUNDARY CONDITION FOR A CURVED TWO-DIMENSIONAL LEAD DETONATION FRONT

Pierre Vidal, Eric Bouton, Henri-Noel Presles

Laboratoire d'Energétique et de Détonique, URA 193 CNRS ENSMA, B.P. 109, 86960 Futuroscope Cedex, France

Detonation wave front dynamics in condensed explosives is currently studied within the framework of evolution equations which relate the geometric and kinematic properties of the wave surface. Basically, two approaches exist. In one of these, the detonation front is represented by a curved partially reactive sonic hydrodynamic discontinuity, and the analysis leads to a hyperbolic evolution equation which relates the mean curvature, the normal velocity and the normal acceleration of the wave front surface. In the other one, the detonation is considered to have a generalized ZND structure. Under the assumption that the flow behind the leading shock is quasi-one-dimensional and quasi-steady, the analysis leads to a parabolic evolution equation which relates the mean curvature and the normal velocity of the lead detonation shock surface. These evolution equations have the common feature of being solely dependent of the explosive material properties. To use these models for studying constant-velocity curved two-dimensional detonations, first, it is necessary to define proper boundary conditions at the edge of the explosive charge which relate the detonation wave front slope to its velocity. The shape and velocity of the detonation wave front are then uniquely defined for a given transverse size of the charge.

413
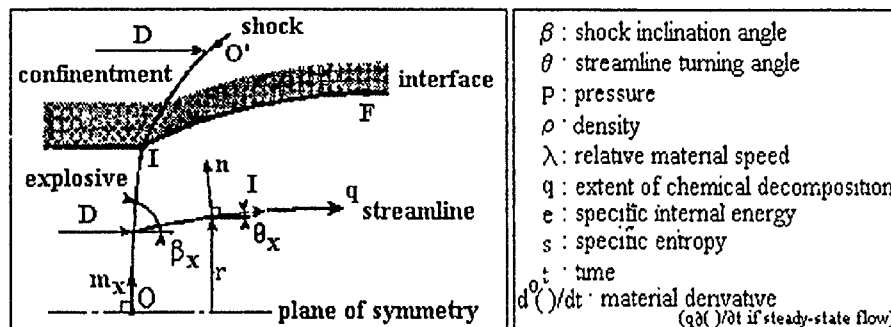
Figure 1: Confined two-dimensional detonation.   Table 1: Nomenclature.

The objective of this short communication is to summarize the principle, the results and the conclusions of the theoretical analysis of the interaction between a constant-velocity curved two-dimensional lead detonation front and the surrounding medium. More specifically, we studied the case of pure refraction, restricting our attention to the interaction point I of the shock fronts in the explosive (X) and its confinement (C) (Fig. 1)

Within the framework of the two-dimensional ZND structure, we first demonstrated that, at point I, exact expressions for all the geometric properties of the shock fronts in X and C (the curvatures C_x and C_c and their 1st, 2nd, ..., n^{th} derivatives along the shock lines) could be obtained as functions of the detonation translational velocity D, the material properties of X and C and, if the flow was axially symmetric, the radius of the explosive charge. These expressions were obtained from the constraints imposed on the flow derivatives of the pressure p and the flow turning angle θ by the conservation laws, the boundary conditions at the curved shock fronts and the contact conditions matching p and θ along the explosive-confinement interface. Thus, in contrast with the models described above, we have shown that there exists a situation where the geometrical properties of a curved detonation wave front depend on the material properties of both the explosive and the confinement.

Next, used these results in our numerical analysis of a polytropic explosive with a one-parameter pressure dependent decomposition rate and an inert polytropic confinement to determine how the relationship between the explosive's interface curvature C_x and the detonation translational velocity D depend on the properties of X and C and on the parameter a of the decomposition rate (Fig. 2). We have found that.

414
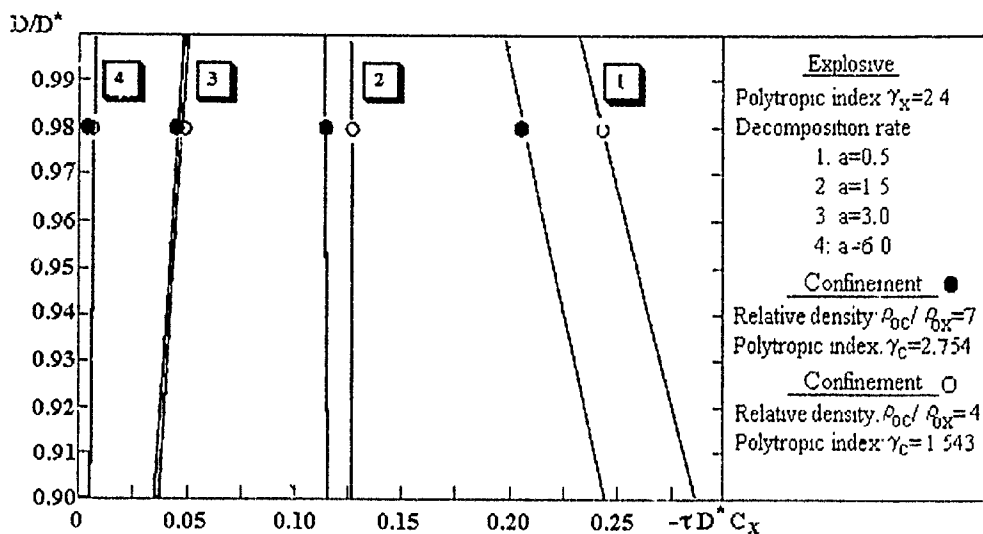
Figure 2: Plots of the nondimensionalized detonation velocity D/D^* versus the nondimensionalized explosive's interface curvature $-\tau D^* C_x$ for a polytropic explosive, two polytropic confinements and the decomposition rate law $w_x = \tau^{-1}(p_x/p_{ref})^a(1-\lambda_x)^b$ in the case of a planar explosive charge configuration. (D^* is the CJ detonation velocity.)

1. For a given velocity D, the absolute value of the explosive interface-shock curvature, C_x, decreases as the confinement density increases. (In our work, C_x denotes the value at point I of the curvature of the explosive's meridian shock line and is defined by $C_x = d\beta_x/dm_x$. Usually, as in our study (Fig. 1), C_x is negative because β_x decreases when m_x increases, so that the concave face of the lead detonation front is oriented towards the reaction zone). Also, the distance between the curves corresponding to two different confinements and the same value of the parameter a decreases as the value of a increases.

2. Depending on the pressure exponent a in the decomposition rate, the slope of the curves can be positive, infinite or negative. Also, an increase in a leads to an increase in the reaction completion time.

3. The same considerations apply to the dependence of the normal detonation velocity $D\sin(\beta_x)$ and the explosive's interface curvature.

Finally, we suggest that one should distinguish between two cases of dynamical behavior for lead detonation fronts propagating in two-dimensional charges under the pure-refraction boundary condition:

In the first case, the explosive has a sufficiently short reaction zone, so that only a very narrow domain in the vicinity of the explosive–confinement interface has a signif-

415

icant influence on the lead detonation front geometry. Consequently, the dynamic behavior of such explosives would be correctly described by evolution equations uniquely determined by the properties of the explosive.

In the second case, the explosive has a sufficiently long reaction zone, so that a wide flow region in the explosive receives information from the explosive–confinement interface. In this case, it seems reasonable to expect that the domain of the dependence of the lead detonation front geometry on the confinement material properties evidenced in our work is not restricted to the close vicinity of the interaction point but extends to a large part of the lead detonation front and, presumably, even includes the explosive charge axis. Consequently, the dynamic behavior of the lead detonation front would obey more complicated evolution equations than in the first case.

References

[1] Brun L. R. *CEA–DAM, CEV–DPM*, DO89023, 1989.

[2] Klein R. *SIAM J. Appl. Math.*, **53**, 5, 1401–1435, 1993.

[3] Vidal P. 1993 (submitted).

ANALYSIS OF THE DETONATION PRODUCTS OF INSENSITIVE HIGH EXPLOSIVES

F. Volk

Fraunhofer-Institut für Chemische Technologie (ICT), Pfinztal, 76327 Germany

The detonation products of high explosives depend on pressure and also on the confinement under which the detonation reaction proceeds. To determine the detonation products of less sensitive high explosives such as TNT/nitroguanidine (NQ) and PBX charges with polybutadiene (PB) binder containing RDX together with or without aluminum (AL), experiments have been performed in a stainless steel chamber of volume 1.5 m^3. These experiments were done under various ambient argon pressures up to 0.1 MPa. The gaseous reaction products were analyzed by mass spectrometry and chemiluminescence analysis. The solid reaction products were analyzed for measuring the carbon residue.

Table 1: Unconfined Charges of 45% TNT/55% NQ at Different Argon Pressures.

Sample No.		1450/1c	1450/2c	1450/3c
Ar pressure [MPa]		Vac.	0.05	0.1
Composition			45% TNT/55% NQ	
O_2 Balance [%]			−47.6	
Charge Weight [g]		331	332	331
ΔH_f [kJ/kg]		−661	−662	−657
Products [mol %]	H_2	20.7	8.3	5.3
	CH_4	0.04	0.1	0.24
	CO	32.1	17.9	14.3
	CO_2	3.7	7.9	10.3
	N_2	27.5	26.1	25.6
	NO	0.1	0.1	0.13
	HCN	0.3	3.2	3.6
	NH_3	0.5	3.0	4.9
	C_2H_2	0.02	0.03	0.1
	H_2O	10.7	19.6	20.0
	C_3	4.4	13.8	15.9
ΔH_{det} [kJ/kg]		2999	3653	3763
C in Residue [% of total C]		10.8	32.2	35.7
Gas formation [mol/kg]		44.5	37.9	35.7

In has been found that the detonation products were highly dependent on the ambient pressure of argon. The most important changes in the reaction products and therefore also in the energy output have been found between vacuum and atmospheric pressure of argon. With increasing pressure, H_2 and CO decrease, and CO_2, H_2O, C_3, NH_3 and CH_4 increase together with the reaction enthalpy. By analyzing the physical structure of the carbon residue, diamonds have been observed between 4 and 7 nm in diameter. In more detail, the following main results have been found:

Unconfined Charges of 45% TNT/55% NO

Table 1 shows the reaction products of TNT – nitroguanidine (NQ) mixtures formed by detonation in vacuum, under 0.05 MPa (0.5 bar), and 0.1 MPa of argon. There is a very clear change in the products with the pressure varied from vacuum to 0.1 MPa of argon (1 bar Ar).

With increased argon pressure we see a distinct decrease in H_2 and CO and a strong

Table 2: Charges of 45% TNT/55% NQ in Class Confinement at Different Argon Pressures.

Sample No.		1451/1	1451/2	1451/3
Ar pressure [MPa]		Vacuum	0.05	0.1
Composition		45% TNT/55% NQ		
O_2 Balance [%]			−47.6	
Charge Weight [g]		332	335	332
ΔH_f [kJ/kg]		−656	−658	−658
Products [mol %]	H_2	8.7	4.2	3.1
	CH_4	0.2	0.4	0.44
	CO	15.9	10.2	9.3
	CO_2	7.9	11.9	12.7
	N_2	27.3	26.0	25.6
	NO	0.06	0.05	0.14
	HCN	1.35	2.4	1.1
	NH_3	1.15	4.7	5.3
	C_2H_2	0.07	0.1	0.13
	H_2O	20.5	20.7	21.0
	C_3	16.8	19.2	21.3
ΔH_{det} [kJ/kg]		3779	3960	4003
C in Residue [% of total C]		39.8	43.3	47.2
Gas formation [mol/kg]		37.1	34.4	33.0

increase in CO_2, H_2O and solid carbon (C_3). The energy output increases markedly from vacuum to 0.05 MPa argon, but only slightly from 0.05 MPa to 0.1 MPa of argon. In the same direction, the gas formation decreases.

Charges of 45% TNT/55% NO in a Glass Confinement

Table 2 shows the results of the same composition of the explosive charge, but packed into a glass tube with the wall thickness of 9 mm. In this case, we also see a decrease in H_2 and CO, but a smaller increase in CO_2, H_2O, C, and the energy output. The reason for this behavior is that the glass confinement by itself increases the energy release, as indicated by the comparison between the vacuum experiments of Tables 1 and 2. This means that the glass confinement increases the efficiency of the argon pressure when going from vacuum to one bar of argon.

Table 3: PBX Charges of 80% RDX/20% PB.

Sample No.		HX 72/1	HX 72/2	HX 72/3
Ar pressure [MPa]		Vacuum	0.05	0.1
Composition		20% PB/80% RDX (10 μm)		
O_2 Balance [%]			−73.3	
Charge Weight [g]		329	328	330
ΔH_f [kJ/kg]		−94	−90	−95
Products [mol %]	H_2	33.5	15.0	12.3
	CH_4	0.1	0.7	2.9
	CO	34.4	17.3	13.1
	CO_2	1.2	3.5	6.6
	N_2	18.8	18.0	18.8
	NO	0.05	0.03	0.02
	HCN	0.1	0.8	0.9
	NH_3	0.5	2.9	2.8
	C_2H_2	—	0.06	0.5
	H_2O	4.8	19.6	19.9
	C_3	6.6	22.2	22.2
ΔH_{det} [kJ/kg]		2949	4214	4440
C in Residue [% of total C]		15.7	49.9	47.3
Gas formation [mol/kg]		52.1	42.0	39.7

Composite Charges of 80% RDX/20% PB

Composite explosive charges consisting of 80% RDX and 20% polybutadiene binder (PB) were investigated under unconfined conditions. From Table 3 it is clear that composite explosive charges exhibit the same behavior of the detonation products as the mixtures consisting of TNT and nitroguanidine (NQ). This involves an increase in CO_2, H_2O and C_3, combined with an increase in the energy output from 2949 kJ/kg to 4440 kJ/kg due to changing from vacuum to 0.1 MPa of argon.

Future experiments will deal with Al-containing high explosives and their products from underwater detonations.

APPLICATION OF THE GENERALIZED GEOMETRICAL OPTICS MODEL TO DETONATION WAVE PROPAGATION

Gao Wen, Sun Chengwei, Wei Yuzhang, Fang Qing

Laboratory for Shock Wave and Detonation Physics Research, Southwest Institute of Fluid Physics, P.O. Box 523, Chengdu, Sichuan, 610003 China

A simple and efficient Huygens calculation can be used for detonation propagating in high explosive, because the reaction zone effect is so slight that it can be ignored. However, because there is a thicker reaction zone in an insensitive high explosive (IHE), which results in that the reaction rate and detonation velocity in the IHE strongly depend on the detonation wave front curvature. It is necessary to study the reaction zone effects in order to describe the two-dimensional detonation wave propagation.

Beside numerical simulations by using 2-D reactive hydrodynamic code, analytics is a reasonable way to study the reaction zone effects on detonation. Based on the reasonable assumption that the curvature radius of detonation front is by an order of magnitude larger than the chemical reaction zone length, Bdzil [1] and Stewart [2] developed the detonation shock dynamics (DSD) theory, which can be used to describe 2-D detonation wave propagation, especially in IHE. Bdzil, Stewart and Lambourn [3] have proposed different forms of basic equation for DSD, and Sun Chengwei [4] has developed a generalized geometrical optics model and derived a similar evolution for a weakly curved detonation front.

Using the computer code mentioned above, the detonation propagation in IHE charges of two geometric shapes was numerically simulated. The results are compared with the Huygens calculation for the C–J wave and the experimental data as follows.

Figure 1 shows the calculation for the rate-strick explosive charge (20 mm dia.), where circles denote the measured points.

Figure 2 shows detonation propagation in a semi-spherical IHE charge, where solid and dashed lines denote the generalized model and Huygens calculations, respectively.

The calculated and experimental wave forms on the diverging detonation emerging on the charge surface of radius 30 mm are shown in Fig. 3.

The experiments and the GGO model calculations on the explosive charges with more complex geometrical shapes were carried out, and the agreement between them is rather satisfactory. However, the classical Huygens calculations obviously deviate from the experiment on IHE charges.

References

[1] Bdzil J. B., Stewart D. S. *Phys. Fluids A*, 1989, **1** (7), 1261–1267.

[2] Stewart D. S., Bdzil J. B. *Comb. Flame*, 1988, **72**, 311–323.
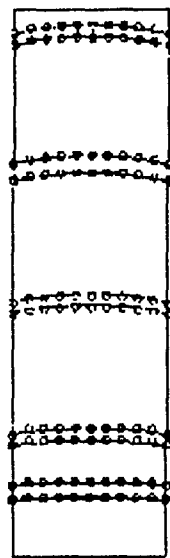
Figure 1: Detonation propagation in a strick explosive.
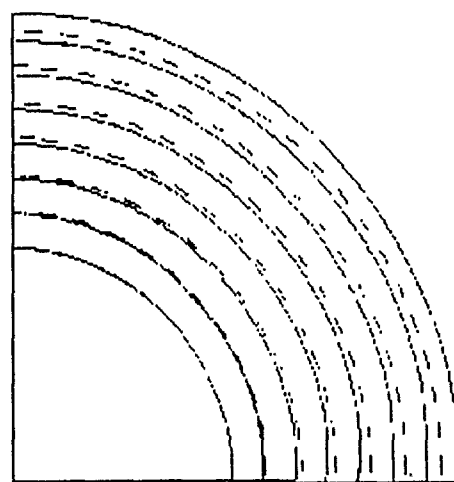
Figure 2: Detonation propagation in a semi-spherical IHE charge.

421
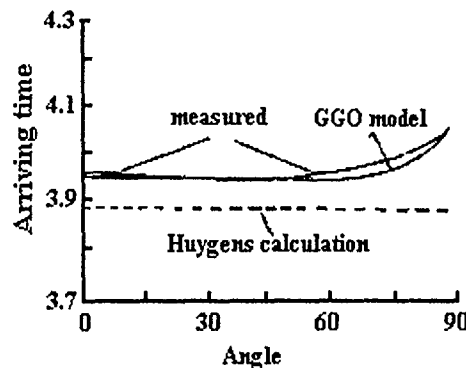
Figure 3: Arrival time of detonation waves at the surface of semi-spherical IHE charge of radius 30 mm.

[3] Lambourn B. D., Swift D. C. *Proc. 9th Symp. (Int.) on Detonation,* Portland OR., Office of Naval Research, 1989, 784–797.

[4] Sun C. W. *Explosive and Shock Waves*, 1992, **12** (1), 89–96.

IMPULSE PRODUCED BY GAS DETONATION IN OPEN CHAMBER

S. A. Zhdan, V. V. Mitrofanov, A. I. Sychev

Lavrentyev Institute of Hydrodynamics Novosibirsk, 630093 Russia

There are several known schemes of detonation combustion applied in the corresponding jet engines:

a) oblique detonation jump in a combustion chamber of ramjet, first considered by Ya. B. Zel'dovich in the 1940's [1],

b) transverse detonation waves in circular or cylindrical combustion chambers of rocket motor, the scheme of B. V. Voitsekhovskii [2],

c) single or repeated explosion of a detonating propellant charge in open conical nozzle, the scheme of G. Varsi *et al.* [3].

The latter scheme was studied for condensed high explosives. Presented below are the results of experimental and numerical studies of reactive impulse produced by detonation of gaseous acetylene–oxygen mixture in cylindrical chamber with an open end.

Experimental

The experiments have been performed by using the "ballistic pendulum" assembly, which is an explosive chamber (EC) suspended at a long thin steel wire. EC is a cylindrical steel tube of inner diameter 107 mm. One end of the tube was closed, while the other could be shutted off by a diaphragm (lavsan film 100 μm thick). The diaphragm provided a possibility to vacuumize the EC before filling it with gaseous mixture ($C_2H_2 + 2.5O_2$). The initial gas pressure in the chamber was $p_0 = 1$ atm.

Detonation was initiated in EC by transmitting a detonation wave from the initiating tube (4 mm inner diameter) into the chamber. To intensify the process, a reflecting screen (a disc 15 mm in diameter) was placed in the initiating tube at the distance of about 10 mm from the tube exit. When the gaseous mixture was ignited, the pressure in EC increased resulting in diaphragm bursting and gas outflow from the open chamber end, and, hence EC deflecting in the opposite direction. The deflection of EC (used for estimating the impulse of the products of gaseous detonation) was measured by drawing of thin thread fixed to it. The height of the chamber suspension (3.4 m) ensures its deflection for 20–60 cm, which made it possible to determine the value of the impulse with the accuracy of ±2–3%.

Numerical Simulation

The motion of a detonating gas in EC was described by two-dimensional nonstationary equations of gas dynamics in axisymmetrical statement [4]. In the equation of state the dissociation and recombination of combustion products were taken into account by using the equation of chemical equilibrium [5]. The numerical algorithm is based on the method of S. K. Godunov [4]. Calculations were carried out for the mixture $C_2H_2 + 2.5O_2$. In calculations the force $F(t)$ acting on the EC end wall and impulse $J(t)$ were determined as follows:

$$F(t) = \pi \int\limits_0^{r_0} (p(0, r, t) - p_0)dr^2, \qquad J(t) = \int\limits_0^t F(t)dt.$$

The following parameters were varied in the experiments and calculations:

a) the chamber volume;

b) the extent of filling the chamber volume by reacting mixture;

c) the place of initiation of gaseous detonation.

423

Table 1.

N	L_0/cm	x_0/L_0	x_*/L_0	I_{exp}	I_{cal}	I_1^{max}	I_1^{min}
1	12.5	1	0	198 ± 5	160	179.3	158.4
2	25	1	0	198 ± 3	163.2	174.7	162.9
3	25	1	1/2	196 ± 3	158	169.5	157.6
4	25	1	1	194 ± 3	—	—	—
5	50	1/2	0	250 ± 5	245	258.3	243.0
6	50	1/2	1/2	245 ± 5	226	239.2	223.7
7	37.5	1/3	0	300 ± 10	295	321.1	294.9
8	75	1/3	0	315 ± 5	307	321.6	304.9
9	100	1/4	0	375 ± 5	364	377.3	358.9
10	62.5	1/5	0	415 ± 10	391	416.8	388.1
11	87.5	1/7	0	505 ± 10	465	490.9	456.5
12	125	1/10	0	—	540	573.4	528.2

Results

Pressure records taken at the closed end of EC are of oscillatory character, which is indicative of reciprocating gas flows. The predicted thrust $F(t)$ is also nonmonotonic and, furthermore, it is of alternating sign. Such a dependence of F on time implies that the impulse $J(t)$ and, consequently, the specific impulse $I(t) = J(t)/(g\rho_g V_0)$ are nonmonotonic functions. The impulse $I(t)$ attains first its maximum value I_1^{max}, then decreases, and, passing through minimum I_1^{min}, slightly oscillates with rapidly damping amplitude. Relative amplitude of the second impulse oscillation does not exceed 1–2%, contrary to the HE explosion in cone [3]. Experimental (I_{exp}) and asymptotic calculated (I_{cal}) values of specific impulses are presented in the Table 1. The value I_{exp} was determined from relationship:

$$I_{exp} = \frac{m_c l(rg)^{-\frac{1}{2}}}{\rho_g V_0},$$

where ρ_g and V_0 are the density and volume of mixture, respectively, g is the acceleration of gravity; m, l, and r are, respectively, the mass, deviation and suspension height of EC, L_0 is the length of EC, x_0 is the chamber part filled with detonable mixture; x_* is the distance from the closed end to the point of detonation initiation.

The calculated and experimental results show that I significantly depends on the extent of filling the chamber by the active mixture, x_0/L_0 As this ratio decreases, the maximum and asymptotic values of specific impulse increase. At $x_0/L_0 < 1/3$ the specific impulse in the cylindrical EC becomes higher than under stationary outflow of combustion products of the same mixture from the chamber with Laval nozzle, where

$I \in (280\text{–}320)$ s [6] when the pressures in the chamber and at the nozzle section are with in the range 20–100 bar. When the extent of filling is 1/10, the impulse gain is 1.5-hold (see Table 1). Limiting value of impulse J_{cal}^{∞} at $L_0 \to \infty$ may be obtained from the formula $J_{cal}^{\infty} = (\gamma - 1)E_0/c_0$ [7], where γ and c_0 are, respectively, the adiabat index and sound speed in air, E_0 is the effective explosion energy transmitted to the shock wave. From our calculations for the mixture $C_2H_2 + 2.5O_2$, the limiting specific impulse is $I_{cal}^{\infty} = 689$ s.

The influence of the initiation point location is insignificant both with and without air "ballast" in EC. For $x_0/L_0 = 1$ the experimental values exceed the calculated ones due to the influence of the bursting diaphragm mass. We failed to obtain specific impulse higher than that for cylindrical chamber by varying the EC geometry (the calculations were also performed for the EC with the shape of truncated cone and semisphere).

The research was supported by Russian Foundation for Fundamental Research (No.93-013-17360).

References

[1] Zel'dovich Ya. B. *Zhurnal Technicheskoi Fiziki*, 1940, **10**, 17, 1453 (in Russian).

[2] Voitsekhovskii B. V. *Dokl. Akad. Nauk SSSR*, 1959, **129**, 6, 1254 (in Russian).

[3] Back L. H., Dowler W. L., Varsi G. *AIAA J.*, 1983, **21**, 10, 1418.

[4] Godunov S. K., Zabrodin A. V. *et al. Numerical Solution of Multidimensional Problems of Gas-Dynamics.* Moscow, Nauka, 1976 (in Russian).

[5] Nikolaev Yu. A., Fomin P. A. *Fizika Gorenia i Vzriva*, 1982, **18**, 1, 66 (in Russian).

[6] Alemasov V. E. *Theory of Rocket Engines.* Moscow, Oborongiz, 1962 (in Russian).

[7] Stanyukovich K. P. *Unsteady Motion of Continuum.* Moscow, Nauka, 1971 (in Russian).

A COMPREHENSIVE CRITERION FOR SHOCK INITIATION OF HETEROGENEOUS HIGH EXPLOSIVES

Wang Zhiping, Wei Yuzhang

Laboratory for Shock Wave and Detonation Physics Research, Southwest Institute of Fluid Physics P.O. Box 523–61, Chengdu, Sichuan 610003, China

By investigating various shock initiation criteria and experimental data for the HNS-I$_4$ and JO9159 explosives, a comprehensive criterion for shock initiation of detonation in heterogeneous high explosives is suggested and the critical curves of shock pressure p vs pulse duration τ are plotted.

The competition of energies released by chemical reaction and consumed by rarefaction and their influence on shock initiation are discussed.

Various shock initiation criteria have been proposed during past decades, for example,

(1) for 1-D sustained-duration shock waves in thick explosive slabs [1]:

$$p = p_c; \qquad (1)$$

(2) for 1-D short-duration shock waves in thick explosive slabs [2]:

$$p^n \tau = N; \qquad (2)$$

(3) for 2-D sustained-duration shock waves induced by the impact of small projectiles [3]:

$$p^m a = M. \qquad (3)$$

4. The POP plot suggested by Ramsay and Popolato [4],

$$p^b x = B, \qquad (4)$$

can be regarded as the criterion for thin explosive slabs initiated by 1-D shock waves, because, when the explosive slab is thinner than the run distance to detonation corresponding to the shock pressure, it can not be initiated. Therefore, the run distance to detonation is the critical thickness of the explosive slab in this case.

5. As for the criterion suggested by Stresau and Kennedy [5]

$$(p^n - p_c^n)\tau = N, \qquad (5)$$

it appears to be a generalized form of Eqs. (1) and (2).

In these expressions, p is the shock pressure, τ is the pulse duration, a is the loading area, X is the thickness of explosive slabs, and the other parameters are constants.

The above criteria are good for particular cases. However, there are some gaps concerned in practice, such as the behavior of an explosive of finite thickness and shock initiated by a thin flyer of small diameter, where both the flyer thickness and its diameter affect the initiation threshold.

Based on the afore mentioned criteria and extensive experimental data for the HNS–I_4 (HNS–I/additive = 97.5/2.5, $\rho_0 = 1.57$ g/cm^3) and JO9159 (HMX/additive = 95/5, $\rho_0 = 1.86$ g/cm^2 explosives, a comprehensive criterion for shock initiation of heterogeneous high explosives has been suggested in the general form

$$p^{2n} = \left(\frac{B}{x}\right)^{\frac{2n}{b}} + \left(\frac{N}{\tau}\right)^2 + \left(\frac{M}{a}\right)^{\frac{2n}{m}}. \tag{6}$$

The shock initiation threshold pressure in HNS–I_4 and JO9159 loaded by the electric gun were measured for various durations (flyer thicknesses) and loading areas (flyer diameters). The initiation thresholds were determined by the "up-down" procedure (Bruceton method). Thus, we obtained the coefficients in Eq. (6) for the HNS–I_4 explosive (d is the flyer diameter):

$$p^{4.63} = 90 + \left(\frac{160}{d^2}\right)^{1.70} + \left(\frac{0.835}{\tau}\right)^{2.65}, \tag{7}$$

and for JO9159

$$p^4 = 600 + \left(\frac{3000}{d^2}\right)^{1.6} + \left(\frac{5.4}{\tau}\right)^2 \tag{8}$$

The fitting deviation was smaller than $\pm2\%$ for HNS–I_4 and $\pm5\%$ for JO9159 (see Fig. 1 and Fig. 2).

From Fig. 1 and Fig. 2, it is concluded that

1. For the thin flyer, τ is small, and the side rarefactions can be neglected as compared with the back rarefactions. The initiation threshold obeys the criterion $p^n\tau = N$.

2. With increasing τ, the side rarefaction gains influence, both back and side rarefactions affect the behavior of $p \sim \tau$ curve which changes from the 1-D to 2-D case and is called as "2-D short duration shock initiation".

3. As τ is increased further, the side rarefaction becomes dominant and the bask rarefaction can be neglected. The p-τ curve evolves into that corresponding to the 2-D shock initiation by a small diameter projectile impact, and can be described by the criterion $p^m a = M$.

4. Finally, as both the flyer thickness and diameter are increased, the p-τ curve tends to a constant pressure plot similar to the 1-D sustained-duration shock initiation, where the criterion is $p = p_c$.
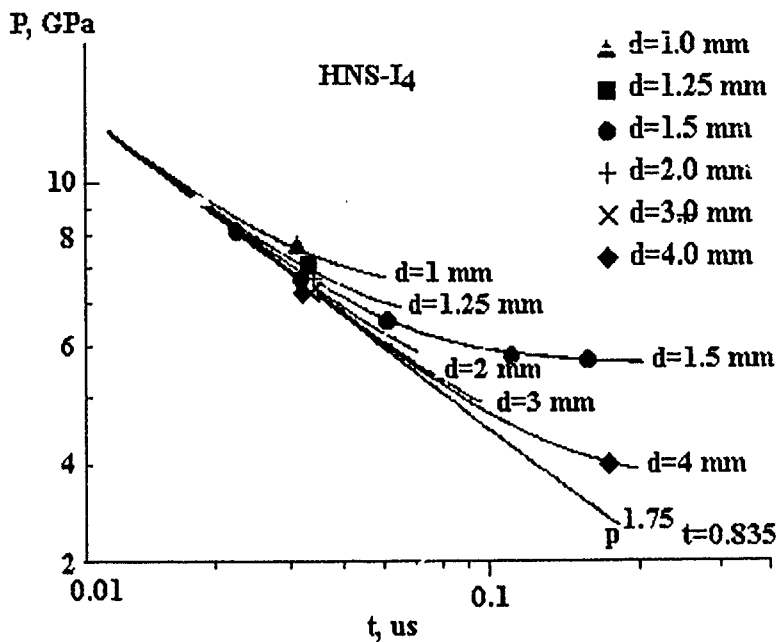
Figure 1: The $p \sim \tau$ curve for HNS–I_4 explosive, $(\rho_0 = 1.57 \text{ g/cm}^3)$.
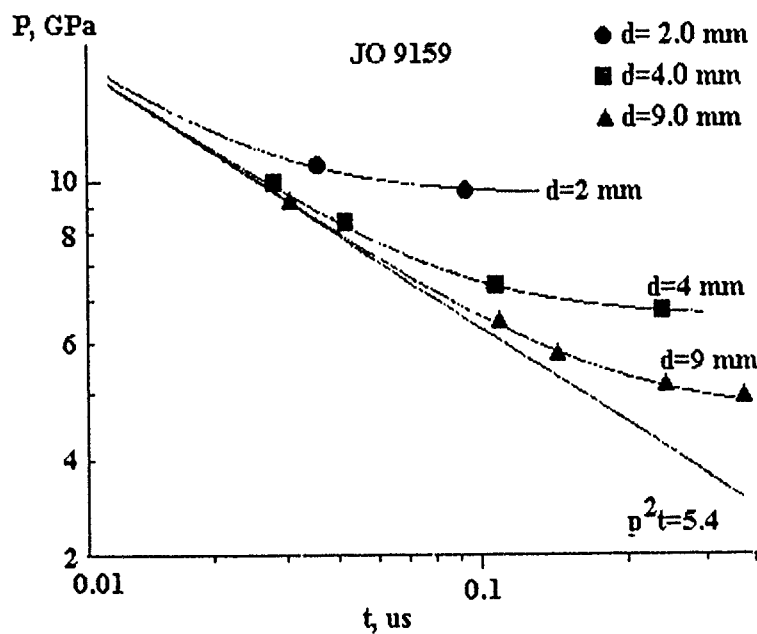
Figure 2: The $p \sim \tau$ curve for explosive JO9159, $(\rho_0 = 1.86 \text{ g/cm}^3)$.

Consequently, Eq. (6) gives a comprehensive description of the shock initiation behavior of heterogeneous explosives, generalizing the previous criteria Eqs. (1)∼(5).

The $p \sim \tau$ curve reflects the competition between the energy released by chemical reaction and the energy consumed by rarefaction. When the released and consumed energies achieve a critical condition, steady detonation can develop. This critical condition is the true shock initiation threshold.

Recently, the critical condition for initiation of detonation in explosives penetrated by small projectiles have been investigated by Zhao Feng *et al.* [7]. An initiation criterion taking into account the geometry of the projectile was also deduced, which employed only one fitting parameter — critical energy.

References

[1] Seay G. E., Seely L. B. *J. Appl. Phys.*, 1961, **32**, 8, 1092.

[2] Walker E. F., Walsley R. J. *Explosivestoffe, 17 Janr.*, 1969, 1, 9.

[3] Moulard H. *Proc. 7th Symp. (Int.) on Detonation*, **1**, 128, 1981 (preprint).

[4] Ramsay J. B., Popoloto A. *Proc. 4th Symp. (Int.) on Deton.*, 1965, 233.

[5] Stresau R. M., Kennedy J. E. *Proc. 6th Symp. (Int.) on Detonation*, 1976, 68.

[6] Zhao Feng, Sum Chengwei, Wei Yuzhang. *Chinese J. Explosion and Shock Waves*, 1993, **13**, 1, 41.

SESSION 7. Combustion and Detonation Analogies

RECURRENCE FORMULAS FOR THE COEFFICIENTS IN THE MARSHAK BOUNDARY CONDITION FOR ONE-DIMENSIONAL THERMAL RADIATION MODELLED BY THE METHOD OF SPHERICAL HARMONICS

Flemming M. B. Andersen

Laboratory of Heating and Air Conditioning, Technical University of Denmark, Building 402,
DK-800, Lyngby, Denmark

The method of spherical harmonics is a standard method for solving the thermal radiation problem in absorbing, emitting and scattering material. The method yields a system of differential equations to be solved usually by numerical methods. The boundary conditions of the system of differential equations are usually derived by tedious hand integrations using the Marshak method, although other methods are available [1].

This paper focuses on the Marshak boundary condition for thermal relation in a one-dimensional layer of absorbing, emitting and scattering material with azimuthal symmetry. The boundaries are assumed to be opaque, grey surfaces which reflect the incoming radiation both diffusely and specularly. The emitted radiation by these surfaces is also assumed to be diffuse.

In this paper, recurrence formulas for the coefficients in Marshak boundary condition will be derived. These formulas will easy the application of the method of spherical harmonics.

Figure 1 shows the geometry and nomenclature. The radiation properties of walls 1 and 2 are given subscripts or superscripts $w1$ and $w2$, respectively. The subscripts s and d indicate specular and diffuse walls, respectively. The other symbols are consistent with the symbols frequently used in the literature on thermal radiative heat transfer.

The exact boundary conditions for a diffusely and specularly reflecting wall, which also diffusely emits thermal radiation for wall 1 are as follows:

$$i(\mu) = \rho_{w1,s}i(-\mu) + 2\rho_{w1,d}\int_{-1}^{0} i(\mu')\mu'\,d\mu' + \frac{\epsilon_{w1}}{\pi}\sigma T_{w1}^4 \quad \text{for} \quad 0 \leq \mu \leq 1, \quad (1)$$

and for wall 2

$$i(\mu) = \rho_{w2,s}i(-\mu) + 2\rho_{w2,d}\int_{0}^{1} i(\mu')\mu'\,d\mu' + \frac{\epsilon_{w2}}{\pi}\sigma T_{w2}^4 \quad \text{for} \quad -1 \leq \mu \leq 0. \quad (2)$$
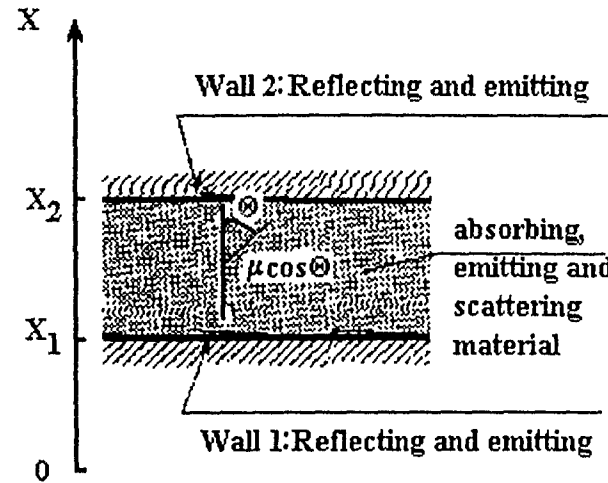
Figure 1: A one-dimensional layer of absorbing, emitting and scattering material and its boundaries of emitting and reflecting opaque walls.

The Marshak condition specifies that odd-order moments, i.e. $n = 1, 3, 5, \ldots, N$, where N is the order of approximation, of these equations are satisfied, thus yielding for wall 1

$$\int_0^1 i(\mu)\mu^n \, d\mu = \int_0^1 [\rho_{w1,s} i(-\mu) + 2\rho_{w1,d} \int_{-1}^0 i(\mu')\mu' \, d\mu' + \frac{\epsilon_{w1}}{\pi}\sigma T_{w1}^4]\mu^n \, d\mu, \qquad (3)$$

and for wall 2

$$\int_{-1}^0 i(\mu)\mu^n \, d\mu = \int_{-1}^0 [\rho_{w2,s} i(-\mu) + 2\rho_{w2,d} \int_0^1 i(\mu')\mu' \, d\mu' + \frac{\epsilon_{w2}}{\pi}\sigma T_{w2}^4]\mu^n \, d\mu. \qquad (4)$$

In the method of spherical harmonics the intensity is expanded into a sum of products of known Legendre polynomials P_m and unknown functions, ψ_m as follows

$$i(x,\mu) = \sum_{m=0}^N \frac{2m+1}{4\pi} P_m(\mu)\psi_m(\mu). \qquad (5)$$

The Legendre polynomials are functions of the direction cosine, μ, only, and the unknown functions are functions of the location, x, only.

Substituting Eq. (5) into Eqs. (3) and (4) yields for wall 1

$$\sum_{m=0}^N \psi_m(x)[a_{m,n}^{w1} - \rho_{w1,d} b_{m,n}^{w1} - \rho_{w1,s} c_{m,n}^{w1}] = d_n^{w1} \epsilon_{w1}\sigma T_{w1}^4, \qquad (6)$$

and for wall 2

$$\sum_{m=0}^N \psi_m(x)[a_{m,n}^{w2} - \rho_{w2,d} b_{m,n}^{w2} - \rho_{w2,s} c_{m,n}^{w2}] = d_n^{w2} \epsilon_{w2}\sigma T_{w2}^4, \qquad (7)$$

431

The remaining part of the paper is concerned with deriving formulas for the coefficients a, b, c and d (with subscripts and superscripts) of Eqs. (6) and (7). These formulas are derived using

$$P_m(\mu) = \frac{2m-1}{m} P_{m-1}(\mu)\mu - \frac{m-1}{m} P_{m-2}(\mu) \tag{8}$$

and

$$P_m(-\mu) = (-1)^m P_m(\mu). \tag{9}$$

Integral expressions for a, b, c and d are obtained by comparison of Eqs. (6) and (7) to Eqs. (3) and (4) and taking Eq. (5) into account. For wall 2, we thus obtain

$$a_{m,n}^{w2} \equiv \frac{2m+1}{4} \int\limits_{-1}^{0} P_m(\mu)\mu^n \, d\mu =$$

$$\frac{2m+1}{4} \int\limits_{-1}^{0} \left[\frac{2m-1}{m} P_{m-1}(\mu)\mu - \frac{m-1}{m} P_{m-2}(\mu) \right] \mu^n \, d\mu = \tag{10}$$

$$\frac{2m+1}{m} a_{m-1,n+1}^{w2} - \frac{2m+1}{2m-3} \frac{m-1}{m} a_{m-2,n}^{w2}.$$

In order to start the recurrence of Eq. (10), formulas for $a_{m,n}^{w2}$ are derived for $m = 0$ and $m = 1$ using the definition of $a_{m,n}^{w2}$ also in Eq. (10),

$$a_{0,n}^{w2} = \frac{1}{4} \int\limits_{-1}^{0} P_0(\mu)\mu^n \, d\mu = \frac{(-1)^n}{4(n+1)} \tag{11}$$

and

$$a_{1,n}^{w2} = \frac{3}{4} \int\limits_{-1}^{0} P_1(\mu)\mu^n \, d\mu = \frac{3}{4} \frac{(-1)^{n+1}}{n+2}. \tag{12}$$

The other coefficients for wall 2 are as follows:

$$b_{m,n}^{w2} \equiv \frac{2m+1}{2} \int\limits_{-1}^{0} \left[\int\limits_{0}^{1} P_m(\mu')\mu' \, d\mu' \right] \mu^n \, d\mu = 2\frac{(-1)^{n+m+1}}{n+1} a_{m,1}^{w2}, \tag{13}$$

$$c_{m,n}^{w2} \equiv \frac{2m+1}{4} \int\limits_{-1}^{0} P_m(-\mu)\mu^n \, d\mu = (-1)^m a_{m,n}^{w2} \tag{14}$$

and

$$d_n^{w2} \equiv \int\limits_{-1}^{0} \mu^n \, d\mu = \frac{(-1)^n}{n+1}. \tag{15}$$

For wall 1 the coefficients are related to $a_{m,n}^2$ as follows:

$$a_{m,n}^{w1} \equiv \frac{2m+1}{4} \int\limits_0^1 P_m(\mu)\mu^n \, d\mu = (-1)^{m+n} a_{m,n}^{w2}, \qquad (16)$$

$$b_{m,n}^{w1} \equiv \frac{2m+1}{2} \int\limits_0^1 \left[\int\limits_{-1}^0 P_m(\mu')\mu' \, d\mu' \right] \mu^n \, d\mu = \frac{2}{n+1} a_{m,1}^{w2}, \qquad (17)$$

$$c_{m,n}^{w1} \equiv \frac{2m+1}{4} \int\limits_0^1 P_m(-\mu)\mu^n \, d\mu = (-1)^n a_{m,n}^{w2} \qquad (18)$$

and

$$d_n^{w1} \equiv \int\limits_0^1 \mu^n \, d\mu = \frac{1}{n+1}. \qquad (19)$$

It has been shown that the coefficients in the Marshak condition can be found by first calculation of $a_{m,n}^{w2}$ for $m = 0$ and $m = 1$ using Eqs. (11) and (12) and then using the recurrence formula in Eq. (10). At each m the $a_{m,n}^{w2}$ are calculated for $n = 1, 2, \ldots, (2N - m)$. It is thus necessary to calculate values for $a_{m,n}^{w2}$ which are not to be applied in the Marshak condition, since these values are required in the recurrence equation, only.

The other coefficients of Eqs. (6) and (7) are found using the formulas given in Eqs. (11)–(19) relating the coefficients to $a_{m,n}^{w2}$. The coefficients are easily calculated by recurrence up to any approximation order N of the spherical harmonics approximation.

In general, the derived formulas are easier to apply than integrating manually the equations for basic definitions of the coefficients given in Eqs. (10), (13), (14), (16), (17) and (18). These manual integrations are by no means difficult, only tedious and lengthy and thus errors are easily introduced.

A general computer program for solving the radiation problem using the method of spherical harmonics has been developed for arbitrary approximation orders using finite differencing and a block matrix solver. The solution functions near the walls are converging as it is expected when higher-order approximations are applied.

References

[1] Ozisik M. N. *Radiative Transfer and Interaction with Conduction and Convection.* John Wiley and Sons, 1973.

MODELING OF DETONATION FRONT DYNAMICS

A. A. Borissov, E. A. Pirogov, O. V. Sharypov

Novosibirsk State University, Novosibirsk-90, Russia

The investigation of combustion and detonation in gases leads to the problem of dynamics of finite-amplitude perturbations. From the thermodynamic point of view, these are highly nonequilibrium processes. The characteristic feature of the systems with such processes is the capability of spontaneous change of regimes. A variation of a "governing parameter" can result in a catastrophic transformation of the type of solution. An excellent example of this behavior is the thermodiffusional instability of a plane combustion front. (A great contribution thereto has been made by Ya. B. Zel'dovich with co-authors [1].)

The present paper contributes to theoretical modeling of the spatiotemporal structure of detonation fronts in gases. The objective of the work was to develop a simplified nonlinear time-dependent model (in line with Zel'dovich's approaches), which provides the formulation of criteria, the analysis of detailed physical mechanisms and the possibility for numerical simulation of the solution dynamics.

It is shown that a solution to the linearized problem of plane (ZND) detonation front stability can be represented by a surface resulting from superposition of sinusoidal "standing waves":

$$F = a_j \cos(k_j y + \varphi_j) \cos(g_l x + \psi_l) \cos(\omega_{jl} t + \theta_{jl}) \exp(\Omega_{jl} t).$$

The period of pulsation for each harmonic is proportional to the wavelength ($\omega_{jl} \propto \sqrt{k_j^2 + g_l^2}$). In addition, the infinitesimal perturbations of wavelengths comparable with the size of chemical conversion zone are unstable ($\Omega_{jl} > 0$). The short and long-wave harmonics are damped by a gas-dynamic mechanism ($\Omega_{jl} \propto -\sqrt{k_j^2 + g_l^2}$) (the same as that responsible for the stability of plane shock waves [2]). The expressions for the increments and "phase velocities" of the harmonics are derived.

The paper takes into account a nonlinear mechanism of interaction between harmonics (similar to the mechanism proposed by Zel'dovich for the flame surface [3, 4]):

$$F_t = (F_t)_{linear} + b(F_y^2 + F_x^2).$$

Based on the analytical results, a numerical algorithm is constructed to simulate the spatiotemporal structure of detonation fronts in two or three dimensions. The discrete Fourier transform method is used (it is verified by solving Burgers equation).

The expression for the governing parameter is derived. It depend on the dimensionless activation energy, the shock wave intensity, and the adiabatic exponent (in
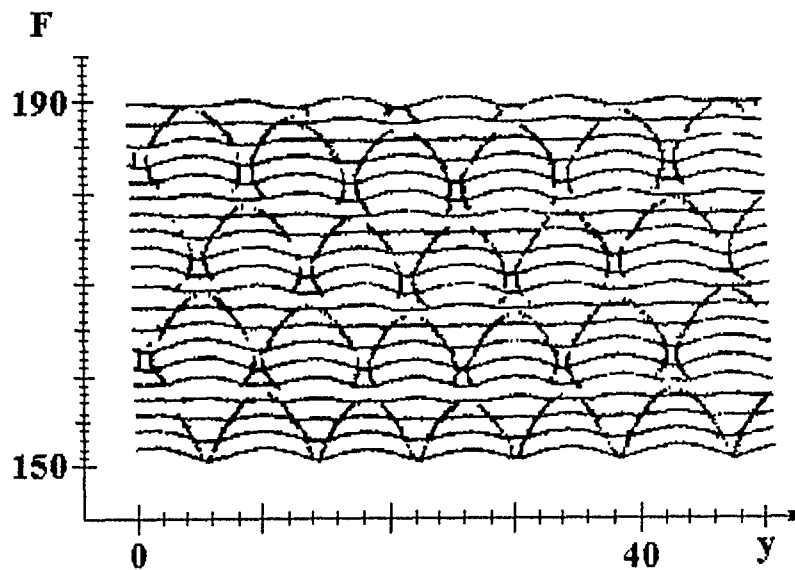
Figure 1: Numerical cellular detonation dynamics. Dotted lines show trajectories of cell junctions.

accordance with [5]). Numerical calculations have shown that a critical value of the governing parameter exists. It divides regimes with more and less regular spatial and temporal structure of the solution. The calculated criterion corresponds to the experimental data [6] for the 2D case.

The constructed model and numerical algorithms can be used to simulate the influence of boundary conditions (walls) on the propagation of detonation in a duct or its passing from a duct to an unconfined space (the problem of detonability limits). Furthermore, the chaotic behavior of the solution described by the model is of interest in its own right.

References

[1] Barenblatt G. I., Zel'dovich Ya. B., Istratov A. G. *Zhurnal Prikladnoi Mekhaniki. Tekhnicheskoi Fiziki*, 1962, **4**, 21 (in Russian).

[2] Dyakov S. P. *Zhurnal Experimentalnoi Teoreticheskoi Fiziki*, 1954, **27**, 3, 288 (in Russian).

[3] Malomed B. A. *Zhurnal Tekhnicheskoi Fiziki*, 1984, **54**, 2, 233 (in Russian).

[4] Sivashinsky G. I. *Acta Astronautica*, 1976, **4**, 11, 1177.

[5] Vasil'ev A. A., Mitrofanov V. V., Topchiyan M. E. *Fizika Goreniya Vzriva*, 1987, **23**, 5, 109 (in Russian).

[6] Manzhalei V. I. *ibid,* 1977, **13**, 3, 470 (in Russian).

ON THE SELF-ORGANIZATION PHENOMENA IN SOME MODELS OF RELAXING MEDIA

V. A. Danylenko, V. A. Vladimirov

Subbotin Geophysical Institute of the Ukrainian Academy of Sciences, Division of Geodynamics of Explosion, Kiev, Ukraine

The aim of this presentation is to analyze the self-similar solutions of hydrodynamics equations (HDE) describing fast processes in active and relaxing media. It is obvious that the classical set of HDE derived under the assumption of complete thermodynamic equilibrium is not appropriate for this purpose. In the late 30s, M. A. Leontovich [1] proposed to allow for relaxation processes, irrespective of their nature, by introduction of internal variables formally satisfying the equations of chemical kinetics.

Assuming that the equilibrium equation of state has the form $p = A\rho^\sigma + B$, we can write out a hydrodynamical set of equations for relaxation processes in the following form:

$$\rho\frac{du}{dt} + \frac{\partial p}{\partial x} = \mathcal{F}, \qquad \frac{d\rho}{dt} + \rho\frac{\partial u}{\partial x} = 0,$$

$$\frac{dp}{dt} + \sigma p\frac{\partial u}{\partial x} = a\rho Q, \qquad \frac{d\lambda}{dt} = Q(\rho, p, \lambda) \tag{1}$$

where u is the velocity, ρ and p are the density and pressure, respectively, $d/dt = \partial/\partial t + u\partial/\partial x$, $\mathcal{F}$ is the external force.

To transform the starting set of partial differential equations (PDE) to a set of ordinary differential equations (ODE), we introduce a special ansatz suggested by the symmetry properties of (1). If $Q = g(\lambda)\varphi(p/\rho)/t$ and $\mathcal{F} = \rho\gamma/t$, using the ansatz

$$u = U(\omega) + \omega, \qquad \omega = \frac{x}{t},$$

$$\rho = \exp[S(\omega)], \qquad p = Z(\omega)\rho, \qquad \lambda = L(\omega) \tag{2}$$

436

enables one to obtain the following dynamical system (DS) satisfied by self-similar solutions of the starting set of PDE:

$$\frac{dU}{d\tau} = U(\psi - \sigma Z - (\gamma - U)) \equiv U\Phi, \tag{3a}$$

$$\frac{dZ}{d\tau} = \Delta(\Psi + \kappa Z) + \kappa Z\Phi, \tag{3b}$$

$$\frac{dL}{d\tau} = \Delta Q, \tag{3c}$$

where $\psi = aQ$, $Q = g(L)\varphi(Z)$, $d/d\tau = U\Delta d/d\omega$, $\Delta = \sigma Z - U^2$, $\kappa = 1 - \sigma$. In the case of $Q = g(\lambda)\varphi(p/\rho)$ and $\mathcal{F} = \rho\gamma$, the ansatz

$$u = W(\omega) + D, \qquad \omega = x - Dt,$$

$$\tag{4}$$

$$\rho = \exp(\xi t + S(\omega)), \qquad p = Z(\omega)\rho, \qquad \lambda = L(\omega)$$

leads to the dynamical system

$$\frac{dW}{d\tau} = W(\xi Z + \gamma W - \psi) \equiv W\Phi, \tag{5a}$$

$$\frac{dZ}{d\tau} = \Delta\Psi + \kappa Z\Phi, \tag{5b}$$

$$\frac{dL}{d\tau} = Q, \tag{5c}$$

where $\psi = aQ$, $Q = g(L)\varphi(Z)$, $d/d\tau = W\Delta d/d\omega$, $\Delta = -(\sigma Z - W^2)$, and $\kappa = 1 - \sigma$.

When Q does not depend on λ, equations (3a,b) as well as (5a,b), form a closed set. As will be shown below, these sets have families of quasiperiodic solutions. Using the Andronov–Hopf bifurcation theorem, one can show that the following statements are true [2]:

Theorem 1. If in neighborhood of a point $Z_1 > 0$ the kinetic function $\psi(Z)$ has the decomposition

$$\psi = (\sigma - 1)Z_1 + \xi(Z - Z_1) + \eta(Z - Z_1)^2 + \chi(Z - Z_1)^3 + \ldots$$

and the parameters ξ, σ satisfy the inequality $\xi > (\sigma^2 + 1)/(\sigma - 1)$, then there exists an open interval $I \in R^1$ in the neighborhood of the critical value $\gamma_{cr} = sgn Re(C_1)\sqrt{Z_1}(\sigma - 1)\left(\sqrt{\xi^2 - \xi(\sigma - 1) - \sigma}\right)^{-1}$, where C_1 is the first Floquet exponent [3] such that for $\gamma \in I$ set (3.a,b) has a family of stable quasiperiodic solutions.

Theorem 2. If the function $\psi(Z)$ intersects transversally the OZ axis at a point $Z_1 > 0$, then there exists an open interval $J \in R^1$ such that for $\gamma \in J$ set (5a,b) has a family of stable quasiperiodic solutions.
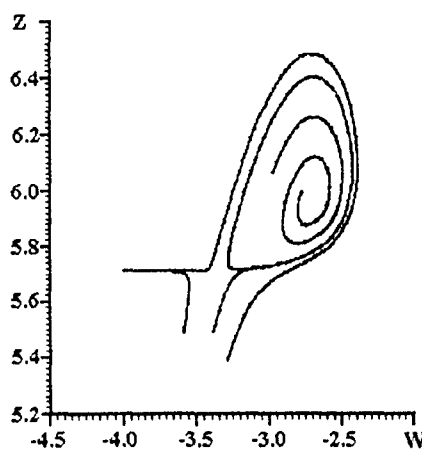
Figure 1: Phase plane of set (5a,b), obtained by straightforward numerical calculation for $\gamma = 1.1$, $\gamma_{cr} = 1$, $\sigma = 2$. $\psi(Z) = 2\sin(\pi(Z - Z_1))\exp(0.7(Z - Z_1)^2)$ if $|Z - Z_1| \leq 2$, and $\psi(Z) = 0$ otherwise.

The phase plane of the set (5a,b) in the neighborhood of the critical point is shown in Fig. 1.

In the case of $\partial Q / \partial \lambda \neq 0$, the self-similar solutions of set (1) are governed by the third-order dynamical systems (3a–c) and (5a–c). It is easy to show that, under the conditions of Theorems 1 and 2, the eigenvalues of the linearization matrices of these sets for the critical values of the bifurcation parameter will be double degenerate, namely one eigenvalue is zero and the other two become pure imaginary. Such degeneracies were carefully studied in [4]. It has been shown that, in the neighborhoods of the critical values of the parameters, a stable quasiperiodic and deterministic–chaotic regimes exist under certain conditions.

Based on the results obtained, we can conclude that set (1), in contrast to the classical hydrodynamics equations without relaxation, can be of use in describing self-organization phenomena.

References

[1] Leontovich M. A. *An Introduction to Thermodynamics.* Moscow, GITTL Publ. 1950 (in Russian).

[2] Danylenko V. A., Sorokina V. V., Vladimirov V. A. *J. Physics, Ser A: Math & Gen.*, 1993, **26**, 7125–7135.

[3] Hassard B. D., Kazarinoff N. D., Wan Y.-H. *Theory and Applications of Hopf Bifurcation.* London–New York, Cambridge University Press, 1981.

[4] Guckenheimer J., Holmes P. *Nonlinear Oscillations, Dynamical Systems and Bifurcations of Vector Fields.* New York, Springer–Verlag, 1984.

HOW USEFUL IS THE ANALOGY BETWEEN GASEOUS AND MELT/WATER EXPLOSIONS?

D. F. Fletcher

Department of Mechanical and Mechatronic Engineering, University of Sydney, NSW 2006
Australia

1 Introduction

The destructive potential of the interaction of a hot metal with cold water is now well-known [1]. Attempts to develop models for the explosion process have met with only limited success [2] because of the complexity of the physical processes to be modelled, the uncertainty concerning the initial conditions, and the difficulty of experimental validation. Here we seek to highlight the similarities and differences between gaseous and physical explosions. This will be done at various levels, with the comparison covering: (i) the basic physics, (ii) the mathematical modelling framework, and (iii) the experimental database.

2 The Conceptual Picture

The conceptual picture of detonations, as originally proposed by Zel'dovich, von Neumann and Döring [3, 4], was adapted by Board, Hall and Hall [5] to provide a model for the propagation stage of a physical explosion. Here we will assume that the reader is familiar with ZND theory and simply note how this is applied to physical explosions. This subject has been addressed extensively in Fletcher and Anderson [2] and Frost, Lee and Ciccarelli [6]. In summary, the conceptual picture is as shown in Fig. 1, with a shock front causing collapse of the vapour layer around the melt and the subsequent relative acceleration of the melt droplets and water causing fine-scale fragmentation and heat transfer. In the Board–Hall model, as in the ZND model, the propagation velocity and the final pressure can be determined from the initial conditions and the equation of state of the reactants, provided that use is made of the Chapman–Jouguet condition.

Immediately, concerns are raised as to which sound speed should be used in a two-phase mixture and the applicability of assuming homogeneous conditions and complete 'combustion'. It is evident that the multiphase system is much less well mixed than the gaseous system, and that there are a number of significant lengthscales, i.e. the inter-droplet spacing, the droplet size and the length of the reaction zone. These obviously play an important role in the propagation behavior, since if the inter-droplet spacing is too large the propagation will fail.

stationary zone	self-similar expansion zone	fragmentation zone	undistructed region

a) Physical picture

b) Pressure field
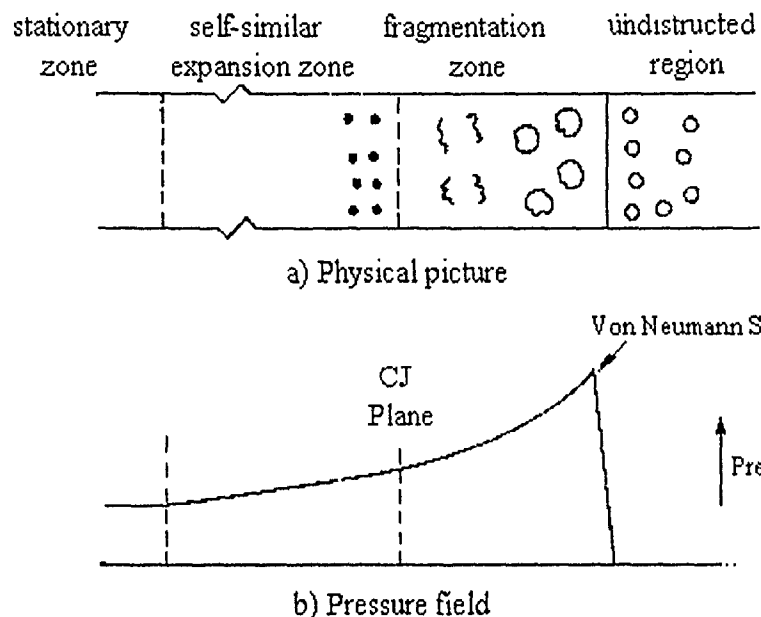
Figure 1: The conceptual picture employed in the Board–Hall model.

One is immediately led to the need to distinguish between a system which is a multiphase continuum, to which the above analysis **may** apply, and that which is not, to which the above analysis certainly does not apply. An example of the latter system is the 'propagation' along an array of droplets as examined by Frost and Ciccarelli [7]. We will return to the issue of continuum behavior later.

The one-dimensional nature of the model must also be questioned, if for no other reason than the fact that any real mixture is inhomogeneous, and such mixture inhomogeneities have been shown computationally to reduce propagation pressures significantly [8]. In addition, the very existence of a steady-state solution depends on the initial conditions, and if t~ much vapor is present no steady-state exists [9].

It is also important to realize that whilst the ZND model provides a reasonable estimate of, for example, detonation velocities, the physical picture is incorrect, with detonation propagation being governed by the behavior of 3D detonation cells [4]. Thus there is no reason to believe that the simple 1D picture will apply in the melt/water explosion case. Frost *et al.* [10] have postulated that, if this analogy holds, it should be possible to determine critical expansion ratios beyond which propagation fails. They also postulated that multiphase deflagrations may provide a better analogy than detonations for physical explosions. Fletcher [11] has performed 'scoping' calculations which suggest that the detonation-like solution gives pressure transients closer in shape to those observed experimentally. However, clarification requires detailed experimental data.

3 The Computational Framework

All attempts to calculate either the detailed variation of properties across a propagation front or the t. ansient escalation from a trigger have employed multiphase equations [2]. These equations assume that the system can be represented as an interpenetrating continuum, the properties of each phase varying smoothly in space. All phases are assumed to 'share' a common pressure. Simple order of magnitude estimates show that pressure equilibration is fast, since a typical sound speed is of the order of 100 m/s and a typical dimension in a computational volume is 10 mm, giving a characteristic timescale of 0.1 ms.

However, temperature variations are much greater, with a typical thermal boundary layer thickness around a melt fragment being of order $\sqrt{\alpha t}$, where α is the thermal diffusivity of the water and t is the time since the fragment formed. Thus, in 1 ms, the typical boundary layer thickness developed is 0.1 mm. Baines [12] performed an analysis along these lines to explain the behavior observed in tin-water propagations. More recently, Theofanous and co-workers [13] have used a combination of optical and X-ray photography to determine the rate at which fragments mix with water, and have shown that this partial mixing, which they refer to as 'microinteraction', must be allowed for if the escalation rate is to be correctly predicted.

The conservation equations used to model multiphase flow have been the subject of considerable debate, since, as with turbulence modelling, there are many unknown quantities which have to be represented. The equation set used by most workers ignores many of these effects, but are capable of predicting wave propagation behavior. Theofanous *et al.* [13] have used this set of equations augmented in such a manner that the fragments and heated water form one phase at a common temperature, and the unheated water form another. They allow mass and momentum transfer between these phases in order to represent the local mixing between the fragments and water. Such complexities are not required in the gaseous explosion case, and, consequently, many fewer constitutive relations are needed.

The choice of fragmentation model largely determines the predicted behavior. The different mechanisms of hydrodynamic (based on relative velocity fragmentation) and thermal (based on, for example, water entrapment and/or bubble collapse) are usually used [2]. Whilst it is clear that thermal mechanisms play a role in single droplet fragmentation, and therefore most likely in triggering, it seems impossible that a propagation can be sustained by such a mechanism, since thermal fragmentation rates are too slow and the density difference between vapor and liquid disappears at high pressure. The fact that changing the water viscosity and surface tension can have a dramatic affect on the propagation behavior has yet to be addressed in propagation models.

4 Experimental Database

The main reason why so many questions remain is the difficulty of performing well-

instrumented experiments. Only recently have experiments been performed which show the details of the fragmentation behavior and allow quantitative data on the fragment mixing rate to be determined. Experiments in which a well-defined initial condition has been achieved are few in number, but progress is being made in Ispra [14] and at the University of Wisconsin [15]. With continued experimental advances it should be possible to validate propagation models for a 1D tube geometry. However, even here it is necessary to distinguish between the two-phase propagations which occur in, say, the tin-water system [15] and the supercritical propagations observed in some cases when a more energetic melt is used [14]. Validation of complex multi-dimensional behavior will take much longer, as will the quantification of the venting effect observed in shallow water pools.

This is in contrast to the study of gaseous detonations, where detonation cell sizes are now routinely measured and, for example, critical tube diameters are well-established. The single phase nature of this problem has clearly facilitated this task.

5 Conclusions

Application of the ZND model of gaseous detonations to physical explosions generated a framework for the modelling of physical explosions which has proved to be very useful. It has stimulated considerable model development, which has allowed many of the complexities of multiphase explosions to be investigated. Current models produce qualitative results only, but validation work underway should improve this situation considerably. It is now the correct time to take a step back and decide what advances made in the gaseous detonation field, especially in terms of numerical methods, can be utilized by multiphase explosion researchers.

References

[1] Corradini M. L., Kim B. J., Oh M. D. *Prog. Nucl. Energy*, 1988, **22**, 1.

[2] Fletcher D. F., Anderson R. P. *Prog. Nucl. Energy*, 1990, **23**, 137.

[3] Zel'dovich Ya. B., Kompaneets A. S. *Theory of Detonations*. Moscow, Gostekhizdat, 1955 (in Russian).

[4] Strehlow R. A. *Combustion Fundamentals*. New York, McGraw-Hill, 1984.

[5] Board S. J., Hall R. W., Hall R. S. *Nature*, 1975, **254**, 319.

[6] Frost D. L., Lee J. H. S., Ciccarelli G. *Shock Waves*, 1991, **1**, 99.

[7] Frost D. L., Ciccarelli G. In: *Prog. Astronaut. Aeronaut.*, 1988, **114**, 451.

[8] Fletcher D. F. *Int. J Heat Mass Transfer*, 1991, **34**, 2449.

[9] Gelfand B. E., Bartenev A. M., Frolov S. M., Tsyganov S. A. In: *Prog. Astronaut. Aeronaut.*, 1993, **154**, 459.

[10] Frost D. L., Bruckert B., Ciccarelli G. *Proc. 1993 OJI Seminar on Physics of Steam Explosions*, Tomakomai, Japan, 1993.

[11] Fletcher D. F. *Shock Waves*, 1994, **3** (in press).

[12] Baines M. *Inst. Chem. Eng. Symp. Series*, 1984, **86**, 97.

[13] Yuen W. W., Theofanous T. G. *Proc. CSNI Specialist Meeting on Fuel-Coolant Interactions*, Santa Barbara, USA, 1993.

[14] Hohmann H., Magallon D., Schins H., Yerkes A. *ibid.*

[15] Park H. S., Yoon C., Corradini M. L., Bang K. H. *Proc. 1993 OJI Seminar on Physics of Steam Explosions*, Tomakomai, Japan, 1993.

THE PHENOMENOLOGICAL THEORY OF NONSTEADY BOILING OF VAPOR-IMBUED LIQUIDS

Yu. A. Gostintsev, L. A. Sukhanov

Semenov Institute of Chemical Physics, Moscow, Russia

Nonsteady boiling is a widespread phenomenon in nature and technology. It takes place, for example, when cryogenic liquids spill on relatively warm surfaces (accidents with heavy rockets at launching sites, leakage from storage facilities and tankers containing liquified gases and so on) or when highly heated bodies interact with colder liquids (flows of volcanic lava in contact with water, accidents in metallurgy, etc.). If the heated bodies have well-developed surfaces (e. g., aggregates of the small particles) their interaction with liquid can lead to the so-called steam explosion. This phenomenon is usually accompanied by fast pressure rise and distruction of the vessel walls (which is possible in the case of heavy accident with the nuclear power plant reactor). In any case, the nonsteadiness of the vapor-imbued liquid boiling is a consequence of the time variation of the temperature jump at the "boiling liquid – underlying material" contact surface (internal factor) and the variability of external factors (pressure, acceleration,

etc.). The term "temperature jump" mentioned above describes the difference between the temperature of the underlying material surface and that of the boiling liquid at the given pressure.

There are, in general, two approaches to the problem of quantitative description of nonsteady boiling.

The first one involves formulation and analysis of the complete set of equations adequately describing the boundary problem for the processes of heat and mass transfer in the vapor–liquid and underlying media simultaneously. Such approach has not been implemented as of yet.

The second, phenomenological approach, can be based on experimental or theoretical data on the steady regimes of boiling, if the heat and mass transfer processes in the vapor–liquid can be treated as quasisteady as compared to the thermal relaxation in the underlying material and to the time-varying external factors. The mathematical description of the nonsteady boiling is substantially simplified in this case, since the problem mentioned above (approach one) can be reduced to a single time-dependent equation for heat transfer in the underlying material. The boundary condition at the contact then can be taken from the data of steady-state experiments or theory.

The approach described here is similar to that used in the phenomenological theory of the nonsteady combustion of powder, developed by Ya. B. Zel'dovich and his followers [1-3].

The quantitative analysis of the applicability region of the phenomenological approach to nonsteady vapor-imbued liquids boiling on heat conducting media, the mathematical model formulation, and the calculations for water, oxygen, nitrogen and methane boiling on various materials performed in the present investigation were partly published in [4].

It has been shown that the "rigid" quasisteadiness condition imposed on the vapor–liquid phase is well satisfied for any regime of noticeable boiling on thermally highly active metals and is violated for the materials with relatively low values of $\lambda_s \rho_s C_s$ (for example, asbestos or paraffin).

Note that the characteristic variation times of the external disturbing factors for the quasisteady vapor–liquid phase must be (for the different "liquid – underlying material" pairs) more than 10^{-2} to 10^{-3} s.

References

[1] Zel'dovich Ya. B. *Zhurnal Eksperimentalnoi Teoreticheskoi Fiziki*, 1942, **12**, 11–12 (in Russian).

[2] Novozhilov B. V. *Unsteady Burning of Solid Rocket Propellants*. Moscow, Nauka, 1973 (in Russian).

[3] Gostintsev Yu. A., Sukhanov L. A., Pokhil P. F. *Zhurnal Prikladnoi Mekhaniki Tekhnicheskoi Fiziki*, 1971, 5–6 (in Russian).

[4] Gostintsev Yu. A., Sukhanov L. A. *et al. Dynamics of Spillage and Evaporating of Liquefied Gases.* Preprint of the Institute of Chemical Physics, Chernogolovka, 1991 (in Russian).

A MODEL OF CHEMICAL CONDENSATION IN THE DIRECT FLOW CVD REACTOR

Yu. M. Grigoryev[*], A. A. Markov[†], I. A. Filimonov[*]

[*] *The Institute for Structural Macrokinetics, Chernogolovka, Russia*
[†] *The Institute for Problems in Mechanics, Moscow, Russia*

The processes of chemical condensation from gas mixtures have so far been described only at the stage of primary nuclei formation [1–4] or at the final moments of new phase generation [5, 6]. Within the framework of the Frenkel–Zel'dovich theory [1, 2] and quasi-chemical models [3, 4], supersaturation in the reacting medium is considered as a constant, the effects of interface boundaries and transfer processes being not taken into account. The Lifshits–Slezov theory [5, 6] deals with the case of negligibly small supersaturation. Thus, the kinetics of new phase generation accompanied by the change in the degree of supersaturation (the intermediate stage of gas-to-solid conversion) has not been considered as of yet, except for some particular problems concerning vapor condensation and mass crystallization. Nevertheless, it is the intermediate stage which determines the condensed product dispersion. The process of chemical conversion in a gas mixture flow in a cylindrical tube with smooth walls at a constant temperature was modeled applying to the theory of CVD reactors. The initial temperature of the walls was assumed to be equal to that of the gas mixture flowing in and chemical conversion is negligibly small. Thus, a hydrodynamic Poiseuille flow with uniform distributions of temperature and mixture components occurs in the tube. At some moment, the wall temperature is instantaneously increased to remain constant during the entire process. The gas mixture consists of reacting and inert gases with fine particles of a condensed product uniformly distributed in the gas at the initial moment. Due to the heterogeneous chemical reaction, the size of condensed particles varies. The chemical conversion of gas-to-solid type takes place both in the gas volume

(homogeneously) and on the reactor walls or the suspended particles (heterogeneously).

On the macroscopic scale, the problem was posed for a continuum, which includes the diffusion equations for temperature and gas concentrations with chemical sources, the equations of continuity and momentum, and the equation of state.

The microscopic gas fluxes induced by heterogeneous chemical condensation give rise to nonzero macroscopic fluxes of the gas components. Assuming that the heterogeneous chemical conversion on the particle surface is quasistationary and the approximation of independent diffusion is correct, the average values of the microscopic gas fluxes were calculated. The particle curvature effect on the surface concentration of saturated vapor was taken into account for the condensed product. An ordinary differential equation describing the evolution of the particle radius has been obtained for the case of spherical condensed particles.

A new parabolization technique was developed in order to provide a stable algorithm for numerical simulation of combustion. As a result, the processes on scales different from one another by orders of magnitude were analyzed.

By virtue of simultaneous numerical analysis of the process on both macroscopic and microscopic scales, the possibility of analyzing the modes of chemical conversion, the thermal features of the process, the conditions of transition from heterogeneous to homogeneous condensation, and the disper-

Figure 1: Premixed acetylene–argon combustion in a tube: (a) temperature isolines; (b) isolines of particle radius; (c) isolines of gaseous product concentration.

sion of the condensed particles has been demonstrated. As an example, premixed acetylene–argon combustion widely used in practice was simulated (see Fig. 1).

References

[1] Frenkel Ya. I. *The Kinetic Theory of Liquids*. Moscow–Leningrad, USSR Acad. Sci. Publ., 1945 (in Russian).

[2] Zel'dovich Ya. B. *Zhurnal Eksperimentalnoi Teoreticheskoi Fiziki*, 1942, **12**, 545 (in Russian).

[3] Smoluchowski M. V. *Zeitschrift für Physikalische Chemie*, 1917, **92**, 129.

[4] Gordiets B. V., Shelepin L. A., Shamotkin Yu. S. *J. Chem. Phys.*, 1982, **10**, 1391.

[5] Slezov V. V., Sagalovich V. V. *Uspekhi Fizicheskikh Nauk*, 1987, **151**, 1, 67 (in Russian).

[6] Lifshits E. M., Pitayevski L. P. *Physical Kinetics*. Moscow, Nauka, 1979 (in Russian).

FRONT DYNAMICS IN NONEQUILIBRIUM PATTERNS

A. Hari*, B. A. Malomed†, A. A. Nepomnyashchy*, L. M. Pismen‡

*Department of Mathematics, Technion — Israel Institute of Technology, Haifa, 32000 Israel
†Department of Applied Mathematics, School of Mathematical Sciences, Tel-Aviv University, Ramat-Aviv, 69978 Israel
‡Department of Chemical Engineering, Technion — Israel Institute of Technology, Haifa, 32000 Israel

The ideas developed in combustion theory have been successfully applied to front propagation problems in different branches of physics[1]. In the present contribution, we consider the propagation of fronts between competing patterns in a nonequilibrium system.

447
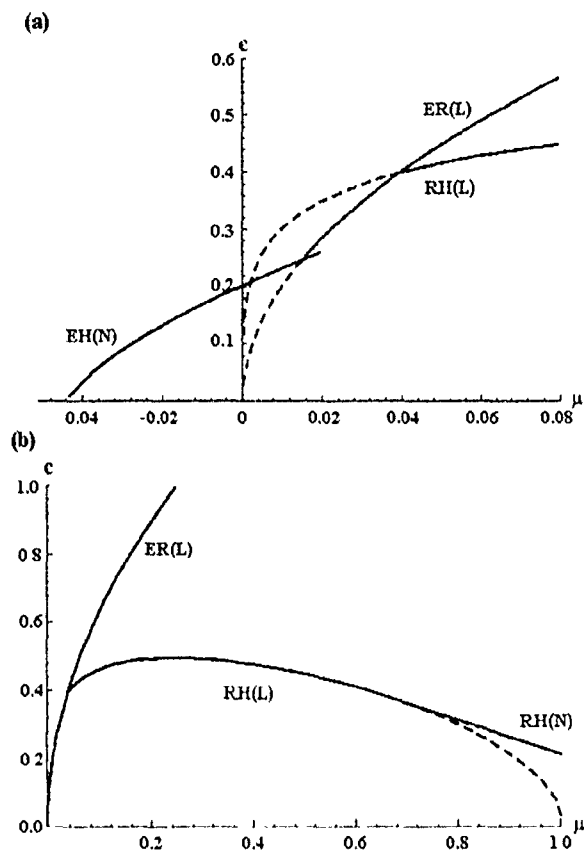
Figure 1: The velocity of propagation of linear (L) and nonlinear (N) equilibrium-rolls (ER), equilibrium-hexagones (EH), and rolls-hexagons (RH) fronts as a function of the parameter μ: (a) near the critical point $\mu = 0$; (b) at large μ; $\nu = 2$. The segments actually determining the propagation velocity are shown by solid lines.

We will focus on convection patterns in a horizontal layer of fluid heated from below, which provide a typical example of dissipative structures. The crucial feature of this system is its rotational symmetry, which leads to a variety of competing patterns (rolls, square patterns, hexagonal patterns etc.). Different kinds of patterns can arise

448

in different spatial domains. These domains are separated by intermediate zones, which can be called "domain boundaries" of "fronts".

The dynamics of such fronts resembles the dynamics of the frontal propagation of chemical reactions or phase transition. Near the instability threshold, the convection patterns can be described by amplitude equations [2, 3] similar to the Landau–Khalatnikov kinetic equation:

$$\frac{\partial a_j}{\partial t} = -\frac{\delta F}{\delta a_j^*}, \quad j = 1, \ldots, N, \tag{1}$$

$$F = \int dx \, dy \left[\frac{1}{2} \sum_{j=1}^{N} |n_j \cdot \nabla) a_j|^2 + V(a_1, \ldots, a_N) \right], \tag{2}$$

where a_j is the envelope function corresponding to a system of rolls with the wavevector n_j.

The planar front

$$a_j = a_j(z), \quad z = x - ct \tag{3}$$

moves always in the direction of patterns characterized by higher density of the Lyapunov functional. One should distinguish two kinds of fronts:

(i) fronts between two locally stable patterns corresponding to different minima of V;

(ii) fronts between a stable pattern and an unstable one, which corresponds to a saddle point or a maximum of V.

In the former case the front solution is usually unique, whilst in the latter case there is an infinite number of solutions (3) with different values of c. However, even in the latter case, for "typical" initial conditions, the limit velocity of the front (as $t \to \infty$) can be determined uniquely by means of some criteria. The first criterion is linear; it selects the pattern generated at the leading edge of the propagation front [6, 7]. The second one is essentially nonlinear and selects the so-called "nongeneric front" [8]. The front with the larger propagation velocity eventually prevails. Figure 1 shows the typical dependence of front velocities on the control parameter [9]. The problem is described by the system of Eqs. (1), (2) with $N = 3$,

$$V(a_1, a_2, a_3) = -\frac{1}{2}\mu \sum_{j=1}^{3} |a_j|^2 - (a_1 a_2 a_3 + a_1^* a_2^* a_3^*) + \frac{1}{4} \sum_{j=1}^{3} \sum_{k=1}^{3} \nu_{jk} |a_j|^2 |a_k|^2,$$

$$\nu_{jk} = \nu + (1 - \nu)\delta_{jk}.$$

An important peculiarity of front propagation in nonequilibrium patterns is the anisotropy caused by cellular patterns. The velocity of the front between two different patterns depends on the direction of its propagation. This is especially important for the case of curved front [10]. If the difference between Lyapunov functional densities $[V]$

of the coexisting patterns is sufficiently large, the curvature effects are unimportant, and every point of the front moves at a certain normal velocity depending on the direction of the local normal vector. In this case, the problem of front propagation can be solved exactly by the method of characteristics. For small or zero differences, the curvature effects should be taken into account, and the normal velocity depends on the orientation of the normal vector and distortion of the front. In the latter case, the front tends typically to flatten in the long run.

Two phenomena specific for the problem of pattern formation should be mentioned. The first one is the effect of the wavenumber selection generated by fronts [5, 6]. It turns out that the front produces patterns with a quite definite wavenumber. The other effect is the interaction between the "large-scale" front and the underlying small-scale convection structure; this effect is an example of nonadiabatic effects [4]. This interaction is most important for small $[V]$ and can lead to a "pinning" of the front by the small-scale structure [5]. As a result, one obtains a motionless front between two structures with different densities of the Lyapunov functional [11].

References

[1] *Dynamics of Curved Fronts.* (Pelce P. Ed.), Boston, Academic Press, 1988.

[2] NewellA. C., Whitehead J. A. *J. Fluid Mech.*, 1969, **38**, 279.

[3] SegelL. A. *J. Fluid Mech.*, 1969, **38**, 203.

[4] Pomeau Y. *Physica D*, 1986, **23**, 3.

[5] Malomed B. A., Nepomnyashchy A. A., Tribelsky, M. I. *Phys. Rev. A*, 1990, **42**, 7244.

[6] Dee G. T., Langer J. S. *Phys. Rev. Lett.*, 1983, **50**, 383.

[7] Van Saarlos W. *Phys. Rev. A*, 1988, **37**, 211.

[8] Van Saarlos W. *Phys. Rev. A*, 1989, **39**, 6367.

[9] Pismen L. M., Nepomnyashchy A. A. Submitted to *Europhys. Lett.*

[10] Hari A., Nepomnyashchy A. A. Submitted to *Phys. Rev. E.*

[11] Nepomnyashchy A. A., Tribelsky M. I., Velarde M. Submitted to *Phys. Rev. E.*

THE ZEL'DOVICH PROBLEM FOR KPP EQUATIONS (KOLMOGOROV–PETROVSKII–PISKUNOV EQUATIONS)

S. I. Khudyaev

Syktyvkar State University, Syktyvkar, Russia

A wave solution of the heat balance equation

$$t_\tau = t_{xx} + \varphi(t) \tag{1}$$

of the type $t(x, \tau) = t(x + u\tau)$, where u is the constant speed to be determined, satisfies the ordinary differential equation [1]

$$t_{\xi\xi} - ut_\xi + \varphi(t) = 0, \qquad \xi = x + ut. \tag{2}$$

The above equation is further investigated under the boundary conditions

$$t(-\infty) = 0, \quad t(+\infty) = 1. \tag{3}$$

In [1], the problem described by Eqs. (2), (3) was thoroughly investigated assuming that

$$\varphi(0) = \varphi(1) = 0, \quad \varphi(t) > 0, \quad 0 < t < 1, \tag{4}$$

$$\varphi(t) \le \varphi'(0) \cdot t, \quad 0 < t < 1. \tag{5}$$

In fact, the more restrictive boundary condition $\varphi'(t) \le \varphi'(0)$ for $0 < t < 1$, was used in [1] instead of Eq. (5). However, the results of [1] on the solvability of the problem (2), (3) for the semi-infinite speed spectrum $u \ge u_0 > 0$ and the formula

$$u_0 = 2\sqrt{\varphi'(0)} = u_{KPP} \tag{6}$$

for the lower boundary of the spectrum are valid if Eq. (5) is fulfilled. The semi-infinite speed interval [2] has been known to appear only with Eq. (4) satisfied. However, generally speaking, Eq. (6) is not applicable to the lower boundary u_0. Nevertheless, it was noted in [3] that Eq. (6) remains valid when Eq.(5) is violated. Therefore, in 1979 Ya. B. Zel'dovich put forward the problem of extension of the KPP class of equations (Eqs. (1) or (2) with function $\varphi(t)$ obeying Eqs. (4), (5)), for which Eq. (6) would remain valid as the lower boundary of the speed spectrum.

With Eq. (4) satisfied, the solution $t(\xi)$ to the problem (2), (3) is monotonically increasing [1, 2] so that $q(t) = t_\xi(\xi)$ is the positive solution of the equation

$$\frac{dq}{dt} = u - \varphi(t)q^{-1}, \quad q(0) = q(1) = 0. \tag{7}$$

Thus, if $uq > 0$, it follows from Eq. (7) that

$$q(t) < \left(2 \int_t^1 \varphi(\tau)\, d\tau \right)^{\frac{1}{2}} \equiv \phi(t). \tag{8}$$

Integrating Eq. (7) term by term and taking into account Eq. (8), we obtain

$$u = \int_0^1 \frac{\varphi(t)}{q(t)}\, dt > \int_0^1 \frac{\varphi(t)}{\phi(t)}\, dt = \int_0^1 d(-\phi(t)) = \left(2 \int_0^1 \varphi(\tau)\, d\tau \right)^{1/2}.$$

Thus, to solve the problem (2), (3) with conditions (4), the inequality

$$u \geq \left(2 \int_0^1 \varphi(t)\, dt \right)^{1/2} = u_{ZFK} \tag{9}$$

must be satisfied. In combustion theory [3], the right-hand side of Eq. (9) represents the well-known approximate Zel'dovich–Frank-Kamenetskii formula for the flame speed. Inequality (9) is valid for the lower boundary u_0. Consequently, to satisfy Eq. (6), the inequality

$$\varphi'(0) \geq \frac{1}{2} \int_0^1 \varphi(t)\, dt \quad (u_{KPP} \geq u_{ZFK}) \tag{10}$$

must be observed. It should be noted that condition (5), being sufficient for Eq. (6) to be valid, satisfies the inequality

$$\varphi'(0) \geq 2 \int_0^1 \varphi(t)\, dt \quad (u_{KPP} \geq 2u_{ZFK}). \tag{11}$$

We present here one extension of the class of functions (4), (5), as well as the conditions necessary for satisfying Eq. (6) in the form

$$\varphi'(0) \geq \int_0^1 \varphi(t)\, dt \quad (u_{KPP} \geq \sqrt{2}u_{ZFK}). \tag{12}$$

The Zel'dovich problem is not solved herewith. Nevertheless, the example considered in [3] shows that the necessary condition (12) is nearly sufficient, and the class of functions to be investigated is of interest.

Let us start with the following auxiliary proposition. Let $\varphi(t)$ be a positive function of $0 < t < t_\ast$, continuous and smooth in the neighborhood of $t = 0$, and suppose that

452

$\varphi(0) = 0$, $\varphi'(0) > 0$. Let $q(t)$ be the positive solution to Eq. (7) in the interval $0 < t < t_*$ under the condition that $q(0) = 0$ with some $u \geq u_{KPP}$. Suppose further that

$$\varphi(t) \geq ct, \quad 0 < t < t_*, \tag{13}$$

for some $c > 0$, and λ is the positive root of the equation

$$\lambda^2 - u\lambda + c = 0. \tag{14}$$

Then, in the interval $0 < t < t_*$, the inequality

$$q(t) \leq \lambda t \tag{15}$$

holds.

First of all, it should be noted that Eq. (13) entails the inequality $c \leq \varphi'(0)$, such that $u^2 - 4c \geq 0$, and Eq. (14) has a positive root λ. Let us assume for a while that the strict inequality $c < \varphi'(0)$ is satisfied. Then (see Eq. (7)),

$$\lambda > q'(0) = \frac{u}{2} \left(1 + \sqrt{1 - 4\varphi'(0)u^{-2}} \right). \tag{16}$$

Function $q_*(t) = \lambda t$ satisfies the equation

$$q'_* = u - ctq_*^{-1}. \tag{17}$$

Taking into account Eq. (13) we obtain from Eqs. (7) and (17) that

$$(q - q_*)' = -\frac{\varphi(t) - ct}{q} + ct \left(\frac{1}{q_*} - \frac{1}{q} \right) \leq \frac{c}{\lambda q}(q - q_*),$$

whence

$$q(t) - \lambda t \leq (q(\epsilon) - \lambda\epsilon) \exp\left(\frac{c}{\lambda} \int_\epsilon^t \frac{ds}{q(s)} \right), \quad \epsilon < t < t_*,$$

for arbitrary small ϵ. Taking into account Eq. (16), we have $q(\epsilon) - \lambda\epsilon < 0$, thereby satisfying Eq. (15). The assumption $c < \varphi'(0)$ can now be easily dropped by means of the increasing sequence $c_n \to \varphi'(0)$ as $n \to \infty$.

At $u = u_{KPP}$, $c = \varphi'(0)$, and inequality (15) holds for $\lambda = \sqrt{\varphi'(0)}$.

Based on Eq. (15), the following results can be obtained.

In the class of functions $\varphi(t)$ obeying conditions (4) and the inequalities

$$\varphi(t) \geq \varphi'(0)t, \quad 0 < t < t_*, \tag{18}$$

$$\varphi(t) \leq \varphi'(0)t, \quad t_* \leq t \leq 1 \tag{19}$$

for some t_*, $0 \leq t_* \leq 1$, the inequality (12) is necessary for satisfying Eq. (6).

When $t_* = 0$, Eq. (18) is dropped, Eq. (19) being reduced to (5). In this case, Eq. (11) holds, and so does Eq. (12). Therefore, it suffices to consider $t_* > 0$. From Eq. (7), we have

$$u \int_0^{t_*} q \, dt = \int_0^{t_*} \varphi(t) \, dt + \frac{q^2(t_*)}{2}. \tag{20}$$

Condition (18) makes it possible to use inequality (15) at $c = \varphi'(0)$. At $u = u_{KPP}$, we have $q \leq \sqrt{\varphi'(0)}t$, $0 < t < t_*$. Therefore, it follows from Eq. (20) that

$$\varphi'(0) \geq \frac{1}{t_*^2} \int_0^{t_*} \varphi(t) \, dt + \frac{q^2(t_*)}{2} \geq \frac{1}{t_*^2} \int_0^{t_*} \varphi(t) \, dt. \tag{21}$$

If $t_* = 1$, then inequality (12) is valid. Let $t_* \leq 1$. Consider the function

$$\psi(s) = \frac{1}{s^2} \int_0^s \varphi(t) \, dt. \tag{22}$$

From Eq. (21) it follows that $\varphi(0) \geq \psi(t_*)$. Let us show that $\psi(s) \leq \psi(t_*)$ at $s > t_*$. We write out the equation

$$\psi(s) = \psi(t_*) + \frac{1}{s^2} \int_{t_*}^s \varphi(s) \, ds - \left(1 - \frac{t_*^2}{s^2}\right) \psi(t_*). \tag{23}$$

From Eqs. (18) and (19), we have

$$\psi(t_*) \geq \frac{1}{2}\varphi'(0), \quad \int_{t_*}^s \varphi \, ds \leq \varphi'(0)\frac{s^2 - t_*^2}{2}, \quad (s > t_*).$$

Then, from Eq. (23), we obtain at $s > t_*$:

$$\psi(s) \leq \psi(t_*) + \frac{s^2 - t_*^2}{s^2} \left(\frac{\varphi'(0)}{2} - \psi(t_*)\right) \leq \psi(t_*).$$

If $s = 1$, then Eq. (21) yields Eq. (12).

For example, the function $\varphi(t) = \alpha t + \beta t^n$ for $t < 1$, $\varphi(1) = 0$ $(n > 1, \alpha > 0, \beta > 0)$ satisfies Eqs. (4), (18), (19) with $t_* = 1$. Inequality (5) does not hold at any $t_* \in (0, 1)$. However, the problem (2), (3) is solvable and the formula (6) is quite true at $\beta \leq \alpha$. Inequality (12) is $\beta \leq (n + 1)/2 \cdot \alpha$ for the above function.

454

References

[1] Kolmogorov A. N., Petrovskii I. G., Piskunov N. S. *Bul. Moscow University, Sect. A*, 1937, 16, 1 (in Russian).

[2] Vaganov D. A., Khudyaev S. I. *Fizika Goreniya Vzriva*, 1969, 2, 167 (in Russian).

[3] Aldushin A. P., Khudyaev S. I., Zel'dovich Ya. B. *Archivum Combustionis*, 1981, 1, 1/2, 9.

OPTICAL DEFLAGRATION IN WATER VAPOR

G. I. Kozlov, V. A. Kuznetsov

Institute for Problems in Mechanics, Moscow, Russia

In studies of the interaction between powerful laser beams and water a new effect was discovered, termed optical deflagration in water vapor. The experiments were conducted using a CO_2 laser with output power 7 kW. The laser beam was focused by a lens at some distance above water surface inside a quartz tube 60 mm in diameter, half-filled with water.

At the initial moment of laser beam action on the water surface, we observed intense boiling and vaporization with formation of vapor flow in the tube with velocity about 1-2 m/s. The pattern of the interaction was determined by the focus location above water surface. At small distances (5-10 cm) in the focusing region a pattern typical for laser breakdown of gases was observed. Probably, the laser breakdown in water vapor was initiated by the contaminant microparticles existing in the water. In our experiments, the breakdown plasma may serve as a "match" for the ignition of optical deflagration.

With an increase of distance between focus and water surface over 15 cm, the ignition and development of optical deflagration flameball occurred. Figure 1a shows a photograph of these flameballs forming sequentially near the focus and moving upward along the tube. A periodical regime of optical deflagrational combustion established, with the frequency of flashes increasing with an increase in the distance between focus and water surface.
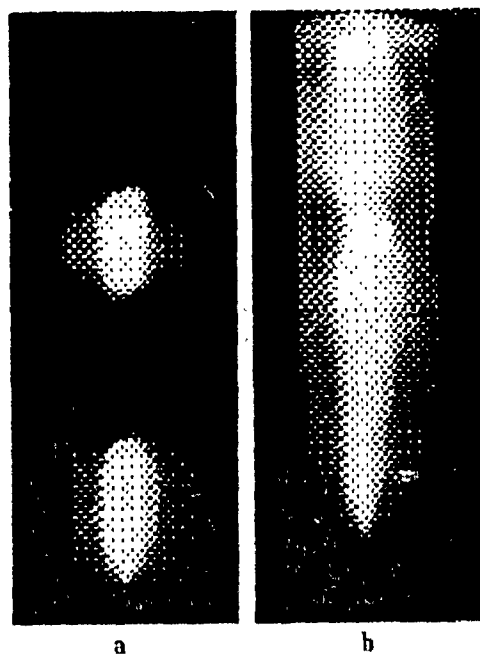
Figure 1.

Finally, when this distance was increased to about 25 cm, the periodical process transformed into a stationary torch of optical flame. A photograph of this flame is s shown in Fig. 1b.

Figure 2.

It is important to emphasize the fact that the optical deflagration occupied only the laser beam cone. It can be seen that flame front is absent and combustion is of distributed nature. Taking this into account, we can conclude that the deflagration flame torch is a realization of an equilibrium process involving heating and dissociation of water vapors. The water dissociation and hydrogen formation in the laser beam has been proved by chromatographic analysis.

Evidently, the nature of optical deflagration is related to the heating of water vapor by laser energy input into vibrational degrees of freedom of water molecules. In the ground state, a water molecule absorbs CO_2 laser radiation only by a small amount,

but with increasing vapor temperature the absorption coefficient χ also increases. To measure the value of χ in deflagration flames, we performed experiments with a wide vapor flow created by a special steam boiler.

The results of this experiment are presented in Fig. 2 where the length of deflagration flame L, absorbed power ΔP, and the absorption coefficient χ are shown as functions of laser beam power P. We can see that the length of deflagration increases with the power increase from 2 to 5 kW, χ is almost constant and equals 0.15 mm^{-1}. With a gradual increase in the laser power, the length remains almost constant, but χ increases sharply, which may be due to an increase in torch temperature and intensification of hydrogen combustion process.

The analysis of deflagration requires a joint consideration of energy balance and physicochemical kinetics equations and is very complex for a general case. We can assume, as the first approximation, that in our experiments the V–T relaxation processes dominate and sustain the system in a virtually equilibrium state. In this case, the values of concentrations determine χ and, in any case, the equilibrium concentration of absorbing molecules will be determined by Boltzmann factor $n_1 = n_0 e^{(-E_1/kT)}$. Thus, heat release per unit volume is given by $\sum \sigma_i n_i I$ (where σ_i is the absorption cross section area and I is the intensity of laser radiation). Then the steady-state temperature of the system will determine the following energy balance equation for a cylindrical volume, assuming that heat losses are determined by heat conductivity:

$$\chi(T)P = A\theta(T), \qquad \chi = \sum \sigma_i n_i, \tag{1}$$

where $\theta(T)$ is the heat flux potential and A is a numerical coefficient, depending on the radial profile of T.

Equation (1) admits several stationary solutions for the same power. If the concentration of absorbing particles is low, the heat release is also weak, and the heat is removed from the system by heat conductivity without heating the mixture. At high temperatures, there are many absorbing particles and high power is released, which is removed from the system by heat conductivity with high temperature gradient. The onset of periodic regime is also possible in the system.

Note that ignition of optical flame requires that water dissociation to be noticeable, which ca be the case at temperatures about 2000 K and higher. This temperature determines the power threshold value P_t for ignition of deflagration torch. It can be determined from Eq. (1), if we assume that the absorption coefficient is $\chi = 0.15$ mm^{-1}, according to our measurement results. Then, assuming that $A = 2$ and $\theta(2000\ \text{K}) = 2.4$ W/cm, we can obtain $P_t \approx 1$ kW from equation Eq. (1), which agrees well with the above mentioned experimental data.

NONSTEADY PROCESSES IN TWO-PHASE GAS–DROPLET PERFECT MIXING REACTOR

V. N. Pushkin, A. M. Rubanov

Ukhta Industrial Institute, Ukhta, Komi Republic, Russia

The analysis of nonsteady processes proceeding in reacting volume is a matter of principle for the theory of perfect mixing reactors. It serves as a basis for detecting the trends characteristic of the period of reactor initiation and is necessary for studying the stability of steady-state operation with respect to large disturbances, as well as operation of the reactors under free-running conditions [1, 2]. The steady-state operation of a two-phase gas–droplet perfect mixing reactor were investigated earlier [3] using the methods of thermal theory of combustion. The present paper is focusing on the nonsteady processes of heat and mass transfer in the reactor. The key results are obtained in numerical experiments simulating the development of the processes mentioned. The emphasis is placed on the dependence of reactor operation on the regime parameters characterizing the flow rate, conditions of heat exchange with surroundings and the structural properties of the gas–liquid mixture. The reactor model is based on assumptions including the monodisperse nature of the starting mixture, the equality of inlet and outlet volumetric flow rates, low mass fraction of the dispersed phase, the preheating of a single-component liquid fuel, the attachment of the droplets to the gas, the dependence of the gas-phase reaction on a single deficient component (fuel vapor). According to the assumptions, the distribution of the droplet residence time z can be considered as independent of the droplet size. Then it is easy to show that the equation describing this distribution admits a self-similar solution $\phi = \exp(-z)$, and the nondimensional mathematical model of reactor takes the following form:

$$\frac{dc_b}{d\tau} = -Da\,c_b \exp\frac{\theta}{1+\beta\theta} + c_{b0} + c_{20} - c_b - c_2, \tag{1}$$

$$\gamma(1-c_2)\frac{d\theta}{d\tau} = Da\,c_b \exp\frac{\theta}{1+\beta\theta} - \frac{Da}{Se}(\theta-\theta_w) - \gamma(1-c_{20})\theta, \tag{2}$$

$$\frac{d\bar{r}^2}{d\tau} = -\frac{\theta-\theta_2}{\omega}, \tag{3}$$

$$c_2 = c_{20}\int_0^{\tau_v} \bar{r}^3 \exp(-z)\,dz. \tag{4}$$

Here, c_b is the fuel vapor concentration; c_2 is the liquid phase concentration; θ is the gas temperature; θ_w is the reactor wall temperature; Da, Se, β, γ are the conventional

parameters of combustion theory; $\bar{r}$ is the radius of droplets dependent of residence time z; τ_v — the residence time of the currently vanishing droplets; ω is the scale of heterogeneity (proportional to the second power of the initial droplet radius r_0^2). The droplet temperature θ_2 is assumed to be uniformed and constant. The suffix 0 refers to the starting mixture parameters.
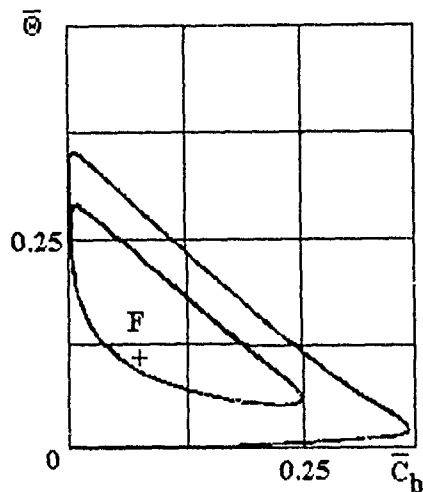
Figure 1: The phase plane of the problem at $\gamma = 0.001$; $\beta = 0.05$; $Da = 0.1525$; $Se = 0.025$; $\omega = 3$; $c_{20} = 0.04$; $c_{b0} = 0.01$, where $\bar{\theta} = \theta\gamma/(c_{20} + c_{b0})$; $c_b = c_b/(c_{20} + c_{b0})$.

Differential equations (1) to (3) were integrated by a modified Runge–Kutta method simultaneously with the computation of droplet size distribution at every step of integration. The performed computations confirm the conclusions based on the analysis of a steady-state model. Furthermore numerical procedure can be used to determine characteristics of theoretical and practical importance, such as induction time for transition to steady-state operation, period and amplitude of oscillations in the free-running case.

Figures 1 to 3 illustrate the scope of the proposed mathematical model. Figure 1 shows the phase curve $\theta(c_b)$ for one of the computed variants. The unstable focus F in Fig. 2 corresponds to the chosen values of the parameters. As is shown, the phase trajectory winds about the limit cycle (with the period $\tau_{cyc} = 1.51$), enveloping the singular point. The latter fact means that after the induction period expiration ($\tau_{ind} = 29.59$) the thermal mode of reactor operation assumes an oscillatory pattern. Figure 2 allows to retrace the evolution of droplet size distribution for the case under study. The $\bar{r}^2(z)$ distribution corresponding to the non-realized steady-state condition is represented by the straight line AB. The parametric diagram providing a basis for prediction of the mode of reactor operation in terms of steadiness and heat-release rate is shown in Fig. 3. The multiplicity curve (solid) and the Andronov–Hopf curve (dotted) are shown in the (Da, Se) plane. The former divides the quadrant into regions with different numbers of steady-state conditions. At crossing the Andronov–Hopf curve, the bifurcation of steady-state conditions occurs. The stable limit cycles are realized inside the loop H. Point P in the diagram corresponds to the variant of analysis presented above.

Figure 2: The history of droplet size distribution under conditions of Fig. 1. $— \tau = 0; 2 — 5; 3 — 15; 4 — 25; 5$ — 29.6; $6 — 30; 7 — 30.35; 8 — 31.05$.
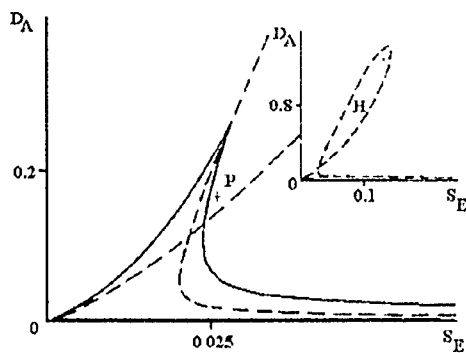
Figure 3: The bifurcation diagram of stable states at $\gamma = 0.001$; $\beta = 0.05$; $\omega = 3$; $c_{b0} = 0.01$; $c_{20} = 0.04$.

References

[1] Aris R. *Analysis of the Processes in Chemical Reactors*. Leningrad, Khimiya, 1967 (in Russian).

[2] Abramov V. G., Merzhanov A. G. *Teoreticheskie Osnovy Protsessov Khimicheskoi Tekhnologii*, 1975, **9**, 6, 863 (in Russian).

[3] Pushkin V. N., Sukhov G. S., Yarin L. P. *Fizika Goreniya Vzriva*, 1993, **29**, 1, 54 (in Russian).

UNSTABLE OSCILLATIONS IN THE SIMPLEST CONTINUOUS-FLOW STIRRED TANK REACTOR (CSTR)

V. K. Ryabinin

Chelyabinsk State University, Chelyabinsk, Russia

Ya. B. Zel'dovich was the first to investigate combustion multistability in a flow system [1]. Further developments in this line by various authors have helped to construct
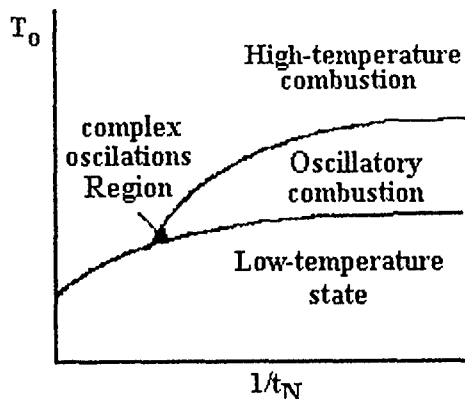
Figure 1: Typical location region of unstable oscillations in the plane of wall temperature T_0 and Newtonian cooling time t_N; mean residence time is fixed.

the theory of nonsteady exothermic reactions in continuous-flow chemical reactors, certain results of which have been summarized in [2–5].

It is well known that, for certain combinations of parameters, the thermal explosion limit in a continuous-flow combustor can transform into a more or less wide region of oscillatory combustion lying between low- and high-temperature steady states. In simplest two-variable models of CSTR, oscillations can only have the form of simple limit cycles [2–5]; more complex models (3 variables and more) can generate oscillations with complex periods or even chaotic behavior [3].

Previous numerical simulations of oscillatory hydrogen oxidation in CSTR have revealed several types of complex oscillations under conditions of chain [6] and thermal [7] ignition; the localization region for such oscillations, in the case of thermal ignition, is shown in Fig. 1. In spite of the comparatively high dimensionality of the CSTR model employed (9 variables), there were reasons to suppose that the complex character of oscillations is due not to the model dimension, but rather to the fact that the phase–plane trajectory intersects the ignition limit curve at a very acute angle. As a result, the coordinates of the intersection point (and ignition conditions) are very sensitive to small perturbations, even such as computational errors [6, 7].

If this conjecture is true, similar effects must be displayed by the simplest CSTR model [4, 5]

$$
\begin{aligned}
\gamma \frac{d\theta}{d\tau} &= (1-\eta)^n \exp\left(\frac{\theta}{1+\beta\theta}\right) - \frac{\theta}{Se}, \\
\frac{d\eta}{d\tau} &= (1-\eta)^n \exp\left(\frac{\theta}{1+\beta\theta}\right) - \frac{\eta}{Da},
\end{aligned}
\tag{1}
$$

where θ, η, τ are the dimensionless temperature, concentration and time, respectively, n is the reaction order, and Se, Da, γ, and β are the combustion theory parameters. Integration of Eqs. (1) was performed by the Gear method.

461
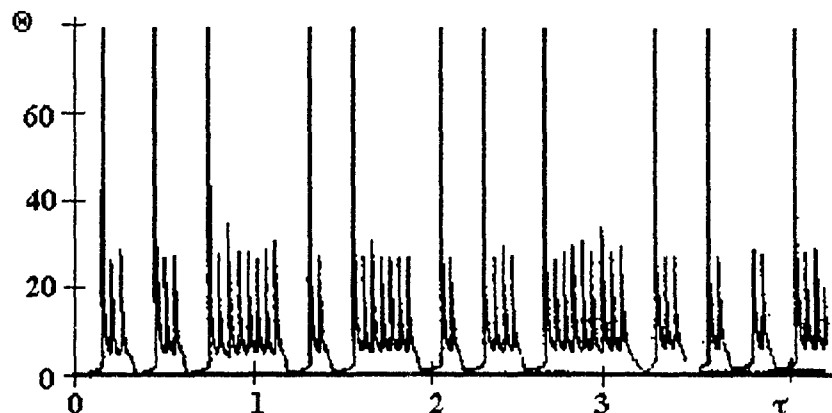
Figure 2: Unstable oscillations in Eq. (1) at $\gamma = 0.01$, $\beta = 0.05$, $Da = 0.051663$, $Se = 0.49665$, and $n = 1$; computational accuracy $\varepsilon = 10^{-5}$.

The search for the region of complex oscillations by the method shown in Fig. 1 has resulted in some examples of unstable bimodal oscillations; one of which is shown in Fig. 2. Such processes are observed in an extremely narrow range of parameters Se and Da restricted to the 4th or even 5th significant digit. Figure 3a shows the phase plane trajectory for the example shown in Fig. 2 in comparison with the thermal equilibrium isocline $d\theta/d\eta = 0$ the isocline $d\theta/d\eta = \infty$. The isoclines intersection point S is a single and unstable stationary state, which is the reason for oscillations [4, 5]. One can see that, after complete reactant consumption, the phase plane trajectory is almost equivalent to the thermal equilibrium isocline but lies slightly below it. Such location of the phase plane trajectory makes it very sensitive to small perturbations, which can either deflect it upwards resulting in intensified reaction and a small-amplitude flash, or downwards with ensuring reaction break, extensive departure from the thermal equilibrium, and a subsequent large amplitude flash. The instability of oscillations is determined by the random character of perturbations due to computational errors which is confirmed by the fact that with decreasing computational accuracy the region of unstable oscillations markedly expands; moreover, even at fixed values of the parameters of Eqs. (1), changing initial conditions, computational accuracy, or the order of operations in formulas leads to noticeable changes in the simulated pattern. However, even a small deviation from the regime of unstable oscillations makes system (1) robust with respect to these perturbations. A corresponding example is shown in Fig. 3b.

The results obtained are unusual, because unstable oscillations cannot occur in the reactor model (1) without dynamic perturbation of its parameters [2–5]. We can only conjecture that under the conditions described, owing to the extraordinary sensitivity of Eqs. (1), calculation errors can act as an external dynamic perturbation destabilizing the oscillations [3]. Perhaps, similar effects can manifest themselves in real reactors due to small fluctuations in cooling and feeding; the main difficulty in their observation is the
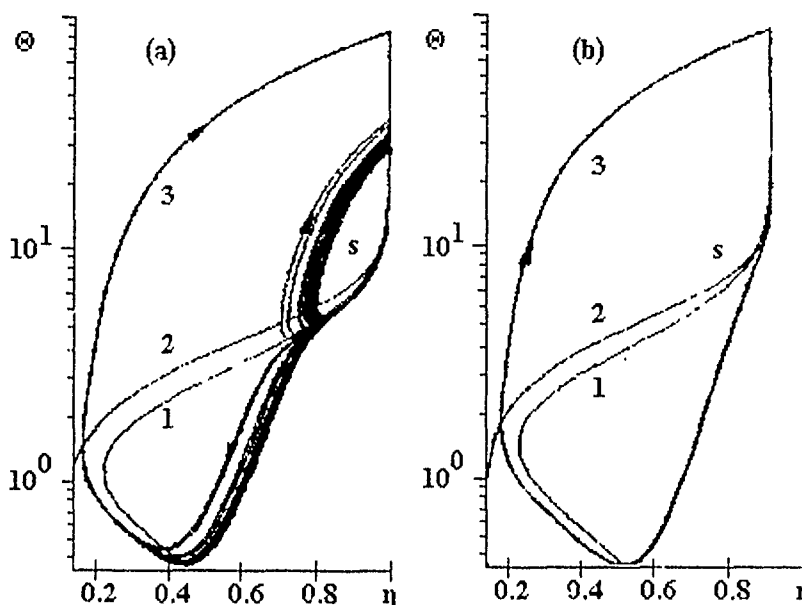
Figure 3: Thermal equilibrium isocline $d\theta/d\eta = 0$ (*1*), $d\theta/d\eta = \infty$ isocline (*2*) and phase plane trajectory (*3*) for (*a*) example of Fig. 2; (*b*) the same parameters, except for $Da = 0.055$ and $Se = 0.5$.

extremely narrow range of existence. For example, bimodal oscillations experimentally found for hydrogen oxidation in CSTR under the conditions of the second (chain) ignition limit were described in [8]; the nature of these oscillations may admit a similar explanation [6].

References

[1] Zel'dovich Ya. B. *Zhurnal Tekhnicheskoi Fiziki*, 1941, **11**, 493 (in Russian).

[2] Vol'ter B. V., Sal'nikov I. E. *Stability of the Operating States of Chemical Reactors.* Moscow, Khimia, 1972 (in Russian).

[3] *Oscillations and Travelling Waves in Chemical Systems.* (Field R. J. and Burger M., Eds.). Moscow, Mir, 1988 (in Russian).

[4] Merzhanov A. G., Abramov V. G. *Chem. Eng. Sci.*, 1977, **32**, 475.

[5] Vaganov D. F., Samoylenko N. G., Abramov V. G. *Chem. Eng. Sci.*, 1978, **33**, 1133.

[6] Vilyunov V N., Ryabinin V. K. *Fizika Goreniya Vzriva*, 1991, **27**, 2, 79 (in Russian).

After expanding of the right-hand side of Eq. (1) in the powers of θ up to the third order we have

$$\frac{d\theta}{d\tau} = 2\left(v - \frac{\rho}{3 - \sqrt{3}}\right) - \frac{\rho\theta}{2 - \sqrt{3}} - \frac{\theta^3}{2}, \tag{2}$$

where $v = (V - V_c)V_c^{-1}$ and $\rho = (R - R_c)R_0^{-1}\exp(-\varepsilon T^{-1})$. Since the stationary patterns are given by the zeroes of the right-hand side of Eq. (2), this corresponds to van der Waals equation of state.

Temperature θ plays the role of order parameter (density), the quantities v and ρ are the "pressure" and "temperature", respectively. Let v be

$$v = \rho - (3 - \sqrt{3})^{-1} + \frac{h}{2}, \tag{3}$$

h being proportional to $\exp(-i\omega t)$. Then, on linear approximation, we have for the Fourier components

$$\theta_\omega = \chi(\omega)h_\omega, \qquad \chi(\omega) = [\rho(2 - \sqrt{3}) - i\omega]^{-1}. \tag{4}$$

The quantity $\chi(\omega)$ is a generalized susceptibility [3]. At low frequencies, χ can reach an infinitely large value with ρ approaching the critical point from above (Curie–Weiss law).

The anomalous susceptibility is obviously due to the increase in thermal relaxation time in the vicinity of the critical point. This increase follows from Eq. (2) and is characteristic of the order parameter behavior. Since the relaxation time is large, one can assume the temperature fluctuations to be quasisteady. Hence, if h is now a random field, its fluctuations can be treated as δ-correlated and, according to [3], we obtain

$$\langle(\delta\theta)^2\rangle = (2 - \sqrt{3})(h^2)_\omega(2\rho)^{-1} \tag{5}$$

for the temperature fluctuations. Here $(h^2)_\omega$ is constant (does not depend on ω). For example, we have

$$\langle(\delta\theta)^2\rangle = (\frac{2}{3})kT_c[c(T_c - T_0)\rho]^{-1}$$

for thermal (Nyquist) noise and

$$\langle(\delta\theta)^2\rangle = eT_c^{-1}\left(\frac{\varepsilon R_c}{ct_0}\right)^{1/2}\rho^{-1}$$

for fractional noise. Here, k is Boltzmann's constant and e is the electron charge.

References

[1] Frank-Kamenetskii D. A. *Sov. Phys. Tech. Phys.*, 1939, **9**, 1457.

After expanding of the right-hand side of Eq. (1) in the powers of θ up to the third order we have

$$\frac{d\theta}{d\tau} = 2\left(v - \frac{\rho}{3 - \sqrt{3}}\right) - \frac{\rho\theta}{2 - \sqrt{3}} - \frac{\theta^3}{2}, \tag{2}$$

where $v = (V - V_c)V_c^{-1}$ and $\rho = (R - R_c)R_0^{-1}\exp(-\varepsilon T^{-1})$. Since the stationary patterns are given by the zeroes of the right-hand side of Eq. (2), this corresponds to van der Waals equation of state.

Temperature θ plays the role of order parameter (density), the quantities v and ρ are the "pressure" and "temperature", respectively. Let v be

$$v = \rho - (3 - \sqrt{3})^{-1} + \frac{h}{2}, \tag{3}$$

h being proportional to $\exp(-i\omega t)$. Then, on linear approximation, we have for the Fourier components

$$\theta_\omega = \chi(\omega)h_\omega, \qquad \chi(\omega) = [\rho(2 - \sqrt{3}) - i\omega]^{-1}. \tag{4}$$

The quantity $\chi(\omega)$ is a generalized susceptibility [3]. At low frequencies, χ can reach an infinitely large value with ρ approaching the critical point from above (Curie–Weiss law).

The anomalous susceptibility is obviously due to the increase in thermal relaxation time in the vicinity of the critical point. This increase follows from Eq. (2) and is characteristic of the order parameter behavior. Since the relaxation time is large, one can assume the temperature fluctuations to be quasisteady. Hence, if h is now a random field, its fluctuations can be treated as δ-correlated and, according to [3], we obtain

$$\langle(\delta\theta)^2\rangle = (2 - \sqrt{3})(h^2)_\omega(2\rho)^{-1} \tag{5}$$

for the temperature fluctuations. Here $(h^2)_\omega$ is constant (does not depend on ω). For example, we have

$$\langle(\delta\theta)^2\rangle = (\frac{2}{3})kT_c[c(T_c - T_0)\rho]^{-1}$$

for thermal (Nyquist) noise and

$$\langle(\delta\theta)^2\rangle = eT_c^{-1}\left(\frac{\varepsilon R_c}{ct_0}\right)^{1/2}\rho^{-1}$$

for fractional noise. Here, k is Boltzmann's constant and e is the electron charge.

References

[1] Frank-Kamenetskii D. A. *Sov. Phys. Tech Phys.*, 1939, **9**, 1457.

[2] Zel'dovich Ya. B. *Selected works*, 1. Princeton, Princeton Univ. Press, 1992.

[3] Landau L. D., Lifshitz E. M. *Statistical Physics*. Oxford, Pergamon Press, 1969.

PRESPINODAL THERMAL DECOMPOSITION OF HIGHLY ENERGETIC MATERIALS

O. F. Shlensky[*], E. F. Vainshtein[†]

[*]*Mendeleev University of Chemical Technology, Moscow, Russia*
[†]*Semenov Institute of Chemical Physics, Moscow, Russia*

The upper boundary of thermodynamic stability of solids and liquids is determined by equating the second derivative (variation) of Gibbs free energy to zero, e.g., $\delta^2 G = 0$ [1]. This condition can be used in determining the temperature T_{sp} on the spinodal line as a function of pressure. Because of thermolysis, the properties of chemically unstable substances have not been thoroughly investigated in the vicinity of the spinodal line. Conventional methods of thermal analysis are of little use for the analysis in vicinity of the spinodal line.

The method of contact heating [2–4] makes such an investigation possible. In this method, a small sample of a substance is placed in contact with a substrate (solid or liquid) heated to a constant high temperature. If the sample is sufficiently thin (2–5 μm), the average heating rates attained exceed $10^4 \ldots 10^5$ K/s. Owing to its small size, the sample fits tightly to the substrate. If the sample size is smaller than critical, thermal explosion does not occur [3].

Using this unique contact method, we were able to show for the first time that explosion-type reactions take place before the limiting temperature T_l of thermolysis is reached for a given substance [2–4]. In subsequent investigations, probe methods were used [5] to determine T_l. The results obtained by the probe method confirm that explosion reactions take place when the temperature T_l is reached [5–7]. However, probe methods have certain drawbacks. They cannot be used in studying solids, in analyzing the kinetics of thermolysis near T_l, and in exothermic processes.

Using the contact and other methods, we have identified the following two types of fast thermolysis:

- processes due to the weakening of intermolecular forces and the "cage" effect (in the case of linear and cross-linked polymers);

- processes characterized by homogeneous nucleation [8].

Table 1: Limiting temperatures for some compounds.

No.	Sample	$T_l/°C$	$E/(\text{kJ/mole})$	No.	Sample	$T/°C$
1	Trotyl	335	130	7	Polystyrene	530
2	Octogen	350	215	8	Glycerine	460
3	Ammonium nitrate	340	240	9	Polyethylene glycol,	
4	Ammonium dichromate	295	250		mol. mass 2500	465
5	NaN_3	550	320	10	Oil (Oilfield	
6	TATB	460	110		"Alaninskoye"	500

Both processes may involve changes in the chemical reaction mechanism. They proceed within a narrow temperature range near T_l. As pointed out in [4, 5], an analysis of the equation of state shows that $T_l < T_{sp}$. Herein lies a certain similarity between the discovered effect and the prespinodal explosive boiling of superheated metastable liquids. However, the main distinctive characteristic of explosive thermolysis is the change in the chemical composition of the superheated substance.

In this communication, we present the results obtained in measurements of the limiting temperatures, T_l, and activation energies of thermolysis for a number of highly energetic substances. The results are summarized in Table 1 (left column). In the same table the temperatures T_l for some non-explosive substances in which thermal decomposition occurs with heat absorption (right column) are given.

The limiting temperature of polystyrene corresponds to the value T_l that has been calculated by the equation of state for linear polymers [2, 4]. Temperatures T_l of the samples No. 4, 8, and 9 agree, within several degrees, with the data obtained by other investigators [6, 7, 9]. The problems of accuracy of the contact method have been addressed in [2, 4].

The discovery of the previously unknown explosive prespinodal effect has brought to the forefront a more thorough examination of physical and mathematical models of combustion. In particular, it is necessary to set a limit to the temperature range where the Arrhenius law is valid for a given material, i.e.

$$k = z \exp\left(-\frac{E}{RT}\right), \quad \text{if} \quad T < T_l;$$

$$k = k_0, \quad k_0 = 10^{10} \div 10^{12}, \quad \text{if} \quad T = T_l,$$

These two expressions can be unified by a single Arrhenius equation with variable activation energy: $E = E(T)$, e.g., $E = E_0(1 - T/T_l)^n$. Here E_0 is the value of E at $T \ll T_l$, parameter $n = 0.01$.

The same correction must be made in the heat release function W in the equations of heat and mass transfer:

$$W = Qz \exp\left(-\frac{E(T)}{RT}\right).$$

At $T = T_l$, we have $W = Qz$, where Q is the thermal effect. The temperature T_l determines the extreme value of the adiabatic induction period t_{ad} of slow thermolysis of certain materials:

$$t_{ad} = \frac{c_p}{Qz} \int_{T_0}^{T_1} \exp\left(\frac{E}{RT}\right) dT \simeq \frac{c_p}{Qz} \frac{RT_l^2}{E} \exp\left(\frac{E}{RT}\right).$$

Above T_l, the sample completely turns into gaseous products. The limiting temperature T_l is a fundamental property of explosive materials. Unlike the ignition temperature, the concept of the limiting temperature T_l is of simple physical nature, based on fundamental thermodynamic laws [1, 5]. Some applications of the discovered effect have been discussed in [2].

References

[1] Muenster A. *Chemische Thermodynamik*, Berlin, Akademie-Verlag, 1969.

[2] Shlensky O. F., Shashkov A. G., Aksenov L. N. *Thermal Decomposition of Materials*. Amsterdam, Elsevier, 1991.

[3] Shlensky O. F., Yundev D. N. *Teplofizika Vysokikh Temperatur*, 1993, **31**, 4, 685–686 (in Russian).

[4] Shlensky O. F., Matyukhin A. A., Vainshtein E. F. *J. Therm. Anal.*, **31**, 1986, 107.

[5] Pavlov P. A. *Boiling Dynamics of Superheated Liquids*, Ural Div. Acad. Nauk SSSR, 1988 (in Russian).

[6] Skripov P. V., Begishev V. P. *Vysokomol. Soedineniya*, 1992, **A34**, 1, 140–145 (in Russian).

[7] Skripov P. V., Ryutin S. B., Begishev V. P. *Inzhenerno-Fisicheskii Zhurnal*, 1992, **62**, 2, 276–282 (in Russian).

[8] Shlensky O. F., Zyrichev N. A. *Kchimiya Vysokikh Energii*, 1994, **18**, 3, (1994), 1–7 (in Russian).

[9] Enikolopyan N. S., Aleksandrov A. J., Gasparyan E. E. *Dokl. Akad. Nauk SSSR*, 1991, **319**, 1384–1389 (in Russian).

[10] Shlensky O. F., Murashov G. G. *ibid*, 1983, **269**, 6, 1406–1409 (in Russian).

THE RADIATIVE HEAT TRANSFER IN THE 22-HOLE YONTAN BRIQUETTES BOILER

Eung K. Shon

Combustion Engineering Research Lab., Korea Institute of Energy Research, P.O.Box 5, Tsedok Science Town, Taejon

Introduction

The most important use of Korea Anthracite Coal is to make 22-hole briquettes (Yontan) for panel heating of Korean type (Ondol). Since the mid-70s, this panel heating system has been investigated by many institutes and schools not for the design of Yontan boiler but only in the course of development of hot water pipe systems and the relevant materials. The technical and engineering aspects of boiler design and combustion mechanism have not been studied, which has resulted in the shortage of data for standard boilers and makes boiler design at the maker's convenience very difficult.

An empirical and theoretical approach to a better design of boilers requires fundamental knowledge of heat transfer and interaction affects of several variables in the Yontan boiler. These variables are the distance between the combustion tube and the water chamber, the length of the water chamber and the materials of the combustion tube and the reflector.

Two approaches were proposed to develop a better design of the Yontan boiler. The first one was aimed at developing a standard model and calculating the heat distribution, and the second one was an experiment that should be carried out by varying the parameters to study the effect of each parameter. Finally, we examined the differences between the theoretical and experimental results and obtained the data required for the development of a better design of the Yontan boiler.

Theoretical and Experimental Approach

For the theoretical analysis, the most popular type of Yontan boiler in this country which consisted of two Yontan briquettes stacked in a cylindrical combustion tube was chosen as a model. As shown in Fig. 1, the lower part of the combustion tube was left out of consideration. Inasmuch as combustion is taking place in the upper part of the combustion tube, it is assumed that the temperature of the lower part of the combustion tube is negligible, and so is the effect of the radiation heat transfer between the water chamber and the combustion tube. The combustion tube was divided into five parts, 1–5, corresponding to the radiating areas on the exterior surface of the combustion tube tested.
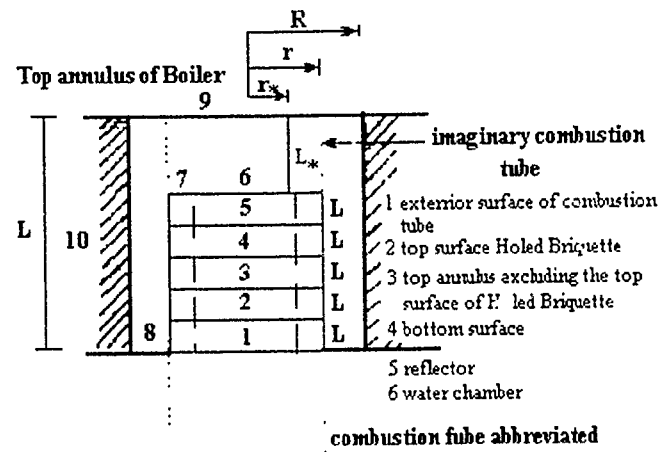
Figure 1: Sketch of the standard model for Yontan boiler.
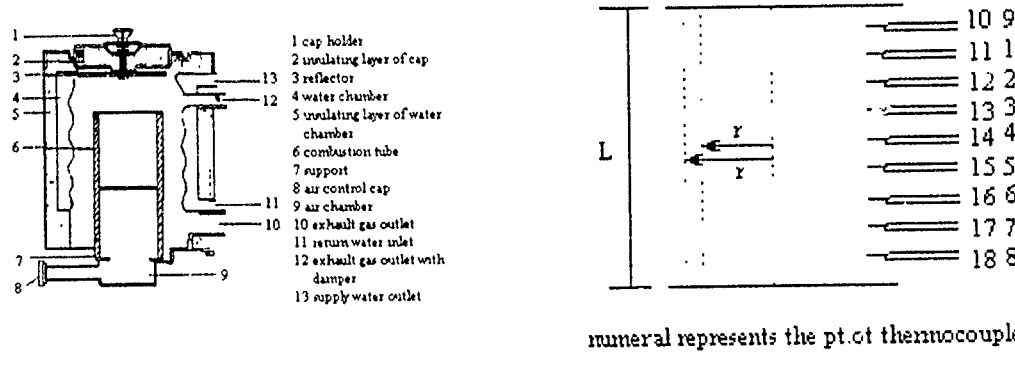
Figure 2: Section diagram of test boiler.

Figure 3: T/C arrangement on the interior and exterior surfaces of combustion tube.

Table 1: Experimental Results.

Item	Combustion Tube Type I	Combustion Tube Type II	Combustion Tube Type III
Wt. of Briquette	3.128 g	3.295 g	3.112 g
Wt. of Igniter	199"	196"	195"
Carbon burn-out	999 g	1.186 g	1.251 g
Burning time	8 h	8 h	8 h
Outdoor temp.	22.3 °C	23 °C	23.9 °C
Exhaust gas temp.	49.5 °C	49.5 °C	48.2 °C
Excess air ratio	3.88	4.4	4.32
Air flow	1.540 gmole	2.052 gmole	2.143 gmole
Temp at extinction	600 °C	650 °C	640 °C
Return water temp (supply)	35.1 °C	35.5 °C	34.6 °C
Water outlet temp	47.1 °C	49.1 °C	49.8 °C
Water flow	66.5 kg/h	66.8 kg/h	67.1 kg/h
Boiler surface temp.			
1	72.4 °C	76.3 °C	81.1 °C
2	59.2 °C	59.9 °C	60.8 °C
3	33.3 °C	33.6 °C	32.3 °C
Thermal conductivity (kcal/mh °C)	—	0.398	0.370
Temp. Diff. between Interior and Exterior surfaces of tube	—	109 °C	194 °C
Heat release (kcal/8 hr)	9.072	10.362	10.969
Heat of hot water (kcal/8 hrs)	6.386	7.238	8.185
Heat transfer to tube surface (kcal/8 hrs)	—	2.325	3.364
Heat of exhaust gas (kcal/8 hrs)	2.958	4.435	3.364
Heat of briquettes preheating	208	301	260
Heat of tube heating	—	206	304

In this study, however, the combustion tests was performed in the standard boiler equipped with three different tubes. The test boiler and combustion tubes are shown in Figs. 2 and 3, respectively. The test procedures were based on the 'Experimental Method of the Performance of Yontan Boiler' and 'Korean Standard of Yontan Briquettes and Char Coal'.

Results and Discussion

In Table 1, the experimental conditions are specified and the test results are shown. The heat conductivities of combustion tube II and III have been measured by transient

heat flow method with Model HC–60 high-temperature thermal conductivity tester.

The relationship between the heat recovery in the 3 different combustion tubes and the effects of water chamber length, the effect of reflector material and the effect of distance between the combustion tube and the water chamber were investigated. In addition, the radiative heat flux in the Yontan boiler was analyzed.

Summary

The fractions of the heat transfer to the water chamber were about 70% of the radiation heat flux and less than 30% of the convection heat flux. For the radiation heat transferred to the water chamber, about 42–44% comes from the top surface of the combustion tube and 22-hole briquette, 27–35% and 25–30% come from the reflector and the exterior surface of the combustion tube, respectively.

There was no effect of variation of the water chamber length and the distance between the combustion tube and the water chamber on the radiative heat transfer.

A stainless steel reflector installed under the cap of the combustion tube improved the radiative heat transfer to the water chamber by about 6% as compared to the SB 41 reflector.

MACROSCOPIC MECHANISM OF INTERFACE STRUCTURING UPON SOLIDIFICATION

A. G. Varlamov

Institute for Structural Macrokinetics, Chernogolovka, Russia

Heterogeneous solidification is, generally, a very complicated physical and chemical process. The approaches used to describe it may be tentatively divided into two groups: thermal-diffusional and geometrical-statistical [1–2]. The fundamental problem of geometrical-statistical approaches is the description of mother-medium space occupation by the condensed phase taking into consideration the properties of the space and phase interface [2] In this report, condensed phase structure formation in the heterogeneous solidification viar the layer-by-layer and normal growth mechanisms is reviewed within the framework of geometrical-statistical approach.

1 The Layer-by-Layer Growth Mechanism

Polycrystalline layer formation is modeled as follows. The substrate, forming an infinite plane, is in equilibrium with the mother medium susceptible to heterogeneous
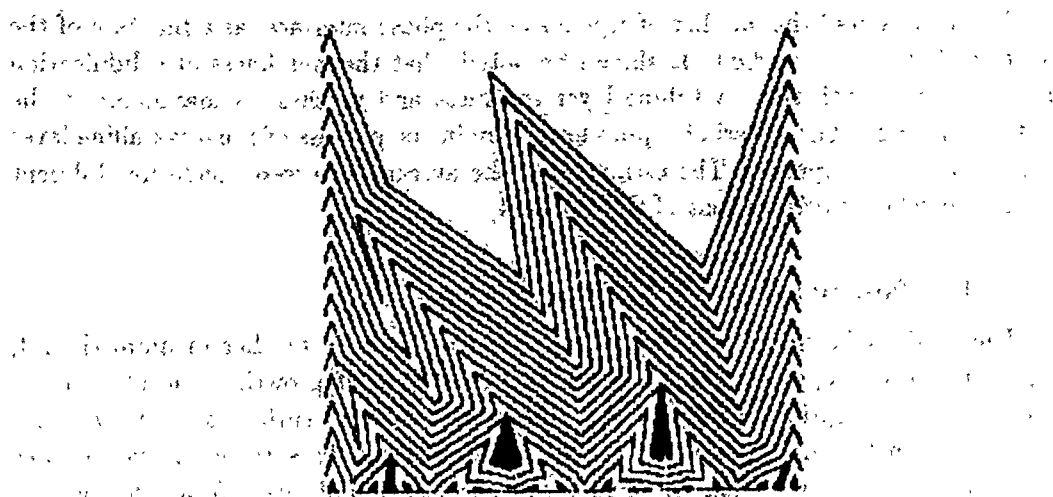
Figure 1: Structure formation in the heterogeneous solidification via the layer-by-layer growth mechanism.

solidification via the layer-by-layer growth mechanism. At the initial moment, freely oriented crystalline nuclei exist on the substrate. Their growth occurs via parallel motion of facets (following the Stenon law) at a certain rate. The growth of crystals leads to their collisions. The fragments of crystal surfaces isolated from the mother medium do not grow. After all the crystals have collided with each other, a continuous polycrystalline layer is formed. The growth of the layer thickness leads to a decrease in the number of crystallites due to "geometrical selection" [4].

Figure 1 shows the numerical results. The growth of the crystals leads to their collisions, isolation of part of the crystal surfaces from the mother medium, and growth arrest for some of the crystals. Other crystals exist on the phase interface at any layer thickness. These were termed "growth leaders". At late stages of the process, the phase interface is formed by the "leaders" only. The "geometrical selection principle" introduced by G. G. Lemlein [3] is refined using the concept of the "growth leader". The new formulation is as follows. In the process of polycrystalline layer formation, the crystals ("growth leaders") for which the projection of facets or top moving rate vector on the substrate plate normal is the largest [4], remain on the phase interface. The individual stages of the polycrystalline layer formation process have been singled out. They are:

(1) free crystal growth (before collision);

(2) collision between the crystals;

(3) overgrowth stage;

(4) stationary stage.

The variation of the number of crystals on the phase interface, as a function of the layer thickness, was studied. It should be noted, that the roughness of solidification front increases with the crystalline layer thickness and reaches its maximum at the stationary stage. The criteria for pore formation in the process of polycrystalline layer formation were proposed. The estimates of the average size were made for different forms and relative orientations of the nuclei [4].

2 The Normal Growth Mechanism

The model of formation of the layer deposited from the mother medium (liquid, vapor) is the concept of the normal mechanism of deposit growth. The idea of the macroscopic description underlying the concept is that every surface point moves at a certain rate in the direction of the mother medium along the surface normal [5]. Let $F(x_0, y_0, z_0) = 0$ be the equation of substrate surface. Solidification front propagation is governed by the following equations:

$$(x - x_0)^2 + (y - y_0)^2 + (z - z_0)^2 = \left[\int\limits_0^t V_n(T, C, \ldots)\, dt \right]^2 \tag{1}$$

$$\frac{x - x_0}{F'_{x_0}} = \frac{y - y_0}{F'_{y_0}} = \frac{z - z_0}{F'_{z_0}} \tag{2}$$

where $V_n(T, C, \ldots)$ is the normal velocity of front propagation, and $\int_0^t V_n(T, C, \ldots)\, dt$ is the distance covered by the front during the time t. The process of phase interface structure formation for the most general case of the substrate surface has an irregular form at $V_n = const$. Two stages of the process can be identified:

1. **The irregular stage.** The number of convex portions of the phase interface decreases and their dimensions increase with increasing layer thickness. The decrease in the number is due to the "geometrical selection" [5]. Solidification fronts of heterogeneities of higher amplitude occupy larger portions of the free space and hinder the propagation of low-amplitude heterogeneities. Finally, the heterogeneities connected with the highest amplitude substrata heterogeneities remain on the interface. They were named "growth leaders".

2. **The regular stage.** The phase interface consists of "growth leaders" only. The number of the convex portions of the interface does not change. Their curvature radius increases with increasing coating thickness, which leads to surface smoothing. At a certain layer thickness, cusps (projections of front intersection lines on to the plate) appear, dividing the phase interface into separate elemental spherolites. The analytical expressions relating specific surface and macroroughness to the thickness and substrate characteristics have been obtained [5]. It should be noted that the solidification front roughness decreases with increasing crystalline layer thickness and asymptotically tends to a smooth surface [5].

474

References

[1] Kurz W. Fisher D.J. *Fundamentals of Solidification*. Trans. Tech. Publications, Switzerland–Germany–UK–USA, 1986.

[2] Belenkii V. S. *Geometrical-Statistical Crystallization Model*. Moscow, Nauka. 1980 (in Russian).

[3] Lemlein G. G. *Doklady Akad. Nauk SSSR*, **48**, 3, 1945, 177–180 (in Russian).

[4] Varlamov A. G, Grigoryev Yu. M., Logachov A. B. *Paper Dep. VINITI No.3233B92* (in Russian).

[5] Varlamov A. G., Grigoryev Yu. M., Shkadinskii K. G. *Poverkhnost*, 1, 1991, 123–129 (in Russian).

SESSION 8. Intensive Shock Waves and Extreme States of the Matter

DESENSITIZATION OF RDX CHARGES AFTER PRESHOCKING BY A COMPRESSION WAVE IN A SiC–CERAMIC ROD

I. A. Balagansky[*], E. F. Gryaznov[†]

[*]Novosibirsk State Technical University, K. Marx ave., 20, Novosibirsk, 630092 Russia
[†]Bauman Moscow State Technical University, 2-nd Bauman str., 5, Moscow, 107005 Russia

The phenomenon of desensitization of multiply shocked explosives is well known [1]. R. N. Mulford et al [2] have described the experiments with double-shocking initiation of detonation in PBX–9404, PBX–9502 and PBX–9501 by a composite projectile consisting of a soft thin layer on the front surface of a high-impedance backing material. The soft layer is PMMA and the high-impedance material is multicrystalline pressed alumina. After double-shocking loading of PBX–9502 in experiments where the precursor shock was 3.7 GPa and the second shock was 7.95 GPa, this explosive was an inert material. For PBX–9404 in the experiments where the precursor shock was 2.3 GPa and the second shock 5.6 GPa, a detonation wave was observed. But desensitization is clearly evident, with the run to detonation showing an increase of 270% over that expected from the Pop plot, when both the precursor and the second shock are considered. R. E. Setchell [3] used VISAR diagnostics to monitor the behavior of materials subjected to preshocking by ramp waves which subsequently develop into shocks. The ramp waves appear to gradually compress granular materials without provoking reaction at a pressure of 5.1 GPa. Even after the shock formation, a considerable delay in the transition to detonation was observed, as compared to initiation by a single shock. The authors of [2] examined the nature of desensitization as regards pore collapse, temperature changes, and changes due to chemical reaction behind the first wave.

One possible means to produce ramp waves is to use high modular ceramics having sufficient values of sound velocity (C_s) and Hugoniot elastic limit (HEL). In particular, for SiC–ceramics, $C_s = 11.2$ km/s and HEL = 8 GPa. Some interesting features of propagation of shock waves in elastic bodies of finite size, due to the inertia of cross section, are described in the monograph [4]. For example, if the boundary condition at the end of a semi-infinite elastic rod is given by a step function, then this step is smoothed due to propagation along the rod. The thickness of the smoothed front, d, approximately equals $d = (r^2 x)^{1/3}$. Here r is the radius of the rod, x is the run of the front. The profile of the smoothed front is shown in Fig. 1 versus the nondimensional coordinate ξ.

In connection with the data presented, we conducted a series of experiments designed to study the initiation capability of compression waves in rods made of self-sustained silicon carbide. We used the rods of square cross section custom-made at
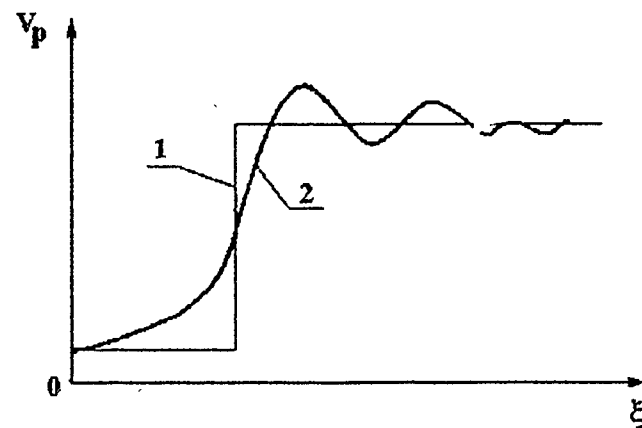
Figure 1: Profile of smoothed front: *1* — step function; *2* — smoothed front.
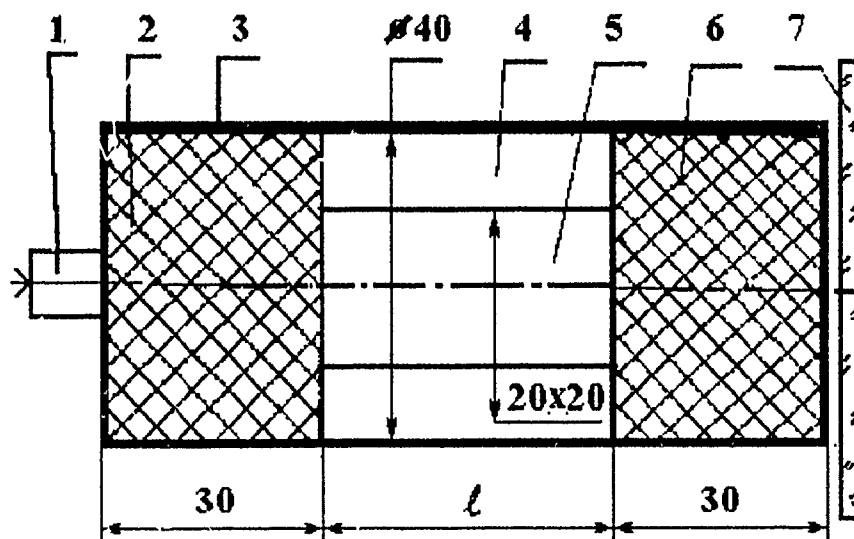
Figure 2: Schematic of experimental assembly: *1* — detonator; *2* — active charge (stabilized RDX of density 1.64 g/cm^3); *3* — aluminum shell; *4* — inert matter; *5* — ceramic rod; *6* — passive charge (stabilized RDX of density 1.64 g/cm^3); *7* — PMMA.

Table 1: The results of experiments with ceramic rods.

No.	Inert matter	Length of rod l, mm	Detonation
1	Epoxy resine	80	No
2	Air	40	No
3	Air	20	No
4	Air	10	No

Kiev Institute for Problems of Materials for our experiments. The butt ends of the rods were polished. Active and passive high explosive charges were prepared by moulding stabilized RDXX. The experimental assembly is shown in Fig. 2. The main results of experiments are given in Table 1 for ceramic rods of different length. A rotating-mirror camera was used to record detonation in the passive charge.

The distance between the active and passive charges for reliable propagation of detonation in air is approximately 75 mm for stabilized RDX of density 1.60 g/cm^3 [5]. Similar distances for water, steel, and aluminium are within 15–20 mm.

Thus, we have observed the low capability of an advanced compression wave in the ceramic rod of initiation of detonation in passive charges of stabilized RDX. In addition, we observed the desensitization of RDX charges after preshocking by a compression wave in the rod of SiC–ceramic due to the absence of detonation after the second shocking by a shock wave in air at the distance of 10 mm between the active and passive charges.

References

[1] Campbell J. R., Davis W. C., Ramsay J. B., Travis J. R. *Phys. Fluids*, 1961, **4**, 4, 511.

[2] Wulford R. N., Sheffield S. A., Alcon R. R. In.: *Proc. 10th Symp. (Int.) on Detonation*, 1993, 415.

[3] Setchell R. E. *Comb. Flame*, 1981, **43**, 3, 255.

[4] Rabotnov Y. N. *The Mechanics of Deformation of the Solid Bodies*. Moscow, Nauka, 1979 (in Russian).

[5] Baum F. A., Stanyukovich K. P., Shechter B. I. *The Physics of Explosion*. Moscow, Fizmatgiz, 1959 (in Russian).

478

FAST SHOCK TUBE WITH EXPLOSIVE (FSTE)

A. Yu. Dolgoborodov

Semenov Institute of Chemical Physics, Kosygin St. 4, Moscow, 117977 Russia

Attempts to accelerate plates to higher velocities continue to hold interest of those doing equation-of-state research. Extensive data have been obtained for common metals over the last thirty years, most of which are limited to pressures 4 Mbar or lower. Data for conditions above this pressure come slowly and are much less abundant than the lower pressure data. Recently, efforts have been directed at developing a relatively small explosive system capable of driving metal impactor disks to velocities of 9 km/s.

Fast Shock Tube (FST) was proposed in Los Alamos National Laboratory [1–3]. FST is a new type of cylindrical convergent high explosive device which creates well behaved gases with energy levels far above those attainable with conventional high explosives. In its simplest form, the FST consists of a hollow cylinder of high explosive (HE) surrounding an inner cylinder of a propellant material such as polystyrene foam.

A plane-wave explosive lens detonates the HE cylinder. As the detonation propagates along the HE, a Mach disk is formed in the foam. The velocity of this shock equals or exceeds the HE detonation velocity. The gas expanding from this highly shocked foam accelerates the plate on the face of this system.

We proposed to investigate a new FST, which we call Fast Shock Tube with Explosive (FSTE). Instead of the foam core, we proposed to use a low-density explosive (LDE) with the highest content of light components (such as hydrogen and water) in detonation products. We also proposed to use a high-density explosive (HDE) in the first part of the core to prevent backward slipping of a part of the products and to increase compression of LDE.

The proposed FSTE configuration is shown in Fig. 1. In our works [4, 5], we investigated formation of Mach disks in nitromethane and its mixtures in HE cylinders and found that the best conditions for formation of Mach disk were obtained if the ratio of the normal detonation velocities was about 0.8 (1 — core, 2 — HE cylinder). This condition determines the choice of HE and HDE.

The experiments were carried out with HMX/TNT (64/36) at density 1.74 g/cm^3 as the HE, HMX/tungsten (50/50, 3.2 g/cm^3) as the HDE, and nitromethane as the LDE. An SFR–1 streak camera was used for visualization. A duralumin flyer plate was accelerated to 8 km/s, and a steel plate was accelerated to 7 km/s.

The FSTE can be used to investigate the behavior of matter under high dynamic pressures and the mechanism of hypervelocity penetration, as well as for tests of materials used for protecting against hypervelocity elements.
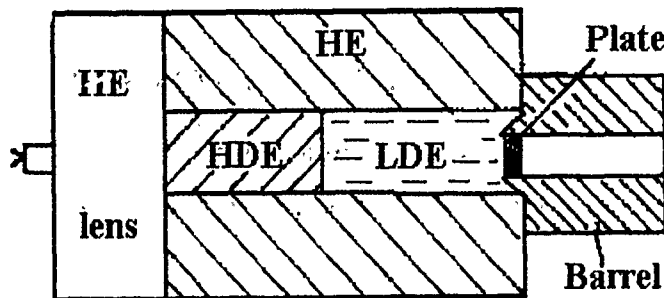
Figure 1: Fast shock tube with explosives (HE — high explosive, HDE — high density explosive, LDE — low density explosive).

References

[1] Steel R. P., Tan T.-H. *Shock Waves in Condensed Matter*, 1987.

[2] Meies J. K., Kerrisk J. F. *Shock Compression of Condensed Matter*, 1991.

[3] Marsh S. R., Tan T.-H. *ibid*.

[4] Gogulya M. F., Voskoboinikov I. M., Demchenko N. G. *Fizika Goreniya Vzriva*. 1981, **17**, 1, 153 (in Russian).

[5] Voskoboinikov I. M., Gogulya M. F., Dolgoborodov A. Yu. *ibid*, 1981, **17**, 5, 133 (in Russian).

SIMULATION OF COMBUSTION INITIATION IN A SHS SYSTEM UNDER HIGH VELOCITY IMPACT

V. A. Gorel'skii, S. A. Zelepugin

Tomsk Branch of the Institute of Structural Macrokinetics, Russian Academy of Sciences, 8 Lenin Square, GSP-18, Tomsk, 634050 Russia

Shock-wave treatment of SHS systems is very promising for producing modified materials. Of special interest are chemical reactions (synthesis) combined with shock-wave treatment. Their products may have improved properties due to the effect of high

pressure [1, 2]. The nature and characteristics of this process are of interest from both applied and fundamental points of view. The objective of this work is to develop a mathematical model for compaction processes and initiation of exothermic combustion reactions in the stoichiometric Ti-C powder system. Based on fundamental conservation laws, the mathematical models allow us to analyze combustion wave propagation and to predict the behavior of an SHS system under given conditions.

A model of porous medium was used in calculations; it is characterized with the possibility of voids formation and growth. The solid part W_c of the medium characterized by density ρ_c, and voids, occupying the volume W_*, in which the density is assumed to be zero, constitute the total medium volume W. The mean density of porous medium is related to the input parameters by $\rho = \rho_c W_c / W$. The porosity of medium is characterized by the specific volume of voids $V_T = W_* / (W\rho)$. The growth rate of specific volume of voids was determined to be as follows [3]

$$\dot{V}_T = -\text{sign}(P_c)K_4 \left[|P_c| - P_k \frac{V_1}{V_1 + V_T} \right] (V_2 + V_T), \tag{1}$$

where P_c is the pressure in the solid component, K_4, P_k, V_1, and V_2 are constants. The set of governing equations is

$$\dot{\rho} = -\rho \left(v_{,z} + u_{,r} + \frac{u}{r} \right), \tag{2}$$

$$\rho\dot{u} = S_{rr,r} + S_{rz,z} + \frac{S_{rr} - S_{\theta\theta}}{r} - P_{,r}, \tag{3}$$

$$\rho\dot{v} = S_{rz,r} + S_{zz,z} + \frac{S_{rz}}{r} - P_{,z}, \tag{4}$$

$$\rho\dot{E} = P\frac{\dot{\rho}}{\rho} + S_{zz}v_{,z} + S_{rr}u_{,r} + S_{\theta\theta}\frac{u}{r} + S_{rz}(u_{,z} + v_{,r}) + \rho\dot{Q}, \tag{5}$$

$$\dot{Q} = \Delta H \frac{d\eta}{dt}, \tag{6}$$

$$\frac{d\eta}{dt} = 0, \qquad T < T_m \quad \text{or} \quad \eta = 1, \tag{7}$$

$$\frac{d\eta}{dt} = K_0, \quad (T \geq T_m \text{ and } \eta < 1) \text{ or } (P > P_* \text{ and } \eta < 1), \tag{8}$$

where ρ is the density, u and v are the components of the particle velocity, r and z are the coordinates, t is time, P is the pressure, E is the specific internal energy, $\dot{Q}$ is the rate of heat release from chemical reactions, and ΔH is the specific heat release of Ti-C formation, η is the reacted fraction, K_0 is the rate constant having the dimension of time^{-1}. For the subsequent calculations, the averaged properties were defined as

$$\frac{1}{\rho} = V = \sum m_i V_i, \qquad E = \sum m_i E_i,$$

481

where m_i is the mass fraction of the i-th material. The equation of state was modified to include the evolution of the internal state variables, governed by a phenomenological kinetic equation for chemical reactions in inorganic powder mixtures. The heat release was included into the energy conservation equation, and contributed to pressure ries through the equation of state. We assumed that the average pressure in the solid mixture could be computed from the specific volume of the solid and the internal energy using the Mie–Gruneisen equation

$$
\begin{aligned}
P_c \;=\; & \rho_0 a^2 \mu + \rho_0 a^2 \left[1 - \frac{\gamma}{2} + 2(b-1) \right] \mu^2 + \\
& \rho_0 a^2 \left[2 \left(1 - \frac{\gamma}{2} \right)(b-1) + 3(b-1)^2 \right] \mu^3 + \gamma \rho E,
\end{aligned}
\tag{9}
$$

where $\mu = [V_0/(V - V_T)] - 1$, $V/\gamma = \sum m_i(V/\gamma)_i$, a and b were specified by the shock velocity – particle velocity relationship, $u_s = a + bu_p$ [4], as function of the reacted fraction in the mixture. The average pressure in a cross section of the porous mixture can now be related to the pressure in the solid components by the relationship $P = P_c \rho / \rho_c$, where P is the average pressure in the section and ρ is the average density of the porous mixture.

The behavior of the Ti–C system under impact loading was studied. A steel capsule with the Ti–C stoichiometric powder mixture impacted steel plate. The steel capsule has the outer diameter 12.5 mm and length 50 mm. The stoichiometric mixture was formed into a cylinder 5 mm in diameter and 40 mm long. The cylinder was inserted into the capsule. Fast reaction started if the mixture temperature attained 1944 K or the pressure exceeded 7 GPa [5]. Under favourable conditions, the maximum rate of heat release from chemical reactions was equal to 313 GJ·kg^{-1}s^{-1} up to complete conversion of the reactants. Figure 1 presents the configurations of the projectile and the target plate during interaction. As illustrated by Fig. 1, the deformation of the plate is comparable with that of the projectile for impact velocity 1500 m/s. The projectile penetrates the target by compressive yielding the material in its path. The effects of chemical reaction on the pressure and temperature histories are shown in Figs. 2 and 3. As illustrated by Fig. 2, the heat released is not large enough to cause observable changes in the pressure curve. The temperature of the mixture is observed to rise slowly after the initial jump resulting from the shock heating. The temperature rise is much greater when the reaction near the impact interface is observed. Calculated temperature was limited by 4140 K at maximum.

The curves also reflect the fact that, for the rate of heat release of 313 GJ·kg^{-1}s^{-1}, the process can be divided on several stages. At the first stages, the reaction proceeds because the mixture pressure exceeds 7 GPa (see Fig. 2). Afterwards, the reaction is resumed because the mixture temperature reached 1944 K.
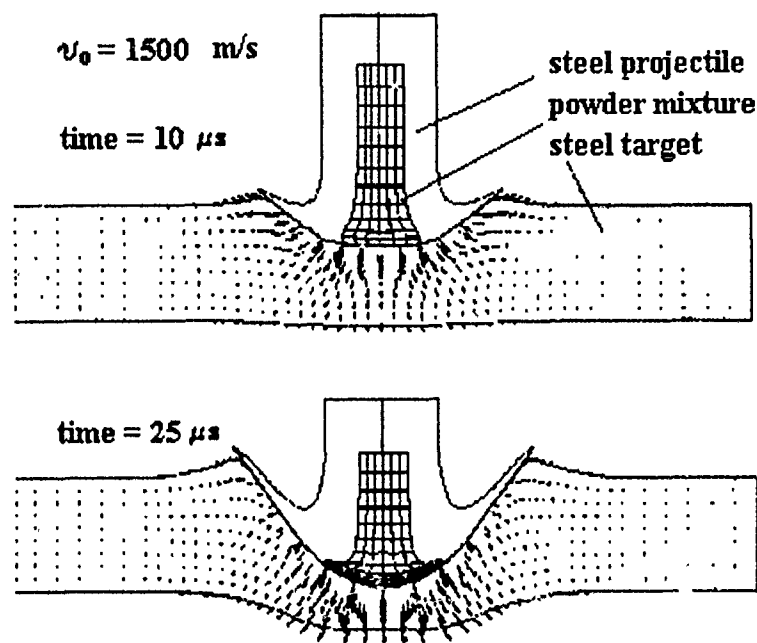
Figure 1: Penetration of a steel target by a projectile with powder reactants.
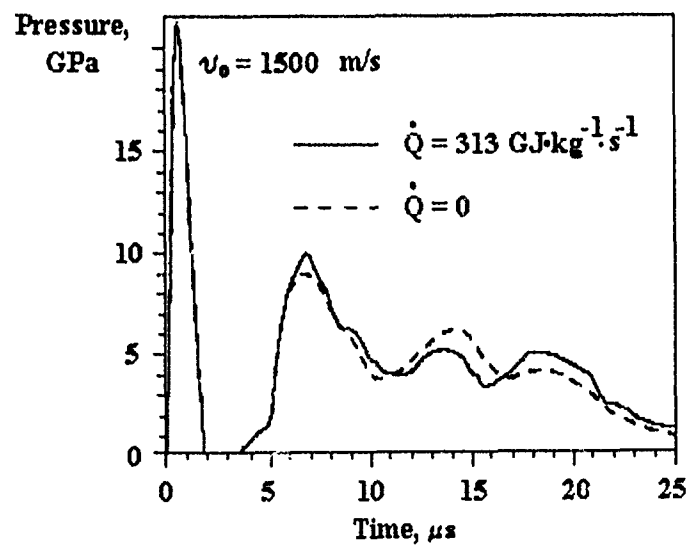
Figure 2: Calculated pressure histories near the contact surface in the powder mixture.
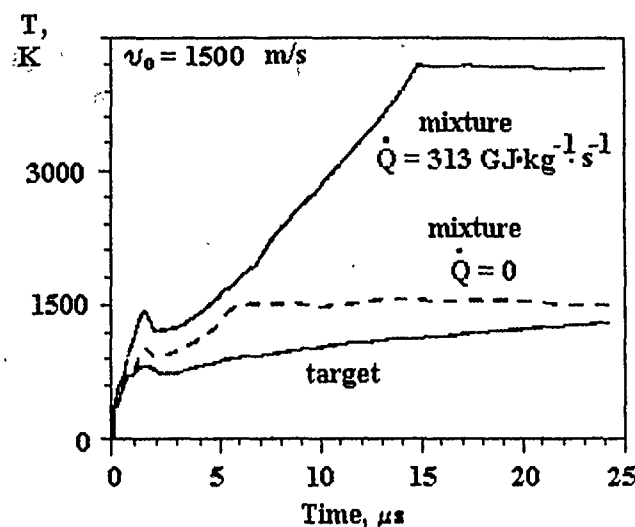
Figure 3: Calculated temperature histories near the contact surface in the target and in the reactants.

References

[1] Adadurov G. A., Borovinskaya I. P., Gordopolov Yu. A., Merzhanov A. G. *Inzhenerno-Fizicheskii Zhurnal*, 1992, **63**, 5, 538 (in Russian).

[2] Horie Yu., Kipp M. E. *J. Appl. Phys.*, 1988, **63**, 12, 5718.

[3] Gorel'skii V. A., Zelepugin S. A. *Khimicheskaya Fizika*, 1993, **12**, 8, 1140 (in Russian).

[4] Zel'dovich Ya. B., Raizer Yu. P. *Physics of Shock Waves.* Moscow, Nauka, 1966 (in Russian).

[5] Gryadunov A. N., Shteinberg A. S., Dobler E. A. *Dokl. Akad. Nauk SSSR*, 1991, **321**, 5, 1009 (in Russian).

THE CAPTURE OF PRODUCTS OF A GAS REACTION BY SHOCK WAVE

S. V. Kulikov

Institute of Chemical Physics in Chernogolovka, Chernogolovka, Russia

The Monte Carlo method was used to compute the zone of translational and chemical nonequilibrium in a planar steady shock wave at the Mach number of 5 for a mixture of four components A, B, C, and D. The cases were considered where only the components A and B were present in the upstream gas mixture at the ratio of molecular number densities equal to 100. With the rise of temperature in the front, the reactions $A + B \rightleftharpoons C + D$ begin, and products C and D are formed. The energy threshold of the forward and backward reactions were set at $14kT_1$ and $4kT_1$. (Here k is the Boltzmann constant, T_1 is the temperature of the upstream flow.)

The method of modeling with variable weighting factors was described in [1, 2]. The collision stage was simulated using the ballot-box scheme. Molecules of all sorts were assumed to be hard spheres of equal diameters without internal structure. It was assumed that a reaction occurred if the energy of the relative motion of colliding molecules along their center line at the moment of impact was higher than or equal to the reaction threshold. The computations were performed for the molecular mass ratios of components A, B, C, and D: (1) 4:16:19:1; (2) 10:10:19:1; (3) 16:1:15:2. In these cases, total thermodynamic equilibrium was reached behind the shock wave within the simulation region. The simulation region along the x axis was divided in 80 cells of the size $\Delta x = 0.3\lambda$. (Here λ is the mean free path in the undisturbed flow ahead of the wave.) The average number of the test particles of each component in the cell ahead of the wave was 20. The splitting time of the collision and displacement stages was $\Delta t = 0.0311\lambda/u$ where u is the most probable thermal velocity of lightest component particles ahead of the wave.

The results of calculations for the case (1) are shown in Fig. 1. Here, solid curves 1, 2, 3, and 4 are the profiles of the concentrations (n) of components A, B, C, and D, respectively. (The concentrations of components A and B were normalized with respect to their concentrations in the upstream flow. The concentrations of reaction products C and D were normalized with respect to their equilibrium concentrations in the downstream flow.) Dot-and-dash lines 5 and 6 are the profiles of the velocities V of components A and B. Broken curves 7 and 8 are the profiles of the velocities of components C and D, respectively. (All velocities were normalized with respect to u. The distance x along the stream was normalized with respect to λ). The results shown in the Fig. 1 are in many ways similar to those obtained for the cases (2) and (3). As one moves deeper into the shock wave, the concentration of the main component A increases due to the compression of the gas mixture in the wave front. The influence
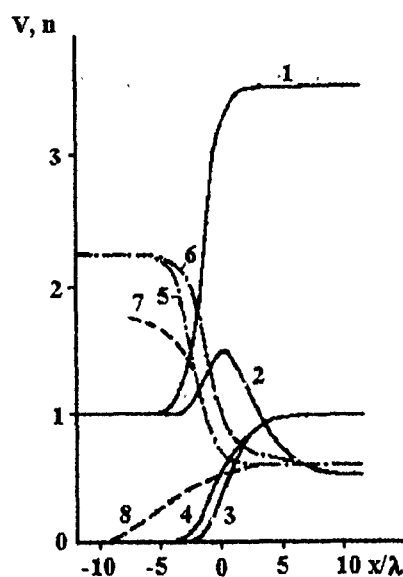
Figure 1: Profiles of concentrations and velocities of components A, B, C, and D for their molecular mass ratio 4:16:19:1.
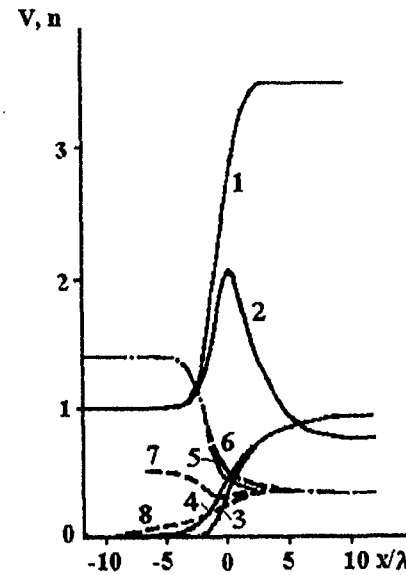
Figure 2: Profiles of concentrations and velocities of components A, B, C, and D for their molecular mass ratio 10:10:19:1.

of chemical reaction on the density of component A is negligible. Only small fraction on this component was consumed in the chemical reaction. However the concentration of the low-concentration additive B, was affected more substantially. It first increased due to compression and then decreased due to the fast reaction.

Figure 2 shows the results for case (2). The notation is the same as in Fig. 1. In this case, the separation of components A and B did not occur, but the results were similar to those in Fig. 1.

In all cases, the velocity of the newly formed component D differed appreciably from the velocity of the gas as a whole. As one moved upstream, this difference of velocities increased and the velocity of component D decreased in the coordinate system attached to the wave front. At the boundary of disappearance of product D, the velocity of this component reached the same value as the velocity of the wave. Thus, a little amount of the light reaction product D was carried by the front. So, the concentration behind the shock, where product D had the same velocity as that of shock wave, was about 0.0003–0.001%. The velocity of product C increased in all cases with the velocity of the mixture flow.

This behavior of velocity of light product D was not the case in previous simulations with the molecular mass ratios of components A, B, C, and D 1:10:8:3 [1, 2]. The computed effect could be caused by the collisions of the light reaction product with

the heavier component dominating in the flow ahead of the wave. The effect can significantly accelerate a complex chemical process in comparison with equilibrium downstream conditions. For example, this can be the case if a radical created in a chain reaction is placed far off ahead of the front and its velocity differs significantly from velocity of other reactants involved in the branching reaction of the chain process.

The predicted effect can occur for example, in a weakly ionized gas. Similar phenomenon was considered in [3], where the electrical conductivity of air was measured in a shock wave. In this case, the wave was formed by the motion of a copper piston. The authors of [3] explained the results obtained by assuming, that the shock-wave front captures copper ions released at the moment of wave formation.

References

[1] Genich A. P., Kulikov S. V., Manelis G. B., Chereshnev S. L. *Sov. Tech. Rev. B: Therm. Phys.*, 1992, **4**, 1, 1.

[2] Genich A. P., Kulikov S. V., Manelis G. B., Chereshnev S. L. *Proc. 17th Symp. (Int.) on RGD*, 1991, 175.

[3] Trofimov V. S., Trofimova G. P., Dremin A. N. *Fizika Goreniya Vzriva*, 1972, **8**, 490 (in Russian).

TWO-TEMPERATURE CHEMICAL KINETIC MODELS FOR STRONG SHOCK WAVES IN OPEN AIR

S. A. Losev, V. N. Makarov, M. Yu. Pogosbekian

Moscow State University, Moscow, Russia

The problem of description of chemically reacting systems in the absence of thermal equilibrium between the vibrational and translational degrees of freedom of the reacting molecules is analyzed with the view of the mathematical modeling of physicochemical processes occurring in strong shock waves in open air.

At high temperatures, when characteristic times of dissociation and vibrational relaxation are of the same order, the dissociation proceeds while vibrational relaxation is

not complete, so that the vibrational temperature T_ν is lower than the gas temperature T.

The relaxation time τ for O_2 has been measured up to $T = 10500$ K, and for N_2 up to 15500 K [1, 2]. The extrapolation of this data to higher temperatures was made using Schwarts–Slawsky–Herzfeld (SSH) theory which takes into account nonadiabatic collisions. It has been shown that, at $T > 25000$ K for O_2 and at $T > 40000$ K for N_2, the vibrational relaxation time τ increases and the "single-collision limit" is not attained.

The results of two-temperature dissociation rate constant measurements for O_2 (up to 10500 K) [1] and N_2 (up to 17000 K) [2] are extrapolated to higher temperatures on the basis of numerical solution of the collision problem for diatomic molecules in terms of classical mechanics and using analytical models of two-temperature dissociation, in particular the β-model:

$$K_d(T, T_\nu) = Z(T, T_\nu) \cdot K_d^o(T), \tag{1}$$

$$Z(T, T_\nu) = \frac{1 - \exp(-\Theta/T_\nu)}{1 - \exp(-\Theta/T)} \left[\exp\left(-E^*\right)\left(\frac{1}{T_\nu} - \frac{1}{T}\right)\right],$$

where $E^* = D - \beta T$, Θ is the characteristic vibrational temperature, D is the dissociation energy (in Kelvins), $K_d^o(T)$ is the equilibrium dissociation rate constant.

The results of experimental investigation of N_2 and O_2 dissociation in shock waves under conditions of vibrational nonequilibrium are well described by the β-model with the parameter being constant ($\beta = 1.5$ for O_2, $\beta = 3$ for N_2). For temperatures higher than those in experiments, it is necessary to take into account the dependence of β on T. For this purpose, the Gordiets model is used:

$$\beta(T) = \frac{3}{2}\frac{D}{\gamma_0 T} \ln\left(\frac{4D}{T}\right), \qquad \gamma_0 = 0.32\frac{\Theta}{\alpha}\left(\frac{m_A}{T}\right)^{1/2}, \tag{2}$$

where m_A is the mass of one atom in the dissociating homonuclear molecule A_2 (in atomic mass units), α is the inverse interaction radius in the exponential repulsive potential for the A_2–A_2 system, γ_0 is the adiabatic parameter (Massey parameter). The effect of molecular rotation of the dissociation rate constant at high temperature is taken into account by substantially reducing the dissociation energy due to the centrifugal effect, so that $D = D(T)$.

A simulation of one-dimensional inviscid flow of multicomponent gas mixture behind a plane shock wave front was carried out. The complete set of chemical and vibrational kinetics equations with expression (1) for $K_d(T, T_\nu)$ and expression (2) for parameter β were used. The calculated value of T_ν under quasi-stationary conditions is close to that obtained experimentally.

Exchange chemical reactions with vibrationally nonequilibrium molecules (such as $N_2(\nu) + O \to NO + N$) are very important for high-temperature air. The rate constants of these reactions in thermal nonequilibrium are estimated in two ways:

- in terms of the Macheret model taking into account the change in the reaction threshold value depending on the N_2 vibrational energy;

- from an accurate solution of the appropriate dynamical model by the method of classical trajectories.

In simulating the gas flow behind shock wave front, it was assumed that the vibrational energy changes not only in VV- and VT-exchange processes, but also in dissociation, recombination and exchange chemical reactions. The vibrational energy e^*, lost through dissociation, recombination and exchange chemical reactions, is

$$e^* = \frac{1}{\Theta} \sum_\nu E_\nu P_\nu, \qquad P_\nu = \frac{K_\nu \exp(-E_\nu/T_\nu)}{\sum_\nu K_\nu \exp(-E_\nu/T_\nu)},$$

where E_ν is the vibrational energy corresponding to the vibrational number ν, P_ν is the reaction probability for molecules on the ν-th level.

In the two-temperature approximation with the reaction rate constant represented as $K(T, T_\nu) = Z(T, T_\nu) \cdot K^\circ(T)$, it is assumed that

$$\frac{K^\circ_f(T)}{K^\circ_r(T)} = k_{eq}(T),$$

where $K^\circ_f(T)$ and $K^\circ_r(T)$ are the equilibrium rate constants of the forward (f) and reverse (r) reactions at $T_\nu = T$ and $k_{eq}(T)$ is the equilibrium constant for a given reaction in the thermodynamic equilibrium state.

In addition to the reactions between neutral particles, the model of the processes in strong shock waves takes into account the associative ionization, electron impact ionization, charge exchange and ion–molecular reaction. For collisions with electrons, the rate constants are calculated by averaging the known cross sections of these reactions over the Maxwellian electron energy distribution.

The results obtained using the adopted kinetics model are illustrated. As the most typical example, the shock wave propagation in the Earth atmosphere at a velocity of $V_s = 9$ km/s and a height of $H = 70$ km was considered.

Thus, the mechanism of the processes in air at temperatures up to 90000 K is presented. This mechanism includes 64 reactions.

By solving the problem with the definite goal function, it is possible to determine the key reactions and reduce the number of reactions necessary to calculate the goal function within the desirable accuracy. For example, the translational temperature is given within 10% by the reduced mechanism including the following reactions:

$$O_2 + M \rightarrow 2O + M \qquad (M = O, O_2)$$
$$NO + M \rightarrow N + O + M \quad (M = N, O, N_2)$$
$$O + N_2 \rightarrow N + NO$$
$$N + e \rightarrow N^+ + 2e$$
$$O + e \rightarrow O^+ + 2e$$
$$N + N \rightleftarrows N_2^+ + e$$
$$O + O \rightarrow O_2^+ + e$$
$$O^+ + N \rightarrow N^+ + O$$
$$NO + N^+ \rightarrow N_2^+ + O$$
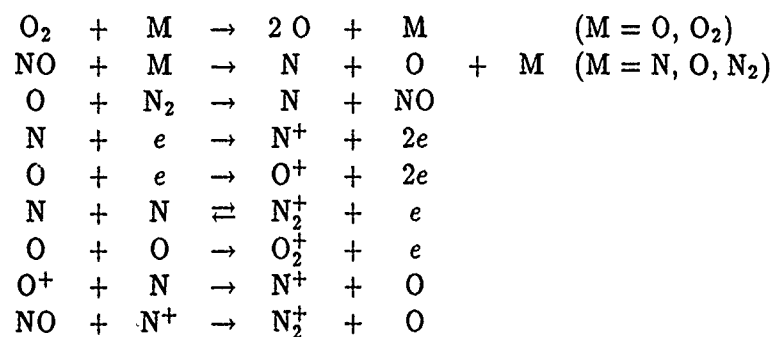
References

[1] Losev S. A., Shatalov O. P. *Khimiya Vysokikh Energii*, 1970, **4**, 3, 263 (in Russian).

[2] Yalovik M. S., Losev S. A. *Sci. Proc. of Institute of Mechanics, Moscow State Univ.*, 1972, **18**, 4 (in Russian).

Autho. Index

Contents

SESSION 7. Combustion and Detonation Analogies   430

If you want
to prepare your manuscript professionally

CALL US

Russian Section of the Combustion Institute
Semenov Institute of Chemical Physics
Kosigin Str., 4, Moscow
117977 RUSSIA
Phone: (007–095) 939–7228, –7253
Fax: (007–095) 938–2156
e-mail: kinet@glas.apc.org